AERO RESEARCH AVENUE

DISCOVERING THE WORLD

JUNE 2023

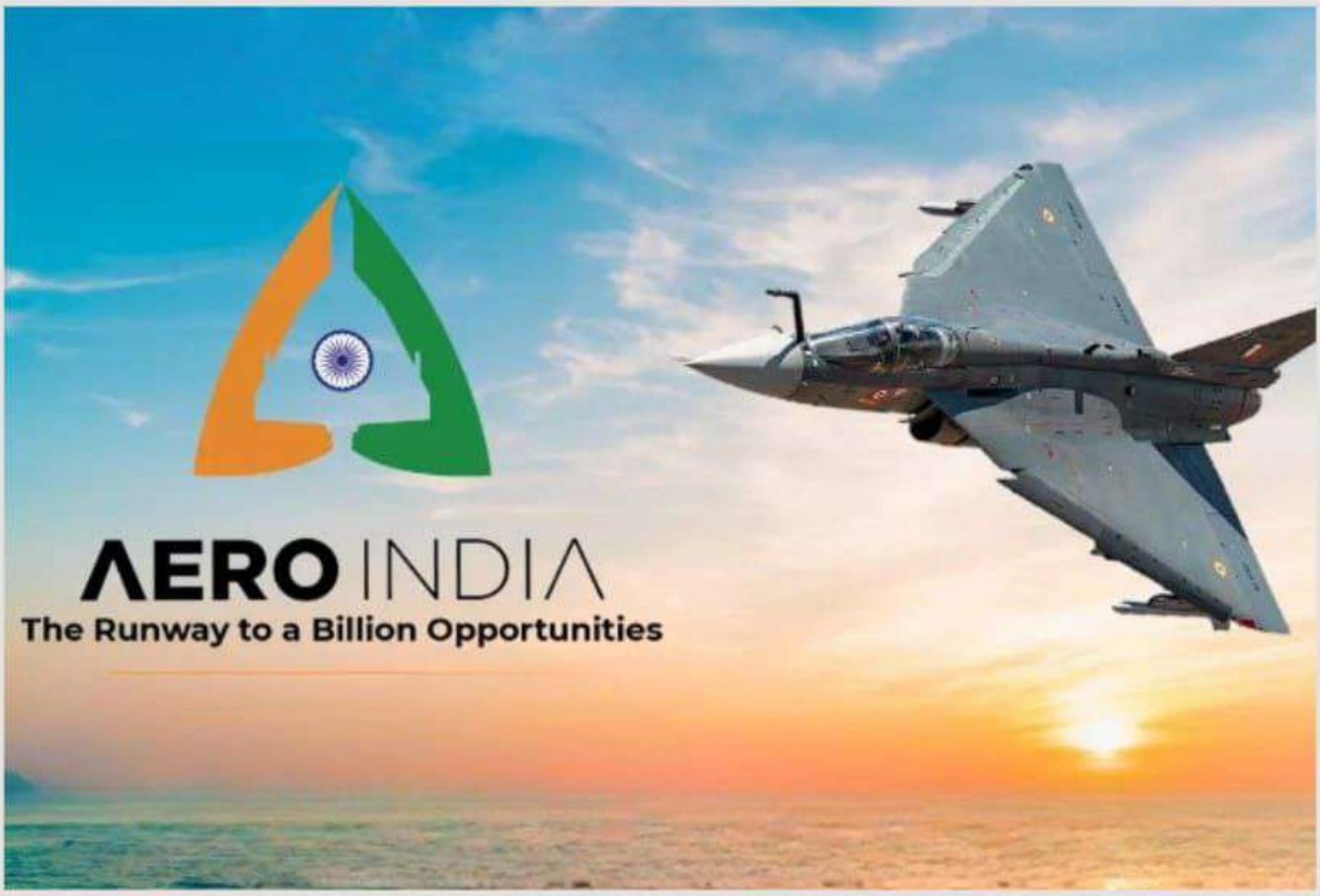

STUDENT CO-ORDINATOR'S
SHREE LAYA
SURESH

FACULTY CO-ORDINATOR
MR A SAI KUMAR

MLR INSTITUTE OF TECHNLOGY

DEPARTMENT OF AERONAUTICAL ENGINEERING

"AERO RESEARCH AVENUE"

2023

MARRI LAXMAN REDDY
GROUP OF INSTITUTIONS
MLR
Institute of Technology

Institute Vision:

Promote academic excellence, research, Innovation, and entrepreneurial skills to produce graduates with human values and leadership qualities to serve the nation

Institute Mission:

Provide student-centric education and training on cutting-edge technologies to make the students globally competitive and socially responsible citizens.

Create an environment to strengthen the research, innovation and entrepreneurship to solve societal problems.

Vision of the Department:

To be a centre of excellence in Aeronautical engineering with emphasis on Research & Innovation to serve the needs of industry with human values to build strong nation. The department's vision is derived from the institute vision and it vouches to help the institute in fulfilling its vision by becoming a center of excellence in Aeronautical Engineering.

Mission of the Department:

The mission statements are the action statements; the department intends to implement in fulfilling its vision. The key components are quality oriented technical education, multidisciplinary skills and Research & Innovation activities with human values.

M1. Provide quality oriented education, well-grounded in the fundamental principles of Aeronautical Engineering.

M2. Consistently produce top quality Aeronautical engineers with core and multidisciplinary skills, who can become ace leaders and successful entrepreneurs with human values.

M3. Continuously strive for knowledge; undertake Research and Innovation that will contribute to the industrial development of the nation.

RESEARCH ARTICLE | MAY 22 2023

Wear characterization of AA2219 titanium carbide reinforced composites

J. Edwin Raja Dhas ✉; K. Anton Savio Lewise; M. Satyanarayana Gupta

AIP Conference Proceedings 2492, 040057 (2023)
https://doi.org/10.1063/5.0113707

Wear Characterization of AA2219 Titanium Carbide Reinforced Composites

J. Edwin Raja Dhas[1,a)], K. Anton Savio Lewise [2,b)], M Satyanarayana Gupta [3,c)]

[1]*Department of Automobile Engineering, Noorul Islam Centre for Higher Education, Kumaracoil-629180, India*
[2]*Department of Aeronautical Engineering, Noorul Islam Centre for Higher Education, Kumaracoil-629180, India*
[3]*Department of Aeronautical Engineering, MLR Institute of Technology, Hyderabad, India.*

[a)] Corresponding Author: edwinrajadhas@rediffmail.com
[b)]kaslewise@gmail.com
[c)] msngupta.m@gmail.com

Abstract. In the modern world the requirement of Metal Matrix Composites is high because of its high strength to weight ratio, thermal and wear resistance properties. Production of composites by economically and efficiently is highly challenging. Titanium carbide is one of the hardest and wear resistant metals which can be used as a reinforcement metal for the manufacturing of Aluminum metal matrix composite. Composites with titanium carbide as reinforcement are likely to overcome the deformation and wear problems arise in automobile field. This work aims to produce composite by mixing aluminum and titanium carbide using modified stir casting method. Design of experiments by response surface methodology was used to find the effect of % of (Titanium Carbide) TiC_p at various sliding velocity and loads in the wear behavior of the specimen. The effect of TiC_P on AA2219 was investigated in terms of mechanical properties and confirmed by SEM and EDAX analyses. From the investigations it was found that strength of the developed AA2219 composite was increased by the addition of TiC_p but increase of TiCp increases the wear rate. It was found that the wear rate of the material increases with the increase of normal load, and sliding velocity. Hence reinforced aluminum matrix composite is recommended for fabrication of secondary components for machine parts which is used in stone crushing, grinding and scrap industries.

Keywords- Metal Matrix Composite; Modified Stir Casting; Wear Study.

INTRODUCTION

The challenge and need for producing Metal Matrix Composites for use in underlying and useful applications including automobile, aerospace industries, defense etc. have fundamentally expanded in the new occasions. There is a need to produce composites with simple manufacturing and better mechanical properties overcome the limitations of present aluminum-based composites by modifying the experiment procedures in its design. This leads to attain improvements performance, reliability and overall efficiency by improving the strength-to-weight ratio. Because of this reason, the materials of low density, high stiffness and high tensile strength is needed.

MMC can be classified into two one is matrix component, which is continuous phase such as aluminum, magnesium and the another one is discontinuous phase such as fibers, whiskers or particles called as reinforcement. The aim of producing metal matrix composites is to obtain the superior character of metal and particulates. Generally, matrix binds the particles together and particles are used to obtain better mechanical properties.

Normally, Aluminium Matrix Composites can be used more than other materials due to its properties like high wear resistance, high strength to weight ratio and better thermal properties. There are various methods of preparation of composites [1] Among this stir casting is a liquid metallurgy process having various advantages [2]. Utilizing various stirring times and stirring speeds in stir casting process aluminium alloy–silicon carbide metal matrix composite material was successfully synthesized [3]. Aluminum Alloy (6063) is cast with alumina by the stir casting

Advancements in Aeromechanical Materials for Manufacturing: ICAAMM-2021
AIP Conf. Proc. 2492, 040057-1–040057-10; https://doi.org/10.1063/5.0113707
Published by AIP Publishing. 978-0-7354-4438-6/$30.00

technique. Tensile strength, hardness value, impact strength shows that the developed composite is superior to base Al alloy 6063 [4]. The tribological, mechanical, metallurgical properties of the prepared composite by mixing Al alloy with SiC, Al_2O_3, and graphite particles using stir casting process exhibit better results than base matrix Al alloy [5]. It was observed that the mixing of frit particles in Al6061 alloy gives better tensile strength, compressive strength and hardness properties comparing with unreinforced matrix [6]. Increase in reinforcement of Al_2O_3 particulate Al6061with significantly increases the mechanical properties of the base metal [7]. Reinforcing of Aluminum based composites with particle like SiC improves mechanical properties [8]. A trial was taken to produce aluminium matrix silicon carbide particulate with an aim to develop uniform mixing of particulate and improvements in mechanical properties are achieved by the selection of various parameters of the reinforced material [9]. The tensile strength of Aluminum alloy matrix with titanium carbide particulate composite was increased [10].

Even though MMC are manufactured using stir casting method it is necessary to validate the developed composite when subjected to fluctuating loads. Hence the wear nature of the material should be addressed to meet the challenge of the developed composite during mechanical or automotive applications. The wear rate of AA6061 Titanium Carbide particulate composite increases as the percentage of titanium carbide increases [11]. In case of AA6061 alloy with metal coated carbon fibers and silicon carbide particles it was noticed that the wear resistance increases by the addition of metal coated fibers [12]. Hybrid combinations of granite dust with Al6061 alloy delivered better hardness, higher tensile strength and significantly increases wear resistance [13]. The behavior of TiC_p on dry sliding wear behavior and microstructure shows that the TiC_p affect the sliding wear behavior of the AA6082/TiC_p AMCs [14]. Investigation has been done on Al6082 alloy composites developed by conventional stir casting method for dry sliding behavior. Results reflected that the sliding distance is the most persuasive factor and load is the factor which affects the wear [15]. The wear characteristics of the reinforcement of ultra-high molecular weight polyethylene with talc particles shows that the rate of wear is minimized by the inclusion of talc [16].

AA2219 is widely used in aerospace especially in fuel tanks for storing liquid cryogenic. AA2219 has improved mechanical properties such as high strength, less weight, good weld ability and better cryogenic character [17-19]. This work aims to prepare AA2219 alloy reinforced with TiC_p and do its wear characterization.

FABRICATION AND WEAR CHARACTERISATION

This work plans to do the manufacturing of an Aluminium alloy based composite material and to test its wear properties. Different composition of TiC_p reinforced with AA2219 alloy using modified stir casting machine. The mechanical property of the casting was examined using tensile test. The wear property of the cast composite was analyzed and validated using mathematical model.

Experimental Setup

The machine used to cast AA2219 alloy with TiC_p was known as modified stir casting machine was shown in Fig.1. This has the advantages of proper mixing and metal pouring than the conventional stir casting setup. The machine has crucible, stirrer and holder for TiC_p. Heating was done electrically. For the MMC AA2219 alloy was selected as matrix and TiC_p as the reinforcement particle. AA2219 was kept in the crucible and made it to melt to the liquid state by keeping the temperature of the crucible as 600^0C.

FIGURE 1. Modified stir casting machine.

The angle of the stirrer blade was of 45degree and the set RPM is 60. The stirrer blade was introduced into the molten AA2219. TiC_p of 3% to 7% is introduced into the molten AA2219 along the side of the stirrer. 1% of magnesium power was inserted in to the molten pool to raise the wettability. Argon gas protects the molten pool by preventing the reaction of magnesium with the atmosphere. The well stirred mixture of molten AA2219 alloy and TiC_p was vacated into the die with complete caution and allowed to cool at the room temperature for 30 minutes. After cooling the specimens are fragmented out from the die of size 100 mm x50 mm x 50 mm.

The casted specimens of various percentage of TiCp are tested for investigating their properties. The tensile test specimens were cut by a milling machine as per the ASTM E8 standard. The specimen was subjected to tensile test and wear test from which the ability of the composite material was determined in various load conditions. As the TiCp % increases the specimens' tensile strength also increases.

Wear Characterization

The design of experiments by response surface methodology was used to obtain the effect of % of TiC_p at various sliding velocity and loads in the wear behavior of the specimen. Box–Behnken type was used. There are two methods of RSM one is Box Behnken type and another one is concrete type. Minimum 15 samples are required to complete the experiments in Box Behnken type. But, minimum 20 samples are required for concrete type. Since less number of samples is required in Box Behnken type this method is selected. The experiments are decided as per the response surface methodology and plotted in the table.1.

FIGURE 2. Modified stir casting machine.

The disc arrangement and pin is used for testing the wear is shown in Fig.2.The disc material is En-32 having a hardness value of 65HRC.The cylindrical pins were prepared from the casting having 50mm length and 6mm diameter. The pins were held in the pin holder to make contact with the rotating disc of 100 mm diameter.

The LVDT transducer of accuracy 1.0 μm was used to find the wearing of the pin. The removed loose wear particles were weighed with an accuracy having 0.0001g in a balance. The volumetric wear loss was calculated from the wear particles of the pin Wear rates reflect wear mass loss, volume loss or linear dimension change under applied normal force and sliding distance. The observations from wear test are shown in table.1. Three trails were conducted to find the average value for volumetric wear loss. By the formula $W=V/\rho D$ the wear rate was find out. Where ρ is the density of the material V the weight loss and D is the material sliding distance.

The specific wear rate was calculated by the formula w=W/L. where L was the applied load. The density of the composite for 3% to 7% varies from 2800 Kg/m3 to 3000 Kg/m3 and the sliding distance is kept constant as 1m. The composite wear pattern can be observed through scanning electron microscope after wear test.

The mathematical modeling of AA2219 TiCp composite for wear rate was analyzed using MINITAB software. The parameters selected were normal load, percentage of TiCP and sliding velocity. Three levels were used. The coefficients of the mathematical model were obtained from table 1. The sufficiency of the regression model was verified by estimating F ratio and 95% trust level and was contrasted and the comparing standard classified value. The model was observed to be satisfactory. The following equation indicates the developed regression model with significant coefficients.

The wear rate function is shown as

$$D = -100.473+A*6.23382+B*2.31190+C*59.0765+A*A*0.0679167-B*B*0.0103271-C*C*9.20528+A*B*0.147563+A*C*0.255278-B*C*0.133667$$

Where D is the average of responses and A, B, C are the response coefficients that depend on respective main and interaction effects of parameters as in the above equation.

% TiC_p

B- Normal Load in N

C- Sliding Velocity in m/sec

D- Wear Rate in mm^3/m

RESULTS & DISCUSSION

The effect of TiCP on AA2219 was investigated regarding mechanical properties and conformed by micro structural studies. The wear particles were measured after every test. The minimum and higher wear rate was observed at various conditions.

The Fig 3 shows the SEM image of the composite having the percentage 7% of TiCp. Three images were shown to identify the presence of TiCp at various points of the sample.

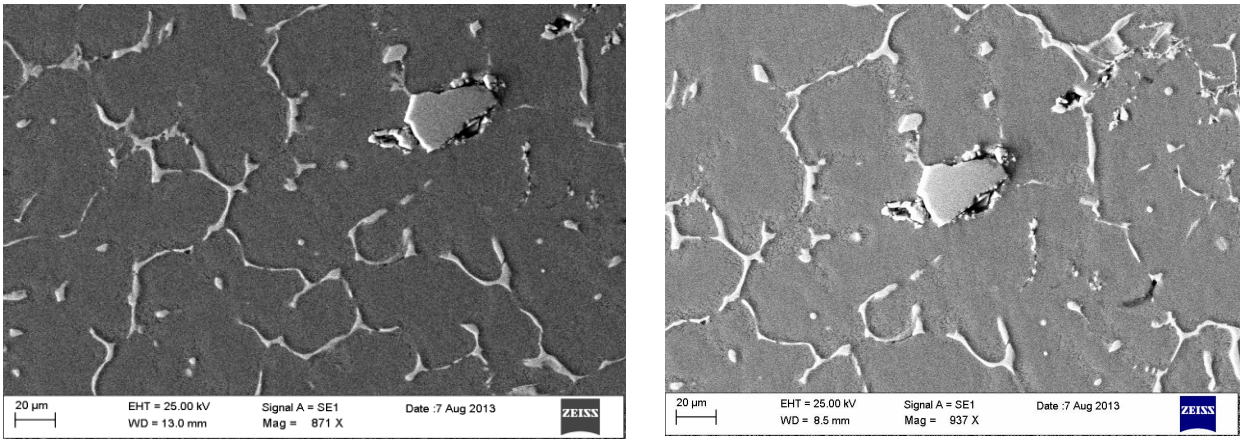

(a) (b)

FIGURE 3. SEM model for AA2217+7% TiCp composite

This leads to understand the uniform mixing of TiCp in the composite. Ordinary Metallographic strategies utilizing various grades of emery papers and last cleaning with one-micron diamond paste. Etching with Keller's Reagent to describe the structure and the observations were included under Scanning electron microscope.

The formation of AA2219 + TiCp composite was confirmed through EDX test which shows the percentage of aluminium matrix and TiCp for spectrum 1. The composition also given in the Table 2. The fig.4 indicates the spectrum1. The EDX graph is shown in Fig. 5. This points shows the presence of TiCp. Also it was conformed that no foreign particles were included in the composite.

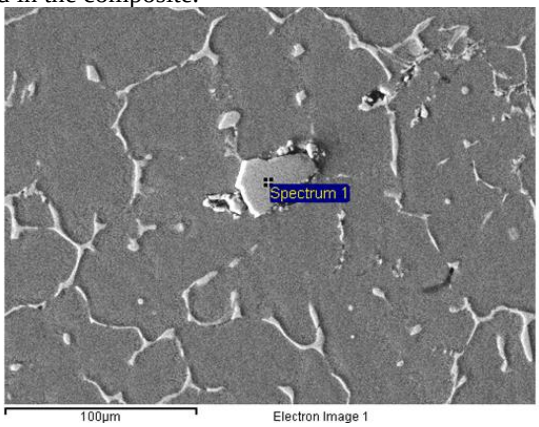

FIGURE 4. Spectrum 1

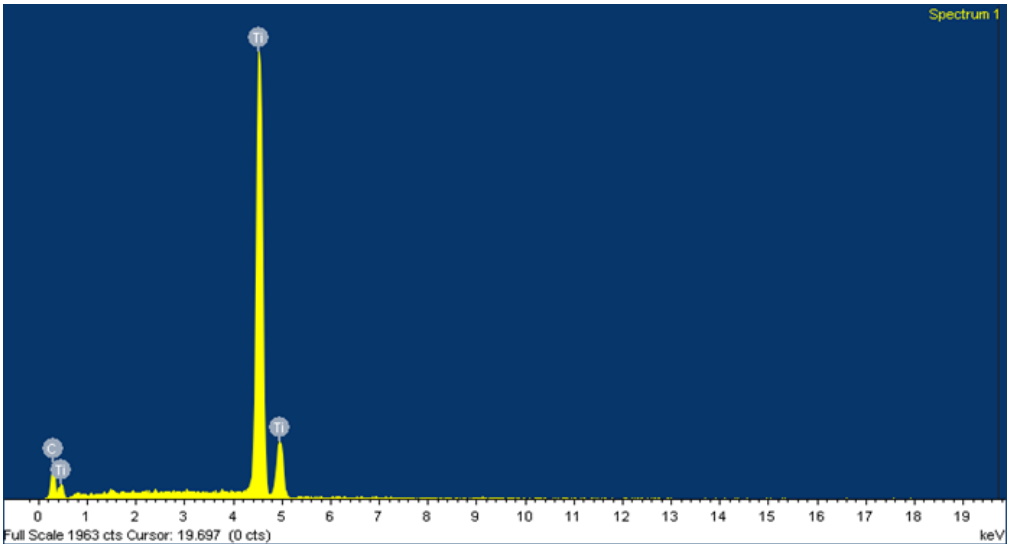

FIGURE 5. EDX for Spectrum 1

Experimentation was done to know the effect of %TiCp on tensile strength. The relationship of % TiCp and average tensile strength was shown in Fig. 6. It was known that the tensile strength of the composite increases with the increase of % in TiCp because TiCp is providing the resistance to plastic deformation. At 6 and 7 percentages of TiCp maximum tensile strength was observed.

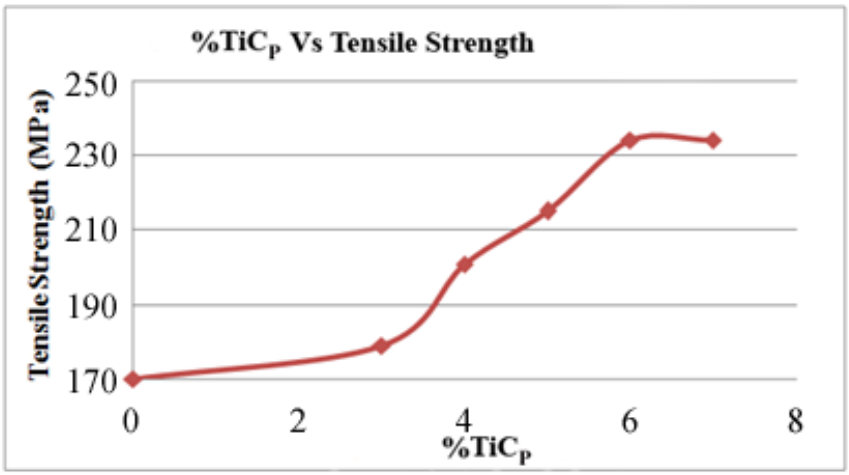

FIGURE 6. Tensile strength Vs % TiCp

Figure.7 indicated the effect of %TiCp on wear rate. It can be observed that the increment of % TiCp, which influences that the increment of wear rate. This may be due to the effect of the hard particles of TiC_p. The particles are hard and the elasticity of the particles also less this may lead to more wear.

The effect of normal load on wear rate which is indicated in Fig.8. The wear rate increases as the normal load increases. This was due to the increase of friction by the increase of the normal load. As the normal load increases the coefficient of friction increases this makes the wear rate to be higher. The particle size also increases at higher loads. So the normal load has more effect on the wear rate. The loads selected were 10N, 30N, 50N.When the load increases the size of the wear debris increases. So the wear rate increases at higher loads.

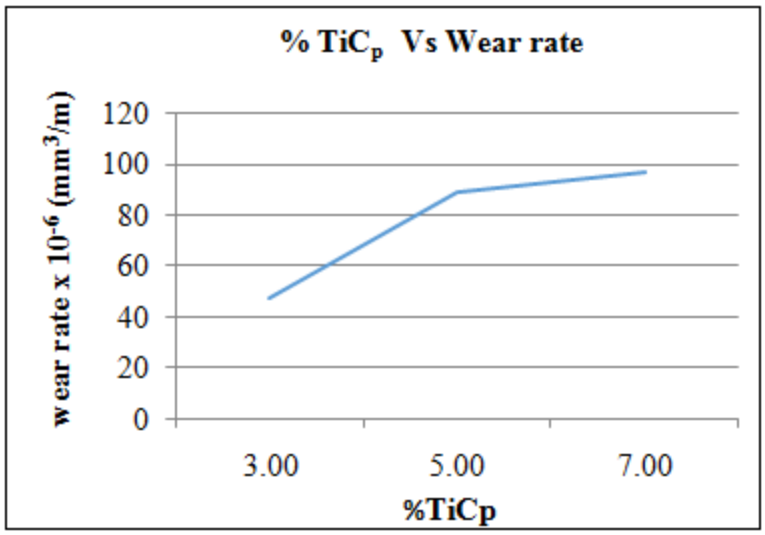

FIGURE 7. Wear rate Vs % TiCp

The effect of velocity on wear rate was shown in Fig.9. The increment of sliding velocity which slightly increases the wear rate. This may be due to plastic deformation on the surface and the formation of high temperature because of high velocity. At higher velocity the temperature increases due to this thermal softening takes place and this leads to more wear. The sliding velocity selected were 2 m/s, 2.5 m/s,4 m/s.

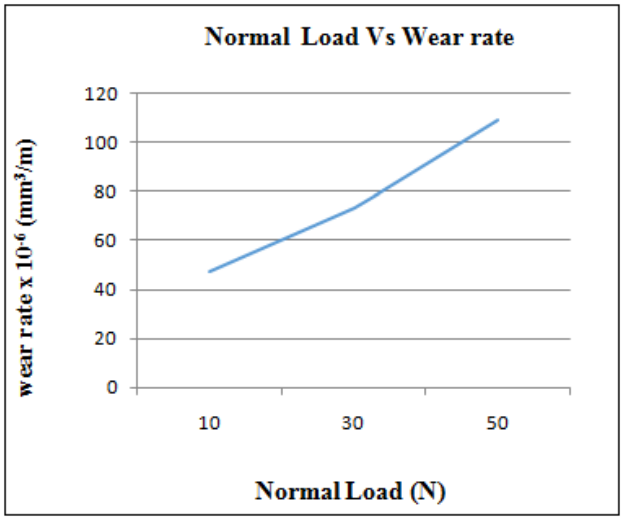

FIGURE 8. Normal Load Vs Wear Rate

The SEM images of the developed composite can be observed through Scanning Electron Microscope. Standard colour metallographic technique was used to study the sem image of wear specimen. The sem image of 3% TiCp shows that the sliding wear occurs by plastic deformation. Fig.10 and Fig.11 shows that in 3% TiCp the scratches are relatively lesser. In the sliding direction scratches and parallel grooves were observed.

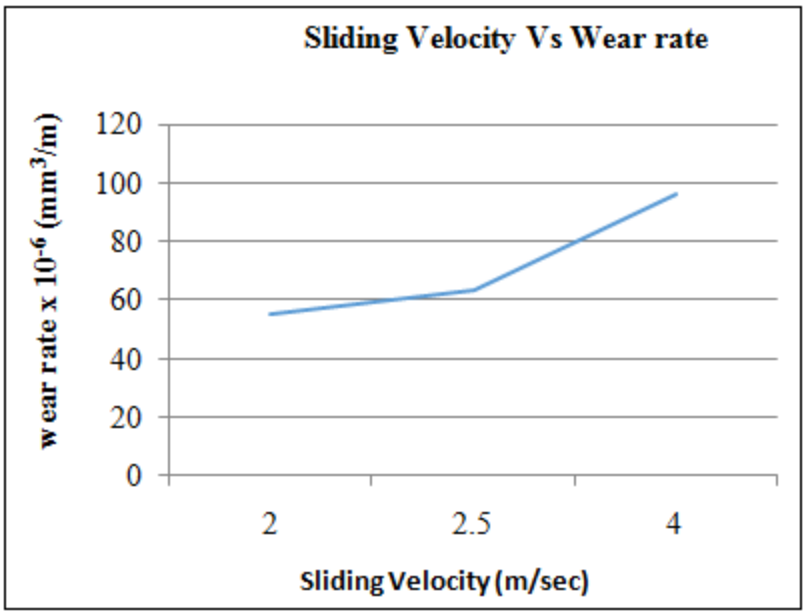

FIGURE 9. Sliding Velocity Vs Wear Rate

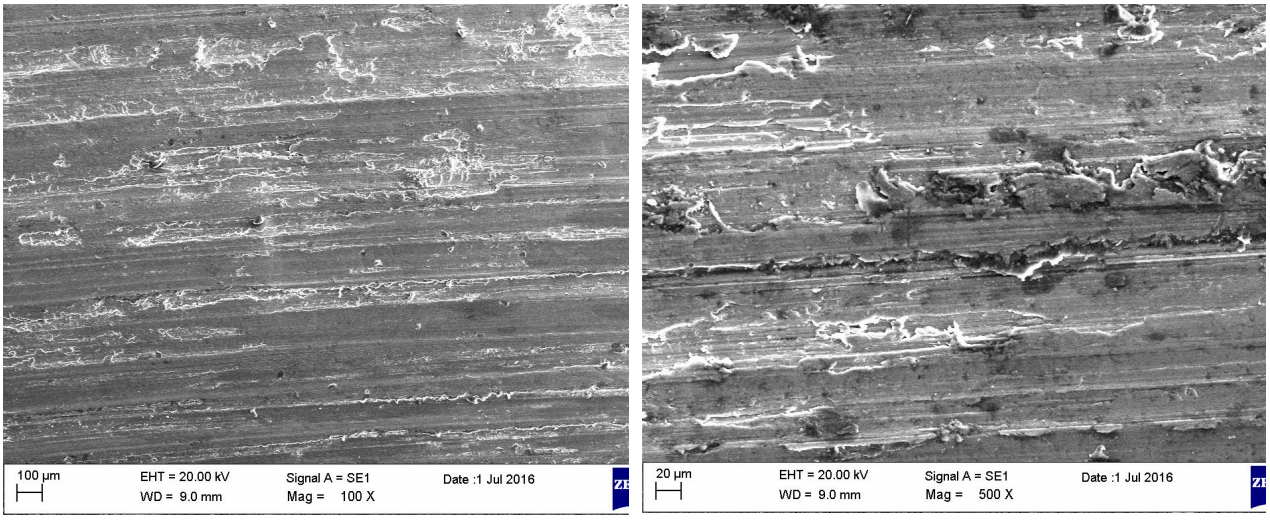

(a) (b)

FIGURE 10. Specimen's SEM image after wear test (3% TiCp) at (a) 100X and (b) 500X

The SEM images providing magnification up to 100X and 500X allowing submicron scale feature to be seen rapid, high-resolution imaging with identification of elements present. Characterization of particulates and defects. SEM provides detailed high resolution images of the sample by rastering a focused electron beam across the surface and detecting secondary or backscattered electron signal. The SEM is also capable of performing analyses of selected point location on the sample.

Some of the microstructural images shows that the titanium carbide percentage is increases, and reducing the porosity level in various zone which results in less casting defects.

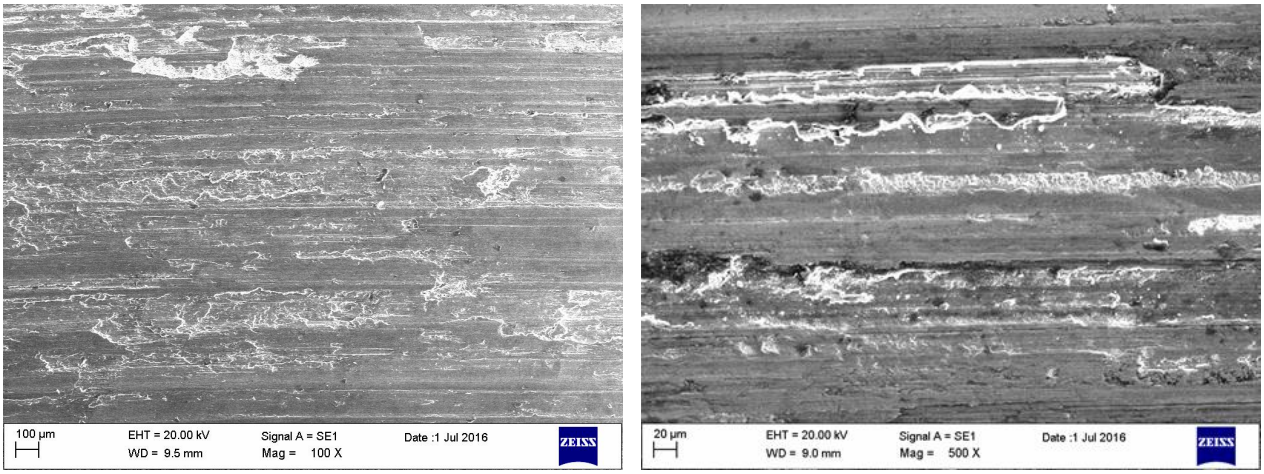

(a) (b)

FIGURE 11. Specimen's SEM image after wear test (7% TiCp) in (a) 100X, (b)500X

TABLE 1. Observations from Wear study

Sl.No	A % TiC_p	B Normal Load (N)	C Sliding Velocity (m/sec)	Average Weight Loss (mg)	D wear rate x 10^{-6} (mm^3/m)	Specific Wear Rate x 10^{-6} (mm^3/mN)
1	3	10	2.5	0.132009	47.146	4.714
2	7	10	2.5	0.189079	63.026	6 .302
3	3	50	2.5	0.237866	84.952	1.699
4	7	50	2.5	0.326787	108.900	2.178
5	3	30	2.0	0.275787	98.492	3.287
6	7	30	2.0	0.291331	97.110	3.237
7	3	30	4.0	0.205103	73.251	2.441
8	7	30	4.0	0.289282	96.427	3.214
9	5	10	2.0	0.159434	54.977	5.497
10	5	50	2.0	0.256354	88.379	1.767
11	5	10	4.0	0.192141	66.255	6.625
12	5	50	4.0	0.26088	89.958	1.799
13	5	30	2.5	0.146941	50.669	1.688
14	5	30	2.5	0.276787	95.443	3.181
15	5	30	2.5	0.200636	69.184	2.306

TABLE 2. Weight percentage for spectrum 1

Element	Weight%	Atomic%
C K	20.74	51.06
Ti K	79.26	48.94
Totals	100.00	

CONCLUSIONS

Modified stir casting process is probably the best interaction to create the specimen with low cost and less wastages and the process requires less time to mold the specimen when comparing to other processes. The castings

produced by modified stir casting method were found to be defects free by the addition of TiCp in the aluminum alloy the tensile strength increases. But it decreases on the earlier studies of composites with AA2219 [21]. So Aluminium is a light weight material and it is reinforced by TiCp to make it more strong and hard. Through wear test it is concluded that

- The strength of the developed AA2219 composite is increased by the addition of TiC_p but the increases in the % TiC_p increases the wear rate.
- The increment of normal load, sliding velocity and the % TiCp which influences the increment of wear rate.
- So depending on the application to meet the required tensile strength and wear rate the suitable percentage of TiC_p in AA2219 alloy composite can be selected.

REFERENCES

1. Suraya, S., Sulaiman, S., Nur Najmiyah, J., & Nor Imrah, Y, *Studies on Tensile Properties of Titanium Carbide (TiC) Particulates Composites* (Advanced Materials Research, 2014) Vol. 903, pp. 151-156. https://doi.org/10.4028/www.scientific.net/AMR.903.151.
2. Siddesh Kumar N.G, Ravindranath V.M, Shiva Shankar G. S, *Mechanical and Wear Behavior of Aluminum Metal Matrix Hybrid Composites*. (Procedia Materials Science, 2014) Vol. 5, pp. 908-917. https://doi.org/10.1016/j.mspro.2014.07.378.
3. Balasivanandha Prabu S, Karunamoorthy L, Kathiresan S, Mohan B, *Influence of Stirring Speed and Stirring Time on Distribution of Particles in Cast Metal Matrix Composite* (Journal of Materials Processing Technology, 2006) Vol. 171, pp. 268-273. https://doi.org/10.1016/j.jmatprotec.2005.06.071.
4. Ajaya K. Singh and L. Kumar and M. Chaudhary and Omar Narayan and PallavSharma and P. Singh and Bhaskar Chandra Kandpal and Som Ashutosh, *Manufacturing of AMMCs using Stir Casting Process and Testing its Mechanical Properties*. (International Journal of Advanced Engineering and Technology, 2013), iv(iii), pp. 26-29.
5. Rajeshkumar G. Bhandare, Parshuram M. Sonawane, *Preparation of Aluminium Matrix Composite by Using Stir Casting Method and its Characterization* (International Journal of Current Engineering and Technology, 2014) sp. 3, pp. 148-155.
6. Ramesh D, Swamy R.P, Chandrashekar T.k, *Effect of Weight Percentage on Mechanical Properties of Frit Particulate Reinforced Al6061 Composite* (Journal of Engineering and Applied Sciences, 2010) 5(1), pp. 32-36**.**
7. Bharath V, Mahadev Nagaral, Auradi.V, *Preparation, Characterization and Mechanical Properties of Al2O3 Reinforced 6061Al Particulate MMC's* (Int. J. Eng. Res. Technol., 2012), 1, pp. 1-6.
8. Mallesh G, Manjunatha H.S, Pradeep Kumar V.G, Rakesh D. R, *Mechanical and TribiologicalProperties ofAluminium A16061 Alloy Reinforced with SiCp*. (Int. J. Eng. Res. Technol., 2015), 5, pp. 111-117.
9. Shubham Mathur, AlokBarnawal, *Effect of Process Parameter of Stir Casting on Metal Matrix Composites* (Int. J. Sci. Res., 2013), 2, pp. 395-398.
10. Malek Ali, Fadhel M.I, Alghoul M.A, Zaharim A, Sopian K, *Synthesis and Characterization of Aluminum Matrix Composites Reinforced with Various Ratio of TiC for light* devices. (Int. J. Model. Methods Appl. Sci., 2012), pp. 169-174.
11. Gopalakrishnan S, Murugan N, *Production and Wear Characterization of AA6061 Matrix Titanium Carbide Particulate Reinforced Composite by Enhanced Stir Casting Method*, (Compo. Part B., 2012), Vol. 43, pp. 302-308.
12. Urena A, Rams J, Campo M, Sánchez M, *Effect of Reinforcement Coatings on the Dry Sliding Wear Behavior of Aluminium/SiC Particles/Carbon Fibres Hybrid Compsites (*J. Wear.,2009), Vol. 266(11), pp. 1128-1136.
13. Anand Pai, Sathya Shankar Sharma, Raynor Errold Silva, Nikhil R. G, *Effect of Graphite and Granite Dust Particulates as Micro-Fillers on Tribological Performance of Al6061-T6 Hybrid Components* (Tribol. Int., 2015) Vol. 92, pp. 462-471. DOI: 10.1016/j.triboint.2015.07.035.
14. Thangarasua A, Murugan N Dinaharan I, *Production and Wear Characterization of AA6082 -TiC Surface Composites by Friction Stir Processing* (Procedia Eng., 2014), Vol. 97, pp. 590- 597.
15. Pardeep Sharma, Dinesh Khanduja, Satpal Sharma, *Dry Sliding Wear Investigation of Al6082/Gr Metal Matrix Composites by Response Surface Methodology*, (J. Mater. Res. Technol., 2015) DOI: 10.1007/s11661-015-2881-9.

16. Boon pengchang, HazizanMdAkil, RamdziahBtNasir,AbbasKhann ,*Optimization on Wear Performance of UHMWPE Composites using Response Surface Methodology* (Tribol. Inter., 2015), Vol. 88, pp. 252-262. DOI10.1016/j.triboint. 2015.03.028
17. Malarvizhi.S, Balasubramanian.V, *Effect of Welding Process on AA2219 Aluminium Alloy Joint Properties*. (J. Trans. Nonferrous Met. Soc. China., 2011) Vol. 21(5), pp. 962 -973.
18. Elangovan.K ,Balasubramanian.V, *Influences of Tool Pin Profile and Welding Speed on the Formation of Friction Stir Processing Zone in AA2219 Aluminium Alloy*. (J. Mater. Process. Technol.,2008) Vol. 200, pp. 163-175.
19. Koilraj.M, Sundareswaran.V, Vijayan.S, Koteswararao.S.R, *Friction Stir Welding of Dissimilar Aluminium Alloys AA2219 to AA5083-Optimization of Process Parameters using Taguchi technique* (Mater. Des., 2012) Vol. 42, pp. 1-7.
20. Jenkins Hexley Dhas. S, Edwin Raja Dhas. J, *Processing and Characterization of AA 2219-TiC$_p$ Reinforced Composite* (Int. J. Eng. Res., 2015) Vol. 26, pp. 8989-8995.
21. Elangovan.K, Balasubramanian.V,Babu.S, *Developing an Empirical Relationship to Predict Tensile Strength of Friction Stir Welded AA2219 Aluminium Alloy* (J. Mater. Eng. Perform., 2008) Vol. 17, pp. 820-830.

RESEARCH ARTICLE | MAY 22 2023

Investigation of mechanical behavior of aluminum metal matrix composite reinforcement with graphene nano fillers

M. Ganesh ✉; P. Issac Prasad

AIP Conference Proceedings 2492, 040076 (2023)
https://doi.org/10.1063/5.0113359

Investigation of Mechanical Behavior of Aluminum Metal Matrix Composite Reinforcement with Graphene Nano Fillers

M Ganesh [1, a)], and P Issac Prasad[2]

[1] *Department of Aeronautical engineering, MLR Institute of Technology, Hyderabad, Telangana, India.*
[2]*Department of Mechanical Engineering, KL University, Vijayawada. India.*

[a)] Corresponding author: ganesh.manikonda@gmail.com

Abstract: Graphene is an extraordinary material being the lightest and strongest material, it has an incredible mechanical properties. It being allotrope of carbon also has exclusive optical and thermal properties, which make it evident filler for producing multipurpose composites significantly metal matrix composites. Aluminum contributing to highly used metal due its cost effectiveness, corrosion resistance and light weight in numerous industries. Aiming to synthesize aluminum metal matrix reinforced with graphene nano filler and to investigate its mechanical behavior by using stir casting method. By varying the weight percentages of graphene nano particulates (0.2%,0.4%,0.6%,0.8%, 1.0% and 1.2% by weight) are used to fabricate metal matrix composite by using 6061. Aluminum grade. The developed nano composite is further verified by metallurgical microscopic images to discuss the distribution of reinforcement in the metal matrix base. The strength of the developed composite is determined by tensile test, hardness of the material by Brinell's hardness test and toughness by impact test. The interference of two material causing various properties to change in the material and helps in choosing the best combination for our required material for the product

Keywords. Composite, grapheme, Al6061, Properties, castingetc.

INTRODUCTION

On the bases of different field in the industries in engineering have a high utility of aluminum due to its cost effectiveness, abundance, and the light weight property? By various techniques and different composition of aluminium, material properties can be changed a sperour requirements .As we know graphene is one of the most distinctive materials with extraordinary electrical, mechanical, thermal properties among the carbonaceous material [4].

The electronic structure of graphite was the first step to understanding graphene by physicist R. Philip in 1947. The designation graphene was a result of combination of word graphite and suffix -ene (referring to aromatic hydrocarbons), in 1986 by chemists Ralph Setton, Eberhard Stumpp, Hanns-PeterBoehm. Isolation of a single-layer graphene was exfoliated using an extremely simple method by physicist of University of Manchester Konstantin Novoselov and Andre Geim in the year of 2004 [6]. The top layers from the graphite sample were removing by adhesive tape and then the layers were applied to substrate material.

Aluminium is a silvery white metallic which is the most abundant metal in the earth crust which belongs to the 13th group the boron family of the main periodic table. The moon surface also features large amount of Aluminium. It was once called king of metals and was discovered in 1825 in Denmark. Aluminium being a light weighted metal is used majorly in aerospace industry [3]. Boeing -747 contains 66,000kg of Aluminium. Pure aluminium does not have high strength so, highly alloys of aluminium is used in various industries. Aluminium reflects 98% of infra-red

Advancements in Aeromechanical Materials for Manufacturing: ICAAMM-2021
AIP Conf. Proc. 2492, 040076-1–040076-9; https://doi.org/10.1063/5.0113359
Published by AIP Publishing. 978-0-7354-4438-6/$30.00

rays. Aluminium is one third times lighter than steel and copper. It is the 3rd most common element in the earth crust which can be easily recycled [7].

Through this research we attempt to combine both remarkable material aluminum and graphene as one by aluminum being the matrix material and graphene nano filler acting as a reinforcement of the composite. By different testing method we try to validate the composite material properties with different ratios of matrix and reinforcement and optimize the most efficient out of all the compositions. Through this the obtained results can be considered as a choice of material selection for various applications of aerospace, automobile, marine and many more growing industries [10].

COMPOSITE

Simply to put, Combination of different components is a composite. The combination of two or more natural or artificial elements with non-identical physical or chemical properties that make the material well-built as a team than as individual players [11]. The components combine and contribute their most useful traits to enhance the final product outcome, without losing their individual identities by not merging together completely. Just like the saying hitting two birds with one stone, through composites we attain different features in a single material. Which make reason for use of composites over traditional material? Matrix and reinforcement material are the different phases in composite. When reinforcement or the filler is added to the matrix, the matrix acts as the binder [2].

GRAPHENE

One of the most promising nanomaterial emerged in the recent decades is Graphene because of it extraordinary characteristics and unique combination of excellent properties. More elastic than rubber yet harder than diamond, lighter than aluminium yet tougher than steel. Strongest and the thinnest material known to man till date is Graphene [12].

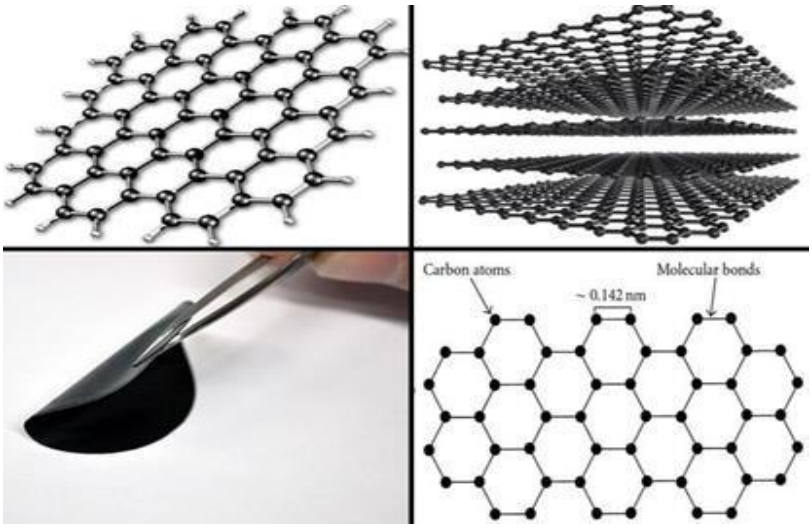

FIGURE 1.Graphene and its properties

Aluminium 6061

Aluminium 6061 is an alloy where aluminium is the base metal and 6xxx aluminium, which entails those alloys which use silicon and magnesium as the primary alloying elements. Second digit designates the degree of impurity control for Al base and “0” specifies that thebulk of alloy is commercial aluminium. Designators for individual alloys are simply specifying the last two digits. Aluminium 6061 has increased strength, toughness, conductivity and furthermore is heat treatable, easily formed and good at resisting corrosion [13].

FIGURE 2. Aluminium6061 and its properties

FABRICATION PROCESS

The key ingredients for manufacturing are materials, which are the driving force behind the technological revolutions. Casting process manufactures objects with high compressive strength. Creates any complex and complicated structure economically and easily [2]. Isotropic structures are formed with accuracy and wide varying range of properties. Significantly, it is the low-priced and object size is not limited among all the manufacturing process.

FIGURE 3. Stir casting process

We used a modern stir casting method rather than choosing conventional type, as it results in higher quality product with fine mixing of reinforcement and formation of less voids in the grain structure. Stirring occurs in a medium

frequency induction furnace. The furnace contains a non-conductive crucible made out of graphite which can melt nearly 15Kgs of metal.

MACHINING AND TESTING

We have selected CNC (Computer numerical control) machine due to its increased efficiency speed production and also ensures accuracy and consistent product quality. By removal of material using rotary cutters by advancing the workpiece, this type of machining is milling. Each casted block of composite is machined with CNC Milling machine. We obtain three specimens in every individual block, all together eight-teen specimens [14].

Tensile Test

Tensile properties frequently are included in material specifications to ensure quality and they are often measured during development of new materials and processes, so that different materials and processes can be compared. Tensile tests are used in selecting materials for engineering applications; their results come in handy during selection process. The material is tested on the basis of ASTM B557 - 15 Test Methods for Tension Testing Wrought and Cast Aluminium-and Magnesium-Alloy Products [15].

FIGURE 4.UTM (Universal testing machine)

Impact Test

Studying the toughness of material relies on the factor of the materials ability to absorb energy during plastic deformation. Toughness is measured by testing the material with impact testing machine. More brittle the material less is the materials toughness and that means the material results to endure only small amounts of plastic deformation [8]. Often the impact energy of a material is decreased, at lower temperatures as impact value of material can also change with temperature. The test procedure was on the basis of IS 1757(Part-1)2014and the type of impact was Charpy– V grooved at room temperature.

FIGURE 5. Charpy Impact Testing Equipment and its specimen

Hardness Test

The hardness test is, by far, the most valuable and most widely used mechanical test for investigating the properties of metals and other materials. Resistance to permanent indentation of a material usually is considered hardness [9]. The primary purpose of the hardness test is to determine the suitability of a material for the application that has been taken into consideration, or the particular treatment to which the material has been subjected. The simplicity with which this mechanical test can be made has made it the most common method of inspection for metals and alloys. The test is conducted on Rockwell cum Brinell hardness machine, with an indenter of 5mm and with a load of 250 Kg. According to the test procedure of IS 1500-201

FIGURE 6. Brinell's Hardness equipment and its Work Pieces

Microscopy Grain Structure Test

The mechanical and technological properties of materials are directly linked to the grain size and orientation. Graphene nano particulates distribution also causes a primary factor for different measure of properties. The fine distribution of graphene causes progressively high strength than the non-uniform distribution of particulates. The specimens have been tested as per the ASTM E112 standards. The area analysed is 0.5791mm2, with magnification of 100Xandby adding the Kellerre agent as the etchant.

RESULTS

The load versus elongation graphs is developed according to the ASTM B577 standards for the tensile test. All the six specimens having varying graphene percentage reinforced into aluminium metal matrix. The specimen is flat having dimension 150x20x12.6mm and with a gauge length of 50mm. The ultimate load, ultimate tensile strength, elongation, yield load and yield stress are evaluated.

The maximum yield strength and ultimate tensile strength obtained are 116.48Mpa and152.6Mpaat 0.8 % GNP respectively.

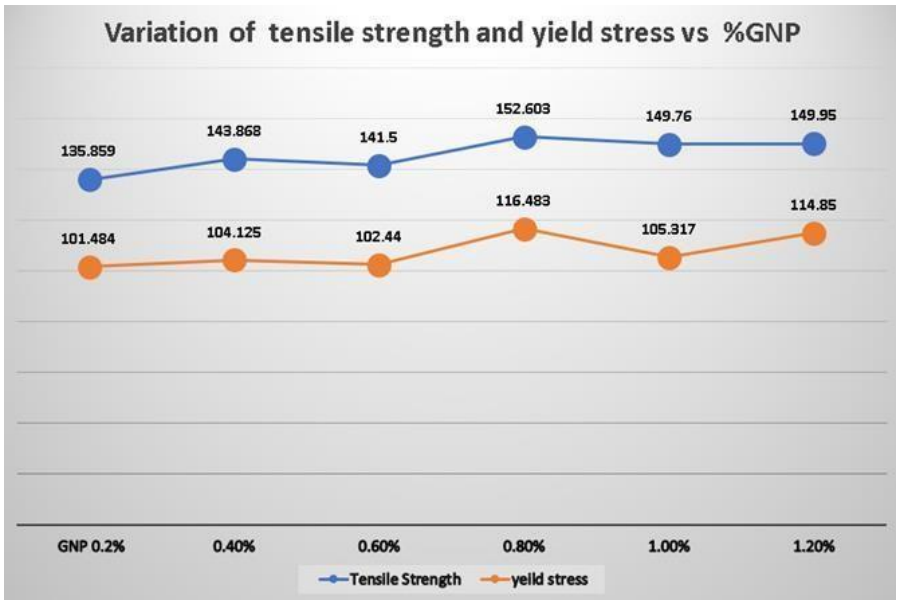

FIGURE 7. Variations of tensile strength and yield stress vs %GNP

As per IS 1757 (part-1): 2014 the impact test is done by using Charpy-V Impact Test equipment having 2mm deep notch with a notch angle of 45° and with dimension of10x10x55mm,at room temperature.

We can observe from the tensile test that at 0.8% GNP the material has high yield strength and ultimate tensile strength, the fact that the composites impact energy will be seen to decrease if the yield strength is increased. The maximum impact energy seen is at reinforcement mixed with 1.0%.

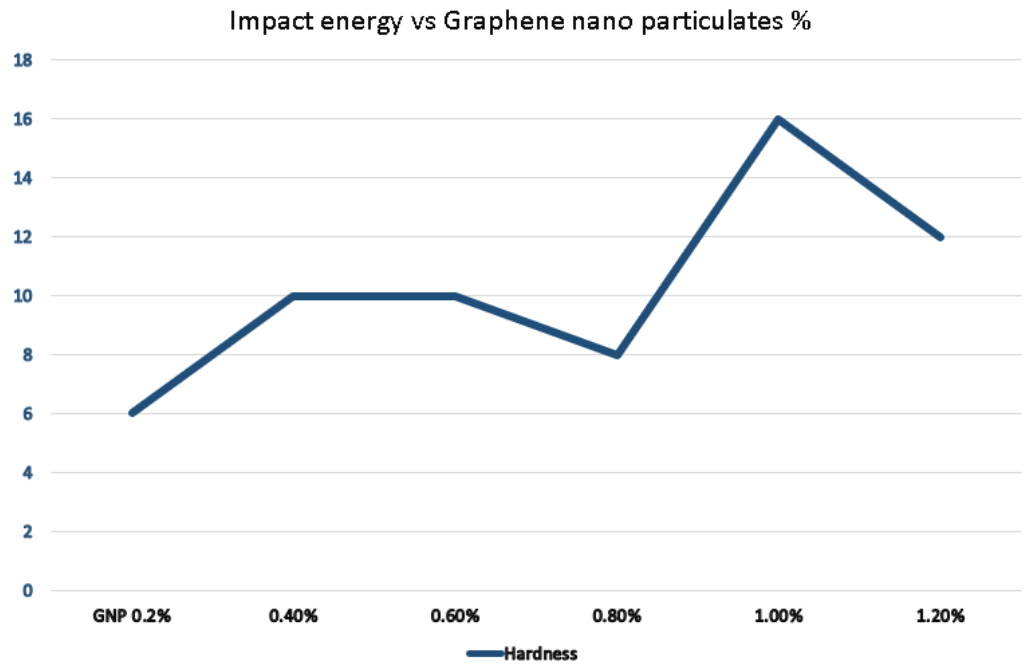

FIGURE 8. Impact energy vs %GNP

At room temperature, the specimens are tested and the obtained results are plotted in graphical form. The Brinell's test is done with an indenter of 5mm with an applied load of250 Kg according to the IS 1500 standards. Each specimen is tested in three different locations of the specimen with the indenter.

The microstructure of grain shows the clusters and agglomeration formed in the grain and it has particle diameter of 10 μm (micro-microns). The mixing of the reinforcement in the base matrix leads to various morphology transition and the columnar microstructure proceeds toward equiaxed micro structure with increasing percentages of graphene. But homogenous mixing is reported mostly in 0.2, 0.6 and0.8 weight% grapheme nano particulates fraction.

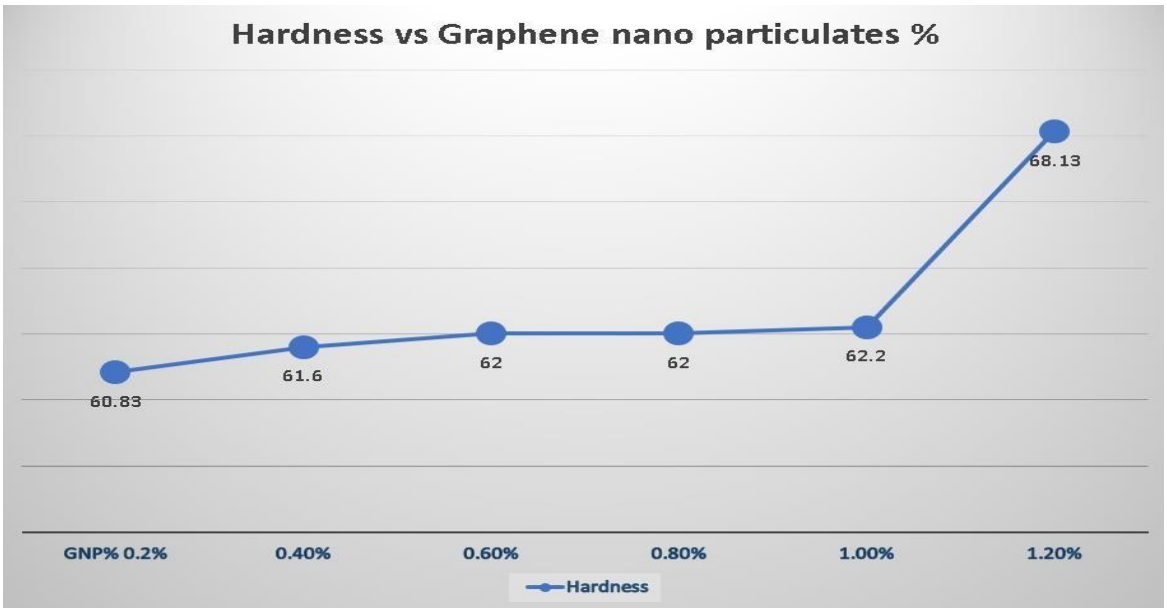

FIGURE 9. Hardness vs %GNP

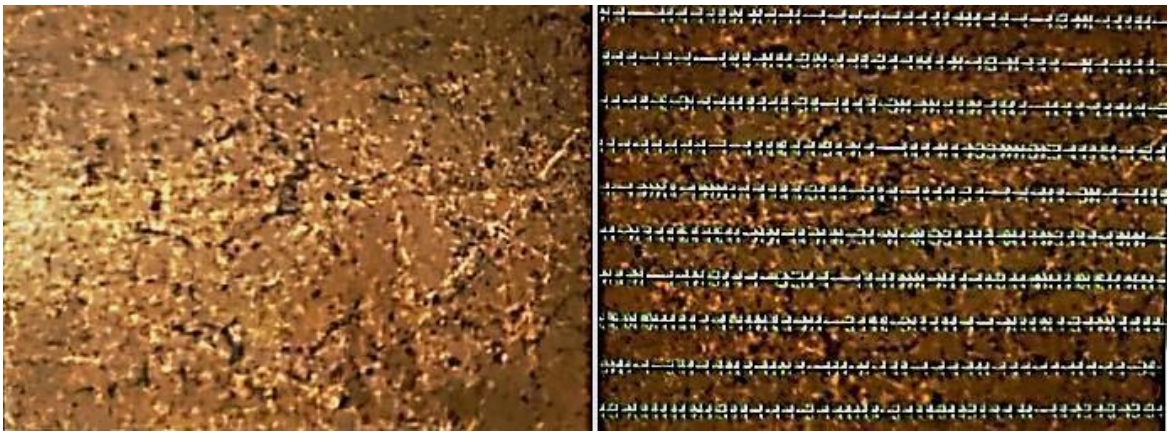

FIGURE 10. Metallurgical Microscopy (10µm) of Aluminium6061-0.8% GNP

CONCLUSION

The investigation and development of Aluminium metal matrix composite reinforced with varying weight percentages of graphene nano particulates is done successfully. The develop samples are Al6061 with 0.2%, 0.4%, 0.6%, 0.8%, 1.0% and 1.2% GNPs were validated by metallurgical microscopy images to discuss the distribution of the reinforcement throughout the matrix material. The mechanical properties such as tensile strength, hardness and toughness were obtained.

Graphene nano particulates distribution throughout the metal matrix phase has been observed. The grain size, boundaries, size are seen and measured. Additionally, observed the effect of clustering of GNPs and also seen agglomeration of GNPs in the specimens produces from the imaging, they can be comparatively low and can be avoidable.

The yield strength and ultimate tensile strength values show an increasing trend when compared to the increasing percentage of graphene nano particulates percentage. The maximum yield strength and tensile strength reported are 116.48Mpa and 152.6Mpa, respectively, for 0.8 % GNP-Al6061 metal matrix. As compared to the raw aluminium 6061the strength has significantly increased. It is observed that due to the increase of reinforcement the materials brittleness also increases grapheme reinforced composite. The maximum value of Brinell's hardness number is 10 seen in the material at 1.0% of GNPs. To the whole, the aluminium – graphene reinforced composite when compared the pure aluminium grade its mechanical properties have enhanced. While the material itself is showing a good behaviour at mixing the graphene nano fillers 0.8 % where the tensile strength is high, the brittleness is low that is ductility is good and has good impact strength, owing to the observation of further improvement in strengthening the material around that region of mixing of reinforcement percentage of grapheme nano fillers.

REFERENCES

1. Tensile behaviour of aluminium alloy (AA7050) metal matrix composite reinforced with graphene fabricated by stir and squeeze cast processes. Venkatesan, M.Anthony Xavior
2. Mechanical Characterization of Stir Cast Al-7075/B4C/Graphite Reinforced Hybrid Metal Matrix Composites B.Jayendraa, D.Sumantha, G. Dinesha, Dr.M.Venkateswara Rao
3. Investigations on Al 7075 /nano- Sic / B4C hybrid reinforcements using liquid casting method S. Sunil Kumar Reddy C. Sreedhar, S.Suresh
4. Investigating aluminium alloy reinforced by graphene nano flakes S.J. Yan, S.L. Dai, X.Y.Zhang,C. Yang, Q.H. Hong, J.Z. Chen, Z.M. Lin
5. Metal matrix composites: production by the stir casting method J. Hashim, L.Looney, M.S.J.Hashmi
6. Effect of Graphene nanoparticles on micro structural and mechanical properties of aluminium based nano composites fabricated by stir casting Bajaj Institute of Technology and Management
7. Effect of silicon carbide particulates on wear resistance of graphitic aluminium matrix composites S. Suresha, B.K. Sridhara

8. Effect of graphene nano platelets on the mechanical properties of aluminium metal matrix composite Sharma, A., Vasudevan, B., Sujith
9. Effect of graphene reinforcement on mechanical and microstructure behaviour ofAA8030/ graphene composites fabricated by stir casting technique L. Natrayan, S.Yogeshwaran,L. Yuvaraj, and M. Senthil Kumar
10. A bottom-up strategy toward metal nano-particles modified graphene nano plates for fabricating aluminium matrix composites and interface study by Tielong Han, Enzuo Liu ,Jiajun Li, Naiqin Zhao, Chunnian He
11. Interface evolution and mechanical properties of nickel coated graphene nano flakes/ pure titanium matrix composites by Y.X.Ge, H.M.Zhang, X.W.Cheng, Q.B.Fan, Z.H.Zhang,
12. X.N.Mu, L. Liu,Y.N. Liu, B. Wang Reinforcement with graphene nano sheets in aluminium matrix composites by J. Wang, Z.Li,G. Fan, H. Pan, Z. Chen, D. Zhang.
13. Madhavi, K Sreelakshmi and M. Satyanarayana Gupta," Evaluation of Ply Orientation on Failure of Composites", *IJCIET*, ISSN Print: 0976-6308 and ISSN Online: 0976-6316, Volume 8, May2017.
14. N Madhavi, B Niharika M Satyanarayana Gupta "Evaluation of ply orientation on failure of Kevlar Epoxy149" *IJCIET*, ISSN Print: 0976-6308 and ISSN Online: 0976-6316, Volume 8, May2017.
15. Vivek Anand A, Gollakota S, Hariprasad V, Shunmugavelu N, Ahifkhan & Arumugam V, "Role of Micropatterns on Wettability and Corrosion Characteristics of SS304 Steel Surfaces", *International Conference on Materials, Manufacturing and Machining* (ICMMM - 2019), 8 & 9 March 2019, BIT Sathy, India

RESEARCH ARTICLE | MAY 22 2023

Interpretive structural modeling based analysis of factors influencing implementation of lean and sustainability concepts in aerospace sector

N. Vinay Kumar; J. Pavan Kalyan; Md. Saqlain Rahil; Md. Mustafa Haroon; A. Vivek Anand; G. Sivaraj

AIP Conference Proceedings 2492, 040005 (2023)
https://doi.org/10.1063/5.0113286

Interpretive Structural Modeling Based Analysis of Factors Influencing Implementation of Lean and Sustainability Concepts in Aerospace Sector

N Vinay Kumar[1], J Pavan Kalyan[1], Md. Saqlain Rahil[1], Md. Mustafa Haroon[1], A Vivek Anand[1] and G Sivaraj[2, a)]

[1]*Department of Aeronautical Engineering, MLR Institute of Technology, Hyderabad, India*
[2]*Department of Aeronautical Engineering, Bannari Amman Institute of Technology, Sathyamangalam, India*

a) Corresponding author: togsiva@gmail.com

Abstract. The detailed study was conducted on the application of Interpretive Structural Modelling (ISM) for analyzing the factors influencing implementation of lean and sustainability concepts in aerospace sector. The implementation of lean concepts in Aerospace sector especially in manufacturing domain will augment its overall production/inspection process efficiency and provides competitive advantage in the global market. Based on literature survey and computation, 15 major factors are identified which affects the lean and sustainability concepts in Aerospace sectors. MICMAC analysis was performed to divide the influencing factors into 4 categories and the relation between the influencing factors are identified. The results were validated by conducting case study.

Keywords: Lean manufacturing; Sustainable manufacturing; MICMAC analysis; Interpretive Structural Modelling; Waste elimination

INTRODUCTION

Lean and sustainability concepts are new and growing vastly in aerospace sector, aims at minimizing wastage and environmental impact of aerospace components. The implementation of green and lean manufacturing in aerospace sector is still a difficult task which is influenced by certain factors [1]. The broad prior art survey was conducted in our work to determine those factors influencing Lean and sustainability concepts in aerospace sectors. The adoption of lean technique with Maintenance Repair Overall Organization (MROs) are subjected to both demand in internal and external fluctuations by lean implementation, the consequence of these variables can be minimized by implementing suitable model [2] .

Romaniw and Bras [3] conducted survey on common factors influencing the implementation of sustainability concepts in aerospace manufacturing industries. The results showed that common influential factors are classified into facility practices and manufacturing practices. The authors concluded that successful implementation of above mentioned factors helped in influencing sustainability concept in aerospace sectors. The studies showed that lean concepts can be implemented for both manufacturing and business process in aerospace sector. Barbosa et al [4] performed a study that focuses on implementing lean techniques in aerospace manufacturing process aiming production automation. The authors conducted literature review on lean manufacturing in aerospace industries and concluded that implementing lean techniques helps in reducing time and wastage. They found that seven waste and methods to minimise waste through lean manufacturing.

Higher order management commitment is the most dominant variable and relative cost benefits as the least dominant variable. Mathiyazhagan et al [5] attempted a first step to determine the huddles in implementing supply chain management (green) using ISM approach. Based on the literature survey and inputs from the academicians

Advancements in Aeromechanical Materials for Manufacturing: ICAAMM-2021
AIP Conf. Proc. 2492, 040005-1–040005-7; https://doi.org/10.1063/5.0113286
Published by AIP Publishing. 978-0-7354-4438-6/$30.00

and industrial experts, the authors found 26 barriers. By following general step in ISM, they formulated an ISM model which indicates the dominant barriers. The results showed that challenges lies in maintaining and creating environmental awareness among suppliers as the most dominant huddle. Qureshi [6]-[10] performed ISMon barriers that affect the application of Total Quality Management (TQM). From literature review and expert advice, about 12 barriers were identified that influence TQM. By performing general ISM, the barriers were prioritized into different levels. The findings showed that lack of higher order management involvement and commitment as the most dominant huddle and high turnover at management level and employee's resistance to change as least dominant barriers in implementation of TQM [21]. The objectives of the current work is to identify the factors influencing lean and sustainability concepts implementation in aerospace sector and to establish interrelationship among factors.

INTERPRETIVE STRUCTURAL MODELLING (ISM) METHODOLOGY

Interpretive Structural Modeling (ISM) is a systematic approach to establish relation among the factors. ISM methodology starts with identifying the influencing factors for implementing lean and sustainable manufacturing in aerospace sector. Table 1 shows the identified factors based on literature review and discussion with experts. The relationship between the factors are mapped using structural self-iteration matrix (SSIM)

TABLE 1. Factors Used in the Study [7-19]

Factor No.	Factors
F1	Mindset and Behaviour (MSB)
F2	Operations Standardization (OS)
F3	Management Infrastructure (MI)
F4	Pull System (PS)
F5	Worker Empowerment (WE)
F6	Training (T)
F7	Group Problem Solving (GPS)
F8	Continuous Improvement (CI)
F9	Market Trends (MT)
F10	Competition (C)
F11	Customer Pressure (CP)
F12	Government Support (GS)
F13	Adoption of Clean Technologies (ACT)
F14	Product Design with Minimal Environmental Impact (PDMEI)
F15	Compliance with Legal Environmental Regulations (CLER)

After constructing the final reachability matrix [20], factor level iterations is performed [10]. Level partitions consist of antecedent set, reachability set, intersection set and level to each factor. The few iterations are shown in tables 2-5. From table 2, shows the intersection set of factors 13 and 14 and reachability set are similar and are assigned level I. Iterations are continued till all factors are positioned at appropriate levels. From table 5, it can be seen that factor 3 and factor 11 are positioned at level X. Higher level factors are placed in top of ISM model and least level factors form the base of ISM model.

TABLE 2. Factor Level Iteration- I

Factor	Reachability Set R(Fi)	Antecedent Set A(Fi)	Intersection R(Fi)∩ *A(Fi) Set*	Level
F1	1,5,6,7,8,10,11,12,13,14	1,2,3,4,5,7,9,11,12,15	1,5,7,11,12	
F2	1,2,4,5,6,8,9,10,12,13,14,15	2,3,4,5,7,9,10,11,12,13,14,15	2,4,5,9,10,12,13,14,15	
F3	1,2,3,4,5,6,7,8,9,10,11,12,13,14,15	3,5,7,10,11,12,13,14,15	3,5,7,10,11,12,13,14,15	
F4	1,2,4,5,6,8,9,10,13,14	2,3,4,6,7,9,10,11,13,14	2,4,6,9,10,13,14	
F5	1,2,3,5,6,7,8,10,13,14	1,2,3,4,5,7,9,10	1,2,3,5,7,10	
F6	4,6,7,8,9,10,11,13,14	1,2,3,4,5,6,7,9,10,11,12,13,14,15	4,6,7,9,10,11,13,14	
F7	1,2,3,4,5,6,7,8,10,11,13,14,15	1,3,5,6,7,9,10,11,12,15	1,3,5,6,7,10,11,15	
F8	8,10,13,14	1,2,3,4,5,6,7,8,9,11,12,13,14,15	8,13,14	
F9	1,2,4,5,6,7,8,9,10,13,14,15	2,3,4,6,9,10,11	2,4,6,9,10	
F10	2,3,4,5,6,7,9,10,13,14	1,2,3,4,5,6,7,8,9,10,11	2,3,4,5,6,7,9,10	
F11	1,2,3,4,6,7,8,9,10,11,13,14,15	1,3,6,7,11	1,3,6,7,11	
F12	1,2,3,6,7,8,12,13,14,15	1,2,3,12,13,14,15	1,2,3,12,13,14,15	
F13	2,3,4,6,8,12,13,14,15	1,2,3,4,5,6,7,8,9,10,11,12,13,14,15	2,3,4,6,8,12,13,14,15	**I**
F14	2,3,4,6,8,12,13,14,15	1,2,3,4,5,6,7,8,9,10,11,12,13,14,15	2,3,4,6,8,12,13,14,15	**I**
F15	1,2,3,6,7,8,12,13,14,15	2,3,7,9,11,12,13,14,15	2,3,7,12,13,14,15	

TABLE 3. Factor Level Iteration- II

Factor	Reachability Set R(Fi)	Antecedent Set A(Fi)	Intersection R(Fi)∩ *A(Fi) Set*	Level
F1	1,5,6,7,8,10,11,12	1,2,3,4,5,7,9,11,12,15	1,5,7,11,12	
F2	1,2,4,6,5,8,9,10,12,15	2,3,4,5,7,9,10,11,12,15	2,4,5,9,10,12,15	
F3	1,2,3,4,5,6,7,8,9,10,11,12,15	3,5,7,10,11,12,15	3,5,7,10,11,12,15	
F4	1,2,4,5,6,8,9,10	2,3,4,6,7,9,10,11	2,4,6,9,10	
F5	1,2,3,5,6,7,8,10	1,2,3,4,5,7,9,10	1,2,3,5,7,10	
F6	4,6,7,8,9,10,11	1,2,3,4,5,6,7,9,10,11,12,15	4,6,7,9,10,11	
F7	1,2,3,4,5,6,7,8,10,11,15	1,3,5,6,7,9,10,11,12,15	1,3,5,6,7,10,11,15	
F8	8,10	1,2,3,4,5,6,7,8,9,11,15	8	
F9	1,2,4,5,6,7,8,9,10,15	2,3,4,6,9,10,11	2,4,6,9,10	
F10	2,3,4,5,6,7,9,10	1,2,3,4,5,6,7,8,9,10,11	2,3,4,5,6,7,9,10	**II**
F11	1,2,3,4,6,7,8,9,10,11,15	1,3,6,7,11	1,3,6,7,11	
F12	1,2,3,6,7,8,12,15	1,2,3,12,15	1,2,3,12,15	
F15	1,2,3,6,7,8,12,15	2,3,7,9,11,12,15	2,3,7,12,15	

TABLE 4. Factor Level Iteration- III

Factor	Reachability Set R(Fi)	Antecedent Set A(Fi)	Intersection R(Fi)∩ *A(Fi) Set*	Level
F1	1,5,6,7,8,11,12	1,2,3,4,5,7,9,11,12,15	1,5,7,11,12	
F2	1,2,4,5,6,8,9,12,15	2,3,4,5,7,9,11,12,15	2,4,5,9,12,15	
F3	1,2,3,4,5,6,7,8,9,11,12,15	3,5,7,11,12,15	3,5,7,11,12,15	
F4	1,2,4,5,6,8,9	2,3,4,6,7,9,11	2,4,6,9	
F5	1,2,3,5,6,7,8	1,2,3,4,5,7,9	1,2,3,5,7	
F6	4,6,7,8,9,11	1,2,3,4,5,6,7,9,11,12,15	4,6,7,9,11	
F7	1,2,3,4,5,6,7,8,11,15	1,3,5,6,7,9,11,12,15	1,3,5,6,7,11,15	
F8	8	1,2,3,4,5,6,7,8,9,11,15	8	**III**
F9	1,2,4,5,6,7,8,9,15	2,3,4,6,9,11	2,4,6,9,	
F11	1,2,3,4,6,7,8,9,11,15	1,3,6,7,11	1,3,6,7,11	
F12	1,2,3,6,7,8,12,15	1,2,3,12,15	1,2,3,12,15	
F15	1,2,3,6,7,8,12,15	2,3,7,9,11,12,15	2,3,7,12,15	

TABLE 5. Factor Level Iteration- X

Factor	Reachability Set R(Fi)	Antecedent Set A(Fi)	Intersection R(Fi)∩ *A(Fi) Set*	Level
F3	3,11	3,11	3,11	**X**
F11	3,11	3,11	3,11	**X**

Conical matrix is formed by arranging factors based upon their level obtained in factor level iteration. Conical matrix help in formulating ISM model based on level partitions. Top level factors are arranged in top of conical matrix respectively. From table 6, it can be seen that factors 13 and 14 are at highest level and they are placed on top of conical matrix. Also, factors 3 and 11 are at lowest level and are placed in bottom of conical matrix and other factors are positioned between them.

TABLE 6. Conical Matrix

Factor	F13	F14	F10	F8	F6	F5	F1	F2	F4	F15	F7	F9	F12	F3	F11
F13	0	1	1	1	0	1	0	1	0	0	0	1	1	1	1
F14	0	1	1	1	0	1	0	1	0	0	0	1	1	1	1
F10	0	1	1	1	1	1	1	0	1	1	0	0	1	1	0
F8	0	0	0	0	0	0	0	1	0	1	0	0	1	1	0
F6	0	0	0	1	0	1	1	1	1	0	0	0	0	0	0
F5	1	1	1	0	1	1	1	1	0	0	0	0	1	1	0
F1	1	0	0	0	1	1	1	1	0	1	1	1	1	1	0
F2	1	1	0	1	1	1	0	1	1	1	0	1	1	1	1
F4	1	1	0	1	1	1	0	1	1	1	0	0	1	1	0
F15	1	1	1	0	0	1	1	1	0	0	0	1	1	1	1
F7	1	1	1	1	1	1	1	1	0	1	1	0	1	1	1
F9	1	1	0	1	1	1	1	1	1	1	0	0	1	1	1
F12	1	1	1	0	0	1	1	1	0	0	0	1	1	1	1
F3	1	1	1	1	1	1	1	1	1	1	1	1	1	1	1
F11	1	1	1	1	0	1	1	1	1	1	1	0	1	1	1

MICMAC ANALYSIS

MICMAC analysis is performed to analyse driving power and dependence power of factors which influence the implementation of lean and sustainable concepts in aerospace sectors. A graphical model is developed showing factor wise dependence power and driving power. MICMAC analysis is carried out from final reachability matrix. Driving power and dependence power obtained in final reachability matrix are developed into a graph. The graph consists of four quadrants. Quadrant I denote autonomous factors, quadrant II denote dependent factors, quadrant III denote linkage factors and quadrant IV denote independent factors as shown in Figure II.

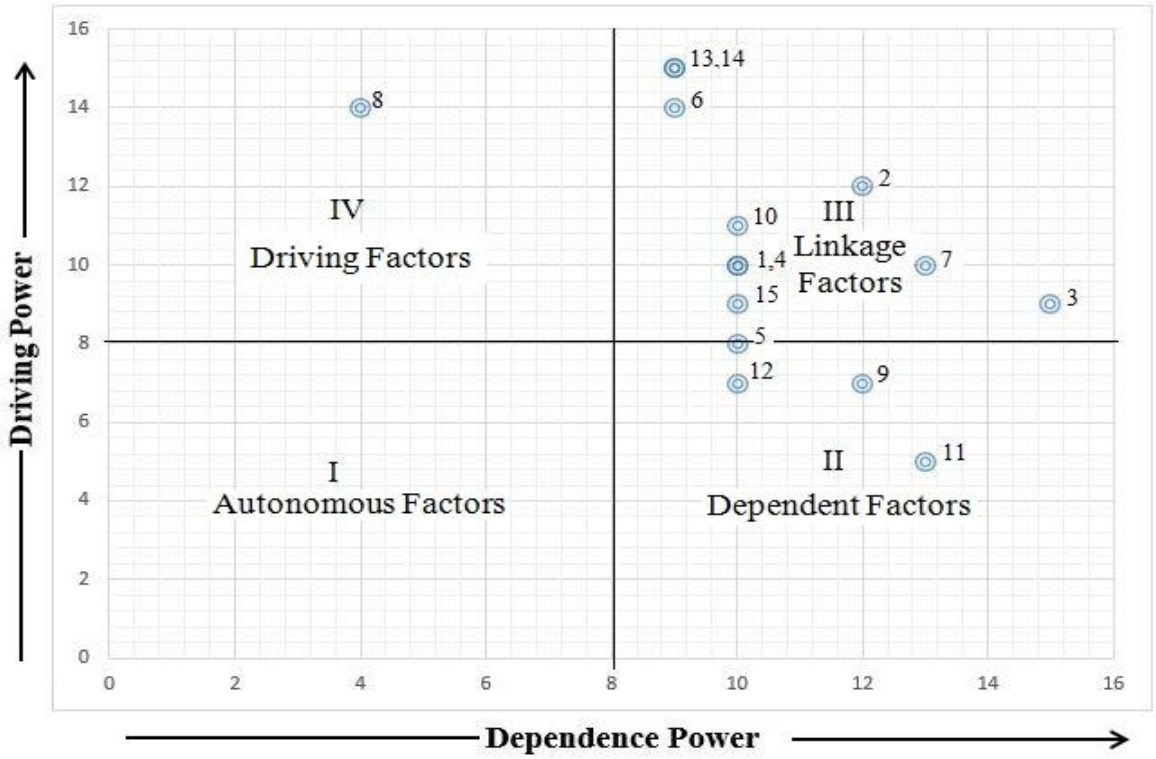

FIGURE 1. Driving and Dependence Diagram

Driving and dependence diagram (Figure 1) shows dependence power and driving power of factors influencing lean and sustainable concepts in aerospace sectors. Observations from driving and dependence diagram are discussed as follows:

- Figure 1 shows that there are no independent factors in driving and dependence diagram. Their absence shows that all 15 factors are important in implementing lean and sustainable concepts in aerospace sector.
- In quadrant II, there are four dependent factors which show that, these factors have stronger dependence power and are easily influenced by other factors.
- In quadrant III, there are 10 linkage factors which show that, these factors have stronger dependence power and also stronger driving power. So these factors are most important factors which can influence others and influenced by others.
- In quadrant IV, there is only one independent factor which has influence on all other factors and does not affected by other factors. These factors have strong driving power.

The conduct of the study enabled the industry practitioners to systematically analyze the factors influencing lean and sustainable concepts implementation. The developed structural model clarifies the interrelationship among factors influencing the application of lean and sustainable concepts. MICMAC analysis enabled the categorization of factors into four categories and further enabling analysis of those factors.

CONCLUSION

The implementation of lean and sustainability concepts in the manufacturing/maintenance companies in Aerospace sector provides strategic advantage to compete in the global market. The wastage in the manufacturing process can be minimized by combining lean and sustainability concepts. The 15 major influencing factors were identified based on literature survey in implementing lean and sustainability concepts in Aerospace sector. The interrelation between these factors were identified by implementing Interpretive Structural Modelling (ISM). The conical matrix was used to do level partition in influencing factors. Based upon ISM (iteration-X) clearly indicates management infrastructure (F3) and customer pressure (F11) are the most influencing factors in implementing lean and sustainability concepts in Aerospace sector.

REFERENCES

1. AL-Najem.,Dhakal, H., Labib, A. and Bennett, N, "Lean readiness level within Kuwaiti manufacturing industries", International Journal of Lean Six Sigma, 4 (3) (2013), pp. 280 – 320.
2. Ayeni, P., Baines, T., Lightfoot, H. and Ball, P, "State-of-the-art of 'Lean' in the aviation maintenance Repair overhaul industry", Journal of Engineering Manufacture, 225 (11) (2011), pp. 2108-2123.
3. Romaniw, Y. and Bras, B, "Survey of Common Practices in Sustainable Aerospace Manufacturing for the Purpose of Driving Future Research", 19th CIRP International Conference on Life Cycle Engineering, Berkeley (2012).
4. Barbosa, G.F., Carvalho, J and Filho, E.V.G, "A proper framework for design of aircraft production system based on lean manufacturing principles focusing to Automated processes", International Journal of Advance Manufacturing Technology, 72 (2014), pp. 1257–1273.
5. Mathiyazhagan, K., Govindan, K., Haq, A.N and Geng, Y, "An ISM approach for the barrier analysis in implementing Green Supply Chain Management", Journal of Cleaner Production, 47 (2013), pp. 283-297.
6. Qureshi, F.T.Z.R.M.N,"Analysis of interaction among the barriers to total quality management implementation using interpretive structural modeling approach", Benchmarking: An International Journal, 18 (4) (2011), pp. 563 – 587.
7. Kodal, N.V.K.J.R,"Validity and reliability of lean manufacturing frameworks", International Journal of Lean Six Sigma, 5 (4) (2014), pp. 361 – 391.
8. Begam, M.S., Swamynathan, R. and Sekkizhar, J, "Current Trends on Lean Management-A review", International Journal of Lean Thinking, 4 (2) (2013). pp. 15-21.
9. Bhuiyan, N. and Baghel, A, "An overview of continuous improvement: from the past to the present", Management Decision, 43 (5) (2005), pp.761 – 771.
10. Catalin, N.A.E, "Advanced Aerodynamic Technologies for future green regional aircraft", Incas Bulletin, 6 (1) (2014), pp. 99 – 110.
11. Cudney, E. and Elrod, C, "A comparative analysis of integrating lean concepts into supply chain management in manufacturing and service industries", International Journal of Lean Six Sigma, 2 (1) (2011), pp.5 – 22.
12. Degirmenci, T, "Standardization and Certification in Lean Manufacturing", MASTER THESIS: Waterloo, Ontario, (2008), Canada.
13. Drew, J., Macallam, B. and Roggenhofer, S, "Journey to Lean: Making Operational Change Stick", International Journal of Production Research, ISBN 978-1-4039-4841-0.
14. Georgescu, D.D, "Lean Thinking and Transferring Lean Management- The Best Defence against an Economic Recession?", European Journal of Interdisciplinary Studies, \31 (1) (2011), pp. 4-20.
15. Govindan, K., Azevedo, S.G., Carvalho, H. and Cruz-Machado, V, "Lean, Green and Resilient Practices Influence on Supply Chain Performance: Interpretive Structural Modelling Approach", International journal of Environmental Science and Technology, 12 (2013), pp. 15–34.
16. Jadhav, J.R., Mantha, S.S and Rane, S.B, "Development of Framework for Sustainable Lean Implementation: An ISM Approach", Journal of Industrial Engineering International, 10 (2014), pp. 72.
17. Jadhav, J.R., Mantha, S.S and Rane, S.B, "Roadmap for Lean Implementation in Indian Automotive Component Manufacturing Industry: Comparative Study of UNIDO Model and ISM Model", Journal of Industrial Engineering International, 11 (2015), pp. 179–198.
18. Jadhav, J.R., Mantha, S.S. and Rane, S.B,"Exploring barriers in lean implementation", International Journal of Lean Six Sigma, 5 (2) (2014), pp. 122 – 148.

19. Kasavaa, N.K., Yusofa, N.M., Khademia, A. and Samana, M.Z.T, "Sustainable Domain Value Stream Mapping (SdVSM) Framework Application in Aircraft Maintenance: A Case Study", Procedia CIRP, 26 (2015), pp. 418 – 423.
20. A Vivek Anand, G Sivaraj, P Velmurugan, Koppula Srinivas Rao, Muhammed Anaz Khan and P S Prem Kumar, "Interpretive Structural Modelling Approach: Implementation of Sustainability Concept and Lean in Aerospace Sectors", International conference on materials research in science and technology (KMRSE'21), Coimbatore, India, 23-25 July 2021.
21. Garre P., Nikhil Bharadwaj V.V.S., Shiva Shashank P., Harish M., Sai Dheeraj M, "Applying lean in aerospace manufacturing", Materials Today: Proceedings, Volume 4, Issue 8, 2017, Pages 8439-8446.

RESEARCH ARTICLE | MAY 22 2023

Analysis of performance characteristics on a motorcycle with an external air induction system

S. Ajay ✉; T. Rajagopal; S. Rajmohan; P. T. Saravanan; M. N. V. S. Swetha Bala

AIP Conference Proceedings 2492, 040065 (2023)
https://doi.org/10.1063/5.0113415

Analysis of Performance Characteristics on a Motorcycle with an External Air Induction System

S Ajay[1, a)], T Rajagopal[l], S Rajmohan[1], PT Saravanan[1], MNVS Swetha Bala[2,b)]

[1]*Department of Mechanical Engineering, Kongu Engineering College, Perundurai, Erode, India*
[2]*Department of Aeronautical Engineering, MLR Institute of Technology, Hyderabad, India.*

[a)] Corresponding Author: ajusuku.405@gmail.com
[b)] swethabalamlr@gmail.com

Abstract. A supercharger is a compressor that is powered by the bike's battery's electrical supply. The project includes a supercharger that is connected to the carburetor which produces pressurized air for improved fuel combustion. Furthermore, the engine's compression can be lowered below that of detonation while still providing a surplus of power, decreasing heat losses in the water jacket. The engine is a single cylinder 4 stroke engine with a displacement of 159.7cc. For the first two gears, output parameters such as brake power, specific fuel consumption, brake thermal efficiency, and mechanical efficiency are measured. The loads are applied through manual loading using a rope brake with a maximum load capacity of 5 kg. Calculations are made on engine running with and without supercharger fitted to the carburetor. The mechanical efficiency of the engine is increased 5% and 3% in gear 1and 2 and input powerhas decreased 18 and 12 % respectively. Also, specific fuel consumption has decreased about 6and 4% for gears 1 and 2 and brake thermal efficiency has increased 6 and 2% respectively. Thus, the results gave no lag time, higher horse power and increased power in lower gears withthe supercharger.

Keywords: Battery, Electric motor, IC Engine, Intake Manifold, Supercharger, etc.,

INTRODUCTION

It is understood that at the beginning of the compression stroke, with an increase in the amount of air or mixture in the cylinder, an engine's power output rises, so it allows more fuel to be burned. The amount of air induced per unit time can be raised by raising engine speed or increasing air density during the suction stroke. A turbocharger or turbo is a forced induction system used to generate more power for a given size of an engine. The main distinction between a turbocharger and a traditional supercharger is that the latter is mostly driven mechanically from the engine from a belt linked to the crankshaft, while the exhaust gas turbine of the engine powers a turbocharger. The use of turbochargers allows smaller displacement engines to be used by manufacturers. This is possible because the performance of the engine is related to the force acting on the piston that generates work and thus torque.

A turbocharger unit consists of two main components: a turbine and a compressor and is intended to improve the performance of the combustion chamber in terms of volume. The improved combustion process would produce a more energetic pulsating exhaust gas that flows into the turbine that drives the compressor through the exhaust manifold. The turbocharger turbine creates a high back pressure on the exhaust manifold, resulting in higher exhaust gas pressure than atmospheric pressure. The

energy generated due to the exhaust gas expansion is then used to rotate the turbine impeller thatdrives the compressor directly. When they launched the 2002 in 1973, BMW was the first to use turbo-charging in a production passenger car. Turbocharging technology is today regarded as a promising way to conserve energy and minimize CO_2 for internal combustion engines. In the project, the additional system is an intercooler. Turbocharger's target is to

- Increase the efficiency of an IC engine by lowering the fuel consumption.
- Reducing the carbon di oxide emission and pollution of atmosphere.

Advancements in Aeromechanical Materials for Manufacturing: ICAAMM-2021
AIP Conf. Proc. 2492, 040065-1–040065-10; https://doi.org/10.1063/5.0113415
Published by AIP Publishing. 978-0-7354-4438-6/$30.00

PROBLEM IDENTIFICATION AND SOLUTION

Problem Identification

The current system uses the turbocharger to increase the mechanical efficiency and volumetric efficiency. However, there's serious disadvantage of turbo lag.

- The period between a turbocharged engine mashing the throttle and feeling the torque rushis turbo lag.
- The lag comes from the moment the engine takes to create ample exhaust pressure to spin the turbo and pump the compressed intake air into the engine and is the longest until the engine is in a very low-rpm, low load cruising situation.
- If any dirt particles are present within the hot exhaust gases, it will damage the turbocharger that in sequence damages the engine.

Problem Solution

In order to improve the mechanical efficiency and to decrease the fuel consumption rate we use super charger. There is no chance of turbo lag. When the engine starts the supercharger also starts there will not be any delay time for the impeller rotation. The supercharger gains input power from the battery not from the exhaust gas. Hence, exhaust gas has no effect on the supercharger as well as engine.

DESIGN AND SPECIFICATION

TABLE 1 Engine Specification

Parameters	Specifications
Engine type	4 strok esingle cylinder
Displacement	159.7cc
Bore	62mm
Stroke	52.9mm
Compression ratio	9.5:1
Maximum power	15.2bhp at 8500rpm
Maximum torque	13.1nm at 4000rpm
Battery capacity	12v-9a

TABLE 1 explains the engine specification of the bike used to produce the results of superchargerfitted with the carburettor of the injection system.

TABLE 2 Supercharger Specification

Parameters	Specification
Product style	Round tapered, universal air filter
Flange inside diameter	5.5 in(140mm)
Flange length	1 in (26mm)
Flange type	Center
Base outside diameter	7 in(180mm)

TABLE 2 shows the supercharger configuration that is attached to the carburettor.

Carburettor Design:

FIGURE 1 views of carburetor

The carburetor design is given above which was designed using SOLIDWORKS 2018. Basically, The working of carburetor is to mix both air and fuel in internal combustion engines. The intake of carburetor is air and fuel, the air here is forced by the supercharger with high volume and so the powerof engine gets increased.

Design Of Supercharger

FIGURE 2 Supercharger

The above design of supercharger is also designed by SOLIDWORKS 2018. This is nothing but an air compressor which increases the air density supplied to carburetor. Result is increase in power.

Assembly and Experimental Setup

FIGURE 3. Assembly of Supercharger and Carburetor

The diagram shows that the both supercharger and the carburetor are assembled using SOLIDWORKS2018. This is driven by the engine power itself. The output power of supercharger is delivered through a pulley and a belt. This can be used where there is necessity of quick and instant delivery of power without any lag.

FIGURE 4. Experimental Setup

The above image is the experimental setup of the supercharger fitted to the carburetor of the bike. Thereadings are noted and further calculations are done accordingly.

MECHANICAL LOADING

Rope Brake

The rope is a basic system for an engine's bp calculation. It consists of a number of rope wound turnsconnected to the output shaft around the revolving drum. One side of the rope is linked to a spring balance and also the other to a loading system. The strength is absorbed by friction between the rope and also the drum. Thus, the drum needs cooling. However, due to changes in the friction coefficient ofthe rope with temperature, the rope brake is inexpensive and simple to produce, not a very precise technique

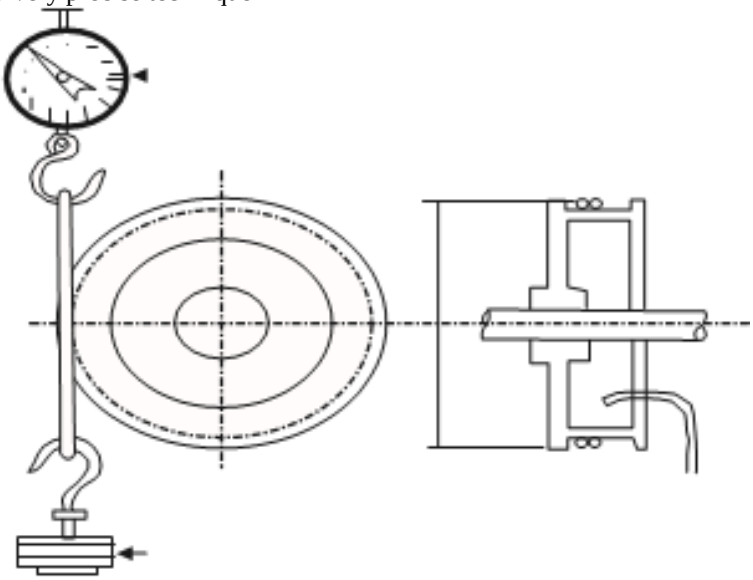

FIGURE 5. Rope brake

Observation

TABLE 3. Observation Table

Characteristics	Results
Specific gravity of fuel	0.754
Calorific value of fuel	47,693kJ/kg
Brake power	15.2BHP (11.34KW)
Cylinder area	3.02 * 10-3m2
Maximum load	5.63kg

TABLE 3 explains the engine oil characteristics, brake power of the engine and the maximum loadapplied to the engine through rope brake.

Calculation Of Friction Power

Williamson Line Method

This approach is also referred to as the extrapolation phase of the fuel rate. A graph of fuel consumption (vertical axis) versus brake power (horizontal axis) is drawn in this drawing and measured on the negative axis of braking power. The negative axis intercept is the friction force of the engine at that rpm. As shown in the figure, in most of the power range, the relationship between fuel consumption and brake power is linear when engine speed is held constant and this creates extrapolation. In addition, if the engine does not develop power, that is, brake power = zero, it consumes a certain amount of fuel. This power was expended on overcoming the friction in the fuel.

The calculated negative intercept of the horizontal axis is therefore the work that describes theaccumulated losses as a consequence of friction, pumping, and is called the frictional loss of theengine as a whole. This measurement technique of friction strength can only be good for a certain speed and is mainly applicable to compression ignition engines. The major downside of this approach is that the long distance to be extrapolated from data between the weight of five and forty to the fuel input zero rows. The error directional margin is very large since the graph is not exactly linear.

RESULTS AND DISCUSSION

Gear 1(Brake Power Vs Input Power with and without Supercharger)

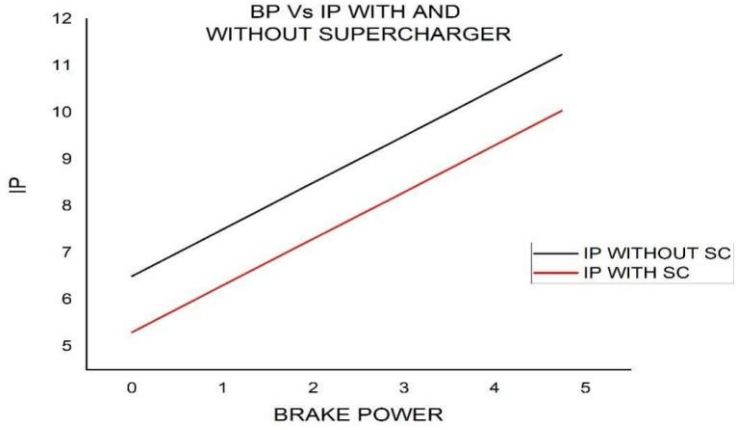

FIGURE 6. BP Vs IP with and without supercharger for gear 1

The Figure 6 is the comparison of engine with and without supercharger with respect to Brake power and Input power in Gear 1. In gear 1 there is 18% decrease in input power when compared with valuesof without supercharger.

Gear2 (Brake Power Vs Input Power with and without Supercharger)

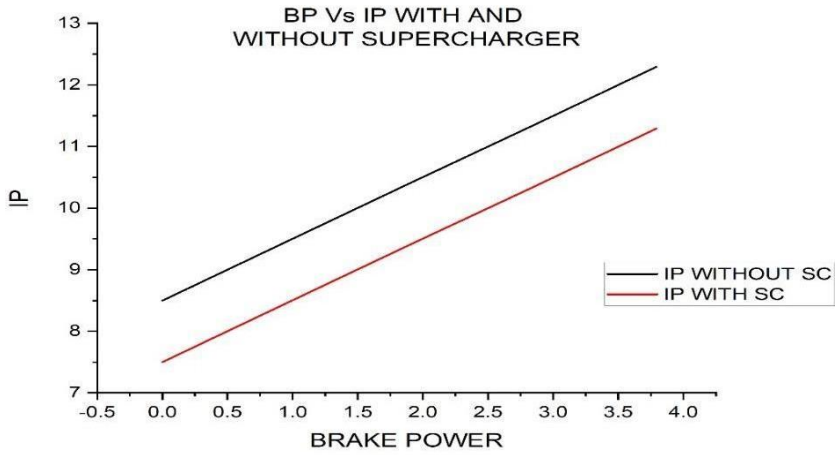

FIGURE 7 BP Vs IP with and without supercharger for gear 2

FIGURE 7 is the comparison of engine with and without supercharger with respect to Brake power and Input power in Gear 2. In gear 2 there is 12% decrease in input power when compared with valuesof without supercharger.

Gear 1 (Brake Power Vs Mechanical Efficiency With and without Supercharger)

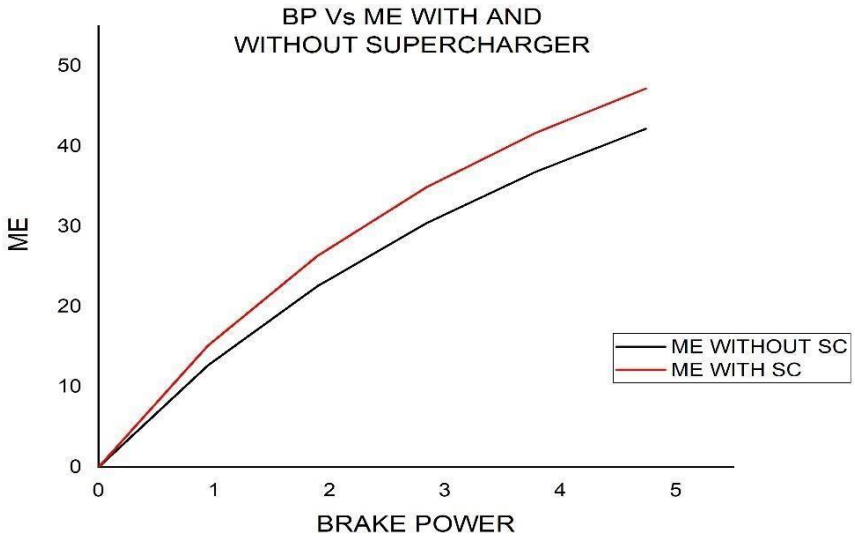

FIGURE 8 Brake power vs mechanical efficiency with and without supercharger for gear 1

FIGURE 8 is the comparison of engine with or without supercharger with respect to Brake power andMechanical Efficiency in gear 1. In gear 1, we can easily identify from the above graph that the

mechanical efficiency with supercharger is higher than the mechanical efficiency without superchargerof about 5% difference.

Gear2(Brake Power Vs Mechanical Efficiency with and without Supercharger)

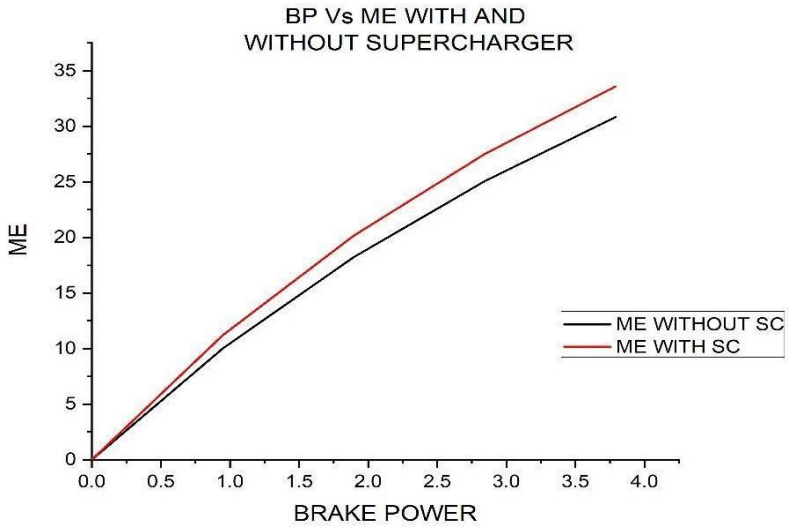

FIGURE 9. brake power vs mechanical efficiency with and without supercharger for gear 2

The Figure 9 is the comparison of engine with or without supercharger with respect to Brake power and Mechanical Efficiency in gear 2. In gear 2, we can easily identify from the above graph that the mechanical efficiency with supercharger is higher than the mechanical efficiency without superchargerof about 3% difference.

Gear 1(Brake Power Vs Specific Fuel Consumption with and without Supercharger)

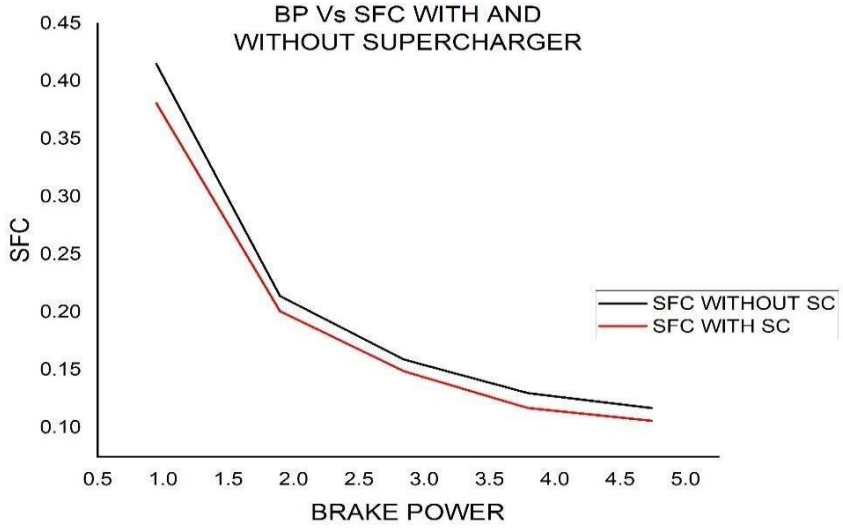

FIGURE 10 Brake power vs sfc with and without supercharger for gear 1

The Figure 10 is the comparison of engine with and without supercharger with respect to Brake power and specific fuel consumption in Gear 1. In gear 1 there is 6% decrease in specific fuel consumption when compared with values of without supercharger.

Gear 2 (Brake Power Vs Specific Fuel Consumption With And WithoutSupercharger)

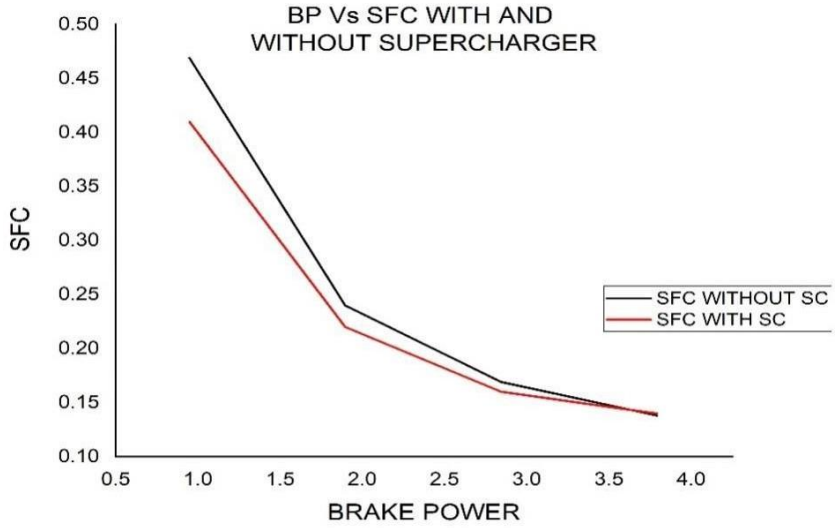

FIGURE 11. brake power vs sfc with and without supercharger for gear 2

The Figure 11 is the comparison of engine with and without supercharger with respect to Brake power and specific fuel consumption in Gear 2. In gear 2 there is 4% decrease in specific fuel consumption when compared with values of without supercharger.

Gear 1 (Brake Power Vs Brake Thermal Efficiency with and WithoutSupercharger)

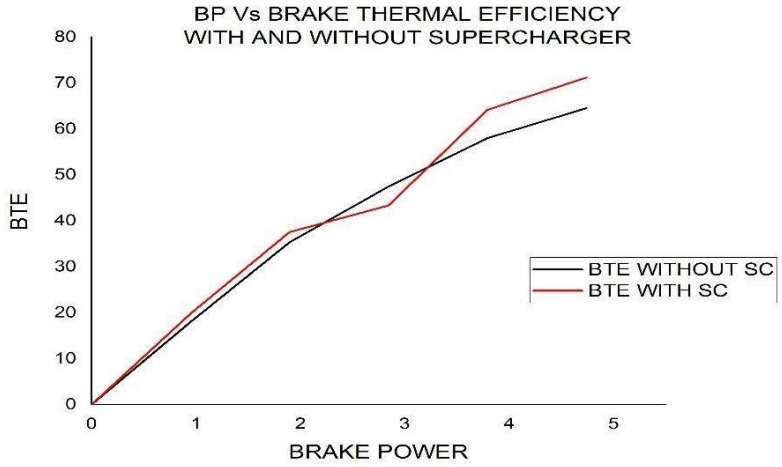

FIGURE 12. brake power vs brake thermal efficiency with and without supercharger for gear 1

The Figure 12 is the comparison of engine with and without supercharger with respect to Brake power and specific fuel consumption in Gear 1. In gear 1 there is 6% increase in brake thermal efficiency when compared with values of without supercharger.

Gear 2 (Brake Power Vs Brake Thermal Efficiency with And WithoutSupercharger)

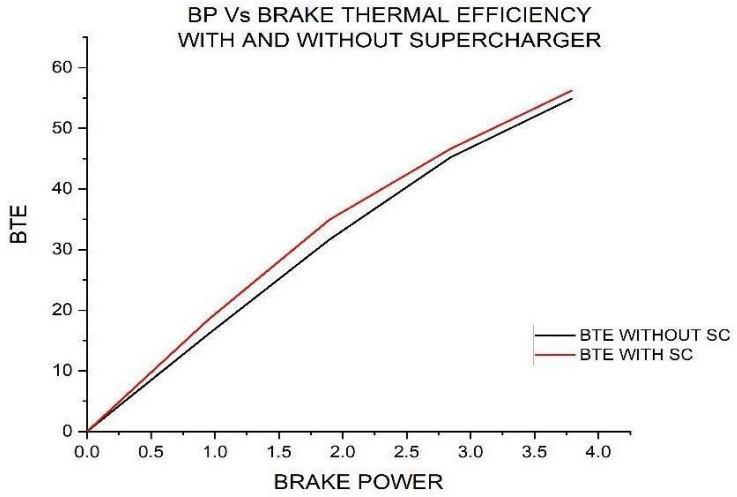

FIGURE 13. brake power vs brake thermal efficiency with and without supercharger for gear 2

The Figure 13 is the comparison of engine with and without supercharger with respect to Brake power and specific fuel consumption in Gear 2. In gear 2 there is 2% increase in brake thermal efficiencywhen compared with values of without supercharger.

In India, the most of the places are in heavy traffic due to high population growth. We have consideredonly two gears because the most of them drive in first two gears due to the heavy traffic conditions.

Merits

There is no lag time due to increased compression rate produced by the supercharger. Increased horse power is obtained by adapting to the supercharger technique. High combustion of fuel at low fuel consumption provides more power even in low rpm. Moreover, the setup is easily installed.

Demerits

Since we use the electric supercharger the connections must be given properly otherwise the supercharger will not run. We can overcome the demerits by running the pump using brake power of engine

CONCLUSION

By adapting to supercharger, the performance characteristics have improved widely. The following observations are obtained by installing supercharger to the injection system:

- The mechanical efficiency has increased 5% and 3% in gear 1 and 2.
- Brake thermal efficiency has improved 6% and 2% for the gears 1 and 2 respectively.
- The indicated power for the same load has been reduced in gears 1 and 2 by 18% and 12%using the supercharger.
- Fuel consumption in gears 1 and 2 with the supercharger has given 6% and 4% reduction.
- Since supercharger is attached to the carburetor, combustion of fuel is greatly maximizedwhich gives higher economy.

Thus, the project has allowed us to find a better way run two-wheeler with improved overall efficiency.

REFERENCE

1. AhirNischal A, Sofia Ali A, Darshan S Shah, Sneh R Prajapati (March 2017) "Fabrication of Turbocharger for Two-Wheeler", *International Journal of Scientific Research in Engineering (IJSRE) Vol.1(3).*
2. Mohammed Israr, AmitTiwari, Mahendra Labana, Anshul Gangele(March 2015) "Performance Analysis And Fabrication on a Turbocharger in Two Stroke Single Cylinder Petrol Engine,IJETI *International Journal of Engineering and Technology Innovations,Vol.2.*
3. B.Jnana Deepak, N Krishna Priya, B Revanth, K S Jaya Prakash,BHemanth Kumar(2014),"Fabrication And Performance Test of Turbocharger for Two Wheeler", *International Journal of Mechanical Engineering and Robotics.*
4. AlokGhud, KetanDeshpande, NileshBelokar(July 2013) "Detachable Supercharger Kit for Two Wheeler", *International Journal of Engineering Research and Technology.*
5. P Balashanmugam, E Elakiya, Sunayana Sharma (November 2013) "Performance Analysis on a Turbocharged Two Wheeler Engine" *International Journal of Engineering and Science and Technology, (Vol.2).*
6. T Prakash, G Arun Kumar, S Arun Kumar, R Manoj Kumar, M G Midhun(2016) "Fabrication of Supercharger in Two Wheeler Engine",*IJARIE-SSN(O).*
7. Prashanth.N.Pakale, S U Patel, "Performance Analysis Of IC Engines Using Supercharger and Turbocharger",*IJRET.*
8. N R Karthik, B Gowtham (September 2016), "A Review on Turbocharger and Supercharger", *International Journal of Engineering Trends in Engineering and Development,Vol(5).*
9. A Kusztelan, Y F Yao, D R Merchant, Y Wang "A Review of Novel Turbocharger Concepts or Enhancements in Energy Efficiency", International Journal of Thermal and Environmental Engineering,vol(2)
10. B Jnana Deepak, N Krishna Priya, B Revanth, K S Jaya Prakash, and B Hemanth Kumar "Fabrication and performance test of turbocharger for two wheeler"
11. MohdMuqeem and Dr. Manoj Kumar, "Turbocharging of IC engine."
12. YogeshGaikwad, RohitJadhav, Abhishek Shinde, Pradeep Mane, Sager patil "Fabrication and implimentation of tuebocharger on two stroke vehicle."
13. ViditSaxena, Shivpratap Singh Hada and Sourabh Jain "Analysis of supercharger and turbocharger using ethanol gasoline blend."

RESEARCH ARTICLE | MAY 22 2023

Mechanical testing of coconut sheath fibre reinforced polymer composite in effect to various treatments with alkaline solutions

G. Manikandan ✉; P. Senthil Kumar; N. Dhavaneeswaran; R. Vinothini; R. K. Yokesvaran; M. R. Harish Kumar; M. Srikanth

AIP Conference Proceedings 2492, 040068 (2023)
https://doi.org/10.1063/5.0113219

Mechanical Testing of Coconut Sheath Fibre Reinforced Polymer Composite in Effect to Various Treatments with Alkaline Solutions

G. Manikandan[1 a)], P. Senthil Kumar[1], N. Dhavaneeswaran[2], R. Vinothini[2], R.K. Yokesvaran[2], M.R. Harish Kumar[2], M. Srikanth[3]

[1] *Department of Automobile Engineering, Kongu EngineeringCollege, Perundurai, Tamil Nadu, India.*
[2] *Department of Automobile Engineering, Kongu Engineering College,Perundurai, Tamil Nadu, India.*
[3]*Department of Aeronautical Engineering, MLR Institute of Technology, Hyderabad, India*

[a)] Corresponding author: manikandan.auto@kongu.edu

Abstract. Regular fiber strengthened polymer composites have arisen as a potential ecofriendly and financially savvy option in contrast to engineered fiber fortified composites. Over the previous decade, huge uses of characteristic fiber composites are utilized in significant ventures, like the development, bundling and car enterprises have shown an extensive interest in the advancement of new regular fiber fortified composite materials. The accessibility of normal fiber and the simplicity of assembling have enticed to consider the attainability of their application as fortification. Thus, the work towards is to study the mechanical properties of fiber made from coconut sheath and it is tested for tensile, flexural, impact and compressive load behaviors for the application in automotive bumpers. The Fiber Reinforced Polymer (FRP) composite was manufactured by hand layup technique after the NaOH solution treatment of coconut tree sheath. The manufactured samples are finished and tested according to the ASTM standards. The results obtained are compared with conventional materials (thermoplastic olefins, polyesters and polyurethanes) and found be greater than these materials. Thus the usage of coconut sheath fiber reinforced epoxy composite in automotive parts will be ecofriendly to the environment.

INTRODUCTION

It is clearly found that the characteristics of composite material rely on the fiber content, loading and orientation of the fiber. Pure epoxy resin has moderate wear resistance and impact strength. Natural fibers are added with the epoxy resin considerably enhances the tensile, compressive, impact properties. Tensile, compressive, wear resistance and impact strength differ as fiber functions and fibertreatment. The reason for treating fibers with NaOH solution i.e., improves fiber bonding with epoxy matrix. The characteristics like impact and tensile strength of coconut sheath fibers in epoxy matrix is comparatively good than other natural fiber. Hence the reinforcement of coconut sheath fibers is used in our project to get improved mechanical properties of the material.

FIBRE DESCRIPTION

The coconut sheath fibers (figure 1) are available plenty from Tamil Nadu and Kerala. These fibers areextracted by either by hand picking or mechanical cutting. The filaments were cleaned with water in the wake of splashing for 30 minutes. The strands were additionally dried in regular daylight to eliminate dampness content and long uniform filaments were acquired. Table 1 shows the propertiesof coconut sheath fiber. Coconut sheath filaments are effectively realistic in fiber and texture structures with great warm and mechanical properties among various normal strands. The inherent properties of coconut sheath fiber like low thickness, low lengthening at break, high pliable modulus, its particular solidness and strength similar to glass fiber.

Advancements in Aeromechanical Materials for Manufacturing: ICAAMM-2021
AIP Conf. Proc. 2492, 040068-1–040068-8; https://doi.org/10.1063/5.0113219
Published by AIP Publishing. 978-0-7354-4438-6/$30.00

FIGURE 1. Coconut Tree, Coconut Sheath Fiber

TABLE 1. Properties of Coconut Sheath Fiber

Properties (physical & mechanical)	Coconut sheath(experimental data)
Wax content (%)	0.41
Cellulose content (%)	68.36
Lignin content (%)	20.63
Moisture content (%)	8.79
Ash content (%)	1.04
Maximum stress (MPa)	119.8 – 128.6
Young's modulus (GPa)	7 – 18
Elongation (%) at break	5.5 – 6.8

PREPARATION PROCESS

Preparation of fibers and matrix

The coconut sheath fibers are cut at 19 cm × 19 cm (l×b) and it is used as reinforcement. For each sample of composite 3 layers of coconut sheath is used as reinforcement. Totally 3 samples of composite are made. Out of those samples first one is dry sample which consists of only coconutsheath layers, the second sample is treated with 2% NaOH and the third sample is treated with 4% NaOH. The coconut sheath fibers are immersed in NaOH for 10 to 15 minutes and then taken. The coconut sheath fiber samples are shown in the figures below.

FIGURE 2. Raw Coconut Sheath

FIGURE 3. 2% NaOH Treated Sheath

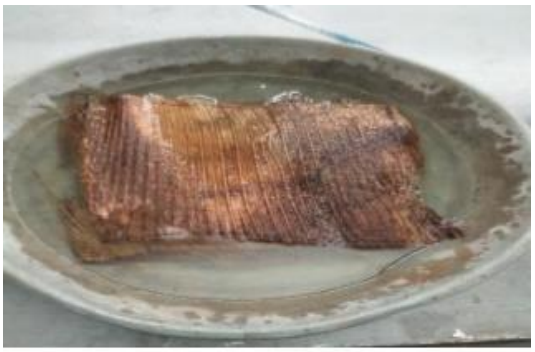

Figure 4. 4% NaOH Treated Sheath

Composite Preparation

In this, the composites are created by utilizing epoxy resin as a grid and coconut sheath fiber as a fortification material. Absolutely 3 examples were set up in various organizations to consider the mechanical properties of the coconut sheath fiber strengthened epoxy composites. The composite material was set up by customary hand lay-up method in mellow steel shape (75 mm × 75 mm × 10 mm) at room temperature. The form is extraordinarily intended to create 10 mm thickness plate. Here7 mm thickness composite example is readied. Epoxy resin LY 556 and hardener HY 951 wereutilized as the network materials. Figure 5 shows the resin and the hardener utilized. The pitch and hardener were blended and mixed precisely in a proportion of 10:1 by weight. The layup composite creation procedure is utilized and stacked layers one over the other is kept. Absolutely 3 layers of coconut sheath is kept and afterward, the resins were filled the shape and shut firmly. The materialwas permitted to fix in room temperature for around 10 to 12 hours. The test examples were set up according to ASTM guidelines. Figure 5. shows the example subsequent to cooling in the room temperature.

FIGURE 5. Composite Specimen

Preparation of Specimen According to Standards of ASTM

The examples are sliced to the accompanying measurements according to ASTM principles appearedin figure 6.

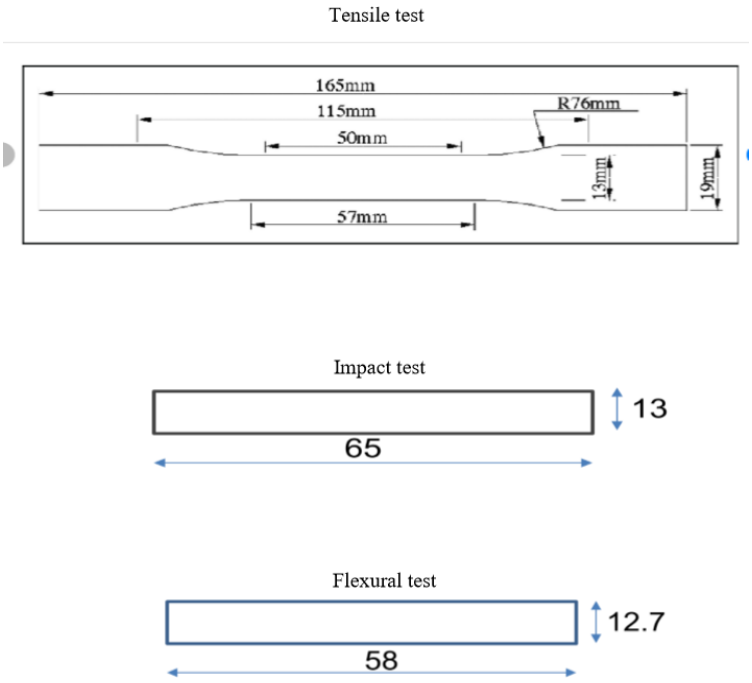

FIGURE 6. ASTM Standard Dimensions for Testing

SPECIFICATIONS OF SAMPLES

1.MATRIX	-	**Epoxy resin**
2.REINFORCEMENT	-	**Coconut sheath fiber**
3.VOLUME FRACTION	-	
Sample 1 - **Dry coconut sheath fiber**		
Sample 2 - **2% NaOH treated fiber**		
Sample 3 - **4% NaOH treated fiber**		
4.PATTERN TYPE	-	**Vertical orientation**
5.PROCESS METHOD	-	**Hand lay-up**

Figure 7. Specification of samples

TESTING

Impact Testing

An Izod impact testing was performed to research the effect strength of the overlays utilizing an effect analyzer as per ASTM D256 norms with an example size of 65×13×7 mm3. Six indistinguishable examples were analyzed under every classification, and the normal qualities were accounted for. The consumed energy during impact is the measure of energy needed to crack the example totally. The examples recorded in the creation table are exposed to Izod impact test according to ASTM D256 guidelines. The determinations of the machine utilized for impact testing is given in the table 2.

Table 2. Specification of Impact Testing Machine

System status	Digital
Span length of charpy vice	Adjustable from 40 mm to 100 mm
Impact speed	3.46 m/s
scales	2 J, 5 J, 10 J, 15 J, 25 J
Results expressed in terms	J/mm
Hammers	Two hammers for Izod test

The impact strength graphs for the samples are shown in the above figures. The average impact strength is obtained from those graphs and finally the impact strength for dry sample, 2% NaOH sample and 4% NaOH samples have been plotted in the figure 8.

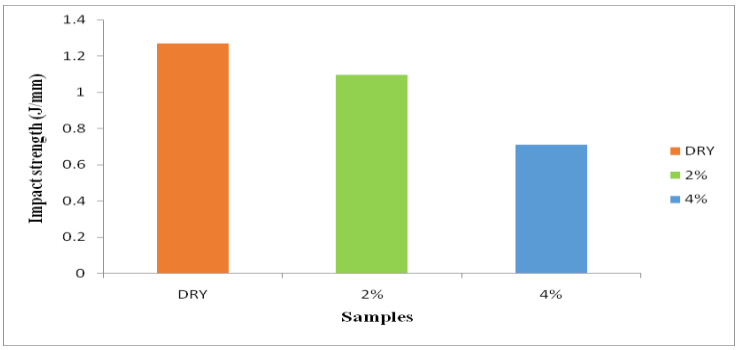

FIGURE 8. Impact Strength (J/Mm)

From the bar chart, it is inferred that 4% NaOH treated sample has very low impact strength when compared to remaining samples. The 2% NaOH treated sample and 4% NaOH treated sample exhibit 1.097 J/mm and 0.709 J/mm respectively. Pure dry coconut sheath fiber reinforced epoxy composite exhibited higher impact strength 1.269 J/mm. It was discovered that from the figure, there was abrupt drop in the effect strength because of expansion of NaOH in the composites. This shows that by expansion of NaOH, de-holding happens and the effect strength lessens. All the examples are contrasted and surmised and each other based on effect strength acquired. Accordingly, from the inference obviously the expansion of NaOH to the coconut sheath fiber strengthened epoxy composite diminishes the effect strength.

Tensile Testing

TABLE 3. Specification of Universal Testing Machine (Tensile)

Capacity	10 kN
Maximum cross head travel	1100 mm
Testing speed range	0.001 to 1000 mm/min
Maximum cross head speed	500 mm/min
Jog speed	0.001 to 1000 mm/min
Return speed	0.001 to 750 mm/min
Dimension (H × W × D)	1600 mm × 650mm × 450 mm

The tensile strength graphs for the samples are shown in the above figures. The tensile properties of composites for the most part rely upon the weaving idea of the texture, the layering design, the thickness, and the fiber/lattice grip. The average tensile strength is obtained from those graphs and finally the tensile strength for dry sample, 2% NaOH sample and 4% NaOH samples have been plotted in the figure 9.

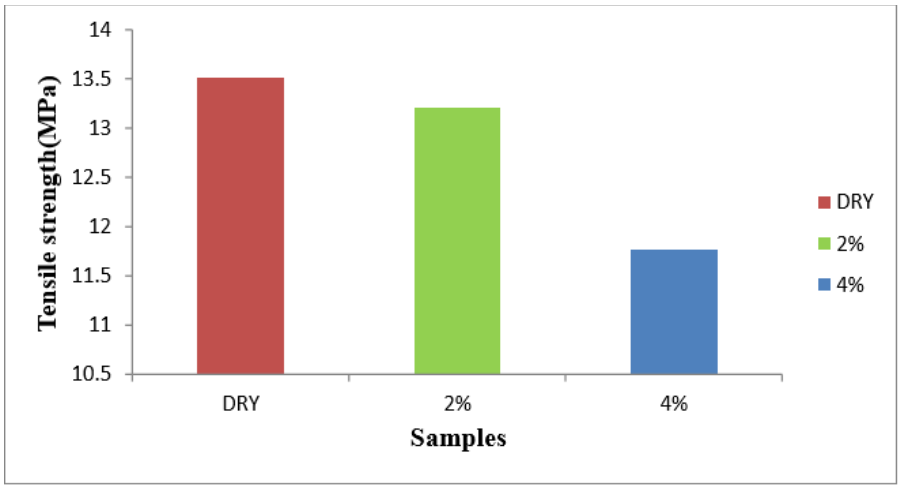

FIGURE 9. Tensile Strength (Mpa)

From the bar chart, it is inferred that 4% NaOH treated sample has very low tensile strength when compared to remaining samples. The 2% NaOH treated sample and 4% NaOH treated sample exhibit

13.21 MPa and 11.76 MPa respectively. Pure dry coconut sheath fiber reinforced epoxy composite exhibits higher tensile strength of about 13.51 MPa. It was discovered that from the figure, there was unexpected drop in the effect strength because of expansion of NaOH in the composites. This shows that by expansion of NaOH, bond property of fiber misfortunes and the elasticity diminishes. Accordingly, from the inference unmistakably the expansion of NaOH to the coconut sheath fiber strengthened epoxy composite diminishes the rigidity.

Flexural Test

Table 4. Specification of Universal Testing Machine (Flexural)

Capacity	10 kN
Maximum cross head travel	1100 mm
Testing speed range	0.001 to 1000 mm/min
Maximum cross head speed	500 mm/min
Jog speed	0.001 to 1000 mm/min
Return speed	0.001 to 750 mm/min
Dimension (H × W × D)	1600 mm × 650mm × 450 mm

The flexural strength graphs for the samples are shown in the above figures. The average flexural strength is obtained from those graphs and finally the flexural strength for dry sample, 2% NaOH sample and 4% NaOH samples have been plotted in the figure 10.

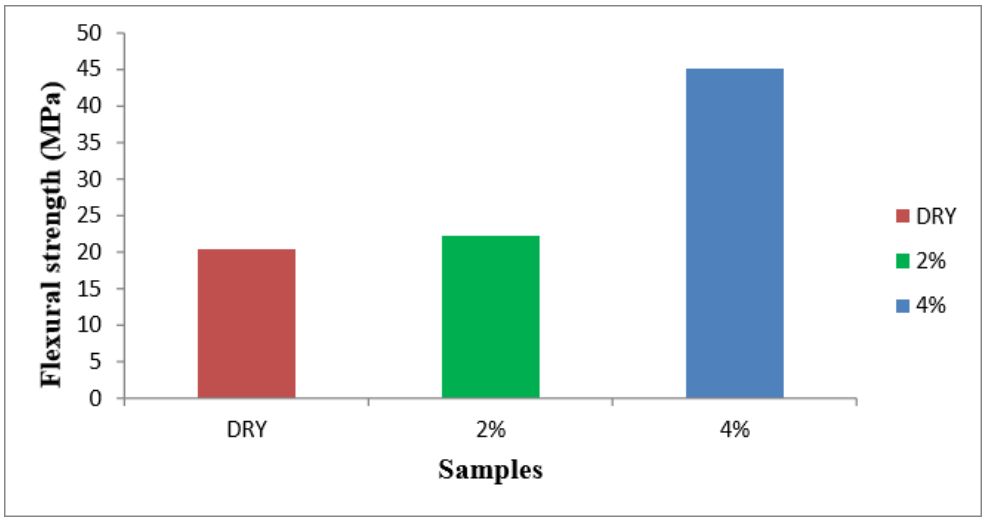

FIGURE 10. Flexural Strength (Mpa)

From the bar chart, it is inferred that 4% NaOH treated sample has very high flexural strength when compared to remaining samples. The 2% NaOH treated sample and dry sample exhibit 22.21 MPa and

20.35 MPa respectively. The 4% NaOH treated coconut sheath fiber reinforced epoxy composite exhibits higher flexural strength of about 45.07 MPa. Due to both tension and compression stresses acting on a bending specimen, it was found that both dry and 2% NaOH treated composite specimens were failed due to de-lamination. The flexural strength of composite plate specimen (4% NaOH) treated has better strength compare to other plates.

CONCLUSION

Fiber treatments were vital factor to fabricate common fiber composites since it can improve the flexural properties indeed by making great interfacial holding among strands and network. This implies that entomb surface assumes a predominant part in flexural and holding properties in a composite. The maximum value of impact strength is 1.269 J/mm which is identified in dry sample, the maximum value of tensile strength is 13.51 MPa which is exhibited in dry sample, the maximum value of flexural strength is 45.07 MPa which is exhibited in 4% NaOH treated sample. It is seen that the mechanical conduct of the composites for example, elasticity, and bowing strength of the composites are vitally biased by the treatment of NaOH to the fibers. The comparison with other material shows that coconut sheath fiber composites can be used as a replacement for automotive components.

REFERENCES

1. Naresinajan.M.P, Rajmohan.B, Devarajulu.S, “Effect of ingredients on mechanical and tribological characteristics of different Brake Liner Materials”. International Journal of Mechanical Engineering and Robotic research, IJMERR, ISSN 2278 – 0149.
2. Marimuthu.K.P, Kumar.S.M and Govindaraju, “Characterization of Mechanical Properties ofEpoxy Reinforced with Glass Fiber and Coconut Fiber”. Materials Today: Proceedings, Pg. (661-667)
3. Sinha.A.K, Narang.H.K and Bhattacharya.S, “Mechanical properties of natural fibre polymer composites”. Journal of Polymer Engineering, Pg. (879-895), 2017.
4. Zhezhen, Shicheng et al., “Jute fibers and powderized hazle nut shells as natural fibers innon-asbestos organic non-metallic friction composites”. Sciverse science direct – material and design, Pg. (847-853), 2013.
5. Albert.Y.M.L, Marc.A.M and Kenneth.S.V, “Mechanical properties and structure of Strombus gigas, Tridacna gigas, and Haliotis rufescens sea shells a comparative study”. Journal of Materials Science and Engineering, pg. (1380 – 1389), 2006.
6. C.W.Chin, B.F.Yousif et al., “Potential of kenaf fibers as reinforcement for tribological applications. Science direct – Wear, Pg. (1550-1557), 2009.

7. Siva Sravanan. S, V.K.Bupesh Raja et al., “Impact characterization of epoxy LY 556/ EGlassfiber Nano clay hybrid nano composite materials. Science direct, Procedia Engineering, Pg. (968-974), 2014.
8. Akhil. A.B et al., “Preparation and characterization of banana reinforced phenol formaldehyde composite”. Journal of Materials Science and Engineering, pg. 1380 – 1389, 2006.

RESEARCH ARTICLE | MAY 22 2023

Comparison of flow analysis over different wings

Linga Mallu D.; Syed Khader Basha; Bhoopal Reddy D.; Ravi T.; Swetha Bala M. N. V. S.

AIP Conference Proceedings 2492, 020003 (2023)
https://doi.org/10.1063/5.0113347

Comparison of Flow Analysis over Different Wings

Linga Mallu D[1], Syed Khader Basha[1], Bhoopal Reddy D[1] and Ravi T[1] and Swetha Bala MNVS[1, a)]

[1]*Department of Aeronautical Engineering, M L R Institute of Technology, Hyderabad India*

[a)] **Corresponding Author**: swethabalamlr@gmail.com

Abstract. The imperative job of the wing in lift age is reliant with wing boundaries. It has been seen that there have been changes in the wing setup throughout the long term and more often than not is spent on improvement. In this exploration, we expect to approve and improve the wing effectiveness utilizing various methodologies specifically computational, mathematical and test on various kinds of wings. Computational investigation is performed utilizing ANSYS Fluent Software, the mathematical examination is accomplished utilizing diverse addressing techniques and the exploratory examination is done utilizing wing setup testing. The outcome acquired in this examination project yield plots and qualities for CL and CD with various stream shapes. Eventually, the report made would furnish us with a superior viewpoint on the extent of advancement in different regions. Three diverse wing plans with a similar airfoil, range, and mean streamlined harmony are investigated. Different Aerodynamics attributes like lift and drag are to be inspected and thought about for these three unique wings. The three wings are rectangular, tightened, and cleared made in CATIA V5 and its investigation is done in Ansys Fluent.

Keywords. Rectangular, Tapered, Swept, Elliptical, NACA, Sweep angle

INTRODUCTION

Airplane fundamental plan is the second step in plan measure which was presented. Three not set in stone during starter plan, in particular: airplane most extreme drop weight (WTO); motor force (P), or motor push (T); and wing reference region. The third step in the plan interaction is the detail plan. During subtlety configuration, significant airplane part like wing, fuselage, level tail, vertical tail, impetus framework, landing stuff and control surfaces are planned individually. [3]Every airplane part is planned as a singular element at this progression, yet in later plan steps, they were coordinated as one framework airplane and their communications are thought of. The wing might be considered as the main part of an airplane, since a fixed-wing airplane can't fly without it. Since the wing math and its elements are affecting any remaining airplane parts; we start the detail configuration measure by wing plan. The essential capacity of the wing is to produce adequate lift power or just lift (L). Be that as it may, the wing has two different creations, to be specific drag power or drag (D) and nose-down pitching second (M). [1]While a wing architect is hoping to amplify the lift, the other two (drag and pitching second) should be limited. Indeed, wing is expected promotion a lifting surface that lift is delivered because of the tension distinction among lower and upper surfaces. Fundamentaly, the standards and approaches of "frameworks designing" are continued in the wing configuration measure. Restricting elements in the wing configuration approach, start from plan prerequisites like execution necessities, soundness and control necessities, producibility necessities, functional prerequisites, cost, and flight security. Significant execution prerequisites incorporate slow down speed, greatest speed, take-off run, reach and perseverance. Essential security and control necessities incorporate sidelong directional static strength, horizontal directional powerful soundness, and airplane controllability during likely wing slow down. [2]

The wing should deliver adequate lift while produce least drag, and least pitching second. One of the vital devices in the wing configuration measure is a streamlined procedure to compute wing lift, wing drag, and wing pitching second.Assortment of instruments and programming dependent on optimal design and mathematical techniques have been created before. The CFD Software dependent on the arrangement of Navier-Stokes' conditions, vortex grid

Advancements in Aeromechanical Materials for Manufacturing: ICAAMM-2021
AIP Conf. Proc. 2492, 020003-1–020003-8; https://doi.org/10.1063/5.0113347
Published by AIP Publishing. 978-0-7354-4438-6/$30.00

technique, flimsy air foil hypothesis, and course are accessible. Accordingly, wing boundaries will change a few times Un blends of all plan prerequisites are met.
The air foil we are utilizing is NACA 4-Digit 2412. We created air foil cross segments by bringing in the directions of NACA 2412 from airfoiltools.com to CATIA.

We created three diverse plan of wing utilizing the cross segment.

- •Rectangular wing
- •Tapered wing
- •Swept back wing

With respect to tightened and cleared wing the harmony length doesn't stay steady along the range so rather than utilizing the term harmony length we will utilize the term Mean Aerodynamic Chord. Length and Mean Aerodynamic Chord of every one of the three wings are same. Length of all the wing is 400mm and mean streamlined mean harmony is 200mm.The produced wings are investigated for lift and drag in ansys programming at 18 degree (approx.) approach. We analyzed the lift and drag qualities of three wings and confirmed it with the proposed hypothesis.

LITERATURE SURVEY

The attributes of flying birds are with the end goal that they can change their wing shape in a split second. They do it by expanding and getting their wing and tips of essential quills. Toward the finish of essential plumes, tips twist evenly just as upward, giving an opened wing planform. This is the situation for the taking off birds over lands yet not in the birds which rise above seas who have pointed sharp tips. These essential plumes with opened wingtips are thought to decrease the streamlined drag[7] was first to actually take a look at this speculation by probing genuine birds. He showed that as a general rule, these opened wing tips decreased the actuated drag.

NACA series:

The airfoil shapes created by the National Advisory Committee for Aeronautics (NACA) are called NACA airfoils. The state of the NACA airfoils is portrayed utilizing a progression of digits following "NACA". The boundaries in the mathematical code can be gone into conditions to exactly produce the cross-segment of the airfoil and compute its properties. In Four-digit NACA series, the [5]

1.First digit communicates camber in percent harmony.

2.Second digit gives area of most extreme camber situated in 10th of harmony.

3.Last two digits give thickness in percent harmony.

Air foils terminology:

Coming up next are the terms identified with airfoil terminology. [4]

- The pull (or upper) surface is normally connected with low static strain and high speed.
- The tension (or lower) surface has a higher worth of static strain when contrasted with that of the pull surface.
- The math of an airfoil is portrayed utilizing the accompanying terms.
- The point at the front of the airfoil with most extreme bend, called the main edge.
- The point at the back of the airfoil with least ebb and flow, called the following edge.

The straight line interfacing the main and the following edge, called the harmony line. The length of the harmony line is known as the harmony length. The state of the air foil is characterized by the locus of focuses, halfway between the upper and lower surfaces of the air foil, called the camber line.

PROCEDURE

Rectangular wing

The plan of the Rectangular wings starts by taking the directions of the NACA four series (0010 air foil) from air foil instruments. The Rectangular wing plan in Catia involved Single air foil in it, they being root, midspan, detachable and mixed air foil as displayed in underneath picture. The air foil is taken as for wing.

First we created a rectangular wing. For it we imported directions of air foil for harmony length 200mm from airtools.com. Then, at that point, utilizing GSD_PointSplineLoft from Excel strategy to plot every one of the focuses

and spline (joining every one of the focuses) in CATIA. After that utilizing the expel order to make 400mm wing length. Reference plane is made w.r.t a, the plane is made and the locus for the tip air foil is created. Also, math is created with spline instrument and surface from wireframe multisection.

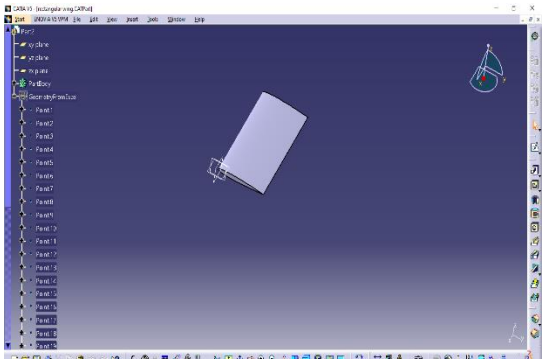

FIGURE 1. Final design view of the Rectangular wing in 3D.

The above figure in the xy and yz plane shows the components of the Rectangular wing in mm. This is picked to give better streamlined outcome for decreasing the prompted drag.

The determinations are

•Airfoil distances of wingspan is 400mm

•Airfoil distances of harmony length is 200mm

•Airfoil thickness of 10% at 30% harmony

The last 3D plan of the Rectangular wing is gotten in the Catia part utilizing multisection as displayed previously.

Tapered wing

The plan of the Tapered wing starts by taking the directions of air foil NACA four series (0010 air foil) from air foil devices. The Tapered wing plan in Catia involved single air foil in it, The Tapered wing is planned regarding wing with wingspan length. The directions are brought into the Catia programming, we imported directions of air foils for harmony length 200mm. Then, at that point, utilizing multi segment and evenness order to produce a wing of length 400mm and afterward the locus of the air foil organizes is plotted on the plane. Concerning tightened and cleared wing the harmony length doesn't stay steady along the range so rather than utilizing the term harmony length we will utilize the term Mean Aerodynamic Chord. Range and Mean Aerodynamic Chord of every one of the three wings are same. Length of all the wing is 400mm and mean streamlined mean harmony is 200mm.The produced wings are dissected for lift and drag in ansys programming at approx.: 18 degree approach. We looked at the lift and drag qualities of three wings and confirmed it with the recommended hypothesis

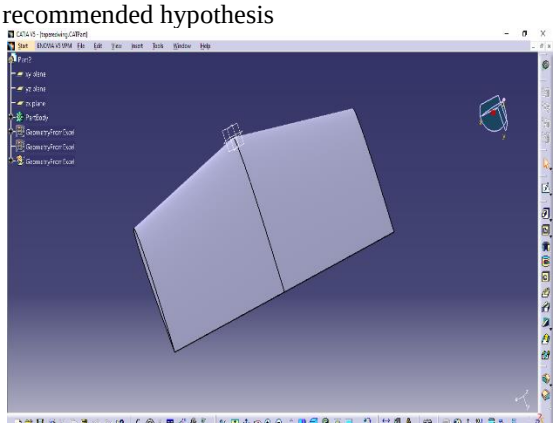

FIGURE 2. Final design view of the Tapered wing in 3D.

The above figure in the xy and yz plane shows the elements of the mixed winglet in mm. The distance of the tip harmony is 160mm and the root harmony is 200mm. This is picked to give better streamlined outcomes for lessening the actuated drag. [3]

The particulars are

- Airfoil distance of root harmony is 200mm
- Airfoil distance of tip harmony is 160mm
- Airfoil distance of wingspan is 400mm
- Airfoil distance of harmony length is 200mm

The last 3D plan of the mixed winglet is acquired in the Catia part utilizing multisection as displayed previously.

Swept wing

The plan of the cleared wing starts by taking similar directions of the NACA four series (0010 air foil) from air foil devices. The cleared wing plan in Catia involved single air foil in it, they being root, midspan, detachable and mixed air foil as displayed in beneath picture. The cleared wing is planned as for wing with wingspan 400mm.

The directions are brought into the Catia programming and for producing cleared wing rehash a similar strategy of tightened wing .Just a certain something while at the same time creating the directions of air foil for 200mm harmony length in airfoiltools.com, change the beginning %. This will prompt sideways removal of one air foil concerning other and give clear point to the wing. In this the breadth point is 18 degree (approx.).then the locus of the air foil facilitates is plotted on the plane. Spline instrument is utilized to interface the singular air foil are framed. Wireframe and surface instrument utilizing multi area alternative these singular air foil is chosen and consequently surface is produced. Reference plane is made w.r.t a, the plane is made and the locus for the tip air foil is produced. Furthermore, math is created with spline device and surface from wireframe multisection.

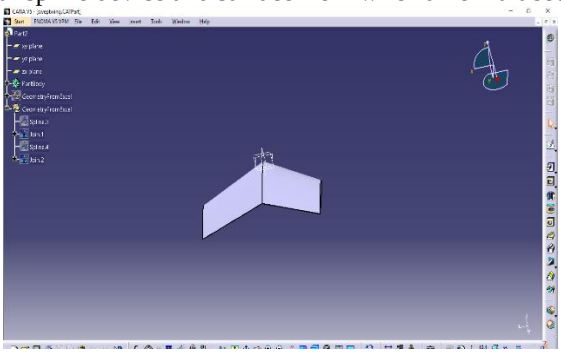

FIGURE 3. Last plan perspective on the Swept wing in 3D.

The above figure in the xy and yz plane shows the elements of the cleared wing in mm. The dispersing between the airfoils is in reverse cleared with a wingspan of 400mm. This is picked to give better streamlined outcomes for diminishing the initiated drag.

The details are

- Airfoil distance of root harmony is 200mm
- Airfoil distance of tip harmony is 160mm
- Airfoil distance of wingspan is 400mm
- Sweep point is 18 degrees (approx.)

The last 3D plan of the cleared wing is gotten in the Catia part utilizing multisession as displayed underneath.

RESULTS

The investigation was finished with 1000 emphases and limit conditions like temperature and tension are equivalent to standard ocean level conditions.

Velocity=10 m/s

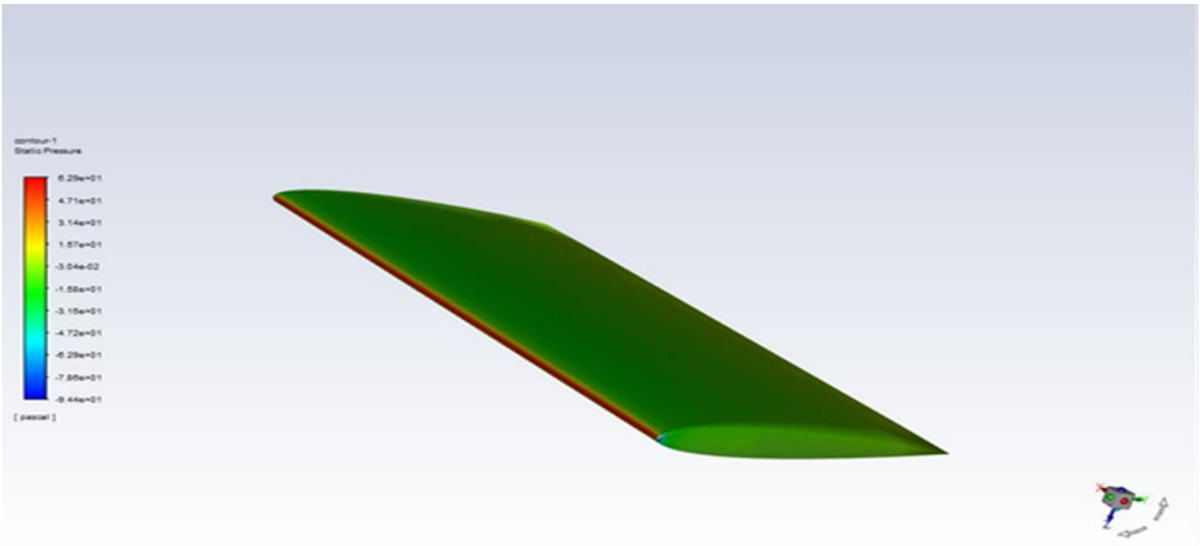

FIGURE 4. Analysis of rectangular wing

Figure 4 shows the rectangular wing planform over which the flow is analysed.

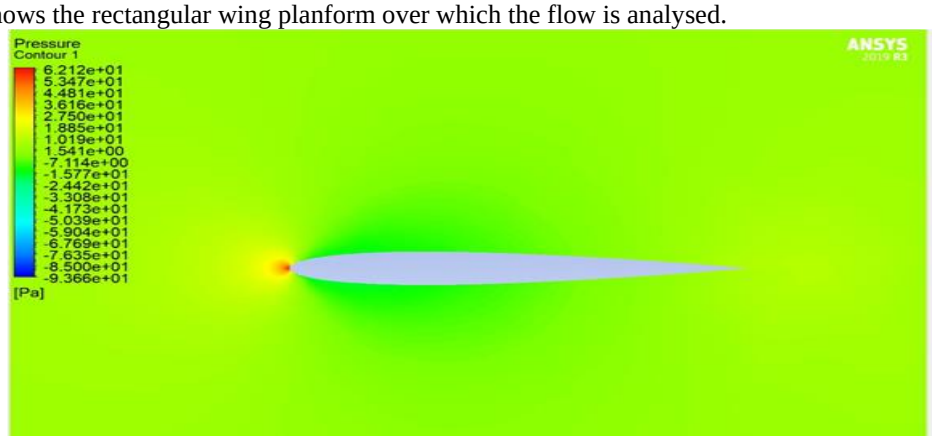

FIGURE 5. Pressure contour of rectangular wing

The pressure contours over the rectangular wing are observed in figure 5.

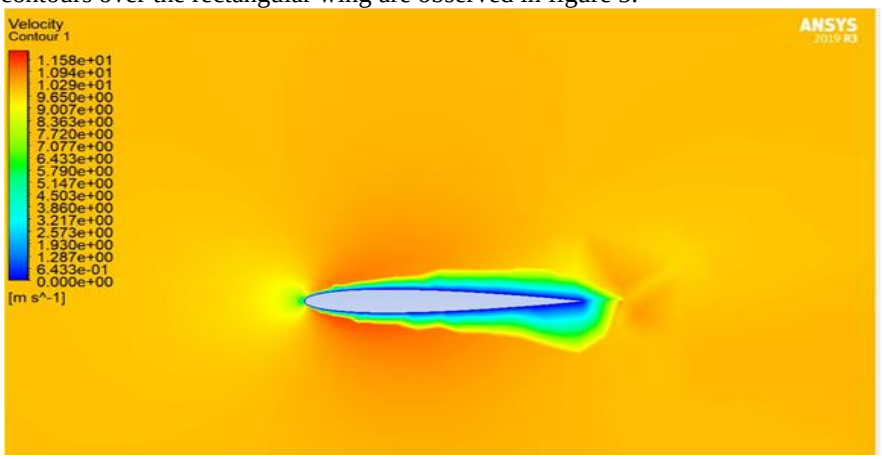

FIGURE 6. Velocity contour of rectangular wing.

The velocity contours are given in figure 6

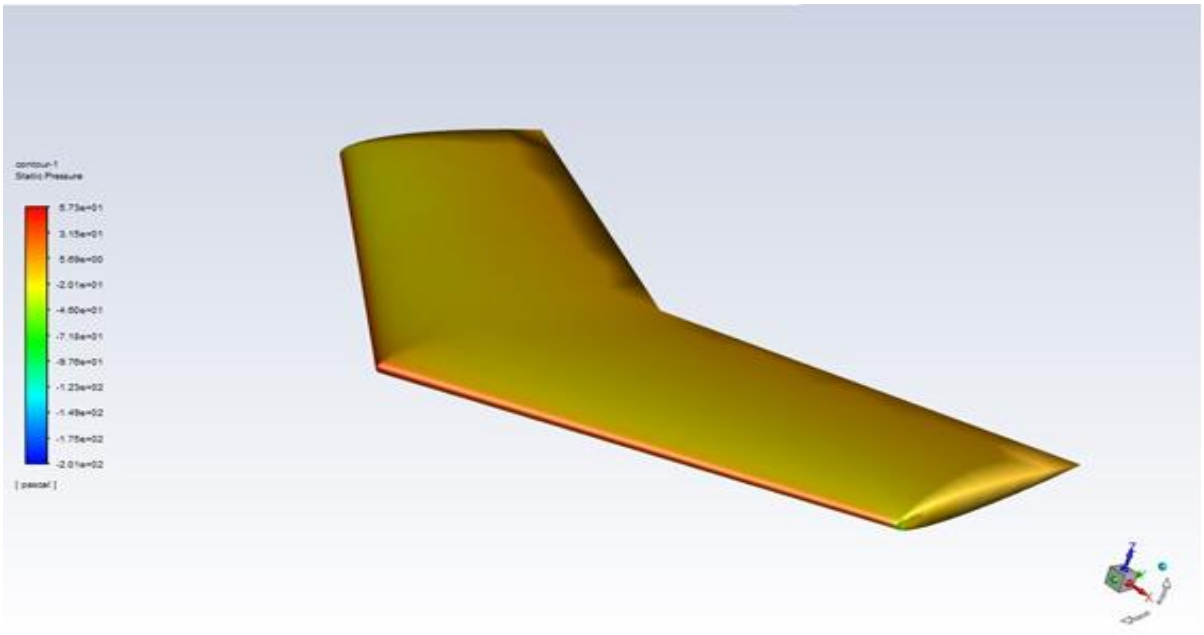

FIGURE 7. Analysis of Swept wing.

- Lift: 0.01035366
- Drag: 0.1593728

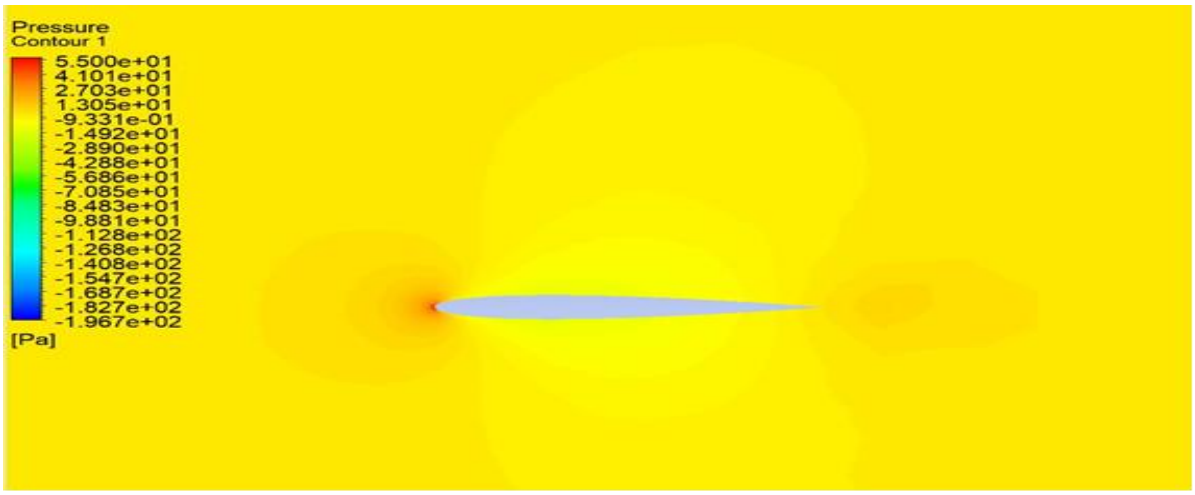

FIGURE 8. Pressure contour of swept wing.

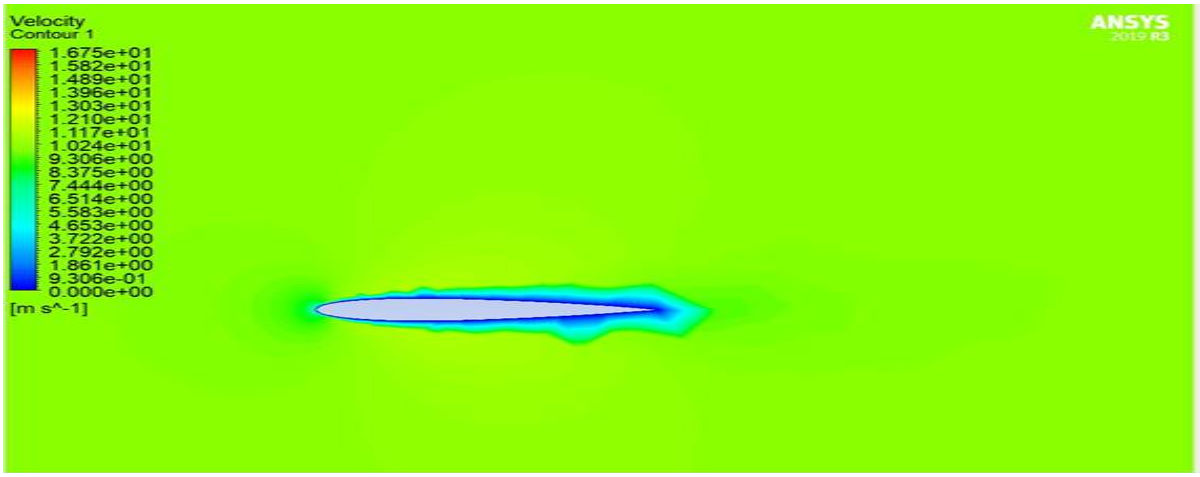

FIGURE 9. Velocity contour of swept wing.

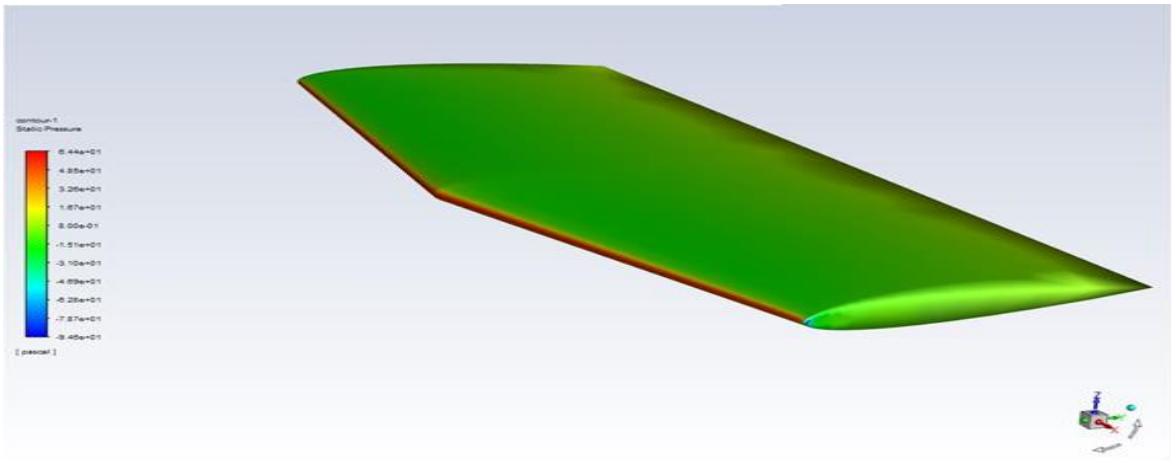

FIGURE 10. Analysis of tapered wing.

- Lift: 0.97724092
- Drag: 0.14046897

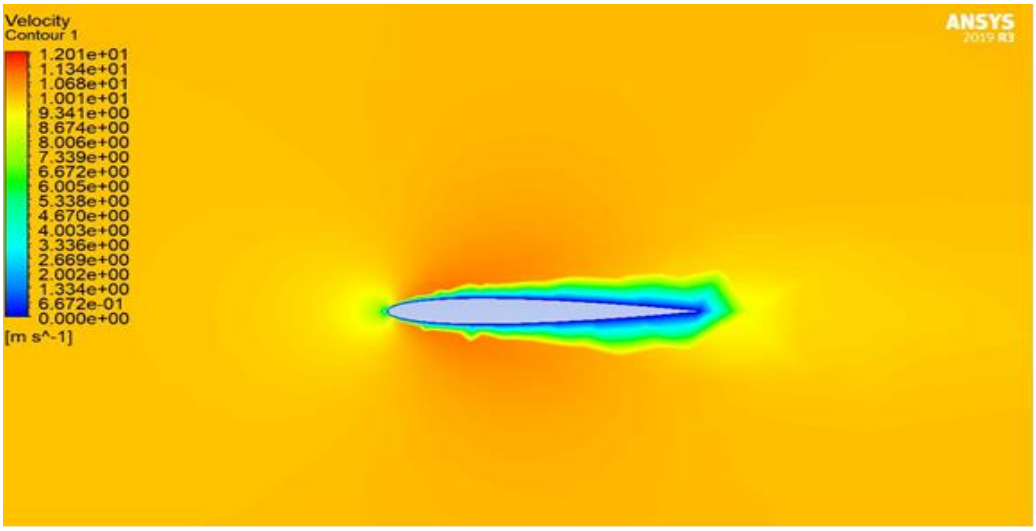

FIGURE 11. Velocity contour of tapered wing.

The outcomes are agreeing

TABLE 1: Lift and Drag values:

WINGS	LIFT(N)	DRAG(N)
RECTANGULAR	0.17300877	0.15521151
SWEPT	0.01035366	0.1593728
TAPERED	0.97724092	0.14046897

From the table 1, it is evident that the lift over a tapered wing is more when compared to that on a recatangular wing. Also, the drag over the rectangular wing is higher. The swept back wing has moderately acceptable values.

CONCLUSION

From the outcomes we got we reasoned that lift and drag are most elevated for the rectangular wing, least for cleared wing and middle for the tightened wing.

REFERENCES

1. A. Sai Kumar et al, "Design and Fabrication of 150 mm Fixed Wing MAV" in *IJST, Vol. 3 Issue 3, December 2013.*

2. A. Sai Kumar et al, "Design and Fabrication of 150 mm Fixed Wing MAV" at *ICRAMAV 2013 Conference*

3. Zubin Zaheer, K E Reby Roy, Gopakumar S Nair, Vineeth Ragipathi, U V Niranjan. "CFD analysis of the performance of different airfoils in ground effect*", Journal of Physics: Conference Series, 2019*

4. John D Anderson , "Fundamentals of Aerodynamics" . *Tata McGraw Hill Publication, Edition 2010*

5. Daniel T. Valentine "Aerodynamics for engineering" Ph.D.*, E. L. Houghton, P. W. Carpenter, Steven H. Collicott (Daniel T. Valentine, 2017)*

6. Snorri Gudmundsson General Aviation Aircraft Design: *Applied Methods and Procedures*

7. Matin Alexande Jones, "CFD Analysis and Design Optimization f Flapping Wing flows" ,Doctor of Philosophy, Disseratation submitted *toSchool of Graduate studies, North CarolinaAgricultural and Technical State University.*

RESEARCH ARTICLE | MAY 22 2023

Experimental and analytical investigation on natural composite materials

K. Arunkumar ✉; G. Sravanthi; A. Udaya Deepika; M. Srikanth

AIP Conference Proceedings 2492, 040043 (2023)
https://doi.org/10.1063/5.0113390

Experimental and Analytical Investigation on Natural Composite materials

K Arunkumar[1, a)], G Sravanthi[1], A Udaya Deepika[1] and M Srikanth[1]

[1]*Department of Aeronautical Engineering, MLR Institute of Technology, Hyderabad, India*

[a)] Corresponding author: arunkumar.samy@mlrinstitutions.ac.in

Abstract: The composite is made up of two or more materials joined together by resin forms composite material. The composite material can be formed by natural fibers or artificial fibers. The main aim is to investigate the mechanical properties of natural composite material. In the present research work banana fiber as the major fiber and coconut coir as an additional fiber to improve the mechanical properties of polymer composite using simple supported beam analysis by applying pressure of 100 N/M^2

Key words: Banana fiber, Coconut coir, Yield stress, Von mises stress, Displacement, Static strain, Static nodal stress.

INTRODUCTION

The first known usage of composite material in 3400 B.C in Egypt in which the Egyptians used wood strips were glued together to form plywood. While the first significant usage of composites in commercial aircrafts was in 1983 by Airbus in A300 and A310 fleets. Composite materials have shown more strength per unit weight than compared to metals. Composites are 70% lighter than steel. Corrosion resistance in these composite materials is higher than steel, composites tend to show non-conductive nature and are considered as super insulators. Tensile strength is defined as the maximum load that a material can support without fracture when being stretched divided by the original cross-sectional area of the material [6].

Composites are materials that are made up of two or more components that are chemically different at the macroscopic scale, have distinct interfaces, and have properties that cannot be achieved by any of the components, individual activities. Composite materials have become fundamental planning materials and are arranged and created for various applications including auto sections, flight parts [1-3]. The advancement in composite use moreover worked out as expected because of extended care concerning thing execution and extended challenge in the overall market for lightweight segments. Among all materials, composite materials replace commonly used steel and aluminium, generally with better performance. Replacing steel pieces with composite chips saves up to 60-80% of the weight of cross section, by exchanging aluminium parts 20% of the weight can be reduced [4].

Composite materials can be classified based on the matrix material (metal, ceramic, and polymer).

Metal Matrix Composite (MMC): Metal matrix composites are composed of a metallic matrix (aluminium, magnesium, iron, and cobalt, copper) and a dispersed metal phase (lead, tungsten, molybdenum).

Ceramic Matrix Composite (CMC): Ceramic matrix composites are composed of a ceramic (matrix) and embedded fibers of other ceramic material (dispersed phase).

Polymer Matrix Composite (PMC): Polymer matrix composites are composed of polymer matrices: thermoset (unsaturated polyester, epoxy) or thermoplastic (polyvinyl chloride, polystyrene) and reinforcement in the form of fibers (glass, carbon, steel, Kevlar fibers etc.) or fillers (talc, mica, CaCO3Etc.). They can further be classified into thermoset composites, thermoplastics composites and natural fiber composites.

Advancements in Aeromechanical Materials for Manufacturing: ICAAMM-2021
AIP Conf. Proc. 2492, 040043-1–040043-7; https://doi.org/10.1063/5.0113390
Published by AIP Publishing. 978-0-7354-4438-6/$30.00

FIGURE 1. Composite structure

Importance of composite materials

- Composites can be very strong, stiff and very light in weight.
- The ratios strength to weight and stiffness to weight are several times of greater than steel or aluminium
- Fatigue properties are generally better than for common engineering materials.
- Toughness is often greater too.
- Composite can be design that does not corrode like steel.

Natural fibers are obtained from the plants which are used to make composites. Generally, the fibers are long using resin and additional fiber the composite material is made. The properties of fibers are strong and stiff. The resin bounds the two types of fibers that is main fiber and additional fiber. The natural fibers can be wood and bone: wood consists of cellulose fibres in a lignin matrix and bone consists of hydroxyapatite particles in a collagen matrix

For better properties the composite materials are formed by combining two different materials, man-made composite materials, used in the aerospace and other industries, are carbon- and glass-fibre reinforced plastic (CFRP and GFRP respectively) that consist of carbon and glass fibres, both of which are stiff and strong (for their density), but brittle, in a polymer matrix, which is tough but neither particularly stiff nor strong [7]. Very simplistically, by combining materials with complementary properties in this way, a composite material with most or all of the benefits (high strength, stiffness, toughness and low density) is obtained with few or none of the weaknesses of the individual component materials [13]. Natural fibers like banana, coconut coir, sisal, jute, kneaf, hemp, ramie, flax, cotton, coir, abaka etc can be used in composite materials [10].

Nowadays there is no field of engineering without the foot-print of composite materials in some form [5].

- Aerospace applications
- Road and Rail transport applications
- Offshore accord water vehicles
- Building and other civil structures
- Chemical Industries
- Electrical, Electronics and communication applications
- Mechanical systems and machine elements
- Consumer durable products and sports applications
- Biomedical applications

DESIGN

The design is done using solid works the main fibre used is coconut coir and the banana fibre used for the additional strength. The natural fibres are abundantly available in nature which can be used in various engineering applications.

The analysis is done to evaluate the stresses and strains of the composite material using solid works.

Model

The test specimen is designed according to ASTM D3039 standards [4]. It is the most common specimen standards used to test the model. The specimen size of 250mm*50mm*10mm bar and over a span length of 100cm and a fibre composite of (coconut coir, banana fibre, epoxy and Hardener) [3].

Properties of banana fiber:

- Density = 1.12g/ cm^3

Properties of coconut coir:

- Bulk density = 0.28g/cm^3
- The composite density of two fibers is calculated, the overall density applied is = 0.66g/cm^3

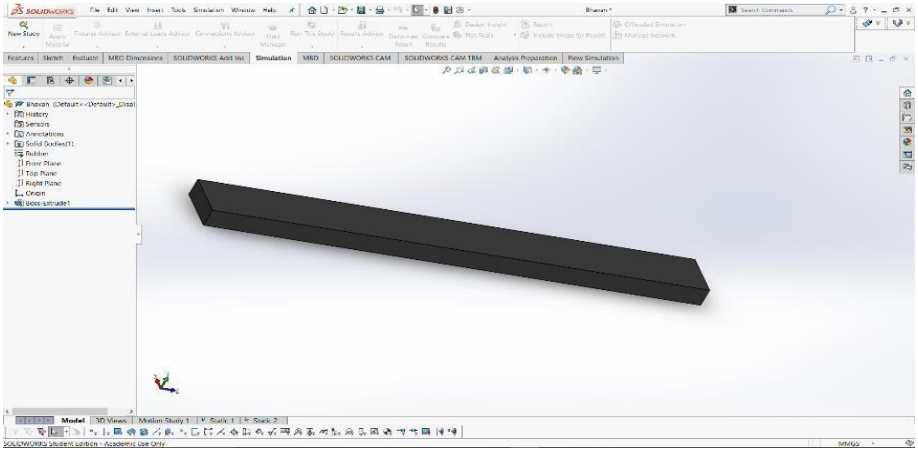

FIGURE 2. Model of composite material

Meshing

Meshing is done for the model for analyzing the beam, the approximate results are evaluated. The beam is divided into 'n' number of elements of tetrahedral structure. The stiffness matrix is calculated for tetrahedral elements, the desired results are obtained [11].

- Mesh type: Solid mesh
- Load type : Pressure Load =100N/m^2

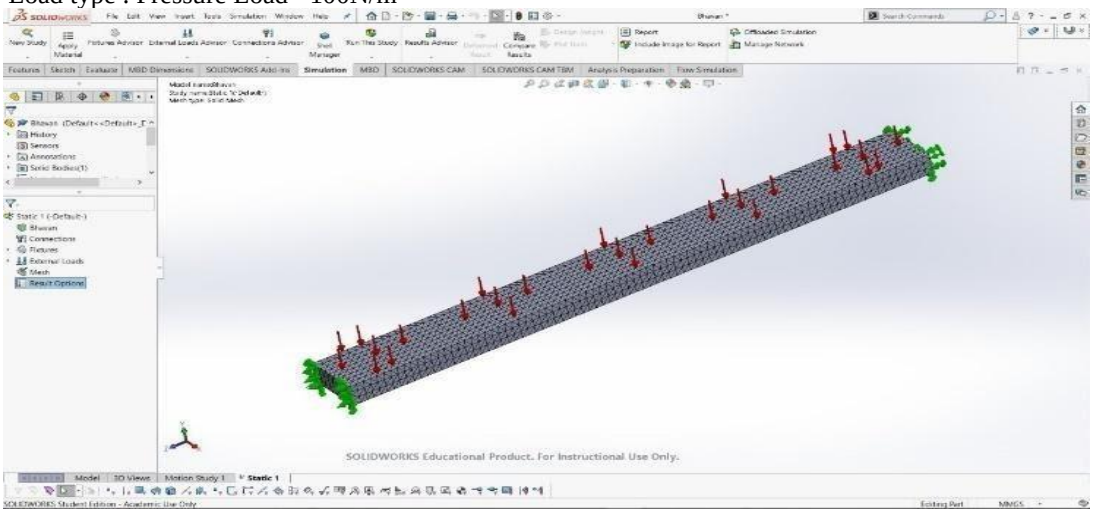

FIGURE 3. Meshing and application of loads

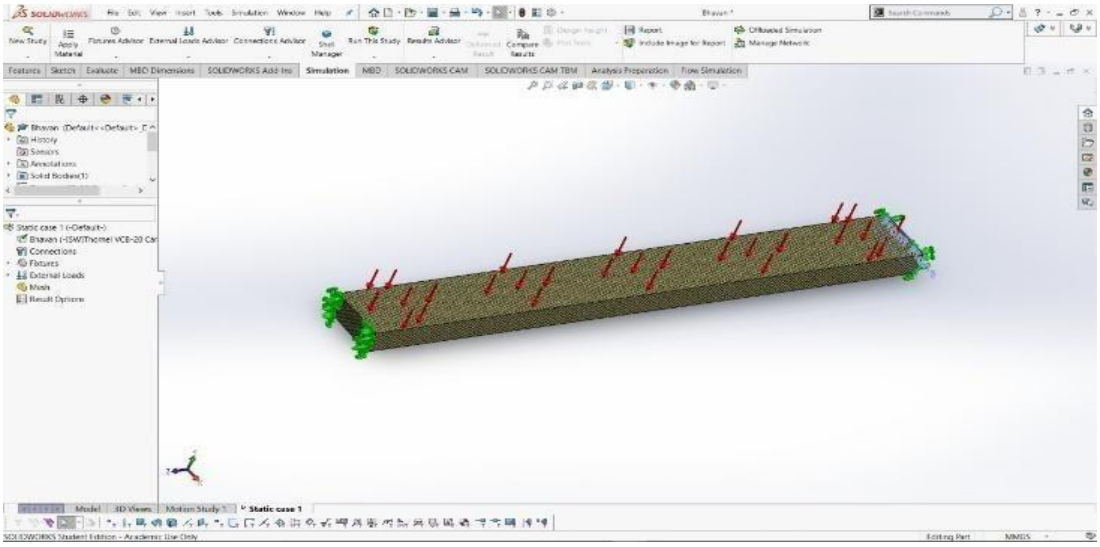

FIGURE 4. Meshing and application of loads

ANALYSIS

The specimen designed, is tested in solid works. Simple supported beam analysis is done on the model. The degrees of freedom given at both ends are zero [9]. The specimen is tested to know the reactions, stresses, displacements produced inside the beam. The meshing is applied for determining the stresses induced in the specimen for accuracy. Tetrahedral mesh is applied for accurate results. The elements are arranged accordingly in unstructured mesh type.

Static Displacement

Max Displacement = 1915e+00m & Min Displacement= 1.00e-20m

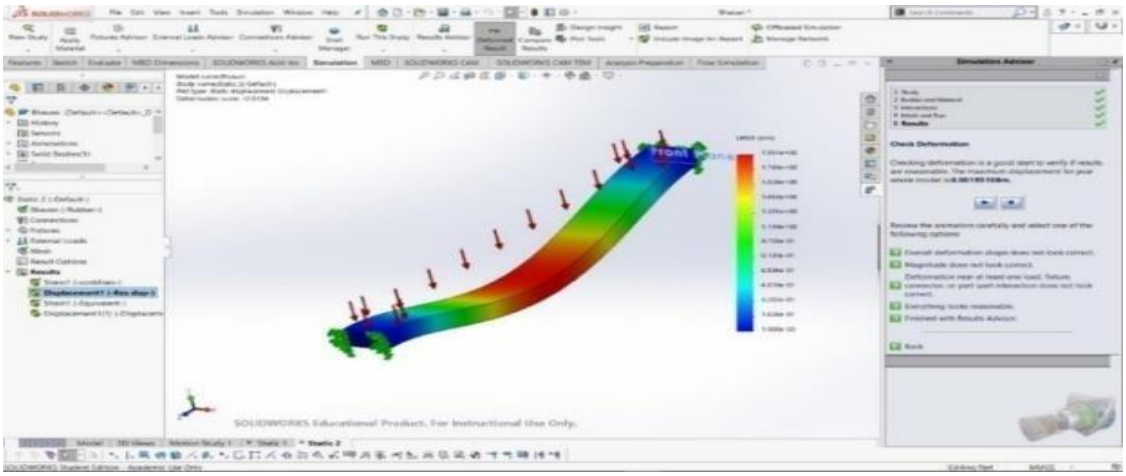

FIGURE 5. Static displacement of composite material

Static Strain

Max Static Strain=4.128e-03 & Min Static Strain=1.064e-01

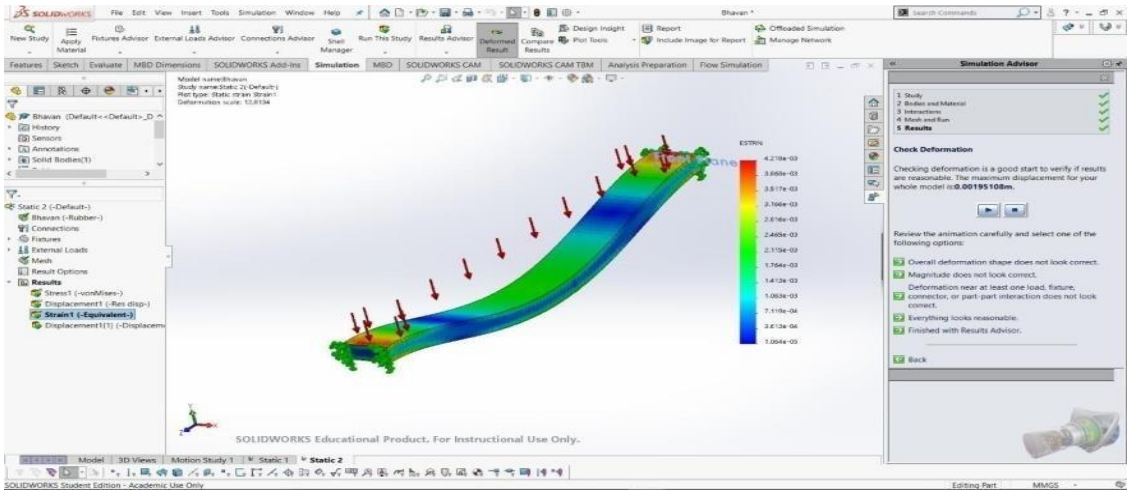

FIGURE 6. Static Strain

Static Nodal Stress

Max Static Nodal Stress=3.245e+04 N/m2 & Min Static Nodal Stress=4.258e+01 N/m2

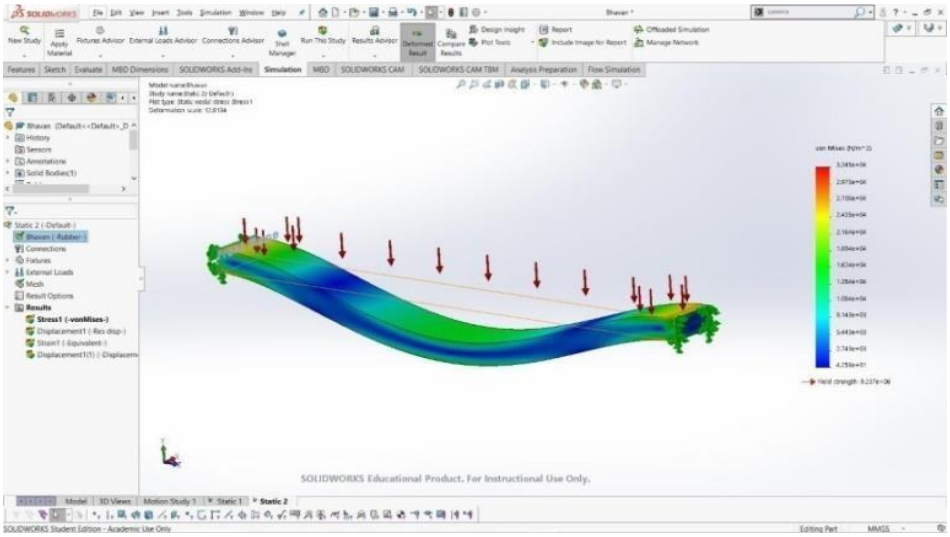

FIGURE 7. Static Nodal Stress

RESULTS AND DISCUSSION

The deformation of the model of static stress, static displacement of composite material, static strain, and static nodal stress is observed [8]. The stress analysis of maximum yield strength is an indication of the stress sustained by the material without undergoing plastic deformation, von mises stress.

Stress Analysis

Max Yield strength=9.237e+06 N/m^2, Max Von Mises Stress=9.245e+04 N/m^2, Min Von Mises Stress=4.25e+01N/m^2 and Max Displacement = 0.0019151mm.

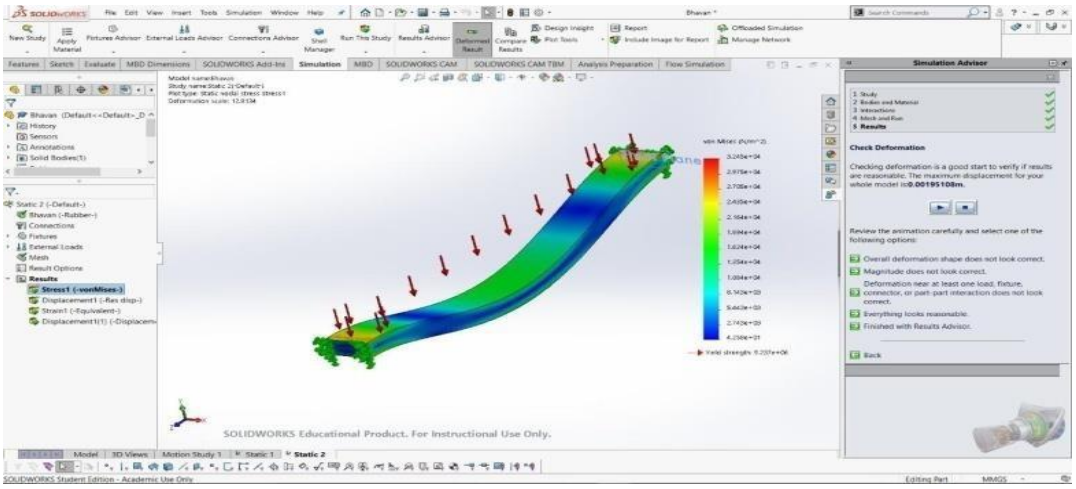

FIGURE 8. Stress Analysis

The simple supported beam analysis is done on the composite material; the maximum displacement of the beam is seen at midpoint, due to the application of load [12]. The uniformly distributed load of 100 N/m^2 is applied. The beam bent downwards, the maximum yield strength, maximum von mises stress, minimum von mises stress, maximum displacement is calculated. The composite materials have more strength compared to individual materials, the properties are improved. The composite materials application can be used in various industries like automobile, electrical components, aircraft interiors, electronic circuit boards etc.

CONCLUSION

A lot of research, work & study have been done by many researchers in the field of design, analysis & experimental investigation of leaf spring. Many of authors have given various methods of design, analysis & experimental investigation of natural composite materials. Various authors concluded that the composites with various combination of banana fiber and coconut coir percentage. Thus it is observed that, there is increase in the tensile and flexural strength of the composite.

The component is designed and analyzed using solid works software. The strength of the mixed composite is evaluated by using the values of von mises stress, displacement stress, equivalent strain, pressure load, resultant displacement, static nodal stress. The maximum displacement is observed at mid span of the composite model, therefore the maximum stress can be seen at the mid span. The reactive forces from both ends of the beam acts upward direction to balance loads and moments.

REFERENCES

1. Ashik, K.P. and Sharma, R.S., 2015. A review on mechanical properties of natural fiber reinforced hybrid polymer composites. *Journal of Minerals and Materials Characterization and Engineering*, 3(05), p.420.
2. Fuqua, M.A., Huo, S. and Ulven, C.A., 2012. *Natural fiber reinforced composites*. Polymer reviews, 52(3), pp.259-320
3. Haneefa, A., Bindu, P., Aravind, I. and Thomas, S., 2008. Studies on tensile and flexural properties of short banana/glass hybrid fiber reinforced polystyrene composites. *Journal of composite materials*, 42(15), pp.1471-1489.
4. A Vivek Anand, R Arvind Singh, S Jayalakshmi, K Srinivas Rao and Xizhang Chen, 2020, "Mechanical and Tribological Properties of Natural Fibre Reinforced Polymer Composites", *Taylor and Francis* - CRC Tribology and Sustainability Book.
5. Holbery, J. and Houston, D., 2006. Natural-fiber reinforced polymer composites in automotive applications. Jom, 58(11), pp.80-86.
6. Madhavi, K Sreelakshmi and M. Satyanarayana Gupta," Evaluation of Ply Orientation on Failure of Composites", *IJCIET*, ISSN Print: 0976-6308 and ISSN Online: 0976-6316, Volume 8, May2017.

7. Kumar, R., Choudhary, V., Mishra, S. and Varma, I.K., 2008. Banana fiber-reinforced biodegradable soy protein composites. *Frontiers of Chemistry in China*, 3(3), pp.243-250.
8. Malhotra, N., Sheikh, K. and Rani, S., 2012. A review on mechanical characterization of natural fiber reinforced polymer composites. *Journal of engineering research and studies*, 3(1), pp.75-80
9. Saheb, D.N. and Jog, J.P., 1999. Natural fiber polymer composites: a review. Advances in polymer technology, 18(4), pp.351-363.
10. Sakthivel, M. and Ramesh, S., 2013. Mechanical properties of natural fiber (banana, coir, sisal) polymer composites. Science Park, 1(1), pp.1-6.
11. Santhosh, J., Balanarasimman, N., Chandrasekar, R. and Raja, S., 2014. Study of properties of banana fiber reinforced composites. *International Journal of Research in Engineering and Technology*, 3(11), pp.144-150.
12. Sapuan, S.M., Harimiand, M. and Maleque, M.A., 2003. Mechanical properties of epoxy/coconut shell filler particle composites. Arabian Journal for Science and Engineering, 28(2), pp.171-182
13. Sathishkumar, T.P., Navaneethakrishnan, P., Shankar, S., Rajasekar, R. and Rajini, N., 2013. Characterization of natural fiber and composites–a review. *Journal of Reinforced Plastics and Composites*, 32(19), pp.14571476.

RESEARCH ARTICLE | MAY 22 2023

Experimental analysis of green composite material using hand lay-up technique

A. Udaya Deepika ✉; Mekhala Abhishek Varadanam; B. Aniketh; A. Aruna Kumari; E. Lakshmi Nagesh

AIP Conference Proceedings 2492, 040063 (2023)
https://doi.org/10.1063/5.0117127

Experimental Analysis of Green Composite Material Using Hand Lay-Up Technique

A. Udaya Deepika[1, a], Mekhala Abhishek Varadanam[1], B Aniketh[1], A Aruna Kumari[2] and E Lakshmi Nagesh[3]

[1]*Department of Aeronautical Engineering, MLR Institute of Technology, Hyderabad, Telangana, India*
[2.]*Department of Mechanical Engineering, JNTUH, Hyderabad, India*
[3]*Department of Mechanical Engineering, Netaji Institute of Engineering and technology, Hyderabad, India*

[a)] Corresponding Mail:udeepika.aero4825@gmail.com

ABSTRACT. As there is diminish of reserves of artificial sources and their imperishable quality, people are searching on substitutes for artificial fiber and system of resin. Few of the emulations are utilized to replace synthetic fiber got successful by considering natural fibers .so researchers are started their work on natural fibers. Their work got improved and the effective performances of natural fiber composites are very impressive. But when compared with artificial fibers they are not achieving the performance of synthetic fiber. So researchers are working on different compositions of organic fibers to achieve the same benefits of artificial fiber (6, 7, and 8). Apart from the advantages of natural fibers they also have a few limitations such as less strength, low thermal stability and moisture properties (8, 9). In this paper we are working on some of the commercially used fibers available in nature like kenaf, combined with resins which are natural. The properties of material and some of the techniques used for strengthen the fiber made it strong as artificial fiber. Bio Chemical treatment used in the fabrication process and loading mechanical methods is used to improve the strength of the natural available fibers. Bio-degradable and abundantly available at lower cost are the main advantages of naturally available fiber and for bio resin system. Natural fiber composites material has gained success commercially in many applications such as aircraft industry, automobiles, goods in sporting, and other appliances are quite dependent on natural fiber-reinforced plastics. By using naturally available fibers in combination with natural resins, the bio-based composites had improved the properties of the material mechanically and can potentially employed for structural purpose then synthetic fiber like UG/BF.

INTRODUCTION

Vignesh kumar mentioned in his paper mentioned that hybridization of naturally available fibers, natural fillers with polymer matrix provides a notable improvement in mechanical properties. They have used Banana/sisal/rice husk/polyester hybrid composite provides a better strength when compared to banana fiber/rice husk/polyester and sisal fiber/rice husk/ polyester. Flexural strength found to be marginal in sisal fiber/ rice husk/polyester and banana fiber/polyester composites. Maximum flexural strength was given by banana/sisal/polyester hybrid composite. Impact energy was too high for sisal/rice husk/polyester hybrid composite and banana fiber/rice husk/ polyester has lowest impact energy measure (6).

A Udaya Deepika in their review work mentioned that the kenaf materials which they had chosen goes with the economic viability changes such as low production cost and less labor work(1). R, S. K in their paper mentioned that composite of kenaf fiber reinforcement with different weight fractions of raw fibers using hand layup technique and had undergone by compression in a mold to identify the fiber optimum content and also the kenaf fiber mats were kept in contact with NaOH and KOH solutions at various proportions. The composites were fabricated with optimum fiber weight ratio and considered the mechanical properties of it.KFRE composites with NaOH combined with kenaf fiber content exhibited higher mechanical properties (10).

Advancements in Aeromechanical Materials for Manufacturing: ICAAMM-2021
AIP Conf. Proc. 2492, 040063-1–040063-7; https://doi.org/10.1063/5.0117127
Published by AIP Publishing. 978-0-7354-4438-6/$30.00

In this paper we considered, kenaf fiber as a reinforcement and epoxy/resin as a matrix for the component to construct a composite material and comparing it with UG/BF. Basically, kenaf fiber has good water absorbent capacity and having a greater yield in comparison to other widely used non wood fibers such as hemp, jute, flax. The two distinct fibers found in kenaf fibers are bast and core. Fibers from the bast are thick and long cells. These composites play a keen role in fabrication of aircraft's in aerospace industry and automobile industry. Basically, we use composite materials for having less weight and high strength i.e; it should have good mechanical and physical properties such as tensile strength, inter laminar shear strength, good load bearing capacity. In this we use 60:40 proportions for the preparation of composite material. The most important aspect of preparing this composite material is replacement of epoxy glass composite with this kenaf fiber composite. As composite materials typically have probability of getting material imperfections if we go with metal matrix composite also we use stir casting machining process at that point.(2) but as we are using natural fiber we need not to undergo with any machining process.

Most of the aircraft components are now fabricated using these composite materials. Up to now 50% of composition of aircraft is prepared by using composite material. The main aim in preparing of future aircraft's is having less weight aircraft with high strength. In this aspect, we are using composite materials in aircraft's. Aircraft's that are using composites in its fabrication of parts are BOEING DREAMLINER, AIRBUS, The most parts of Boeing can be manufactured using composites. The parts such as, wings and fuselage .In this, fabrication of material using kenaf fiber, we use filler material to increase strength of the fiber to some more extent. These fibers are Eco- friendly and environment. Ayensu in their paper mentioned that fabrication of composite materials is a easy task with natural fibers (11). Natural fibers with low density, greater specific strength specifies that natural fibers are eco-friendly in nature (4).

MATERIALS USED

- Kenaf fibres
- snail shells powder
- Bio epoxy
- Hardener

TABLE1. Mechanical properties of kenaf fibre [12].

Density (g/cm^3)	Tensile strength (MPa)	Tensile modulus (GPa)	Elongation (%)
–	692	10.94	4.3
–	930	53	1.6
1.45	930	53	1.6
1.4	284–800	21–60	1.6
1.5	350–600	40	2.5–3.5
0.75	400–550	-	-
0.6	-	-	-
0.749	223–624	11–14.5	2.7–5.7
1.2	295	-	3–10

Working With Hand Layup Technique

Gel coat is laid on the mold by using a brush. Next fiber reinforcement is placed manually on the mold. Once gel coating has cured sufficiently. The laminating resin is poured and brushed by using a paint roller. Rollers are used in wet the reinforcement and remove it by entrapped air. Subsequently to build a laminate one by one layer is added to fiber reinforcement to get particular thickness. To stiffen the laminate low density core materials are commonly used.

Characterization

Tensile Testing:

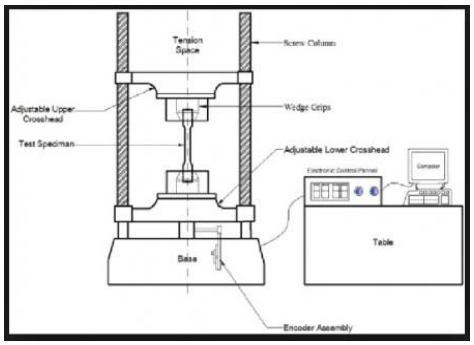

FIGURE 1. UTM

Tensile testing is a destructive engineering testing of materials. In this process sample is tested by applying a load for proof testing until it fully fails. We are not performing tensile test on UTM but we are doing the test using ANSYS software.

Universal testing machine

Tensile testing is carried out on the specimen of standard unit ASTM 790. This test was carried for force-displacement data which will be obtained for computation stress-strain response of the composite using ANSYS.

Designing

Flexural test is carried out with the help of three point bending test using UTM according to the standard ASTM 790. Specimen length is 120mm and width is 10mm.

ANSYS includes different kinds of meshing [13]. Basing on the parameters such as geometry shape and dimensions, material properties the element type and meshing will be given in the software and solid models also involve typical solid elements where the material is assigned to all regions of the model [14]. Various solid and shell elements in ANSYS are available [15]. We had applied solid 20 nodes 186 for material with meshing parameter as hexa mesh on our model.

FIGURE 2. Pressure loading Analysis

Flexural testing

Flexural strength and modulus are measured using flexural testing. Flexural strength is maximum on the specimen as the stress at the outermost fiber due to compression or either tension force applied on the specimen. Flexural modulus can be calculated from the slope of the specimen. T**est** results are slightly different from manual to anlaysis using softwrae.

Based on composite system there are total 3 different compositions analysed. They are:

- Modified composite with CaO 0.1 wt % (case 1)
- Modified composite with CaO 0.25 wt % (case 2)
- Modified composite with CaO 0.5 wt % (case 3)

We are doing testing on 3 different compositions.

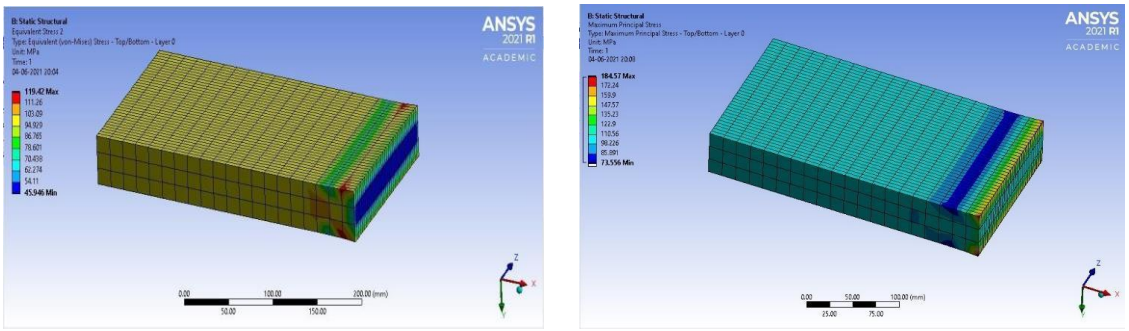

FIGURE 3. Maximum principal stress for case 3

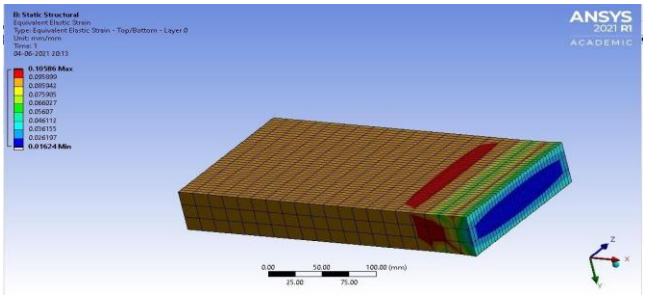

FIGURE 4. Vonmisses stress case 3

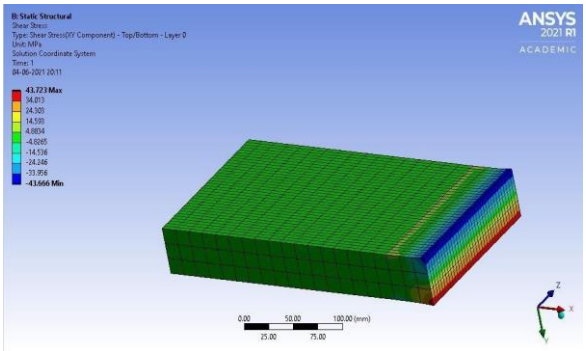

FIGURE 5. Shear stress case 3

First four fiber layer should be made without adding CaO to it and then these layer should go through three different testing's which are tensile strength, impact strength, and flexural strength., these four fiber will have less mechanical properties compare to the other. Next four fiber should be made by adding 0.1 wt % of CaO to it (case 1). Then these layer will go with the same procedure like before of different testing and these layers mechanical properties will be little better than the first four fiber. Next four fiber will go with same process but with adding 0.25 wt% of CaO to it (case 2)and these layers will be too go through all the testing's and it will be much stronger compared to the last fibers.Last stage will be another four fiber, in this 0.5 wt% of CaO will be added to it(case3). And will be tested which is stronger, CaO to the material will bring advantages but also slide disadvantages to it too. At the end there will be total 12 fibers with which are gone through three different testing and with different weightage of CaO. Here we are showing analysis result for only case 3 and comparing it with the analysis done on fibers of banana and glass for unidirection.

Comparing with analysis done on fibers of banana and glass composite in unidirection made by using epoxy resin LY556 and the hardener HY951 is stirred with a ratio of 10:1. This solution is used as a matrix. The catalyst was added to the epoxy and the stirred properly to get a perfect mixture with correct timing before applying into the mold. The molds should be cleaned for dust before applying epoxy. The glasses were used as reinforcements along with unidirectional fibers of banana. The analysis of these two laminates was done by using the basic hand lay-up technique (4).

RESULTS AND DISCUSSION

In theoretical model, as the content of fiber increases, its strengthens the composite accordingly. Mechanical strength of composite material deteriorates when Volume fraction of fiber increases over a specific value. The tensile strength of green composites increases when it is reinforced by Kenaf fiber and the matrix resin with CaO filler material. In the result it is shown that the maximum tensile strength at a load of 60KN was applied in all cases for kenaf fiber were recorder at baseline composite with 0.1 wt% CaO, which exhibited the value of 18.9 MPa, respectively. The strength of the composites started to increase with further adding of CaO. With 0.25 wt% of CaO to the composite material the tensile strength result is increased to 30.5MPa and with 0.5 wt% of CaO to the composite material the tensile strength result increases to 50.8MPa. The flexural strength of neat PMCs with reinforcement of kenaf fiber and epoxy resin with CaO of 0.1 wt% is 121MPa and increases to 209.2 MPa after adding more percent of CaO that is of 0.25 wt%. and after adding more filler material of 0.5 wt% flexural strength increases to 400.5 wt%.

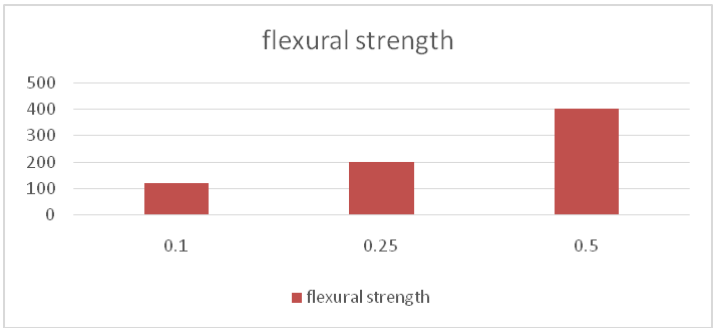

FIGURE 6. Graph for flexural testing on kenaf and CaO

In the test it is noticed that graph doesn't increase every time the CaO is added. When the reinforced kenaf fiber with matrix epoxy and CaO is been tested for impact strength it was shown that when 0.1 wt% CaO is added to the material then the minimum deflection will be 1.03 mm. And when the CaO of 0.25 wt% is added then the minimum deflection of the material will be 1.16 mm. And then in final case CaO of 0.5 wt% is added to the material the min deflection will be 1.10 mm, and filler material is increasing it produces more cracks to the material. So the filler material should be used with balance. The properties of the kenaf fiber of polymer material composite has been investigated and it was shown that using kenaf fiber there is much more advantage in tensile and flexural strength but in the impact strength filler material can be used in balance to avoid the cracks on the composite material and as

kenaf is also known as hibiscus cannabinus. There is more advantages of finding them in any kind of weather, just because of this they have advantage of moisture absorption. Kenaf fiber is also exhibited comparable strength to the E- glass fiber. But it can have the advantages of being Eco-friendly. By adding CaO as a filler material it was shown that the tensile strength and impact strength of kenaf fiber polymer material composite has been increased. In future more research works can be conducted on modification of kenaf fiber, particularly to use as a reinforcement it in polymer composite matrix for further enhance the properties of the green composites which can be really used keeping future as perspective.

The fibers of banana and glass for unidirection composite possess higher tensile strength and withstand the strength up to 295.38 MPa for the load 65 KN and in ANSYS Von- misses stress value is 616.69 MPa for banana and glass for unidirection composite. The load to displacement is found as 11 mm as average value for banana and glass for unidirection composite, hence for moderate strength it can be utilized.(4)

Using ANSYS software and manual testing the results based on experimental and numerical data analysis can be deviate. It is due to the assumptions in numerical analysis such as increase of bonding, aligning of fibers, porous free members, uniform diameter of fibers and predicted tensile value to be higher for banana and glass for unidirection composite and composite with CaO 0.5 wt % composition.

In experimental analysis flaws in composites (voids, cracks, matrix and fiber fracture, poor bonding, improper matrix distribution and nonalignment of fibers) are the basic causes for obtaining lower tensile value for banana and glass for unidirection composite and kenaf with CaO 0.5 wt % composite when compared with the numerical analysis. We may enhance the strength of the composites material by chemically treating natural fibers. Medium strength is required in usage of natural fibers replacing the synthetic fibers. The natural fibers are ecofriendly hence research is required to make a composite material having natural fiber in which tensile property is moderately equal to fiber like glass.

CONCLUSION

Tensile test is carried out on green composite with CaO 0.1 wt % (case 1), modified composite with CaO 0.25 wt % (case 2), modified composite with CaO 0.5 wt % (case 3) using ANSYS software and compared with the analysis on unidirectional banana fiber composite.

Tensile test is carried out on green composite and the valu is 400 Mpa for load of 60 kN and unidirectional banana fiber composite it is 295.38 MPa at a load 60 kN.

The ANSYS Von -misses stress value is 433.72 MPa, green composite CaO 0.5 wt % (case 3) and 616.69 MPa for banana and glass for unidirection composite.

REFERENCE

1. A. Udaya Deepika, Sd Esmail, B. Manmada Rao and Vibhav Kumar Trivedi, A review on the usage of green composite with other composites *AIP Conference Proceedings* 2317, 020015 (2021); https://doi.org/10.1063/5.0036438
2. M. Satyanarayana Gupthaa), G. Akhilb), V. Reshmac), P. Harshitha Laxmid), and J. Jawahar, Fabrication and comparision of AA7005/SiC-Al2O3 and other composite materials using different methods, *AIP Conference Proceedings* 2317, 020030 (2021)
3. "Preparation and characterization of starch-based composite films reinforced by cellulose nanofibers". *International Journal of Biological Macromolecules*. 116: 272– 280. doi:10.1016/j.ijbiomac.2018.04.186. PMID 29729338.
4. A Shadrach Jeyasekaran, K Palani Kumar and S Rajarajan, Numerical and experimental analysis on tensile properties of banana and glass fibers reinforced epoxy composites, Sadhana¯ Vol. 41, No. 11, November 2016, pp. 1357–1367.
5. OJ Gbadeyan, S Adali, G Bright, B Sithole, Prabashni Lekha, Mechanical, microstructure, and dynamic mechanical analysis of nano-shell and plant fiber hybrid biocomposite, *Journal of Composite Materials*, May 3, 2021 Research Article
6. Experimental analysis on mechanical behaviour of natural fiber reinforced composites using filler material, January 2018, *Journal of Mines, Metals and Fuels* 2018(SRM IST Special Issue 2018 Part I), sn, Vigneshkumar, Kannan, Gokul, Subramanian, C, Duraisamy, Boopathi, 2018/01/11

7. Väisänen, Taneli, Antti Haapala, Reijo Lappalainen and Laura Tomppo: 'Utilization of agricultural and forest industry waste and residues in natural fiber-polymer composites: A review'. Waste Management 54 (2016): 62-73.
8. Ihueze, Christopher C., Okafor Christian E. and Okoye Chris I.: 'Natural fiber composite design and characterization for limit stress prediction in multiaxial stress state'. *Journal of King Saud University-Engineering Sciences* 27, no. 2 (2015): 193-206.
9. Pan, Yihui and Zheng Zhong: 'A micromechanical model for the mechanical degradation of natural fiber reinforced composites induced by moisture absorption'. *Mechanics of Materials* 85 (2015): 7-15.
10. R, S. K., & Durgam Muralidharan, N. (2020). Mechanical Characteristics Study of Chemically Modified Kenaf Fiber Reinforced Epoxy Composites. *Journal of Natural Fibers*, 1–11. doi:10.1080/15440478.2020.1818350
11. Ayensu A 2000 Interfacial debonding of natural fibre reinforced composites. Q. Sci. Vis. 6(1): 25–34
12. RezaMahjoubaJamaludin MohamadYatimbAbdul RahmanMohd SambSayed HamidHashemic,Tensile properties of kenaf fiber due to various conditions of chemical fiber surface modifications, *Construction and Building Materials*, Volume 55, 31 March 2014, Pages 103-113
13. Meyghani B, Awang M, Emamian SS, Nor M, Khalid M, Pedapati SR. A comparison of different finite element methods in the thermal analysis of friction stirs welding (FSW). Metals. 2017; 7(10):450. Search in Google Scholar
14. Fragassa C, Vannucchi de Camargo F, Pavlovic A, Minak G. Explicit numerical modeling assessment of basalt reinforced composites for low-velocity impact. Compos B Eng. 2019; 163:522–35. Search in Google Scholar
15. Wenbin Y. An introduction to micromechanics. Appl Mech Mater. Trans Tech Publications, Ltd. Mar. 2016; 828:3–24. doi: 10.4028/www.scientific.net/amm.828.3. Search in Google Scholar

RESEARCH ARTICLE | MAY 22 2023

Review on phase change materials and their applications

P. Thangavel ✉; S. Panneerselvam; V. Hariharan; D. Deepa; B. Manideep

AIP Conference Proceedings 2492, 040069 (2023)
https://doi.org/10.1063/5.0114431

Review on Phase Change Materials and Their Applications

P Thangavel[1,a)], S Panneerselvam[1], V Hariharan[2], D Deepa[3]and B Manideep[4]

[1]*Department of Mechanical Engineering, Kongu Engineering College, Perundurai-638060, Tamil Nadu, India.*
[2]*Department of Mechatronics Engineering, Sri Krishna College ofEngineering and Technology, Coimbatore 641008, Tamil Nadu, India.*
[3]*Department of Electronics and Communication Engineering, Bannari Amman Institute of Technology, Sathy 638401, Tamil Nadu, India.*
[4]*Department of Aeronautical Engineering, MLR Institute of Technology, Hyderabad, India*

[a)] Corresponding author: ptvel.mech@kongu.edu

Abstract. Through the use of Phase Change Material (PCM), thermal energy is stored in the form of latent heat. PCMs have the capacity to store a large amount of energy in a compact package. The amount of energy contained within PCMs is determined by the charging temperature and time.Organic, inorganic, and eutectic PCMs are the different categories of PCMs currently used in cooling and heating applications. PCMs have been used widely in latent heat storage systems for HVAC (Heating, Ventilation and Air Conditioning), textiles, helmets, heat pumps, spacecraft, electronic chips, and building applications. The subcooling cycles with phase change materials are used to improve the Coefficient of Performance (COP) of refrigeration cycle. The theoretical resultshows that improvement of COP for different operating temperature of the condenser is in the range of 4-25%. Other than refrigeration and air conditioning applications, PCMs can be used in many applications such as a temperature damper in electronic chips by preventing it from overheating. PCMs can be employed for cooling of buildings by maintaining the constant temperature during the day. The numerous methods of thermal energy storage and PCM applications in various fields are discussed in this article.

Keywords: Phase Change Materials; Applications; Refrigeration System; COP.

INTRODUCTION

Continuous increases in the degree of greenhouse impact and increases in fuel prices are key factors in identifying alternative energy options for various applications in day-to-day life. There is a need for large-scale energy storage devices in renewable energy storage. The use of Phase Change Materials (PCM) to store thermal energy in the form of latent heat is a new alternative. A PCM is a material with a high heat of fusion capable of retaining and releasing vast quantities of thermal energy when melting and solidifying at a certain temperature. As the transition of phase of a PCM, heat is either absorbed or released. During a constant-temperature operation, latent heat is the energy emitted or consumed by a PCM or thermodynamic device. For a slight change in temperature, a significant amount of energy can be emitted due to phase change. This paper reviews various types of PCMs and their applications in various fields such as refrigeration and air conditioning, cooling of buildings, etc. Also reviews the influence of nano particles in the properties of PCMs and performance improvement of system by mixing it with them.

MATERIALS AND METHODS

Thermal Energy Storage

Mechanical and electrical energy are examples of different types of energy [1]. Compressed air storage, hydro power storage and fly wheels are generally used mechanical energy storage. In this type of storage system, power is stored when inexpensive off-peak power is available, and it is utilized when insufficient supply of power. Generally, batteries are the main electrical storage system; most commonly used batteries are lead acid battery, Ni-Cr battery. Then the thermal energy is stored in two ways as shown in fig 1. Thermal energy storage is carried out in various ways like change in internal energy, sensible heat, latent heat etc. Thermal energy is stored by raising the temperature of a

Advancements in Aeromechanical Materials for Manufacturing: ICAAMM-2021
AIP Conf. Proc. 2492, 040069-1–040069-8; https://doi.org/10.1063/5.0114431
Published by AIP Publishing. 978-0-7354-4438-6/$30.00

solid or liquid. The amount of heat emitted or consumed by a material after a temperature shift is known as sensible heat. For charging and discharging, a sensible heat storage device makes use of the material's heat power and temperature adjustment. The amount of heat deposited is determined by the material's specific heat and temperature shift.

$$Q = mC_p(T_2 - T_1) \quad (1)$$

When phase change occurs, then there is a heat absorption or release in latent heat of material. The storage capacity of various LHS with PCM [2] is given by

$$Q=m[C_{ps}\ (T_{mean}- T_{intial}\ )+ a_m\ \delta h_{mean}+ C_{pi}\ (T_{final}\ -T_{mean})]\ ) \quad (2)$$

The latent heat of transition for solid – gas and liquid – gas transitions are higher, but it necessitates a large container for the manufacture of the system with complicated issue. Solid–liquid transitions provide limited latent heat storage, proving that they are commercially viable for thermal energy storage systems.

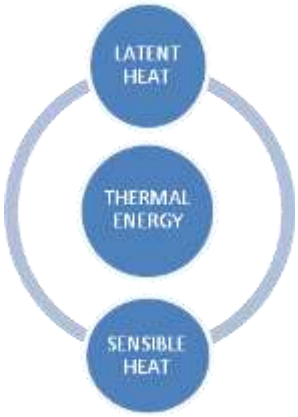

FIGURE 1. Thermal energy storage methods

Phase Change Materials

Latent heat storage materials are also known as phase change materials. When a solid change to a liquid or a liquid changes to a solid at a steady temperature, thermal energy conversion happens. PCMs act as traditional storage materials in their initial state. At a constant temperature, PCMs can absorb and release the heat. PCM's can store 5-14 times more heat per unit volume than the sensible storage materials like water and rock [3]. PCM's are used in refrigerator for improving the COP. PCM's are used in building construction applications, electronic device manufacturing, food processing and storage industries and transportation of food and dairy items etc. PCM's should have properties like thermal properties, kinetics and chemical properties [4].

Classifications of Phase Change Materials

Organic, inorganic, and eutectic are the major classification of PCMs and shown in fig 2. Inorganic compounds usually have about twice the volumetric latent heat storage ability of organic compounds. Organic compounds have the capacity of (128 – 200 kg/dm3), but inorganic compounds have more capacity than organic (250 - 400 kg/dm3). Organic PCMs are again classified into paraffin compounds and non – paraffin compounds. Paraffin is economic, reliable, less expensive, noncorrosive and chemically inert. It is stable below 500□C. Due to these properties paraffin having long freeze melt cycle [5]. But paraffin having some drawbacks such as it is having low thermal conductivity, somewhat inflammable. Because of these drawbacks we can go for non-paraffin. Non-paraffin compounds have wide variety of properties.

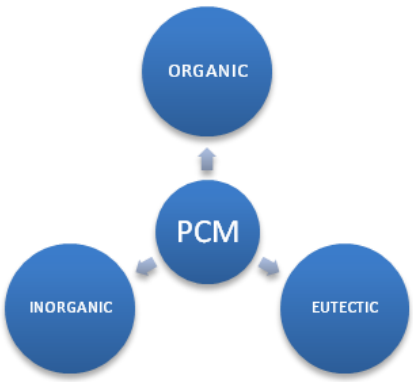

FIGURE 2. Classification of phase change materials [4]

A study of organic materials was performed, and a variety of fatty acids and alcohols appropriate for storage were discovered [4, 7]. Fatty acids have higher heat of fusion, when compared to other paraffin. It is having the capabilities of reproducibility and freezing behavior also freeze without super cooing [8, 9]. But main drawback is corrosive nature and cost. So the next preference is given to inorganic phase change materials. It is again subdivided into two groups; they are salt hydrates and metallic. Salt hydrate is the most important type of PCM. This salt hydrate has additional appealing properties, such as a high latent heat of fusion per unit volume. The paraffin is almost doubled because it has a high thermal conductivity. They are non-corrosive and compliant with plastics, but they are slightly toxic [10]. But it is having some drawbacks such as super cooling and it is suitable for thermal storage, melt incongruently. To overcome the super cooling and segregation of salt hydrates [11], a study has discussed through an experiment with rolling cylinder heat storage system. Metallic are the combination of low melting metals and metal eutectics. Due to weight, it is not commonly used in PCM technology, but it has a high latent heat of fusion per unit volume and thermal conductivity. Relevant heat and vapour pressure are lower. A minimal melting composition of two or more elements is called eutectic. During crystallization, each component melts and freezes at the same time, resulting in a mixture of component crystals. [12].

Some of the important required properties of PCM are mentioned below.

- Latent heat of fusion per unit mass is high for PCMs, so it can store large amount of energywith lesser amount of materials.
- High specific heat of PCMs provides an extra sensible heat conservation effect while stillpreventing subcooling.
- It should have a high thermal conductivity to reduce the temperature differential needed tocharge the storage material.
- High density, allowing the product to be keeps in a lower container capacity.
- The PCM should not be flammable (poisonous, inflammable and explosive).
- There is no chemical decomposition, guaranteeing the longevity of the system.
- Working components should not be corroded.
- During freezing, PCM should not be subjected to excessive cooling.

Various Applications of Phase Change Materials

Thermal energy storage is one of the most efficient storage methods for improving energy efficiency and save the energy. Thermal energy can be retained in a variety of ways, including sensible, latent, and thermochemical gas, or a combination of all three. Because of its high storage capacity and ability to store heat at a constant temperature, latent heat storage by PCM is one of the most common heatstorage methods.

The PCMs can be used in building applications for enhancing thermal comfort of the inside the atmosphere where the latent heat thermal energy storage applications. [13, 14]. In building applications there are two methods used for incorporation of PCM's within the concrete structure [15]. First one is incorporation of PCM's in the building materials during manufacturing process. Another one is adding of building materials in PCM's. In building application among the various PCM's, Fatty acids are used due to their great latent heat capacity, non-toxicity, low vapour pressure [16-20]. They can be directly incorporated into conventional building materials. Recent years PCM added

with walls in interior surface of building and walls has gained impacts in maintenance of thermal comfort inside the room. There was a comparative study has been made walls with PCM and without PCM [21]. Fatty acids based mixture capric acid of 82% and lauric acid of 18% and having melting temperature of 20.394^{o}C and freezing temperature of 19.138^{o}C used as PCM in this study. That implementation shows good thermal comfortand warm during winter season. Later that new kind of PCM based tiles used for maintaining indoor air temperature in winter season [22].

Temperature control of electronic device is very important one for improving their life and reliability. Temperature is the main factor to cause failure of electronic components. 1% increase in temperature will reduce its reliability by 4% [23]. Many statistics shows that 55% of electronic components failure occurs due certain relation with temperature [24]. For this purpose thermal control is provided in electronic components. PCM can effectively use for phase change thermal control in electronic devices. PCM's can absorb or release the heat when electronic device working in high temperature or below the working temperature. It will prevent the electronic device from overheating and it maintains proper temperature fluctuation. PCM can also be used to store thermal energy during the day and release it later in the day in solar power plants. Microencapsulated PCM's can be used in textile fibres. It will provide great enhanced thermal protection in cold as well as hot environments [25]. PCM's can be used in motor vehicles. In this application there is a latent heat storage module which is included tostore energy during engine stop condition and it can be used to preheat the engine at new start. Engine canreach the optimum temperature within a shorter time [26].

Another application is food processing and transportation. For improving food quality, food taste and nutrition value during transportation and storage the freezer is used. Due to food transportation at lower temperature, the freezer plays an important role. The time and amplitude of cooling cycles in low-temperature storage chambers such as refrigerators and freezers have an effect on food quality and energy use. If there is any temperature fluctuation inside the chamber or freezer then the food quality will be affected during storage and transportation [27]. So the temperature control is important factor in food storage and transportation. In this review mainly focused on refrigeration and air conditioning application,these two are main household appliances in all houses. Because of continuous operation it consumes morepower than any other appliances.

Amorphous and crystalline phase shift materials are commonly available with its physical properties. By heating the substance past its crystallization temperature, it is very simple to turn the state of these phase transition materials from amorphous to crystalline. Amorphous phase is derived from crystalline by melt-quenching. Phase shift materials are also commonly used in all modern opticalrewritable recording formats, including Compact Discs (CDs), DVDs, and Blu-ray disks. PCMs have recently been used in solid-state memory systems to store more data due to their significant variance in electrical resistivity [42,43]. Thermal mass is used to lower peak-power demand and minimize cooling device size. Then, instead of using high-energy cooling sources, use low-energy cooling sources. Wide thermal energy storage systems have previously been used to compensate for the limitations of alternative cooling sources or to avoid high demand costs. However, PCMs are now often added with gypsum sheet, cement, or other wall-covering materials. As a result, it is now incorporated into the framework of the house. The main benefit of PCMs is that they can increase thermal energy storage capability and allow forisothermal discharge. As a result, it can reach high levels of energy storage without drastically altering theroom's temperature. Since the heat is stored inside the house, no additional transportation energy is needed. [44,45].

TABLE 1. List of commercially available PCM's for cooling and heating applications.

Material	Type	Melting Temperature (^{0}C)	Heat of fusion (kJ/kg)	Reference
RT 20	Paraffin	22	172	[45]
RT 25	Paraffin	26	232	[45]
RT 26	Paraffin	25	131	[45]
RT 27	Paraffin	28	179	[45]
RT 32	Paraffin	31	130	[45]
Climsel c23	Salt hydrates	23	148	[46]
Climsel c24	Salt hydrates	24	216	[46]
Climsel c32	Salt hydrates	32	212	[46]
STL 27	Salt hydrates	27	213	[46]
S 27	Salt hydrates	27	207	[46]

Methods to Improve the COP of Refrigerator

Losses from compressor on/off cycles are caused by refrigerant movement as the compressor starts and stops. This phenomenon results in a 5-30% loss of energy. At the time of compressor start most of the refrigerants are accumulated in evaporator. So the evaporator is in positive temperature nearly a cabinet temperature. Since accumulation of refrigerant in evaporator cause more mass flow from the evaporator. Finally, the capillary tube is filled with refrigerant vapour. As a result, refrigerant accumulatesin the condenser, and refrigerant enters the capillary tube in a liquid condition. The above-mentioned losses can be reduced by increasing the thermal inertia of the refrigerator, as well as the identified 11 % improvement in cooling power. [13].

For improving COP of refrigerator, additional insulation has introduced for door and cabinet which will reduce the heat loss. Vacuum Insulation Panels integrated with cabinet and 25% of average energy is obtained. Manufacturing of the experiment is the main drawback of the system. COP of refrigerator varies with change in thermal load and the results shows effect of PCM on COP at different thermal load [14]. Then, in order to improve COP, a high-efficiency compressor was developed. Ordinaryrefrigerators employ hermetic compressors, which usually run at partial load, resulting in lower output and longer cycle times. To monitor the refrigerating power, Variable Speed Compressors (VSC) and Variable Capacity Compressors (VCC) are also used. [23]. The result shows that 45% of energy saving is obtained by replacing ordinary compressor by VCC compressor. Use of latent heat storage is the option for improving the COP [14] [15]. In general heat transfer occurs by natural convection and radiation with low heat transfer coefficient [16]. The addition of a PCM slab to one side of an evaporator improves efficiency due to conduction inside the PCM. Also, a refrigerator with less PCM in the evaporator was simulated, resulting in a COP improvement of 12% [16].

Experimental analysis had completed with adding thickness of PCM slab on the back side of evaporator. It increases the 25% of COP and significant decrease in compressor start and stop. PCM can absorb large amount of heat during melting at constant temperature [20-22] and PCM is used to reducethe temperature fluctuation in many applications like in domestic refrigerator and freezer [23, 24]. Theuse of PCM can reduce product and air temperature fluctuations inside refrigerator freezer [27]. PCM wasincorporated into a domestic freezer and the study was focused on the use of readily available PCM (Sodium chloride with Water). This PCM is more vulnerable to corrosion and undercooling. [25]. A prototype of refrigerator with PCM has developed and placed PCM in heat exchanger at various locations.Experiment result shows 6-8% increase in COP [26]. PCM panels were incorporated into the interior walls of a domestic refrigerator [24] and results indicate an 8% drop in energy consumption over thedefrost cycle.

INFLUENCE OF NANO PARTICLES IN PHASE CHANGE MATERIALS

With the development of nanotechnology an innovative fluid called nano fluid arises. It is formed by metal or metal oxide nanoparticles in a base fluid. While considering PCM's, there are various drawbacks of properties such as poor thermal and electrical conductivity [28-31] super cooling nature etc, are identified. Basically nano particles are used to get constant thermal conductivity and high heat transfercoefficient. In order to increase the thermal properties of PCMs, the nano particles are embed with it.Nano particles would affect the thermal and physical properties of PCM. The degree of super cooling of PCM is influenced by dispersion of nanoparticle. Nucleation process is used for dispersing Nano particle and PCM. From the available materials best candidate material is used as nucleating agent. This would increase nanoparticle dispersion in PCM. A tiny structure may also allow nanoparticles to have a wide surface area, which coincides with their physical and chemical properties and reacts on thermal-physical properties of PCM. Inorganic compounds like salt hydrates are used as PCM. They are chemically stable and non-ignitable but the main problem behind these materials are super cooling and poor thermal conductivity. For improve their properties nano particles are embedded into PCM [32].

In some fields especially in latent heat microencapsulated PCM's had not well done under repeated cycling because of large particle size. Microencapsulated PCM not only increase the viscosity also crushed during pumping. Because of these reasons nano encapsulated PCM's with smaller size is developed. In this experiment, graphene-based nanoparticles are used. The surface area of graphene, defines the best thermal physical properties for nano-enhanced phase change materials [38].

The Photovoltaic panel efficiency mainly depends on the material of photovoltaic panel and its operating temperature. When there is a rise in operating temperature the electricity generation of photovoltaic cell drops tremendously and vice versa. In order to increase the electricity generation coolingis required. The cooling can be provided by Nano encapsulated PCMs [37]. Photovoltaic technology also used in Building-Integrated Concentrated

Photovoltaic (BICPV) which experiences a loss in the electrical efficiency with an increase in temperature that may also lead to the degradation over the time. Micro-fins, PCM, and Nano material Enhanced PCM are used in hybrid passive cooling solution for BICPV (n- PCM). Under normal convective heat transfer conditions, the thermal output of an un-finned metallicplate was first compared to that of a micro-finned plate, and then to that of applied PCM and n-PCM. When comparing micro-fins with PCM and micro-fins with n-PCM, the average temperature in the system's center was lowered by 10.7°C and 12.5°C respectively. As compared to natural convection heat transfer, the result of using PCM and n-PCM with the un-finned surface shows a temperature reduction of 9.6°C and 11.2°C respectively [41].

PCM's biggest difficulty is its poor thermal conductivity. This paper discusses the methods for improving the thermal conductivity of an organic phase change material used in low-temperature thermal energy storage applications. Carbon powder and the use of aluminum and graphite fins are used to increase the thermal conductivity of polyethylene glycol PCM. Experiments of flat and cylindrical configurations were carried out, and thermal conductivity increments were measured [44].

CONCLUSION

The available thermal energy storage technology with PCMs in various applications is the main focus of this review article. These PCM-based applications are now very useful to increase the energy efficiency. This paper also discusses recent studies in this area of refrigeration, with a special emphasis onevaluating the thermal properties of different PCMs and also focused on various applications like buildingusage for cooling, heating, heat pump, and electronics etc. In all applications PCM plays an important rolein heat transfer and influence of nano technology with PCMs for enhancing thermal conductivity is also reviewed in this article.

REFERENCES

1. Khartchenko N V, Advanced energy systems, Berlin: Institute of Energy Engineering & Technology University; 1997.
2. Lane GA, Solar heat storage latent heat materials, vol. I. Boca Raton, FL: CRC Press, Inc.; 1983.
3. Abhat A, Low temperature latent heat thermal energy storage: heat storage materials, Solar Energy, 1981; 30 (4), 313–32.
4. Buddhi D, Sawhney RL, Proceedings on thermal energy storage and energy conversion; 1994.
5. Hale DV, Hoover MJ, O'Neill MJ, Phase change materials hand book, Alabaa: Marshal SpaceFlight Center; 1971.
6. Abhat A, et al., Development of a modular heat exchanger with integrated latent heat storage.Report no: BMFT FBT 81-050, Germany Ministry of Science and Technology Bonn; 1981.
7. Lane GA, Glew DN, Heat of fusion system for solar energy storage Proceedings of the workshopon solar energy storage subsystems for the heating and cooling of buildings. Virginia: Charlothensville; 1975. p. 43–55.
8. Herrick S, Golibersuch DC. Quantitative behavior of a new latent heat storage device for solarheating/cooling systems, General International Solar Energy Society Conference; 1978.
9. Lane G.A. et al, Macro-encapsulation of PCM, Report no: ORO/5117-8. Midland, Michigan:Dow Chemical Company; 1978. p. 152.
10. Lane GA, Rossow HE, Encapsulation of heat of fusion storage materials, Proceedings of thesecond south eastern conference on application of solar energy; 1976. p. 442–55.
11. Telkes M. Thermal storage for solar heating and cooling, Proceedings of the workshop on solar energy storage sub-systems for heating and cooling of buildings, University of Virginia, Charlottesville; 1975.
12. Shilei L, Neng Z, Guohui F, Impact of phase change wall room on indoor thermal environment inwinter. Energy and Buildings 2006, 38: 18–24.
13. Ceron I, Neila J, Khayet M, Experimental tile with phase change materials (PCM) for building use. Energy and Buildings 2011, 43:1869–74.
14. Colvin.D.P and Bryant Y.G., Protective clothing containing encapsulated phase change materials,Proceedings of the 1998, ASME international mechanical engineering congress and exposition. Anaheim. CA, USA 23-32.
15. Manini Paolo, RizziEnea, Pastore Guido, Advances in VIP design for super insulation of domestic appliances, Proceedings of 4th International Appliance Technical Conference (IATC), West Lafayette, USA, 2003.

16. Laguerre, O, Ben Amara, S, Moureh, J, Flick, D, Numerical simulation of air flow and heat transfer in domestic refrigerators, Journal of Food Engineering 2007, 81, 144–156.
17. Cerri, G., Identification of domestic refrigerator models including cool storage, Proceedings of 20th Int. Cong. of Refrigeration, Washington, 2003.
18. Azzouz, K., Leducq, D., Guilpart, J., Gobin, D., Improving the energy efficiency of a vapour compression system using a phase change material, Proceedings 2nd Conference on Phase Change Material & Slurry, 2005.
19. Azzouz, K., Leducq, D., Gobin, D., Performance enhancement of a household refrigerator by addition of latent heat storage, International journal of Refrigeration 31, 2008, 892- 901.
20. Azzouz, K., Leducq, D., Gobin, D., Enhancing the performance of household refrigerators with latent heat storage: an experimental investigation. International Journal of Refrigeration 2009, 32, 1634-1644.
21. Zalba, B., Marı´n, J.M., Cabeza, L.F., Mehling, H., 2003. Review on thermal energy storage withphase change: materials, heat transfer analysis and applications. Appl. Therm. Eng. 23,251-283.
22. Oro´ , E., de Gracia, A., Castell, A., Farid, M.M., Cabeza, L.F. Review on phase change materials(PCM) for cold thermal energy storage applications, Applied Energy, in press
23. Gin, B., Farid, M.M., Bansal, P.K., 2010. Effect of door opening and defrost cycle on a freezerwith phase change panels. Energy Convers, Manag 51, 2698-2706.
24. Onyejekwe, D., Cold storage using eutectic mixture of NaCl/H2O: an application to photovoltaiccompressor vapours freezers. Sol. Wind Tech. 6, 1989, 11-18.
25. Wang, F., Maidment, G., Missenden, J., Tozer, R. The novel use of phase change materials inrefrigeration plant. Part 1: experimental investigation. Appl. Therm. Eng. 2007, 27, 2893-2901.
26. Herald Mehling and Luisa F Cabeza, “Heat and Cold Storage with PCM, An up to dateintroduction into basics and application” Springer, 2008
27. Xie H, Wang J, Xi T, et al. Thermal conductivity of suspensions containing Nano sized SiCparticles. Int J Thermo phys, 2002; 23: 571–80.
28. Zhu H, Zhang C, Liu S, et al. Effects of nanoparticles clustering and alignment on thermalconductivities of Fe_3O_4 aqueous nanofluids, Appl Phys Lett 2006; 89: 023123.
29. Beck MP, Yuan Y, Warrier P, et al. The effect of particle size on the thermal conductivity ofalumina nanofluids, J Nano part Res 2008, 11: 1129–36.
30. Corcione M. Empirical correlating equations for predicting the effective thermal conductivity anddynamic viscosity of nanofluids, Energy Convers Manage 2011; 52: 789–93.
31. Kalaiselvam S, Parameshwaran R, Harikrishnan S. Analytical and experimental investigations of nanoparticles embedded phase change materials for cooling application in modern buildings. Renew Energy 2012; 39:375–387.
32. Vellaisamy Kumaresan, Ramalingam Velraj, Sarit K. Das, The effect of carbon nanotubes in enhancing the thermal transport properties of PCM during solidification 2012.
33. Qinbo He, ShuangfengWang ,Mingwei Tong, Yudong Liu., Experimental study on thermo physical properties of nanofluids as phase-change material (PCM) in low temperature cool storage 2012.
34. George A. Hand book of thermal design. In: Guyer C, editor. Phase change thermal storage materials, McGraw Hill Book Co.; 1989 [chapter 1].
35. K.Biswas, Nano-based phase change materials for building energy efficiency, The Smart Eco- Efficient Built Environment 2016, Pages 183-211.
36. Preet, B Bhushan, T Mahajan, Experimental investigation of water based photovoltaic/thermal (PV/T) system with and without phase change material (PCM), Solar Energy, 2017.
37. Ahmad Tajuddin Mohamad and Nor Azwadi Che Sidik, Nano-enhanced phase change material effects on the super cooling degree improvement, published under licence by IOP Publishing Ltd.
38. M.Abdollahzadeh M.Esmaeilpour, Enhancement of phase change material (PCM) based latent heat storage system with nano fluid and wavy surface, International Journal of Heat and Mass Transfer, Volume 80, January 2015, Pages 376-385
39. V.Kumaresan, P.Chandrasekaran, MaitreyeeNanda, A.K.Maini, R.Velraj, Role of PCM based nanofluids for energy efficient cool thermal storage system, International Journal of Refrigeration, Volume 36, Issue 6, September 2013, Pages 1641-1647
40. S.Sharma, L.Micheli, W.Chang, A.A.Tahir, K.S.Reddy, T.K.Mallick, Nano-enhanced Phase Change Material for thermal management of BICPV, Applied Energy, Volume 208, 15 December2017, Pages 719-733.

41. SimoneRaoux Robert, M.ShelbyJeanJordan-Sweet, BeckyMunoz, MartinSalinga, Yi-ChouChen, Yen-HaoShih, Erh-KunLai, Ming-HsiuLee, "Phase change materials and their application to random access memory technology",Microelectronic Engineering, Volume 85, Issue 12, December 2008, Pages 2330-2333.
42. M.H.Mahfuz, M.R.Anisur, M.A.Kibria, R.Saidur, I.H.S.C.Metselaar, Performance investigation of thermal energy storage system with Phase Change Material (PCM) for solar water heating application, International Communications in Heat and Mass Transfer, Volume 57, October 2014,Pages 132-139.
43. Randeep Singh, Sadegh Sadeghi, Bahman Shabani, "Thermal Conductivity Enhancement ofPhase Change Materials for Low-Temperature Thermal Energy Storage Applications energies article, 27 December 2018.

RESEARCH ARTICLE | MAY 22 2023

Design and analysis of propeller

Sreekanth Sura ✉; K. Prudhvi; M. Sri Ram Chaitanya; R. Anil Kumar; S. Praveen

AIP Conference Proceedings 2492, 020064 (2023)
https://doi.org/10.1063/5.0113394

Design and Analysis of Propeller

Sreekanth Sura[1, a)], K. Prudhvi[1,b)], M. Sri Ram Chaitanya[1,c),] R. Anil Kumar[1,d),] S. Praveen[1,e)]

[1]*Department of Aeronautical Engineering, MLR Institute of Technology, Hyderabad, India.*

Corresponding Author: [a)]sreekanthsuramlrit@gmail.com
[b)]prudhvikosanapk@gmail.com,
[c)]m.sriramchaitanya@gmail.com,
[d)]anilkumarraopally@gmail.com,
[e)]praveendattu5@gmail.com

Abstract. Propeller is the key component of an engine to provide thrust. The design of propeller plays a major role in guiding the airflow. And the material used need to with stand the structural loads and forces acting on it. The objective of this project is to generate thrust force at different RPM values ranging from 0 to 8,000 for UAV. To design a propeller using solid works software and to do computational fluid dynamics analysis at the sea-level conditions in Ansys software. To design a propeller many variables are to be taken into consideration such as chord distribution, flow angle, pitch angle at different spans of blade & the twist distribution from root to tip. Blade element theory is used to perform the different spans and took the optimum result for producing high thrust with minimal loss. And based on the obtained results the parameters were taken into consideration.

INTRODUCTION

The aim of this thesis is to investigate the UAV propeller aerodynamic design and analysis to achieve better output at lower RPM's by changing the blade angles according to the plane position and at wider range of operating conditions. In order to achieve the exact blade angles and aerodynamic design composite materials are used. Through which even the material properties of propeller increase. As a result, the aerodynamic characteristics are also improved[1].

The design is optimized based on specific aerial vehicle characteristics, as well as conceivable operations of related aircraft propellers. Initially, all computations will be carried out to establish the ideal blade geometry utilizing existing blade element theories, taking into account a literature analysis of previous years' research and related studies. Preliminary observation will include analytical computations depending on its conditions on the blade element theory with basic initial input data. A propeller is designed using these results, and flow analysis is performed to validate and verify the analytical approaches used[2].

All of the study results were taken into consideration, and they were then used to carry out additional finite element analysis of a propeller with ideal blade geometry in order to determine propeller deflections under a given load condition[3]. A number blade angles were considered at the plane sections taken all the flow characteristic were taken into consideration, thus the optimal design is finalized. And then the RPM is altered and Study is done at which RPM the thrust output is higher the usual. Dynamic Fluid-Structure Iteration Analysis methodologies will be developed to further examine the deflections, with outputs and recommendations for future development.

Advancements in Aeromechanical Materials for Manufacturing: ICAAMM-2021
AIP Conf. Proc. 2492, 020064-1–020064-10; https://doi.org/10.1063/5.0113394
Published by AIP Publishing. 978-0-7354-4438-6/$30.00

DESCRIPTION OF PROPELLER

A propeller is a device which converts rotational energy to the propulsive energy. It has a hub and blades to form helical spiral. The rotational motion of the blades is converted into thrust power by creating pressure differences between the two surfaces. propeller makes aircraft move through the air[4-5]. propeller consist of two or many blades attached to the hub. These Blades are connected to hub and to engine shaft.

A propeller consists of tip, root, leading edge and trailing edge. Where tip is the farthest or the edge of the propeller portion, root is the nearest portion to the hub, leading edge is the cutting edge of the airfoil as it cuts the flow of air over the blade and camber side, trailing edge Is the rear edge of the airfoil.

The blade angle is between the chord or blade face of element and rotation plane. As the blade twists the angle changes and gives different speed.

The blade element is made up of airfoil sections that are emplaced of one other to produce the blade airfoil. These elements are arranged at various angles in the plane of rotation.

METHODOLOGY

Blade Element Theory

One of the most common methods for studying the aerodynamic design and performance of propellers is blade element theory. This theory is built on the foundation of wings and standard airfoil theory. The wing of a propeller is rotating with some angle of twist. And the angular speed with its spanwise elements in sloid-body rotation is $\omega=2\pi n$. As the distance from the axis of rotation increases linearly the speed of rotation increases, hence there is need for twist, to regulate flow conditions. As a result of rotation, each blade section is exposed to relative flow magnitude and blade angles, just as the blade element theory assumes. A propeller blade is made up of a series of airfoil sections that observe the relative flow and generate local torques and aerodynamic[6-7] .

The aerodynamic performance of each segment is determined by the local relative airfoil shape from figure 1, flow speed, Reynolds number and angle of attack depending on the relative speed. The propeller and elemental velocity vectors in X and Y directions, as well as the angles with elementary aerodynamics velocity, pressure and other components, are depicted

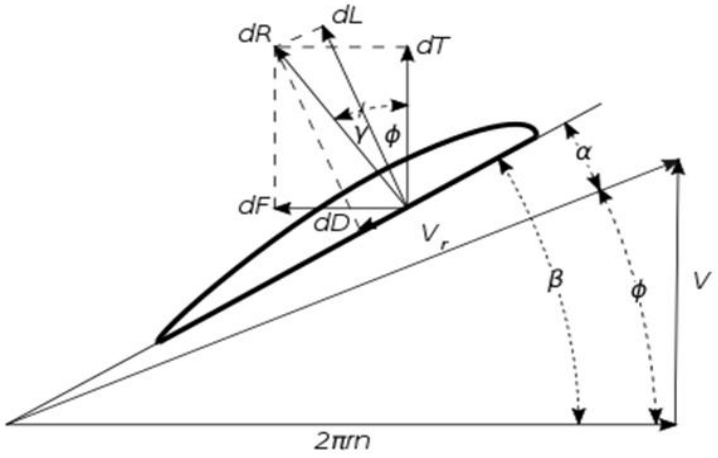

FIGURE 1. Blade Element

First and foremost, the Blade Element Scientific theory and formulations are used to do all analytical computations. Because a propeller blade is nothing more than the stacking of multiple airfoil sections, we split it into several tiny airfoil sections based on the propeller's span. NACA 4412 was chosen as the proper angle of attack for the airfoil, i.e., at the maximum L/D, say 7.00 degrees, for the most efficient functioning. And as we move from the root chord to the tip, the angle of the blade decreases to provide a more effective thrust by minimizing drag. The Angle of Attack is a function of the optimum pitch angle of the blade section. As a result, each part's rotational

speed varies, but forward speed remains constant since the pitch angle is designed to vary from root to the edge to maintain the optimum angle of attack at each section. The Table 1 shows airfoil specifications.

DESIGN

Table 1. Airfoil specifications

S.No.	Name of the property	Property's value
1	Number of blades (B)	2
2	Station radius (r)	15mm
3	Blade length (L)	155mm
4	Blade chord (c)	37mm
5	Propeller diameter (D)	340mm
6	Free airstream velocity (V)	25m/s
7	Reynolds number (Re)	50,000

SOLIDWORKS

Solidworks is a modeling software of CAD (computer aided design) and CAE (Computer-aided engineering) and it is used for designing and analysis software, and product data management software. It makes key role across many industries like aerospace, civil or construction, automotive, robotics and animations etc...

Solidworks is so simple to use, easy to learn and user-friendly. It has windows graphical user interface by this designer can easily copy and paste or drag and drop. Many icons and options are so similar and familiar to operate. It is published by Dassault Systems. SolidWorks is of three types: part, assembly and drawing mode. In figure 2 the solid work model shown.

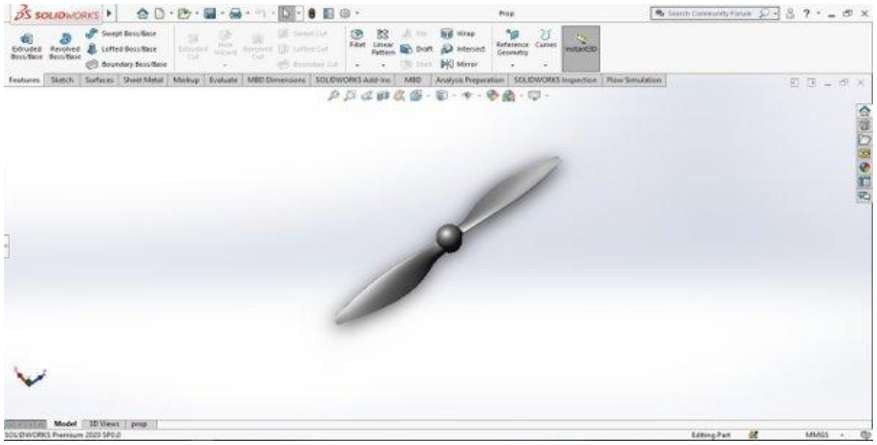

FIGURE 2. Solidworks Model

Steps involved

Step 1: Create a new plane (plane1), select right plane as 1st reference
Step 2: Taking plane1 as reference and create plane2 and repeat the same for 6 planes
Step 3: Now insert NACA 4412 points on each plane and convert entities
Step 4: Sketch a circle on plane1, and make this coincident with the origin point
Step 5: Hide all the planes and create loft for all the points (NACA 4412)
Step 6: Create circle with diameter=15mm on top plane
Step 7: Create boss-extrude for circle and choose mid plane direction
Step 8: Create circular-pattern loft and select the parameters to loft
Step 9: Create dome with depth=30mm

Step 10: Draw a circle around the propeller and Bose-extrude it (used for simulation).

ANALYSIS

Computational Model

There are two components to the computational domain. Upstream and downstream, the static domain takes up more space than the propeller's diameter. The length-wise diameter of domain is ten times that of the span-wise diameter propeller. The inlet, exit, and outside area of the propeller are all stationary. The spinning domain has a diameter of 38cm and a height of 40cm and is cylindrical in form. Individual meshes for the static and spinning domains could be seen in Figure 3. At an 8000rpm propeller rotation speed, a variety of mesh structures were utilized to ensure outcomes based on surface function independency. The produced thrust has a maximum difference of just 0.26 percent between the fine mesh and the coarse mesh. As a result, the mesh chosen has no bearing on the outcome. As a result, for the proposed propeller, the fine mesh type is utilized in CFD simulation. The figure 3 shows Rotating and Stationary Domain.

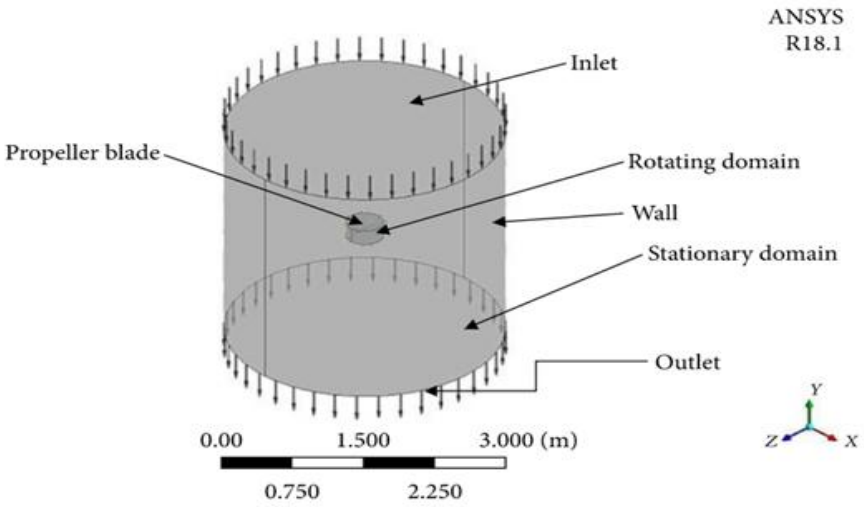

FIGURE 3. Rotating and Stationary Domain

The figure 4,5,6,7,8 shows Static Domain Solid View, Static Domain Wireframe View, Rotating Domain Solid View, Rotating Domain Wireframe View, Static and Rotating Domain Wireframe View and Table 2,3 gives details of mesh attributes, Rotating Zone Conditions.

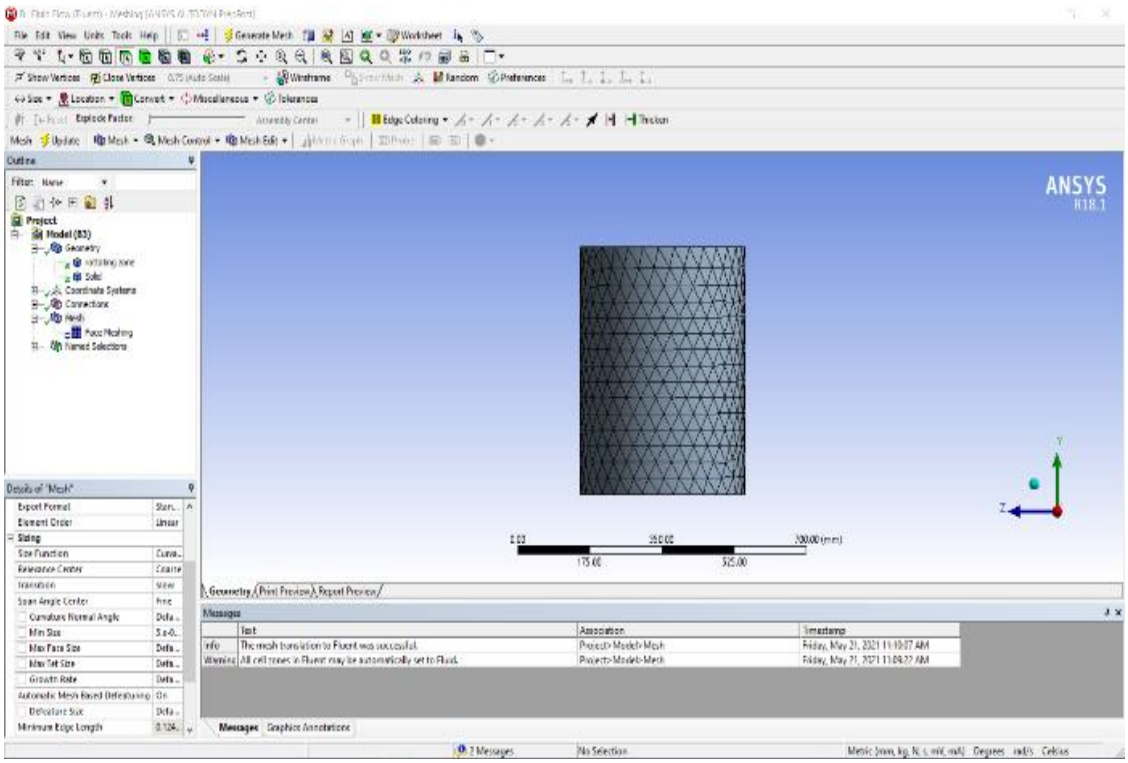

FIGURE 4. (a) Static Domain Solid View

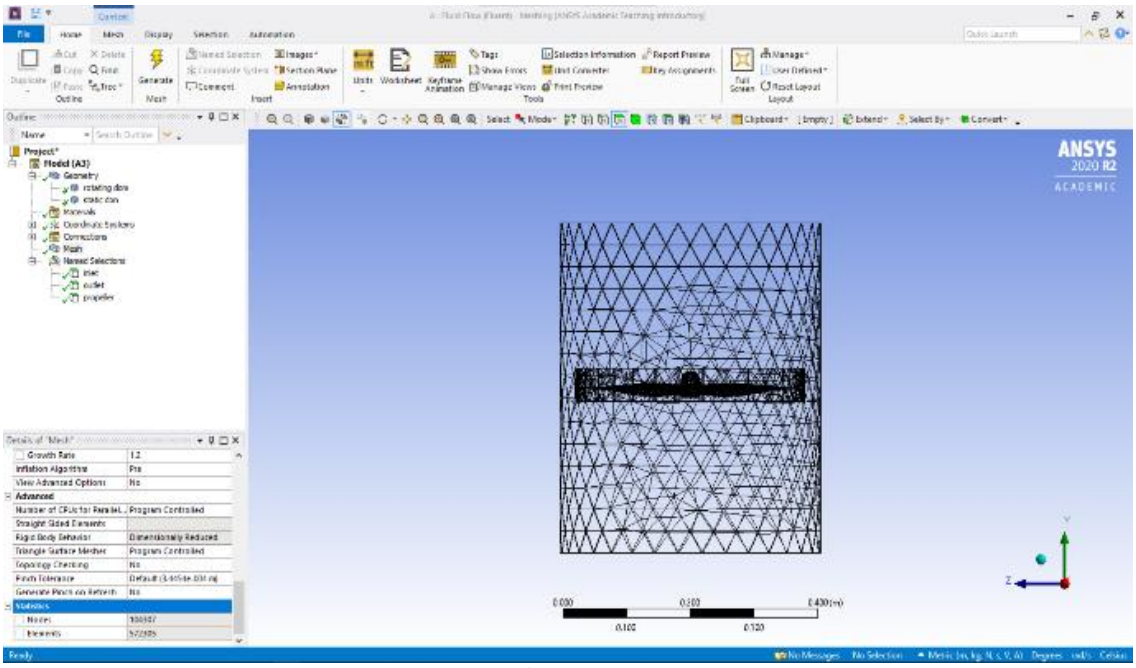

FIGURE 5. Static Domain Wireframe View

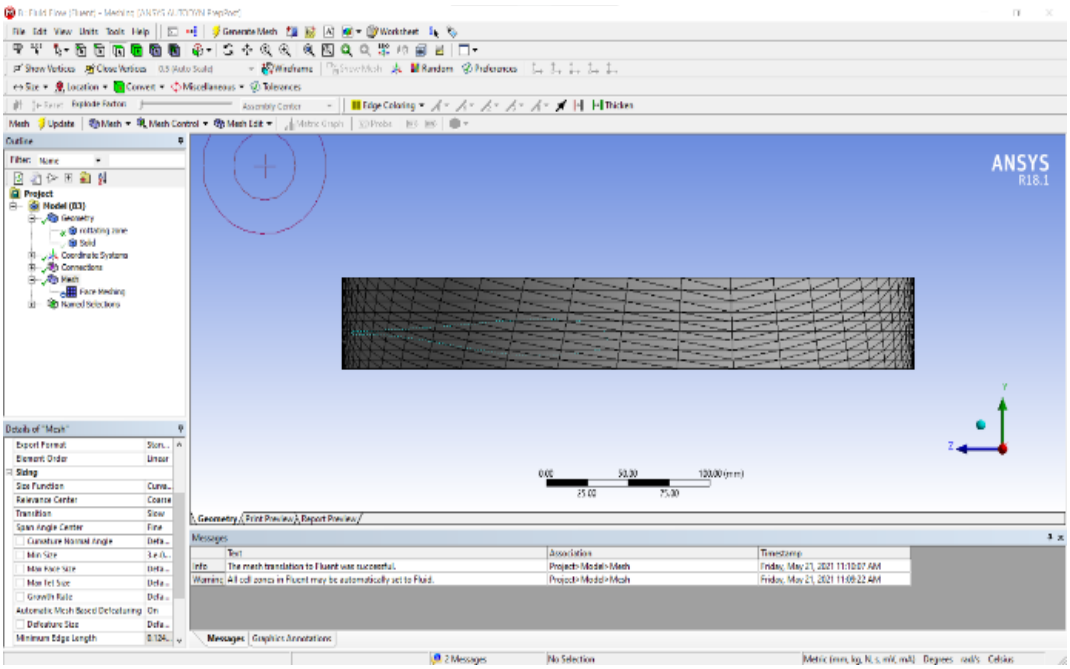

FIGURE 6.Rotating Domain Solid View

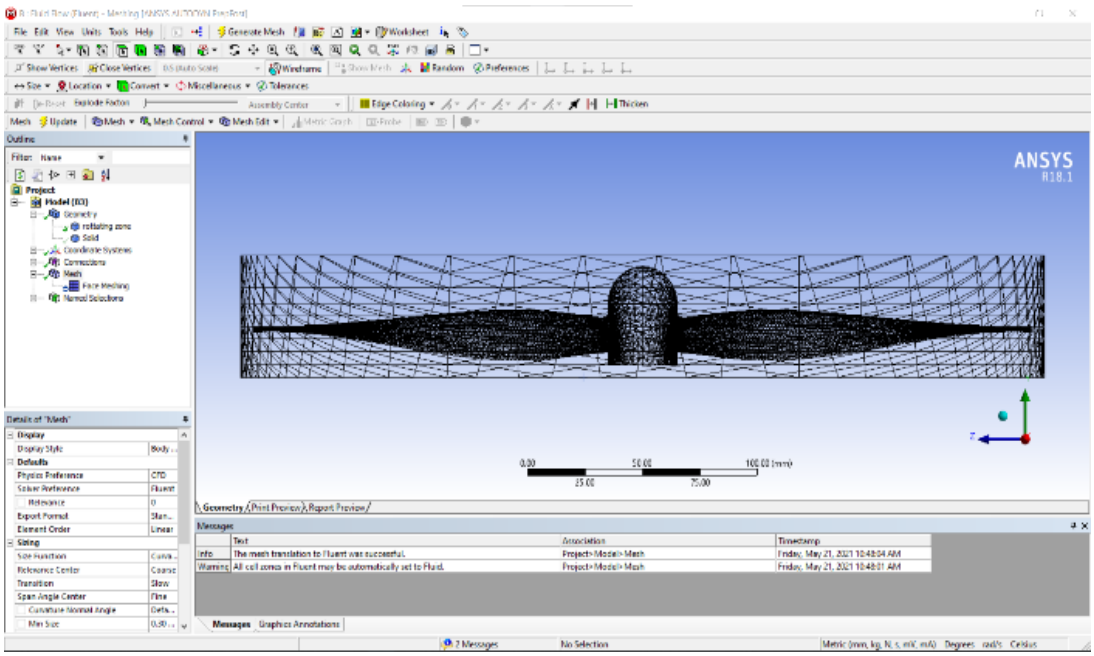

FIGURE 7. Rotating Domain Wireframe View

Table 2. Mesh Attributes

S.No	Property	Value
1	Number of nodes	15508
2	Number of elements	79849
3	Growth rate	1.2
4	Transition ratio:	0.272
5	Minimum size	3.0mm
6	Solver preference	Fluent
7	Target skewness	0.900

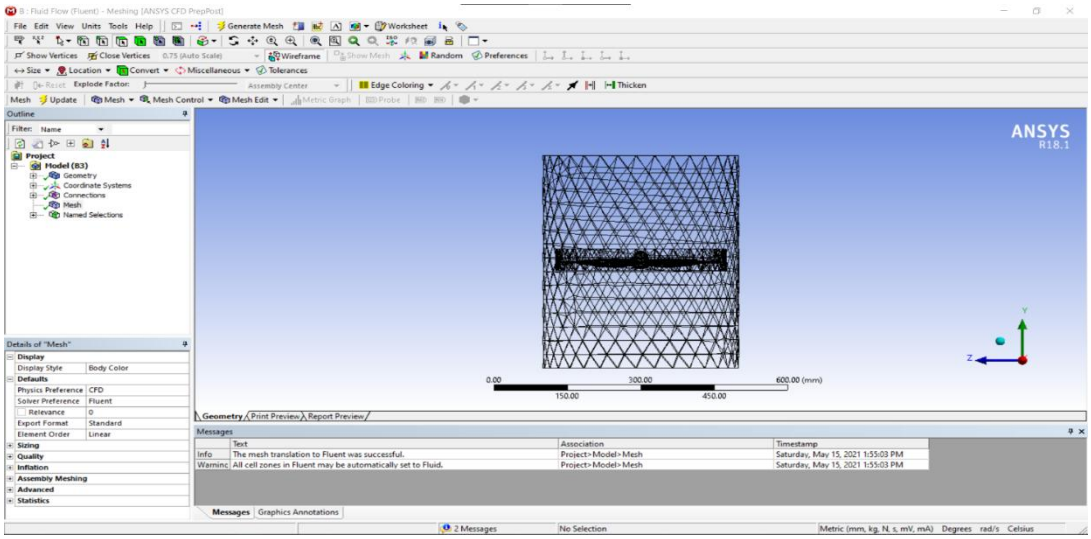

FIGURE 8. Static and Rotating Domain Wireframe View

Table 3. Rotating Zone Conditions

S.No	Material	Air
1	Relative to cell zone	Absolute
2	Rotational velocity	8000(rpm)

Table 4. Reference Values

S.No	Compute form	Rotating zone
1	Area	1m2
2	Density	1.225
3	Temperature(k)	288.16
4	Velocity(m/s)	1

RESULTS

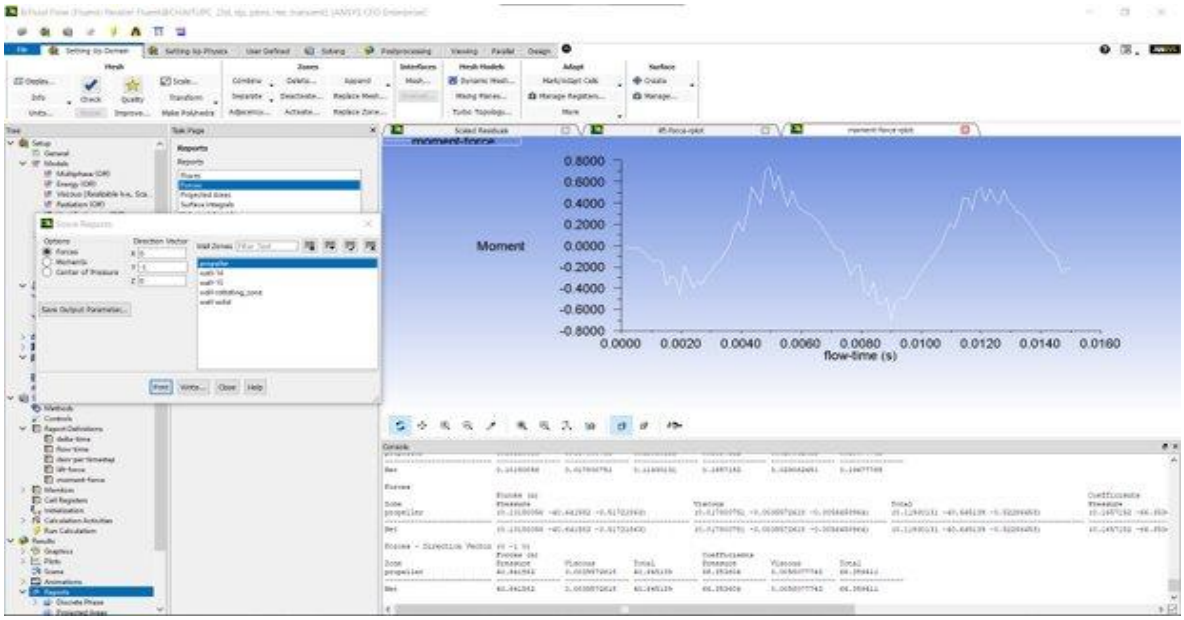

FIGURE 9. Moment Force Graph

This above figure 9 defines about the moment force generated by the propeller at around 8000 RPM. In the graph we can observe the moment is not constant.

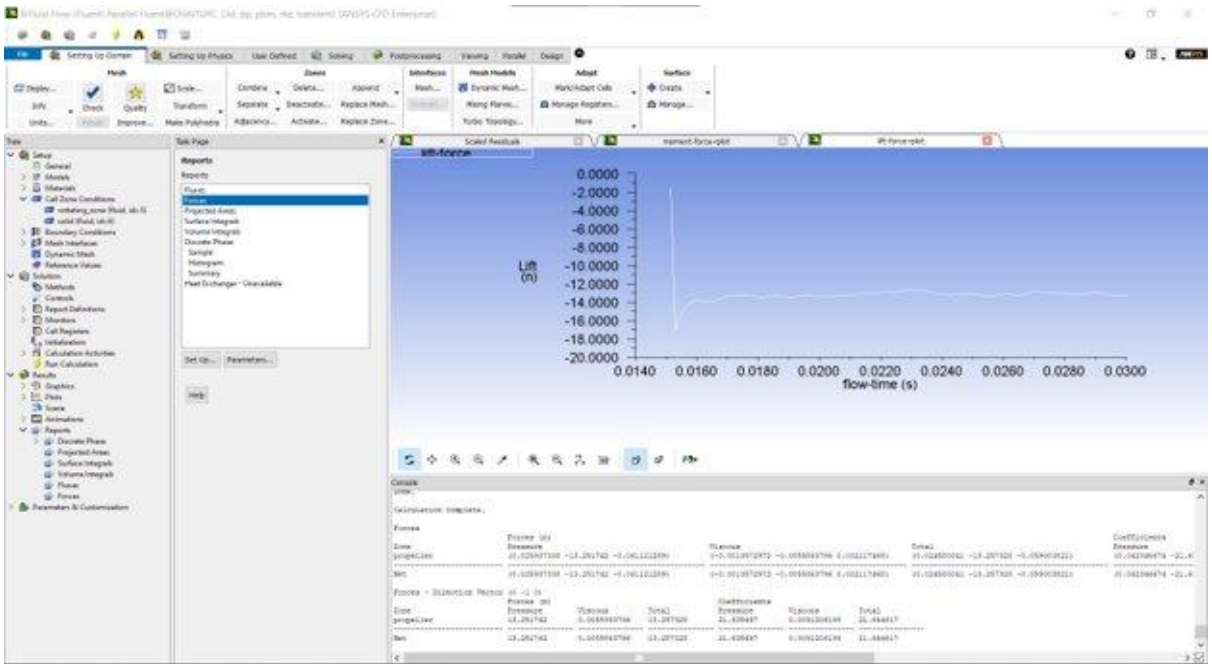

FIGURE 10. Lift Force Graph

This above figure 10 defines about the lift force vs flow time of the propeller around 8000 RPM which is operated at sea level.

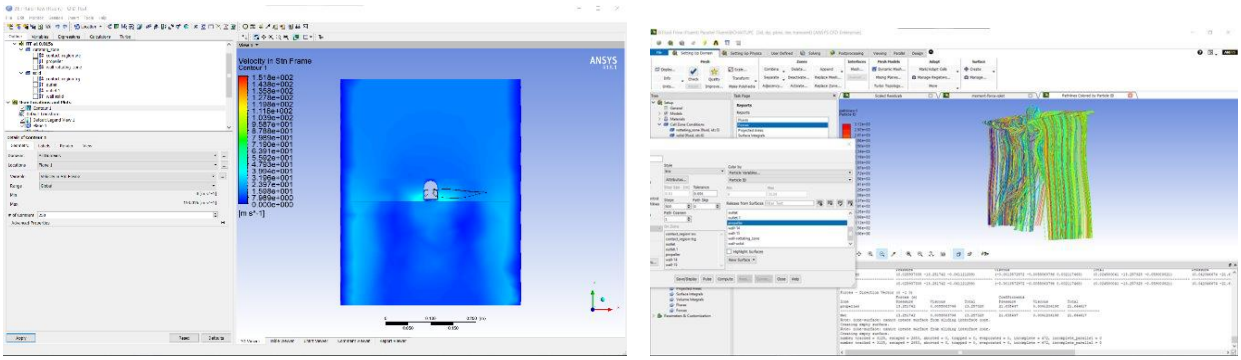

(a) (b)

FIGURE 11. (a) Velocity in Contour (b) Path Lines Particle ID

This above figure 11 defines about the particle density variation behind the propeller when the air flow starts. As we can observe the density of the flow particles is varied at different positions from the hub. Near the hub the density of flow is high due to the structural behavior of the propeller and blade angle.

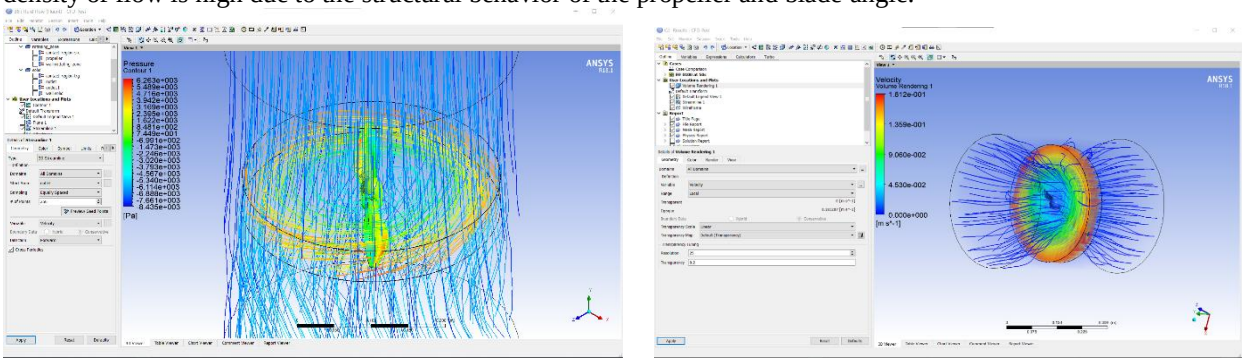

(a) (b)

FIGURE 12. (a) Velocity Stream Line(b) Velocity Volume Rendering

This above figure 12 defines about the pressure around the propeller inside the rotating domine and we can also observe the pressure on the propeller as we can observe that the portion where air particles leaving the propeller at the trailing edge the pressure is higher than the other portions because of randomness of the particles at the trailing edge.

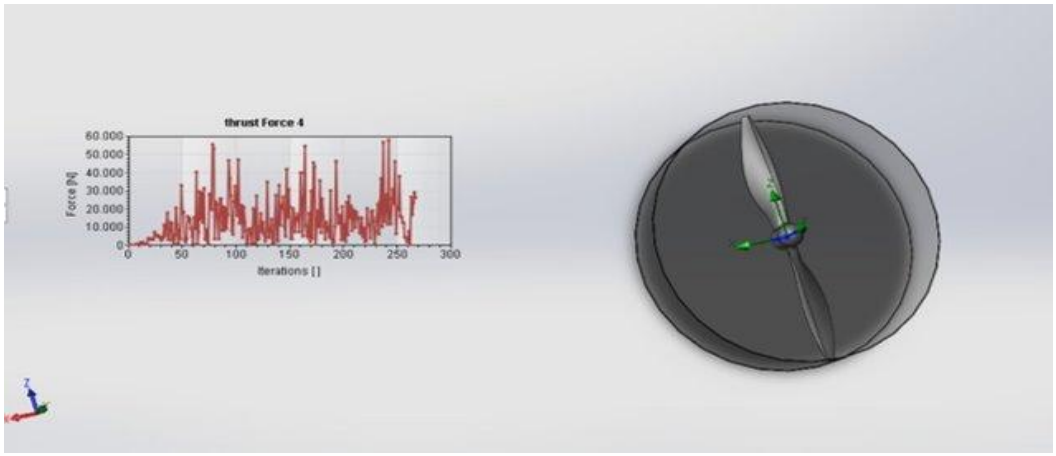

FIGURE 13. Trust Force Representation

The figure 13 trust force representation and flow analysis is done on the designed propeller at the sea level conditions at different RPMs. From 2000 to 4000 RPM the lift generated is constant. From 4000RPM to 8000RPM the rise in lift is rapid. After 8000 RPM again the there is no rise in the lift and the lift force started reducing as we continued to increase the RPM. The analytical and theoretical results are obtained from a propeller rotating from 0 to 8000 RPM are determined and the maximum thrust values are found at 8000 RPM. The values are found to be,

Theoretical Thrust values = 25.8 N
Computational Thrust values = 26.3 N

CONCLUSION

A propeller is designed with NACA4412 airfoil using Solid works software and the Computational Fluid Dynamics analysis at the sea-level conditions is done using Ansys software. The thrust force is generated at 0-8000 RPMs and the computational values are found to be greater than the theoretical values as the impacts of the wake upon the sections of blade are not included in the Blade Element Approach. Furthermore, analysis of numerical results differs significantly from analytical results in this case. We can see that using a mesh with a larger element size gives us more accuracy in results. As a consequence, more research is recommended in order to decrease the discrepancies in the results.

REFERENCES

1. M. K. Rwigema, "Propeller blade element momentum theory with vortex wake deflection," 27th International congress of the aeronautical sciences, vol. 1, pp. 727–735, 2010.
2. S.J. Krishna Murthy, R. Prathapan Ayaka, N. Vinod Kumar, N. Harikrishna, Jyotsana. M. Sharma, Jayant Lavhe, "Design and Development of Propeller for NAL-Micro Air Vehicle" NAL, Bangalore, PD-PR-0914, May 2009.
3. Drela, Mark. "QPROP formulation." Massachusetts Inst. of Technology Aeronautics and Astronautics, Cambridge, MA (2006)
4. Zondervan, G. J. D. "A review of propeller modelling techniques based on Euler methods." Series 01: Aerodynamics 05 (1998).
5. Mr. Sreekanth sura, Alka Sawale, M. Satyanarayana Gupta "Dynamic Analysis of Cantilever Beam" International Journal of Mechanical Engineering and technology (IJMET), date: 05-05-2017, volume no:8.
6. K Shiva Shankar, B Nagaraj Goud, Sreekanth Sura, Ch Harish, B Pravalika, "An UAV with Twin Propellers Driven by Single Motor", International Journal of Innovative Technology and Exploring Engineering (IJITEE), ISSN: 2278-3075, Volume-9 Issue-2, December 2019.
7. Mr. Veeranjaneyulu Professor Manohar Satti, " Design and Analysis of Missiles*" Page 1570-1577 Volume No,3 Issue No.10 & ISSN: 2348-4845 IJMETMR Oct 2016*

RESEARCH ARTICLE | MAY 22 2023

Modeling and static structural analysis on stiffened panel for an aircraft structure

B. Nagaraj Goud ✉; Sreekanth Sura; Swetha Bala M. N. V. S.; B. Manideep

AIP Conference Proceedings 2492, 040007 (2023)
https://doi.org/10.1063/5.0113300

Modeling and Static Structural Analysis on Stiffened Panel for an Aircraft Structure

B. Nagaraj Goud [1, a)], Sreekanth Sura[1, b)], Swetha Bala MNVS[1, c)], B. Manideep [1, d)]

[1]*Department of Aeronautical Engineering, MLR Institute of Technology, Hyderabad, India.*

[a)] Corresponding Author*: nagaraj2107@gmail.com*
[b)] *sreekanthsuramlrit@gmail.com*
[c)] *swethabalamlr@gmail.com*
[d)]*manideepbalusani.9@gmail.com*

Abstract. The paper is focused on the modeling and analysis of an aircraft stiffener by using ANSYS. The stiffener of an aircraft is mainly used to support the structure of the aircraft. It is normally made using a metal of aluminum, steel and titanium. In this regard, the stiffener is made with aluminum alloy and is compared with steel material. and performed static structural analysis and analyzed material performance. To improve the structural stability of a stiffened panels are to be determined on account of their weight saving. When these stiffeners were permitted to buckle at ≤ to the design yield load. The response of stresses and deformation of the Stiffened Panel are addressed and the response of the structure. When the design is efficient, the constraint can be adjusted to allow local buckling at the design limit load, as long while the structure doesn't really fail at even a load lesser than the design maximum applied load. Improved structural integrity by supported by hat section arrangements to the stiffened panel. Therefore, the simulation analysis results for the stiffener supported by the hat section members were presented.

Key words: Aircraft, Stiffener, Design load, Static Analysis, ANSYS

INTRODUCTION

Stiffeners are secondary plates or sections that are attached to flanges or beam webs to strengthen the members against out-of-plane deformations[1]. Stiffeners will be installed on nearly all key bridge beams. Most, however, will have transverse web stiffeners connected to the web, so instead of vertical stiffeners. Longitudinal web stiffeners are often used in deep beams. Flange stiffeners are typically utilized on long length box girder bridges; however, they are infrequent elsewhere[2]. Weaving process through its thickness of the dry graphite-epoxy composite material can significantly decrease the effort required for panel fabrication and assembly. The pre-stacked skin portions, ribs, stringers, intercostals, and spar caps are stitched together across the thickness of the skin. Stitching provides a way to decrease damage progress caused by low-speed or discontinuous source impact, and mechanical fasteners are almost removed entirely. Conventional composite materials have used no-damage-growth technique and are tailored to withstand design limit loads in discrete-source-damaged components without damage dispersion[3]. As the structures that are partially noticeable after an impact can support the design of maximum load without damage occurs. The assembly constraint requires that allows the less strain than would be required in an original construction, resulting in a heavier structure and the composite material of stiffening panels are becoming more attractive in the aerospace applications[4].

The different types of stiffeners are used to stiffen the composite plate. These are divided into two categories: open form as well as closed form or box type. The open form is torsionally less, whereas the closed or box type is torsionally tough. Unless this design restriction could be altered to allow local buckling at design limit load, as far as

Advancements in Aeromechanical Materials for Manufacturing: ICAAMM-2021
AIP Conf. Proc. 2492, 040007-1–040007-6; https://doi.org/10.1063/5.0113300
Published by AIP Publishing. 978-0-7354-4438-6/$30.00

the component doesn't really fracture at such a load is below design maximum load, lighter, greater weight- and cost-efficient constructions can be produced[5]. The structural panels can be built in such a way that they are considered to handle loads far greater than that of the buckling loading and remain unchanged. The main aim of this research study about to see how considerable weight may be saved by allowing strengthened panels to buckle at loads lower than their bearing capacity as far as the panel doesn't quite fail. When the damage begins and growth on a local level, as well as nonlinear behaviour of post-buckling, If the structure fails due to the load is considered to be the ultimate load, it should be evaluated[6]. The method used in this study was to evaluate the behaviour of single-stiffener materials both analytically and experimentally then predict structural stability improvements for multi-type stiffened panels using analytical methods[7]. Stiffeners are divided into two categories. They are stiffeners that run the length of the web and are aligned in the span direction and other one is transverse stiffeners are placed perpendicular to the span direction of the beam as shown in figure.1

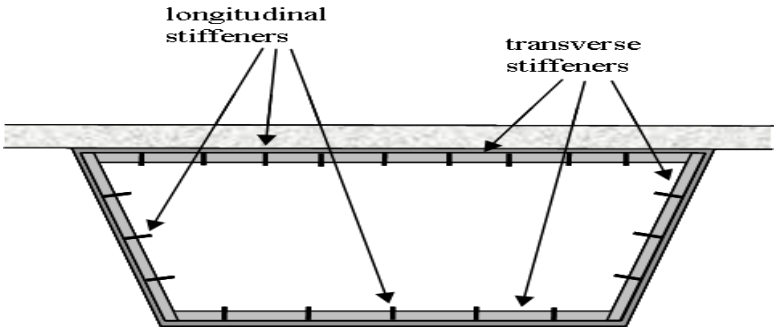

FIGURE.1 stiffener

Stiffeners have been utilized in the past in a number of ways, but the simple flat stiffener is virtually usually employed in the latest designs. The Stiffeners could be applied to one edge of the plate (single sided) or both edges of the plate (double sided) [8]. Joint stiffeners are commonly double-sided, while middle web shear walls are usually single. Stiffeners could be doubled, tripled, quadrupled, or even multi-legged. For the purpose of coupling torsional stiffening in between beams in a practical way, intermediate stiffeners on major beam webs are frequently required. If this is the case, the stiffener positions will be determined by the bracing locations[9]. However, for beams that do not requires including such transverse girders in the ladder deck bridge or if the design bracing is employed, intermediate stiffeners could be required. beam as shown in figure.2

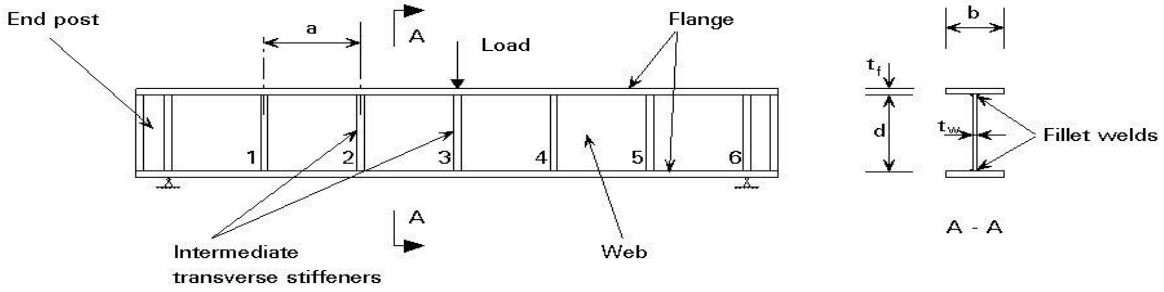

FIGURE.2 Intermediate transverse web stiffeners

In 1940, Massonnet presented a research study of the elastic stability of simply supported rectangular plates subjected to pure bending and strengthened with a 1/4 longitudinal stiffener. These studies concentrated primarily on the theory of optimal stiffener rigidity[10]. Later, Kromm and Chawla refined the minimum strength requirements for panel stiffeners by examining a longitudinal stiffened panel during pure bending[11]. Milosavljevic has developed a comprehensive study on treatment of the elastic stabilisation of a simply supported rectangular panel was subjected to an axial stress, shear stress and combined bending that strengthened to two transverse stiffeners and one longitudinal stiffener. The key was found by applying a series technique to the plate's differential equation. the stiffeners in the transverse direction at the 1/3 wide locations, the special situations of pure bending and bending

with shear were solved after a year. According to Dubas ideal portion of the stiffener in longitudinal direction which act a simply supported panel exposed to the pure bending is at 1/5, The American and British Specifications have since accepted this position.

DESIGN AND MATERIAL PROPERTIES

The design work in this research focuses on building and expanding the possibilities of those computational tools using the proposed methodology to improve modelling, design and development, thus the stiffened panel is designed entirely or in its discrete required components as shown in figure.3

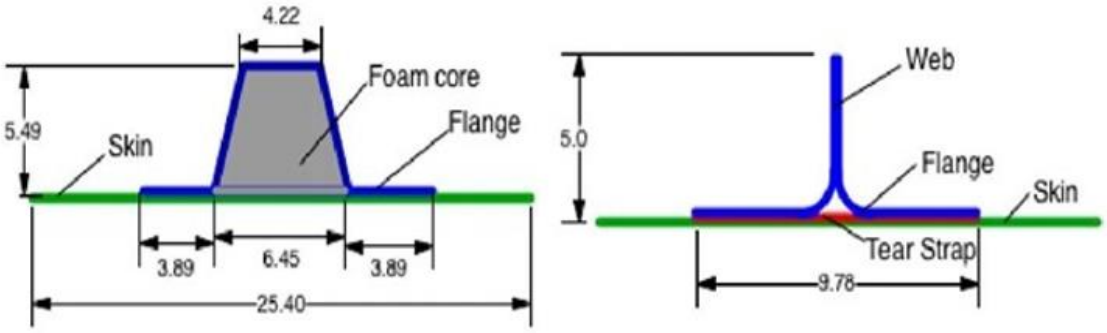

FIGURE.3 Hat and blade frame stiffener

The hat section stiffener design using CATIA and It includes a step-by-step simulation that demonstrates the main component with dimensions and their characteristics as shown a wireframe in figure.4 and the design part workbench in figure.5

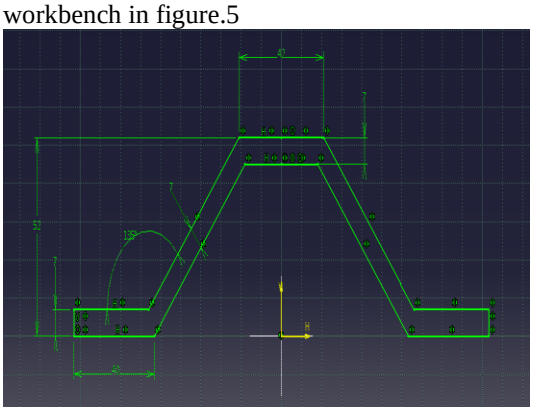

FIGURE.4 Geometry of the Hat section stiffener

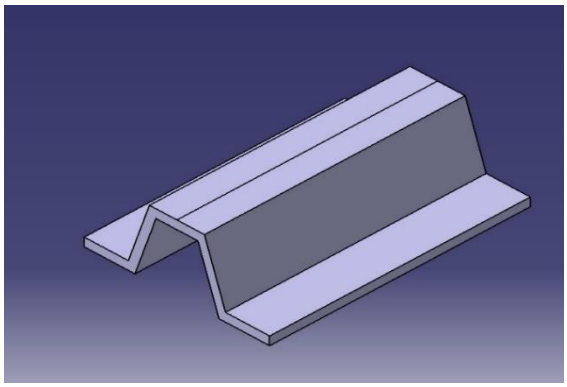

FIGURE. 5 Model of Single Hat section stiffener

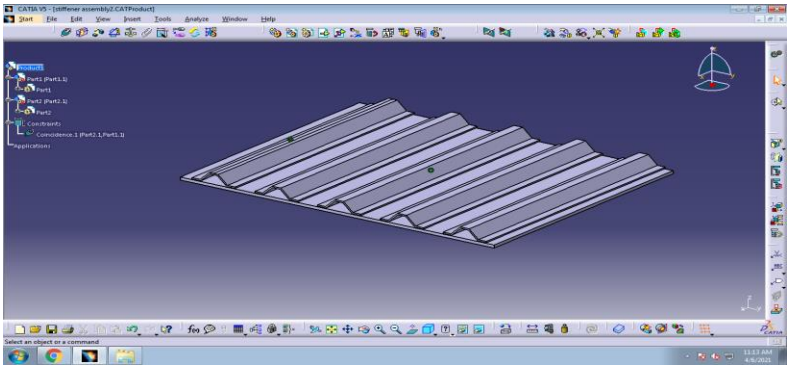

FIGURE.6 Model of Hat section stiffener

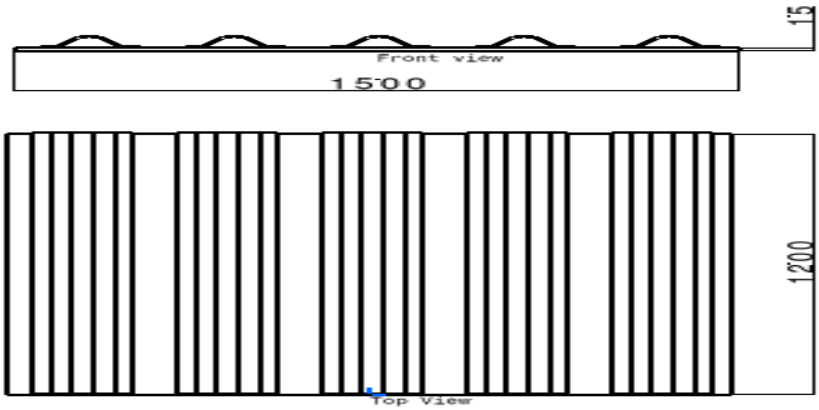

FIGURE.7 Front view and Top View of the Hat section stiffener

TABLE1. Shows the Material properties

Material	Poisson's Ratio	Modulus of Elasticity (GPa)	Density (kg/m^3)
Structural Steel	0.27	200	7850
Aluminium Alloy	0.33	70	2770

RESULTS AND DISSCUSSIONS

Based on selected materials and designs, the finite element analysis package ANSYS workbench was imported from CATIA and as per the required dimensions. Meshing, boundary conditions were applied, the rectangular panel was fixed at both ends and uniformly distributed pressure was applied, and static structural simulation analysis was performed for both aluminum alloy and steel materials.

For the given set of loading condition, the Maximum Deformation value was observed 40.092mm on the Aluminum stiffened panel and the minimum value was observed 4.45mm and von Mises stress, the Maximum value was observed 337.91Mpa and minimum value was observed 1.596Mpa as shown in figure.8 and 9.

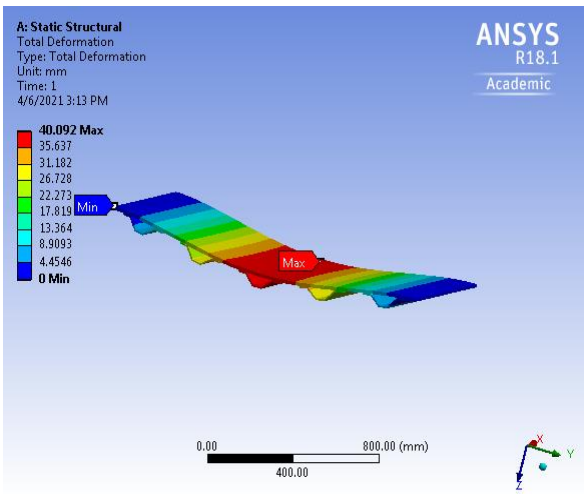

FIGURE.8 Maximum Deformation of an Aluminum Alloy Material

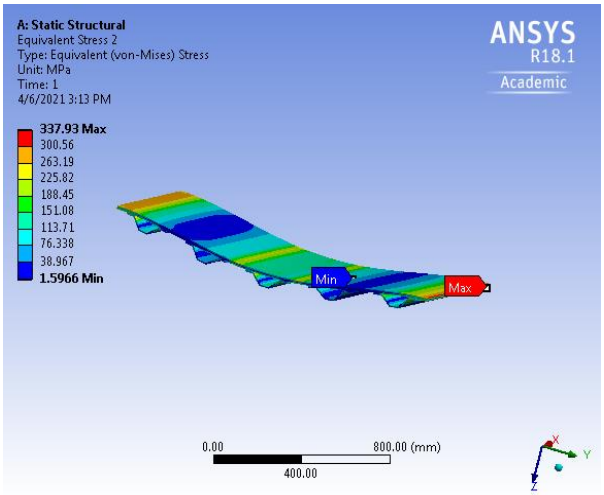

FIGURE.9 Von Mises stress of an Aluminum Alloy Material

Similarity on steel material, the given set of loading condition, the Maximum Deformation value was observed 14.68mm on the Steel stiffened panel and the minimum value was observed 1.6mm and von Mises stress, the Maximum value was observed 375.9Mpa and minimum value was observed 1.43Mpa as shown in figure.10 and 11.

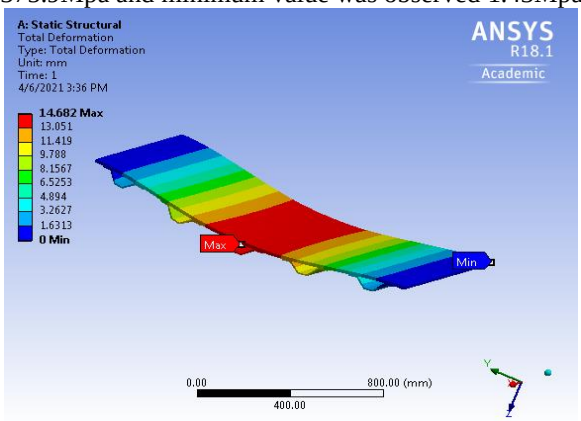

FIGURE.10 Maximum Deformation of the Steel Material

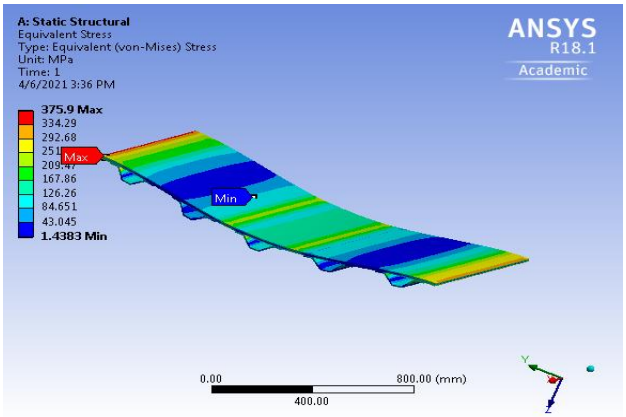

FIGURE.11 Von Mises stress of the Steel Material

The results of the static analysis presented in the form of total deformation and Von mises stresses under the pressure of 1atm was applied on the fixed rectangular plate carrying uniformly distributed load calculated by ANSYS.

TABLE 2. Shows the Stresses and Deformation Results

Materials	Pressure (MPa)	Von Misses Stresses (Mpa)	Displacement (mm)
Aluminium Alloy (AA6082)	0.101	337.93	40.09
Steel Alloy (Ferrium m54)	0.101	375.90	14.68

CONCLUSION

Aluminum is the primary material used in the manufacturing of aircraft in this article. However, larger aircraft manufacturers such as Boeing and Airbus have started to use carbon fiber in their planes. The FEA of the structural analysis for a fixed rectangular plate with uniformly distributed pressure load applied for both steel and aluminum material was performed in this work, and the following conclusions were reached. The total deformation and stress analysis results for a fixed stiffened panel are compared for two material qualities by ANSYS. By static analysis, von mises stress values are lower in aluminum than in steel stiffened panels, and overall deformation results are lower in aluminum than in steel stiffened panels.

REFERENCES

1. Uday Deepika A, Veeranjaneyulu K. Buckling analysis of stiffened panel for aircraft fuselage. *Int J Mech Prod Eng Res Dev*. 2018;8(1):1299-1308. doi:10.24247/ijmperdfeb2018150
2. Uday N, Goud R, Sawale A, Rakham B. Buckling Load Predictions of Panel and Shell using Vibration Correlation Technique. *Int J Eng Adv Technol*. 2019;9(2):1842-1845. doi:10.35940/ijeat.b2679.129219
3. Kumar DM, Madhavi N, Sushma M. Thin walled C-Sectional Beam under Axial Load. *Int J Innov Technol Explor Eng*. 2020;9(3):498-499. doi:10.35940/ijitee.c8512.019320
4. Ko WL, Jackson RH. Shear Buckling Analysis of a Hat-Stiffened Panel. *Nasa Tm-4644*. 1994;(November 1994).
5. A A V. Parametric study of castellated beam with varying depth of web opening. *Int J Sci Res Publ*. 2012;2(8):2250-3153. www.ijsrp.org
6. Kumar. Static and Dynamic Analysis of Aircraft Stiffened Panel. 3(2):134-139.
7. Kothapalli AKR, Mohanty A, Adika SRK. Finite Element Modeling And Analysis Of Fuselage Stiffened Panel Subjected To Cabin Pressurization. *ResearchgateNet*. 2012;(January):678-681. http://www.researchgate.net/publication/246546122_Finite_Element_Modeling_And_Analysis_Of_Fuselage_Stiffened_Panel_Subjected_To_Cabin_Pressurization/file/e0b4951d9b5233ed5e.pdf
8. Li X, Jia D, Meng C. Buckling analysis of airframe jointed panel under combined loading. *Int J Appl Mech Eng*. 2018;23(4):1035-1042. doi:10.2478/ijame-2018-0060
9. Anupriya B, Jagadeesan K. Shear strength of castellated beam with and without stiffeners using FEA (ANSYS 14). *Int J Eng Technol*. 2014;6(4):1970-1981.
10. Massonnet, C. (1940). "La Stabilite' De L`Ame Des Poutres Munies De Raidisseurs Horizontaux Et Sollicitees Par Flexion Pure (The Web stability of Longitudinally Stiffened Plate Girders Subjected to Pure Bending)."
11. Kromm, A. (1944). "Zur Frage der Mindeststeifigkeiten Von Plattenaussteifungen (On the Problem of Optimum Rigidity of Stiffened Plates)." Stahlbau, 17, p. 81.

RESEARCH ARTICLE | MAY 22 2023

Development of an efficient process for recycling of lithium-ion batteries

R. Sathish Kumar ✉; R. Manoj Kumar; B. Saravanan; D. Pavithran; B. Siddharthan; N. Uday Ranjan Goud

AIP Conference Proceedings 2492, 050038 (2023)
https://doi.org/10.1063/5.0140810

Development of an Efficient Process for Recycling of Lithium-Ion Batteries

R Sathish Kumar[1,a)], R Manoj kumar[1], B Saravanan[2],D Pavithran[3],B Siddharthan[4], N. Uday Ranjan Goud[5]

[1]*Departmentof Mechatronics Engineering Dr.Mahalingam College of Engineering and Technology,Pollachi, India*
[2]*Department of Automobile Engineering,BannariAmmanInstituteofTechnology, Sathyamangalam, India*
[3]*Departmentof Production Engineering, Dr.Mahalingam College of Engineering and Technology, Pollachi, India*
[4]*Department of Mechatronics Engineering, BannariAmmanInstituteofTechnology, Sathyamangalam. India*
[5]*Department of Aeronautical Engineering, MLR Institute of Technology, Hyderabad, India*

[a)] Corresponding Author: sathishk951@mcet.in

Abstract. Lithium-ion batteries (Libs) are used now a days in notable quantities in the automotive industry, as these batteries are anticipated to last the life time of the vehicle, they will be essential in large numbers for another 10-15 years. Hence, this project addresses the issue by treating the Li-ion battery scraps in a hydrometallurgical process. The process incorporates leaching, solution purification, Co-Ni-MnretrievalandLi$_2$CO$_3$precipitation.The section-wise leaching procedure reveals the extraction rates of Li, Co, Ni, Mn and Al are higher than 95 % at optimum leaching conditions. The extraction rate of Cu varied between 40 % and 50 % without presence of hydrogen peroxide. The solution of purification step is obtained by modifying the pH of the leaching solution. Al, Cu and Fecan be precipitated from the solution in the form of metal hydroxide by increasing the pH of the solution to 5.5(40 °C). The lithium's be bringingoutfromthesolutionbyaddingNa$_2$CO$_3$ at95 °C.

INTRODUCTION

In the automobile industry, scientists began to focus on pure electric vehicles (EV), Hybrid-electric vehicles (HEV) and Plug-in hybrid electric vehicles (PHEV) which are assumed as the best alternatives for conventional vehicles. In the decade, the need for automotive lithium-ion batteries (LIBs) will increase dramatically. However, the problem arises is recycling of batteries. Lithium-ion batteries contains more important metals, such as lithium, cobalt, nickel, manganese, copper and aluminum. Many processes and procedure, including pyro metallurgical and hydrometallurgical methods, had been done to recycle spent LIBs. However, they need more process for winning the valuable metals more efficiently, economically and environmentally friendly. Lithium-ion batteries for vehicles are the better and good choice for electric vehicles. The density of energy per unit volume is (Wh/l) and per unit weight is (Wh/kg) of various recharging batteries. The capacity and efficiency of lithium-ion batteries are important to lead acid and nickel cadmium batteries. The voltage of a lithium-ion battery will be around 3.7 V, which is three times that of standard nickel batteries, such as Ni-Cd, Ni-MH. Other than, Lithium-ion batteries no batteries have memory effect and have high cycle times. The electrical energy requirements of lithium-ion batteries are different depending upon type of vehicles. For pure electric vehicles, a large amount of energy must be stored in place to transfer the vehicle over an acceptable distance. Electrical Vehicle battery pack store on the order of 35 kWh. The energy storing is possible as much energy as desired in batteries by simply increasing their number, but this increases the weight to unacceptable high values. High-power lithium-ion batteries at recent time achieve a specific power greater than 1300 W/kg and a power density greater than 2700W/L. There action in the lithium-ion battery cell system with a $LiCoO_2$-cathode is

$$charging \qquad LiCoO_2 + C_6 \rightarrow \text{------} \rightarrow Li_{1-x}CoO_2 + Li_xC_6 \qquad \textbf{(1)}$$

$$discharging \qquad Li_{1-x}CoO_2 + Li_xC_6 \rightarrow \text{----------} \rightarrow LiCoO_2 + C_6 \qquad \textbf{(2)}$$

Advancements in Aeromechanical Materials for Manufacturing: ICAAMM-2021
AIP Conf. Proc. 2492, 050038-1–050038-7; https://doi.org/10.1063/5.0140810
Published by AIP Publishing. 978-0-7354-4438-6/$30.00

EXPERIMENTAL PROCEDURES

In the solution purification step, copper and aluminium are first extracted by hydroxide precipitation. The co-precipitation and adsorption of Co/Ni in the precipitate is attempted to be intercept. With an correct temperature and reaction time, the equilibrium could be reached. The $Cu(OH)_2$ and $Al(OH)_3$ particles can grow and aggregate to a sufficient size. Subsequently, the solution can be shortlisted, and the residual is supplied to copper and aluminum production. At moment, the Al and Cu is brought out together, it will be tried to remove them from the solution separately in future. After the step 1, Ni, Co and Mn are removed from Li with hydroxide or sulphide precipitation methods. The Ni, Co and Mn containing concentrate is filtered and supplied to other metal recovery processes. The step 2.1isthe removal of Co, Ni and Mn with hydroxide precipitation method.

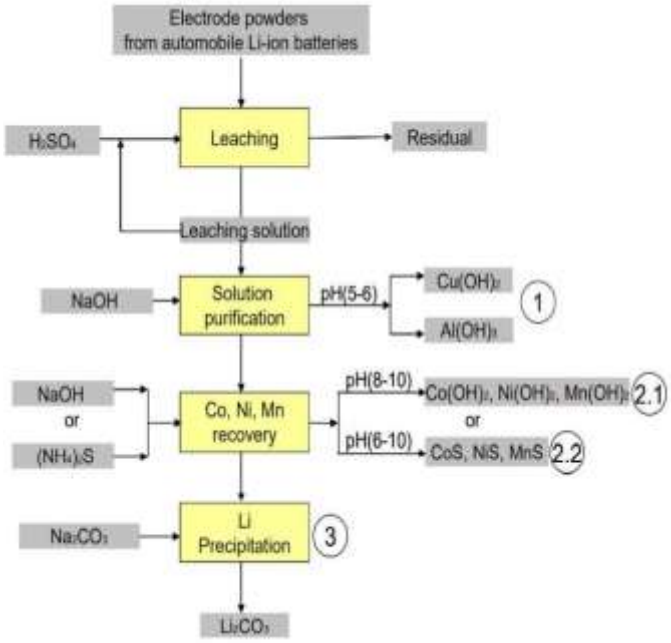

FIGURE1: The flow process

With good amount pH value by adding the neutralization reagent, the Co, Ni and Mn hydroxide will form in the solution. The other step 2.1 is by using sulphide precipitation, step 2.2. The solution of Ammonium sulphide provide as the sulphide ions supplier. The quantity of ammonium sulphide must be precisely controlled else the rest of ammonium sulphide can influence the following lithium recovery process. In step 3, the lithium ions are recovered in the form of lithium carbonate by inducing saturated soda solution. The electrode powder is a combination of metal oxide compound and metal scrap particles which comes from various cathode types of automobile batteries. The spent lithium-ion batteries are separated to different plastic, steel casing and electronic scrap from the cell. In the coming deactivation step, the cells are treated for five hours at temperature500°C.The electrolyte in the cell will degrade and become volatile. The deactivated cells are transferred to crushing and sieving processes. Ferrous scrap is subsequently magnetically separated. The non-ferrous metals, such as Copper and Aluminium scraps are created by sieving. Nickel and cobalt are 17.9 wt-%and 4.15 wt-% respectively in the given electrode powder, Lithium had taken 3.95 wt-% of the whole electrode powder. Even if copper, aluminium and iron can be separated mechanically, they can still sediment into the prepared electrode powder. The rest of electrode powder in carbon which is morethan36 wt-% of the powder.

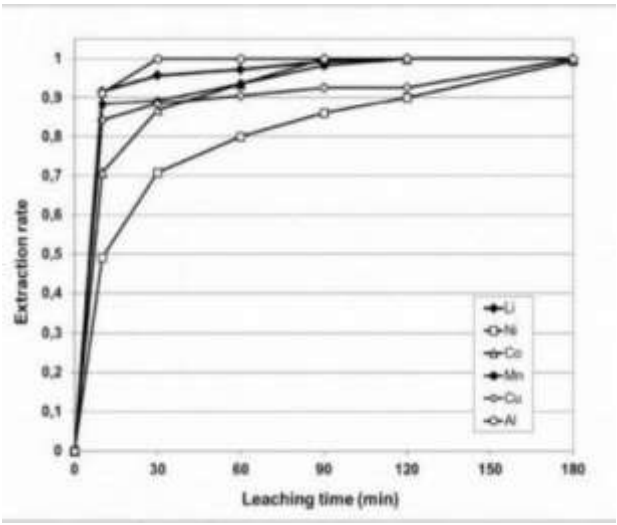

FIGURE2: Influence of leaching time on extraction of Metals

FIGURE3: Copper particle from residual of leaching without H_2O_2

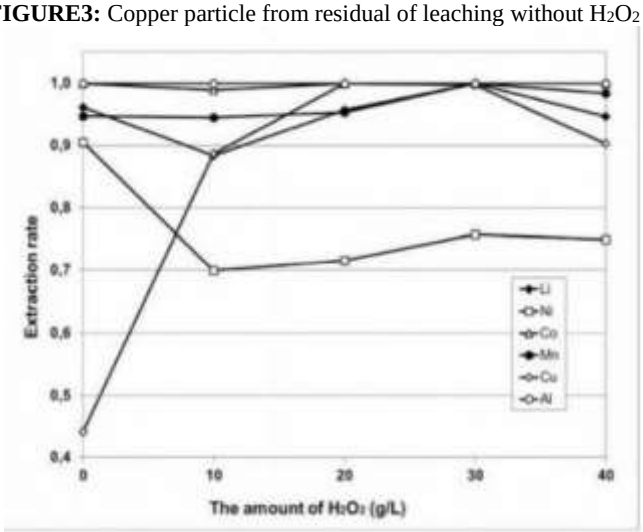

FIGURE4: Influence of H_2O_2 on extraction of metals

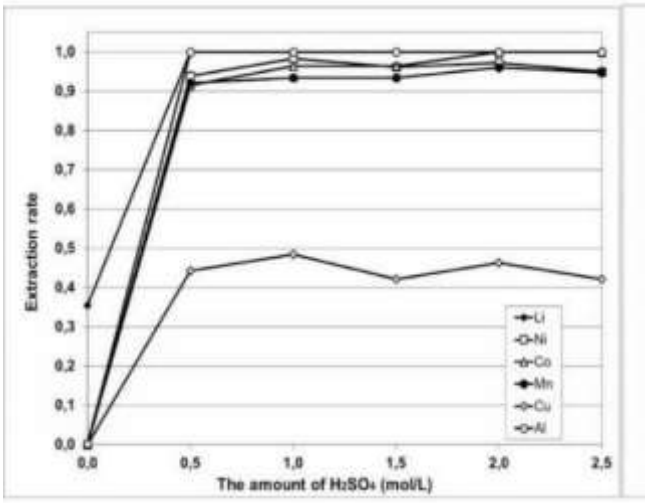

FIGURE5: Influence of Sulphuric acid concentration on extraction of metals

The leaching reaction is carried out at the conditions: 60 °C, 2 mol/L H_2SO_4, 20 g/L H_2O_2, 50g/L solid liquid ratio. The concentrations of extracted metals are tested by the separately Coupled Plasma (ICP-OES). The metal extraction changes with different leaching time. Hydrogen peroxide(H_2O_2) has a high oxidation potential and can oxidize some relative noble metals. The nickel extraction have decreased from 0.98 (without H_2O_2) to 0.72 (with 10 g/L H_2O_2). There is no large difference with further adding H_2O_2.With presence of H_2O_2, the extraction of copper can be improved and meantime the dissolution of nickel is relatively hindered in the limited reaction time (1h). Lithium and Aluminium are relatively easier and good soluble elements, which could reach a high extraction level at a lower acid concentration. The copper extraction stays between 40 % and 50 %. It is not significantly influenced by acid content. According to the above discussion, the formed H_2SO_4 concentration is 1-2 mol/L to maintain a high leaching efficiency.

Leaching with different temperature

As the leaching of electrode powder that is connected to the diminishing particles model, there action temperature plays an important role in the leaching process. A little foam is formed at the starting of the leaching experiment. In addition, the exothermic effect is not significant. It suggests that at very low temperature can hinder the reaction kinetics. The increase of temperature is favoured by leaching of metals. The copper, aluminium and lithium extraction are somewhat influenced by temperature. At higher temperature high leaching efficiency was found but also causing high energy consumption. According to the above discussion, the suited leaching temperature is 60~80 °C to maintain a fast-leaching reaction.

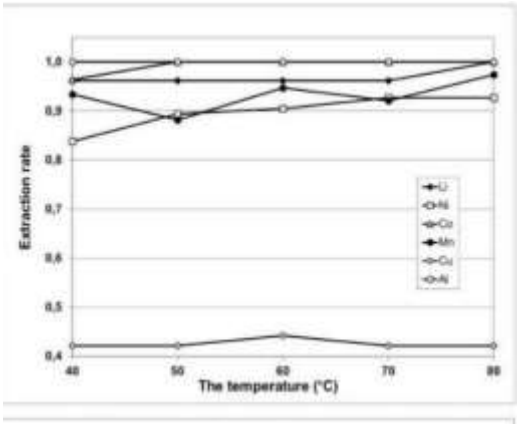

FIGURE 6: Influence of temperature on extraction of metals

SOLUTION PURIFICATION AND METAL RECOVERY

The solution purification process proceeds with changing pH values of the solution at 40 °C. With addition of sodium hydroxide solution, the pH of the solution will increase slowly. Solid particles are formed in the solution. The sample part of the solution is taken at equilibrium pH of 1.39,1.92, 2.88, 4.33, 5.07, 5.56, 6.00, and 6.93 in the full solution purification process. The effect of pH on the precipitation of metals has been found out. The chart has said aluminium, iron and copper are successfully precipitated from the solution. Even co-precipitated cobalt, nickel and manganese are at very low level. In Principle, Lithium could not form any compounds with other ions. The loss in lithium is usually produced by sampling and absorption; So that, lithium is not included in this diagram. The cobalt, nickel and manganese successfully removed from the solution after adding 6 ml of NaOH solution (1 mol/L). The remaining aluminium and copper had also co-precipitated at the same time. Now there is only Li left in the solution. The obtained solution can be directly supplied to the lithium recovery process. The experimental result has demonstrated that the hydroxide precipitation at pH>10canrecoverCo, Ni and Mn as a valuable mixture of three metals.

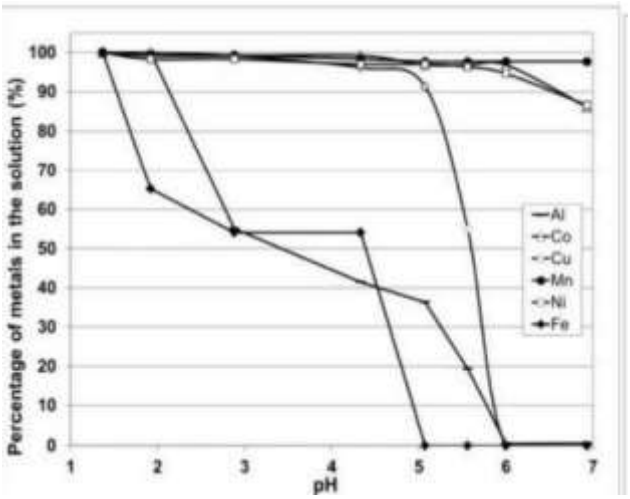

FIGURE7: Effect of pH on removal of impurity metals

TABLE1: Experimental result of Co-Ni-Mn

Concentration of Metal ions	Al mg/L	Co mg/L	Cu mg/L	Fe mg/L	Li mg/L	Mn mg/L	Ni mg/L
Purified solution	6.6	589	4.57	<1	583	1077	2446
Li-ion solution	<1	<1	<1	<1	620	<1	<1

Element	Li	$Ni(OH)_2$	$CO(OH)_2$	$Mn(OH)_2$	Cu	Al	Fe
Composition (%)	0.5	33.3	8.63	42.3	<0.05	0.16	<0.05

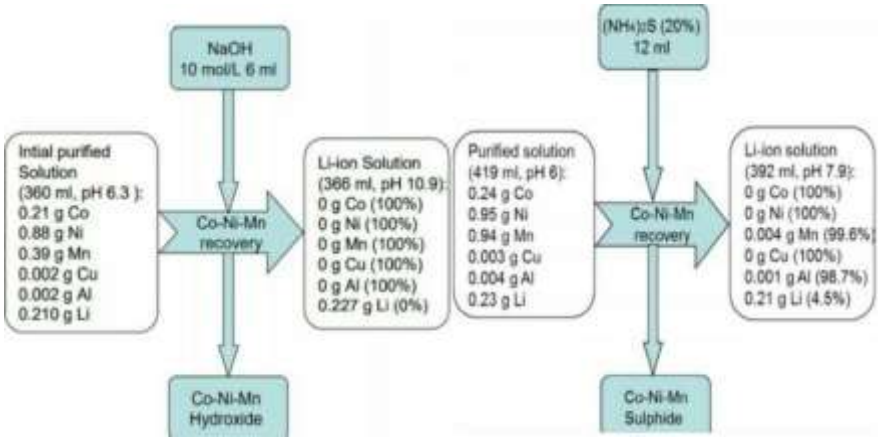

FIGURE 8: Analysis of Experimental result of Co-Ni-M

LITHIUM CARBONATE PERCEPTION

The mass flow for all the metals in the Co-Ni-Mn sulphide precipitation is found. At this step, cobalt, nickel and manganese were fully removed again nearly to 100 %. Only a trace content of Mn and Al present in the solution. Manganese will have concentration of only 10.5 mg/L. Alumni-Cobalt, nickel, copper and iron are completely removed. The obtained Li-ion solution can straightly be used for lithium recovery. The solution after the Co-Ni-Mn retained process is tempered on a heating plate at95°C and at same time treated with a soda solution precipitate lithium carbonate. During heating, the lithium which contains the solution is concentrated by the water evaporation. The crystallization of lithium carbonate starts soon after addition of sodium carbonate. Because the lithium carbonate in the solution has reached the supersaturated state, the lithium carbonate will automatically crystallize. The possibility of formation of other crystals should be considered. There are also sodium and sulphate ions in the solution. The materials which reach supersaturated state first can crystallize from the solution. Thus, the formation of Na_2SO_4 even after cooling down of the rest solution is impossible. It is evidently that manganese is also co-precipitated into the lithium carbonate solids. $MnCO_3$ has a much lesser solubility thanLi_2CO_3.Manganese in the solution can be removed by addition of a small amount of Na_2CO_3. So that the Li-rich solution should be completely purified before Li_2CO_3 crystallization.

TABLE 2: Solubility of all possible crystals

Solubility	**Li_2CO_3(Li) g/L**	**Na_2CO_3 g/L**	**Li_2SO_4 g/L**	**Na_2SO_4 g/L**
20°C	13.3(2.5)	215	348	195
90°C	-	439	309	427
100°C	7.2(1.4)	-	-	425

Element	Li_2CO_3	Ni	CO	Mn	Cu	Al	Fe
Composition(%)	93.6	0.21	0.032	2.16	<0.05	0.024	<0.05

CONCLUSION & RESULT

A hydrometallurgical recycling process of Li-ion batteries has been formed and evaluated. In the leaching step, the suitable leaching temperature to obtain a higher leaching efficiency: 60~80 °C. The suitable Sulphuric acid concentration: 1~2 mol/L; and at the suitable leaching time of 1 hour. With presence of H_2O_2, the extraction of copper can be stabled from 40 %-50 % to almost 100% and mean time the dissolution of nickel is relatively hampered in the limited reaction time (1h). The obtained Cu-Cleaching residual is whish is best suited for copper production. In the solution purification step, the optimum final pH for the solution purification is about 5.5 (40 °C) to precipitate aluminium, copper and iron. Meantime the co-precipitated cobalt, nickel and manganese are no more than 3%.

The precipitated residual can be gathered and supplied to further the separation process. Cobalt, nickel and manganese have been successfully collected from the solution by hydroxide precipitation method. The Co-Ni-Mn mixture is now available for new batteries electrode powder production or further hydrometallurgical separation processes. Even though sulphide precipitation can also recover Co, Ni and Mn at a high degree, the remaining NH^+ and the bad smell of ammonium gas have a negative effect. The lithium recovery from spent

REFERENCES

1. Method and apparatus for recycling lithium-ion batteries (2015) *URL:https://patents.google.com/patent/WO2017091562A1/en?oq=lithium+ion+battery+recycling*
2. Process for recycling li-ion batteries (2013) *URL:ttps://patents.google.com/patent/EP3087208B1/en?oq=lithium+ion+battery+recycling*
3. Xu,"A review of processes and technologies for the recycling of lithium-ion secondary batteries", *Journal of Power Sources, Volume 177,P. 512–527, 2008.*
4. Nishi: "Lithium-ion secondary batteries; past 10 years and the future"; *Journal of Power Sources; Volume100; P.101–106;2001.*
5. Costs of Lithium-Ion Batteries for Vehicles, *URL:http://www.transportation.anl.gov/pdfs/TA/149.pdf*
6. Winter.M;Brodd,R.J.ChemicalReviews,2004,104,4245-*4270Dean:Lange'shandbook of chemistry,ISBN0-07-016384-7, 1999*

RESEARCH ARTICLE | MAY 22 2023

Design and fabrication of automatic emergency braking system

J. Indira Priya Dharshini ✉; A. Nirmal Kumar; G. Prabhu; ... et. al

AIP Conference Proceedings 2492, 040066 (2023)
https://doi.org/10.1063/5.0113868

Design and Fabrication of Automatic Emergency Braking System

J Indira Priya dharshini[1,a)], A Nirmal Kumar[1],G Prabhu[1], V Vignesh Bala[1],T Viknesh[1], A. Sai Kumar[2,b)]

[1]*Department of Mechatronics Engineering, Sri Krishna College of Engineering and Technology, Kuniyamuthur, India.*
[2]*Department of Aeronautical Engineering, MLR Institute of Technology, Hyderabad, India.*

[a)] Corresponding author: indirapriyadharshinij@skcet.ac.in
[b)] ask.mraj@gmail.com

Abstract. Due to rapid increase in population, usage of automobiles is also increasing. Since vehicles are mostly mishandled, it leads to many road accidents. In an average more than 1000 accidents occurs every day in India. Hence, there is a need to develop emergency braking system that will be used in vehicle to reduce the accident. Emergency braking system (EBS) is high tech braking system will slow down the speed of vehicle in case of emergency. Ultrasonic sensor is used to detect the objects at certain distance and applies brake in order to avoid accident. Disc brake is used in emergency braking system due its effectiveness. This emergency braking system was specially designed that it will works when a vehicle reaches over 60 km/hr. and it can be activated either manually or automatically. In this paper, the emergency braking system is developed to ensure the safety of the passenger and driver.

INTRODUCTION

In 2019, around 4.49 lakh road accidents were reported and in which 1.51 lakh people died and 4.51 lakh people suffered from injury (Ministry of Road Transport & Highways, 2019). These accidents also paved way to economic losses in along with loss of lives (Lee and Laun, 2016). The key factor responsible for the most of the road crashing are inadequate breaking time for the driver. Due to sudden occurrence of object in front of the vehicle mostly doesn't allow to think (N.C. Basjaruddin et al., 2016). The greater number of accidents has increased usage more advanced driving-aid system. That caused to create more automated vehicles (Alonso et al., 2011).

Thus, it is mandatory to produce proper braking system to prevent driver as well as vehicle damage (Pawar et al., 2017). The automated Emergency Braking System emerged to reduce the number of accidents due to break failure. Hence, numerous reputable companies had developed some advanced braking systems such as Collision Mitigation Braking System and Collison Warning with Brake system (N.C. Basjaruddin et al., 2016). It is reported that Autonomous Emergency Breaking (AEB) can elude or minimize the crashing of vehicle. Furthermore, it is rate one among 5 best advanced system and had the ability to stop 22% fatal accidents (Koglbauer et a1., 2018). Autonomous Emergency braking system with ultrasonic sensor helps to detect the obstacle at a distance and applies brake in case of emergency (Patil. et al., 2020).

Hence, the objective of the present study was to develop automated emergency braking system with ultrasonic sensor in order to prevent and protect road accidents and improve safety of drivers. This paper discussed the design and performance of fabricated automated emergency braking system.

Advancements in Aeromechanical Materials for Manufacturing: ICAAMM-2021
AIP Conf. Proc. 2492, 040066-1–040066-5; https://doi.org/10.1063/5.0113868
Published by AIP Publishing. 978-0-7354-4438-6/$30.00

Braking System description in Automobiles

Brake is a mechanical device which reduce the speed or prevents motion of a vehicle by means of friction (Ram et al., 2017). To avoid accidents, brake system plays significant role to ensure safety on roads and driver. When the obstacle or pedestrian was detected the vehicle should be stopped. However, if it fails, the automated emergency braking system works and make the vehicle to stop atthe safe distance (Lie et al., 2014) Automated system should be controlled plan to adapted on the road as like drivers. The automated system helps the delivers to predict and act in wisely manner (Koglbauer et al., 2018). In automated emergency braking system, the prime components are sensor which is used to detect the obstacle and controller that will allow the vehicle to decelerate in proper way (Lee and Laun, 2016).

Components Used and Design Methodology

The components used in the present study are,

1. Ultrasonic sensor – using the ultrasonic waves it will detect the object and activate the brake system.
2. Wheel – friction on the road cause motion of the vehicle by wheel.
3. Brake – device used to inhibit or decelerate the motion of the vehicle.
4. Solenoid valve – flow of liquid or gas was controlled electromagnetically.
5. Chain – connected with wheel to transfer the energy.
6. Motor – converts energy into mechanical energy and applies torque to wheel cause motion.
7. Pneumatic cylinder – to provide motion and force to the automated system.

A systematic setup was made by using the above-mentioned components to perform the automated emergency braking system. The assembled setup was drawn in SOLIDWORKS 2019 to show the setup and mentioned (fig. 1).

FIGURE 1. Pictorial representation of automated emergency braking system using SOLIDWORKS2019.

Design Calculation

Rated torque of motor: 50kg-cm = 4.09N.m

Here, N = 250, T = 4.09

$$\text{Requried power} = \frac{2 \times \pi \times \text{N} \times \text{T}}{60}$$

$$= 107.07 \text{ watt} \quad \textbf{(1)}$$

$$\text{Motor power} = \text{Required power} \times \text{K}$$

$$= 160.01 \text{watt} \quad \textbf{(2)}$$

Chassis magnitude: 1.21m (4ft) × 0.6m(2ft)Wheel

distance: 0.70m;

Chassis made up of Steel;

Static load on wheels, $F_s = \mu f \times R_n$

$= 0.6 \times 50 \times 9.81$

$F_s = 294.3N$ **(3)**

Piston rod – Design calculation:

Load as a result of air pressure,

Piston diameter (d) = 40 mm

Pressure (p) $= 6\ kgf/cm^2 \times 0.981$

$= 6\ bar = 0.5886\ N/mm^2$

$= 5.886\ N$ **(4)**

Rod material = C 45(Data book page no 1.12)

Yield stress (σy) = 36 kgf/mm² = 36 × 98.1

$= 3531.6\ bar = 353.16\ N/mm^2$ **(5)**

Safety factor = 2

Force acting on the rod (F) = Pressure x Area

$= P \times (\Pi d^2/4) = 0.5886 \times \{(\Pi \times 40^2)/4\}\ F$

$= 739.6\ N$ **(5)**

Stress (σy) = $\sigma y / F_0 S = 353.16 / 2$

$= 176.5 N/mm^2$ **(6)**

$\therefore d = \sqrt{4F/\pi\ [\sigma y]}$

$= \sqrt{(4 \times 739.6)/\pi\ [176.5]}$

∴ Minimum rod diameter required for the load = 2.3 mm **(7)**

Assuming rod diameter = 15 mm

Piston rod length - Calculation:

Stroke = 160 mm

Threads length= 2 x 20 = 40mm

Extra length including front cover =12 mm

Accommodate head length (extra) -20 mm

Total length of the piston rod = 160 + 40 + 12 + 20

= 232 mm **(8)**

By standardizing,

Diameter of gear:

Piston rod length= 230 mm.

d = zm; da = d + 2 m; df = d - 2.5m;d

= zm = 20 × 2 = 40m

da = d + 2 m = 40 + 4 = 44m

df = d – 2.5 m = 40 – 5 = 35m

a = (d1 + d2) /2;

c = 1.25 m - 1.00 m = 0.25 m

mt = mn / cos β; d = zmn / cos β

diameter – calculation:

Transverse module mt = 2,

Gear teeth z = 30,

Helix angle β = 15° (R)

Reference Diameter d =zmt= 30 × 2 = 60m

Helical gear reference diameter with:

Normal module mn = 2,

Gear teeth z = 30,

Helix angle β = 15° (R)

Diameter of Reference, d = zmn / cos β

= 30 × 2 / cos 15° = 62.117m **(9)**

Hardware setup

Using the calculated data, the components were made it and assembled. On the chassis, wheel was attached. Ultrasonic sensor was attached on the left front of the chassis. Beside the sensor, motor was placed on the right front of chassis which it is attached to the air compressor and sensor. Battery was attached micro controller and sensor to give power supply to work the systems. Pneumatic cylinder was connected to both sensor and air compressor. It was set that theautomated emergency braking system should work when the vehicle exceeds the speed limit of 60km/hr.

When the object was detected by sensor before the wheel, the sensor allots the motor to slow down, thus cause the increase air pressure in pneumatic cylinder which extent its liver and helps to reduce the speed of the wheel. The typical setup of the system was shown (fig. 2).

FIGURE 2. Typical setup of automated emergency braking system

CONCLUSION

From this work, it was concluded that automated emergency braking system has the ability to reduce the accidents and also severity of the accidents. The ultrasonic sensor showed better performance and effective in detecting the obstacles. The pneumatic pump was used to activate the automated emergency brake instantly when there was any object appearance suddenly. Hence, it recommended to use automated emergency braking system in vehicle to avoid most of the accidents. The future work of this project will be, should be installed in a vehicle and should be checked the efficiency in real-time.

REFERENCES

1. Alonso. L., Milanés. V, Torre-Ferrero. C., Godoy. J., Oria. J.P., Pedro. T. "*Ultrasonic Sensors in Urban Traffic Driving-Aid Systems*". Sensors. 11: 661-673,(2011).
2. Basjaruddin. N.C., Kuspriyanto, Suhendar, Saefudin. D, Azis. V.A, Hardware Simulation of Automatic Braking System Based on Fuzzy Logic Control. "*Journal of Mechatronics, Electrical Power, and Vehicular Technology*". 07: 1-6, (2016)
3. Koglbauer. I., Holzinger. J., Eichberger. A, Lex. C, Autonomous emergency braking systems adapted to snowy road conditions improve drivers' perceived safety and trust. " *Traffic Injury Prevention*". 19 (3): 332-337, (2018).
4. Lee. I.H, Luan. B-C, Design of Autonomous Emergency Braking System Based on Impedance Control for 3-Car Driving Scenario. " *SAE International"* . 4271: 1453-1459, (2016).
5. Lie. G., Zejian. R., Pingshu. G, Jing. C, Advanced Emergency Braking Controller Design for Pedestrian Protection Oriented Automotive Collision Avoidance System. *" The Scientific World Journal"*. 1-11.,(2014)
6. Patil. G.S, Thombre. S.R., Rathod. A.B., Sorte. M.B, Design and Fabrication of Automatic Pneumatic bumper and braking using sensor. "*Internation Journal of Robotics and Automation*". 6(1), (2020).
7. Pawar. S., Raut. S, Keni. J., Mhaisdhune. V., Patil. C.R , Review Paper on Automatic Braking System with Pneumatic Bumper." *International Journal of Advance Engineering and Research Development* ". 4(12): 777-779. (2017).
8. Ram. J.V.S., Manikanta. K.M.S.V, Pavanth. G, Jagadeep. B., Kumar. B.R. , Automatic Braking System Using Ultrasonic Sensor. " *International Journal of Innovative Science and Research Technology* ". 2(4): 398 – 405, (2017).
9. Road Accidents in India . Ministry of Road Transport and Highways. Transport Research wing. New Delhi,(2019).

RESEARCH ARTICLE | MAY 22 2023

Wetting behavior of microgroove and micropillar patterned surface

D. Joseph Jeshua ✉; P. Tharun Kumar; A. Sai Kiran; P. Jagadeesh; A. Vivek Anand

AIP Conference Proceedings 2492, 040004 (2023)
https://doi.org/10.1063/5.0113238

Wetting Behavior of Microgroove and Micropillar Patterned Surface

D. Joseph Jeshua[1, a)], P Tharun Kumar[1, b)], A Sai Kiran[1, c)], P Jagadeesh[1, d)], A Vivek Anand[1, e)]

[1]*Department of Aeronautical Engineering, MLR Institute of Technology, Hyderabad, Telangana, India.*

[a)] Corresponding Author: jjjeshua@gmail.com
[b)]tharunkumar5854@gmail.com
[c)]saikiranalaka12@gmail.com
[d)]jagadeeshpj17@gmail.com
[e)]vivekanand7adr@gmail.com.

Abstract. Lotus effect is the natural phenomena where superhydrophobicity can be detected on the outside of a lotus leaf. This is due to the micro protrusions and wax nanocrystals that are present on the outside of a lotus leaf. If observed carefully, the protrusions are like micro pillars. In similar way, another natural superhydrophobic surface is the paddy leaf. When zoomed in oe natural examples, microgroove and micro pillared surfaces are fabricated to conduct wetting study with the idea of achn the surface, there are groove like structures that slide down the water without actually wetting the leaf. Taking the abovieving hydrophobicity on a metal surface that can be used in engineering of various products where it is necessary to have the water not staying at a point. This paper highlights the construction of the two surfaces and conducting wetting study. An ideal ridge width to channel width ratio and optimized microstructure is found to support hydrophobic nature in the surface.

Keywords: Wetting, Hydrophobicity, Micropatterns, Contact angle, Contact diameter

INTRODUCTION

Designing the wettability of a strong surface assumes a significant part in numerous fields, for example, self-cleaning surfaces, surface resistive coatings, and microfluidic gadgets. The wettability of a solid can be determined in terms of contact angle (CA) alongside different boundaries such as contact angle hysteresis, tilting angle [1&2]. In this paper, contact angle of water is considered so whenever contact angle is mentioned, it is to be taken as water contact angle. Contact angle is characterized as the angle between the surface of the solid to the tangent of the surface of the liquid intersection with the solid. The surfaces with contact angle less than 90˚ are called as hydrophilic surfaces which translates to water loving surfaces (hydro – water and philia – like) and the contact angle between 90˚ and 150˚ are called as hydrophobic surfaces which translates to water fearing surfaces (phobia – fear) and the contact angle greater than 150˚ are called as superhydrophobic surfaces[3-7].

The shape of a liquid droplet is determined by the surface tension of the liquid and the intermolecular forces of the liquid. The external forces such as gravity also affect the shape of the droplet. The static contact angle is the contact angle where the liquid droplet stays at a constant place during the period of experimentation. The relation between static contact angle and shape of the droplet can be given from Young-Laplace equation [11] as

$$\cos\theta = \frac{\gamma_{sv} - \gamma_{sl}}{\gamma_{lv}} \quad (1)$$

where, γ_{lv}, γ_{sv}, and γ_{sl} are the liquid-vapour, solid-vapour and solid-liquid interfacial tensions respectively and θ is the contact angle.

Advancements in Aeromechanical Materials for Manufacturing: ICAAMM-2021
AIP Conf. Proc. 2492, 040004-1–040004-9; https://doi.org/10.1063/5.0113238
Published by AIP Publishing. 978-0-7354-4438-6/$30.00

There are two types of wetting modes. They are i) Wenzel mode of wetting and ii) Cassie-Baxter mode of wetting. The Wenzel model deals with the surfaces where when a drop rests on a surface through the surface roughness and reaches the bottom surface without producing any air pockets [8-12]. The Cassie-Baxter model deals with the surfaces where when a drop rests on a surface through the surface roughness and forms air-pockets at the bottom decreasing the contact area. The Wenzel mode wetting has less static contact angle when compared with Cassie mode.

The relation for contact angle in Wenzel state is represented by the equation –

$$\cos\theta_W = r(\cos\theta_e) \tag{2}$$

where, θ_W is the contact angle in Wenzel state, r is the ratio of the wetted area to the planar area ($r > 1$) [5]

The relation for contact angle in Cassie state is represented by the equation –

$$\cos\theta_c = \emptyset(\cos\theta_e + 1) - 1 \tag{3}$$

where θ_c is the contact angle in Cassie-Baxter state, $\emptyset$ is determined as ridge width to channel width ratio in this paper here on.

Contact angle hysteresis is the difference of advancing angle and receding angle which is linked to the titling angle of the liquid[13&14]. This arises from the surface irregularities, chemicals used. The advancing contact angle is used to tell the maximum contact angle the surface can have and the receding angle tells the minimum contact angle the liquid can have. It is essential to have a contact angle hysteresis to be less.

$$H = \theta_a - \theta_r \tag{4}$$

where, H is the hysteresis and θ_a and θ_r are the advancing angle and receding angle respectively [13].

The highest reported contact angle is 175˚. A water contact angle of 173.7˚ is achieved by using FGO based transparent polymeric films on aluminium alloys and an extremely low contact angle hysteresis of 5˚ where FGO stands for fluorinated graphene oxide [2].

Hydrophobic surfaces can be fabricated by using chemical coatings, thin films and by producing patterns over a surface. Using chemical coatings or thin films makes the fabrication process faster but the endurance of the coatings wear off after a period of time. Compared to coatings, micropatterns last longer and also gives a higher static contact angle which makes it a good hydrophobic surface.

Micropatterns can be fabricated by numerous ways. Some of them are micro end-milling [5], laser micromachining [4]. Wet chemical fabrication – chemical etching method, sol-gel method, electroless galvanic deposition, electrodeposition, and chemical functionalization, Lithography - deep ultraviolet lithography, electron beam lithography, X-ray lithography, colloidal lithography, nano-imprint lithography [15], Templating, Chemical vapor deposition, Layer-by-layer deposition, Colloidal aggregation and assembling, electrospinning and electrospraying, phase separation [14].

From the lotus leaf observations, there are small air pockets that limits the contact area of droplet on the surface of the leaf (Cassie wetting state) [5]. These are adapted into the design consideration of a bio-inspired structure with the same mission that is to increase the contact angle. There are two types of surfaces that can be designed which can produce air pockets similar to lotus leaf. They are pillars and grooves. By using pillars, isotropic wetting can be achieved which provides the same distribution of water molecules in all the directions. By using pillars, anisotropic wetting is achieved where the distribution is non-uniform perpendicularly and parallelly which depends on the point of observation.

In the present work, the development and wetting study of isotropic and anisotropic surfaces of mild steel metal is done. The samples are developed using chemical etching process and the geometric measurement of the samples is done by using a 3D optical profilometer. The static contact angle for micropillar surface is only one but the static angle of microgroove surface is divided into two angles namely angle parallel to the grove and angle perpendicular to the groove. The comparison of isotropic and anisotropic wetting is done and an ideal ridge width to column width ratio is found that can be used for similar topographies.

EXPERIMENTAL PROCEDURE

Micropatterned Surface Fabrication Process

Chemical Etching

Chemical etching is a machining process that uses chemical etchants to create highly accurate precision components. Chemical etching is simply removing unwanted materials from the surface to form a required pattern. It

uses high temperature and high pressure to create permanent etched image on metal surface. It has many benefits over other processes as it gives more flexibility and much lower set up costs. High volume of machining can be produced where physical properties of the material remain unchanged.

The chemical etching process is divided into six sub-processes. They are i)cleaning – where the surface is cleared of all surface contaminants. ii) laminating – where the cleaned metal is coated with a UV sensitive photoresist at required places with hot roll laminator at high temperature. iii) exposure – here, the metal that is laminated is exposed to ultraviolet rays that harden the photoresist where the areas are clear. iv) developing – where the resist on non UV exposed area is chemically developed to give away the desired pattern. v) etching – where an etching solution is splashed on the two sides of the metal with high pressing factor. vi) stripping – where the photoresist is removed revealing the required pattern. Further etching processes may be required to fine tune the surface.

Here in this work, chemical etching on stainless steel is done using potassium bi-sulphate as chemical etchant that is acidic in nature. The composition of the etchant is 10gr of potassium metabisulphite combined with 90ml of H_20 (water). For developing the sample, untampered martensite solution is used. For developing isotropic surface, dry etching solution is used and for anisotropic surface, wet etching solution is used.

So, using chemical etching process, microgroove and micropillar designs are made on stainless steel surface.

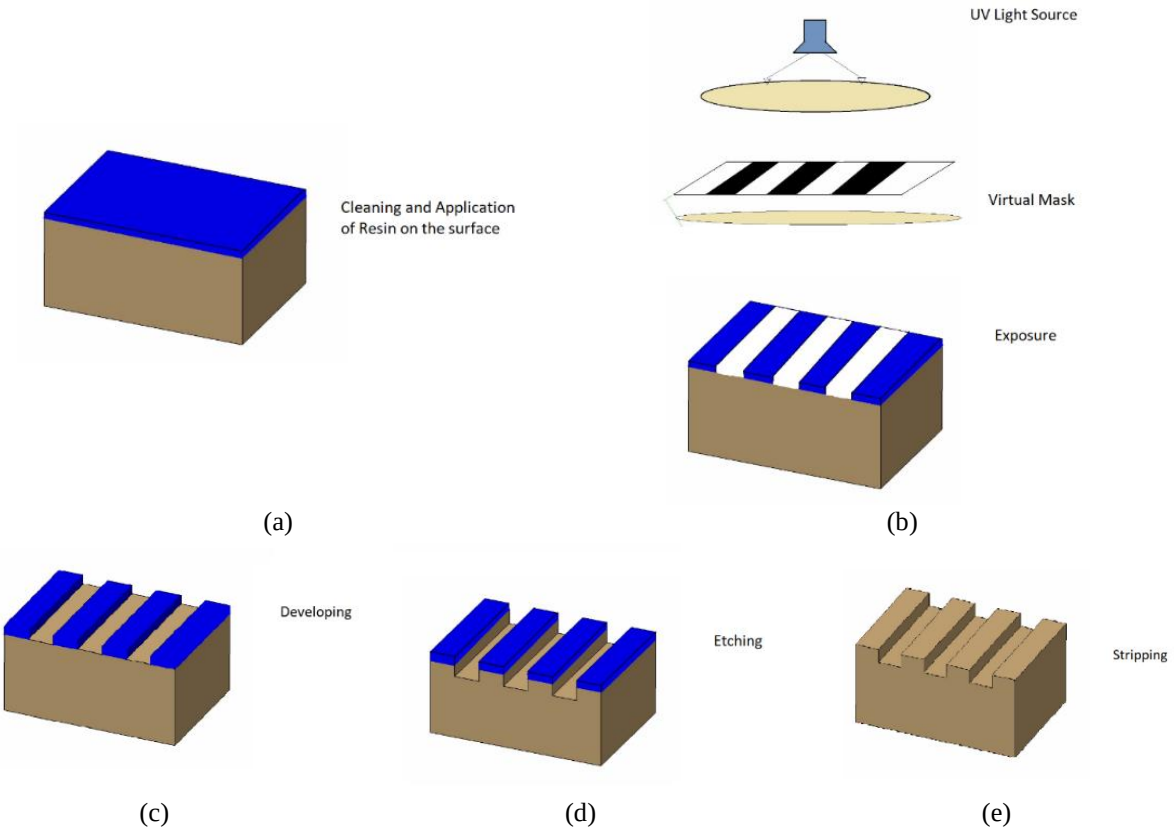

FIGURE 1. Schematic Sketch of Chemical Etching Process (a) cleaning and application of resin on the surface, (b) Exposure of UV light through virtual mask, (c) Developing, (d) Etching and (e) Stripping.

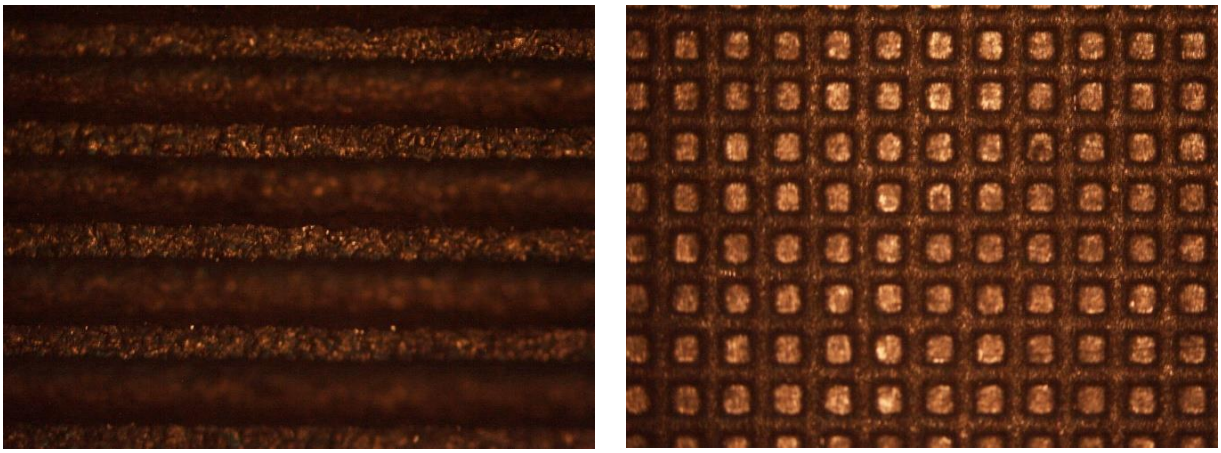

(a) (b)

FIGURE 2. Fabricated Specimen (a) Microgroove patterned surface and (b) Micropillar patterned surface**.**

Characterization of Micropatterned Surface

The surface topography of the micropatterned surfaces are examined with the help of 3D optical profilometer where mathematical boundaries such as ridge width, channel width are taken and arranged in Table 1 and Table 2 for microgroove and micropillar patterned surface respectively. The static contact angle and the contact diameter framed by the water bead shifts relying on the math. The regular arrangement of surface micro asperities such as one dimensional grooves and square pillars were generated on the surface using the chemical etching process.

Groove is a long narrow channel. There are different types of grooves like v-type, concave type etc. But here we are using pillar and square or box type grooves. Significantly the furrow designs perform three capacities. Wipe out commotion, for example, screeching, eliminates the oil film on the outside of the plates and keeps the outside of the grating material provided with oil to help with dispersing energy into the encompassing environmental factors during commitment, which additionally scatters the warmth from the plates.

A 3D optical profilometer uses light instead of probe to map the surface topography. The key component in this technique is to direct the light in a way that it can detect the surface in three dimensional space. In this wettability study we are using a 3D optical profilometer. 3D profilometer is a measuring instrument used to measure the surface roughness and quality of the surface and also measures the critical dimensions like grooves, step, curvature etc. and generate in high resolution.

TABLE 1. Geometrical Dimensions of Microgroove patterned Surface

Specimen	Ridge Width (RW) (μm)	Channel Width (CW) (μm)	RW/CW
MG 1	82.5	173.24	0.4
MG 2	123.3	198.45	0.6
MG 3	145.36	203.35	0.7

TABLE 2. Geometrical Dimensions of Micropillar patterned Surface

Specimen	Ridge Width (RW) (μm)	Channel Width (CW) (μm)	RW/CW
MP 1	102.35	257.05	0.4
MP 2	115.25	185.33	0.6
MP 3	127.43	176.65	0.7

Wetting Study

The wetting study can be done by understanding the static contact angle of a sessile water droplet. The schematic diagram of the setup (Figure 1) can be seen which is used for calculating the static contact angle. A liquid volume of 8 μl was dispensed from a 10 ml syringe via 20 gauge hypodermic needle to form a sessile drop on the micropatterned surfaces, both pillared and grooved. The motion of the syringe piston was carefully controlled by using a height gauge

manually. The surface was cleaned before and after performing the experiment using acetone followed by distilled water to remove any irregularities. The static contact angle that is measured from the liquid drop image on the micropatterned surface is taken by using a high resolution camera setup both parallelly and perpendicularly for microgroove specially.

For each sample, 20 measurements are taken for the static contact angle. The static contact angle is measured by using ImageJ software for each measurement and the average of the contact angle is calculated. For the microgroove patterned surface, 20 measurements are taken for both parallel and perpendicular measurement of the contact angle and the average is listed in Table 3 and Table 4 for microgroove pattern and micropillar pattern respectively.

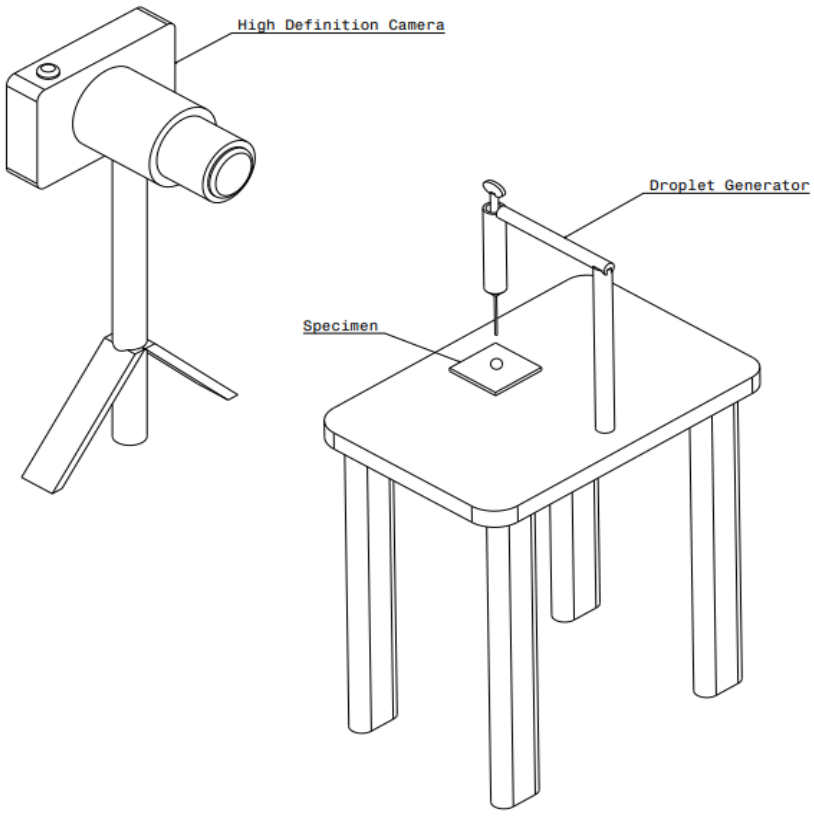

FIGURE 3. Schematic Sketch of Wetting Setup

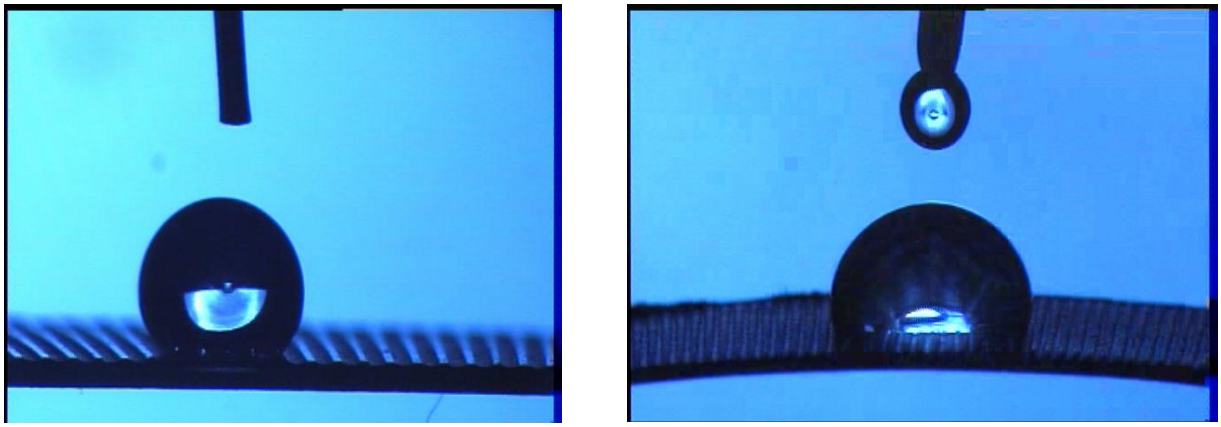

(a) (b)

FIGURE 4. Water Drop on (a) Microgroove Patterned Surface and (b) Micropillar Patterned Surface

TABLE 3. Wetting Characteristics of Microgroove patterned Surface

Specimen	Contact Angle $\theta^{\circ}_{\perp}$	Contact Angle $\theta^{\circ}_{\parallel}$
MG 1	135.85	89.37
MG 2	144.55	94.09
MG 3	119.83	83.49

TABLE 4. Wetting Characteristics of Micropillar patterned Surface

Specimen	Contact Angle θ°
MP 1	139.43
MP 2	145.95
MP 3	123.76

RESULTS AND DISCUSSION

The wetting behavior of stainless steel samples in isotropic surface topography and anisotropic surface topography is investigated in terms of variation of static contact angle, change in geometric dimensions that is represented in the ratio of ridge width to column width. The isotropic surfaces have the same topography independent of measuring direction. The properties are similar in isotropic surfaces at any pillar in all directions. The surface showed identical contact angle when measured in different directions. The etch rate is also observed to be faster than anisotropic etching as it is usually limited by reaction. The anisotropic surface has two angles and the perpendicular contact angle is observed to be greater than the parallel contact angle. Graphs are plotted with respect to RW/CW and the contact angles for both microgroove and micropillar patterned surfaces (Fig. 6 and Fig. 7)

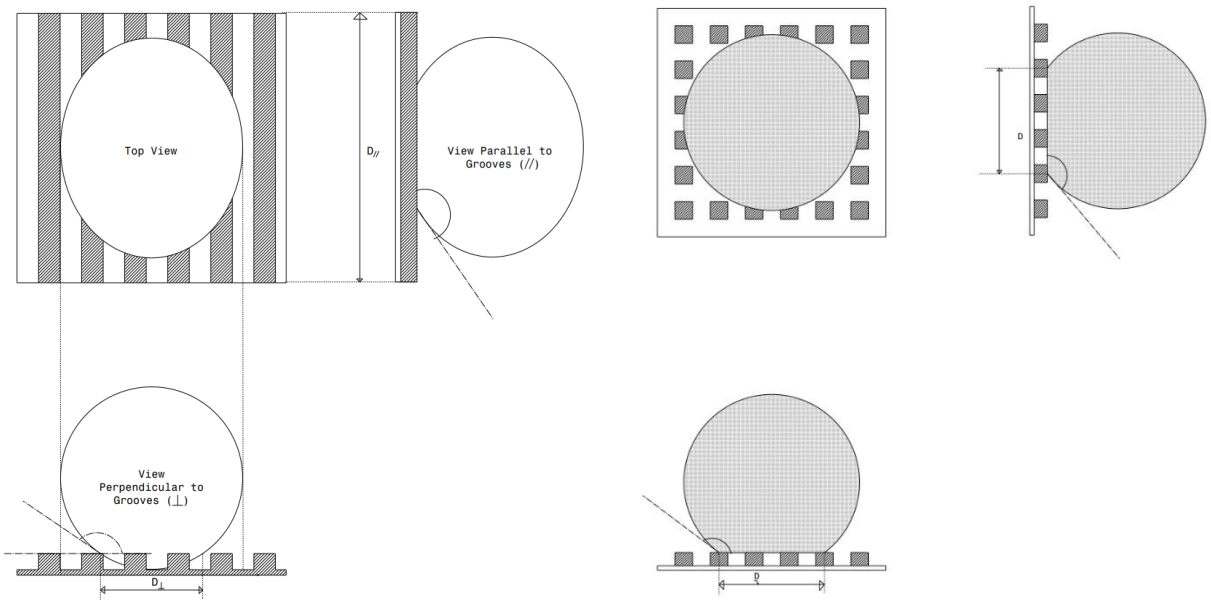

FIGURE 5. Schematic diagram of a water droplet on a) Microgroove Patterned Surface *and* b) Micropillar Patterned Surface

GRAPHS

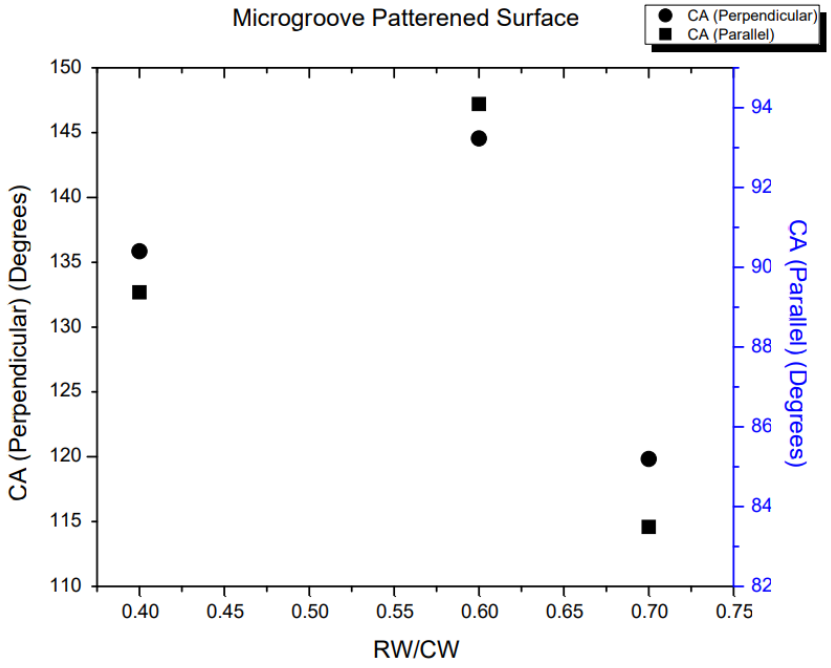

FIGURE 6. Graph showing the relation between contact angle (CA) of water drop measured on microgroove surface with RW/CW

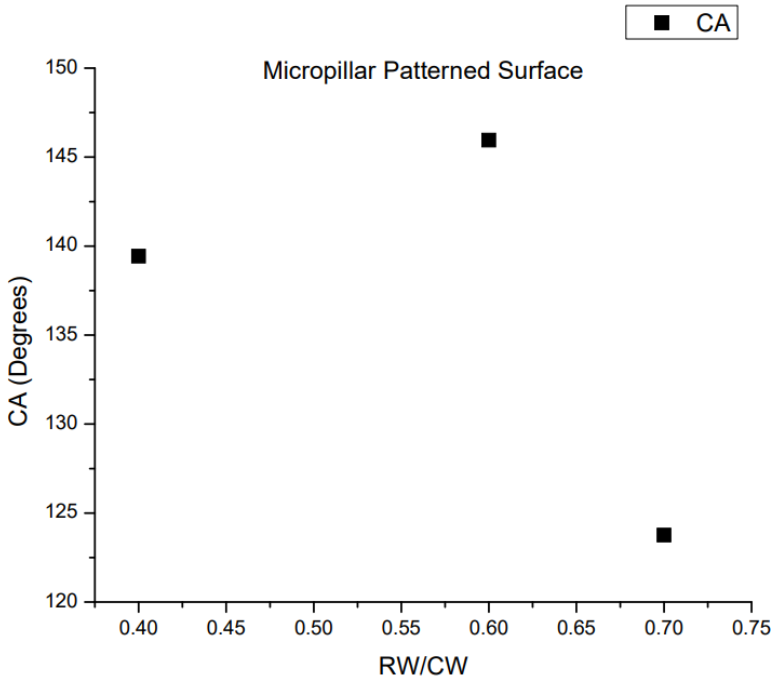

FIGURE 7. Graph showing the relation between contact angle (CA) of water drop measured on micropillar surface with RW/CW

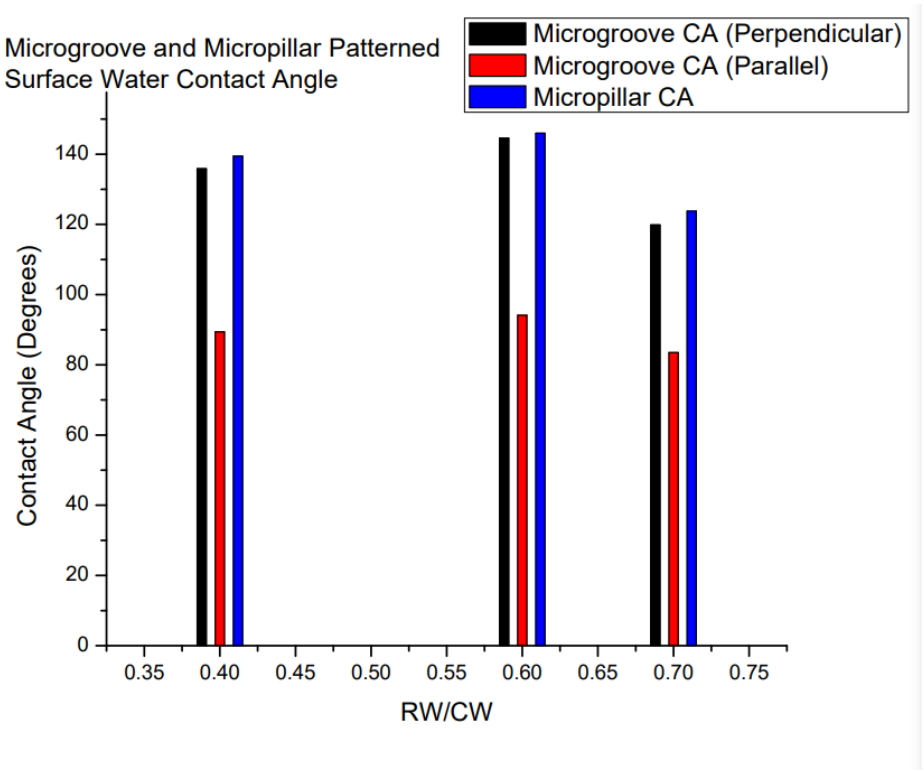

FIGURE 8. Graph showing overall relation of contact angle (CA) of water drop measured on microgroove and micropillar surface with RW/CW

The wetting in the microgroove and micropillar patterned surface can be analyzed as follows from Fig. 8.

The ridge width to channel width ratio is not affecting when observed with respect to microgroove and micropillar patterned surface. In all the three RW/CW, the micropillar contact angle is at the maximum. The perpendicular contact angle is always greater than the parallel contact angle in microgroove pattern surface. The micropillar pattern surface is better at acting as a hydrophobic surface when compared to microgroove pattern surface.

CONCLUSION

A test study is performed to examine the wetting characteristics of isotropic and anisotropic patterned surface topographies by using micropillar and microgroove patterned surfaces respectively in Cassie-Baxter mode. The surface structures are patterned using chemical etching and the geometrical dimensions are examined using 3D optical profilometer. The wetting characteristics which is the static contact angle is measured from a high resolution image of the sessile water droplet formed on the surface of each patterned specimen. The static contact angle shows variation to the change in the ridge width to channel width ratio on both micropillar and microgroove surface. From the observations, isotropic surface i.e., micropillar surface is found to be ideal for a better hydrophobic acting surface at the experimented dimensions. The ideal ridge width to channel width ratio is found to be 0.6 to have a high static contact angle on micropillar patterned surface and the maximum static contact angle is found to be 145.45˚. The ideal ridge width to channel width ratio may change with respect to the geometrical dimensions taken for experimentation.

This study is conducted to examine the influence of patterns on surface for achieving of hydrophobicity. Further studies will be conducted to study the wetting behaviour of nano-structured surface to act as a super hydrophobic surface and achieve a contact angle greater than 150˚.

REFERENCES

1. Anna Maria Coclite, Yujun Shi and Karen K. Gleason, *Super-Hydrophobic and Oleophobic Crystalline Coatings by Initiated Chemical Vapor Deposition*, Physics Procedia 46, 56-61 (2013).

2. T. Bharathidasan, Tharangattu N. Narayan, S. Sathyanaryanan and S.S. Sreejakumari, *Above 170˚ water contact angle and oleophobicity of fluorinated graphene oxide based transparent polymeric films*, Carbon 84, 207-213 (2015).
3. K.J. Kubiak and T.G. Mathia, *Anisotropic Wetting of Hydrophobic and Hydrophilic Surfaces – Modelling by Lattice Boltzmann Method*, Procedia Engineering 79, 45-48 (2014).
4. K.M. Tanvir Ahmmed and Anne-Marie Kietzig, *Drag reduction on laser-patterned hierarchical superhydrophobic surfaces*, Soft Matter 12, 4912-4922 (2016).
5. Md. Ashiqur Rahman, *Wetting and frosting/defrosting study on microgrooved surfaces*.
6. Jun Wu, Jun Xia, Wei Lei and Bao-ping Wang, *Pinning mechanism of advancing sessile droplet on superhydrophobic surfaces*, RSC adv. 4, 35649-35652 (2014).
7. Jaroslaw Drelich and Emil Chibowski, *Superhydrophilic and Superwetting Surfaces: Definition and Mechanisms of Control*, Langmuir 26(24): 18621-3.
8. Anand, A.V., Arumugam, V. and Kannan, R. (2017) *Static wetting characteristics of micro-textured stainless steel surfaces under uniaxial loading condition*, Int. J. Surface Science and Engineering, Vol. 11, No.2, pp.174-190.
9. Vivek Anand A., Arumugam V., Jayalakshmi S. and Arvind Singh R., (2018) *Innovative approach for suppressing corrosion of SS304 steel in saline water environment*, Anti-Corrosion Methods and Materials, Vol. 65 Issue: 5, pp.484-491
10. A. Vivek Anand, S. Gollakota, V. Hariprasad, Ashifkhan, N. Shunmugavelu, and V. Arumugam, *Role of micropatterns on wettability and corrosion characteristics of SS304 steel surface*, AIP Conference Proceedings 2128, 040006 (2019)
11. A.Vivek Anand, S. Gollakota, V. Hariprasad, N. Shunmugavelu, Ashifkhan, and V. Arumugam, *Wettability characteristics of microgroove patterned SS304 stainless steel surfaces*, AIP Conference Proceedings 2128, 040001 (2019);
12. Xuanping Tang, Sonja Richter and Srdjan Nesic, *Study of wettability of different mild steel surfaces*.
13. Yuehua Yuan and T. Randall Lee, *Contact Angle and Wetting Properties*.
14. Sepehr Shadmani, Mehdi Khodaei, Xiuyong Chen and Hua Li, *Superhydrophobicity through Coatings Prepared by Chemical Methods*
15. A Vivek Anand, B Nagaraj Goud, J Sahana, V Hariprasad and K Arunkumar, *Implementing Micropatterned Surface for Drag reduction in UAV*, International Journal for Recent Technology and Engineering, Vol. 8, No. 4, pp.4710-4714 (2019).

RESEARCH ARTICLE | MAY 22 2023

Experimental determination of mechanical properties of a carbon fibre composite plate under hygrothermal environment

N. Uday Ranjan Goud ✉; Y. Vijay Bhasker; M. Ramu; B. Sai Varun; G. Prudhvi Raj

AIP Conference Proceedings 2492, 040032 (2023)
https://doi.org/10.1063/5.0113426

Experimental Determination of Mechanical Properties of a Carbon Fibre Composite Plate under Hygrothermal Environment

N. Uday Ranjan Goud[1,a)], Y. Vijay bhasker[1,b)], M. Ramu[1,c)], B. Sai Varun [1,d)], G. PrudhviRaj [1,e)]

[1] *Department of Aeronautical Engineering, MLR Institute of Technology, Hyderabad, India*

[a)] Corresponding authors: uday.goud@mlrinstitutions.ac.in
[b)] vijayvictorious9999@gmail.com
[c)] ramukumarlucky@gmail.com
[d)] bandivarun8@gmail.com
[e)] prudhviraj2000@gmail.com

Abstract: This Paper is near to investigate the mechanical properties of carbon fiber composite plates subjected to (environmental) hygrothermal conditions. The carbon fiber composites that is 3k 200GSMtwill weaved were fictitious with completely different dimensions by hand-layup methodology. The laminates are cured in forced convection oven for 4hours and at room condition temperatures for 48 hours. The laminates are then subjected to hygrothermal conditions i.e., the laminate plates are placed in an environmental controlled area over an amount time. There is the severe reduction in the Inter lamina shear stress property and also flexural modulus of elasticity due to the heavy environmental exposure. The test results have shown that environmental conditions showed a definite impact on mechanical properties and it also explained that mechanical properties are substantially reduced even by one short term exposure of environmental conditions.

Keywords: Carbon fibre composite, Degradation, Durability, Aging conditions, Hygrothermal conditions, Epoxy resin.

INTRODUCTION

Carbon fibre reinforced epoxy composites obtain high specific strength and stiffness, high strength to weight ratio, corrosion resistance, and good fatigue tolerance. They have been mostly used in composites in the form of woven textiles, continuous fibers, and chopped fibres. Regardless of these advantages and characteristics, there are major concerns on the sustained performance, long term durability, and also in their reduction of a lifetime when handling harsh and change in environmental conditions [1].Normally, fibers will be not affected by moisture or pressure until and unless the polymer matrix is resisted by fibre and due to that, the development of hygrothermal stress occurs [2].

The properties such as compressive strength, interlaminar shear strength, Fatigue, and impact tolerance will be decreased by these external moisture conditions and those properties are completely matrix dominated, which results in the loss of microstructural integrity. From previous experimental observations, it has been concluded that the absorption of moisture on the polymer composites is only a linear function, till the content of moisture is less than 2% [3]. The degradation will be emulated not only in performance but also in the fracture morphology. The common types of environmental conditions which have been exposed are Moisture, temperature, Hygrothermal, UV, Low earth orbit environment, and seawater [3]. For the overall sustainability and to reduce stress concentrations in material better interfacial properties are always required because they provide efficiency in load transfer from matrix to reinforcement [2]. In fiber-reinforced polymer matrix composites, Delamination is one of the severe failure mechanisms, it is arisen

Advancements in Aeromechanical Materials for Manufacturing: ICAAMM-2021
AIP Conf. Proc. 2492, 040032-1–040032-10; https://doi.org/10.1063/5.0113426
Published by AIP Publishing. 978-0-7354-4438-6/$30.00

due to the accumulation of interlaminar stresses and low through thickness strength in the material. Hence, by this delamination, there is a cause of buckling failure under compressive loading. In the material class, the behaviour and its damage redundancy are definite features that are widely spread in nature that are encountered in various damage modes. These damage modes are delamination growth, fractal growth in fibre, and matrix cracking. Hence, it has always been an uphill task to identify the fundamentals of hygrothermal degradation in fiber/polymer composites.

In the field of failure mechanisms, as per the scientist Seth et.al it is proved that the because of thermal conditioning, percentage of interlaminar shear strength decreases during the above ambient temperature testing mode of all loading rates and that leads to expanding the process zone in matric which results in fibre/matrix debonding. The reasons behind studying these conditions are, fiber composites are anticipated to encounter a wide range of environmental conditions during their service time, and moisture absorption changes the stress state and affects the interface of fibre-matrix which results in deterioration [4].

The fibers that are about the size of 0.0002-0.0004 in (0.005-0.010 mm) in diameter and laid back with carbon atoms are called Carbon fibers. One of the main reasons for the great strength in carbon fiber matrix composites are fibers in it, and the justification for that point is because of carbon crystal alignment. The crystals are one which makes the fiber abundantly stronger with its size. The classification of carbon is based on the property of tensile modulus. The reason behind choosing the property of tensile modulus is, because the tensile modulus is a major criterion to predict the material efficiency. The Tensile modulus is generally known as “Modulus of elasticity” or “Elasticity modulus”. Quality control needs to be done firmly on the manufacturing of carbon fiber composite as it involves various applications and its efficiency is of utmost importance [5].

Composite material is a structure of two or more materials which are mixed and accumulated on a macroscopic scale, and produce a new material with different characteristics. The two constituent materials which have been taken for the making of a composite material will have significantly different physical or chemical properties. Composites are formed by reinforcements and matrixes which are, Reinforcement such as Fibers, particles, flakes or fillers and Matrix such as Polymers, Metals or Ceramics [5]. Composites are generally classified into two apparent levels, the first level of classification is composite with matrix constituent and, the second level of classification is composite with reinforcement form. The composite parts are eccentric in a way, such that they are designed to resist the loads from various directions. During the service life of materials, they experience several loads which are exerted on them, and due to that many stresses are imposed on them. It is always important to analyse the sort of stresses which would affect the application of material and decide the material for use in that fabrication. The aerospace applications are the most immense factor in the composites industry since composites materials attain a great strength to weight ratio, high strength, hence the best choice for the aerospace industries would be composite inadequately [7]. One of the main reasons behind the usage of composites is that they can resist with many stresses but not increase the weight.

To meet the required dimensions or design, there are several ways and methods of fabrication process for fabricating composite components. It all depends on the specific part, materials and required application for choosing the method of fabrication. In consideration of these issues as mentioned earlier, this project focused on studying and analysing the conditions of the degradation i.e., reduction in the carbon fibre compounds in the composite, and characterizing the physical and mechanical degradation of carbon fiber-reinforced epoxy composites which are exposed to a heat and moisture conditions. The main objective is to improve the reasonable modes of identifying the degradation that enhances the predictability of service time of materials under these hygrothermal conditions.

EXPERIMENT DETAILS

The experimental process started from gathering and studying the relevant journals, publications, research papers, and books related and required for the project. In detail to the experiment, carbon fiber epoxy reinforced composites are fabricated by using the Hand lay-up manufacturing process. Then the carbon composites are placed in the open environment, for a reasonable cycle of time. The degradation of the carbon fiber plate is observed in ways such as, by comparing the mechanical properties increase or decrease by the increase or decrease in the exposure time and by micrographic observations on surface and also weight loss or gain after the plates are subjected to hygrothermal conditions[8].Hence the degradation of carbon fiber composites is observed and analysed, by the deteriorating effects of mechanical properties on the structure by performing destructive testing methods.

MATERIALS AND ITS PROPERTIES

In this project, a carbon fiber reinforcement is utilized which is in the form of Bi-directional. A 3k carbon fabric 200 GSM of twin weave is selected for fabrication, of 1000 mm width and 3000 mm length. The thickness of the carbon fabric ply is around 0.2 mm. The thermoset polymer epoxy resin is used as a matrix for the fabrication with the carbon fiber. The type of epoxy resin used in the process is Araldite CY 230 which is a low viscosity resin [17]. The amount of 1000 gm epoxy is being bought for this project. One of the best combinations for the epoxy resin CY 230 is Aradur HY 951 hardener. Hardeners are always necessary to make an epoxy resin useful for its intended purpose. Aradur HY951 hardener which has low viscosity, good mechanical strength, good resistance to atmospheric and chemical degradation. It is mixed with epoxy in the ratio of 10:1. The amount of 100 gm hardener is being bought for this project. The Physical, Electrical, and mechanical properties of all the carbon fiber is shown table 1 and, Matrix and hardener in table 2.

TABLE-1 Physical, Electrical and mechanical properties of 3k Carbon fabric [16]

S. No	Property	Value
1	Density	1.76 g/cc
2	Tensile strength	3650 mPa
3	Modulus of elasticity	231 GPA (in tension)
4	Thermal conductivity	8.50 W/m-k
5	Electrical resistivity	0.00180 ohm-^{1} $_{cm}$
6	Elongation at break	1.4 %

The raw materials such as Carbon fiber, epoxy resin, and hardener were supplied from Vaishnav composites Limited, Secunderabad.

TABLE 2 - Properties of Epoxy resin CY 230 and Hardener HY 951[17]

Resin	Viscosity	Specific gravity	Flash point	Mix ratio	Density
Matrix	1350- 2000 mPa*s	1.1- 1.2g/cm³	160℃	100:10	1.19 g/cm^3
Hardener	10 - 20 mPa*s	0.98 g/cm³	110 ℃	100:10	1 g/cm³

FABRICATION AND TESTING

The process involved in fabricating the carbon fiber reinforced composite is the “Hand layup method” as mentioned earlier. The total 3sq.m of carbon fabric has been able to produce a four (4) number of composite plates of dimensions: 300*250 mm, 300*200 mm, 300*125 mm, and 100*100 mm of thickness: 4.5mm, 4.5mm, 4.8 mm and 7.2 mm respectively.It varies from one to one individually, whether to cure in the open room temperature conditions or to subject it to the forced micro-oven and also even to seal the hand layup set up to the vacuum bag. The better equipment we use, the better post curing will happen. The forced convection oven process is one of the reasonable processes for a consistent curing process[9]. The oven is used in this project, after placing for 48 hours of room conditions to every laminate. Laminate is placed in the oven for 4 hours at 60℃ temperatures. The fabrication involves a sequence of operations as shown in the below figure 1.

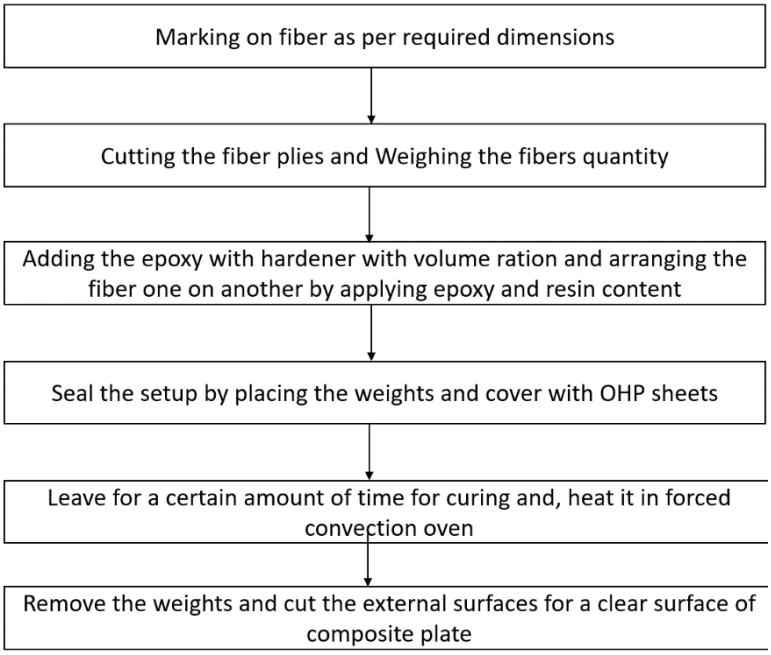

FIGURE 1 - Steps of operations involved in the fabrication

TABLE 3 - Characteristics of final composite plates

S. No	Composite plate dimensions (mm)	Fibers Weight beforehand lay method (gm)	Epoxy used (gm)	Hardener used (gm)	Desired Thickness (mm)	Obtained Thickness (mm)
1	300*250	240	219	22	3	4.3
2	300*200	182	180	18	3	4.3
3	300*125	145	132	13.2	3.6	4.8
4	100*100	65	60	6	6	7.3

The composite plate of all dimensions as desires have been fabricated. Hence by the parts per volume theory the amount of epoxy needed to take for an example, if the weight of fibers will be 219 gm and then the mix ratio to epoxy and hardener is 10:1 and the amount of hardener will be 22 gm. There is a chance of increase in thickness after the fabrication and post curing conditions. The weights of those fiber layers and epoxy hardener ratio are shown in table 3 below, and four final fabricated composite parts are also represented in figure 2.After completion of fabrication, with the objective to study the conditions of composites under heat and moisture absorption. The carbon fiber composite plates have been placed for an open environment under frequent observation, for a 10-cycle period, of which each cycle is equal to 35 hours duration. During this time, all the composite plates were exposed to all sorts of environmental conditions which generally composites are being experienced in their applications. The composites haven't disturbed during their exposure time which could replicate its results. After the expodesired time for the project, composite plates were removed from the environment and stored.

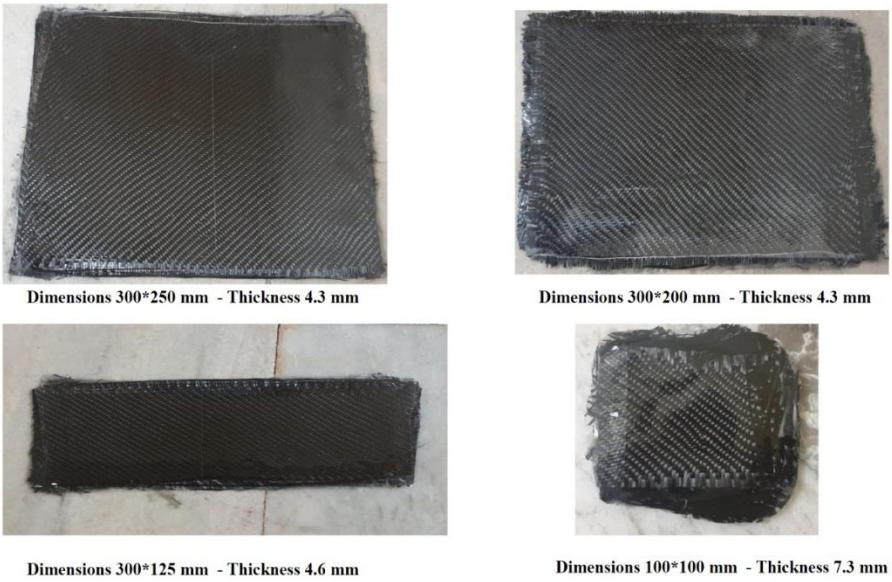

FIGURE 2 - Representation of all four composite plates of various dimensions

Then the composite plates were cut in ASTM standards required for testing and performed the tests which will be discussed further. The results of the tests and studying the role of hygrothermal conditions will be discussed briefly in the Results and Discussions section. All the tests involved in this project are performed in KVS Metallurgical Labs, Hyderabad, Telangana with the help and support of their professional team[15].

Tensile Strength test

The composites have been tested on a Servo Universal testing machine for the tensile test. The properties which are impacted due to tensile forces are identified in this test. The standards used in this tensile test are ASTM D3039, and the test specimens were cut in those standard dimensions and performed the test. The testing machine is shown in figure 3.

FIGURE- 3 - Servo Universal testing machine

Flexural Strength test

It is always important to calculate the failure point or modulus of rupture, for a material. Hence flexural modulus tests have been performed on fabricated composite plates on Universal testing machines. Flexural strength or modulus is one of the dominant properties such that it determines the material resistivity or highest stress experienced in the material before its yield point. Hence, it is a key aspect for the selection of materials as it determines the stress which the material could maintain without breaking. The test specimens were cut in ASTM D790 standards.

Inter Laminar shear strength test

The property that determines the shear stress between the laminates of a structure, is known as Interlaminar shear stress. This test is preferred mainly on layered structures and composites. The composite plate has been cut into standards required such as ASTM D2344. Generally, the shear stress can be observed in the flexure test, but only when the span is small compared to thickness. Hence the shear stress occurs on a small scale in those areas.

Hardness test

The hardness test is carried out on one of the plain surfaces of the fabricated composite plate. The type of hardness test involved in this project is Barcol Hardness, done by Barcol hardness tester and the standards are ASTM D2583. By hardness, we are able to identify the properties such as ductility, wear resistance, and even strength. The major reason for performing Barcol hardness tests is, to define the resistivity of material that is exposed by permanent deformation under penetration of the indentation of another harder material. The test setup is shown in figure 6.

FIGURE 4 - Barcol Hardness Tester set up

Compressive strength test

The compressive properties define the behaviour of a material when they are subjected to compressive loads. It's a simple test, which applies the loads at a uniform rate and then compresses. This test is performed by a Servo Universal testing machine. As a result, stress-strain data is recorded with respect to load applied. The test specimens are cut in the required standard dimensions ASTM D695.

RESULTS AND DISCUSSION

This project necessitated several mechanical tests, which resulted in the properties of carbon fiber composites which are required to estimate the overall reliability and lifetime of the composites. It also discusses the composites which have been exposed for a certain period of time to environmental conditions and their effects on the properties. The properties of the composites are depleted by the reluctant temperature which results in fracture of the material. Numerous solutions have been tendered to tackle these environmental conditions.It's a significant challenge to demonstrate and draw to a conclusion on temperature effects on composite. The present project upholds the fabrication process and mechanical properties of the carbon fiber composites exposed to ambient temperature (+28℃). The tensile strength, flexural modulus of elasticity, Yield strength, compression strength, and inter laminar shear strength has been resolved. The comparative study with the previous test results and present trend result has been also discussed further.

Tensile strength result

Three (3) test specimens were cut as per the ASTM standards from the 4.5 mm thickness carbon fiber laminate. The 3 test specimens were tested on a universal testing machine for tensile tests only, for the better and average result excluding any instrumentation and random error and to obtain the finest result. The data that prevailed through tensile tests are Yield stress, Tensile strength, Yield load, Peak-load, Break(failure) load, and their respective elongations. The average result out of 3 tests for a tensile test is 227.16 MPa of Yield stress and 289.63 MPa. As per many journals and the general properties of carbon fiber, the tensile strength should be more than 360 MPa. A distinctive stress-strain plot for one of the test specimens is shown in figure 7, which has a tensile strength of 324 MPa and 257.8 MPa of Yield stress. Hence it can be assumed that, due to the exposure that has been subjected on carbon fiber laminates

tends to weaken the bond of fiber-matrix interface and results in a reduction of tensile strength, and also yield stress. It is not appropriate to point only to environmental conditions for failure even though it is one of the reasons, but the composition of the fiber weight to the epoxy resin and the fabrication process which involves a faultless post-curing technique is also majorly considered for better performance of carbon composites.

Flexural strength result

The tensile test, flexural stress test, inter laminar shear stress, and Compression stress test, are all performed on the same Servo hydraulic Universal testing machine UTES-40. A total of 5 specimens were used for the flexural strength test which were cut into ASTM standards required for the test. The data analysed from this test are flexural strength at yield and max positions, flexural strain, and flexural modulus of elasticity. It has been observed after testing that there is no such huge or minimal decrease of flexural strength of carbon fiber composites. As the basic flexural strength of carbon fiber is around 350 MPa. The average result for flexural strength obtained through the tests on carbon fiber is 332 MPa. This value replicates and will be also equal to the normal value of certain tests, but it cannot be neglected. There might be a change of reduction in flexural strength after some more high exposure to the environment. But there is a huge decrease in the modulus of elasticity (flexural modulus) obtained in this test, it depicts that due to environmental conditions, maybe the factor of material resistance for bending decreases. Generally, the flexural modulus of carbon fiber composites will be more than 200 GPa. But the test specimens obtain a flexural modulus of elasticity of only 8.007 GPa. The factor of resistivity is very important for consideration and it presents a challenge to improve the properties which gives more flexural modulus

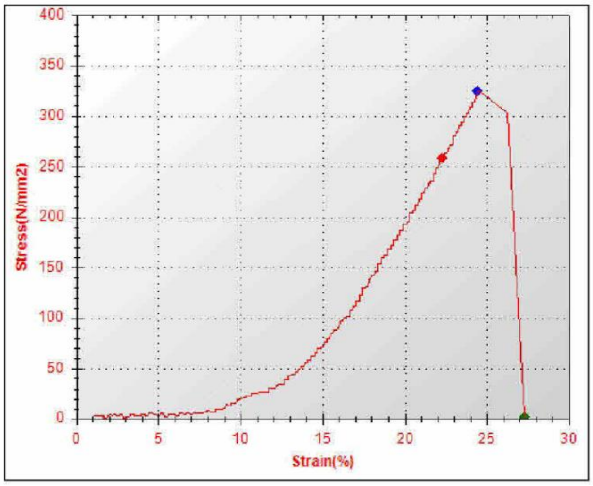

FIGURE- 5 - Graphical representation of Stress vs Strain

.

The flexural strength at yield, Deflection at yield, and load at yield are: 181.3 MPa, 2.60 mm, and 417.7 KN respectively. The factor of maximum elongation which is less than compared to the previous tensile test is 5.46 mm, it shows there is a state of reduction in elongation in flexural tests. The flexural strain which is one of the important factors is maintained with a 0.021 value.

Inter laminar shear stress result

The stresses that act upon normal to the plane of the laminate, and the shear stress which occurs at the edge planes of the laminate are Inter laminar shear stresses. The displacement speed maintained for this test is 1 mm/min. One of the main aspects of discussing this property is that the effect of environmental conditions mainly acts on fiber-matrix bonding and matrix complexion interface. Due to these factors the property completely decreases and tends to premature failure is Inter laminar shear stress. Five (5) specimens were used for the Inter laminar shear stress test which were cut into ASTM standards required for the test. By the number of tests, it has been determined that the minimal load the composite can take during the inter laminar shear stress is 371.3 N, and deflection experienced is only 1.032 mm. A typical load vs deflection graph is plotted and shown in figure 8. Heading to the short beam.

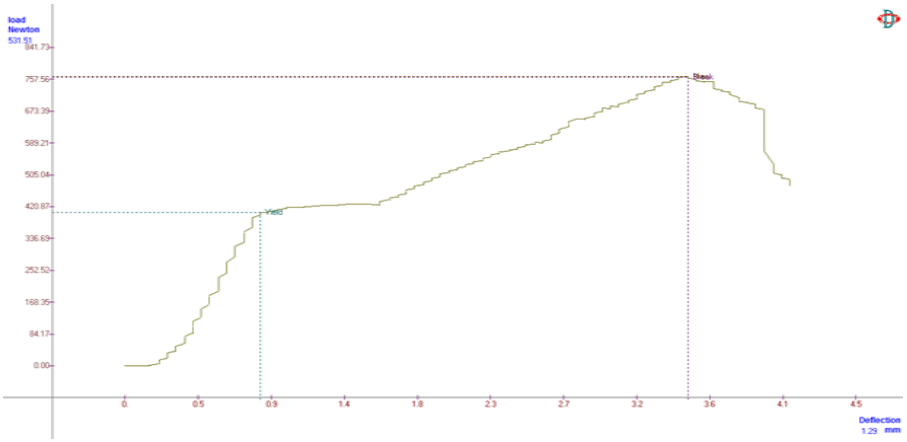

FIGURE 6- Load vs Deflection graph for Inter Laminar shear stress test

strength test, this test is also known as the Short Beam Strength test, The short beam strength(s) that are recorded in this test are 6.186 MPa, 5.66 MPa, 7.82 MPa, 2.5 MPa, and 3.69 MPa. The average short beam strength for the interlaminar shear stress for tests can be determined by an average of results that is 5.17 MPa. It is assumed the laminates do not obtain with a better inter laminar shear stress through the composite structure, there are irregularities and fiber breakage issues even during the test. The short beam strength gradually decreases after some intervals of the test, the exposure of the environment definitely has a part to decrease in this strength, hence the fiber-matrix bonding should be taken care of while predicting this property.

Compressive strength result

One of the major drawbacks of carbon fiber composites is less compressive stresses. Generally, due to the stress concentrations, instability in the composite materials, and loss of stiffness directly tend the material to buckle under compressive loading. The compositions of the epoxy resin and carbon fiber also have a major role in compressive stresses, epoxy is stronger in compression but carbon fiber is weak in compression. The test was conducted on two (2) specimens for compressive strengths. The compressive strength resulted from the average of tests is 15.17 MPa. The peak load that could be achieved by the composites is recorded with 1.3 KN elongation of 16.8 mm is experienced. It is reluctant to experience this certain result after the environmental exposure, as the general compressive strength of carbon fiber composites is more than 800 MPa, hence it can be estimated that the reduction of compressive strength after the environmental conditions is very huge. The compressive strength should be improved in composites with respect to structure reliability and aging conditions.

Hardness test result

Hardness is the property that which resists from the deformation occurring in the material, mostly the deformation on the surface is considered as deformation in polymers. The test was carried on the plain surface of the fabricated carbon composite of cross-sectional area 250*250 mm^2. The indenter of the Barcol hardness tester is placed on the different positions of the specimen and uniform pressure is applied until the indication on the dial gauge reaches the maximum point, hence the points show the hardness of that respective area. The hardness was recorded for 5 times on the specimen for a better value and the various harnesses recorded during the test. It is advised to use Barcol hardness for rigid plastics and composites such as carbon and glass fiber. The average hardness resulted from the specimen is 49. The reduction in hardness might be due to the formation of pores and voids which are formed by placing them in the environment. The void fraction in composites is inversely proportional to the hardness of the material, hence it is important to be careful that the void fraction should be low in composites.

CONCLUSION

In this comparative study, we carried out the effects of environmental exposure on the carbon composite properties under hygrothermal conditions, which is exposed to heat and moisture. The exposed specimen is tested for tensile

strength, flexural strength, hardness, Interlaminar shear strength. The test data is used for comparative study and for predicting the long-term service life of carbon fiber composite. From the experimentation conducted and based on the above results, the following major conclusions are:

Reduction in tensile strength, the experimental data after the exposure when compared shows the tensile strength of a composite generally, that is exposed for 400 hours is 6% - 8% less than the strength of the initial specimen. And the yield stress is decreased by 7-10%.(Average data is taken from 5 tests for a specimen) which is due to the weakening of fiber-matrix bonds. The load at yield and peak are 24.71KN, and 31.51KN and the failure of the composite is due to the axial directional splitting, transverse matrix failure.

Decrease of flexural strength, it has been observed that there is no effective decrease in flexural strength. The test data is compared with the initial results and it says that there is a 5-7% decrease in flexural strength. But there is a huge decrease in modulus of elasticity which may be due to poor dispersion of fiber in the matrix or the voids formed in the laminate. By this, we can understand that due to the extensive environmental conditions, the material resistivity of bending decreases which results with low flexural modulus of elasticity. This focus that the composites need to fabricate which could resist flexural loads accurately.

Interlaminar shear stress and compression tests are conducted and the average short beam strength of interlaminar shear is 5.17MPa which is very low. It is assumed due to the irregularities and fiber breakage in laminates and weak bonding. The main drawback of carbon composite is its poor compressive strength. The composites have a higher tensile strength than compressive strength, under testing the composite not only buckles it also kinks or crushes. In these tests the average compressive strength which is exposed decreased by up to 20% of the initial test average compressive strength.

The degradation of the carbon composite is due to the deterioration of the bonding between the fiber-resin matrix and also resin matrix interface. However, we can expect that over long environmental exposure periods can cause so much damage between fibers matrix resin and owe to matrix erosion and can even result in structural failure.

It can be determined that during service life, composites face various obstacles such as environmental conditions which affect the integrity and decrease the durability of the material. By several researchers and designers throughout the years, there have been numerous improvements made to enhance the resistivity during the environment and also to control the damage conditions of composites.

FUTURE SCOPE

Further study can be extended to understand the degradation of carbon under the microstructure level using powerful microscopes and the percentage of carbon degradation. This project provides an opportunity to compare the results with several other fiber reinforcements, different fiber weight loading composites, and also by stitched laminates for not only estimating its service life span but also to improve it. This project confides a challenge to improve the design methodology and to fabricate a flawless composite which have better reliability and excellent performance.

ACKNOWLEDGEMENT

We gratefully acknowledge the support of the Vaishnav composites limited and KVS metallurgical lab for supplying products and helping in performing tests. We are thankful to Mr. Bhanu Prakash and Mr. Santhosh for assistance in carrying and helping for the fabrication of composite plates. We are also extremely thankful to Mr. N. Uday Ranjan Goud for guiding us throughout the project.

REFERENCES

1. ‘Mr. N. Uday Ranjan Goud’, ‘Dr. N. V. Swamy Naidu’, “Investigation on Buckling of Laminated Composite Plate”, IOSR Journal of Mechanical and Civil Engineering (IOSR-JMCE), e-ISSN: 2278-1684, p-ISSN: 2320–334X, PP 81-87, www.iosrjournals.org, January, 2017.
2. ‘Nayani Uday Ranjan Goud’, ‘Alka Sawale’, ‘Bhupal Rakham’, “Buckling Load Predictions of Panel and Shell using Vibration Correlation Teche”, International Journal of Engineering and Advanced Technology (IJEAT), ISSN: 2249 – 8958, Volume-9, Issue-2, December, 2019

3. ‘Alka Sawale’, ‘Nayani Uday Ranjan Goud’, ‘M.Srinikitha’, “Experimental Analysis of Stress Concentration on V-Notched Plate”, International Journal of Innovative Technology and Exploring Engineering (IJITEE), ISSN: 2278-3075, Volume-9 Issue-2, December 2019
4. ‘Nayani Uday Ranjan Goud’ et al, “Investigation on elliptical crack geometry in a thin plate”, AIP conference proceedings, volume 2317, issue 1, doi.org/10.1063/5.0036433, February 2021.
5. G. Agarwal, A. Patnaik, R. K. Sharma, “Mechanical and thermo mechanical properties of Bi-directional and short carbon fiber reinforced epoxy composites”, Journal of Engineering Science and Technology, October 2014, Vol. 9(5)
6. Bhavesh G. kumar (Department of mechanical engineering), Raman P. Singh (state university of New York), Toshio Nakamura (Stony Brook), “Degradation of carbon fiber reinforced epoxy composites by ultraviolet Radiation and condensation”, June 14, 2002
7. Sanghamitra Sethi, “Environmental Degradation Study of FRP Composites Through Evaluation of Mechanical Properties” Department of Metallurgical and Materials Engineering National Institute of Technology Rourkela - 769008, Odisha INDIA, December 2014
8. M. Meng, M.D.J. Rizvi, S. Grove,H.R.Le, “Effects of Hygrothermal stress on failure of CFRP composites “, Article in Composite Structures 09 April 2018.
9. Cheng Xiaoquan, Yasir Baig, Li Zhonghai, “Effects of Hygrothermal environmental conditions on compressive strength of CFRP stitched laminates”, Journal of Reinforced Plastics and Composites · January 2011
10. Etches J., Potter K., Paul Weaver, Ian Bond “Environmental effects on thermally induced multi stability in unsymmetric composite laminates, Composites Part A: Applied Science and Manufacturing”, Department of Physics Brigham Young University - Idaho December 2018
11. Om. K. Joshi, “The effect of moisture on the shear properties of carbon fiber, Composites” 1983; 14; 196.
12. Akay M, Mun S.K.A, Stanley A. Influence of moisture on the thermal and mechanical properties of autoclaved and oven-cured Kevlar-49/epoxy laminates. Composite Science and Technology 1997; 57; 565
13. Barré S, Chotard T, Benzeggagh ML. Comparative study of strain rate effects on mechanical properties of glass fibre -reinforced thermoset matrix composites. Composites Part A 1996; 27:1169–81.
14. Wang Y, Hahn T.H. AFM characterization of the interfacial properties of carbon fiber-reinforced polymer composites subjected to hygrothermal treatments. J Compos. Sci. Technol. 2007; 67: 92-101
15. Rahul Reddy Nagavally, “History, types, fabrication, techniques, advantages and applications” Kakatiya institute of technology and sciences, Warangal, International Journal of Advances in Science Engineering and Technology, ISSN: 2321-9009, Vol-4, Iss-3, Spl. Issue-2 Sep.-2016
16. https://www.polymercompositesinc.com/products/fabrics/carbon-fiber/carbon-fiber-3k-2x2-twill-weave/
17. https://5.imimg.com/data5/GI/GS/MY-35074384/araldite-epoxy-resin-cy-230-and-hy-951-hardener.pdf

RESEARCH ARTICLE | MAY 22 2023

Performance improvement in thermal conductivity measuring apparatus using spiral heating coil

M. Mahesh ✉; P. Thangavel; M. S. Abdullah; B. Arulpriyan; P. Gokul; D. Mahesh Kumar

AIP Conference Proceedings 2492, 020080 (2023)
https://doi.org/10.1063/5.0113149

Performance Improvement in Thermal Conductivity Measuring Apparatus Using Spiral Heating Coil

M Mahesh[1, a)], P Thangavel[1], M S Abdullah[1], B Arulpriyan[1], P Gokul[1], and D. Mahesh Kumar[2]

[1]*Department of Mechanical Engineering, Kongu Engineering college, Erode, India*
[2] *Department of Aeronautical Engineering, MLR Institute of Technology, Hyderabad, India*

[a)] Corresponding Author mail address: mmahesh.mech@kongu.ac.in

Abstract— Because of the wide range of applications in which metals are used, heat conduction is unquestionably important. Metals have high thermal conductivities because they have a large number of free electrons, which help to transmit heat quickly through the fabric. Metals are commonly utilized as conductors as a result of this ability; in physics, metals are commonly seen as cooking utensils, heat exchangers, and warmth sinks. Engineers and developers need to be able to precisely live the heat conduction of metals in order to decide what type of metal to utilize for a specific application. Regarding these requirements the thermal conductivity measuring apparatus for Cartesian and cylindrical coordinates is proposed for development. Design of testing chamber and heating coil are initiated to accompany the cylindrical and Cartesian coordinate components. Based on the design, the various materials for chamber, heating coil and insulating materials will be selected. Fabrication work to be completed based on the design. Heat supplied is controlled by an Auto transformer which is used to regulate the applied voltage. Voltmeter and Ammeter are connected in the experimental arrangement to note the applied voltage and current respectively. Thermocouples are used to measure the temperature of the specimen surfaces at different locations. After measuring the required values, the values are substituted in the thermal conductivity formula and the thermal conductivity of the specimen is obtained.

Key Words: Chamber, Heating Coil, Material properties, Thermal Conductivity, Performance study

INTRODUCTION

The thermal conduction is outlined as a live of the flexibility of a fabric to transfer heat. Thermal conduction plays a key role in thermal behavior of the fabric. It's an elementary property, freelance of the amount of fabric. Heat is transferred between two surfaces of the fabric because of temperature distinction between them. The magnitude of thermal conduction is depends abreast of energy transferred per unit time, area exposed for warmth transfer and temperature distinction of the surfaces. Thermal conduction of the fabric is to be known before it's applied to sensible applications. Hence, it's necessary to understand the thermal conduction of a fabric. The thermal conduction is often influenced by the material's chemical composition and molecular structure. Material with straightforward chemical composition and molecular structure has higher thermal conduction than the advanced. Because of the wide range of applications in which metals are used, thermal conduction is unavoidable. Metals have high thermal conductivities because they include a large number of free electrons that act to transport heat fast through the fabric. As a result of this ability, metals are commonly utilized as conductors; in physics, metals are commonly used as preparation utensils, heat exchangers, and heat sinks. Engineers and developers need to be able to correctly measure the heat conduction of metals in order to decide which type of metal to utilize. To meet these objectives, thermal conduction measurement equipment for Cartesian and cylindrical coordinates has been developed.

Advancements in Aeromechanical Materials for Manufacturing: ICAAMM-2021
AIP Conf. Proc. 2492, 020080-1–020080-7; https://doi.org/10.1063/5.0113149
Published by AIP Publishing. 978-0-7354-4438-6/$30.00

LITERATURE REVIEW

A work on Thermal Conductivity Measurement of A Bar-like Object was presented by Chuansha DAI et al. (2017). This study proposes a new experimental setup for measuring the effective thermal conductivity of a bar-like structure, as well as a theoretical analysis for data reduction. This method has a number of advantages over other methods: There is no need to cut a measurement sample from the primary object; the system is very reliable since the approach uses multi-position temperature data matching, which includes the hot tank, cold tank, and hot end. This technology is mostly used for theoretical analysis and object thermal conductivity testing.

The measurement of thermal conductivity variation with temperature for solid materials was presented by S.Aksoz et al. (2012). The thermal conductivity change with temperature of solid materials was frequently measured using a linear heat flow equipment. The hot stage, cold stage, and sample holder make up the linear heat flow apparatus. The hot stage is made up of two brass plates that are resistively heated by NiCr wires, which are insulated in alumina tubes and integrally threaded through the plates. Following the completion of all needed temperature measurements during the heat, the cooling procedure was initiated in the same steps down to room temperature. After removing the sample from the linear heat flow apparatus, the longitudinal section of the specimen was checked for porosity, cracks, and casting flaws to ensure that no inaccuracies in the measurements were introduced.

METHODOLOGY

The methodology of this research work has been depicted in Figure.1.

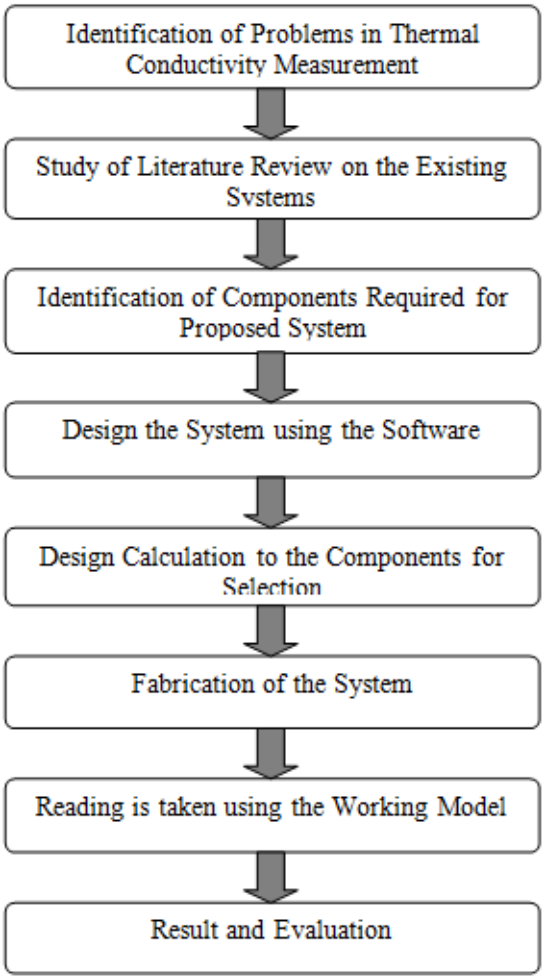

FIGURE 1 Methodology

MATERIALS AND SPECIFICATIONS

TABLE 1 Material and its Specifications

Components	Materials	Specification and use
Ammeter	Fiber Glass and Led panel	Range upto 16A AC Current.
Voltmeter	Fiber Glass and Led panel	For single Phase supply AC Current.
Contactor	Plastic	To Switch on high power in the circuit.
Heating Coil	Nichrome and alloys	Power = 2000W Outer Diameter = 150mm
Temperature Indictor with Controller	Fiber Glass and Led panel	LED display in degree Celsius.
MCB	Plastic	Two Pole MCB. To cut off the Power Supply during failure.
Thermocouple	Nickel and alloys	Sensor used to measure the temperature.
Indication lamp	Light glass	V = 1.5V indicates whether the heater is on (or) not.
Heater on/off Switch	Plastic	Switch to on and off the Heater.
Panel Frame	Heavy Metal	1" X 1" Square rod.
Chamber	Plywood and Asbestos	For Placing the Heating Coil and Specimen.
Base Plate	Mild Steel	Thickness = 3mm Specimen is placed on it.

DESIGN CALCULATION

The ammeter, voltmeter and heating coil selection is based on the calculation listed below.

Power Calculation

The power demand was estimated using the ohm's law.

$$P = V \times I \tag{1}$$

For voltage,

$$V = I \times R \tag{2}$$

Substitute equation 2 in 1

$$P = I^2 \times R \tag{3}$$

Where,

P = Power in Watts

V = Voltage in Volts

R = Resistance in Ohm

I = Current in Ampere

For single phase supply the voltage $V = 230V$

Power rating of the heating coil is given by the manufacturer as $P = 2000W$

For ammeter calculation,

$$I = P/V$$
$$I = 2000/230$$
$$I = 8.48A$$

For verification of theoretical Power rating value,

$$V = I \times R$$
$$230 = 8.48 \times 8.48$$
$$R = 27.12\Omega$$

According to ohm's law,

$$P = V \times I$$
$$P = 230 \times 8.48$$
$$P = 1950.4W$$

The calculated power value is approximately equal to the theoretical power value.

For heating coil range calculation,
Heating filament was assumed to be 100%

$$Q = mc_p \Delta T$$

$$\Delta T = 2000 / (0.01 \times 0.135 \times 1000)$$

$$T = 1481.48 °C$$

The maximum temperature range obtained by the heating coil to be 1481.48°C
Using this calculation the components are selected for the project.

DESIGN ANALYSIS

Different software can be used to carry out the design process, such as Autocad, SolidWorks, Proe, Creo, and so on. The design process in Figure 2 was carried out entirely with the CREO 2.0 Software. This software was chosen because it is more user-friendly and is the most often used solid modelling software.

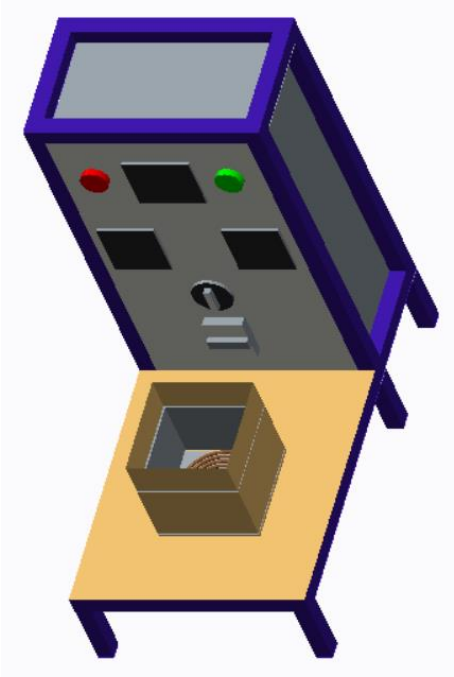

FIGURE. 2 Design of the System

PROPOSED SYSTEM

The frame is made to place the electric panel which holds all electrical parts is shown in figure 3. The plywood placed on the front of the frame in which the heating coil and chamber is placed. The heating coil is placed in the chamber which is made of asbestos and plywood. The base plate made of mild steel is placed on the heating coil to place the specimen on it and the heat is transferred from the heating coil to the base plate and to the specimen.

FIGURE. 3 Fabricated Model

WORKING

The single phase power supply is passed to the contactor and the contactor switches the electrical power circuit. The power is supplied to the heating coil and there is a control button for controlling the temperature of the heating coil. The heating coil temperature is displayed in temperature indicator. The thermocouple is connected to the temperature indicator which will sense the temperature of the specimen. The base plate is placed over the heating coil for placing the specimen on it. The specimen is then selected and it is placed on the base plate. The heating coil gets heated and passes the heat to the base plate and then to the specimen. Then using the thermocouple the temperature of the specimen at the top(T1) and bottom(T2) is measured and displayed in the temperature indicator. The voltage and ampere are displayed in the voltmeter and ammeter for that temperature. By increasing the temperature different readings are taken for the specimen. After completing all readings the calculation process is carried out for the taken readings.

RESULT AND DISCUSSION

The specimen's thermal conductivity is measured with the built thermal conductivity measuring apparatus. The aluminium substance has been chosen as a test subject. The specimen is put on the base plate, and the heating coil is connected to the power source. Cutoff of the power supply to the heating coil controls the temperature. The thermocouple is then used to detect the temperature, and the digital indicator is used to monitor the voltage and current. The thermal conductivity of the specimen is determined using the collected data and the thermal conductivity formula.

$$K = (Q \times L)/(A \times \Delta T)$$

Where,

K is the thermal conductivity of specimen in W/m.K.

Q is the amount of heat transferred through the specimen in Watts.

L is the thickness of the specimen in meter.

A is the surface area of the specimen in square meters.

ΔT is the difference in temperature of the specimen in Kelvin.

For aluminum the thermal conductivity is obtained.

TABLE 2 Experimental Reading

Heating coil T (K)	Current I (A)	Voltage V (V)	Heat Transferred Q (W)	Temperature Difference ΔT (K)	Thermal conductivity K(W/m.K)
313	0.76	232	176.32	0.5	254.92
323	0.88	234	205.92	0.6	248.09
333	0.96	232	222.72	0.7	230.00
343	1.08	230	248.40	0.8	224.45
353	1.23	234	287.82	1.0	208.06

The experimental reading of the specimen is measured and calculated is shown in table 2. Then the experimental value is compared with the theoretical value. The theoretical value of the thermal conductivity of the aluminum is 237W/m.K. The obtained experimental value is compared in the graph shown below.

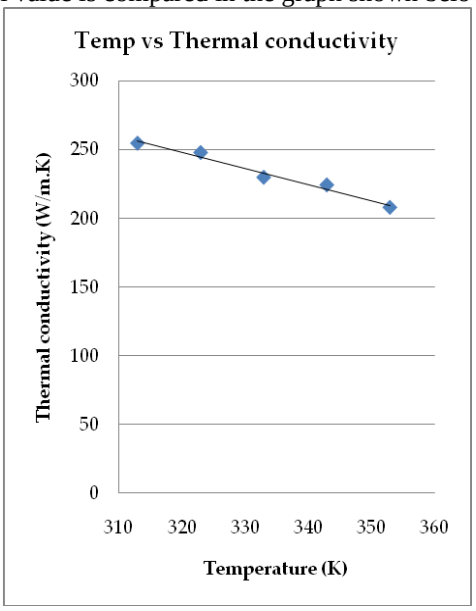

FIGURE. 4 Variation of thermal conductivity with temperature

The graph shown in figure 4 indicates the comparison between the temperature and the thermal conductivity of the aluminum material. In this graph, if the temperature increases the thermal conductivity will get decreased.

CONCLUSION

Significant results relating to metal characteristics and material withstanding temperature have been acquired as a result of this work's investigations. The thermal conductivity value of a material decreases as the temperature of the material rises. This experimental setting yielded a thermal conductivity value that is closer to the material's theoretical thermal conductivity value. Engineers and developers will be able to readily determine which sort of metal to employ for a specific application using this device. The thermal conductivity measurement equipment can be improved further by adding a multilevel temperature sensor to measure temperature at several points and changing the chamber design to improve the accuracy of the material's thermal conductivity value. The manufactured thermal conductivity apparatus is used to determine the thermal conductivity in a simple method, and the thermal conductivity can be easily found using a small piece of specimen. The designed equipment is simple to operate and can be used by anybody to test thermal conductivity. It is also more cost effective than any other currently available device.. The experimental average thermal conductivity value of aluminum is 233.1 W/m.K when the theoretical thermal conductivity value of aluminum is 237W/m.K.

REFERENCE

1. Chuanshan DAI, Xin GUO, Jinhua LU, Haiyan LEI, "Thermal Conductivity Measurement of A Bar-like Object*"*, *Energy Procedia*, 2017. 142: pp. 3975–3981.
2. Yuwang Liu, Mingzhi Yu, Yanfa Tian, Qiang Qin, "Study of thermal conductivity measurement accuracy of wet porous media", *Procedia Engineering*, 2017. 205: pp. 1755-1761.
3. C.L. Hapenciuc, I. Negut, T. Borca-Tasciuc, I.N. Mihailescu, "A steady-state hot-wire method for thermal conductivity measurements of fluids", *International Journal of Heat and Mass Transfer*, 2019. 134: pp. 993-1002.
4. Xiaodong Zhao, Guoqing Zhou, Xiong Jiang, "Measurement of thermal conductivity for frozen soil temperatures, Measurement", 2019.
5. S. Laguela, P. Bison, F. Peron, P. Romagnoni, "Thermal conductivity measurements on wood materials with transient plane source technique", *Thermochimica Acta*, 2014.
6. Mohd Yurzie Nazierul bin Yahaya, Normayati bte Nordin, "The Development of Thermal Conductivity Measurement Apparatus", 2010.
7. Wojciech P. Adamczyk, Ryszard A. Białecki, Tadeusz Kruczek, "Measuring thermal conductivity tensor of orthotropic solid bodies, Measurement", 2017.
8. P. Nagaraju, Sukanta Roy, "Effect of water saturation on rock thermal conductivity measurements", T*ectonophysics*, 2014.
9. Jun Huang, Xiaoxiao Xia, Xuejiao Hu, Song Li, Kang Liu, 'A general method for measuring the thermal conductivity of MOF crystals", *International Journal of Heat and Mass Transfer*, 2019.
10. S. Aksöz, E. Öztürk, N. Maraslı, "The measurement of thermal conductivity variation with temperature for solid materials", Measurement, 2012.
11. Mahesh et al.,, "Performance Improvement of VCRS Using Waste Heat recovery method", 2020, doi: 10.30534/ijeter/2020/81852020
12. Mahesh et al., "Performance Analysis of Cascade Refrigeration System with alternate refrigerants", 2020, doi: 10.30534/ijeter/2020/94852020
13. Mahesh et al., "Performance Evaluation of Portable Mist Humidifier", 2020, doi: 10.1088/1757-899X/995/1/012030

RESEARCH ARTICLE | MAY 22 2023

CFD investigation of rocket exhaust thrust vector control using gas injection

Bedarakota Nikhil Sai ✉; B. Manideep

AIP Conference Proceedings 2492, 020066 (2023)
https://doi.org/10.1063/5.0139062

CFD Investigation of Rocket Exhaust Thrust Vector Control Using Gas Injection

Bedarakota Nikhil Sai[1, a)] and B Manideep [1, b)]

[1]*Department of Aeronautical Engineering, MLR Institute of Technology, Hyderabad, Telangana, India.*

[a)] Corresponding author: neethun62@gmail.com.com
[b)] manideepbalusani.9@gmail.com

Abstract. The research work presents the flow characteristics of the steady flow field of a rocket engine with a nozzle, the objective of the work is to consider one of the rocket engines, simulate and present the variation of Mach, Density, Temperature, Thrust deflection, change in momentum due to the thrust vectoring. A numerical analysis was carried out to characterize the nozzle flow field of secondary injection thrust vector control (SITVC), and a simulation results was set out to analyze the impact of switching the injection position on the SITVC nozzle fluid flow structure and SITVC performance. Parameters. Due to the complexity of the rocket flow investigation, most of the research works are performed using the computational tool. And due to the advent of Computational Fluid Dynamics, the studies involving the fluid flow problem for complex systems has been tremendously helpful. Therefore, the research work has solved numerically the compressible 2-D steady Reynolds Average Navier Stokes equation.

Keywords. The effect of the rocket engine flow aided in the presentation of the wall temperature, static pressure, exit Mach number, this research has also verified the authenticity of the code Fluent, by verifying the results obtained with that of the numerically solved results.

INTRODUCTION

A rocket engine forms a high-speed propulsive jet of fluid, generally high gas, using stored rocket propellants as reaction mass. Rocket engines are reaction engines that generate thrust by ejecting mass backward, as stated by Newton's third law. The majority of rocket engines depends on the combustion of reactive chemicals to provide the necessary energy, however non-combusting forms such as cold gas may be used. The combustion chamber is where chemical energy is produced into kinetic energy. As propulsion systems, there are usually two components: fuel and oxidizer. They are injected into the combustion chamber at very high pressure (because to the high pressure inside the combustion chamber) and mixed before becoming lighted. The chemical energy is converted back into caloric energy, as well as temperature and pressure. The use of readily available software will allow the rocket flight research to progress by private companies and the research community. The objective of this project is to use a commercial CFD code-ANSYS Fluent as a tool for a parametric study of a rocket chamber that incorporates Mach interactions, shock interactions and other supersonic characteristics which initiates during the thrust vector control. A detailed approach to the analysis is documented for rocket flow study enthusiasts to readily simulate their own rocket flow fields.

LITERATURE REVIEW

A rocket combustion chamber [1] was developed with a one coaxial shear injector. The hot firing experiments carried out with gaseous methane and gaseous oxygen at a mass ratio of 2.647 of oxidizing to fuel at a pressure of 2 MPa. Wall temperatures were measured along the chamber's axis, and wall heat fluxes were calculated using the inverse heat conduction method. To conduct a more detailed review of the research. The eddy dissipation concept

Advancements in Aeromechanical Materials for Manufacturing: ICAAMM-2021
AIP Conf. Proc. 2492, 020066-1–020066-8; https://doi.org/10.1063/5.0139062
Published by AIP Publishing. 978-0-7354-4438-6/$30.00

model is adopted to model turbulent combustion. Mesh independency studies have been achieved prior to any further analyses. The ultimate target is to compare the heat fluxes obtained from simulation with the experimental data.

A more accurate picture of the post war soviet rocket propulsion was presented in the [2], the material has supplemented the material of the Russian publications that included the various kinds of rocket engine literature [3], the website had a huge list of the various Ukrainian rocket engines, From this literature the geometrical profile of the RD-106 nozzle was considered for the research work.

Heat transfer studies [4] were presented for a rocket nozzle, to calculate two dimensional two phase flow predictions were presented for convective and radioactive heat transfer, the methodology and design presented were suggested to design new rockets and improvise the existing designs.

A study[5] reported the Numerical simulation of the combustion characteristics of a rocket-based combined-cycle engine combustor running in ramjet mode. The intrinsic unsteadiness of combustion in such a propulsion model is explained using compressible large eddy simulation with liquid kerosene sprayed and evaporated. Results for the combustor's pressure oscillation amplitude and frequency, as well as the wall pressure distribution[7-10]

MODELING AND ANALYSIS

The CAD model was created following the dimensions mentioned, In this case we would need to create a 2-d sketch/plane of the upper section of the rocket engine, and assign the central axis as the axis of symmetry.

The CAD model was created following the dimensions mentioned in the above figure, In this case we would need to create a 2-d sketch/plane of the upper section of the rocket engine, and assign the central axis as the axis of symmetry[10-12].

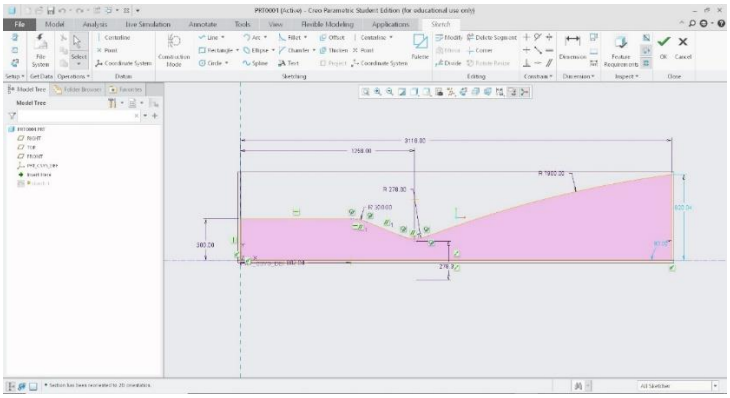

FIGURE 1. The RD-106 Rocket Engine sketch in Creo

The website [3] has presented all the working details of the rocket engine, such as the Chamber Pressure, Chamber temperature, etc., the details are vital in order to perform the necessary hand calculations, the given data is listed below in the following table. These are to be numerically simulated using the Ansys Fluent solver.

In order to perform a numerical study, we needed to assume, the altitude, hence we have assumed the operating altitude of the rocket engine as 6 km.

TABLE 1 Boundary conditions

S.No	Boundary Condition	
1	Chamber Pressure	5.88 MPa
2	Chamber Temperature	2300 K
3	Altitude	20 km
4	Temperature at 20 km	216K
5	Pressure at 20 km	5474.9 Pa

From the dimensions of the rocket engine we have the nozzle are ratio as

Nozzle Area Ratio = Exit Area / Throat Area

20.42 $\boldsymbol{m^2}$

Stagnation Density = $\frac{\boldsymbol{P}}{\boldsymbol{RT}}$

= 8.90 kg/m^3

Throat Velocity = $\frac{\sqrt{\boldsymbol{\gamma RT}}}{\boldsymbol{\Gamma+1}}$

= 877.5 m/s

Therefore, from the equations mentioned in [6] the Exit Mach Number = 4.750

Using the compressible flow relations [7] the Throat Density = 5.6kg/m^3

Similarly, the Exit pressure = 14961 Pa, the exit pressure is less than the atmospheric pressure (at that altitude) , hence the flow is under expanded.

The Exit Temperature can be found using the Isentropic relations, it was found to be, Exit Temperature = 444.8K

The Exit Sound speed was found to be 421.27 m/s (Using a=$\sqrt{\boldsymbol{\gamma RT}}$)

The Exit Velocity was found to be 1923.97 m/s(Using Ve = a* Me)

Introduction to Analysis Tool

Simulation of systems and equipment comprising flow of gases and liquids, heat and mass transfer, chemical reactions and related physical phenomena using computational fluid dynamics (CFD) is a technique used in engineering. It can be used to reduce pressure drops, calculate aerodynamic lift or drag, and predict the rotor thrust, among several other things.

FIGURE 2. Model generated in ANSYS Space Claim

Governing Equation:

$$\frac{\partial}{\partial t}\iiint_{\mathcal{V}} \rho \, d\mathcal{V} + \iint_{S} \rho \mathbf{V} \cdot \mathbf{dS} = 0$$

The Momentum Equation:

The fundamental physical principle used is Newton's second law

The X-Momentum of N-S Equation:

$$\frac{\partial(\rho u)}{\partial t} + \nabla \cdot (\rho u \mathbf{V}) = -\frac{\partial p}{\partial x} + \frac{\partial \tau_{xx}}{\partial x} + \frac{\partial \tau_{yx}}{\partial y} + \frac{\partial \tau_{zx}}{\partial z} + \rho f_x$$

$$\rho\frac{D}{Dt}\left(e+\frac{V^2}{2}\right)=\rho\dot{q}+\frac{\partial}{\partial x}\left(k\frac{\partial T}{\partial x}\right)+\frac{\partial}{\partial y}\left(k\frac{\partial T}{\partial y}\right)+\frac{\partial}{\partial z}\left(k\frac{\partial T}{\partial z}\right)$$
$$-\frac{\partial(up)}{\partial x}-\frac{\partial(vp)}{\partial y}-\frac{\partial(wp)}{\partial z}+\frac{\partial(u\tau_{xx})}{\partial x}+\frac{\partial(u\tau_{yx})}{\partial y}+\frac{\partial(u\tau_{zx})}{\partial z}+\frac{\partial(v\tau_{xy})}{\partial x}+\frac{\partial(v\tau_{yy})}{\partial y}$$
$$+\frac{\partial(v\tau_{zy})}{\partial z}+\frac{\partial(w\tau_{xz})}{\partial x}+\frac{\partial(w\tau_{yz})}{\partial y}+\frac{\partial(w\tau_{zz})}{\partial z}+\rho\mathbf{f}\cdot\mathbf{V}$$

CFD-Post Results of the Rocket Engine

Open Cfx Post Results to Find the Results like Pressure, Velocity, mach ,temperature, density on Body

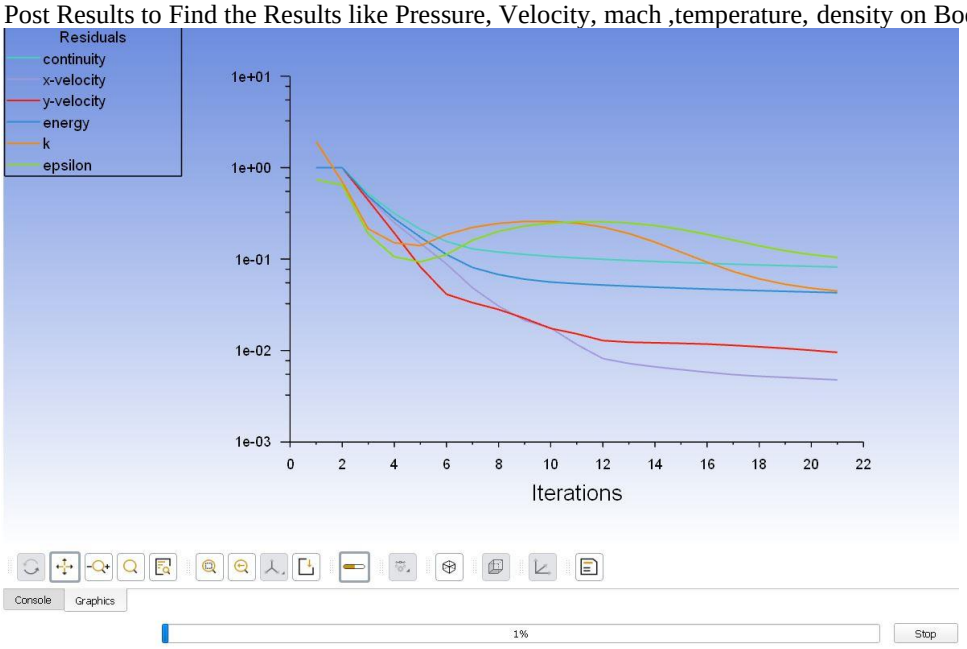

FIGURE 3. Residuals

RESULTS AND DISCUSSION

Comparison of Numerical and Hand Calculations

TABLE 2. Results Data

S. No	Parameter	Hand Calculation	Numerical
1	Exit Velocity	1923.97 m/s	1932 m/s
2	Exit Mach Number	4.750	4.57
3	Exit Temperature	444.8 K	444.125 K
4	Stagnation Density	8.90 kg/m^3	8.95 kg/m^3
5	Exit Pressure	14961 Pa (2.17 psi)	18788 Pa (2.72 psi)

By going through the above table, it is very clear the hand calculations and numerical results obtained from the flow analysis is very nearer.

Now that the mesh study has been verified, the variations of the Mach, Density, Pressure, across the X-direction and Y-direction.

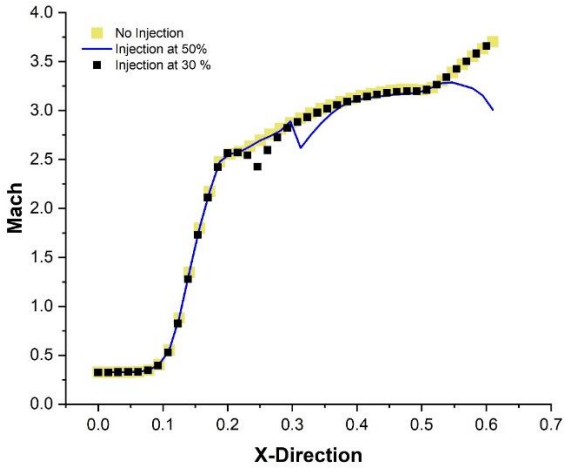

FIGURE 4. Mach along X-direction

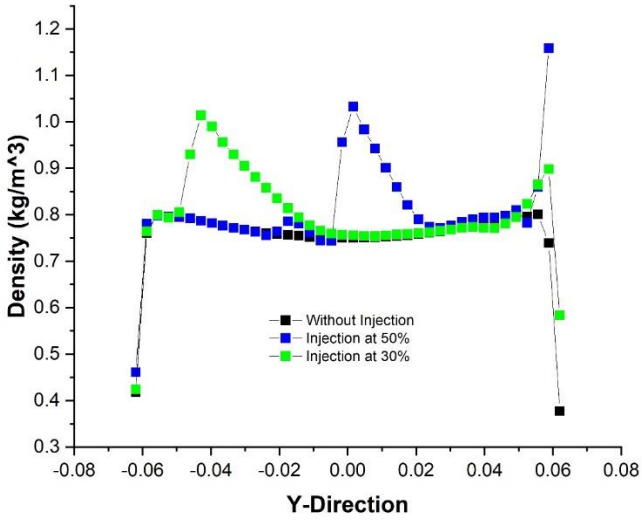

FIGURE 5. Density along Y-direction

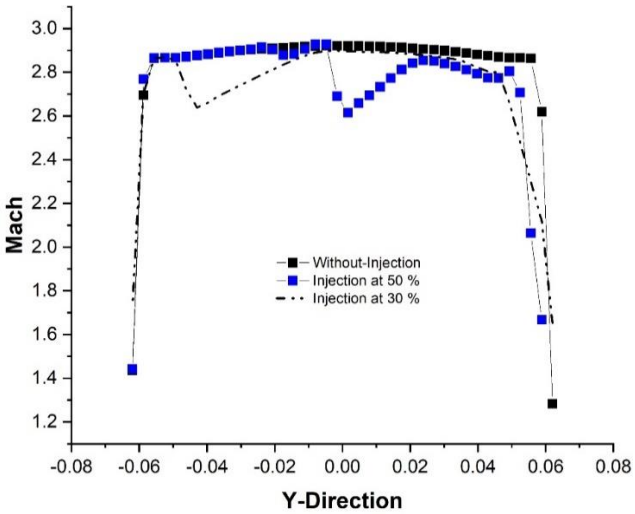

FIGURE 6. Mach along Y direction

The Mach number along Y-direction, shows that for the injection of gas at 30% of the conical nozzle, the mach reduces at the bottom section of the conical nozzle.

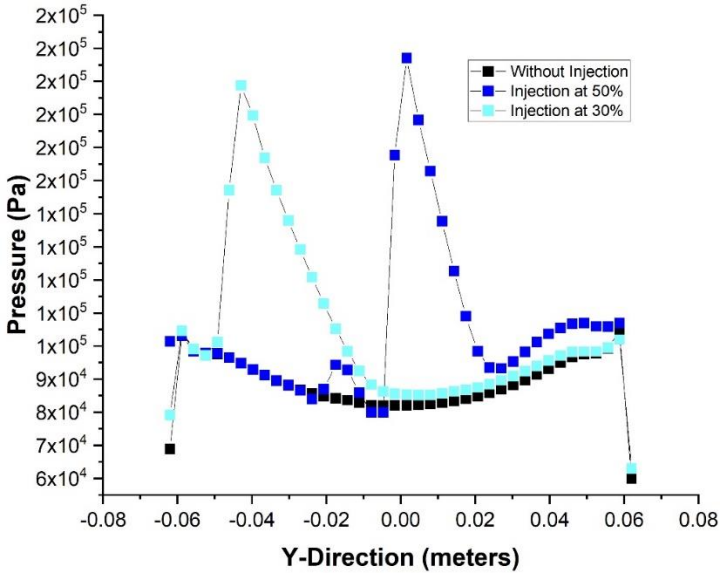

FIGURE 7. Pressure along Y-direction

The side thrust due to secondary injection can be computed by integrating the change in momentum due to the secondary injection induced asymmetry in side velocity at the nozzle exit plane. The product of integrated velocity and mass flow gives the change in momentum of the jet in the transverse direction. Similar calculations in the axial direction give the change in the axial thrust which compared to the no-injection axial thrust gives the axial thrust augmentation.

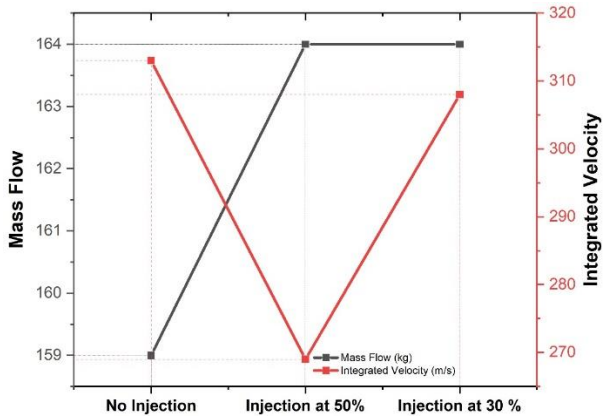

FIGURE 8. Mass flow and Integrated Velocity variation

The above graph represents the mass flow and the integrated velocity at the outlet, the mass flow for the injection case, has more mass due to the addition of the secondary flow, from the secondary inlet. Whereas the integration of the velocity at the outlet, has a variation, the integration of velocity at the injection at 50% is 270m/s.

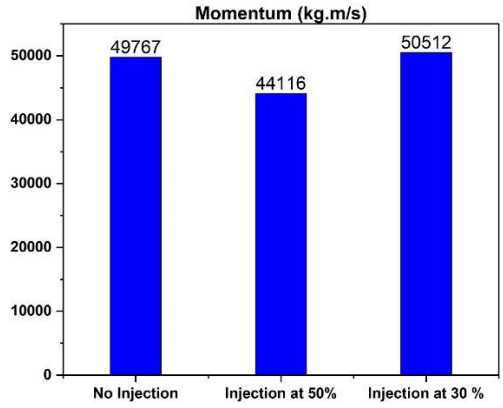

FIGURE 9. Momentum

The product of the integrated velocity and the mass flow, gives the momentum, there is a thrust augmentation in the thrust when the injection of the gas is from the 30% of the conical nozzle, the difference between the thrust is presented in the above figure.

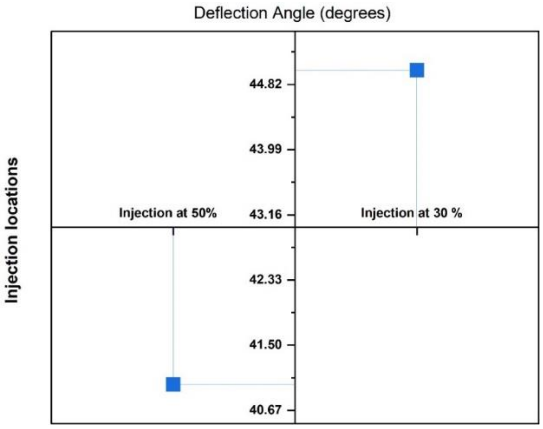

FIGURE 10. Deflection angle of the thrust

It is observed that the thrust varies at an angle of 44 degrees for the injection at 30%, which is higher in comparison with respect to the 50% injection location.

CONCLUSION

A numerical study was performed on commercial CFD software to verify its strengths and weaknesses for the rocket engine internal flow.

In order to simplify and reduce the computational effort the fuel air mixture physics where neglected, this was due to the objective of the investigation, i.e., to analyze the flow variation of the rocket engine chamber and nozzle. Thus, the air was considered as the working fluid, the air was assigned the related chamber pressure and temperature.

The rocket was assumed to be operating at the altitude of 20 km from the mean sea level. The commercial CFD solver, fluent was used for the numerical simulation. The analysis was performed on three different mesh sizes.

The simulation performed was verified for its validity with the hand calculation that involved considering various high-speed flow equations. It was clearly seen that the numerical results obtained from the simulation were matching with the hand calculated values of various parameters.

The flow variables density, pressure, Mach number were extracted at the exit of the nozzle in the Y direction and the thrust deflection due to the secondary injection was analyzed, it was observed that the 30% nozzle length position proved to augment the thrust and create a large thrust deflection angle, in comparison of the 50% injection location.

This research has helped to verify the authenticity of the code in solving the flows involving the rocket fluid study, and has also presented the variation of the temperature acting on the wall of the rocket.

REFERENCE

1. Ross, J. C., and Brauckmann, G. J., 2011, "Aerodynamic and Aeroacoustic Wind Tunnel Testing of the Orion Spacecraft," *29th AIAA Appl. Aerodyn. Conf. 2011, (June), pp. 1–19.*
2. Przybilski, O. H., 2002, "The Germans and the Development of Rocket Engines in the USSR," *JBIS - J. Br. Interplanet. Soc., 55(11–12), pp. 404–427.*
3. "Http://Www.B14643.de/Spacerockets/Specials/Russian_Rocket_engines/Engines."
4. DAS, D. K., MOORE, G. R., and BOYER, C. T., 1988, "Heat Transfer Studies on a Rocket Nozzle for Naval Application," *Nav. Eng. J., 100(1), pp. 29–35.*
5. Huang, Z. W., He, G. Q., Qin, F., Cao, D. G., Wei, X. G., and Shi, L., 2016, "Large Eddy Simulation of Combustion Characteristics in a Kerosene Fueled Rocket-Based Combined-Cycle Engine Combustor," *Acta Astronaut., 127, pp. 326–334.*
6. "Rktthsum @ Www.Grc.Nasa.Gov."
7. "Calc @ Www.Dept.Aoe.vt.Edu."
8. Noaman, H. R., Tang, H. Bin, and Khalil, E., 2019, "Numerical Simulation on the Influence of Injection Location, Injection Angle, and Divergence Half Angle on SITVC Nozzle Flow Field," *Int. J. Aerosp. Eng., 2019.*
9. A Sai Kumar, "Design of Minimum Length Supersonic Nozzle using the Method of Characteristics" in International Journal of Innovative Technology and Exploring Engineering (IJITEE) Volume-9 Issue-2, December 2019
10. Nirmith Kumar Mishra, A Sai Kumar, M Ganesh, Mohd Abdul Rehman Alam', "Design of Minimum Length Supersonic Nozzle using the Method of Characteristics", International Journal of Innovative Technology and Exploring Engineering (IJITEE) ISSN: 2278-3075, Volume-9 Issue-2, December 2019, pp 1370-1374.
11. 'Nirmith Kumar Mishra , Dr S Srinivas Prasad, Ayub Padania', "Modeling & Simulation of Rocket Nozzle" International Journal of Advanced Engineering and Global Technology ISSN No: 2309-4893 Vol-2, Issue-09,September 2014, pp 988- 995
12. 'Y D Dwivedi, B Parvathavadhani K, Nirmith Kumar Mishra', "Design of Supersonic Wind Tunnel Using Method Of Characteristics", International Journal of Futuristic Science Engineering and Technology, ISSN 2320 – 4486, Vol 1 Issue 4 April 2013, pp 250-262

RESEARCH ARTICLE | MAY 22 2023

Optimization of UAV by using tubercles wing configuration

K. Arunkumar ✉; G. Sravanthi; A. Udaya Deepika; M. Srikanth

AIP Conference Proceedings 2492, 020018 (2023)
https://doi.org/10.1063/5.0113387

Optimization of UAV by Using Tubercles Wing Configuration

K Arunkumar [1, a)], G Sravanthi [1], A Udaya Deepika[1] and M Srikanth[1]

[1] *Department of Aeronautical Engineering, MLR institute of technology, Hyderabad, India.*

[a)] Corresponding author: arunkumar.samy@mlrinstitutions.ac.in

Abstract. This paper aims to identify and explore a unified design methodology for the design of a Tubercles wing for an UAV. The majority of experiments using infinite wings have shown positive results. (2D) models and are accompanied by significant lift loss and drag increase in the pre–stall area Finite models (3D) have, On the other side, the total aerodynamic performance was enhanced (increased lift and moment, but decreased drag) Between 500,000 and 1,000,000 Reynolds number. There exists few design methodology for tubercles wing configuration. However, there is no traceable unified design methodology for a swept back wing configuration. Design methodologies from various sources were examined and the most appropriate one is chosen. Aerodynamic Model is constructed and curvature analysis is done by using CATIA V5. Aerodynamic analysis and structural analysis is simulated using Ansys software.

Keywords: UAV, Sinusoidal wing, serrated, tubercles

INTRODUCTION

Nature has long served as a source of inspiration for technical issues been an interest throughout the human history. Tubercles are one of the designs obtained from the nature. Tubercles are nothing but a sinusoidal structure with a constant wavelength which is implemented in edges of the wing. Previous Researchers have shown that incorporating leading-edge tubercles improves airfoil performance [2]. Tubercles are considered to serve as lift enhancers, allowing flow to stay linked for a wide variety of attack angles, delaying stall and increasing maximum lift coefficient with the least amount of drag. A variety of variables contribute to the improved performance of airfoils having tubercles on the leading edge. Increased boundary layer momentum exchange compartmentalization of the flow and subsequent mitigation of tip stall non-uniform separation features change in the pressure distribution over the airfoil surface and vortex lift are examples. Recent study has shown sinusoidal leading-edge (LE) serrations as an efficient passive treatment for reducing an airfoil's broadband noise when subjected to a very turbulent flow[4].This project focuses to design a Tubercles wing with various configuration using computer aided design tools and assess the curvature implementation in the design and also To determine the impact of tubercle installation on UAV wings, a thorough 3D computational research is conducted using CFD techniques that are initially validated and calibrated using experimental data from the literature. Then evaluate the structural property using structural analysis tool considering major factors. In this project, the tubercles are implemented in various parts in different cases. Such as the tubercles is implemented in leading edge in design 1 keeping the wavelength as lower and constant. In design 2, the wing is configured as swept back with an angle and tubercles is implemented in leading edge. Similarly keeping the wavelength constant in design 3 the tubercles is implemented in both leading and trailing edges. Hence, the objectives of this project are to determine the curvature analysis of the tubercles, aerodynamic analysis and structural analysis [5].

There has been an experimental analysis on sinusoidal wave which has been carried out by various authors in various period of time. The study says the serrated wing is effective only in certain Reynolds number such as 100000re

Advancements in Aeromechanical Materials for Manufacturing: ICAAMM-2021
AIP Conf. Proc. 2492, 020018-1–020018-9; https://doi.org/10.1063/5.0113387
Published by AIP Publishing. 978-0-7354-4438-6/$30.00

to 500000.It results shows as there is increase in max lift and decrease in drag, [8] It also increase the stall angle up to 6° to 7° in previous experiments And it is said that there is increase in drag at pre stall region to overcome that we are experimenting with different configurations and different set of wavelength. In other case when there is a completely change in wing structure the strength of structure is varied but there is no proof of such experiments

METHODOLGY

Geometrical design

This section deals with the creation of the geometry using CATIA V5R21.

Sinusoidal tubercles

Swanson et al. proposed a framework for modelling sinusoidal tubercles, which we used. As indicated in Figure 2, the amplitudes are 0.10c, and the wavelength is 0.210c. The airfoil coordinates are altered in the x direction without altering the y coordinates, as indicated in Equation (1) and (2). The clean wing is indicated by the subscript old, and the region of maximum thickness is indicated by the subscripts tm. The Amplitude A is used to change the chord length of the leading edge by a fraction of a chord length [7-9]. Profiles are created in Excel, and then these profiles are imported into CATIA V5R21 using macros to create the wing surface. The Amplitude A is used to reduce the length of a chord's leading edge by a fraction of its original length. To construct the wing surface, profiles are developed in Excel and then imported into CATIA V5R21 through macros [10].

Design Analysis

The designs are generated and the curvatures are asses using curvature analysis and finding out the minimum, maximum and mean value. Which shows us any present of anomalies occurred in structure?

Aerodynamic analysis

Fluent analysis is simulated using Ansys software at a certain velocity in order to find the C_L, C_D, coefficient of lift, coefficient of drag to analyze the aerodynamic efficiency [4]. From this analysis we can determine whether the design is effective or not. This is done to all the three cases and their results are obtained.

Structural analysis

Static structural analysis is simulated using Ansys software. This analysis is carried out to know whether the design is ideal or not in structural strength basis [12]. Some of parameters such as elastic strain, equivalent stress and factors of safety is considered. From this analysis we can determine whether our design can withstand the load or not. The analysis is carried to all the three cases and results are obtained.

GEOMETRICAL DESIGN

Tubercles – sinusoidal calculation

The sinusoidal tubercles have been modeled using the methodology suggested by Swanson
A amplitude of 10% is set as constant for all three designs [11].
X(New) = 15 (+_10%) for Xold > Xnew
= 13.5 , 16.5
Xold = 15
Xnew = 13.5

15 > 13.5

With a span of 900m and chord length of 150 mm and 135mm wing is constructed

Wing Design

FIGURE 1. Modeling based on Gaussian value 0.000678mm (Case 1)

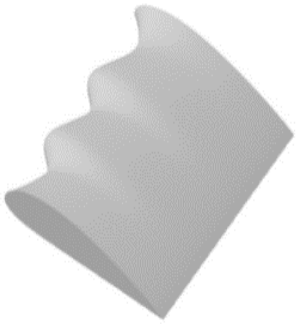

FIGURE 2. Modeling based on Gaussian value 0.000429mm (Case 2)

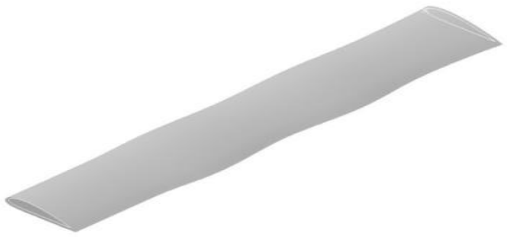

FIGURE 3. Modeling based on Gaussian value 0.00141mm (Case 3)

CURVATURE ANALYSIS

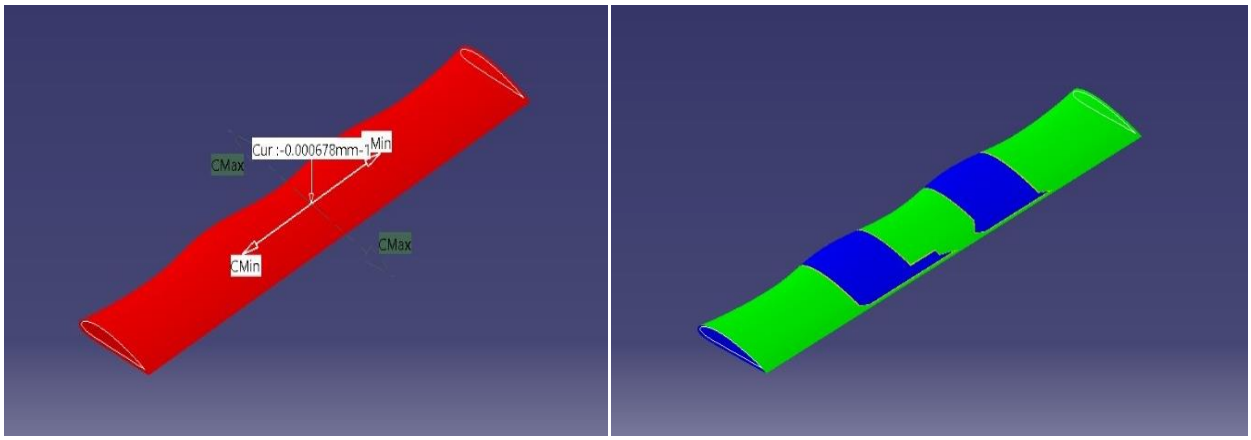

(a) (b)

FIGURE 4. (a) Case 1 Gaussian Value (b) Case 1 Inflection Area

The tangent of the point 0.333mm shows the positive point of the Gaussian curvature touches the surface at single point, where the negative tangent value 0.003mm-1 in the point of negative curvature cuts the surface

There shows no presence of anomalies in this design.

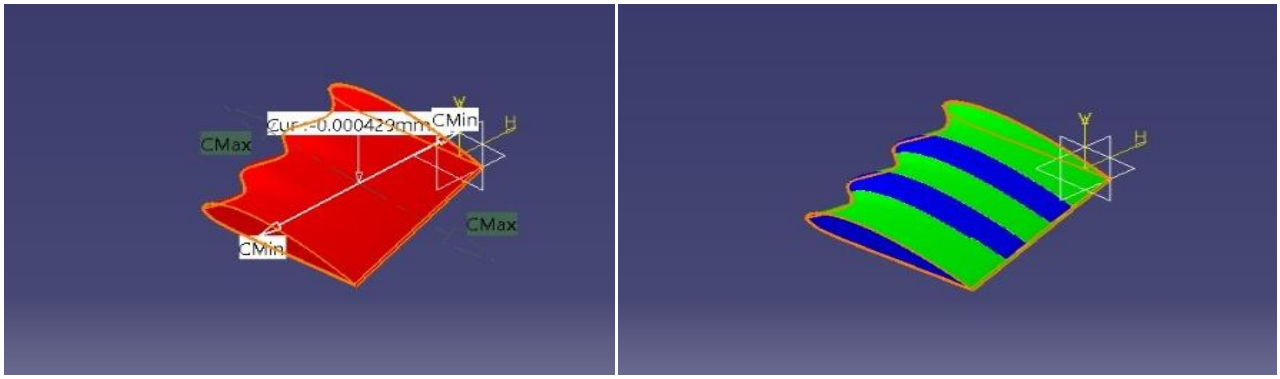

(a) (b)

FIGURE 5. (a) Case 2 Gaussian Value (b) Case 2 Inflection Area

The tangent of the point 0.041mm shows the positive point of the Gaussian curvature touches the surface at single point, where the negative tangent value 0.043mm-1 in the point of negative curvature cuts the surface

There shows no presence of anomalies in this design

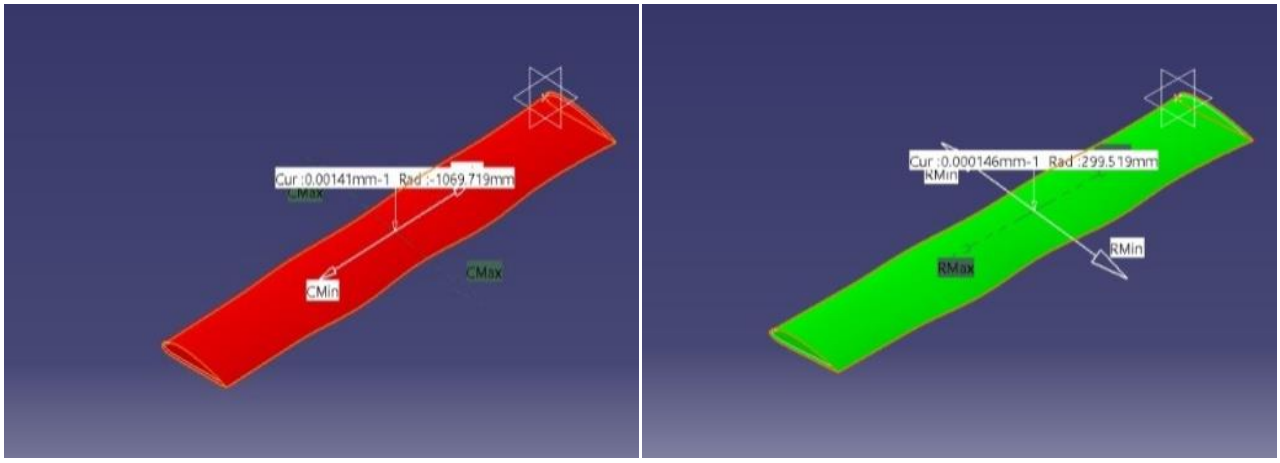

(a) (b)

FIGURE 6. (a) Case 3 Gaussian Value (b) Case 3 Inflection Area

The tangent of the point 0.041mm shows the positive point of the Gaussian curvature touches the surface at single point, where the negative tangent value 0.015mm-1 in the point of negative curvature cuts the surface.

FLUENT ANALYSIS

In fluent analysis, Angle of attack is set has 5 degree angle which was estimated earlier in airfoil comparative charts and the velocity is set to be maintained at 30m/s. For each case, different parameter such as pressure, velocity and velocity streamline has been estimated [10]. From the computational data different parameters such as lift, lift coefficient, drag and drag coefficient is estimated.

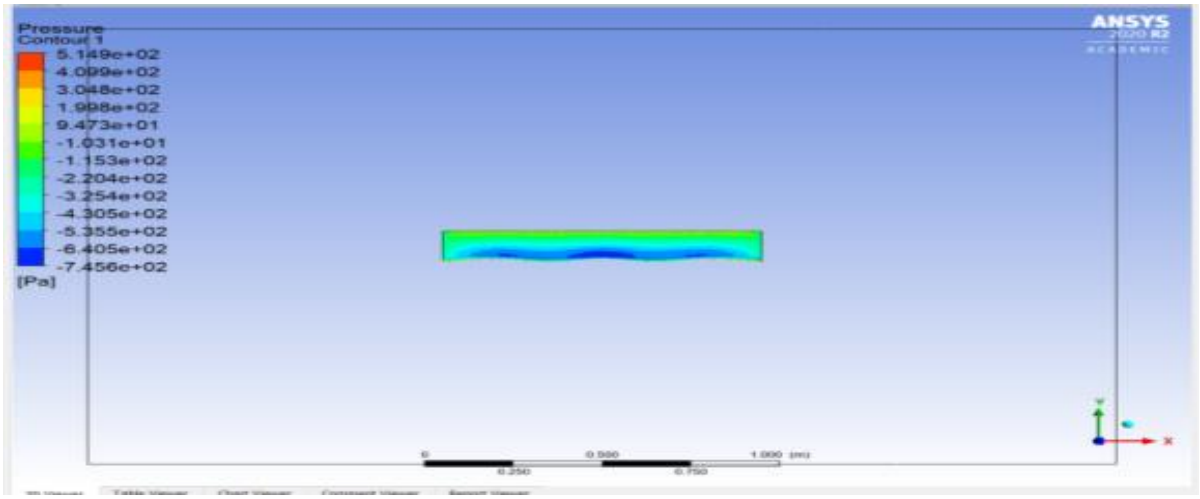

FIGURE 7. Case 1 Pressure Contour

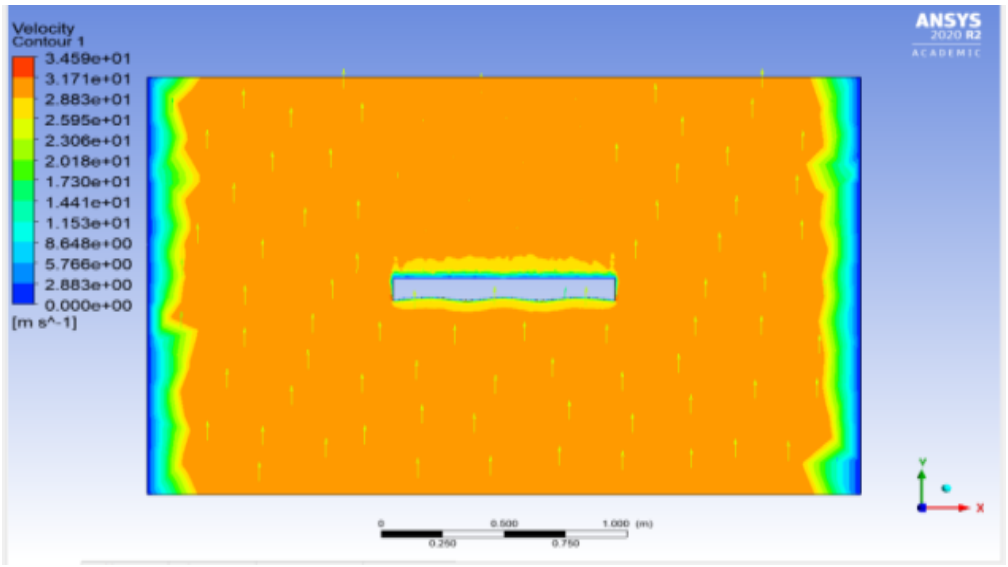

FIGURE 8. Case 1 Velocity Contour

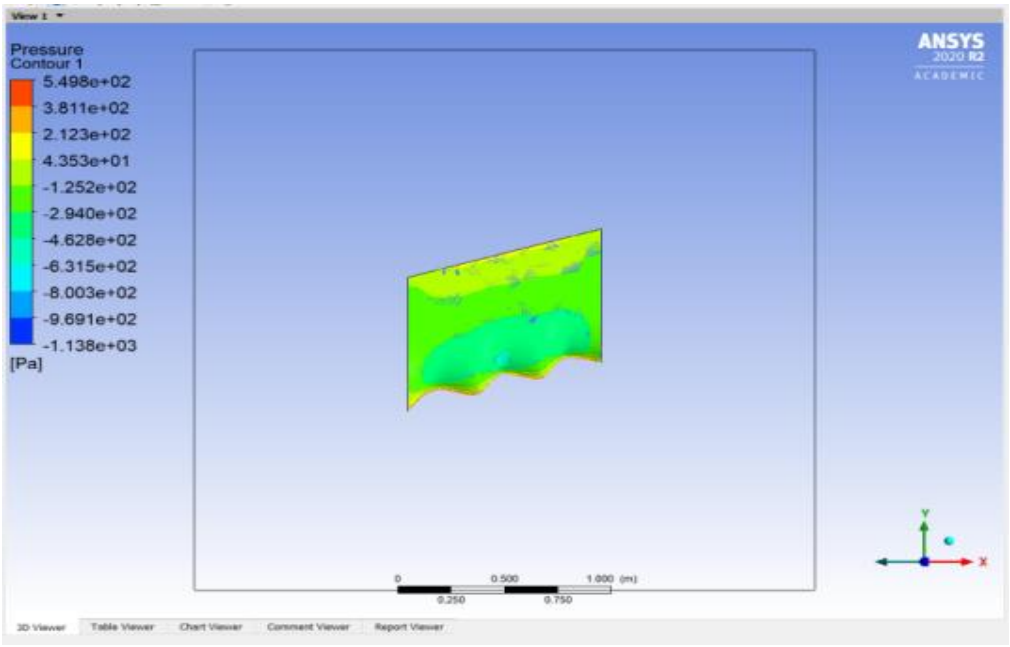

FIGURE 9. Case 2 Pressure Contour

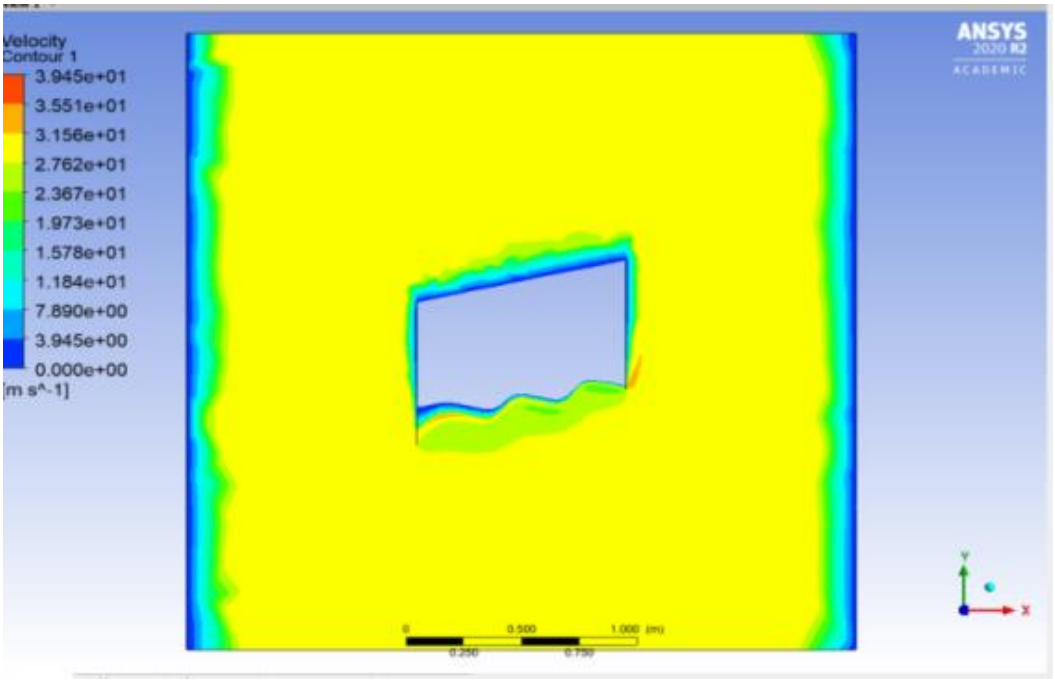

FIGURE 10. Case 2 Velocity Contour

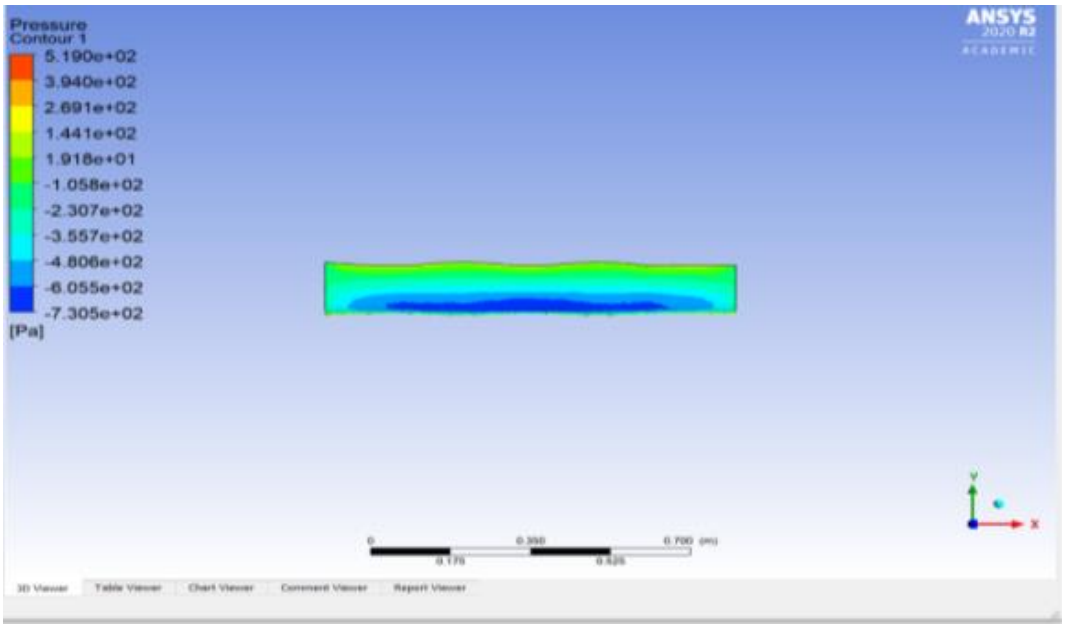

FIGURE 11. Case 3 Pressure Contour

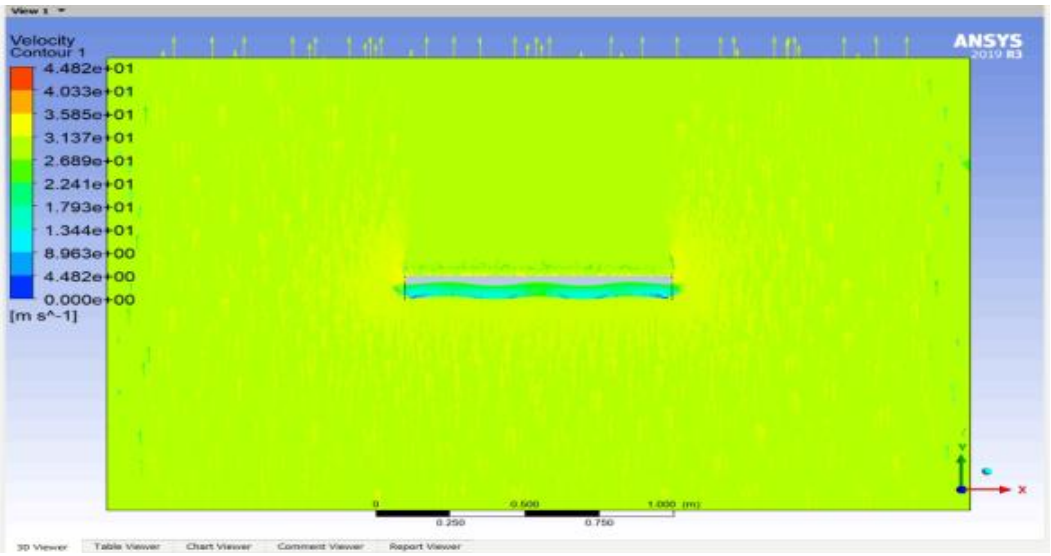

FIGURE 12. Case 3 Velocity Contour

RESULTS

The above pressure and velocity contour are examined to validate the simulation results. At angle of attack 5, a higher velocity profile which corresponds to low pressure region is expected on the top surface of wing and vice versa for the bottom part in all the three cases. The velocity contour determines the discharge of the stream and the velocity streamline flow shows the separation of airflows [1]. There is a present of Vortex a wing tip case 2 comparing the computational data from various cases with the usual wing we can see that there is increase in Lift and decreases in drag.

TABLE 1. Comparison of different cases with conventional wing

PARAMETERS	NORMAL WING	CASE 1	CASE 2	CASE 3
LIFT	52.59	54.903206	129.37034	54.457921
CO OF LIFT	0.095	0.084	0.0211	0.084
DRAG	3.2786	3.3748776	15.955468	3.3572077
CO OF DRAG	0.004	0.00456	0.026	0.00548

CONCLUSION

Design is a fine blend of science, creativity, presence of mind, and the application of each one of them at the appropriate time. The design of anything needs experience and optimistic progress towards the ideal system. The scientific society always looks for the best product design. From the above various simulations such as curvature and surface analysis,

Fluent analysis is evident that sinusoidal wave has shown increase in lift in all the cases. In case 2, it has shown vortex formation in wing tip region which question the structural strength again. Overall comparing the fluent data, there is been a 3% improvement in case 1 and case 3 where as in case 2, there is a 2% of improvement. This can also be increased with an attachment of winglet. Considering curvature results the curvature test proves that there is no anomalies present in the structure.

REFERENCE

1. Charalampos Papadopoulos1,*, Vasilis Katsiadramis2, and Kyros Yakinthos1,2 Numerical 3D study on the influence of span wise distribution of tubercles on wings for UAV applications https://doi.org/10.1051/matecconf/201930402014
2. David S. Miklosovic∗ and Mark M. Murray† U.S. Naval Academy, Annapolis, Maryland 21402-5042 and Laurens E. Howle‡ Duke University, Durham, North Carolina 27708-0300 Experimental Evaluation of Sinusoidal Leading Edges DOI: 10.2514/1.30303 *JOURNAL OF AIRCRAFT* Vol. 44, No. 4, July–August 2007
3. B Venkata Sai Anoop, TV Vineeta, A Sai Kumar, VVS Nikhil Bharadwaj on "Conceptual Design of Hybrid UAV" in *International Journal of Engineering Research Technology* (IJERT) Volume 4 Issue 12, Dec 2015.
4. AA Mehraban1, MH Djavareshkian1 , Y Sayegh1,B Forouzi Feshalami1 , Y Azargoon1, AH Zaree1 and M Hassanalian2 Effects of smart flap on aerodynamic performance of sinusoidal leading-edge wings at low Reynolds numbers DOI: 10.1177/0954410020946903: 23 February 2020; accepted: 9 July 2020
5. Till M. Biedermann 1,* , Pasquale Czeckay 1, Nils Hintzen 1, Frank Kameier 1 and C. O. Paschereit 2 Applicability of Aeroacoustic Scaling Laws of Leading Edge Serrations for Rotating Applications doi:10.3390/acoustics2030030 19 June 2020; Accepted: 21 July 2020; Published: 23 July 2020
6. Mohamad Shorbagy1, Basman El-hadidi2, Gamal El-Bayoumi3, Osama Said4 and Moatasem Fouda5 Experimental Study on Bio-Inspired Wings With Tubercles DOI: 10.2514/6.2019-0848 January 2019 January 2019
7. S.M.A.Aftab, M.F.Abas, K.A.Ahmad*, A.S.Mohd Rafie and N.B.A.Razak Comparative study of Spherical and Sinusoidal Tubercle Leading Edge Modification on NACA 4415 Wing https://www.researchgate.net/publication/319135829 November 2014
8. S. M. A. Aftab1, K. A. Ahmad1,2 CFD study on NACA 4415 airfoil implementing spherical and sinusoidal Tubercle Leading Edge https://doi.org/10.1371/journal. pone.0183456
9. S.M.A.Aftab, M.F.Abas, K.A.Ahmad*, A.S.Mohd Rafie and N.B.A.Razak Comparative study of Spherical and Sinusoidal Tubercle Leading Edge Modification on NACA 4415 Wing https://www.researchgate.net/publication/319135829 November 2014
10. K.L. Hansen, R.M. Kelso, B.B. Dally, E.R. Hassan Analysis of the Stream wise Vortices Generated Between Leading Edge Tubercles https://www.researchgate.net/publication/258246709 December 2011
11. Gianluca Cappanera*, Valerio D'Alessandro, Luca Giammichele, Renato Ricci Acoustic Investigation of Aerodynamic Appendages for Wind Turbine Blades: Fluid-dynamic Tests https://doi.org/10.18280/ti-ijes.632-431 18 April 2019 44
12. Wei Zhaoyu1, New T. H.1, *, Cui Y. D.2 Vortex Structure Analysis of Aerofoil with Leading-edge Tubercles by Proper Orthogonal Decomposition Technique https://www.researchgate.net/publication/284458681 November 2015

RESEARCH ARTICLE | MAY 22 2023

Modeling and structural analysis of two stage gear box with different materials

A. Udaya Deepika ✉; Kasireddy Vamshi; Kalasani Navya; P. Deepika; Swagat Sarbottam Sahoo; A. Aruna Kumari; E. Lakshmi Nagesh

AIP Conference Proceedings 2492, 020081 (2023)
https://doi.org/10.1063/5.0117120

Modeling and Structural Analysis of Two Stage Gear Box with Different Materials

A Udaya Deepika[1,a)], Kasireddy Vamshi[1], Kalasani Navya[1], P.Deepika[1], Swagat Sarbottam Sahoo[1], Dr.A Aruna Kumari[2], Dr E Lakshmi Nagesh[3]

[1] *Department of Aeronautical Engineering, MLR Institute of Technology, Hyderabad, Telangana, India*
[2]*Department of Mechanical Engineering, JNTUH, Hyderabad, India*
[3]*Department of Mechanical Engineering, Netaji Institute of Engineering and technology, Hyderabad, India*

[a)] Corresponding author: udeepika.aero4825@gmail.com

Abstract: An all-terrain car is an off-road vehicle which can travel without any problems on any terrain. These vehicles support some kind of extreme loads while off-road travel. All-terrain cars are equipped with wide tyres with grooves for greater stability on slippery terrain and good ground clearance to prevent obstacles. These cars are designed to also be stronger and longer lasting than commercial vehicles. In Deserts, these cars are widely used. Design of gears, shafts, gearbox cassettes, bearing collection, engine vibration and engine design. The gearbox is coupled to a Continuously-Variable Transmission which is powered by a 7.5KW- four-stroke gasoline engine. The first stage includes parameters calculations to obtain dimensions of the gearbox and its components. The second stage involves design modeling of the components in CATIA V5R21. In next stage, Finite-Element analysis is performed to validate the design in ANSYS 14.5. The final stage involves testing of the gearbox on diverse and harsh terrains. The volume of the all gears and shafts calculated with the classical method is 99.3788 cu.in, while the optimal design solution offers a smaller volume, equal to 67.069 cu.in. i.e. a 32.503% reduction.

Key words. All Terrain Vehicle, Reduction, Computer Aided Design (CAD) Computational Fluid Dynamics(CFD), Finite Element Analysis (FEA).

INTRODUCTION

An electricity supply and power transmission system consist of a machine that provides regulated power application. As an assembling of components, Merriam-Webster describes transmission including the gears and propeller shaft, which transfer power from an engine. The word transmission in British English references to the whole train including the jam, gearbox, prop shaft, differential and end shaft drives.

FIGURE. 1 Gear Box

Advancements in Aeromechanical Materials for Manufacturing: ICAAMM-2021
AIP Conf. Proc. 2492, 020081-1–020081-9; https://doi.org/10.1063/5.0117120
Published by AIP Publishing. 978-0-7354-4438-6/$30.00

In American English, moreover, it is distinct that a trigger is any mechanism that transforms speed and torque, while a transmission is a form of transmission which can "adjust" to shift the speed torque ratio in a dynamic way, for example in a car. The dynamic of a car differs by speed: the inertia of the vehicle's large mass at low speeds, while a wind resistance is dominant at cruise or high speeds.

Usually, cars had 3-speed transmissions by mid-1970s. The equipment is normal. In the 1950s four-speed units started to appear in volume versions and were common and in 1960s; some of the exotics had five-speed models. In the 1970s, with gasoline prices rising and fuel economy being a significant marketing point, over-driven 4th or 5-speed transmissions became available in mass-market vehicles and also in small, Toyota-pioneered pick-up lorries (who advertised the fact by giving each model the suffix SR5 as it acquired the fifth speed). In the early 1990s, 6-speed transmissions in high-performance automobiles began to appear. [1-12] Mass market cars, including small pick-up trucks, pioneered by Toyota, offered 4-speed overdrive 4th gear or 5-speed transmission (who advertised the fact by giving each model the suffix SR5 as it acquired the fifth speed). [3] In high-performances cars in the early 1990s, 6-speed transmissions began to appear. Today, almost every manual automotive mass market transmission has a 5-speed capacity. [quote necessary] Porsche has just revealed that a 7-speed manual gearbox would come for the next generation 911, first of its sort for an average car with the first 6 gear ratios identical to that of the 6-speed gear box and a higher 7th gear. For electric cars (EV's), gearboxes have been commonly anticipated. [4-6].

METHODOLOGY

Gear Ratios

For most automobile applications, the slightly slower gear (assigned '1' of low gear) permit 3 to 4 engine revolutions each (3:1). "High" manual transmission in three or four speeds lets the output shaft turn at the very same speed as engine (1:1). The motor turns less than a complete turn with each shaft revolution and 5 and 6 speeds are sometimes 'overdriven' (0.8:1, for example).[7-9]

External Overdrive

In the fifties, sixty years, and seventies, low engine fuel-efficient highway cruising was often allowed by means of either a separate overdrive module in or behind the rear gearbox on cars with 3- or 4-speed transmissions. It was either enabled by pushing a switch on the gearstick button or the steering column manually when in high gear, or by raising the foot instantly from the speed-up while the car was driving above a certain speed.[10] By means of a flooring accelerator, automatic overdrives were disconnected and a Lockout Control was given to allow the driver to disable the overdrive and run the transmission as normal transmission (non-over shooting) [11].

Gear Patterns

The whole line horizontal is neutral, but it is normally spring loaded so that if it is not shifted to another gear, it would return to a centre of the N spot.

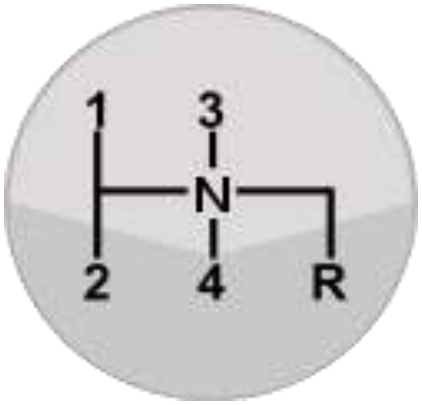

FIGURE 2. Shaft

TABLE.1 Material specification

Materials and Dimensions	
Materials	Cast iron
Cross section	180x81

Gear assembly

The gear box is basic and precise, manufactured by various operations In order to assemble gears for transmission in field vehicles, it is essential.

FIGURE.3 Transmission Box Assembly

WORKING PROCESS

Because once they mesh with an adjacent gear, the teeth of a gear can be regarded as levers. So instead rocking back and forth about short distances, the gears can however be rotated constantly as is normal for the lever. [7-8]. The number and diameter of a gear is determined by its teeth. The equipment linked to the power supply is called that driver and the equipment that the driver uses is the powered equipment. It is always rotating in the opposite direction to that of the engine; since both gears have same number of letters, they spin at the same rpm. However, if the teeth are different the gear will spin quicker with the lesser r number of teeth. Both equipment teeth which have to be correctly mated for work contact must be the same in size and form. FIGURE 2 reveals two gears, one on end of shaft A, with 15 teeth and the other at the end to shaft B, with 30 teeth attached. That 15 teeth of a smaller gear A will map 15 teeth with the greater gear B, but the gear A will allow just the 1/2 revolution of gear B.

COMPONENT AND ASSEMBLY

A roller is made or built around its circumference with even-sized, spaced teeth. In revolving machines, gears are used for transmitting not only movement from one stage to the next, but for the mechanical benefit they provide. A gear train is called two or three gears transferring movement of one shaft to the next and a gear is a series of meshing wheels or cylinders. Gearing is mostly used to convey moving motion and can even be adapted to rotating motion & vice versa. Mechanical components are flexible and can perform various types of power transfer or motion modulation. These are examples,

Gear

An equipment is a circle with a, spaced mesh of teeth. Its materials are highly robust and tuffy, and withstand various forms of loads when meshed.

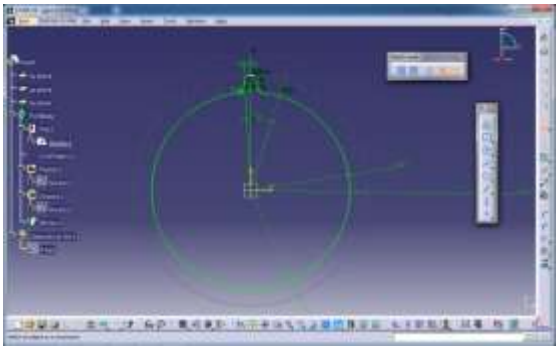

FIGURE.4 Circle

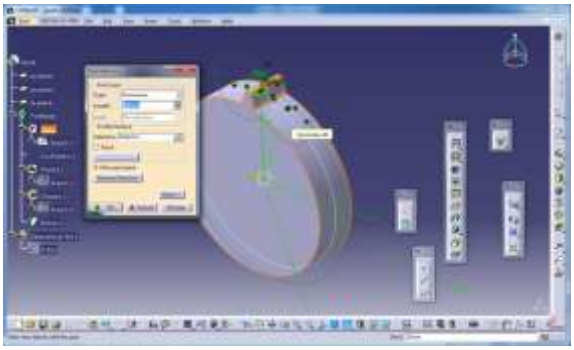

FIGURE .5 Padding Circles

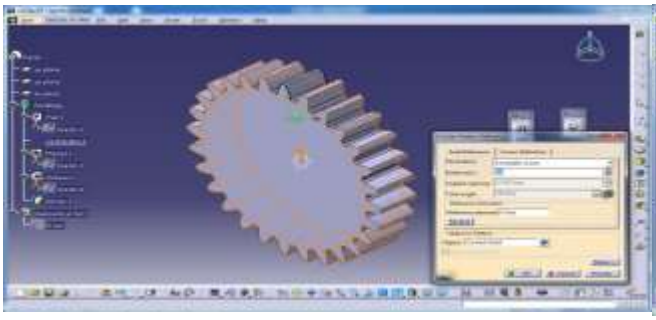

FIGURE.6 Moving circles

FIGURE.7 Gear-1

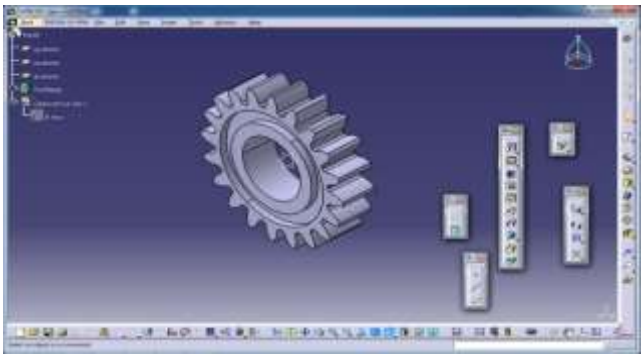

FIGURE.8 Gear-2

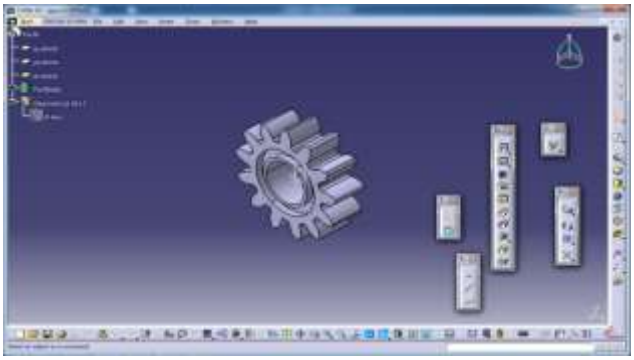

FIGURE.9 Gear-3

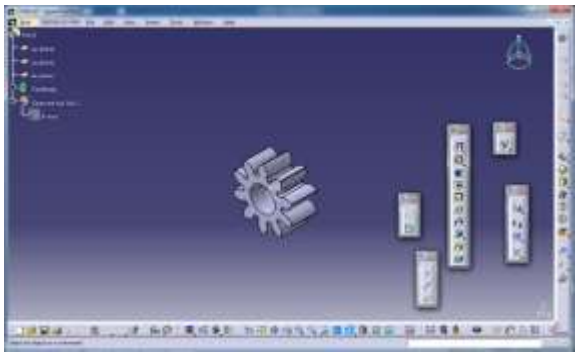

FIGURE.10 Gear-4

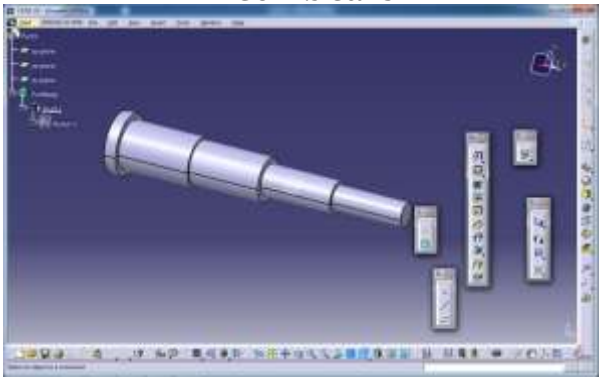

FIGURE.11 Shaft

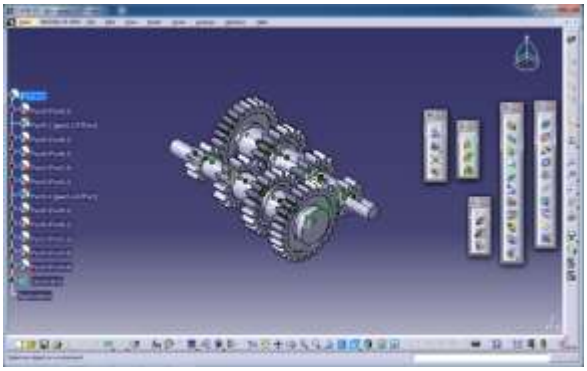

FIGURE.12 Assembly of 2 step gear box

FINETE ELEMENT ANALYSIS

A computational means of solving engineering and statistical mechanics problems was its Finite Element analysis (FEA). Useful for problem areas where analytical solutions are impossible for complex geometries, loading and material properties. The Purpose of FEA to solve the Analytical Solution like Stress analysis is performed on the basis of dramatic simplification and idealization for trusses, beams and other basic structures,

Concentration of mass to the centre of gravity, Simplified as a segment of line (same cross-section). Design focused on idealized structure estimation outcomes and an extensive protection factor (1.5-3), based on practice. The geometry of the design is much more complicated and the requirements for accuracy are much greater. To grasp a complex object's physical behaviors (strength, heat transfer capability, fluid flow, etc.)

Prediction of design results and conduct to measure the protection margin and correct identification of design weaknesses and trust to determine the optimum design.

CALCULATION & RESULT

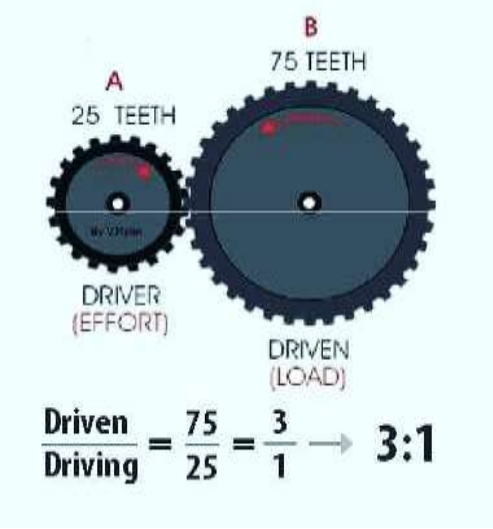

FIGURE.13 Gear Box Result

Take into account,
GR= Numbers of teeth on the drive wheels B/ Number in teeth A
VR = Running equipment speed A/speed driven equipment B

MA = Charging/Exercising

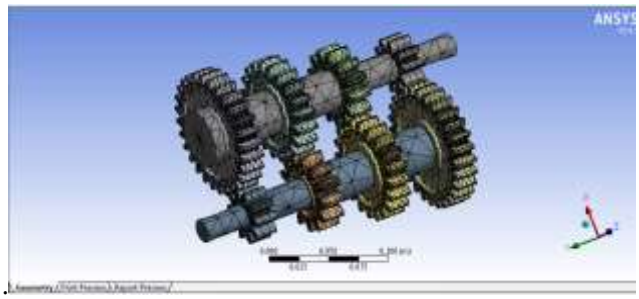

FIGURE.14 Mesh

Steel Moment Structural 100Nm.

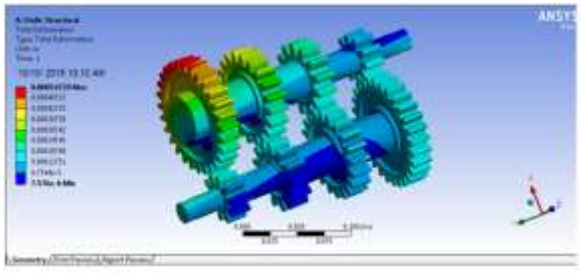

FIGURE. 15 deformations max

The **FIGURE**.15. shows that the maximum deformation is 0.046mm in the bull gear, the red radii on the gear teeth shows that the contact tooth got bent and as a result the gear took a small angular displacement.

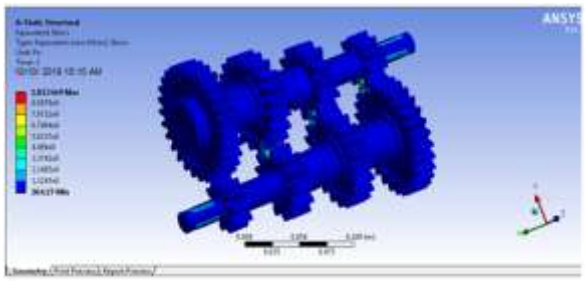

FIGURE.16 Stress150Nm Counterpart

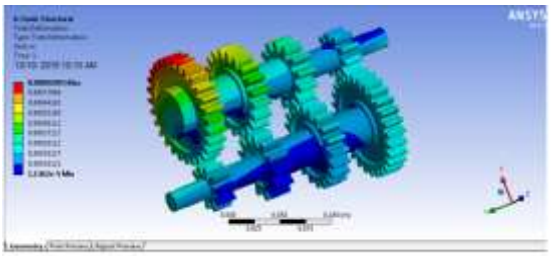

FIGURE.17 Total Distortion

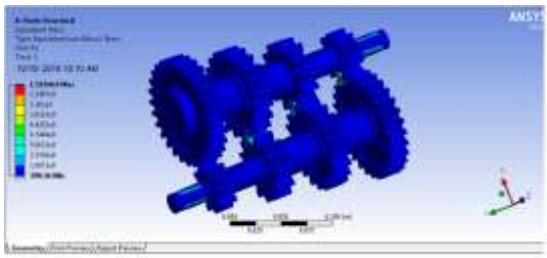

FIGURE. 18 Strength200Nm Equivalent

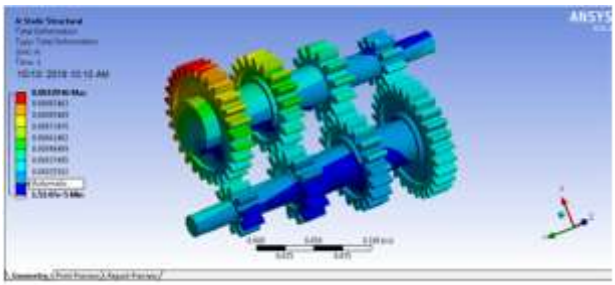

FIGURE. 19 Complete Deformation

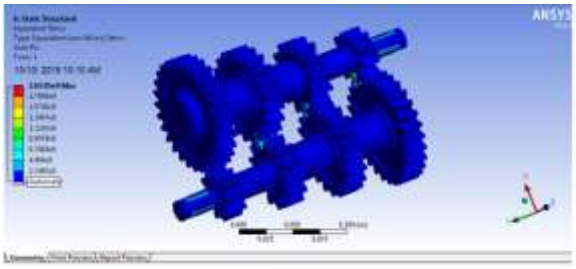

FIGURE.20 Stress Equal

ALLUMINIUM 100Nm

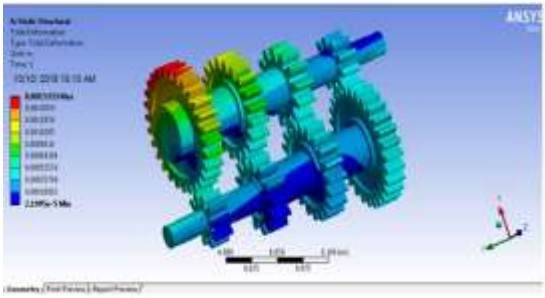

FIGURE. 21 totally deformed

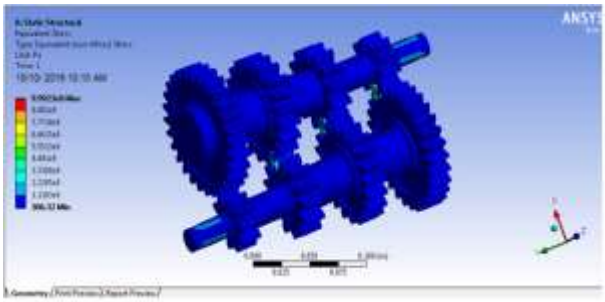

FIGURE.22 Stress150Nm equivalent 19

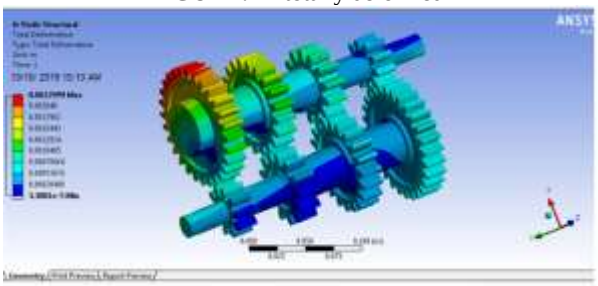

FIGURE. 23 Complete Training

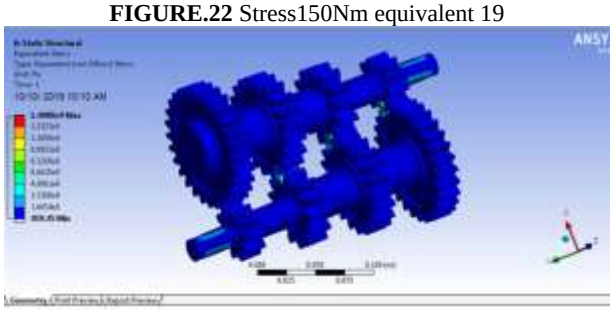

FIGURE. 24 stress counterpart 200Nm

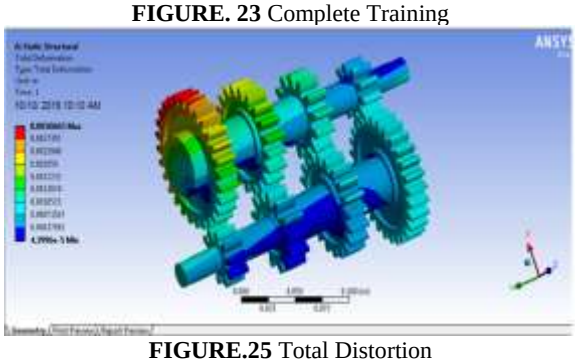

FIGURE.25 Total Distortion

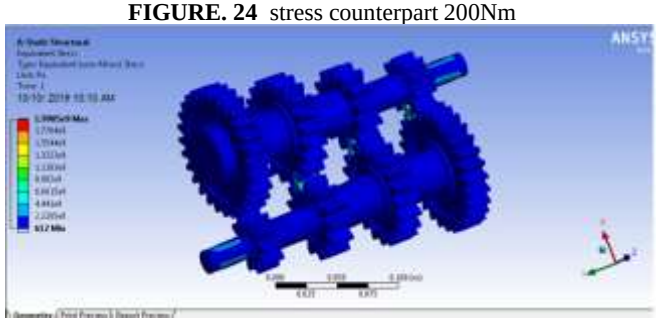

FIGURE.26 Stress Equal

Gray cast iron100Nm

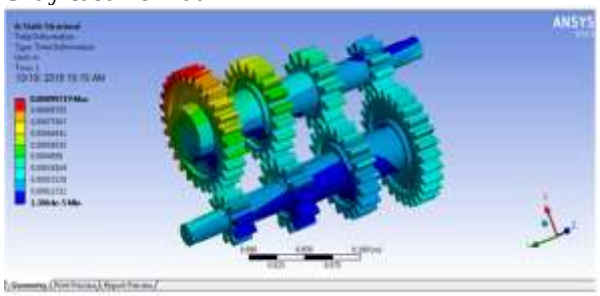

FIGURE.27 Total Distortion

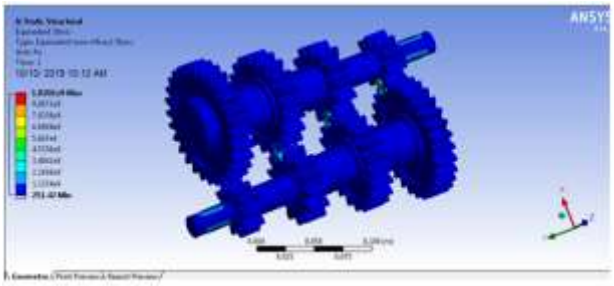

FIGURE.28 Stress150Nm Counterpart

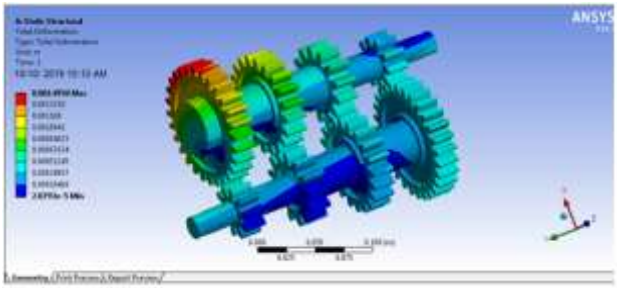

FIGURE.29 Total Distortion

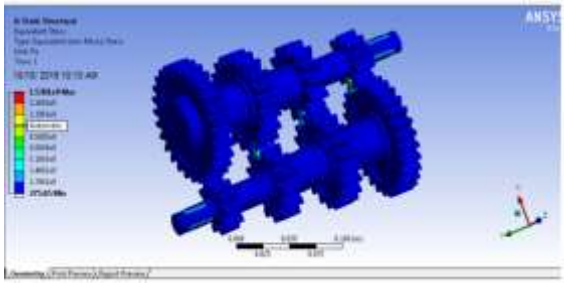

FIGURE.30 Equivalent Stress

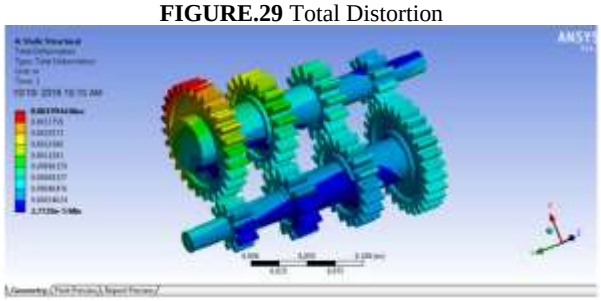

FIGURE.31 Total Distortion

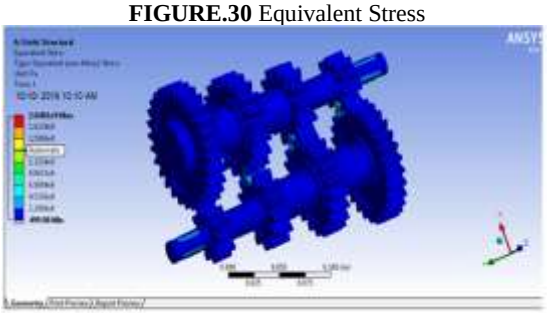

FIGURE. 32 Stress Counter Part

The best material in comparison to steel and aluminum is grey cast iron. When we equate the overall deformations and stresses with all diagrammes, it is fine for cast iron, and even for a body that keeps the lubrication mechanism down.

CONCLUSION

The pressure analysis of its gearbox was performed and pressures also on gear tooth were found to be below the allowed/safe level. The structural analysis was again performed and findings were found well within an acceptable/safe range after a change in the configure ration of the original gearbox. The tension inducing on the gear tooth was considerably minimized by producing the good material of various loads of grey cast iron. The finite element method is best suitable for evaluating and verifying the design. It bridges the gap between design and manufacturing thereby reducing costs and provides an optimum solution. The performance of the gearbox was tested at real time running conditions parameters. The acceleration timings were measured using Arduino-based Data Acquisition System.

The topology optimization has significantly contributed in reducing the overall weight of the vehicle thereby improving the acceleration by 15%. In the first stage dimensions are obtained by calculating the dimensions of the gearbox and its components. In the second stage through CATIA V5R21 design and modeling components created. In next stage, FEM Analysis is performed and validate the design in ANSYS 14.5. The final stage involves testing of the gearbox on diverse and harsh terrains. The volume of the all gears and shafts calculated with the classical method is 99.3788 cu.in, while the optimal design solution offers a smaller volume, equal to 68.069 cu.in. i.e. a 31.503% reduction. The results depict that the value of maximum value of von misses is 652.4 MPa and minimum value of von misses stress is 0.00078 MPa. In the frame it is found that the maximum deformation in the plate is 0.4852 mm. The maximum stress and deformation are occurring near inner side extrusion of the gearbox casing and this can be minimized by providing

more fillet radius. Different modification was tried and the best feasible modification is suggested to shift the natural frequencies of the gearbox casing. The gearbox casing natural frequency 281.93 Hz is shifted to 361.39 Hz by giving external stiffness. Modification Details as follows

- 2 rods of diameter 150 mm & length 1875 mm with 2 nuts of diameter 150 mm and thickness of the each nut is 100 mm fitted in two sides of the casing (attached near to the base)
- 2 rods of diameter 100 mm & length 1875mm welded in two sides of the casing (attached near to the top) As a result of this modification the stiffness of the gear box casing is increased and the natural frequency is shifted away from the resonance band.

REFERENCE

1. N. Godwin Raja Ebenezer, S. Ramabalan & S. Navaneetha santha kumar, *Design optimisation of mating helical gears with profile shift using nature inspired algorithms* (Australian Journal of Mechanical Engineering, 13 May 2020), Pg No:2204-2253
2. N. Godwin Raja Ebenezer, S. Ramabalan, S. Navaneetha santha kumar, *Practical Optimal Design on Two Stage Spur Gears Train Using Nature Inspired Algorithms*, International Journal of Engineering and Advanced Technology (IJEAT) ISSN: 2249 – 8958, Volume-8 Issue-6, August 2019.
3. Ajay Narayankutty , *A review of design and analysis of a 3-stage planetary gearbox*, IJARIIE-ISSN(O)-2395-4396, Vol-2 Issue-3 2016.
4. Praful Kamdi, Akshay Ajmera, Nayan Baheti, Vishwadeep Bhosale, Prof.D.S Choudhari, *Design & Fabrication of Two Stage Reduction Gearbox in All Terrain Vehicles* , 2017 IJRTI | Volume 2, Issue 6, ISSN: 2456-3315
5. V.RamamurtiP.GautamA.Kothari, *Computer-aided design of a two-stage gearbox, Author links open overlay panel,*Advances in Engineering Software, Volume 28, Issue 1, January 1997, Pages 73-82
6. L.Karikalan , K.Mathan , K.Devanand , S.Vijay, *Design and Analysis of Two Stage Reduction Gearbox for All Terrain Vehicles*, International Research Journal of Engineering and Technology (IRJET), Volume: 07 Issue: 05, May 2020
7. L.Karikalan, K.Mathan, , K.Devanand, , S.Vijay, *Design and Analysis of Two Stage Reduction Gearbox for All Terrain Vehicles*, International Journal of Advance Engineering and Research Development, Volume 5, Issue 03, March -2018.
8. A.Y.V. Gopi krishna, R.V. Kiran,*Design and analysis of a two stage reduction gearbox*, International Research Journal of Engineering and Technology (IRJET), Volume: 06 Issue: 12 | Dec 2019
9. Subbaratnam, B., Ramana Reddy, D.V, A Udaya Deepika, Seshagiri Rao, G.V.R, *Dynamic stability analysis of structural members*, International Journal of Mechanical Engineering and Technology (IJMET) Volume 8, Issue 8, August 2017, pp. 892–899.
10. N Madhavi, B Niharika M Satyanarayana Gupta "*Evaluation of ply orientation on failure of Kevlar Epoxy149*" IJCIET, ISSN Print: 0976-6308 and ISSN Online: 0976-6316, Volume 8, May2017
11. Dr. M Satyanarayana Gupta Ms. N. Madhavi, Balaji.S," *Design and Fabrication of Composite Drill and Trim Jig for I/R Holes of Tip Assembly Door*", ijmetmr, ISSN No:2348-4845, Volume 3, Nov2016
12. Babitha Kodavanla,Dr. A. Barai,A. B. S. Dadapeer, Mery Threza,P. Hanuma, and N. Madhavi, "Improvement Of Damping Properties Of Structural Member Using Soft Material At Support", International Journal of Engineering & Technology, Vol. 7, Issue 3,May 2018pp.1216-1219 (ISSN: 2227-524

,

RESEARCH ARTICLE | MAY 22 2023

Fabrication and testing of composite materials

N. Madhavi ✉; G. Ramya Sree; S. Venkata Rami Reddy; T. Praveen Kumar; K. Naga Venkata Satyanarayana

AIP Conference Proceedings 2492, 040001 (2023)
https://doi.org/10.1063/5.0116513

Fabrication and Testing of Composite materials

N. Madhavi[1,a)], G Ramya Sree[1], S Venkata Rami reddy[1], T Praveen Kumar[1], K Naga Venkata Satyanarayana[1]

[1]*Department of Aeronautical Engineering, MLR Institute of Technology, Hyderabad, India*

[a)] Corresponding author: madhunagireddy@mlrinstitutions.ac.in

Abstract: Now a days technology is playing important role in every aspect. In the world of composites, structural proficiency and effectiveness has more importance. Composite materials are very strong and lightweight. The growth of composite applications is increasing in every field. Applications of composite materials have high demand in the areas of aeronautical, aerospace, automobile, medical, civil construction, electronic, submarine industries etc., In this paper the composite materials in the orientation [0/90] fabrication and testing had done to obtain the results. Result shows the strength of composite materials (Jute & E – Glass fiber) for different ply layups. The properties of this composite plates are compared and determined experimentally according to ASTM standards (ASTM D7264) using UTM machine (UNITEK 94100). In this paper hand layup fabrication method are used for fabricating laminates.

Keywords: Composite materials - E-Glass fiber & Natural Fiber (Jute), Epoxy resin, Hardener, Properties of composites.

INTRODUCTION

In the present era usage of composites has been increased and also increasing but, composites are our old tradition because our ancestors are already well known about the composites. Composites were used for different parts of aircraft. Composite materials are far better than the other materials in every aspect. There are different and various composite materials are found compare to past. Not only composite materials are most influence and prominent materials but also there are some other materials like clay materials, metals etc., Composites are having great contribution in resulting the good strength for a product. The composites are becoming part of our life and also providing a great scope for future research and utilizing of them. These materials offering a platform for scholars, youngsters and many others to make a use of it, by discovering various materials with its enormous properties.

The general definition of a composite is binding of different materials as one material, for this process there should be more than one material (same or different materials are used). The composite material is a composition or mixture materials with uncommon properties (physical & chemical), these materials are insoluble in one another. The composite materials will be running with important characters – matrix & reinforcement, matrix will support to pass on or transfer the loads throughout the laminate or reinforcement and gives stability. Reinforcement will provide good strength and stiffness to the material. These composites have additional properties which are anti – corrosive and insulating materials, thermal resistance etc., The composites have enormous properties and the composites having versatile applications[1-2].

There are various advantages by using the composite materials, they have enormous properties where the material can withstand at any situation. There are different types of composites based on their categories. Primary composite materials are based on matrix and secondary composite materials are based on reinforcement[3-7].

Advancements in Aeromechanical Materials for Manufacturing: ICAAMM-2021
AIP Conf. Proc. 2492, 040001-1–040001-7; https://doi.org/10.1063/5.0116513
Published by AIP Publishing. 978-0-7354-4438-6/$30.00

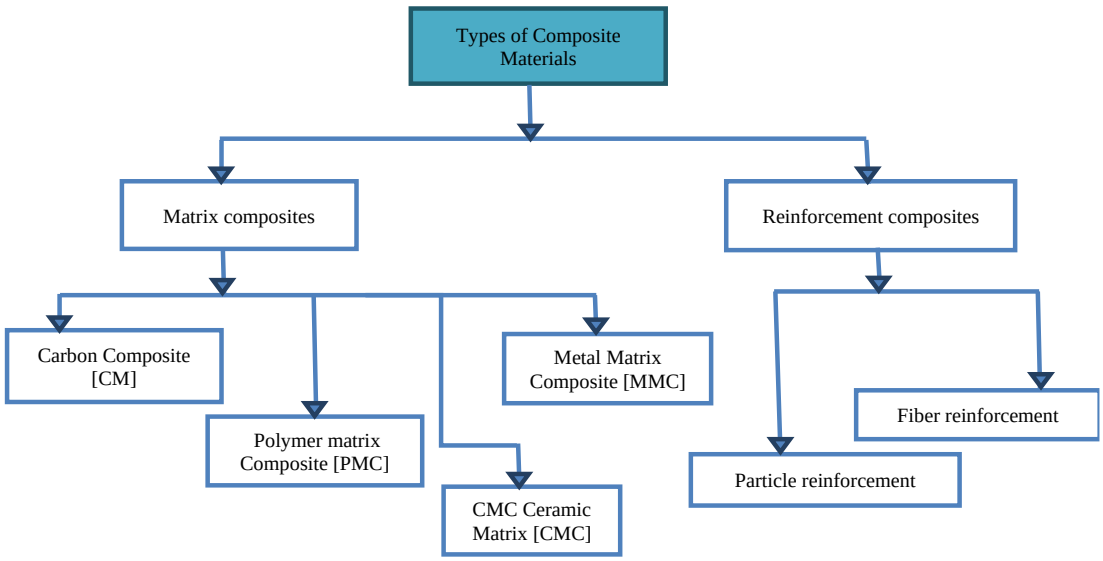

FIGURE 1. Classification of composite materials.

Fabrication methods of composites are mostly depending on three main components.

- Properties of matrix & reinforcement,
- The geometry and bring off clear information about final result or outcome, and

Different types of methods or processes to fabricate the composite materials:

- Hand layup Process or manual layup Process
- Open Molding Process
- Resin Infusion Methods
- Resin transfer molding
- Resin Infusion Methods
- Compression molding
- VARTM (Vacuum- assisted resin molding)
- Pultrusion
- Filament winding
- Tube rolling
- Reaction injection molding[8-10]

These are fabricating methods for the materials of composite. These methods are used according to the material and its application. Some of the fabrication methods are explained below.

Hand Lay – up Method

Hand lay-up process is also called known as manual layup process. It is most common & cost-effective method for fabricating composite materials. This method is easy and simple way to fabricate the composites. In this method the required number of plies are placed over other by applying gel. Consider a mold, place a sheet on mold for good laminate and apply gel or release agent (which is composition of epoxy resin and hardener with a ratio of 100:33) on the sheet. Now, put ply layer on the sheet and again apply gel uniformly using roller. After applying, place another layer of ply and apply gel uniformly repeat this process until the required thickness of laminate with ply layers. At last, again place another sheet on the laminate and kept it in undisturbed place by placing some pressure on it and let it cure by atmospheric or other curing methods[11-14].

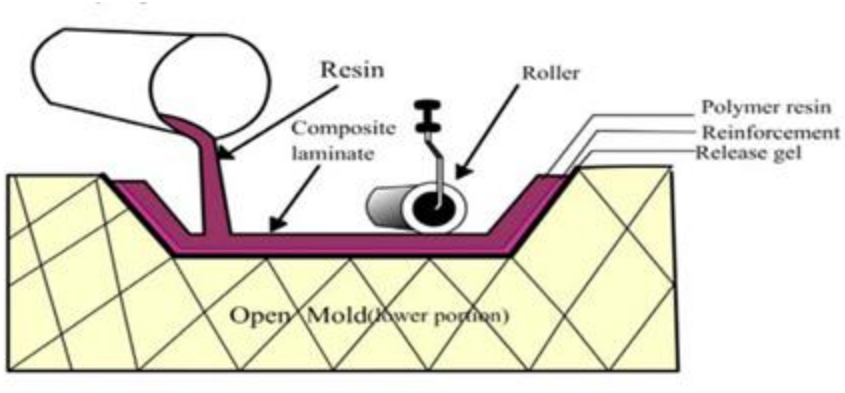

FIGURE 2. Hand Lay- up Method

Open Molding Process

Open molding is also known as contact molding fabricating method. This process is most preferable for glass fiber composites. This method is cost effective and it is a spraying process. In this process release agent is applied on the mold. Now the process of fabrication starts, Place the fabricating material on the mold and spray the gel or releasing agent on the material properly and roller is also used for applying the gel uniformly. In this method, one will be spraying the gel and another sprinkle chopped strands and making uniform using roller on to the molding surface instantaneously. Now place another piece of material and spray the gel, make this up to required number for plies. For the last ply, spray the gel on the top of the ply, so that the material becomes strong and layers stick to one another. Put some pressure on the mold and permit the mold to cure in atmospheric air or different curing methods. Sometimes manual layup process can be used with the spray layup for decreasing the labor and also it will less time consuming [15].

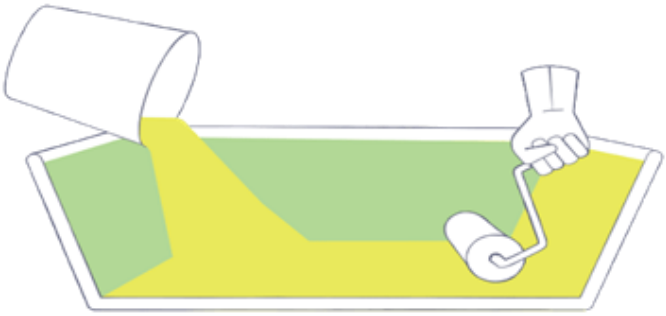

FIGURE 3. Open Molding Process

MATERIALS

This paper is using two – directional composites Jute (0.4 mm) and E – Glass (0.28 mm) fiber materials are used to fabricate the laminate[3]. Epoxy (Araldite LY 556) and Hardener are used to make a perfect laminate. E- Glass fiber is a cost effective and popularly used. In the E – Glass the 'E' represents the insulator of electric. Let us consider Jute as composite – 1**(C_1)** E – Glass as composite – 2 **(C_2).** Some of the properties of composites which are used in this paper are mentioned below.

TABLE 1. Properties of composite – 1 (C_1)

S. No	Properties of Composite – 1 (C_1)	Fiber of Jute
1	ρ of C_1 (g/cm³)	1.4
2	Enlargement (%)	1.8
3	Strength of tensile (MPa)	400 – 700
4	Modulus of elasticity, E (GPa)	15 – 25

TABLE 2. Properties of composite – 2 (C_2)

S. No	Properties of Composite – 2 (C_2)	E – Glass
1	ρ of C_2 (g/cm³)	2.5
2	Enlargement (%)	4.8
3	Strength of tensile (MPa)	2000 – 3000
4	Modulus of elasticity, E (GPa)	70 – 80

Fabrication Procedure

For fabricating the laminates or composite materials, choosing the fabrication method will be based on the material and its properties and applications. Here, for this composite material's manual layup method i.e., (hand layup method) is used for fabricating the laminate because natural fibre jute and E – glass separate laminates will be fabricated (for these materials manual layup method is better method for preparing laminate). Epoxy resin and hardener are used to make the laminate as adhesive, this resin and hardener are made with a ratio of 100:34. The combination of resin and hardener is called as release agent or release gel. The material dimensions are made according to the ASTM standards [ASTM D7264]. Take a mould and place a sheet or ohp sheet to prevent stickiness of laminate to the mould. Apply the release gel on the ohp sheet and spread it, take a ply layer and put on the ohp sheet and apply the gel (mixture of resin and hardener) uniformly using roller. Again, place the 2nd layer of ply [90^0] over the 1st ply layer and apply the gel uniformly using roller. Similarly, do the same process for remaining required ply layers. For the last ply layer apply gel and place ohp sheet on it. Place some pressure on the laminate and keep is aside, let it cure at atmospheric air or by using different curing methods. After curing remove the laminate from the mould and proceed for further process.

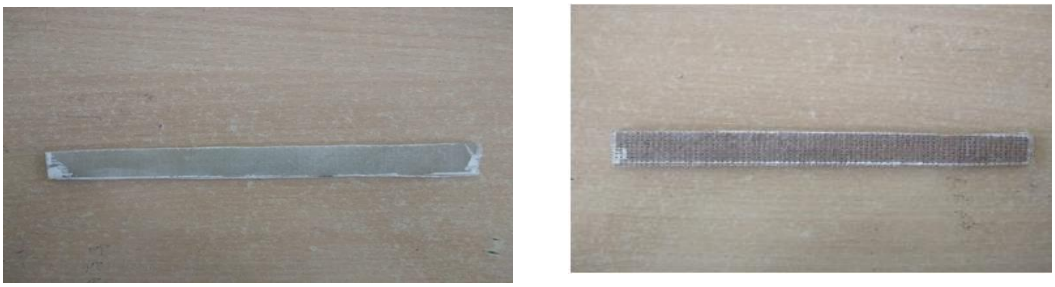

FIGURE 4. Fabrication of E – Glass fiber laminate & The Jute fiber laminates

TESTING

Flexural bending test was performed on the samples of composite – 1 and composite – 2 with dimensions 150 mm x 12.5 mm x 4 mm in ASTM D7264 standards to estimate the maximum load for samples. Testing of a samples were done using Three – point bending test on universal testing machine [UNITEK 94100] with cross head speed 1mm/1min. Samples were placed on the simple supported beam and the cross-head weight was released slowly and accurate flexural strength were noted. Both samples were compared after testing.

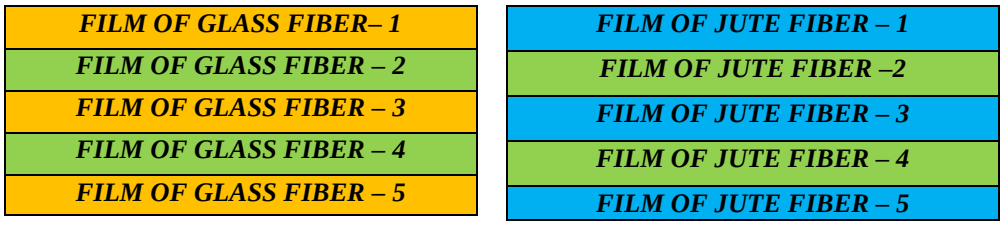

(a) (b)

FIGURE 5. The sample presentation of the Composite – 1 (a); The sample presentation of Composite – 2 (b)

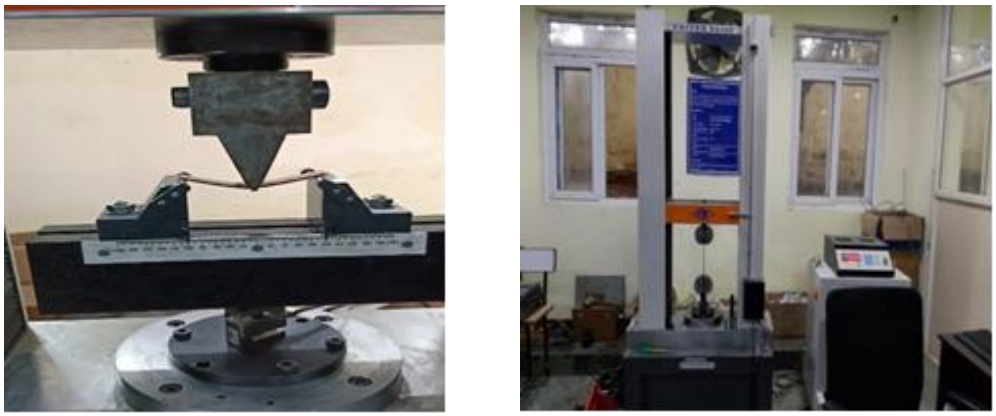

(a) (b)

FIGURE 6. (a) Flexural bending test for Composite – 1 using universal testing machine; (b) Universal testing Machine (UNITEK 94100)

RESULT AND DISCUSSION

- The below graph gives information about the flexural bending test which plotted between load & displacement for E – Glass fiber. The maximum load taken by the composite is 0.105 KN. The maximum displacement is at 17.210 mm.
- The X – axis represents the displacement in mm and Y – axis represents the load in KN. In the graph the displacement is gradually changing (at 9000 mm) from the failure point.

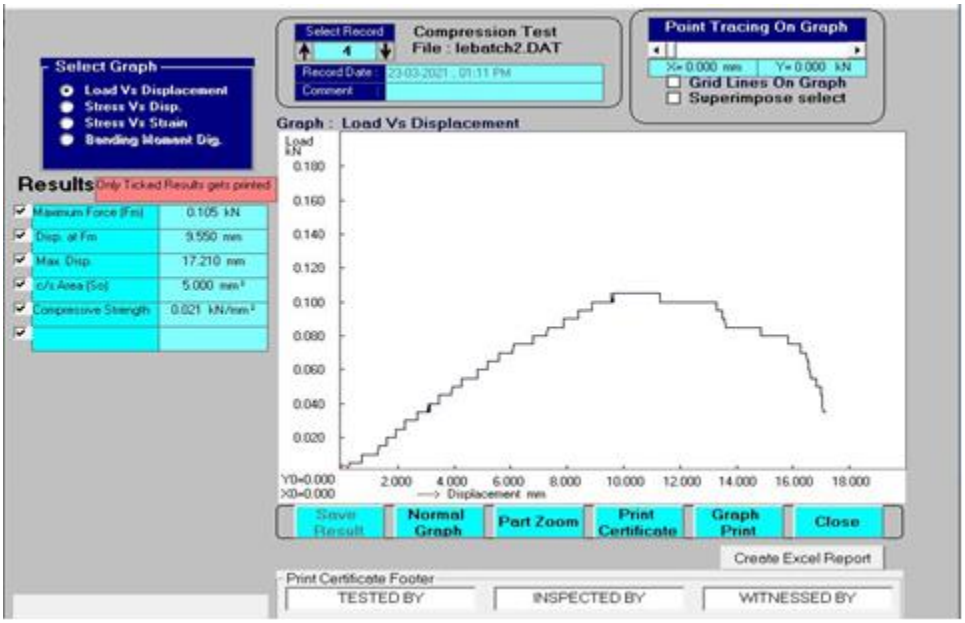

FIGURE 7. The above graph shows the results of flexural bending test for E – Glass fiber

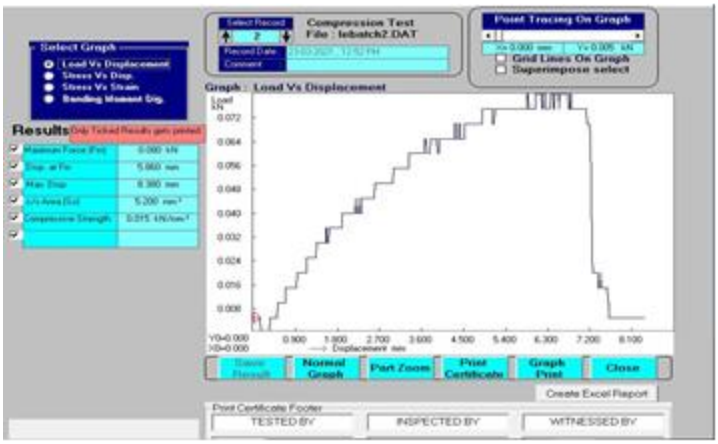

FIGURE 8. The above graph shows the results of flexural bending test for Jute fiber.

- The above graph gives information about the flexural bending test which plotted between load & displacement for natural fiber – jute. The maximum load taken by the composite is 0.080 KN.
- The X – axis represents the displacement in mm and Y – axis represents the load in KN.
- In this graph there is a sudden displacement happened after 7000 mm. The failure or breakage point nearly at 5800 mm.

TABLE 3. Flexural Properties of Composites after testing

S.NO	Composites	Maximum Load (KN)	Flexural strength (KN/mm^2)
1.	Jute	0.080	0.015
2.	E – Glass	0.105	0.012

From the above graphs and table, E – Glass composite material (i.e., laminate) is having more flexural strength than the Jute composite material. In general, the properties like density, modulus of elasticity etc., of jute are having less value of strength but in absorption of moisture the jute has more percent in absorbing this is absorbed from 'Preparation and Mechanical Properties of Jute Fibre Reinforced Epoxy Composites'. Both the composite materials can be used for applications based on the type of usage.

CONCULSION

This paper presents the fabrication and testing of different composite materials using composite – 1 and composite – 2 by using hand layup method and flexural bending test is performed using UTM machine. From the obtained results, both composites (Jute & E – Glass) had their own importance. Meanwhile by comparing the composites E – Glass has more capacity to take heavy loads i.e., 0.105 KN, whereas Jute can resist up to 0.080 KN. The displacement for jute was 8.380 mm and the displacement for E – Glass was 17.210 mm. E – Glass has more displacement compare to Jute. This paper concludes that flexural strength of E – Glass is far better than the Jute.

REFERENCES

1. Vivek Anand A, Venkatesh G & Anand P, 2014, "*Noval method for fabrication of 3-D spacer fabric composite and investigation of mechanical property",* Int. J. Modern Engineering Research, Vol. 1, No. 4, pp. 27-30.
2. R Kannan, Vivek Anand A, Arumugam V, Naveen R et al.," *Strength Enhancement of Sisal Fiber by its Wettability Modification with Cardanol*", Int. Conference on Material Science & Technology (2016), DOI: 10.5185/icmtech.2016, Oral Presentation, Mar 01-04, India.
3. Madhavi, K Sreelakshmi and M. Satyanarayana Gupta, *Evaluation of Ply Orientation on Failure* of Composites, IJCIET, ISSN Print: 0976-6308 and ISSN Online: 0sss976-6316, Volume 8, May2017.

4. K. Sreelakshmi, N Madhavi, M Satyanarayana Gupta, *Analysis of Interlaminar Stresses in a Composite Material with A Circular Hole by Using Finite Element Method*, IJCIET, ISSN Print: 0976-6308 and ISSN Online: 0976-6316, Volume 8, May2017.
5. B. Nagaraj Goud, K. Shiva Shankar, B. Manideep, K. Veeranjaneyulu "*Experimental Test on Glare Composite of an Aircraft Structure under Tensile Strength Failure*", International Journal of Engineering and Advanced Technology (IJEAT) ISSN: 2249 – 8958, Volume-9 Issue-2, December, 2019.
6. P. Anudeep, Babitha Kodavanla, P.Srinivas Rao and Madhavi Nagireddy, *Experimental analysis on treated and untreated Grass/Carbon Hybrid Composite Structures*, International Journal of Applied Engineering Research and Development (IJAERD), Vol. 8, Issue 1 Jun 2018, pp. 1-6 (ISSN (P): 2250-1584; ISSN (E): 2278-9383), Scopus Indexed).
7. A Vivek Anand, V Hariprasad, S Jayalakshmi, R Arvind Singh, V R Ravivarma and S Gollakota, 2018, "*The Sisal/Coir/Glass fiber-based hybrid composite laminate sstructure*", International Journal of Mechanical and Production Engineering Research and Development, Vol. 8, No. 7, pp. 1039-1046.
8. *"Properties of Jute Fibre at Different Portions",* Hindawi Publishing Corporation International Journal of Polymer Science Volume 2015, Article ID 262348.
9. *"Preparation and Mechanical Properties of Jute Fibre Reinforced Epoxy Composites",* Kumar A, Srivastava A (2017) Preparation and Mechanical Properties of Jute Fiber Reinforced Epoxy Composites. Ind Eng Manage 6: 234. doi:10.4172/2169-0316.1000234.
10. *"Flexural bending fatigue of raw and chemically treated jute",* S. K. Kundu, "Flexural bending fatigue of raw and chemically treated jute," *Textile Research Journal*, vol. 57, no. 2, pp. 118–120,1987.
11. Yoldas Seki, Kutlay Sever, Seckin Erden, Mehmet Sarikanat, Go¨kdeniz Neser, Cicek Ozes, 2011, *"Characterization of Luffa cylindrica Fibers and the Effect of Water Aging on the Mechanical Properties of Its Composite with Polyester*", DOI 10.1002/app.34744.
12. Demir H., Atikler U., Balkose D., Tihminhoglu F., 2006, "*The effect of fiber surface treatment on the tensile and water sorption properties of polypropylene -luffa fiber composites*", Composites: Part A 37 (2006) 447–456.
13. Ghali l., Msahli s., Zidi M., Sakli F., 2009, "*Effect of pre-treatment of Luffa fibers on structural properties*", Materials Letters 63 (2009) 61–63.
14. Valcineide O.A., Tanobe, Thais H.D., Sydenstricker, Marilda Munaro, sandro c. Amico.,2005, "*A comprehensive characterization of chemically treated Brazilian sponge-gourds (Luffa cyllindrica)*", Polymer Testing 24 (2005) 474–482.

RESEARCH ARTICLE | MAY 22 2023

Modeling and static structural analysis on stiffened panel for an aircraft structure

B. Nagaraj Goud ✉; Sreekanth Sura; Swetha Bala M. N. V. S.; B. Manideep

AIP Conference Proceedings 2492, 040007 (2023)
https://doi.org/10.1063/5.0113300

Modeling and Static Structural Analysis on Stiffened Panel for an Aircraft Structure

B. Nagaraj Goud [1, a)], Sreekanth Sura[1, b)], Swetha Bala MNVS[1, c)], B. Manideep [1, d)]

[1]*Department of Aeronautical Engineering, MLR Institute of Technology, Hyderabad, India.*

[a)] Corresponding Author*: nagaraj2107@gmail.com*
[b)] *sreekanthsuramlrit@gmail.com*
[c)] *swethabalamlr@gmail.com*
[d)]*manideepbalusani.9@gmail.com*

Abstract. The paper is focused on the modeling and analysis of an aircraft stiffener by using ANSYS. The stiffener of an aircraft is mainly used to support the structure of the aircraft. It is normally made using a metal of aluminum, steel and titanium. In this regard, the stiffener is made with aluminum alloy and is compared with steel material. and performed static structural analysis and analyzed material performance. To improve the structural stability of a stiffened panels are to be determined on account of their weight saving. When these stiffeners were permitted to buckle at ≤ to the design yield load. The response of stresses and deformation of the Stiffened Panel are addressed and the response of the structure. When the design is efficient, the constraint can be adjusted to allow local buckling at the design limit load, as long while the structure doesn't really fail at even a load lesser than the design maximum applied load. Improved structural integrity by supported by hat section arrangements to the stiffened panel. Therefore, the simulation analysis results for the stiffener supported by the hat section members were presented.

Key words: Aircraft, Stiffener, Design load, Static Analysis, ANSYS

INTRODUCTION

Stiffeners are secondary plates or sections that are attached to flanges or beam webs to strengthen the members against out-of-plane deformations[1]. Stiffeners will be installed on nearly all key bridge beams. Most, however, will have transverse web stiffeners connected to the web, so instead of vertical stiffeners. Longitudinal web stiffeners are often used in deep beams. Flange stiffeners are typically utilized on long length box girder bridges; however, they are infrequent elsewhere[2]. Weaving process through its thickness of the dry graphite-epoxy composite material can significantly decrease the effort required for panel fabrication and assembly. The pre-stacked skin portions, ribs, stringers, intercostals, and spar caps are stitched together across the thickness of the skin. Stitching provides a way to decrease damage progress caused by low-speed or discontinuous source impact, and mechanical fasteners are almost removed entirely. Conventional composite materials have used no-damage-growth technique and are tailored to withstand design limit loads in discrete-source-damaged components without damage dispersion[3]. As the structures that are partially noticeable after an impact can support the design of maximum load without damage occurs. The assembly constraint requires that allows the less strain than would be required in an original construction, resulting in a heavier structure and the composite material of stiffening panels are becoming more attractive in the aerospace applications[4].

The different types of stiffeners are used to stiffen the composite plate. These are divided into two categories: open form as well as closed form or box type. The open form is torsionally less, whereas the closed or box type is torsionally tough. Unless this design restriction could be altered to allow local buckling at design limit load, as far as

Advancements in Aeromechanical Materials for Manufacturing: ICAAMM-2021
AIP Conf. Proc. 2492, 040007-1–040007-6; https://doi.org/10.1063/5.0113300
Published by AIP Publishing. 978-0-7354-4438-6/$30.00

the component doesn't really fracture at such a load is below design maximum load, lighter, greater weight- and cost-efficient constructions can be produced[5]. The structural panels can be built in such a way that they are considered to handle loads far greater than that of the buckling loading and remain unchanged. The main aim of this research study about to see how considerable weight may be saved by allowing strengthened panels to buckle at loads lower than their bearing capacity as far as the panel doesn't quite fail. When the damage begins and growth on a local level, as well as nonlinear behaviour of post-buckling, If the structure fails due to the load is considered to be the ultimate load, it should be evaluated[6]. The method used in this study was to evaluate the behaviour of single-stiffener materials both analytically and experimentally then predict structural stability improvements for multi-type stiffened panels using analytical methods[7]. Stiffeners are divided into two categories. They are stiffeners that run the length of the web and are aligned in the span direction and other one is transverse stiffeners are placed perpendicular to the span direction of the beam as shown in figure.1

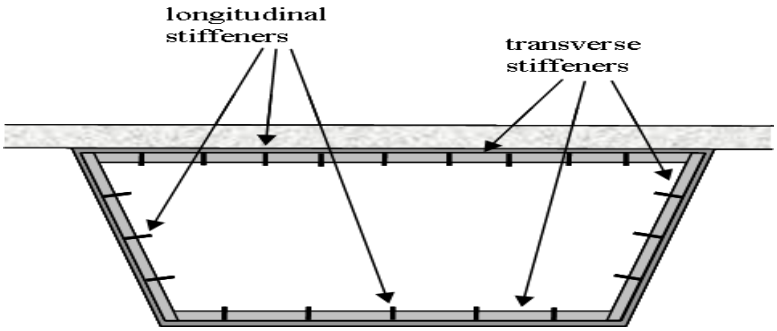

FIGURE.1 stiffener

Stiffeners have been utilized in the past in a number of ways, but the simple flat stiffener is virtually usually employed in the latest designs. The Stiffeners could be applied to one edge of the plate (single sided) or both edges of the plate (double sided) [8]. Joint stiffeners are commonly double-sided, while middle web shear walls are usually single. Stiffeners could be doubled, tripled, quadrupled, or even multi-legged. For the purpose of coupling torsional stiffening in between beams in a practical way, intermediate stiffeners on major beam webs are frequently required. If this is the case, the stiffener positions will be determined by the bracing locations[9]. However, for beams that do not requires including such transverse girders in the ladder deck bridge or if the design bracing is employed, intermediate stiffeners could be required. beam as shown in figure.2

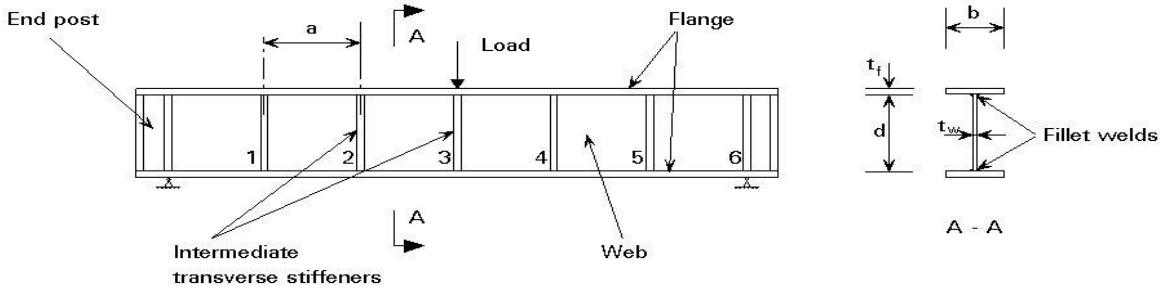

FIGURE.2 Intermediate transverse web stiffeners

In 1940, Massonnet presented a research study of the elastic stability of simply supported rectangular plates subjected to pure bending and strengthened with a 1/4 longitudinal stiffener. These studies concentrated primarily on the theory of optimal stiffener rigidity[10]. Later, Kromm and Chawla refined the minimum strength requirements for panel stiffeners by examining a longitudinal stiffened panel during pure bending[11]. Milosavljevic has developed a comprehensive study on treatment of the elastic stabilisation of a simply supported rectangular panel was subjected to an axial stress, shear stress and combined bending that strengthened to two transverse stiffeners and one longitudinal stiffener. The key was found by applying a series technique to the plate's differential equation. the stiffeners in the transverse direction at the 1/3 wide locations, the special situations of pure bending and bending

with shear were solved after a year. According to Dubas ideal portion of the stiffener in longitudinal direction which act a simply supported panel exposed to the pure bending is at 1/5, The American and British Specifications have since accepted this position.

DESIGN AND MATERIAL PROPERTIES

The design work in this research focuses on building and expanding the possibilities of those computational tools using the proposed methodology to improve modelling, design and development, thus the stiffened panel is designed entirely or in its discrete required components as shown in figure.3

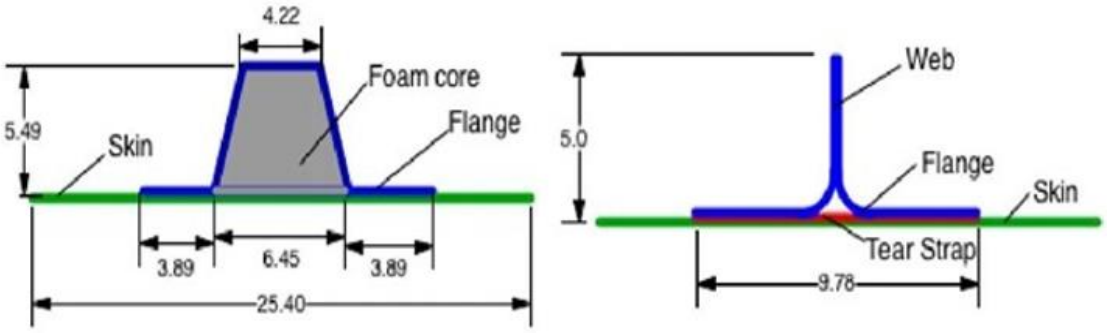

FIGURE.3 Hat and blade frame stiffener

The hat section stiffener design using CATIA and It includes a step-by-step simulation that demonstrates the main component with dimensions and their characteristics as shown a wireframe in figure.4 and the design part workbench in figure.5

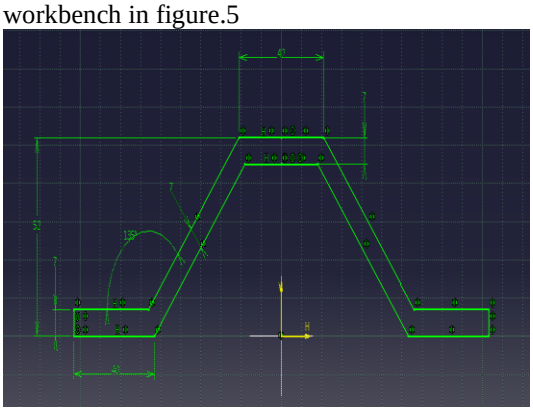

FIGURE.4 Geometry of the Hat section stiffener

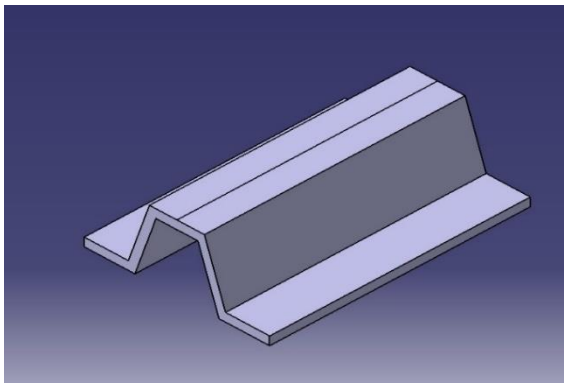

FIGURE. 5 Model of Single Hat section stiffener

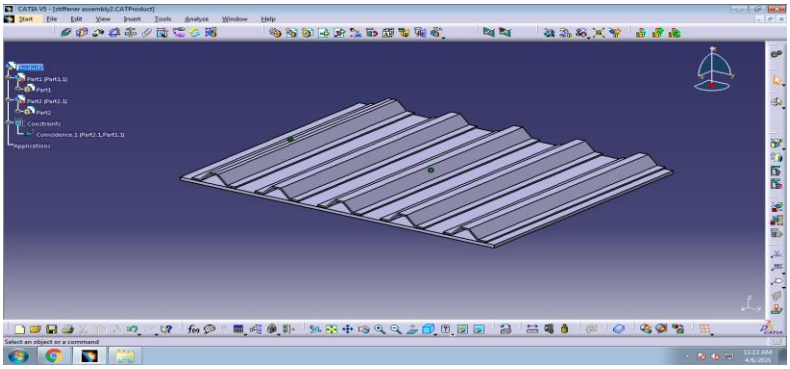

FIGURE.6 Model of Hat section stiffener

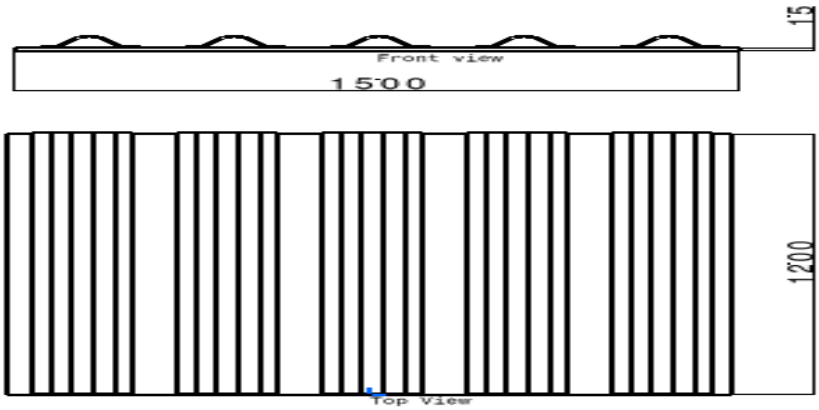

FIGURE.7 Front view and Top View of the Hat section stiffener

TABLE1. Shows the Material properties

Material	Poisson's Ratio	Modulus of Elasticity (GPa)	Density (kg/m^3)
Structural Steel	0.27	200	7850
Aluminium Alloy	0.33	70	2770

RESULTS AND DISSCUSSIONS

Based on selected materials and designs, the finite element analysis package ANSYS workbench was imported from CATIA and as per the required dimensions. Meshing, boundary conditions were applied, the rectangular panel was fixed at both ends and uniformly distributed pressure was applied, and static structural simulation analysis was performed for both aluminum alloy and steel materials.

For the given set of loading condition, the Maximum Deformation value was observed 40.092mm on the Aluminum stiffened panel and the minimum value was observed 4.45mm and von Mises stress, the Maximum value was observed 337.91Mpa and minimum value was observed 1.596Mpa as shown in figure.8 and 9.

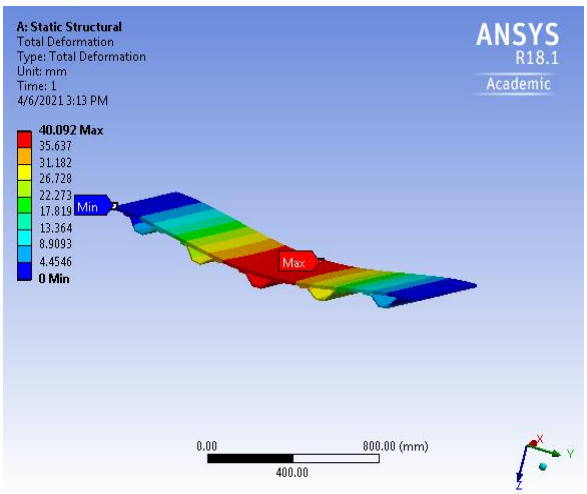

FIGURE.8 Maximum Deformation of an Aluminum Alloy Material

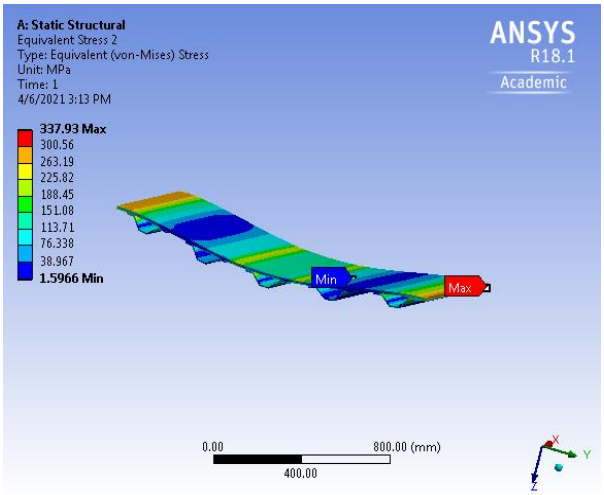

FIGURE.9 Von Mises stress of an Aluminum Alloy Material

Similarity on steel material, the given set of loading condition, the Maximum Deformation value was observed 14.68mm on the Steel stiffened panel and the minimum value was observed 1.6mm and von Mises stress, the Maximum value was observed 375.9Mpa and minimum value was observed 1.43Mpa as shown in figure.10 and 11.

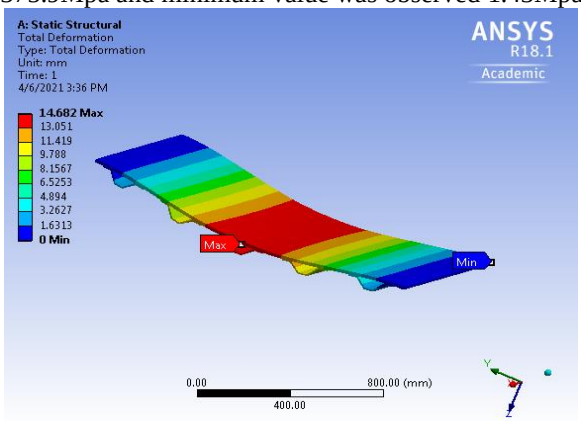

FIGURE.10 Maximum Deformation of the Steel Material

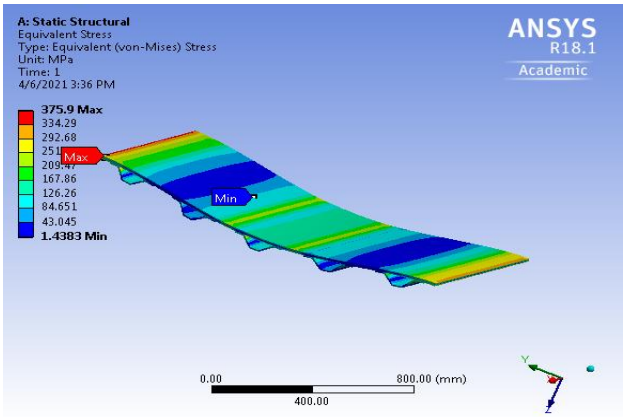

FIGURE.11 Von Mises stress of the Steel Material

The results of the static analysis presented in the form of total deformation and Von mises stresses under the pressure of 1atm was applied on the fixed rectangular plate carrying uniformly distributed load calculated by ANSYS.

TABLE 2. Shows the Stresses and Deformation Results

Materials	Pressure (MPa)	Von Misses Stresses (Mpa)	Displacement (mm)
Aluminium Alloy (AA6082)	0.101	337.93	40.09
Steel Alloy (Ferrium m54)	0.101	375.90	14.68

CONCLUSION

Aluminum is the primary material used in the manufacturing of aircraft in this article. However, larger aircraft manufacturers such as Boeing and Airbus have started to use carbon fiber in their planes. The FEA of the structural analysis for a fixed rectangular plate with uniformly distributed pressure load applied for both steel and aluminum material was performed in this work, and the following conclusions were reached. The total deformation and stress analysis results for a fixed stiffened panel are compared for two material qualities by ANSYS. By static analysis, von mises stress values are lower in aluminum than in steel stiffened panels, and overall deformation results are lower in aluminum than in steel stiffened panels.

REFERENCES

1. Uday Deepika A, Veeranjaneyulu K. Buckling analysis of stiffened panel for aircraft fuselage. *Int J Mech Prod Eng Res Dev*. 2018;8(1):1299-1308. doi:10.24247/ijmperdfeb2018150
2. Uday N, Goud R, Sawale A, Rakham B. Buckling Load Predictions of Panel and Shell using Vibration Correlation Technique. *Int J Eng Adv Technol*. 2019;9(2):1842-1845. doi:10.35940/ijeat.b2679.129219
3. Kumar DM, Madhavi N, Sushma M. Thin walled C-Sectional Beam under Axial Load. *Int J Innov Technol Explor Eng*. 2020;9(3):498-499. doi:10.35940/ijitee.c8512.019320
4. Ko WL, Jackson RH. Shear Buckling Analysis of a Hat-Stiffened Panel. *Nasa Tm-4644*. 1994;(November 1994).
5. A A V. Parametric study of castellated beam with varying depth of web opening. *Int J Sci Res Publ*. 2012;2(8):2250-3153. www.ijsrp.org
6. Kumar. Static and Dynamic Analysis of Aircraft Stiffened Panel. 3(2):134-139.
7. Kothapalli AKR, Mohanty A, Adika SRK. Finite Element Modeling And Analysis Of Fuselage Stiffened Panel Subjected To Cabin Pressurization. *ResearchgateNet*. 2012;(January):678-681. http://www.researchgate.net/publication/246546122_Finite_Element_Modeling_And_Analysis_Of_Fuselage_Stiffened_Panel_Subjected_To_Cabin_Pressurization/file/e0b4951d9b5233ed5e.pdf
8. Li X, Jia D, Meng C. Buckling analysis of airframe jointed panel under combined loading. *Int J Appl Mech Eng*. 2018;23(4):1035-1042. doi:10.2478/ijame-2018-0060
9. Anupriya B, Jagadeesan K. Shear strength of castellated beam with and without stiffeners using FEA (ANSYS 14). *Int J Eng Technol*. 2014;6(4):1970-1981.
10. Massonnet, C. (1940). "La Stabilite' De L`Ame Des Poutres Munies De Raidisseurs Horizontaux Et Sollicitees Par Flexion Pure (The Web stability of Longitudinally Stiffened Plate Girders Subjected to Pure Bending)."
11. Kromm, A. (1944). "Zur Frage der Mindeststeifigkeiten Von Plattenaussteifungen (On the Problem of Optimum Rigidity of Stiffened Plates)." Stahlbau, 17, p. 81.

RESEARCH ARTICLE | MAY 22 2023

Design and fabrication of micro class aerial vehicle with elliptical wing tips

Sreekanth Sura ✉; Pasala Preethi; Sira Sony; Paladugula Koti; Lala Raghuveer

AIP Conference Proceedings 2492, 040052 (2023)
https://doi.org/10.1063/5.0113375

Design and Fabrication of Micro Class Aerial Vehicle with Elliptical Wing Tips

Sreekanth Sura[1, a)], Pasala preethi[1], Sira sony[1], Paladugula koti[1], Lala raghuveer[1]

[1]*Department of Aeronautical Engineering, MLR Institute of Technology, Hyderabad, India.*

[a)]Corresponding Author : sreekanthsuramlrit@gmail.com

Abstract. For the past few years MAV is playing important role in various sectors like civilian and military organisations. They might have a different mission profile according to their usage. MAVs are immensely useful for quick access in difficult and remote areas and for scanning unreachable military bases. They are extremely beneficial in places where a man cannot reach or he is unable to perform a mission in time. It can be used efficiently for defense operations such as surveillance for enemy troops or terrorist activities or to provide support to armed people. For this, it is desired to design a MAV for high endurance with the high lift to drag ratio that is the drag should be minimum. So, in this project it is proposed to study the airfoil and wingtips. Based on the analysis appropriate wingtip is chosen. In present, maximum flying duration in 20 - 30 minutes and accordingly payload is chosen and MAV sizing is carried out. Then the MAV is fabricated and demonstrated.

INTRODUCTION

The main objective of the report is to provide outline of design and fabrication of MAV with elliptical wingtips. RC aircrafts are designed in such a way that it can be carried out quickly launched and full fill mission within prescribed time the main motto is to design and fabricate an aircraft which is cable to achieve the highest payload fractions possible with the lowest empty weight with the three main consideration.

- maximizing lift
- minimizing aircraft weight and drag
- better stability

This section addresses the approach to designing the aircraft and fitting a model that covers factors like weight estimation, wing design, fuselage design, empennage sizing and control surface sizing in order to meet the requirements and figure 1 shows the mission profile.

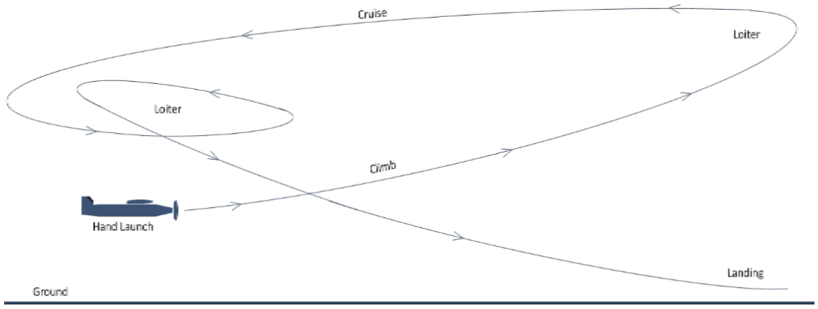

FIGURE1. Mission Profile

Advancements in Aeromechanical Materials for Manufacturing: ICAAMM-2021
AIP Conf. Proc. 2492, 040052-1–040052-7; https://doi.org/10.1063/5.0113375
Published by AIP Publishing. 978-0-7354-4438-6/$30.00

WEIGHT ESTIMATION

Weight of the aircraft should be less than 1.5 kg (We< 1.5 kg),Weight estimation is given below.

Equation of weight:

$W_{total}=W_{emty}+w_{payload}$

Where,

$W_{empty}=W_{structure}+W_{component}$

Since, there will be some misinterpret in fabrication as compared with estimation which can be tolerated and optimized up to 5%-10%.

AIRFOIL SELECTION

Airfoil selection plays a vital role in designing an aircraft as it has to satisfy the minimum requirement like stall and cruise characteristics. After doing a lot of ground work on selecting airfoil, we have selected MH113 figure 2 and we have modified the airfoil using XFLR 5 which provides us all the requirements which are suitable for our wing design at Reynolds number Re =100000.

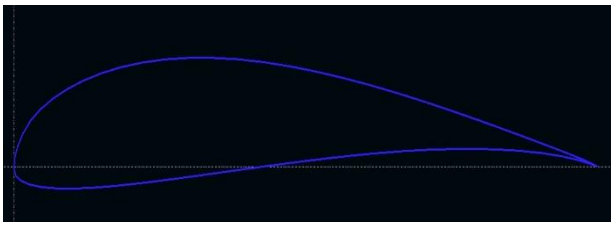

FIGURE 2. Airfoil modified MH113

ASPECT RATIO AND WING AREA

Aspect ratio is the ratio of square of wing span to surface area of the wing.

For Home-built aircrafts, the aspect ratio should rely between 6 to 7.5 as this gives the best aerodynamic efficiency.If the aspect ratio is greater than 7.5 it will have high gliding performance.

Wing surface area should be maximum, so it can able to carry the maximum payload as much as possible. We have selected the rectangular wing configuration with no sweep for its ease of manufacturing and cost efficiency. In order to reduce the alarming amounts of induced drag it produces, we have inculcated the curved and sharp wing tips. The induced drag is reduced by reducing the formation of wing tip vortices.

FUSELAGE AND PAYLOAD SIZING

Fuselage of aircraft is designed to incorporate the payload and electronic components. All of these are placed inside the fuselage by considering the CG (centre of gravity) of the aircraft before and after securing payload. For the ease of fabrication, fuselage with squared section was designed by giving the proper dimensioning of the sections. The motor mount is prepared by sandwiching the plywood in between the balsawood in front of the fuselage to strengthen the nose area so as to overcome the forces produced by the motor. The length and width of fuselage is 0.911m and 0.06m.

TAIL SIZING

One of the most important part of the aircraft is tail which consists of the stabilizers which helps to create and control the yawing and pitching moments of the aircraft. Tail is divided into two parts as horizontal stabilizer and vertical stabilizer in figure 3. To attain adequate stability and control, the conventional tail configuration has been opted for our aircraft.

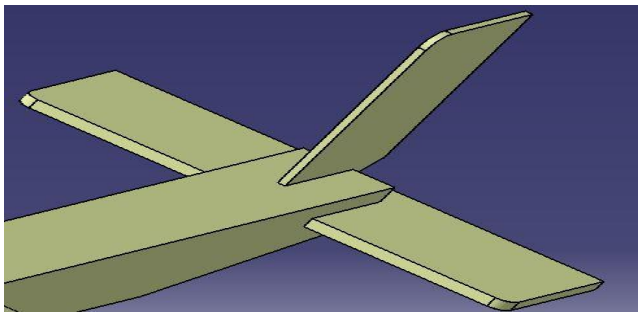

FIGURE 3. Empennage

An aircraft stabilizer is an aerodynamic surface, including one or more movable control surfaces which provides the longitudinal and directional stability.

Horizontal Stabilizer coefficient $(c_{HT}) = L_{HT}S_{HT}/C_W S_W$

Vertical stabilizer coefficient $(c_{VT}) = L_{VT}S_{VT}/b_W S_W$

CONTROL SURFACE SIZING AND SERVO SIZING.

The control surfaces of any aircraft are aileron (produces roll moment), rudder (produces yaw moment), and elevator (produces pitch moment). To maintain the adequate stability of the aircraft, forces acting on it should be precisely manipulated. To manipulate the forces, control surfaces are designed for an aircraft.

Therefore, servo sizing is also important. Many iterations have been conducted with improvements in moment arm length for servo.

PERFORMANCE ANALYSIS

Drag Estimation

The other aerodynamic force experienced by the aircraft is drag. This is the force which opposes the aircraft motion. Generally, drag is created due to the shear stress on the body, formation of trailing vortices at wing tips due to lift (or) induced drag and due to the integrated static pressure which are normal to the surface area of wing. In figure 4 you can see drag distribution at take off.

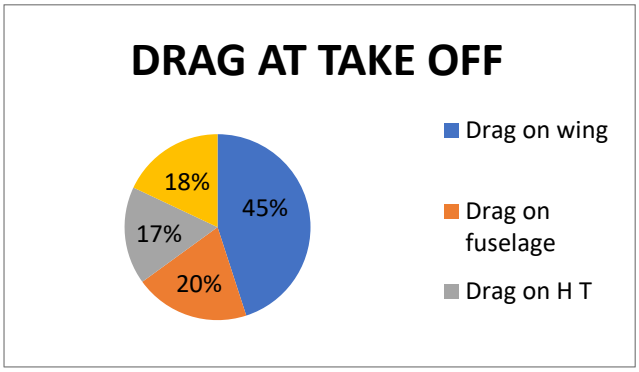

FIGURE 4. Drag at take off

POWER PLANT MATCHING

Power required for an aircraft is characteristic of aerodynamic design and weight of the aircraft. However, the power available is characteristic of the power plant of the engine. Here the actual power is calculated based on the test conducted by the 3^{rd} party evaluators and data sheets provided by the manufacturers.

Power = drag * velocity

THRUST TO WEIGHT RATIO

It is the ratio of thrust produced by selected propulsion system to overcome the drag acting on aircraft to the weight of the aircraft. As we know in level unaccelerated flight thrust must be equal to the drag for better performance of aircraft. The figure 5 represents the Thrust to weight ratio.

$$\frac{T}{W} = \frac{1}{(\frac{L}{D})max} \quad (1)$$

Where, (L/D)max =Aerodynamic Efficiency

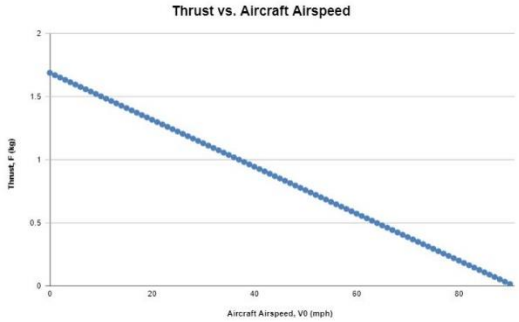

Figure 5. Thrust to weight ratio

WING LOADING

Wing loading of an aircraft is a ratio of the total weight of the aircraft to the surface area of the wing. Depending upon the wing loading. Performance of aircraft varies. Based on wing loading stability, turn performance, and glide performance of an aircraft varies. Wing loading is also known as the biggest determinant of speed. Aircraft with low wing loading factor flies at low speed while the higher wing loading flies at high speed. Wing loading is differed in conventional aircrafts in take-off, cruise and landing conditions. In Figure 6 Wing loading performance graph has been shown.

Wing loading for aircraft at stall speed is 88.2 N/m^2

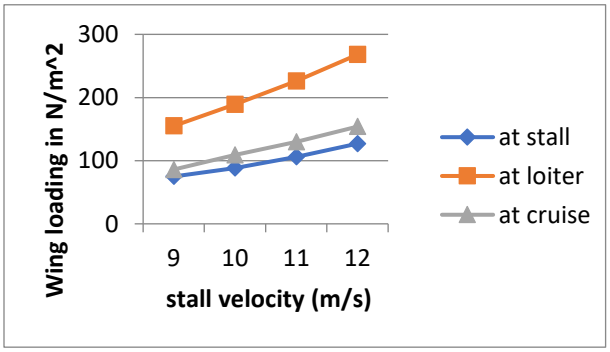

Figure 6. Wing loading performance graph

LOAD FACTOR

The ratio of the aerodynamic force on the aircraft to the aircraft's gross weight is a load factor.While designing a n aircraft, the highest load factors that can be predicted under various
operating conditions in normal operation are calculated and the value at stall velocity is 1.01

$$n = \frac{1}{2} * \rho * V^2 * \frac{CLmax}{\frac{W}{S}} \quad (2)$$

CG ESTIMATION

The Centre of Gravity (C.G) of this aircraft from nose is estimated as (-7.437e-009m, 0.202m, -0.005m).

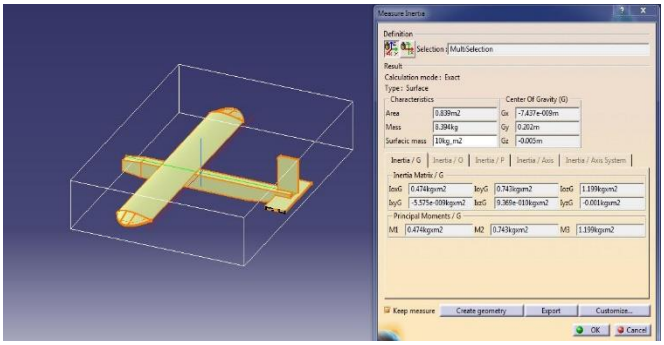

Figure 7. Centre of Gravity estimation

MODELLING ANALYSIS

The Figure is 3D modelling from simulation software are useful for studying the structural dynamics and aerodynamic properties of the aircraft. 3D modelling, CFD (Computational Fluid Dynamics) and Structural analysis were conducted in CATIA V5 and ANSYS workbench respectively.

MODELLING

Each and every part of an aircraft is designed in CATIA – Part design module and all parts are imported in CATIA – Assembly module and the assembly was done. Even the Centre of Gravity of an aircraft is also estimated with payload in CATIA. In figure 8 3D CAD model of the aircraft.

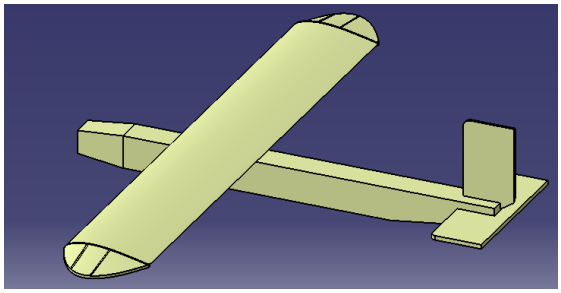

Figure 8. 3D CAD model of the aircraft

COMPUTATIONAL ANALYSIS

CFD analysis is carried out using FLUENT 18.1 at various angles of attack 0”

Condition:

At sea level;V_{stall}= 10m/s

CFD is performed on a 3D model of aircraft at sea level conditions like velocity, pressure and etc; with element count of 73 lakhs and node count of 19 lakhs. And results are shown in below in figure 9,10.

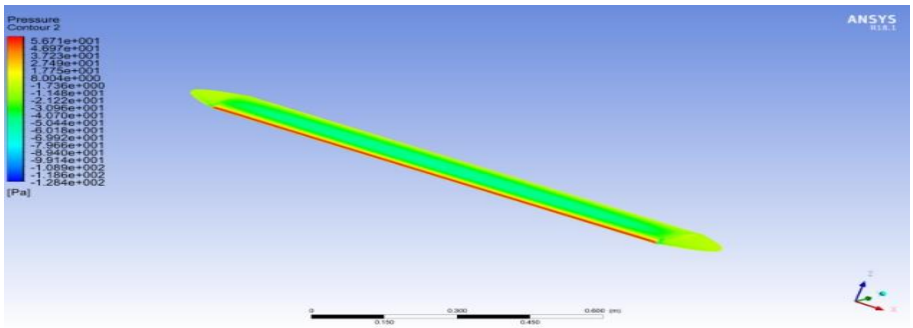

FIGURE 9. Static Pressure

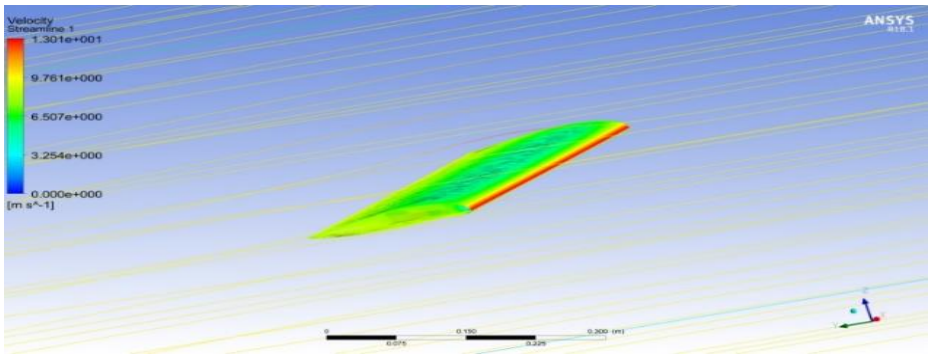

FIGURE 10. Velocity Magnitude

STRUCTURAL ANALYSIS

Condition: Cantilever beam Structural analysis is performed to find Stresses, Forces and Deformation etc., on a body. In figure 11 the Deformation =0.008m.

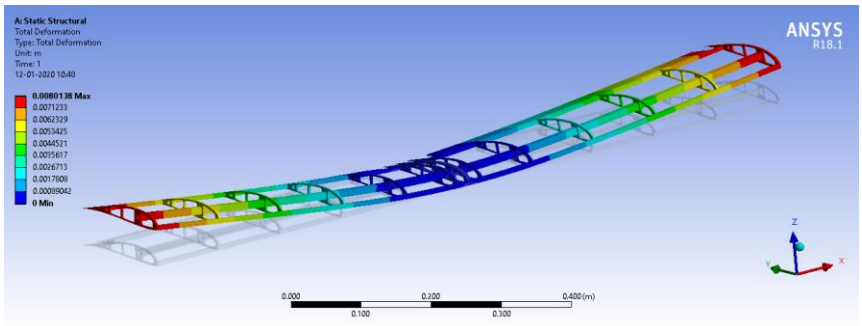

FIGURE 11. CFD and Structural Analysis

FABRICATION

Over the course of this project, many iterations were conducted. Each one iteration allowed us to check the feasibleness to practice the different construction techniques. Before the development began, the balsa sheet components of the aircraft were cut using the optical cutting machine. After that the successive step of the team was to assemble the plane components. Later, the next process is to integrate the electronic components within the aircraft. After the integrating of the electronics the plane will be completely sealed for flight check. In figure 12 you can see the fabricated structure.

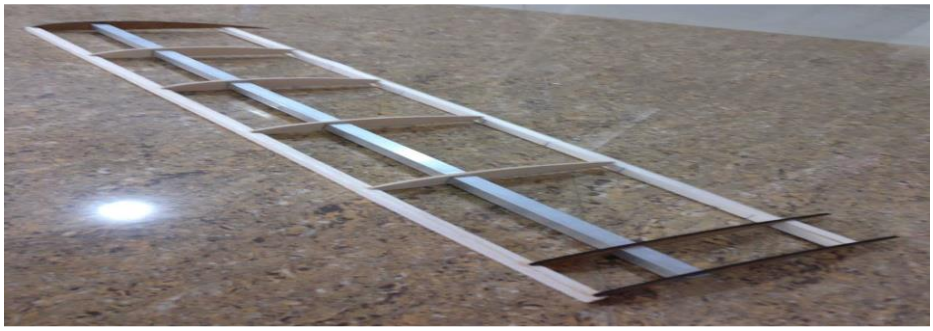

FIGURE 12. Fabrication

CONCLUSION

Designed and fabricated the MCA as per the information provided in following table. We have obtained approximate results according to our design and survey. The payload prediction chart gives the graphical representation of the payload capacity of the UAV as a function of density altitude. The change in the atmospheric properties with increasing altitudes can have great influence on the flight, or specifically considered, on the payload capacity. Though the maximum attainable cruise altitude during the flight test in the competition is well below 50 meters, the payload capability is predicted all the way from 0 to 3000 meters.

REFERENCES

1. Sai Kumar A , P C Bhaskar Reddy, C Vamsi Krishna; " Design and Fabrication of 150 mm Fixed Wing MAV", *International Journal of Science & Technology*, Volume 3, Issue 3, 15-23, 2013
2. Mr.sreekanth sura, a.sai kumar, nirmith kumar mishra, sohail raheman, "design and fabrication of micro air vehicle (mav) with double-bubble fuselage" *international journal of recent technology and engineering* (ijrte) issn: 2277-3878, volume-8 issue-4, november 2019.
3. K Arunkumar, K Veeranjaneyulu, Om Prakash, Sreekanth Sura, M Srikanth," Mechanism and Performance Analysis of Morphing Wing", *International Journal of Innovative Technology and Exploring Engineering* (IJITEE) ISSN: 2278-3075, Volume-9 Issue-3, January 2020
4. Anderson, J. D. (2007, .ISBN 10:0-07-066082-4). "Introduction to Flight". Tata Mc Graw Hill.
5. Gleason, P. G. (2012, ISBN-10: 111997861). Introduction to UAV Systems. WILEY.
6. It's All RC! (2014, February 19). Retrieved from How To Calculate Drag: https://itsallrc.wordpress.com/2014/02/19/how-to-calculate-drag/
7. Kermode, A. C. (2007, ISBN 81-317-1389-X). Flight without formula. Pearson Education.
8. P.Raymer, D. (2006, ISBN:1-56347-829-3.). "Aircraft Design: A Conceptual Approach". AIAA.
9. Prof.T.G.Talapurkara, N. L. (Director). (n.d.). Airplane Design [Motion Picture].Prof.T.G.Talapurkara, N. L. (Director). (n.d.). Flight Mechanics I-II [Motion Picture].

RESEARCH ARTICLE | MAY 22 2023

Mounting plate design for section-IV of an aerospace vehicle under yawing mode

B. Manideep ✉; E. C. Prasad Nidumolu; B. Nagaraj Goud

AIP Conference Proceedings 2492, 040055 (2023)
https://doi.org/10.1063/5.0113329

Mounting Plate Design for Section-IV of an Aerospace Vehicle Under Yawing Mode

B Manideep[1, a)], E C Prasad Nidumolu[2, b)] and B Nagaraj Goud [1]

[1]*Department of Aeronautical Engineering, MLR Institute of technology, Hyderabad, India*
[2]*Department of Mechanical Engineering, MLR Institute of technology, Hyderabad, India*

[a)]Corresponding author: manideepbalusani.9@gmail.com
[b)]Prasadnidumolu555@gmail.com

Abstract. The structure of an aerospace vehicle is a group of several parts. Part IV is one of those sections, which covers electronic subsystems and avionics batteries. Includes a mounting plate interface that can accommodate a thermal battery for power train control and actuation systems. (No.3), 1, main electronic battery, secondary electronic battery pack, contractor box, monitoring circuit battery voltage (BVMC). The thermal battery and main electronic battery are attached to the clamp and holder plate, and the BVMC, secondary electronic battery and contractor box are attached with screws. Modeling was done in ProEngineer Wildfire 5.0 and analysis was done in ANSYS 12.0. The results were analyzed at various loads and, for theoretical calculations, the factor of safety of the mounting plate was within limits, so the overall design was considered reliable and safe.

Keywords— Battery, Analysis, Aerospace, Mounting Plate

INTRODUCTION

Aerospace Vehicle

In aerospace aircraft, the components must be mounted inside the airframe according to the configuration of the system and travel in a defined path with the help of guidance from control electronics must be installed to support all loads. Properties related to mass are important for the aircraft to follow the required path the main mass characteristics of a vehicle are body weight, COG, and MOI. A force exerted by Earth's gravity on the vehicle i.e. Weight. The vehicle's Mass (weight) is distributed efficiently, but knowing the lane distribution and vehicle stability is important. The main thing is to pay attention to the center of gravity and total weight[1-2].

Yaw Motion

During flight, the aircraft usually rotates around its CG. Since the axis of the coordinate system is perpendicular to one another, you must use the centroid to define the 3D coordinate system. The jaw axis is perpendicular to the horizontal and vertical axes. During the yaw movement, the car's nose moves from side to side. Moments can be observed in figure 1[3-4].

The deflection of the rudder of the aircraft allows you to create a yawning motion. The drawbar is articulated at the end of the vertical stabilizer. A slight change in the steering angle at the rudder end will change the lift produced by the longitudinal stabilizer. In the case of the longitudinal stabilizer and the rudder, the lateral force generated depends on the direction of the wing[5]. If the rudder leans towards left, the lateral force acts towards right side.

Advancements in Aeromechanical Materials for Manufacturing: ICAAMM-2021
AIP Conf. Proc. 2492, 040055-1–040055-8; https://doi.org/10.1063/5.0113329
Published by AIP Publishing. 978-0-7354-4438-6/$30.00

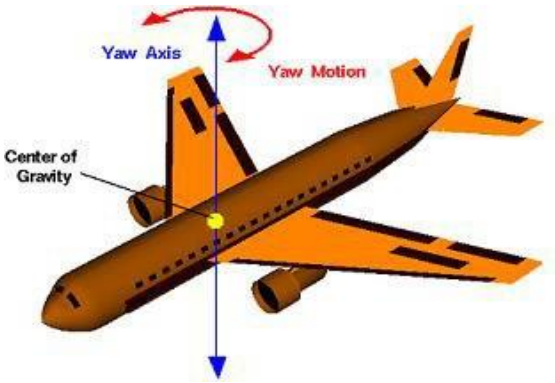

FIGURE 1 Flight Vehicle-Yaw Motion

MODELLING

Aerospace Machinery Part IV Subsystem for Order Fulfillment, Four brackets are used to assemble the section (cell) subsystem.

The Subsystems of mounting Plate are

- Control Actuation System's Thermal Batteries (3No's)
- Battery for Primary Avionics
- Circuit for Voltage Monitoring of BVMC-Battery
- Battery for Secondary Avionics
- Contactor Box.

The total mass of the assembly on the rack is approximately 17.7 kg and the total configuration is depicted as shown in Figure 2[5-8].

The weight of the auxiliary system is transmitted externally to the mounting plate as forces, moments. External load applied is 27.5 g in the vertical direction and 8 g in the horizontal direction, depending on the mass of the subsystem. The mounting plate is design is done and it is tested to check whether it can resist the acceleration loads.

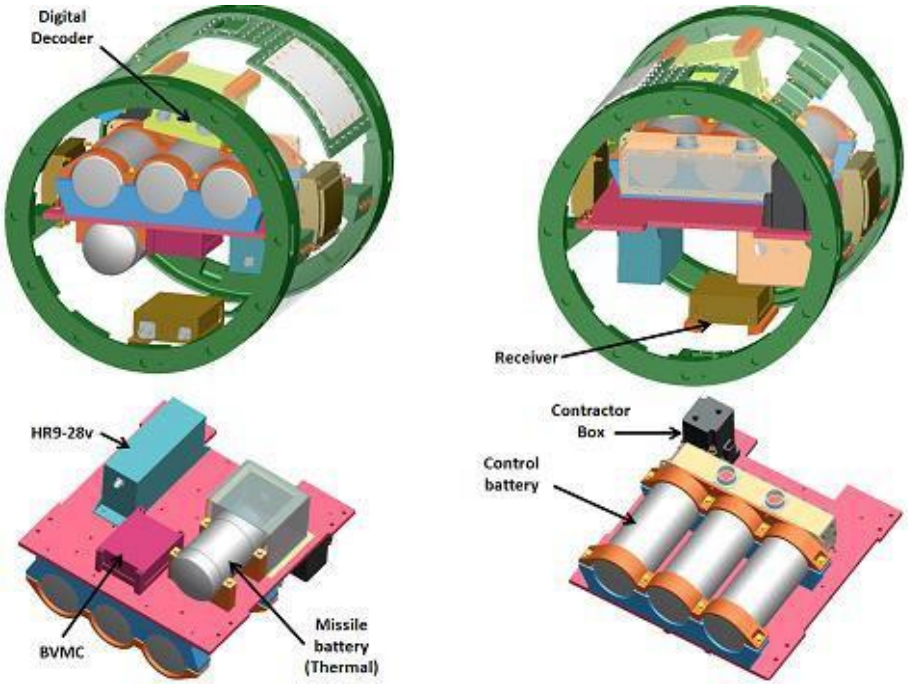

FIGURE 2.Section 4 airframe with packages mounted on plate

INDIVIDUAL PACKAGES DETAILS

Mounting Plate

Plate connected to a subsystem modeled in CAD Pro Engineer as showon in figure 3,

Plate is made up of Aluminium Alloy24345 (WP condition) material, its characteristics are as follows. Plate (IS:736): UTS:405 M Pa, PS:310 M Pa, %e:72

FIGIURE 3. Mounting plate

Control Battery (Thermal) along with Clamp, Brackets

Power for the control operating system is supplied by the control battery (thermostat). The size of the control spindle (thermostat) is Ø80 and 190 in length. The batteries are placed in series as shown in figure 4 with the lower bracket and secured with M5 screws (8 pcs) and upper clamps. Bakelite High Ram Grade F2IS: 2036 material is used for battery mounting and insulation

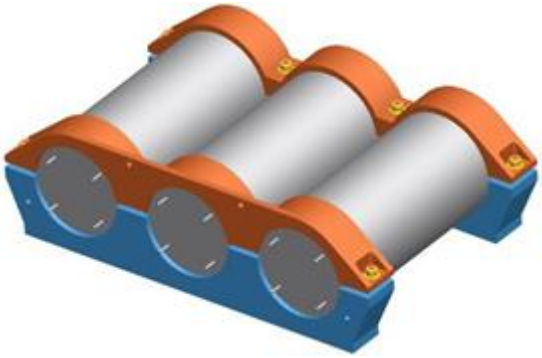

FIGURE 4 Control Battery with Clamps and Brackets

Avionics Battery (Thermal) mounted with Brackets and clamps

Use avionic (thermal) batteries to power the electronic assemblies installed in parts II to IV. The battery size is Ø80 and the length is 145. The battery is on the mounting bracket and is secured with an M5 8 screw and top clamp. Bakelite High Ram Grade F2IS: 2036 material is used for battery assembly and insulation, as shown in figure 5

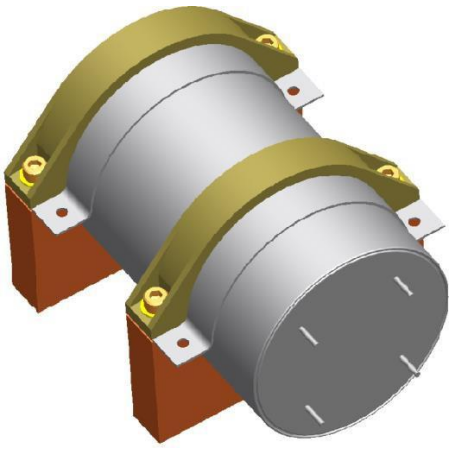

FIGURE 5. 3D Modeling of Avionics Battery Mounted on Clamps and Brackets

BVMC (Battery Voltage Monitoring Circuit) Package

The voltages of the different batteries installed in Part IV are monitored using the BVMC package which is shown in figure 6.For telemetry applications, the battery output voltage is monitored, converted to a digital format and then sent to the built-in computer.

FIGUIRE 6. Model of Battery Voltage Monitoring Circuit Package

HR-59VBattery

The HR59V battery is included to power autonomous aerospace destruction systems, AVDS and 1 Battery provides 5 amps at 9V for external AVDS is required.wchich is as shown infigure 7.

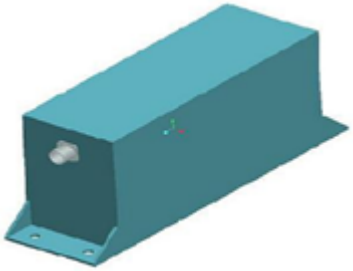

FIGURE:7 Model of HR5-9V

Contractor Box

Use the contractor's box to activate the control pin. Three control pins were connected in series. The battery packs a trigger voltage of 150V. The contractor's box shown in figure 8 receives a command to activate the transmit trigger voltage. These commands are obtained from the built-in calculator.

FIGURE 8. Model of Contractor Box

ANALYSIS

- In the inclined state, the plate experiences an external load and a moment due to the load caused by the packages attached to the plate. The analysis was carried out under inclined conditions [1-8]. The results are observed and tabulated.
- Mounting plates are imported into ANSYS software.
- eight node Shell element(Shell 281) is used to mesh the plate
- Uniform thickness of 8mm is provided.
- Lugs are modeled by a SOLID20, tetrahedral element (SOLID 187).
- The total number of items used in this assembly is 87471.
- No.of elements of plate are 4983.
- No.of elements of Lugs are 82488.

The node of the hole is at the pin level to connect to the stop cell at all degrees of freedom. The plate nodes and the interface holes of the heat sinks are interconnected with all degrees of freedom[9-12]

A Lateral Direction Loading (Yaw)

Each mounted package applies a direct load to each position on the plate, both left and right. Figure 9 shows the boundary conditions and forces acting on the plate. The stresses and flexures that occur on the plates and supports are shown in Figures 10 to 13.

Thermal battery weight (control) with bracket	=8.98Kg
Battery Force in 8g state	= 704.75N
The load onto the plate at each mounting hole	= 88.1 N
Thermal Battery (Avionics) weight with brackets =	2.26Kg
Battery Force in 8g state	= 177.4N
The load onto the plate at each mounting hole	= 44.4N
Battery (HR5-9v) Weight	= 1.95 Kg
Battery Force in 8g state	=150.7N
The load onto the plate at each mounting hole	= 150.7/4

Deflection &stress plot with plate and brackets

BVMC package Weight	= 0.7 Kg
Battery Force in 8g state	= 55 N
The load onto the plate at each mounting hole	= 13. N

Weight of Contact or package = 0.76Kg
Battery Force in 8g state = 59.6N
The load onto the plate at each mounting hole = 29.8 N

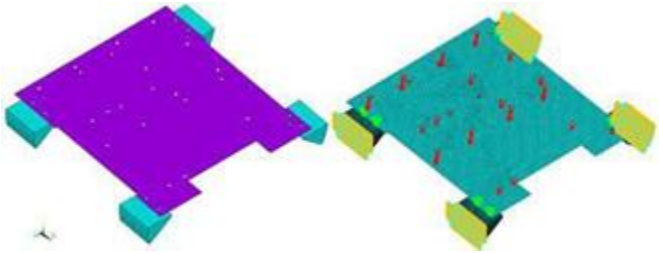

FIGURE 9. FE model and boundary condition plot

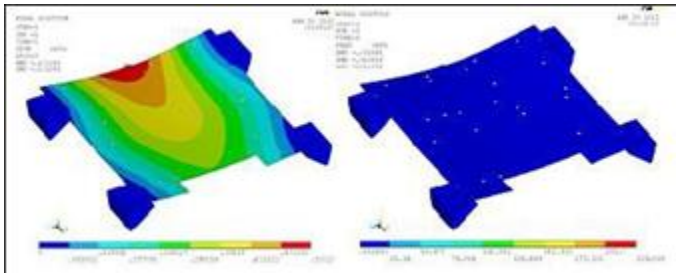

FIGURE 10. Deflection & stress plot with plate and brackets

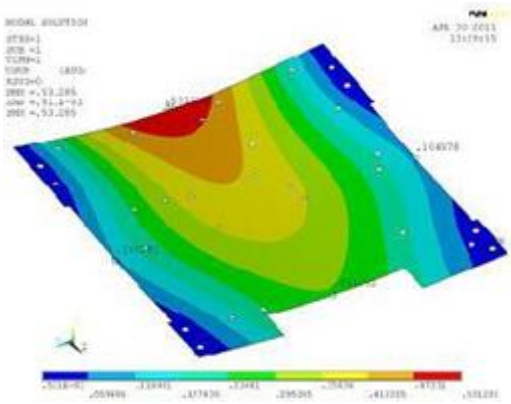

FIGURE 11..Deflection of plate under Yawing

From the Fig11, The max deflection got for Plate is 0.53mm.

RESULTS

The load on the plate is assumed as a rectangular plate having edges loaded in the center. [2], the load of all the packages including plate is 17 Kg. [3-4].

Plate b Length = 400 mm,
Plate a Width = 345mm,b/a = 1.2,
Plate Deflection $=\alpha(p\alpha^2/D)=3282051.3$
Where $\alpha=0.00647$, (based on b/a ratio)
P=Load on the plate= 1334.16 N
$D=Eh^2/\{12(1-\mu^2)\}$
=29.8N

Where E=0.7e5,
h=Thickness of the plate=8mm,
μ=0.3mm
By inducing the above results, Deflection of plate= 0.3 mm
The calculated deviation will be less than the result of FE. This is because the plate is firmly secured on all four sides. Calculations used for qualitative evaluation.

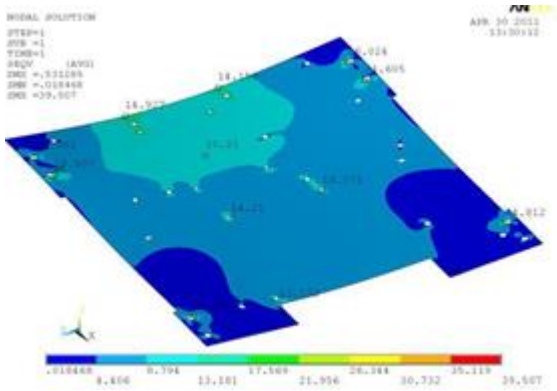

FIGURE 12. Induced Stresses in Plate Yawing

- The maximum deflection achieved with the mounting plate under elevation conditions is 0.055mm.
- The maximum stress obtained for the plate in yawing condition is 66 MPa, with an FOS equal to 4.7.shown in figure 12.

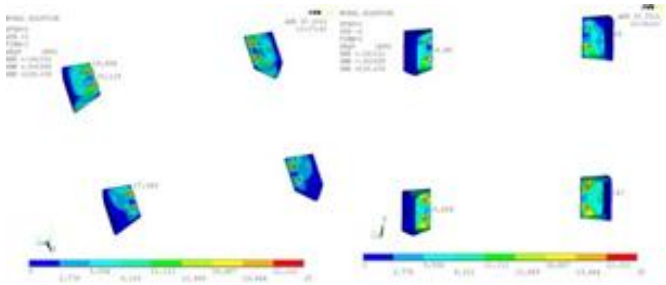

FIGURE13. Induced Stresses on Brackets under Yawing

From Figure 13, Maximum induced Stress for the Plate is =39.51MPa
FOS = 310 / 39.51 =8

CONCLUSION

In general the allowable safety factor for the structural design of aerospace aircraft is considered as 1.5. If the result of maximum deflection achieved with the mounting plate under elevation conditions is concidered, it is within limits, and the maximum stress obtained for the plate in yawing condition is acceptable as the FOS is greater than 1.5. Therefore, the mounting plate design is safe.

REFERENCES

1. *MIL-HDBK-5B, "Metallik Material and Elements for Aerospace Vehicle Structures", Department of Defence (DoD), Washington DC.*
2. "Theory of Plate & Shells-S, Timoshenko", Woinowsky-Krieger, Page No.206, and Table 37)
3. "Introduction to Finite Elements in Engineering Practice" *by "Tirupati R. Chandrapatta and Ashok D. Belugundu"*

4. M Ganesh, Nirmith Kumar Mishra, A. Sai Kumar, V. Vikas, K. Keerthi Krishna "Design and Analysis of UAV for High Payload" in *International Journal of Innovative Technology and Exploring Engineering* (IJITEE) Volume-9 Issue-2, December 2019
5. A. Sai Kumar, M Ganesh, Nirmith Kumar Mishra, Manish Choudhary, Yashwanth Rao Bandari "Design and Development of Man Portable Back Packable Multi-Purpose Drone" in *International Journal of Engineering and Advanced Technology* (IJEAT) Volume-9 Issue-2, December 2019
6. Dhanjal S., Arora R. "Stress analysis of a rectangular plate with circular hole using three dimensional finite element model". *International Journal of Engineering, Business and Enterprise Applications* (IJEBEA), Vol. 12, Issue 1, 2015, p. 77-80.
7. M. L. Pavan Kishore, A. Chandrashekha, M. Avinash and Raunak Das, "Stress analysis of rectangular and square plates with various cutouts",
8. Gunwant D., Singh J. P. "Stress and displacement analysis of a rectangular plate with a central elliptical hole". *International Journal of Engineering and Innovative Technology*, Vol. 3, Issue 3, 2013, p. 387-392.
9. . 'N.Madhavi, Muttangi Sushma, D.Mahesh Kumar, M Satyanarayana Gupta', 'Drones for Agricultural Land prediction', 'International Journal of Innovative Technology and Exploring Engineering (IJITEE)', ISSN: 2278–3075 (Online), Volume-9 Issue-2, December 2019, Page No. 5050-5053.
10. N.Madhavi, Vanaparti Ajay Kumar, Dr. M Satyanarayana Gupta" Design and Analysis of a Fuselage Using Helical Longerons", ijmetmr, ISSN No:2348-4845, Volume 3, sep,2016.
11. N Madhavi, Y.B.SudhirSastry, Pattabhi R.Budarapu," Buckling analysis of thin wall stiffened composite panels", Computational materials sciences, Volume 96, 459-471, Nov2015.

RESEARCH ARTICLE | MAY 22 2023

Flow investigation of a multiple winglet wing model

Swetha Bala M. N. V. S. ✉; Sai Kumar Goud Kalali; B. Nagaraj Goud; ... et. al

AIP Conference Proceedings 2492, 020002 (2023)
https://doi.org/10.1063/5.0113318

Flow Investigation of a Multiple Winglet Wing Model

Swetha Bala MNVS[a)], Sai Kumar Goud Kalali[b)], B. Nagaraj Goud[c)], A Sai Kumar[d)], and M Satyanarayana Gupta[e)]

Department of Aeronautical Engineering, MLR Institute of Technology, Hyderabad, India.

[a)] Corresponding Author: swethabalamlr@gmail.com
[b)] saigoud1034@gmail.com
[c)] nagaraj2107@gmail.com
[d)] ask.mraj@gmail.com
[e)] msngupta.m@gmail.com

Abstract. This study investigates the potential of multiple winglets mounted on a transonic wing. The investigation evaluates the reduction of drag coefficient due to presence of multiple winglets on the basic wing model. Numerical Experiments were adopted for these investigations. The commercial CFD solver ANSYS Fluent was used to perform the aerodynamic investigation. Four different models were evaluated based on the configuration. The first model is a non-winglet model, i.e., the base model. The remaining three models were the wings with the multiple winglets, i.e., 60-Winglet model, 75-Winglet model and 90-Winglet model. The differences in the model were based on the cant angle of the winglet. 3D RANS equation along with one equation Spalart-Almaras turbulence model was used for solving the flow past the wing models. The chord wise pressure distribution, pressure variation over the entire wing, coefficient of lift, coefficient of drag, lift to drag ratio were compared for all the cases.

INTRODUCTION

The aircraft winglets are aerodynamic devices attached to the aircraft wing tips. The purpose of winglet is to reduce drag associated with the creation of lift. Winglet generally facilitate the wing to become more efficient and aerodynamic by producing enhance amount of lift. This implies that the airplane will now require less energy from the engine. This directly results in enhanced fuel economy, low carbon di-oxide emission and most importantly lower operational costs to the airline. A small device incorporated at the wing-tip therefore has huge advantages.

When the airfoil (or the aircraft wing) generates the lift force, the air flows from beneath the wing, moves out around the tip, then to the top of the wing in a circular pattern. Therefore, a circulatory flow is observed at the wing tip. This circulatory fashion air flow is named as “vortex”. And the circulatory pattern of airflow left behind the aircraft wing is technically termed as “wing tip vortices”. Winglet aids to diminish or mitigate the “induced drag”. The aircraft in flight generates a differential in pressure due to the contour of the upper surface and lower surface of the wing. Cut-section of the wing is an airfoil [1]. The air flowing above the airfoil is a low-pressure high velocity air, in comparison with airflow at the lower surface. The air flow in the lower surface is moving slowly with high pressure. The air now tends to move from higher to lower pressure, thereby generating a push force to the airfoil (wing). The difference in pressure (above and lower surface of the airfoil) therefore creates a lift force. This lift force is one of the significant aspects for the successful flight of any aircraft. When the air moves from the lower surface wing root to the upper surface wing root in circulatory fashion, the oncoming air combines with this circulatory air and causes a sudden change in velocity and direction of air. This mixture of air, i.e, spanwise air and chordwise air twists the airflow and hence generates vortices along the trailing edge of the wing.

When the air moves from the lower surface wing root to the upper surface wing root in circulatory fashion, the oncoming air combines with this circulatory air and causes a sudden change in velocity and direction of air. This mixture of air, i.e, spanwise air and chordwise air twists the airflow and hence generates vortices along the trailing

Advancements in Aeromechanical Materials for Manufacturing: ICAAMM-2021
AIP Conf. Proc. 2492, 020002-1–020002-9; https://doi.org/10.1063/5.0113318
Published by AIP Publishing. 978-0-7354-4438-6/$30.00

edge of the wing. induced drag, and imparts downwash. In addition to this the vortices are the vital reason for the wake turbulence. The wake vortices linger in the air for a longer time after an aircraft has passed, being hazardous to the other aircrafts going through these lingering vortices. Hence it is desirous to reduce the induced drag. Generally, a lower induced drag is obtained with elliptical wing, or by increasing the aspect ratio. Therefore, the gliders/long-range airliners have high aspect ratio wings, as a high lift to drag ratio is desirous. Increasing the aspect ratio is not always advantageous, due to structural constraints. The aircraft may also possess low maneuverability. Therefore, the next method to reduce the induced drag, which came into picture is the utilization of winglets.

The winglets increase effective aspect ratio of the wing, thereby changes magnitude and the pattern of vortices. The kinetic energy of the air flow reduces which reduces the quantity of fuel required to perform work on the circulatory air [2]. In the late 1970's, many biologists initiated a study on flying capabilities of birds like eagles, condors, vultures etc., Its was observed that these birds have high-lift wing with feathers that produce slotted wing tips. The study investigated by the biologists revealed that the pin feathers of these birds aided in reducing drag in flight, in addition to these, the pin feathers helped in providing a functionality of ailerons [3].

In the year 1970s, at NASA Langley research centre, Richard Whitcomb investigated the applications of winglets to the modern transport aircrafts. The investigation focused on the presence of vertical fin structure at the wing tip. These investigations were extended with real time flight tests in the years 1979 and 1980. Whitcomb proved that the winglets increased the range of aircraft, by as much as 7% [3]. Spiroid wing tip is a conceptual type of winglet that reduces the induced drag similar to the winglet. It is a closed loop shaped structure [4]. Ilan kroo et al [8] reviewed the various concepts of aircraft types, aerodynamic devices such as winglets, ring and box-wings, to analyze the potential reduction of vortex induced drag without increasing the wing span. Aviation partners tested spiroid winglet on Gulfstream II aircraft and stated that the spiroid winglet reduced the cruise fuel consumption by more than 10 percent. In addition to this, the aviation partners stated that the structure could distort under load which may infer performance loss, Ruhlin, Bhatia and Nagaraja [9] demonstrated that the reduction of flutter speed by adding winglet. The investigation was performed at transonic Mach numbers. The winglets were also proved worthy for low-speed aircrafts such as sail planes.

In addition to the incorporation of winglets for aircrafts, the winglets were proved functional for the hydrodynamic bodies[10]. Winglets were attached to the sailboat keels. The wake downstream of the hydrodynamic boat resembles a biplane system, therefore reducing the induced drag. Imamura et al [11] experimented the application of winglet on the conventional wind turbine and showcased an increase in the power coefficient of the turbine. A multiple-Winglet type of aircraft by Heinz Klug [12] was a created to exploit the non-planar wake geometry and reduces the induced drag and wing stress. In Europe, a special wing was developed named as "Wing-Grid"[13]. In this model, multiple small wing extensions were added to the wing. The multiple wings were incorporated at different angles. So that the vortexes don't interact, and dissipate the vortex energy. In this process the induced drag was reduced.

Colling investigated the incorporation of winglet for the sailplanes[5]. Panagiotou et al. studied the UAV performance with winglet by solving RANS equation. The numerical study investigated the Lift, Drag, and Pitching moment. The improvement in the aerodynamic performance was showcased. Zhang et al analysed winglet configuration for solar aircraft[6]. The study demonstrated the variation of aerodynamic performance of the winglet with different aspect ratios.

The intent of this work is to use ANSYS Fluent for the numerical study of a wing with winglets. By comparison of various design requirements, the most crucial problem is reducing the drag forces developed on the wing. There are huge number of efforts applied for reducing the drag coefficient using winglets as discussed in the literature review. However, it is still a significant interest to research novel configurations of winglet. Therefore, a numerical study i.e., Airflow investigation of different winglet configuration using ANSYS solver are performed, this investigation involves the presence of multiple winglets at the wing tips. To the best of authors knowledge, the multiple-winglet of uniform dimensions were investigated earlier, this research investigate the aerodynamics of multiple winglets of different sizes and at different angle of attack. The aerodynamic evaluation will demonstrate the performance of different winglet configuration. The numerical study of flow-field physics surrounding the winglets and wing are performed using RANS equations and one equation turbulence model will be performed.

METHODOLOGY

The model of the wing employed NACA 66-215 airfoil. The airfoil coordinates were downloaded from airfoil tools website. Appendix-A provides the details of the x, y and Z co-ordinates of the airfoil. To reduce the

computational effort, the model geometry was created with the dimensions compatible to be fitted in any academic wind tunnels. The fig represents the dimensions of the base model, i.e., the wing without any winglets. The root chord of the wing is 165mm, the tip chord is maintained as 80mm. the half span is equal to 330 mm. A sweep of 15 degrees also created.

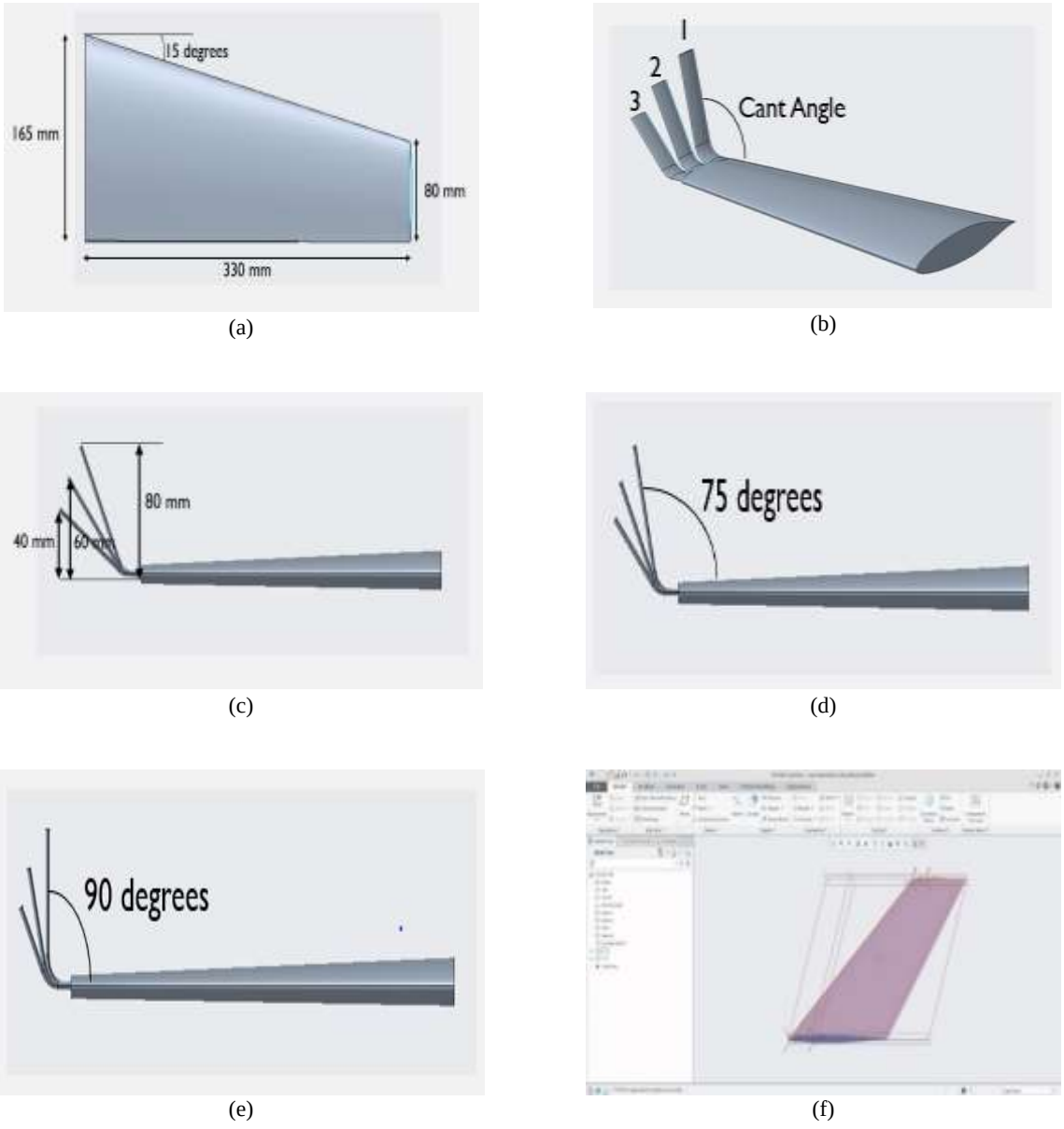

FIGURE 1. (a) Schematic design of the base wing. (b) Multi-winglet model: Winglet number and Cant angle. (c) Geometry of the winglet 60^0 model. (d) Geometry of the winglet 75^0 model. (e) Geometry of the winglet 90^0 model. (f) Final CAD geometry of the ONERA wing.

In addition to the base wing, three other CAD geometries were created to investigate the multiple winglets. The multiple-winglet model were names as Winglet-60-Model, Winglet-75-Model and Winglet-90-Model [17]. Each of the multi-winglet model possessed three winglets (1,2, and 3) as shown in figure. The winglets are inclined at an angle with horizontal, this angle is named as "Cant angle". The winglet has zero twist and zero sweep. The numerical in the name of the winglet-model name corresponds to the cant angle of the first winglet. Therefore,

Winglet-60-Model means the 1st winglet having a cant angle of 60 degrees with horizontal, similarly winglet-75 and 90 model corresponds to the model whose first winglet is having a cant angle of 75 and 90 degrees respectively. The cant angle of winglet 2 and 3 is 15 and 30 degrees higher than the cant angle of 1st winglet respectively. Previous researches investigated the multiple winglets with same lengths. In this investigation, the winglet height with respect to the horizontal was reduced. The first winglet was at a height of 80 mm from the horizontal, the second winglet was at a height of 60mm from horizontal and the third winglet was at 40mm from the horizontal. The figure shows the difference in height for the Winglet-60-Model. The similar height differences were assigned to the other two Winglet-Model.

CFD Validation

NASA Verification and Validation Archive [7] has provided various results that represents geometric configuration and flow condition studies which can be considered during validation of the numerical solver Fluent [14-16]. The ONERA M6 wing is considered in this work for external flows because of its simple geometry. It is also combined with complexities of transonic flow (i.e., local supersonic flow, shocks, and turbulent boundary layers separation). The ONERA M6 wing is a swept, semi-span wing with no twist.

TABLE 1. Boundary Conditions

MACH	Pressure (psi)	Temperature (R)	Angle of Attack (Deg)	Angle of Side-slip (Deg)
0.8395	45.82	460.0	3.06	0.0

Analysis & Numerical Scheme

The numerical solver Fluent is used to perform a flow analysis, for this an experimental case is considered that will be simulated numerically for the code verification, followed by modification of the geometry. To obtain accurate results, it is necessary to select proper solver to perform simulations in order to achieve correct solutions. We selected pressure-based solver over density-based solver. Pressure based solver is generally used for incompressible flow simulation whereas compared to pressure-based solver, density-based solver is used for compressible flow simulations. The main difference between these two solvers is that, the way they couple the energy and momentum equations to obtain accurate result.

We totally considered 4 cases

- Case-1 Normal winglet design
- Case-2 Winglet design with 60^0 Cant Angle
- Case-3 Winglet design with 75^0 Cant Angle
- Case-4 Winglet design with 90^0 Cant Angle

Meshing and creating sections

After creating the mesh, each boundary of the domain is named, the naming of the boundary is performed to assign the boundary type.

For this research work, we have considered the seven boundary types:

Inlet, Outlet, Lower Surface, Upper Surface, Far Field, Symmetry, Winglet.

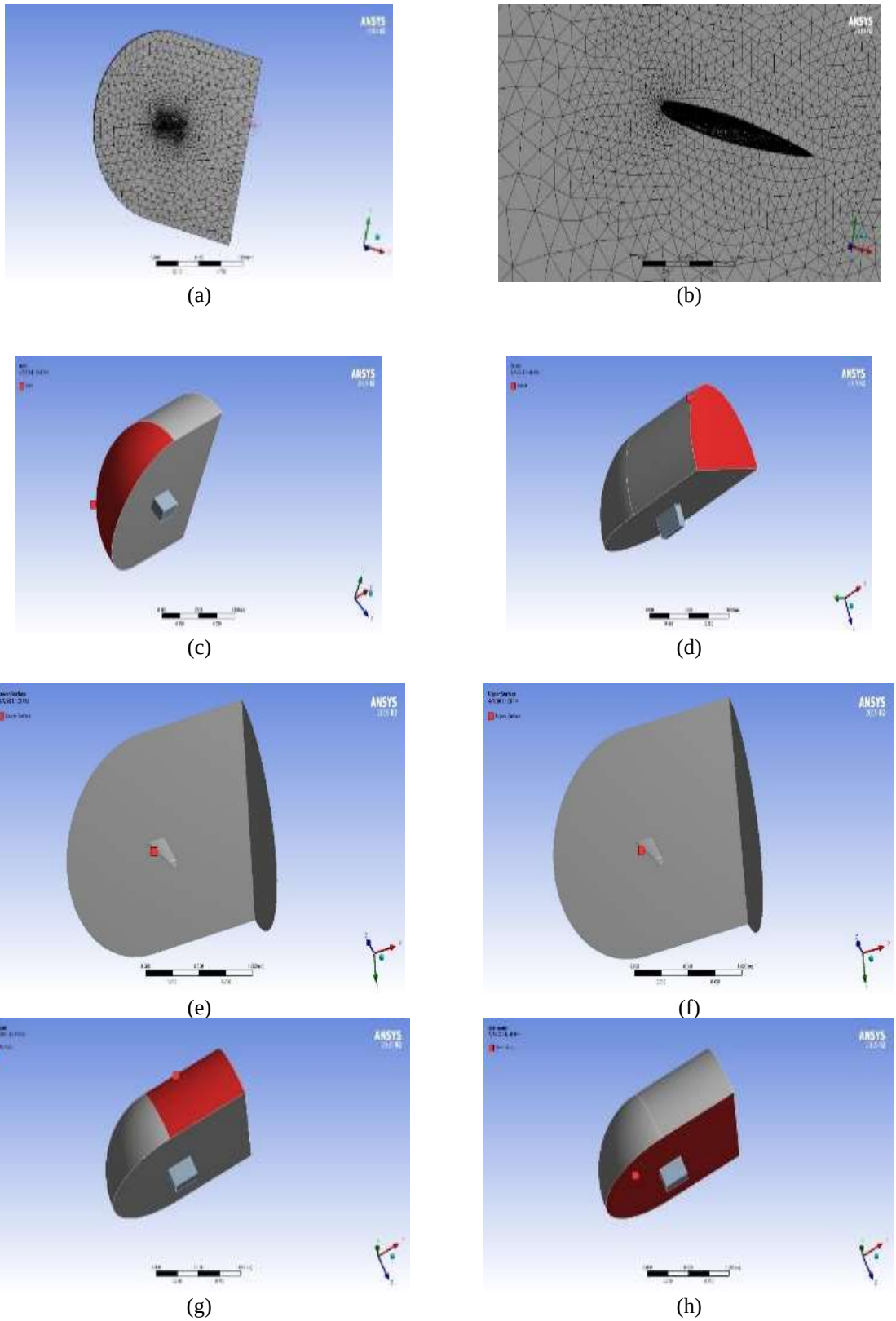

FIGURE 2. (a) Complete mesh of model. (b) Fine mesh. (c) Inlet. (d) Outlet. (e) Lower surface. (f) Upper surface. (g) Far field. (h) Symmetry

Solution Setup

Workbench→ setup→ fluent→ Double Precision→ serial→ ok

- General→ check quality→ report quality→ aspect ratio of mesh found out to be perfect→ solver→ pressure based solver
- Viscous model→ spalart-Allmaras - on→ turbulent viscosity→ none→ vorticity-Based→ On

The Energy model is selected because it accurately combines the velocity with the static temperature for compressible flow.

- Materials→ fluid→ air →create/edit→ rename "air" → change parameters→ ok
- density→ change to → ideal gas.

Under the properties of fluid, fluid is selected as air. The ideal gas equation is chosen for the calculation of density. Three coefficient method is adapted with the reference viscosity = 1.794e-05 kg/m-s.

- Cell zone conditions→ edit→ change medium from "air" → ok
- Boundary conditions→ far Field→ type=inflow→ edit→ Gauge pressure → 45.829 and Mach no 0.8395 → Cartesian coordinate system = (0.9986) in X direction→ (0.0534) in Y direction → turbulent viscosity ratio→ 10→ ok
- OUTLET→ type=Pressure far field→ edit→ Gauge pressure → 45.829 and Mach no 0.8395→ and Mach no 0.8395 → Cartesian coordinate system = (0.9986) in X direction→ (0.0534) in Y direction → turbulent viscosity ratio→ 10→ ok
- Solution initialization→ Standard initialization→ ok→ compute from inlet
- Solution control →modified turbulent viscosity → 4.154059e-05 → temperature → 460
- Calculations→ check case→ everything ok→ give iterations → 15000→ RUN

RESULTS AND DISCUSSION

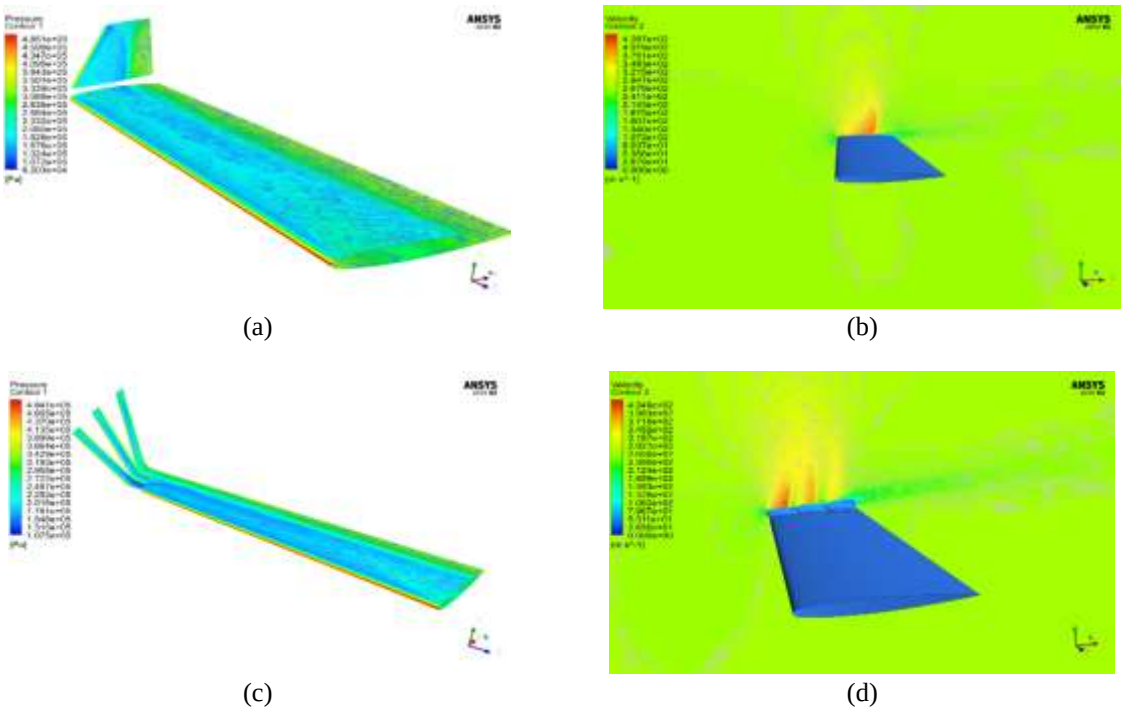

(a) (b)

(c) (d)

FIGURE 3. (a) Pressure contour on winglet case 1. (b) Velocity contour on winglet case 1. (c) Pressure contour on winglet with 60^0 cant angle. (d) Velocity contour on winglet with 60^0 cant angle.

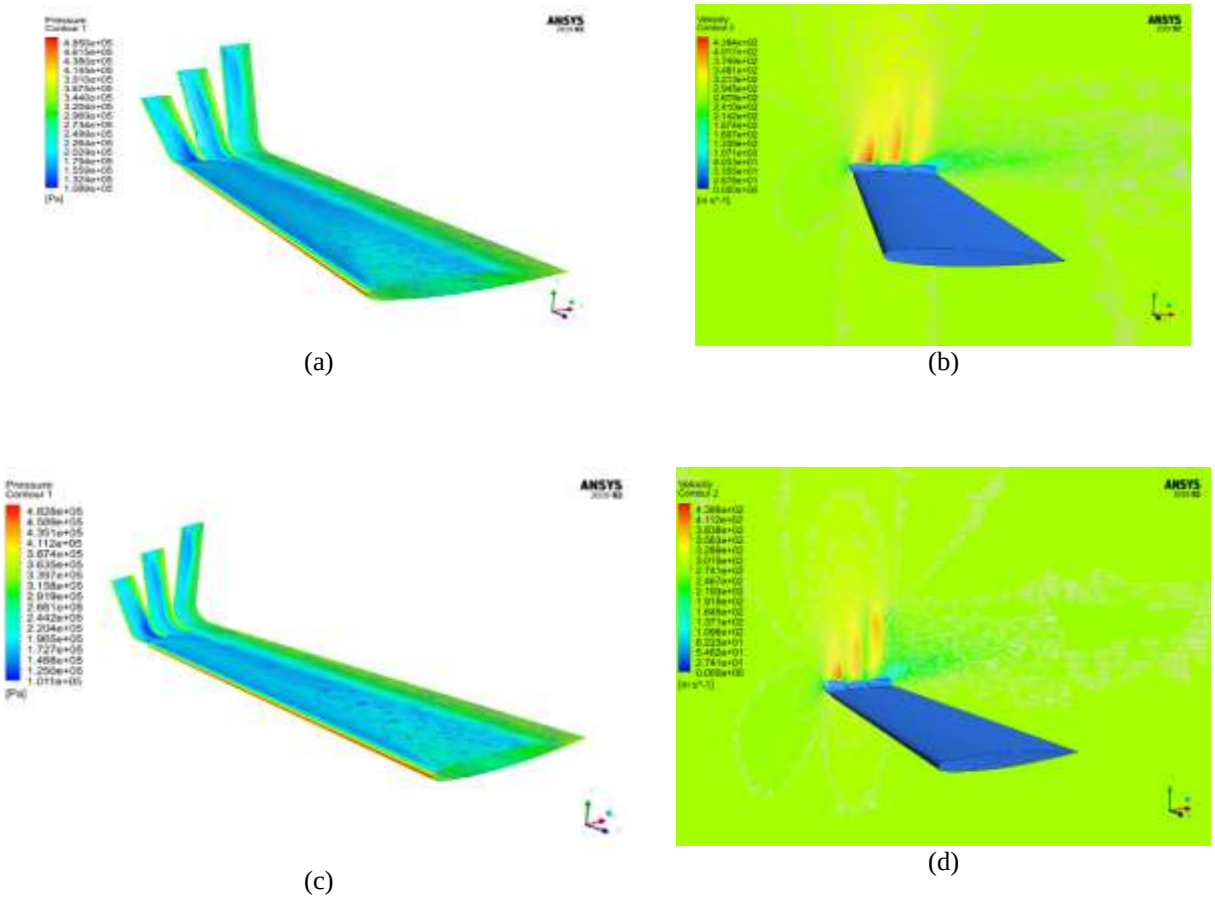

(a) (b)

(c) (d)

FIGURE 4. (a) Pressure contour on winglet with 75^0 cant angle. (b) Velocity contour of winglet with 75^0 cant angle. (c) Pressure contour of winglet with 90^0 cant angle. (d) Velocity contour of winglet with 90^0 cant angle.

According to the mass conservation laws, the amount of air entering the domain must be equal to the amount of air leaving the domain, hence the flux report provides information about the air flow entering the domain through the domain. The figure shows the net difference of the mass flow rate at inlet and outlet, clearly it is visible that the net result is closer to zero. Hence, we may conclude from this report that the mass is conserved in the domain.

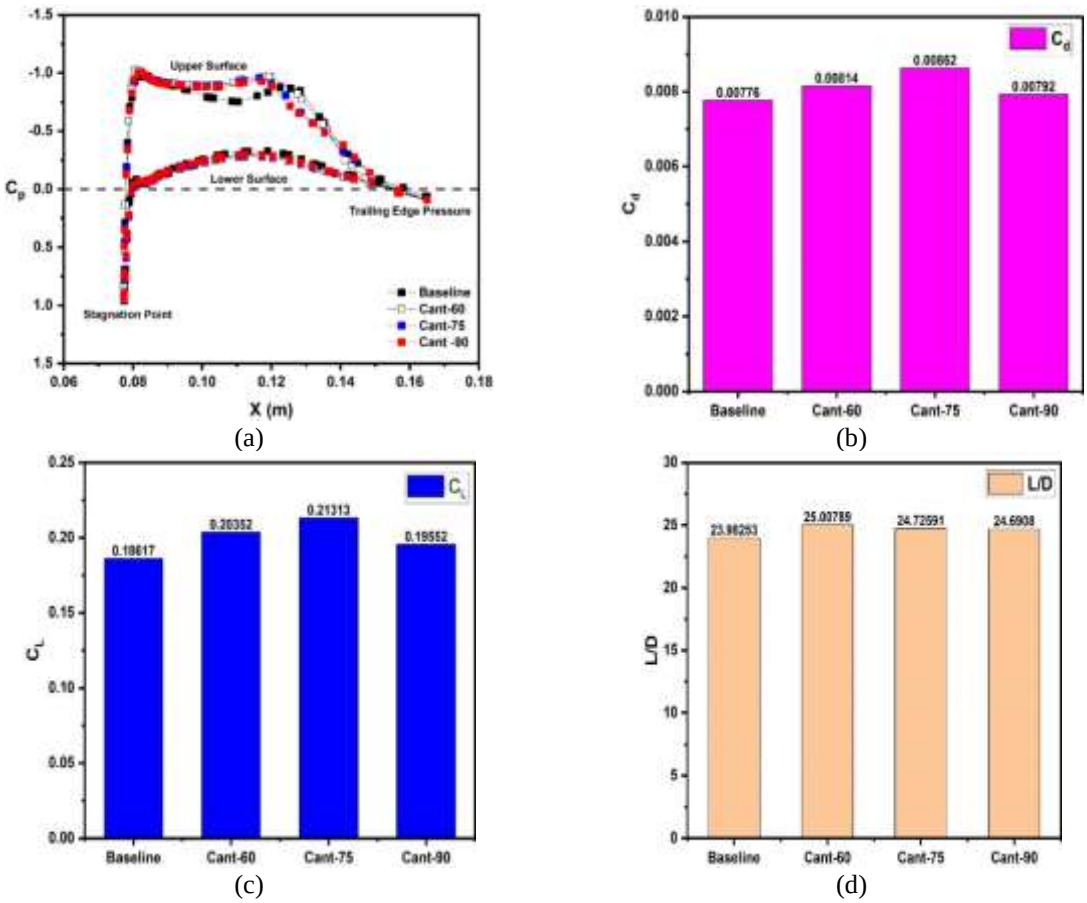

FIGURE 5. (a) Comparison of C_P (vs) X(m). (b) Coefficient of drag. (c) Coefficient of lift. (d) Lift to drag ratio

Fig 5(a), shows the Cp at the end of the wing span, near the winglet. The presence of winglet has increased the suction on the upper layer of the wing. On the closer observation, the Cp above the surface of the Winglet model increases, a higher negative pressure indicates the pressure above the wing surface.

Fig 5(b), shows that the bar chart of coefficient of drag; Maximum drag coefficient was for the cant-75 model.

Fig 5(c), shows that the C_L value is the highest for Cant-75 model. However, the C_L for all the winglet model is seen to gradually increase. The increase in C_L is due to the drop of pressure on the upper surface.

Fig 5(d), shows that the lift to drag ratio of the wing model. Although, Cant-75 model showcased a high coefficient of lift, it has also induced a high co-efficient of drag among all the configurations assessed in the study. The evaluation of L/D will demonstrate the aerodynamic performance of the wing. The below figure shows that the highest L/D ratio was exerted by the 60-winglet.

By the comparison of the coefficient of pressure values in all the models, the winglet 60 model displayed accurate results. The most efficient winglet is winglet 60 model.

CONCLUSION

The numerical experiment has been performed to evaluate the efficiency of multiple winglet wing models. The winglets were mounted at different cant angle with different heights from the horizontal. The C_L, C_d. C_p, pressure distribution was presented in the report. The results of flow visualization are estimated for performance improvement analysis due to the multiple winglet model. The results of flow visualization are presented for performance improvement analysis due to multiple winglet model.

The model with winglet performed low, in comparison with the base line model, i.e., the single-winglet model. The pressure on the upper surface increased further for the models that were equipped with the winglets.

Similarly, the model with winglet attributed to a lower drag, in comparison with the base line model. Among the winglet models, the 60-Winglet model performed sufficiently well. This model possessed the highest L/D ratio, and seemed suitable for the further experimental investigation.

ACKNOWLEDGEMENT

The work was supported by the MLR Institute of Technology. I thank my guide, who greatly assisted the research and improved the manuscript.

REFERENCES

1. J.D..Anderson, Fundamentals of Aerodynamics.
2. Corsiglia, V. R., Rossow, V. J., and Ciffone, D. L. "Experimental Study of the Effect of Span Loading on Aircraft Wakes." *Journal of Aircraft*, Vol.**13**, No. 12, 1976, 968-973.
3. Whitcomb, R. T. *A Design Approach and Selected Wind-Tunnel Results at High Subsonic Speeds for Wing-Tip Mounted Winglets*. 1976.
4. Gratzer, L. B. US Patent: "Spiriod-Tipped Wing," No.5,102,068, Filed 25 Feb. 1991, 2004.
5. Colling, J. D. *Sailplane Glide Performance and Control Using Fixed and Articulating Winglets [Microform]: A Thesis / by James David Colling*.National Aeronautics and Space Administration; National Technical Information Service, distributor, [Washington,DC: Springfield, Va,1995.]
6. SUN, X., HUANG, W., OU, M., ZHANG, R., and LI, S. "A Survey on Numerical Simulations of Drag and Heat Reduction Mechanism in Supersonic/Hypersonic Flows." *Chinese Journal of Aeronautics*, Vol. 32, No. 4, 2019, pp. 771–784.
7. Yates, J. E., and Donald, C. D. *A Fundamental Study of Drag and an Assessment of Conventional Drag-Due-to-Lift Reduction Devices*. 1986.
8. Kroo, I., McMasters, J., and Smith, S. C. "Highly Nonplanar Lifting Systems." *Transportation Beyond 2000: Technologies Needed for Engineering Design*, 1995, pp. 331–370.
9. Ruhlin, C. L., Bhatia, K. G., and Nagaraja, K. S. "*Effects of Winglet on Transonic Flutter Characteristics of a Cantilevered Twin-Engine Transport Wing Model*." *NASA Technical Paper*, 1986.
10. Sloof, J. W. *The Aero- and Hydromechanics of Keel Yachts*.
11. Imamura, H., Hasegawa, Y., And Kikuyama, K. "Numerical Analysis of the Horizontal Axis Wind Turbine with Winglets." JSME International Journal Series B, Vol. 41, No. 1, 1998, pp. 170–176. https://doi.org/10.1299/jsmeb.41.170.
12. Klug, H. G. "Auxiliary Wing Tips for an Aircraft", 1988.
13. Roche, U. La, and Palfy, S. Wing Grid, A Novel Device for Reduction of Induced Drag on Wings.
14. Bara, A.I., Kodavanla, B., Niloufer,, Ruth, E., Satyanarayana Gupta, M, "Natural frequency estimation for unsymmetric cross section of a typical cylindrical shell", International Journal of Mechanical and Production Engineering Research and Development, 2018, 8(4), pp. 45–54
15. Shiva Shankar, K., Satya Narayana Gupta, M., Parthasarathy, G. "Comparative study of CFD solvers for turbulent fuel flow analysis to identify flow nature", International Journal of Civil Engineering and Technology, 2017, 8(5), pp. 386–394
16. Alekhya, N., Prabhu Kishore, N., Satyanarayana Gupta, M., Swetha, Y., Vishnu Vardhan, M., "Comparison of performance of conic and ramp inlet using cfd", International Journal of Mechanical Engineering and Technology, 2017, 8(7), pp. 190–198

RESEARCH ARTICLE | MAY 22 2023

High-speed aerodynamic analysis of a ducted re-entry vehicle

Sai Krishna Konda; Sai Kumar A.

AIP Conference Proceedings 2492, 020001 (2023)
https://doi.org/10.1063/5.0113325

High-Speed Aerodynamic Analysis of a Ducted Re-entry Vehicle

Sai Krishna Konda[1,a)] and Sai KumarA[1, b)]

[1] *Department of Aeronautical Engineering, MLR Institute of Technology, Hyderabad, India.*

[b)] Corresponding Author: *ask.mraj@mlrinstitutions.ac.in*
[a)] k*ondasaikrishna98@yahoo.com*

Abstract. Lower ballistic coefficient offers an optimal re-entry, where the vehicle decelerates higher up in the atmosphere thereby decreasing the imposed aerothermal loads. The current numerical study investigates the effects of an add-on duct to the re-entry vehicle. The add-on duct shall circumvent the vehicle from the shoulder to the base. The add-on duct is expected to improve aerocapture ability of the re-entry vehicle. The drag and ballistic coefficient of the ducted re-entry vehicle will be evaluated and compared with the baseline model. Apart from this, the effect of the distance of the duct from the body will also be investigated. In addition to this the variation of drag and ballistic coefficient due to the change in speed regime will also be investigated. All the investigations will be performed using the CFD solver Fluent. The results reveal that the position-1 has the highest drag when the duct-position is at position-1. When the body is tested at Mach 3, the drag coefficient increased for all the positions. The position-2 showcased the highest drag coefficient for the model. The model tested at Mach 5 revealed that the position-2 of the duct has the highest drag coefficient.

INTRODUCTION

Atmospheric re-entry is a significant aspect in a manned mission. The interplanetary manned mission will require a re-entry into the earth's surface. An efficient re-entry requires an accurate accountability of the re-entry method and trajectory. Care must be taken to determine the gravitational loads acting on the vehicle, the surface temperatures of the body face, most significantly the loads and temperatures shall be withstand able by crew.

Generally, the re-entry in the earth's surface occurs at extreme velocities, velocities that corresponds to the Mach numbers in supersonic and hypersonic regimes. The supersonic and hypersonic flight conditions are related with large number of difficulties, such as aerodynamic problems. There-entry vehicles serves as a tool for space exploration for all the human space missions. The re-entry vehicle must possess emergency abort capabilities, must sustain the crew in the space for a longer period of time, and provide a safe and comfortable re-entry from the deep space into the earth's atmosphere. These versatile characteristics are widely regarded as the basis for justifying the improvement of the re-entry vehicle.

In order to incorporate the basic mentioned attributes in a re-entry vehicle, there is several R & D performed years before the mission is accomplished. The research and development involves the experimental and computational test conducted across various systems of the re-entry vehicle. Apart from the experimental test being performed on the space vehicles of different shapes, there is an excellent computational tool that will allow us to investigate virtually the flow parameters of the various space vehicles. Computational Fluid dynamics [1] has played a significant role in the evaluation of the flow parameters, and research on efficient systems. For the past years, the aerodynamics of space vehicles (re-entry vehicles) has been an interest for the researchers. Especially, the effects on the drag coefficient due to a physical modification in any vehicle has piqued the curiosity of several aerodynamicists. The re-entry vehicles have always been a subject of vital interest by the researchers due to immense number of practical implications.

Axisymmetric Shape - This is a simplest shape being employed or considered by various vehicles. Most commonly the fore-body of this type of vehicles is a spherical shaped blunt body. The bluntness is required to

Advancements in Aeromechanical Materials for Manufacturing: ICAAMM-2021
AIP Conf. Proc. 2492, 020001-1–020001-8; https://doi.org/10.1063/5.0113325
Published by AIP Publishing. 978-0-7354-4438-6/$30.00

allocate the payload in the vehicle, and create enough drag during the landings. It is a combination of Fore-body and Aft-body. The fore-body nose can have any diameter, depending on the requirement and the aft body. The variation of fore-body and aft-body depends on the application of the space vehicle, the number of crew, the payload, etc. Axisymmetric body with lengthier aft body, in comparison with the fore-body/nose.

Various researchers have investigated the aerodynamics of re-entry bodies:

Mehta [2] used numerical simulation to analyses the flow past Apollo and Orex re-entry vehicle. The author demonstrated the flow-field characteristics of bow shock,expansion fan,sonic line,and re-circulating zone in the numerical computations. The effects of module geometrical parameters on the flow field, such as spherical cap radius, shoulder radius, cone angle, and back shell inclination angle, which will provide a useful input for re-entry vehicle optimization.

Mungiguerra and Fedele [3] investigated the MINI-IRENE capsule. The Flight Demonstrator, which is a novel concept capsule. The demonstrated possessed a variable geometry, the purpose of the variable geometry is to enhance the range of available platforms for retrieving the payloads and data from LEO. The significant characteristics of this vehicle was the “umbrella-like" deployable front structure. The purpose of this structure was to reduce the capsule ballistic coefficient, which lead to acceptable wall heat fluxes, mechanical loads, stability and final descent velocity.

Zhou et al. [4] investigated the various aerodynamic configurations of the capsuled for the reentry manned vehicle. The authors stated that the capsule with high L/D ratio have statically stable trim points, and this is undesirable, because when the vehicle flies past the trim point during re-entry the consequence may be disastrous. The authors proposed an effective design methodology for enhancing mono-stability features of re-entry capsules without compromising the lift-to-drag ratio. The results were demonstrated based on CFD analysis to understand the flow characteristics.

Raj et al. [5] used numerical simulations to propose add-on to the existing re-entry vehicle. A circumventing duct was proposed in their work. Different designs were simulated to evaluate the drag-coefficient and ballistic coefficient of the vehicle with the duct. The results revealed that the drag from all the models was increased with the presence of duct circumventing the re-entry model. Sharma et al. [6] performed numerical simulation to investigate a novel concept i.e., a flow-through duct in blunt cylinder replicating a re-entry vehicle. The effects of aerodynamic heating and drag were evaluated by using steady state simulations on the axisymmetric body. The study revealed that the smaller ratio of duct diameter have shown significant reduction of peak surface fluxes.

Savino et al. [7] focused on the design of deployable and thermal protection system. Two sphere cone configurations were investigated from an aerodynamics point of view. An evaluation of thermal and aerodynamics loads was performed to assess the longitudinal stability of the capsule. Chang et al. [8] investigated the aerodynamic characteristics of the re-entry vehicle using CFD. The authors focused on the hypersonic flow regime over a setoff capsule configuration. The results demonstrated a good agreement between numerical and experimental study. The surface heat flux and aerodynamic force predictions for the capsule configurations are discussed in detail.

White et al. [9]compared four different configurations to analyses the aerodynamics of the bionic and capsule configuration. The volumetric efficiency, peak deceleration, peak dynamic pressure, available downrange, available cross range - (all during re-entry), handling qualities and controllability, stagnation point heating rates and temperatures, and technology readiness level were considered as the parameters for evaluating the performance characteristics.

Although numerous works focused on the re-entry vehicle, few works discussed the drag characteristics and ballistics of the bluff body. In this work a quantification with a systematic analysis of the flow over a bluff body is performed to evaluate the drag and ballistic co-efficient of the blunt body with circumventing duct [10&11]. The blunt body considered for this study will be an axisymmetric body.

MODELING OF GEOMETRY

Ballistic coefficient determines the amount of deceleration a body possess. The Fig 1.Illustrates the two commonly used re-entry vehicle. The body on the left is a streamlined body, the stream line bodies have high ballistic coefficient. On the other side, the body is a blunt vehicle with low-ballistic coefficient. Generally, the body with low-ballistic coefficient has higher deceleration forces. Therefore, during re-entry low-ballistic coefficient is preferred. The difference between both the bodies is with respect to the aft body, on the left side the aft-body is increasing its diameter, on the right side, the diameter of the aft body is reducing.

FIGURE 1. Blunt versus Streamlined Vehicle.

In this research, we are investigating the ballistic coefficient and drag coefficient for the body which has a constant aft body diameter, as shown in figure. The body has a diameter of 15mm. The length of aft body is 15mm. The next model, which is targeted to improve the deceleration forces is the model with a duct circumventingaft body of the figure 1model. The figure 2 shows, model with the duct.

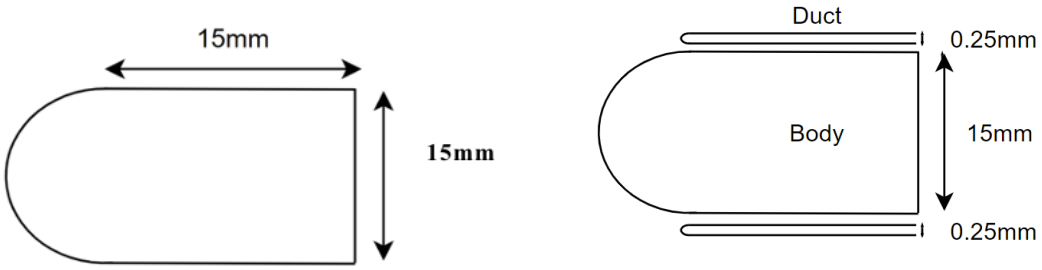

FIGURE 2. Dimensions of the main body; (b) Dimensions of the main body with duct.

The duct is along the length of the model. The lip radius of the duct is 0.125mm. The research involves the investigation of the airflow characteristics i.e., the drag characteristics and ballistics coefficient of the model with duct placed at various positions. The distance between the duct and the aft body is varied as follows:

TABLE 1. Positions of the Duct.

Model	Distance of Model with the body (mm)
1	0.25
2	0.35
3	0.45

Three different models are created by considering the different positions of the duct. The geometry is created in the ANSYS Design modeler. Each position of the duct is investigated for three different Mach numbers 2, 3 and 5.

CFDVALIDATION AND GRIDINDEPENDENCE STUDY

In order to validate the numerical scheme, an experimental study by white[9] is considered. The investigated experimentally, the flow past a bluff body having 4 inches diameter. The experimental study involved the flow of Mach 2.23. The experiment boundary conditions are tabulated.

TABLE 2. Experimental Boundary Condition.

Mach	Angle of Attack	Pressure altitude
2.23	0	32,000 Feet

The dimensions of the experimental model are illustrated in the Figure 3.

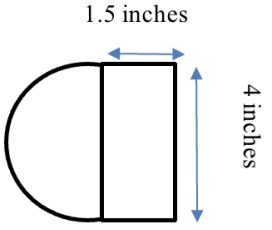

FIGURE 3. Experimental Model.

The Figure 4(a). Illustrated the comparison of local to free-stream pressure ratio on the blunt body.Other graph, clearly illustrates that with the considered numerical scheme, the solver fluent has resulted in identical pressure distribution. Therefore, this demonstrates a successful code verification to perform consequent CFD simulation.

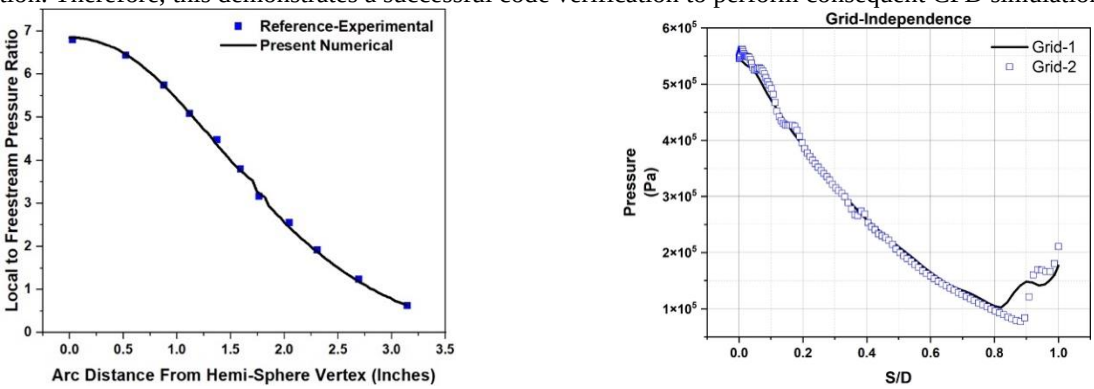

(a) (b)

FIGURE 4. (a) Experimental Vs. Numerical Pressure Distribution; (b) Grid Independence Study.

The domain was discretized into unstructured elements. Inflation layers were applied at the wall. Grid refinement study was performed with 85443 And 185975 (Number of elements), Fig 4(b). Shows the comparison of pressure for the two grid sizes. It is evident from the graph that there is a minimal difference in pressure due to grid refinement. Therefore the grid independence is satisfied. And for the consequent Simulation grid-2 was employed. The first and foremost task in a CFD investigation is the grid independence study. Therefore, in this study the grid independence is performed on the bluff bo.The numerical solver Fluent is used to perform a flow analysis, for the duct is considered that will be simulated numerically, followed by modification of the geometry. In this research work, we considered 3 positions at 3 Mach numbers that is at Mach 02, at Mach 03 and at Mach 05.

ANALYSIS

Modeling capabilities for incompressible and compressible, laminar and turbulent fluid flow issues are provided by ANSYS FLUENT. It is possible to conduct steady-state or transient analyses [10]. ANSYS FLUENT combines the ability to simulate complicated geometries with a wide range of mathematical models for transport processes (such as heat transfer and chemical reactions).Various important elements are offered to allow simulation of fluid flow and related transport phenomena in industrial equipment and processes. Porous media, lumped parameter (fan and heat exchanger), stream-wise periodic flow and heat transfer, swirl, and moving reference frame models are all examples of these. Modeling single or many references is possible with the moving reference frame family of models.

ANSYS FLUENT is powerful CFD software available in the market. It works on finite difference method (FVM) to solve the complex numerical solutions. ANSYS WORKBENCH provides easy accessibility for users. The GUI (graphic user interface) and sequential order of solving the problem is much easier to understand. ANSYS DESIGN MODULAR provides its own set of tools to build and edit the geometry. Using these tools, we can quickly create parts with 2D and 3D wireframe, surface, and solid geometry[9-11]. It also allows importing geometry form other design software like CATIA, SOLIDWORKS, and CREO etc.

For this research work, we have considered the seven-boundary type:

1. Inlet
2. Outlet
3. Axis
4. Duct fore-body
5. Duct rare body,
6. Fore-body,
7. Rare body

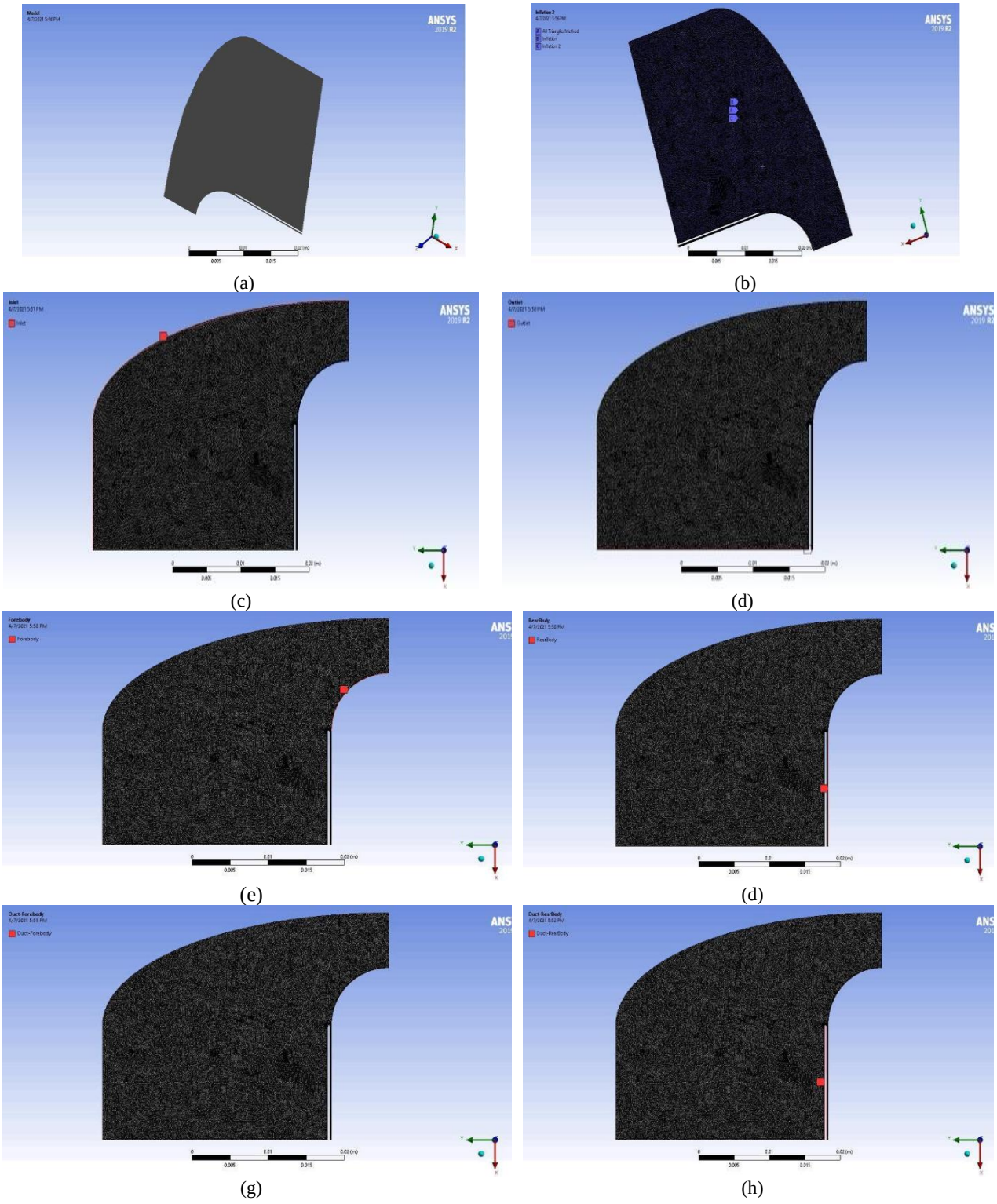

FIGURE 5. (a) CAD Model Generated; (b) Meshing of Model; (c) Named Sections Inlet; (d) Named Sections Outlet; (e) Named Sections Fore body; (f) Named Sections Rare body; (g) Named Sections duct Fore body; (h) Named sections duct rare body.

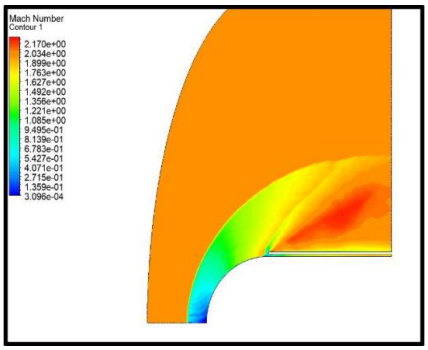

(a)

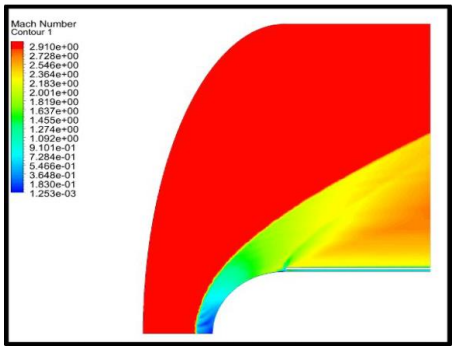

(b)

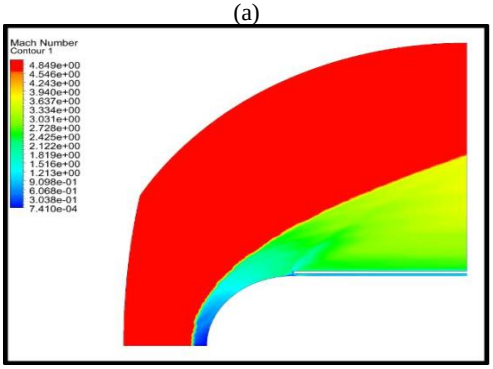

(c)

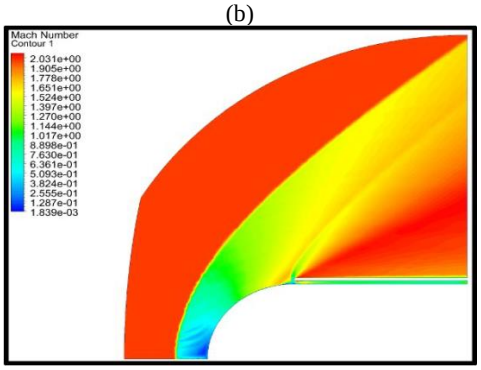

(d)

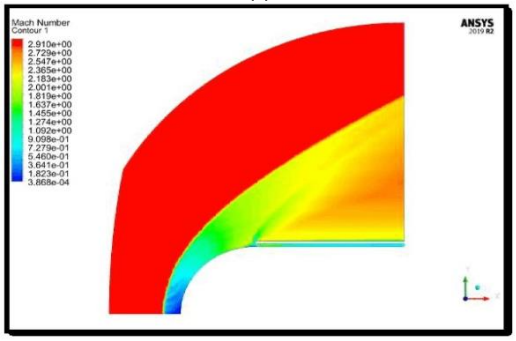

(e)

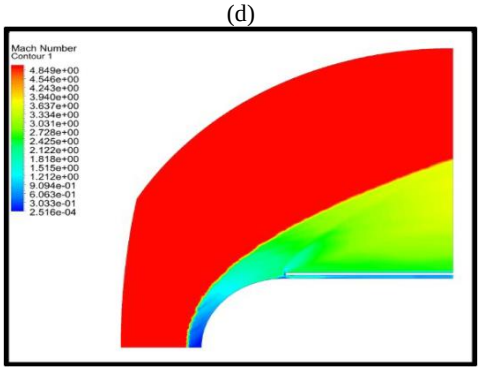

(f)

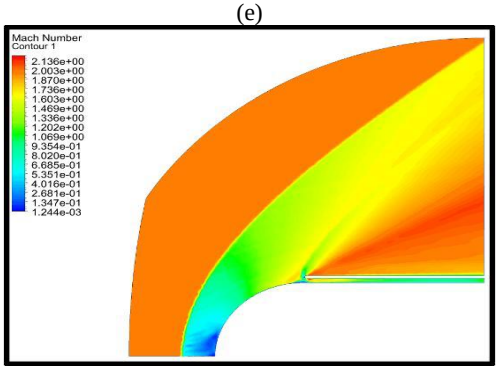

(g)

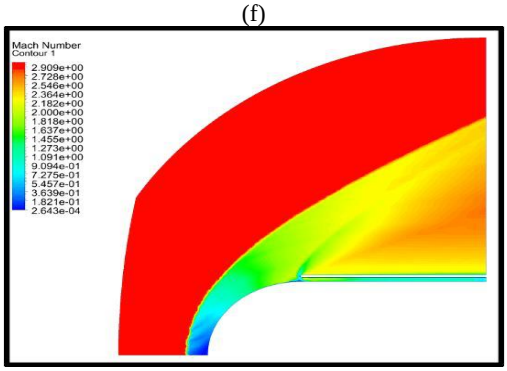

(h)

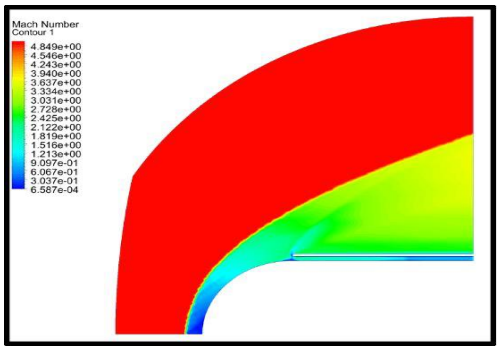

(i)

FIGURE6. (a) Position 1 Mach Contourat Mach 02; (b) Position 1 Mach Contour at Mach 03; (c) Position 1 Mach Contour at Mach 05; (d) Position 2 Mach Contour Mach 02; (e) Position 2 Mach Contour at Mach 03; (f) Position 2 Mach Contour at Mach 05;(g) Position 3 Mach Contour Mach 02; (h) Position 3 Mach Contour at Mach 03; (i) Position 3 Mach Contour at Mach 05.

All constraints are converged. But we are mainly focused on Mach contour. So, we analyse all cases Mach contours.The distance between the duct and the aft body is varied. Three different models are created by considering the different positions of the duct. The geometry is created in the ANSYS Design modeler. Each position of the duct is investigated for three different Mach numbers 2, 3 and 5. Duct Position 1 Mach Contour at Mach 02, Duct Position 1 Mach Contour at Mach 03, Duct Position 1 Mach Contour at Mach 05, Duct Position 2 Mach Contour Mach 02, Duct Position 2 Mach Contour at Mach 03, Duct Position 2 Mach Contour at Mach 05, Duct Position 3 Mach Contour Mach 02, Duct Position 3 Mach Contour at Mach 03, Duct Position 3 Mach Contour at Mach 05.

RESULTS AND DISCUSSION

The results evaluated the aerodynamic characteristics of the model with different duct positions. The figure represents the Cd obtained at different positions of the duct for the different Mach number. The results reveal that the position-1 has the highest drag when the duct-position is at position-1. When the body is tested at Mach 3, the drag coefficient increased for all the positions. The position-2 showcased the highest drag coefficient for the model. The model tested at Mach 5 revealed that the position-2 of the duct has the highest drag coefficient.

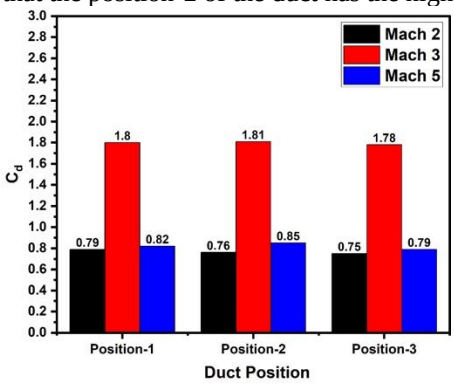

FIGURE 7. Coefficient of Drag vs Duct Positions.

The drag characteristics were different for all the cases. In order to quantify the ballistic coefficient, the drag values along with the reference area is used. The following formula is used to calculate the ballistic coefficient:

$$\beta = \frac{m}{C_D S}$$

M is the mass of the body which is assumed as 75 grams based on the size of the model, $C_d$is the drag coefficient and S is the reference area.

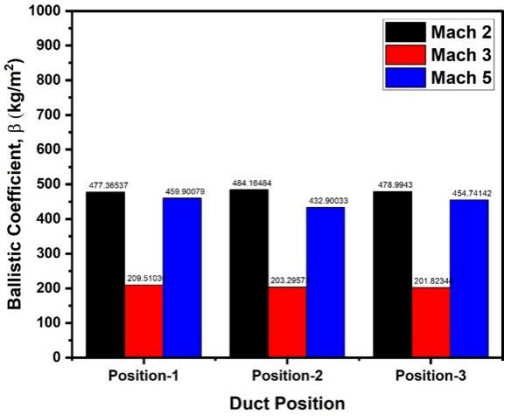

FIGURE 8. Ballistic Coefficient vs Duct Position.

The **Figure** 8. Illustrates the ballistic coefficient vs, the duct position. The lesser the ballistic coefficient the higher the deceleration forces that can withstand the model. The model at Mach 2 revealed that the position-2 has the highest ballistic coefficient. For the Mach-3, the position-1 and for Mach-5 the position-1.

CONCLUSION

Numerical experiments were performed on the blunt model to investigate and account the coefficient of drag acting on the model at different Mach numbers. In addition to the drag coefficient, ballistic coefficient is also evaluated. The study targeted the evaluation of the duct circumventing the aft body of the re-entry vehicle. The circumventing duct was varied with respect to the distance from the aft-body and the circumventing duct.

Three positions were evaluated, at three different mach numbers i.e., 2, 3 and 5. The contours illustrated the shock waves and the various configurations of the flow fields. The drag coefficient revealed different outcome for each position and mach number. The ballistic coefficient revealed that the for Mach-2, the position-1 showed lower values of ballistic coefficient this indicates that this position has the highest deceleration forces. And for Mach-3, the position-3 revealed a lower ballistic coefficient, and at Mach-5 the position-2 has the highest deceleration forces. The model helps to increase re-entry vehicle drag, resulting in a more stable and safe landing.

ACKNOWLEDGMENTS

This research was supported by MLR Institute of Technology. I thank my guide, who provided insight and expertise that greatly assisted the research and improved manuscript.

REFERENCES

1. Van Leer, B., and Powell, K. G. *Encyclopedia of Aerospace Engineering*, (2010).
2. Mehta, R. C. *Indian Journal of Engineering and Materials Sciences*, **15**, 459–466 (2008).
3. Fedele, A., and Mungiguerra, S. *Acta Astronautica*, **151**, 324–333 (2018).
4. Chen, B., Zhan, H., and Zhou, W, *Acta Astronautica*, **106**, 160–169 (2015).
5. Sharma, G., Yadav, R., Studies, E., and Kulkarni, P. 17thAnnual CFD Symposium , August 11-12 , 2015.
6. Carandente, V., Zuppardi, G., and Savino, R. *Acta Astronautica*, **93**, 291–303 (2014).
7. Chang, C. L., Venkatachari, B. S., and Cheng, G. C. Collection of Technical Papers - AIAA/ASME/SAE/ASEE 42nd Joint Propulsion Conference, 6, 4498–4519 (2006).
8. Kumar, A.S., Shivaleela, M., Srilekha, L., Sruthi, B., "Flow field analysis of rudder in CFD" *AIP Conference Proceedings*, 2021, 2317, 040011
9. Sai Kumar, A., Ganesh, M., "Evaluation of effect of shape and length of spike on aerodynamics performance of supersonic axi-symmetric bodies",*International Journal of Mechanical and Production Engineering Research and Development*, 2018, 8(1), pp. 133–144.
10. Ganesh, M., Bindu, G.H., Kumar, A.S., "Modeling and analysis of a composite wing for missile structure",*International Journal of Mechanical Engineering and Technology*, 2017, 8(6), pp. 338–347.

RESEARCH ARTICLE | MAY 22 2023

Mechanical properties of green composites with hemp/sisal fiber and novolac resin

Hrithik Porwal ✉; Gatla Soumya; P. Hastu Sruthi Bhavana; S. Chandrashekhar; A. Vivek Anand

AIP Conference Proceedings 2492, 040009 (2023)
https://doi.org/10.1063/5.0113265

Mechanical Properties of Green Composites with Hemp/Sisal Fiber and Novolac Resin

Hrithik Porwal[1, a)], Gatla Soumya[1, b)], P.Hastu Sruthi Bhavana[1, c)], S.Chandrashekhar[1, d)], A. Vivek Anand[1, e)]

[1]*Department of Aeronautical Engineering, MLR Institute of Technology, Hyderabad, India.*

[a)] Corresponding Author: Hrithikporwal588@gmail.com
[b)] gatlasoumya99@gmail.com
[c)]Phsruthibhavana007@gmail.com
[d)] chandrashekharshedole@gmail.com
[e)]vivekanand7adr@gmail.com

Abstract. The natural fibres are lightweight, economic and easily biodegradable and are eco-friendly due to which a study is performed to prepare a green composite whose both constituents' fibre and matrix are derived from nature. The reinforcement used for this study is Hemp and Sisal which are derived from the leaves of the Hemp and Sisal plant. The composites of these materials have high specific strength and good mechanical properties. The matrix used is Novolac also called Cardanol Phenol-Formaldehyde derived from Cashew nutshell. Composite laminates were prepared using the materials and were tested for their water absorption properties and tensile properties. From the study, it was found that the sisal fibre reinforced with Novolac resin has better water absorption properties than Hemp. Also the tensile strength of the Hemp laminate was greater than the Sisal laminate and Hemp-Sisal laminate. The Hemp-Sisal laminate showed intermediate properties between Hemp laminate and Sisal laminate.

Keywords: Green composite, Laminate, Novolac resin, Hemp fiber, Sisal fiber

INTRODUCTION

The use of natural fibre as reinforcement in composites is greatly reaching its new height nowadays due to the fact that environmental damages caused by the traditional non-renewable polymer-based composites [3]. When the non-renewable polymer-based composites are recycled, they release harmful gases such as etc as these composites use the resin which is derived from petroleum-based products. Due to this reason many of the researchers are developing new materials which are cost-effective, easy to fabricate and can be biodegradable. These materials are green composites fabricated using the natural fibres of the plants. Natural fibres such as Hemp, Sisal, Coir, Jute, Banana fibre, Flax fibre etc are some examples of natural fibres which are most commonly used by researchers and industry. The plant extracted natural fibres has a high strength to weight ratio, low density, good modulus, high specific strength along with that they are economical and are abundantly available in nature.

In aerospace and automobile industries the weight of the material is the most critical parameter since composites of natural fibres are light in weight and economical because of which they are getting more attention from these industries [9]. Apart from the advantages that natural fibres possess they also have some drawbacks which are not so critical but it is very important to know. The natural fibres show different strengths depending on which soil and in which atmosphere they are cultivated and moreover these fibres do not have a constant diameter as other synthetic fibres due to which the properties of the composites may vary [7].

For our work, we have used Hemp and Sisal fibre due to their more abundance and composites of these fibres reinforced with Novolac resin are being tested for water absorption and tensile strength.

Advancements in Aeromechanical Materials for Manufacturing: ICAAMM-2021
AIP Conf. Proc. 2492, 040009-1–040009-8; https://doi.org/10.1063/5.0113265
Published by AIP Publishing. 978-0-7354-4438-6/$30.00

Hemp fibre is also called cannabis Sativa. This fibre mostly cultivated in Asia. This plant has been cultivated res in Asia for more than 12000 years. Apart from Asia now Hemp is grown in the UK, America, Europe, etc. The fibers in the Hemp plant are contained within the tissues of the stem which allows the Hemp plant stem to be erect in doing so the fibres provide high strength and stiffness to the plant [2]. The high strength and stiffness of the fibres make them to be used as fillers for composite materials. The main constituents of the Hemp fibre are cellulose, Hemicellulose, Lignin and Pectin.

Sisal is also called Agave Sisalana. Sisal fibre is extracted from the leaves of the Sisal plant. Moreover, the sisal plants are grown in many countries but are native to Southern Mexico. Similar to the Hemp fibre the fibres of Sisal have high stiffness and strength. Mostly the fibres are used to make ropes but this fibre can act as a better option as reinforcement for the composites. The fibre length of the Sisal plant is small compared to the hemp fibre as well as the fibre diameter of the sisal fibre is lesser compared to hemp. The constituents of the Sisal fibre are similar to that of Hemp fibres but their percentage is different [11].

EXPERIMENTAL PROCEDURE

Specimen Preparation and Fabrication Process

Materials

The matrix material used in this study is Novolac whose physical name is cardanol phenol-formaldehyde supplied by Axotherm Industries Ltd. Hemp and Sisal are the natural fibres that are used as reinforcement. The typical chemical composition of the Hemp and Sisal fibre is presented in Table 1. The mechanical and physical properties of the Hemp and Sisal fibres used in this study are presented in Table 2. The images of the Hemp, Sisal and Resin are shown in figure 1.

TABLE 1. Typical Chemical Composition and Structure Parameters of Hemp and Sisal Fiber [2]

Fiber	Cellulose	Hemi-Cellulose	Lignin	Pectin	Wax	Cell Length	Spiral Length (deg)	Moisture Content (%)
Hemp	74.4	17.9	3.7	0.9	0.8	23.0	6.2	10.8
Sisal	65.8	12	9.9	0.8	0.3	15	10-20	10

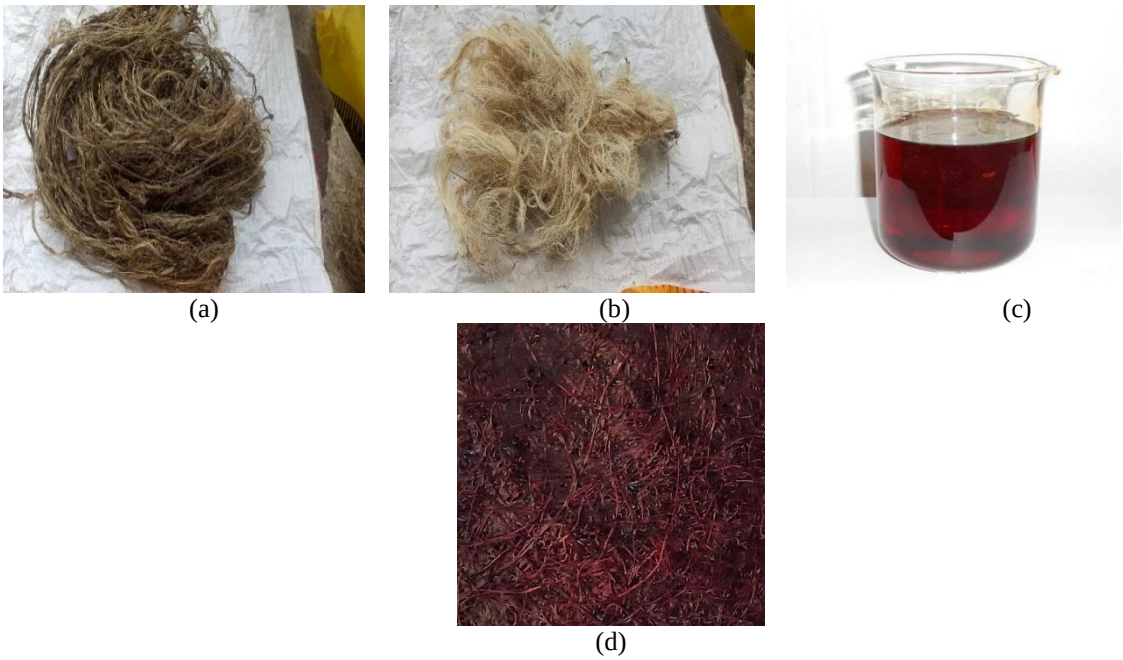

(a) (b) (c) (d)

FIGURE 1. Raw material (a) Hemp fiber (b) Sisal fiber (c) Novolac Resin (d) Laminate Specimen

TABLE 2. Mechanical and Physical Properties of Hemp and Sisal Fiber [2]

Fiber	Density (gm/cm^3)	Elongation to break (%)	Tensile Strength (MPa)	Young's Modulus(GPa)
Hemp	1.14	1.6	690	30-60
Sisal	1.45	5-14	400-700	9-12

Processing

The composite material was prepared using the hand lay-up manufacturing technique [22-24]. Firstly, both the sisal fiber and the hemp fiber were given an alkali treatment with 10% concentrated NaOH solution so that the impurities such as the dust particles, wax, hemicellulose (i.e., stem solid particles) etc. can be removed. The alkali treatment not only removes the dirt but also makes the fibre surface rough which helps in better adhesion of matrix on the fiber and also it makes the diameter of the fiber smaller which increases the aspect ratio of the fiber [16]. In the NaOH solution, the fiber was left for 8 hours and after that, the fibers were cleaned with normal water thoroughly and left to dry in the sun for 24 hours. A measured amount of the Novolac was poured on hemp fiber which was placed in the mould to make laminate which contains equal ratios of both the resin and hemp fiber (i.e,.50% resin and 50% Hemp fiber). The mould was coated with the releasing agent. The same process was adopted to make the sisal reinforced laminate. But for the third laminate, the 50% (weight fraction) fiber ratio was equally divided i.e., 25% Hemp and 25% Sisal to make a hybrid composite and the resin was the same as before mentioned. Therefore three laminate specimens were prepared. The dimensions of the laminate were 120mm x 120mm x 4mm. A hydraulic press machine was used to consolidate the composite panels and left for curing in the machine for 24hours at a room temperature of 25^0C. The constituents of the three composites laminate are shown in Table 3.

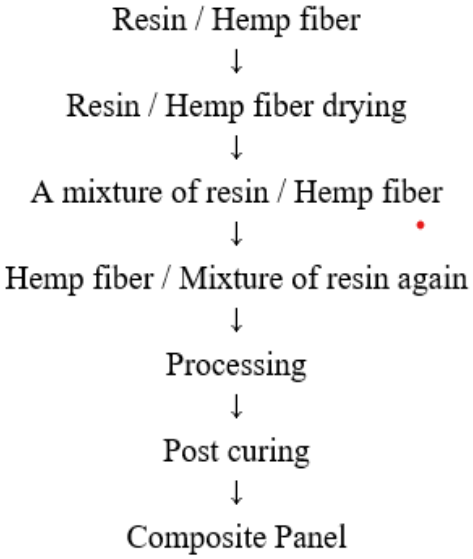

FIGURE 2. Specimen Preparation using Hand Layup Process Route for Hemp Laminate
Note: The above route process can be used for the sisal and the Hemp- Sisal composite laminates

TABLE 3. Major Constituents of Fabricated Specimens

Specimen	Reinforcement	Resin
H	Hemp	Novolac
S	Sisal	Novolac
HS	Hemp and Sisal	Novolac

Water Absorption Test

Water absorption test for the composite made with natural fibres is of at most concern since natural fibre contains more cellulose due to which they can absorb water. The water absorption by the composite affects the mechanical, thermal and physical properties of the composites. The moisture-absorbing ability of natural fibre composite can be reduced by using several chemical agents and surface treatment of fibre such that the composite properties can be enhanced.

Several studies show that the moisture diffusion rate in polymeric based composites is governed by three mechanisms. The first being diffusion of water molecules inside the micro gaps between polymer chains. The second involves capillary transport into the gaps and flaws at the interfaces between the fibre and the matrix. This is a result of poor wetting and impregnation during the initial manufacturing stage. The third involves the transport of micro cracks in the matrix arising from the swelling of fibers (particular in the case of natural fibres composites). Essentially moisture diffusion in a composite constitutes volume fraction of fibre, voids, and the viscosity of matrix, humidity and temperature.

Percentage change of Water absorption in the composite can be calculated using the formula mentioned below [9]:

$$Water\ absorption\ (\%) = \frac{Final\ weight\ of\ the\ specimen\ after\ immersion - Initial\ weight\ of\ the\ specimen}{Initial\ weight\ of\ the\ specimen} * 100$$

The preparation of the specimen for the water absorption test involves the alkali treatment of the fibres (i.e., Hemp and Sisal) with NaOH (10% Solution). The fibres were soaked in the NaOH solution for 8hours. Next, the fibres were washed with the normal distilled water and sun-dried for 24hours. The cleaned fibres soaked in the Novolac resin for 24 hours and after that the resin reinforced fibres dried for 24hours. The specimen was prepared according to the ASTM 570 standards. Reinforced fibres were weighed before soaking in the water and for every 10hour interval, the fibres were again weighed to calculate the amount of water absorbed in percentage change. The specimens were soaked in water for three days till they reached their saturation point. The images of the specimen are shown in the figure below.

(a) (b) (c)

FIGURE 3. (a) Sisal Specimen (b) Hemp Specimen (c) Fibres getting separated due to absorption of water by the specimen

TENSILE TEST

The tensile test of a specimen is a basic and universal engineering test to achieve material parameters such as Young's modulus, percentage elongation, percentage area reduction, Yield strength, Ultimate strength. These are the very important parameters that help in the selection of material for the different engineering applications.

In the tensile test, firstly the composite specimen is prepared according to the ASTM standards. The designation of the ASTM standard followed is D3039 [19]. The Sisal, Hemp and Hemp-Sisal specimens were cut according to the dimensions mentioned by the ASTM D3039 i.e120mm x 25mm x 4mm.

In the tensile test, the specimen is fixed between the jaws of the UTM machine and a uniaxial load that is tensile load is applied on the ends of the specimen. The force applied elongates the specimen, the force is applied till the material gets fractured [5]. The test was performed at a room temperature of $25^{o}C$. The different combinations of the specimens tested on UTM were sisal composite, Hemp composite, Hemp-Sisal composite. The image of the UTM machine is shown below in fig 3.

FIGURE 4. Universal Testing Machine (UTM)

RESULTS AND DISCUSSION

Water Absorption Test

The test of water absorption was conducted on the various fibres reinforced with Novolac resin as matrix such as Sisal-Novolac, Hemp-Novolac. For the test, a bunch of fibres soaked in resin was prepared. For every 10hours interval, the material was weighed and the values were noted. And a plot between Time vs Water absorption in percentage was plotted by considering the Time in Hours on X-axis and Water absorption in percentage change was considered on Y-axis.

From the plot, we can observe that sisal fibre has better water absorption characteristics than hemp fibre. Since the sisal fibre has less cellulose content than hemp fibre due to which it absorbs less water. A fibre containing more cellulose can absorb more water since cellulose is that component that can retain more water in fibre [1]. Here hemp reinforced fibre absorbs more the more water which swells the fibre and causes the crack to develop in the composite and more water penetrates into the composite through these cracks by capillary action which makes the fibre and matrix interface weak due to which the matrix and fibre start to get separate as a result the material fails [2]. Therefore the sisal reinforced fibre absorbs less water as we can see from the graph which makes it better than hemp reinforced fibre composite.

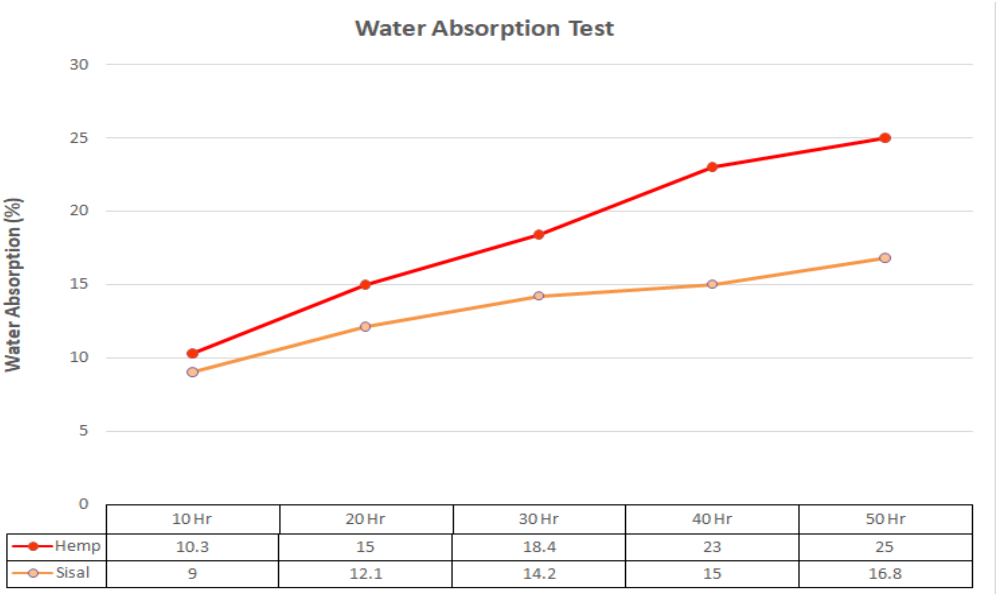

FIGURE 5. Water Absorption Results of Hemp and Sisal fiber

Tensile Strength

Test on the composites for the determination of the tensile strength was performed. The test was performed using UTM following the ASTM D3039 standards. The results of which are shown in fig- 4. From the results, we can observe that the Hemp laminate has a more tensile strength (i.e., Tensile strength of Hemp laminate = 28 MPa) than Sisal and Hemp-Sisal laminates. Since the Hemp fibre has more Young's modulus than the Sisal fibre which is shown in Table 2 also the Hemp has more stiffness i.e., less elongation to break percentage which helps for the laminate to elongate less and can carry more load before fracture.

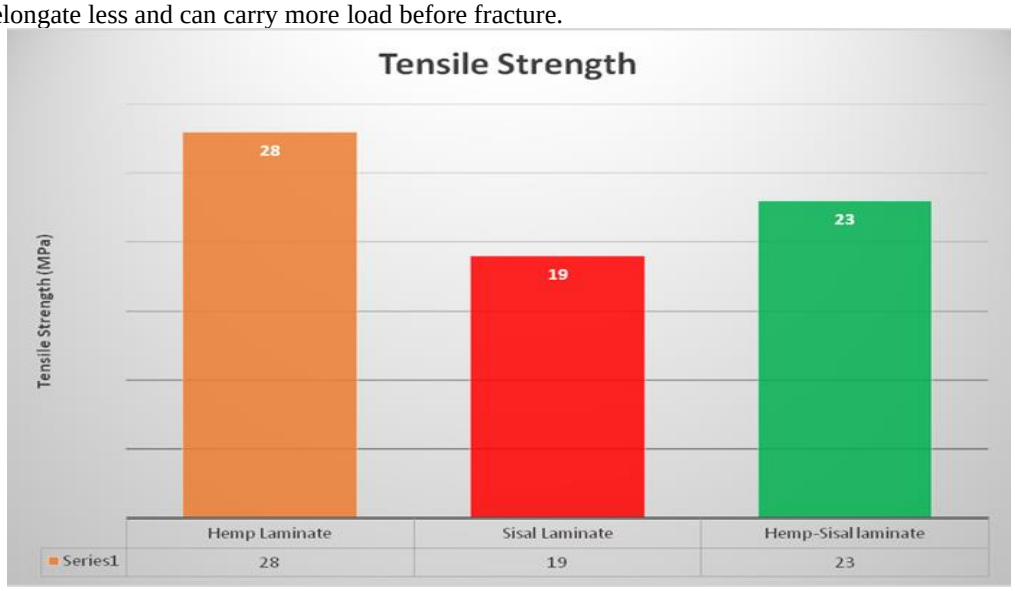

FIGURE 6. Tensile strengths of the Hemp, Sisal, and Hemp-Sisal laminate

The Hemp-Sisal laminate has a more tensile strength than the Sisal laminate since the laminate is composed of the properties of both the fibres and shows the intermediate properties between Hemp laminate and Sisal laminate therefore its tensile strength is less than Hemp laminate but greater than Sisal laminate. The tensile strength of the Hemp-Sisal laminate is 23MPa. The tensile strength of the Sisal laminate is 19MPa.

CONCLUSION

The Green composites have great potential to be used as composites for future use. These composites can be used as material for the construction of the secondary which does not have to carry critical loads since the Green composites have less strength than synthetic composites but using these materials for secondary structures instead of standard plastics then when a vehicle lifetime is completed these materials can be easily recycled without causing more harm to the environment. Also, the sisal laminates can be employed where the working atmosphere has more moisture content since it has better water absorption characteristics than Hemp laminates. Similarly, the Hemp laminates where high tensile strength for the secondary structure is required.

REFERENCES

1. A. May-Pat, A. Valadez-Gonzalez and P.J. Herrera-Franco, *Effect of fiber surface treatments on the essential work of fracture of HPDE-continuous henequen fiber-reinforced composites,* Polymer Tesing, 32 (6) (2013), pp. 1114-1122.
2. H.N. Dhakal *, Z.Y. Zhang, M.O.W. Richardson, *Effect of water absorption on the mechanical properties of hemp fibre reinforced unsaturated polyester composites*. Composites Science and Technology 67 (2007) 1674–1683.
3. Asim Shahzad, *Hemp fibre and its composites – a review*, Journal of Composite Materials 0(0) 1–14.
4. Biljana M. Pejic, Mirjana M. Kostic, Petar D. Skundric, Jovana Z. Praskalo, "The effects of hemicelluloses and lignin removal on water uptake behaviour of hemp fibres".Bioresource Technology 99 (2008) 7152–7159.
5. Girisha. C, Sanjeevamurthy, Gunti Rangasrinivas, *Tensile Properties of Natural Fiber Reinforced Epoxy-Hybrid Composites*. International Journal of Modern Engineering Research (IJMER) Vol.2, Issue.2, Mar-Apr 2012 pp-471-474, ISSN: 2249-6645.
6. Riya Srivastava, Deepak Srivastava, *Mechanical, chemical, and curing characteristics of cardanol– furfural-based Novolac resin for application in green coatings*, J. Coat. Technol. Res., 12 (2) 303–311, 2015
7. S.N. Monteiro , K.G. Satyanarayana; A.S. FerreiraI , D.C.O. Nascimento I , F.P.D. LopesI I.L.A. SilvaI , A.B. BevitoriI , W.P. Inácio, J. Bravo NetoI , T.G. Portela, *Selection of high strength natural fibres*, a, v. 15, n. 4, pp. 488 – 505, 2011.
8. R.Udhayasankar, B. Karthikeyan & A. Balaji, *Comparative mechanical, thermal properties and morphological study of untreated and NaOH-treated coconut shell-reinforced cardanol environmental-friendly green composites*, ISSN: 0169-4243 (Print) 1568-5616
9. R. Kannan, A. Vivek Anand, V. Hariprasad, R. Arvind Singh, S. Jayalakshmi, V. Arumugam, *Effect of Cashew Nut Shell Oil (Cardanol) on Water Absorption and Mechanical Characters of Sisal Fiber*, ISBN:978-93-86256-65-2.
10. Prasanna Kumar Ilankeeran, Preetamkumar M. Mohite, Sudhir Kamle, *Axial Tensile Testing of Single Fibres*, Modern Mechanical Engineering, 2012, 2, 151-156
11. Benítez-Guerrero, M.a* , Pérez-Maqueda, L.A.b , Artiaga, R.c , Sánchez-Jiménez, P.E.b , Pascual-Cosp, J.a , *Structural and Chemical Characteristics of Sisal Fiber and Its Components: Effect of Washing and Grinding*.
12. D. Rouison and M. Couturier, M. Sain, B. MacMillan and B.J. Balcom, *Water Absorption of Hemp Fiber/Unsaturated Polyester Composites.*
13. Dr. Osama Mohammed Elmardi Suleiman Khayal, *Laboratory Experiments Tensile Testing.*
14. O.O.Daramola, O.S.Akintayo, T.A.Adewole, H.K.Talabi, *Mechnaical properties and Water absorption behavior of polyester/soilrettes banana fiber (SRBF) composite*, ISSN: 1584-2665.
15. A. Balaji, B. Karthikeyan, J. Swaminathan & C Sundar Raj, *Effect of Filler Content of Chemically Treated Short Bagasse Fiber-Reinforced Cardanol Polymer Composites*, Journal of Natural Fibers, DOI: 10.1080/15440478.2018.1431829.
16. Samson Rwahwire, Blanka Tomkova, Aravin Prince Periyasamy, Bandu Madhukar Kale, *Green thermoset reinforced biocomposites.*
17. D. Chandramohan, A. John Presin Kumar, *Experimental data on the properties of natural fiber particle reinforced polymer composite material*, Data in Brief 13 (2017) 460 – 468.
18. T. T. Chiao, R. L. Moore, *A Tensile Test Method for Fibers.*

19. G.Velmurugan, D. Vadive, R. Arravindm, S.P. Venkatesh, A. Mathiazhagan, R. Mohamed Rijuvan, *Tensile Test Analysis of Natural Fiber Reinforced Composite*, International Journal of Mechnaical and Industrial Engineering (IJMPE), Volume 2, Issue No.2, ISSN 2231- 6477.
20. M.Longesh, V.Mariselyam, *Evaluation of Tensile Properties of Natural Fibers Composites*, International Journal of Applied Engineering Research, ISSN: 0973-4562 Vol. 10 No.61 (2015).
21. Dr.Karthir.Viswalingam and Dr.F.Emerson Solomon, *A Process for Selective Extraction of Cardanol from Cashew Nut Shell Liquid (CNSL) and its Useful applications*, International Journal of Scientific Reasearch Volume 4, Issue3, March-2013, ISSN 2229-5518
22. Muhammed Anaz Khan, A Vivek Anand, Lokasani Bhanuprakash, A Ravindra and V Hariprasad, 2020, "Mechanical Properties of E-Glass Fiber- Basalt Fiber Reinforced Polymer Matrix Composite", International Journal of Recent Technology and Engineering", Vol. 9, No. 2, pp. 1019-1022.
23. Muhammed Anaz Khan, A Vivek Anand and Lokasani Bhanuprakash, 2020, "Mechanical Properties of Laser Welded SS316 and SS321", International Journal of Engineering and Advanced Technology", Vol. 9, No. 6, pp. 192-195.
24. A Vivek Anand, R Arvind Singh, S Jayalakshmi, K Srinivas Rao and Xizhang Chen, 2021, “Mechanical and tribological properties of Natural fibre reinforced polymer composites”, Taylor and Francis - CRC Tribology and Sustainability Book, 1st edition, eBook ISBN: 9781003092162

RESEARCH ARTICLE | MAY 22 2023

Development of novel SMC based multi input single output boost converter

S. Sathishkumar ✉; M. Rishi Bala; M. Nithiskumar; G. Kannan; T. Logeshwaran; N. Uday Ranjan Goud

AIP Conference Proceedings 2492, 050041 (2023)
https://doi.org/10.1063/5.0140061

Development of Novel SMC based Multi Input Single Output Boost Converter

S Sathishkumar[1, a)], M Rishi Bala[1], M Nithiskumar[1], G Kannan[1], T Logeshwaran[2] and N Uday Ranjan Goud[3]

[1]*Department of EEE, Bannari Amman Institute of Technology, Sathyamangalam, India*
[2] *Department of EEE, Kongu Engineering College, Erode, India*
[3]*Department of Aeronautical Engineering, MLR Institute of Technology, Hyderabad, India*

[a)] Corresponding author: tamilselvan@vitsathy.ac.in

Abstract. This study describes a non-isolated high gain DC to DC converter. The defined project isa multiport boost converter in which it boosts's the input voltage to the required output voltage. Sliding Mode Control (SMC) method is used in proposed converter to control the switch. Diodes and switches in proposed topology operate asynchronously. The non-linear surfaces are put forward which makes sure constant power to be given as output to the load. The existing of the sliding mode control and the stabilization of sliding surfaces were finalized in this projected converter. The effectivity of this sliding mode converter was checked by using the simulation software are taken on different operating condition. The proposed converter is simulated on MATLAB simulation on the laboratory on the multiport DC-DC boost converter.

Keywords. Non-isolated, Gain, SMC, Multiport

INTRODUCTION

Current century is observing larger collaborative effort in creating renewable energy technology. Following the development in the power electronic technologies, there is a current trend in multi converters power system that includes renewable energies and vehicle system (water, earth, sky vehicle) [1, 2]. Direct current Micro grids were receiving more attentions due to the urge on integration of renewable energy source creating DC power like photovoltaic cells, fuel cells, and so on. In addition, the accessibility of productive Direct Current load, availability for storing system in Direct current, non-existence of the reactive power compensations were important drives of the Direct Current micro grid, amongst all other. Still, multi converter power system, including micro grid poses serious stability challenge as for the converter's non-linearity and inter-converter's dynamic, although each converter is steady [1, 3–8].Commonly load in cascade multi-converter consists of dual types as constant power load (CPL) and constant voltage load (CVL). Firmly controlled point-of-load (POL) converter on a flowed multi-converter power system behaves by way of CPL, dipping constant power since input bus and then displays negative incremental impedance characteristic features. In different circumstances, CVL requires constant voltages meant for own process. Strongly controlled POL converter dropping constant power takes destabilizing result in the poorly restrained input LC filter then the source converter working on continuously conducting mode, making fluctuations on the input bus voltages then occasionally leads voltage failure also. Instabilities by way of a result of CPLs were called by way of terrible impedance variabilities [10–18].

Few answers were advised on the writings toward ease poor resistance variabilities which include the load losing, inactive resistance restraining, assignment for capacitances then batteries on Direct Current buses besides controller-primarily built approaches [4, 6]. Few to the existence manipulate reply was built totally at access area process [1,

Advancements in Aeromechanical Materials for Manufacturing: ICAAMM-2021
AIP Conf. Proc. 2492, 050041-1–050041-10; https://doi.org/10.1063/5.0140061
Published by AIP Publishing. 978-0-7354-4438-6/$30.00

17], remarks linearization [13, 14], circle termination [15], pulsation width alteration [12], digital capacitor simulation [11], sliding-mode controller (SMC) [11,12,13] and additional non-lined concept-primarily built methods along with Lyapuinov and Bryton Mayor's blended capability capabilities [14]. Middle book's resistivity standard-built access area result needs redesigning for source or else load resistance toward compensating Constant Power Loads on a minor-sign experience [5, 16]. Controllers' planned this usage of linearizing the flora about equilibrium factor is commonly inadequate for mitigating Constant Power Loads result. So, for mitigating Constant Power Loads brought on variabilities on extremely non-lined Direct Current supply systems, here was necessity to sturdy manipulate plan methods that could make sure system balance in international or semi-international experience.

On this offered paper, they have used Sliding Mode Controller technique for justifying Constant Power Loads produced variabilities on multi-converting Direct Current supply schemes. Sliding Mode Controller was fine installed then ripe approach on layout robust controlling to an expansion on structures which include strength convertors. Sliding Mode Controller approach guarantees sturdiness by appreciate on conflicts also limit differences [17]. Initial outcomes on this projected paper were posted on [15] in which discontinued form for Sliding Mode Controller was given on the converters. The paper offers non-lined shift purpose-built SMC on easing Constant Power Loads impact on the Direct Current enhance convertor. This offered arrangement makes use of a real non-lined thing on controller layout then on showing reality of sliding mode then firmness on shifting feature. On first-rate for author's data, this was initial painting that reports justification on Constant Power Loads impact on Direct Current improves convertor by means of non-lined shifting characteristic-built Sliding Mode Controller.

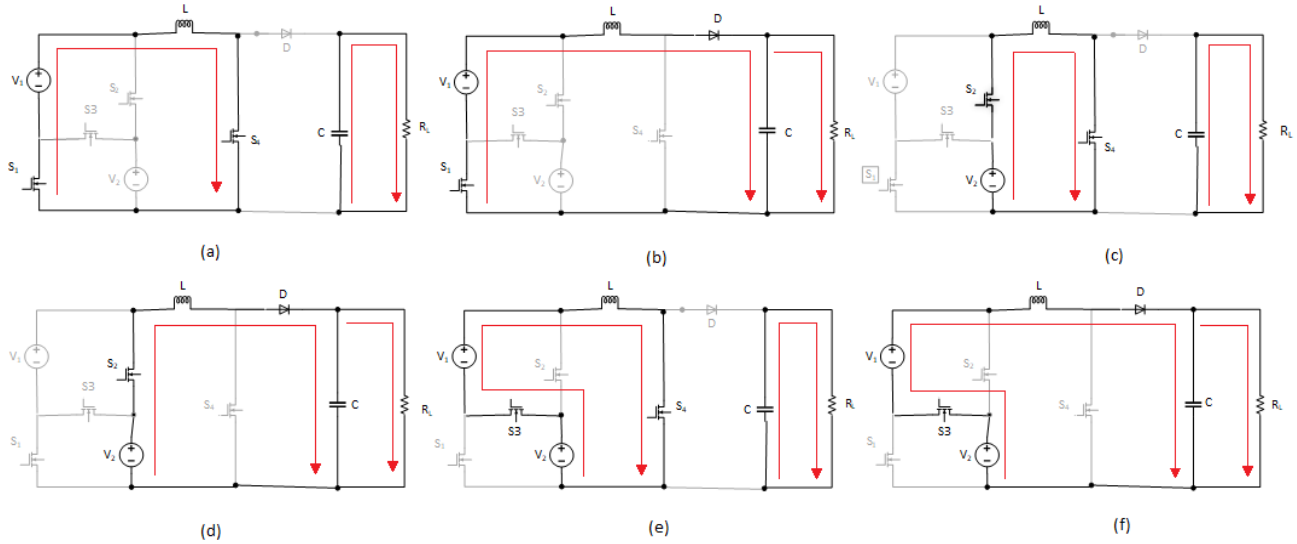

FIGURE 1. Proposed Topology

APPLICATIONS

Solar Array Characteristics

The solar array has a non-linear V-I characteristic which is based on the surrounding conditions: ambience, temperatures and insolation.

The non-linear characteristics of the solar cells are obtained in the given equation:

$$i_{SA} = I_{ph} - I_0 \left\{ \exp\left(\left(\frac{q}{AKT} \right) . (v_{SA} + R_S i_{SA}) \right) - 1 \right\}$$

where I_{ph} was produce current on the ideal state, I_o was reversed saturation current and q was charge on the electron, V_{SA}, i_{SA} were output voltages and output currents on PV cells. A was ideal factor of the P-N junction, K was known as Boltzman's constant, T was temperature, and thenR_S was sequence resistor for PV cells.

Steady State Operational Analysis

First Mode (Input V1 is supplying voltage to the Load)

The S1 switch is kept in ON state and the Switches S2 and S3 are kept in OFF state. Hence, we get V1 as input source. In the above figure (a), the Switch S4 is closed, the current from input source V1 passes through the inductor in clockwise and the inductor induces magnetic field around it as it stores energy. Hence, the left side of the inductor is positive. In the figure (b) the Switch S4 is opened, due to the higher impedance current is reduced. The magnetic field in inductor is reduced in energy to give uninterrupted current to the load. So, the polarity of the inductor is reversed as the right side of it becomes positive. Because of this, inductor passes its energy along with the input source V1 in series resulting in higher voltage to charge the capacitor by passing through the diode D. The switch S4 is turned ON and OFF fast enough, so the inductor is not discharged fully in between S4's ON stages. Hence, this results in higher voltage level maintained in load side when compared to the input side. Also, when the switch S4 is opened, the capacitor connected parallel to the load gets charged by the added-up voltages. And when the switch S4 is closed, the previously charged capacitor is able to give the voltage and energy to output. On this time, the diode which blocks both sides stops the capacitor from discharging to the inductor side through the switch. And the switch S4 is again turned OFF fast enough to stop the capacitor from discharging all of its stored energy to the load, it is then charged again and the process is repeated.

Second Mode (Input V2 is supplying voltage to the Load)

The S2 switch is kept in ON state and the Switches S1 and S3 are kept in OFF state. Hence, we get V2 as input source. In the above figure (c), the Switch S4 is closed, the current from input source V2 passes through the inductor in clockwise and the inductor induces magnetic field around it as it stores energy. Hence, the left side of the inductor is positive. In the figure (d), the Switch S4 is opened; due to the higher impedance current is reduced. The magnetic field in inductor is reduced in energy to give uninterrupted current to the load. So, the polarity of the inductor is reversed as the right side of it becomes positive. Because of this, inductor passes its energy along with the input source V2 in series resulting in higher voltage to charge the capacitor by passing through the diode D. The switch S4 is turned ON and OFF fast enough, so the inductor is not discharged fully in between S4's ON stages. Hence, this results in higher voltage level maintained in load side when compared to the input side. Also, when the switch S4 is opened, the capacitor connected parallel to the load gets charged by the added-up voltages. And when the switch S4 is closed, the previously charged capacitor is able to give the voltage and energy to output. On this time, the diode which blocks both sides stops the capacitor from discharging to the inductor side through the switch. And the switch S4 is again turned OFF fast enough to stop the capacitor from discharging all of its stored energy to the load, it is then charged again and the process is repeated.

Third Mode (Input V1 and V2 both are supplying voltage to the Load)

The S3 switch is kept in ON stage and switch S1, S2 are kept in OFF stage. Hence, we get V1 and V2 as input source. In the above figure (e), the Switch S4 is closed, the current from input source V1 and V2 passes through the inductor in clockwise and the inductor induces magnetic field around it as it stores energy. Hence, the left side of the inductor is positive. In the figure (f), the Switch S4 is opened; due to the higher impedance current is reduced. The magnetic field in inductor is reduced in energy to give uninterrupted current to the load. So, the polarity of the inductor is reversed as the right side of it becomes positive. Because of this, inductor passes its energy along with the input source V1 and V2 in series resulting in higher voltage to charge the capacitor by passing through the diode D. The switch S4 is turned ON and OFF fast enough, so the inductor is not discharged fully in between S4's ON stages. Hence, this results in higher voltage level maintained in load side when compared to the input side. Also, when the switch S4 is opened, the capacitor connected parallel to the load gets charged by the added-up voltages. And when the switch S4 is closed, the previously charged capacitor is able to give the voltage and energy to output. On this time, the diode which blocks both sides stops the capacitor from discharging to the inductor side through the switch. And

the switch S4 is again turned OFF fast enough to stop the capacitor from discharging all of its stored energy to the load, it is then charged again and the process is repeated.

Model of the Boost Converter

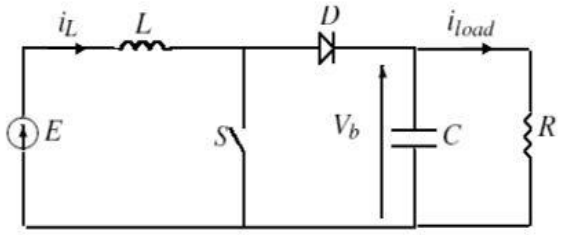

FIGURE 2. Boost Convertor Circuit

FIGURE. 2 displays the circuit of the boost converters. It contains input voltage, E, representing voltages for two inputs used, a flattening inductor L, a switch S which is under control, a diode D, filtering capacitor C, lastly the load that is represented as R. Guessing in which this model was connected on the constant conducting modes, that defines on inductor's current will not go towards zero, this mathematically derived circuit for the boost convertor could derive through following Kirchhoff's law. This derived equation from the model for the boost converter on the continuous conduction mode is:

$$\begin{cases} C\dfrac{dV_b}{dt} = (1-u)i_L - i_{load}, \\ L\dfrac{di_L}{dt} = E - (1-u)V_b, \end{cases} \qquad (1)$$

In which u was switching stage in case on the regular circuit, V_b, i_L were the output voltage and inductor current for the DC-DC convertor. In SMC, we determine the character u as:

$$u = \begin{cases} 1 \; if \; S < 0, \\ 0 \; if \; S > 0, \end{cases} \qquad (2)$$

In which S was sliding surface.

Designing for Sliding Mode Control

The main aim for the DC-DC boost convertor's control was to adjust required output voltage V_b in terms of the reference voltage V_{ref}. The pattern for the sliding mode control (SMC) of the boost convertor will start along sliding surface. As per given in [13], it was known that the directed surfaces V_b-V_{ref} could lean towards the zero only when current is increased simultaneously. Normally, the cascaded control structure will be given to the control boost converters, which causes them toward resolving control problems by means of the two of control loop [12], [13], [17]: This output voltages loop produces reference's current as of the voltage errors also internal current loops control the inductor's current through the sliding modes (Fig. 3).

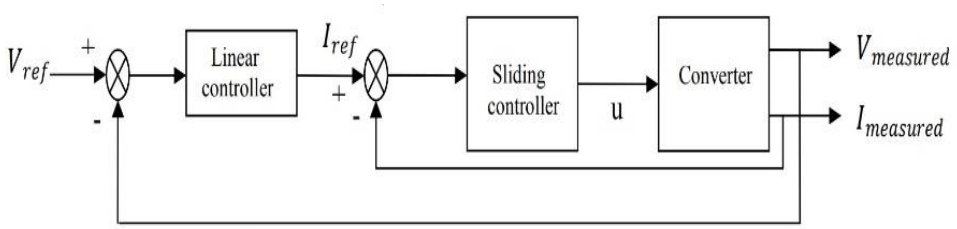

FIGURE 3. Cascade Controller Structure

The control for output voltage for the boost convertor meeting some standards for constancy and the reality for the sliding mode. Although, it was described on [17] which says it will be hard for it to declare gain in voltage loop because the sliding mode was non-linear system. Hence Sliding Mode Control is put into the current regulations, the voltage loop is extra sensitive of higher frequencies' occurrence as well as uncertainty of reference current. In order to increase performance to this controller, we put forward to read the control modes derived from the sliding surface that includes output voltage. Let ($V_{ref}^e, I_{ref}^e = \frac{{V_{ref}^e}^2}{RE}$) to be the required balance point, we get given surface as:

$$S = K_1\left(V_b - V_{ref}^e\right) + K_2\left(i_L - I_{ref}\right), \tag{3}$$

where K_1 and $K2 \in R^+$.

As the reference current is based on operating point, they can be extracted, that is:

$$I_{ref} = \frac{V_{ref}^e i_{load}}{E}, \tag{4}$$

Where $i_{load} = \frac{V_b}{R}$

Sliding surface's coefficients (K_1, K_2) should be chose to make sure that sliding mode belongs least around the required balance points, and dynamic of this system would get to the surface and lean towards balance point.

Existing conditions

The existing conditions for the sliding modes show together S,Ś would be long towards the zero, if it belongs towards infinite, that describes dynamics in system would lean to sliding surface. This existing conditions in sliding mode would be SŚ<0 (on $S \rightarrow 0$), attainment in the difference makes sure that reality in sliding mode is surrounded by linear surface.

Let's write equation for model of convertor in the given state, which is balance point placed in origin. Thus, we can get:

$$\begin{cases} C\ \frac{dx_1}{dt} = (1-u)\left(x_2 + I_{ref}^e\right) - \left(\frac{x_1 + V_{ref}^e}{R}\right), \\ L\frac{dx_2}{dt} = E - (1-u)\left(x_1 + V_{ref}^e\right), \end{cases} \tag{5}$$

Where $x_1 = V_b - V_{ref}^e$ and $x_2 = i_L - I_{ref}^e$

Replacing I_{ref} on the result from (4) on equation for commutation surface (3), we get:

$$S = K_1\left(V_b - V_{ref}^e\right) + K_2 i_L - \frac{K_2 V_{ref}^e V_b}{RE}, \tag{6}$$

$$= \left(K_1 - \frac{K_2 V_{ref}^e}{RE}\right)(V_b) + K_2 i_L - K_1 V_{ref}^e$$

Writing the equation in new coordinate system (x_1, x_2), we get:

$$S = \left(K_1 - \frac{K_2 V_{ref}^e}{RE}\right)(x_1) + \left(K_1 - \frac{K_2 V_{ref}^e}{RE}\right)\left(V_{ref}^e\right) + K_2 x_2 + K_2 I_{ref}^e - K_1 V_{ref}^e, \tag{7}$$

$$= K_1' x_1 + K_2 x_2,$$

$$\text{Where } K_1' = K_1 - \frac{K_2 V_{ref}^e}{RE}.$$

On analyzing SṠ which is negative on u=0, 1, we could finalize in which this sliding region was ranged to given variations:

$$\begin{cases} x_1\left[\frac{-K_1{}'}{RC} - \frac{K_2}{L}\right] + \frac{x_2 K_1{}'}{C} + K_2\left[\frac{E}{L} - \frac{V_{ref}^e}{L}\right] - K_1'\left[\frac{V_{ref}^e}{RC} - \frac{I_{ref}^e}{C}\right] < 0, \\ -\frac{K_1' x_1}{RC} + \frac{K_2 E}{L} - \frac{V_{ref}^e K_1{}'}{RC} > 0, \end{cases} \tag{8}$$

By the both differences as well as the demand to make sure sliding modes belong to the least surrounding balance points ($x_1 = 0$, $x_2 = 0$), the given conditions should be justified:

$$\frac{K_1{}'}{K_2} < \frac{RCE}{V_{ref}^e L}. \tag{9}$$

Stability conditions

The stability for this structure was assured when activity on this structure of the sliding region was flown towards required balance point. The goal was to decide activity on new states x_1, $x_2$during sliding region was got. In this state prototype (5), commuting surface (6), as well as, after Ṡ =0, equal average control which should then substituted on structure, soon system slides through surface was shown as:

$$u_{eq} = 1 - \frac{\frac{E}{L} - \frac{K_1'\left(x_1 + V_{ref}^e\right)}{K_2 RC}}{\frac{x_1 + V_{ref}^e}{L} - \frac{K_1'\left(x_2 + I_{ref}^e\right)}{K_2 C}}. \tag{10}$$

Through changing equal control (10) on state space mode (5), as well as since S = 0, we conclude activityon x_1 on sliding region:

$$\frac{dx_1}{dt} = \frac{E\left(I_{ref}^e - \frac{x_1 K_1{}'}{K_2}\right) - \frac{\left(x_1 + V_{ref}^e\right)^2}{R}}{C\left(V_{ref}^e + x_1\right) - L\left(I_{ref}^e - \frac{K_1'}{K_2} x_1\right)\left(\frac{K_1'}{K_2}\right)}. \tag{11}$$

Let $V = \frac{x_1^2}{2}$ be 6yapunov candidate function, hence we get:

$$\dot{V} = -x_1^2 \frac{E\frac{K_1}{K_2} + \frac{V_{ref}^e}{R} + \frac{V_b}{R}}{C\left(V_{ref}^e + x_1\right) - L\left(I_{ref}^e - \frac{K_1'}{K_2}x_1\right)\left(\frac{K_1'}{K_2}\right)}. \quad (12)$$

The declaration towards the $\dot{V}$ as to being negative was:

$$C\left(V_{ref}^e + x_1\right) - L\left(I_{ref}^e - \frac{K_1'}{K_2}x_1\right)\frac{K_1'}{K_2} > 0 \Rightarrow x_1 > \frac{\frac{LV_{ref}^e}{RE}\left(\frac{K_1'}{K_2}\right) - CV_{ref}^e}{C + L\left(\frac{K_1'}{K_2}\right)^2} \quad (13)$$

The sliding region is given as (8) as well as existing state (9), we could show that state (13) was pleased, besides sliding region for substitution's surface. Built towards constancy proposal on the knowing towards the Lyapuinov, we could tell in which this system was internationally asymptotically steady.

RESULTS AND DISCUSSION

For evaluations and validations of this proposed converter's accuracy and performance, the simulation result is presented below,

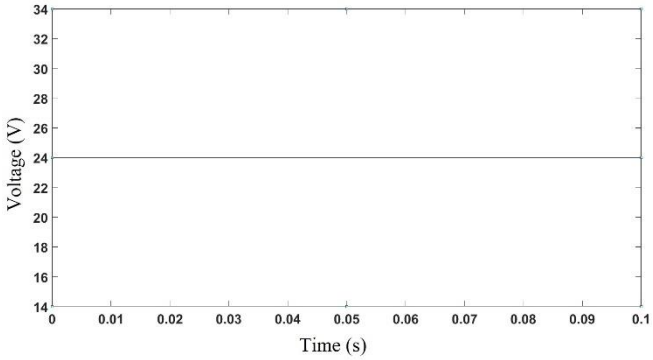

FIGURE 4. DC/DC Input Voltage

The graph for the input voltage is given above. The graph may vary according to the given voltages such as V_1, V_2 or both.

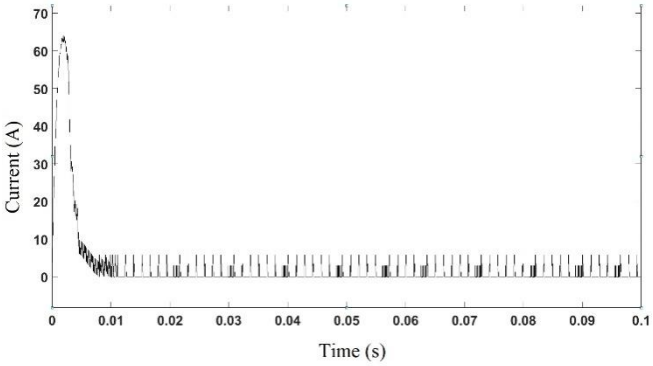

FIGURE 5. DC/DC Input Current

The graphical representation of the input current is represented in the graph above. The value of the current varies due to the overall change in the circuit.

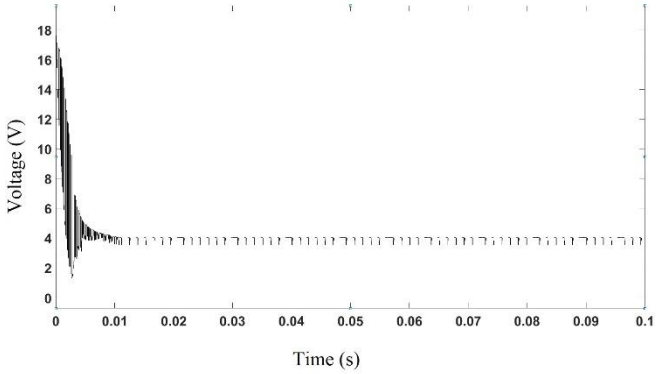

FIGURE 6. Calculated Voltage taken from output and reference Voltage.

The calculated voltage is taken from the output voltage and reference voltage by using K_p, K_d and K_c.

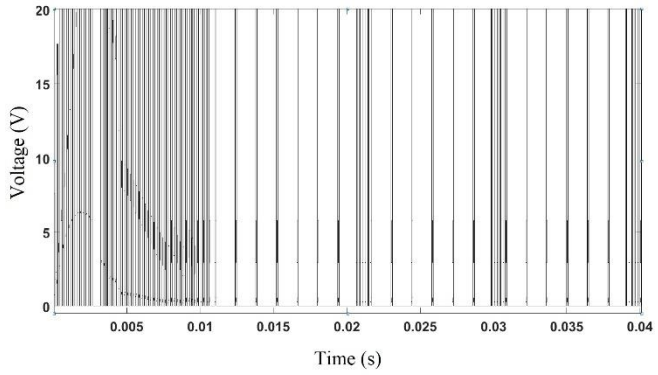

FIGURE 7. Reaction of the MOSFET under the given pulse

The graphical diagram given above represents the switching of the device under the given pulse. The pulse is generated by the Sliding Mode Controller technique and given as input to the MOSFET.

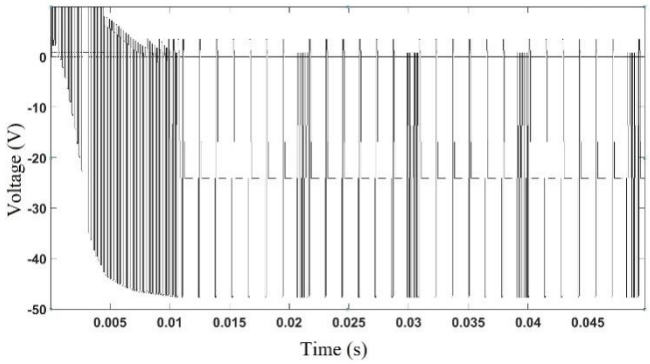

FIGURE 8. Diode Voltage according to the Pulse

The above graphical diagram represents the voltage variations of the diode under the forward and reverse voltages introduced to it. The diode is an important part in the circuit because the reversing of the voltage due to the inductor is stopped by the help of the diode.

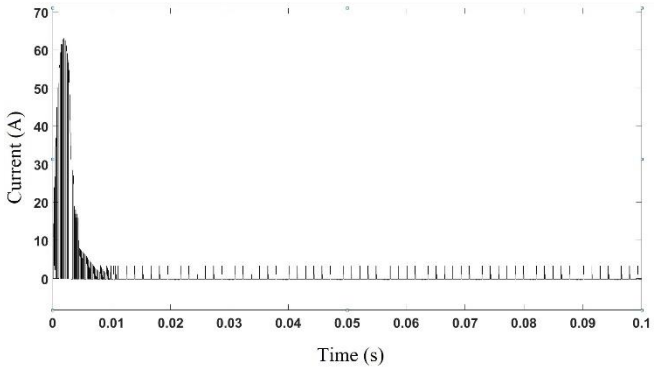

FIGURE 9. Current through the Capacitor

The current through the capacitor is represented in the above graph. It is taken into account to get the desired output voltage. It is also used in the calculation for the MOSFET pulse.

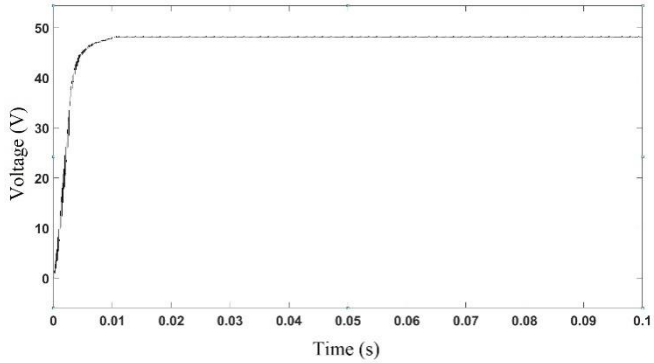

FIGURE 10. DC/DC Output Voltage

By introducing many changes to the circuit, the desired DC to DC output voltage is accomplished. The desired output Voltage of proposed DC to DC convertor was represented on graph above.

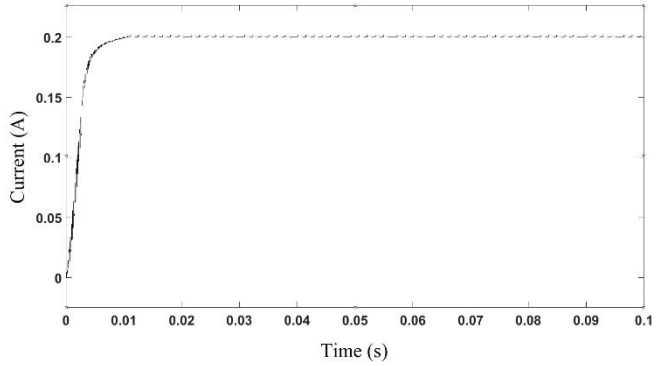

FIGURE 11. DC to DC Output Current

The above diagram is the graphical representation of the Output current.

CONCLUSION

The sliding mode controller proposal on multiport DC-DC convertor is proposed on the presentation. The controller method which increases performance on systems is derived. Their influences on controller parameter in the performance are analyzed. An optimized algorithm was created and developed to derive and calculate the optimal value of the parameter based on previously defined specifications. The important application of this type of controller is to give the supply of electrical bus through super capacitor is proved. Result shows the active reply by controllers, the sturdiness of the load along with the input voltages on larger variation among the nominal value. Future researches may include the focusing of sturdy on thought on load currents, as well as in steadiness of controller's/observers close loop.

REFERENCES

1. S.Arulselvi, G.Uma and M.Chidambaram, "Designing on PID control of convertor", International Power Electronics Meeting (IPEMC 2014), 16 August 2014, China.
2. L.Guo, J.Y.Hung and R.M.Nelms, "Designing as well as implemention on PID control on DC-DC convertor," Proceeding on Intersociety Power Change Meeting, August 2001.
3. H.Mingzhi and X.Jianping, "Non-linear PID on Control Lowly Convertors", Practical power electronic meeting APEC 2020, 25 Feb-1 March 2020.
4. A.J.Foreyth and S.V.Mollov, "Modelling as well as controls on DC-DC converter", IEEE Power Engineering, vol. 12.
5. M.Rashid, Power Electronic Manual, Academics Press, 2001.
6. V.S.C.Racirah and P.C.Sen, "Relative Study on Comparative Important Sliding Modes, as well as Fuzzy Judgment Controllers on Power Converter", IEEE Dealings on Manufacturing Application.
7. Sanjeet Kumar and Dr. P.R.Thakura, "Closed loop PI control of DC-DC Cascode Buck-Boost Converter," International Conference on Innovations in Information, Embedded and Communication Systems (ICIIECS) – 2017.
8. Siw-Chong Tan, Y.M.Lai, Chi.K.Tse, "Common Designs Issue on Sliding Mode Control on DC-DC Converter", IEEE transactions in Industrial Electronic, March 2008.
9. Yanhui Xie,Reza Ghaemi, Jing Sunand James S. Freudenberg, "Model Predictive Control for a Full Bridge DC/DC Converter", IEEE Transactions on Control Systems Technology, Volume-20, No. 1, Jan-2012.
10. D.Cortes and J.Alvarez, "Robust sliding modes controls on convertors", Proceeding of IEEE Global Power Electronic Assembly, 20-24 October 2002.
11. S-C.Tan, Y.M.Lai, Chi K.Tse," Faster reply sliding modes control on the boost convertor on extensive range on functioning condition", IEEE transaction In Manufacturing Electronics, March 2007.
12. Nihat Ozturk and Emre Celik, "Speed control of permanent magnet synchronous motors using fuzzy controller based on genetic algorithms", Electrical Power and Energy Systems, 2012,889–898
13. M.Ahmed, M.Kuisma,"Applying Modest Procedures on regulatory Switching Power supply by means of SMC as controller method", Proceedings on Global Symposium, SIELA, 30 May 2003.
14. H.Gueldemir, "Sliding Modes Controls on Converters", Journals on practical science, 2005.
15. Ayushi Jain, Ashok Kumar Sharma and Kanak Hada, "A PFC Based BLDC Motor Drive using Buck-Boost and Buck-Boost Buck Converter", IEEE International Conference on Smart Technology for Smart Nation 2017.

RESEARCH ARTICLE | MAY 22 2023

Mechanical properties of hybrid composite sandwich structure with sisal and E glass fiber

M. Udaya Sree ✉; S. Sudha; Y. Yamini Reddy; N. Sahasrarchith; A. Vivek Anand

AIP Conference Proceedings 2492, 040008 (2023)
https://doi.org/10.1063/5.0113271

Mechanical Properties of Hybrid Composite Sandwich Structure with Sisal and E glass Fiber

M Udaya Sree[1, a)], S Sudha[1, b)], Y Yamini Reddy[1, c)], N Sahasrarchith[1, d)], A Vivek Anand[1,]

[1]*Department of Aeronautical Engineering, MLR Institute of Technology, Dundigal, Hyderabad, Telangana, India.*

[a)]Corresponding Author: mudaya2017@gmail.com
[b)]sudha2k18@gmail.com
[c)]minniprecious@gmail.com
[d)]nandalasahasrarchith@gmail.com

Abstract. The current world of mechanical industry is in search of new advancements in material constructions involving advanced technology. The new phase of industries began with the replacements of natural fibers with synthetic materials. The introduction to natural fibers is rapidly cruising due to their high performance, recyclable and good properties. The industries are looking for the biodegradable feature due to environmental concerns. According to study, the natural fibers have low weight and moderate mechanical properties when compared to synthetic glass fiber composites. The hybridization of natural fibers with glass fiber reinforced polymers (GFRP), can result in enhancement of mechanical properties of composites in source of strength, low density, impact resistant, corrosive, thermal and bacterial resistant. In this paper the natural fiber sisal is mixed with E-glass fiber to form hybrid composites. The chemical agents epoxy and hardeners are used in required quantity. The sisal and glass fibers are layered in sandwich structure by the use of advanced core materials. The sandwich structure are light materials, with high stiffness and exterior surface transfer load by bending and core material transfer load by shearing. Tensile and flexural tests are carried out to explore the mechanical properties of sandwich structure composites.

Keywords: Sandwich structure, Sisal Fiber, E glass fiber, Epoxy, Tensile strength, Flexural strength

INTRODUCTION

Now a days the deficiencies in material resources has come to picture. The properties that exist in one material does not exist in another. To extract the properties that evolved in each material, combination of the material is important. Each material has their own properties so that we can combine the material which can share their properties to make their material as per the requirements. This combination of material forms a composite material, which is defined as the combination of two or more materials either physically or chemically. [1] While the hybridization of the material is referred as the constituents of the material is combined in microlevel or nano level. Exactly in such situation's fibres play an important role in engineering materials often for manufacturing the strongest materials. [2], [3]

Due to increase in global and environmental risks, natural fibres have been attracting the most of the industrial applications and researchers. The main advantage of these fibres is availability, low cost, renewable, friendly with environment, low density, high specific properties, low energy consumption, excellent thermal properties and are non-abrasive. In recent years these natural fibres are widely used in composite material to extract properties either with other natural fibres or artificial fibres to gain the properties as required for the different applications.[4]

The plant fibre and glass fibres are one of tremendous combinations. The plant fibres which have best properties is coir (coconut fibres) rather than all other fibres but sisal has been preferred over coir because the coir has the

Advancements in Aeromechanical Materials for Manufacturing: ICAAMM-2021
AIP Conf. Proc. 2492, 040008-1–040008-6; https://doi.org/10.1063/5.0113271
Published by AIP Publishing. 978-0-7354-4438-6/$30.00

property of a highest absorption of water about 60% which can cause the composite material to lose its internal resistance. [5] Sisal fiber is derived from the leaves of the plant. It is usually obtained by machine decortications in which the leaf is crushed between rollers and then mechanically scraped. The Fiber is then washed and dried by mechanical or natural means. [6] The dried fiber represents only 4% of the total weight of the leaf. Once it is dried the fiber is mechanically double brushed. The lustrous strands, usually creamy white, average from 80 to 120cm in length and 0.2 to 0.4mm in diameter. [7]

Synthetic fibre is stronger than natural fibres as they are manmade and are durable. These Synthetic fibres have the high resistance to wear and tear and have smooth surfaces. There are Different types of synthetic fibres such as Transformation of natural polymers, synthetic polymers, and other type of fibres which are not polymers. The glass fibres have the higher flexibility and strength which can be possible due to the orientation of the molecules on the surface layer of the glass it will be changing when the fibre glass is pulled out of the molten glass due to its rapid cooling. This type of fibres cannot be easily deformed or damaged. There are different types of glass fibres which has different properties namely A Glass, C Glass, D Glass, E Glass, AR Glass, R Glass, S Glass, S-2 Glass. The most of the glass fibres that are used for industrial applications are E Glass fibre and S Glass fibre. Though S Glass fibre has high tensile strength, E Glass fibres are alkali free which has less than 1% of alkali in it, also has high strength and electrical resistivity. E Glass fibre has low elastic modulus compared to other and low thermal conductivity. [8]

Core material plays an important role in sandwich structure laminate which is skin type material, has stiffness and low weight. These core materials are available in different forms such as end grain balsa wood, PVC foam, urethane foam, non-woven core fabric and honeycomb materials. This light-weight materials are bonded between two composite skins and act as the central member which is referred as the sandwich structure. The core material in the structure increases the sectional modulus which in result increases the stiffness and ability to create a light weight structure.[9]

Honeycomb core materials are manufactured from a variety of materials such as Nomex, aluminium, Thermoplastic and most commonly polypropylene. These are available in different forms of polymers, carbon, aramid, and GRP. These are relatively of low crush materials, high strength and has stiffness, increasing stress with increasing strain. Honeycomb Structure which contains thin foils forming interlocked hexagonal cells with their axes oriented at right angles in the direction of face sheet. The main advantages are high specific strength, stiffness, light weight, lower shrinkage and these are tough but flexible.

A sandwich structured composite is a special class of composite material that is fabricated by attaching two thin stiff skins to a light weight thick core. With a sandwich, less material is required than with a solid structure. Sandwich panel is a kind of layered composite. It consists of core and faces. They are formed by two strong outer sheets. core is layer of less dense material. These materials of sisal fibre, E Glass fibre form a sandwich structure placing a core material as a central member. [9] These are thoroughly fabricated using the resin as epoxy in three different forms such as i) Core material with sisal fibre as faces ii) Core material with E Glass fibre as faces iii) Core material with E glass fibre and sisal and faces on the either side. These sandwiches laminated structures are tested separately according to ASTM standards of testing machines. The materials have gone through the tensile test and flexural test where the results are claimed in terms of tensile strength and the elongation at break of each case. [10]

EXPERIMENTAL PROCEDURE

Specimen Preparation and Fabrication Process

The hybrid composite materials are fabricated by using sisal and E-glass fibres (150mm X 150mm). The sisal short fibres are arranged to required thickness and dried under sun for removal of moisture content. The E-glass fibre sheets are cut into required dimensions. A rectangular mould is prepared as base support, the epoxy and hardener is bonded in 60% to 40% into a container.

Hand layup technique is used for fabrication. It is one of the simplest and effective method for processing small products to large products in large quantity. Firstly, the mould is cleaned by applying releasing jell (poly vinyl alcohol), then the OHP (overhead projected) sheet is placed on mould. The materials are layered in sandwich structure i.e., face sheets sisal and E-glass fibre are layered top and bottom, the core material honeycomb paperboard is layered at centre by adding epoxy appropriately turning it into laminates. Laminates are compressed in compression machine to remove excess resin. The fabricated composite laminates are then cured at room temperature. The dried composites are then shaped into specimen for testing process.

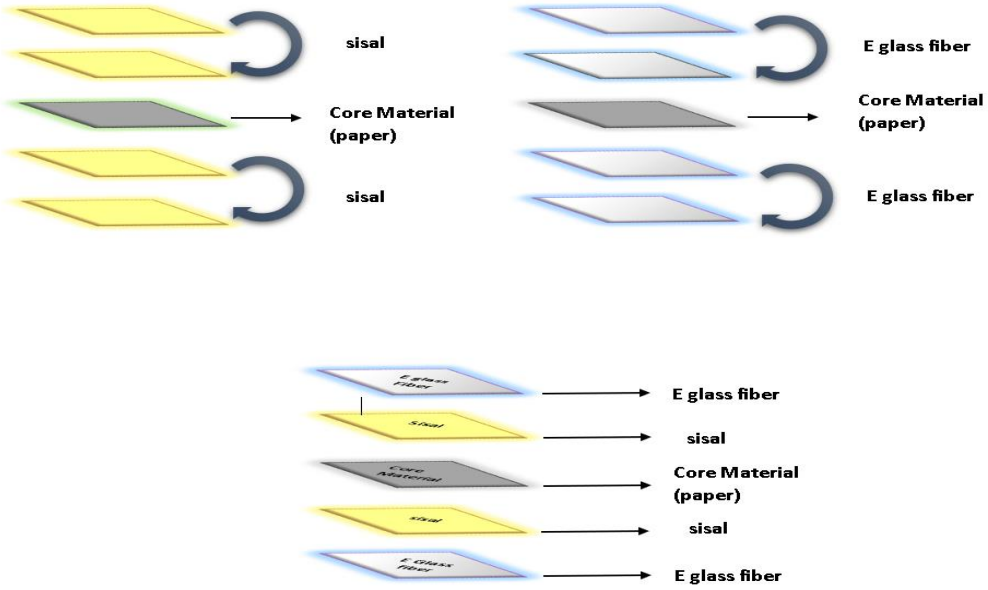

FIGURE 1. Schematic sketch of prepared specimens

TESTING METHODS

Tensile Test

Tensile testing was conducted as per Standard ASTM D3039 to explore its mechanical properties, dimension of the samples 120 mm x 25 mm x 10 mm. Tensile testing is a form of a tension testing where the ends of the composite sample are held between the grips and tension is applied to composite sample until it undergoes fracture. The corresponding load tensile strength and elongation are obtained. The specimens are held between the grips in the Universal testing machine, to avoid fracture the ends of the specimens are covered with very strong adhesive (tabs) and then clamped it between the grippers. The load is applied gradually and the force Vs displacement graph was noted. For a material of different size, it can be directly compared by the force and is usually divided by area of the sample yielding units per pound.[11-15]

Flexural Test

As per Standard ASTM C- 393, composite samples were cut to the dimension 120 mm x 25 mm x 10 mm. Flexural test is also known as three-point bending test or standard flexural test. The test is subjected by placing a composite sample across the two supports and then pressing on the top of the sample. The test determines the behaviour of the specimen when it is subjected to loading and also determines the maximum stress induced in the outermost fibre. The pressing is done with a single point of contact. The ASTM C-393 permits the use of either single loading, or two-point loading and they are usually termed as three -point and four- point flexure respectively. The fixtures are used in either configuration, one loading head being removed and the remaining one centred on the loading beam to perform three-point loading. The standard long beam flexure fixtures can also be customized.

During the flexural test, the deformation of specimen with respect to increasing in force is measured to calculate bending stress-strain curve. The test is being conducted on simply supported beams of constant cross-sectional areas.

RESULTS AND DISCUSSION

Tensile Strength

The tensile test is performed on three different combinations of sisal and epoxy, E-glass fiber and epoxy, sisal, E-glass fiber and epoxy. And the results are obtained in following table.

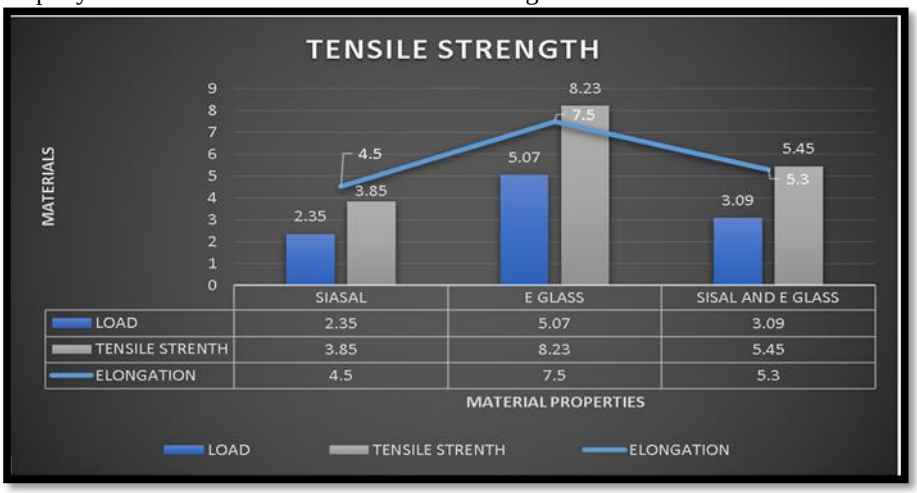

FIGURE 2. Tensile strength of the fabricated specimens

The tensile test result of hybrid composite is plotted. It is observed that there is no increment in tensile property of sisal-epoxy, due to the low adhesiveness between sisal and epoxy. Comparatively the Eglass fiber with epoxy shows good increase in tensile strength. In according to this the sisal and Eglass fibers are combined with epoxy which shows an enhancement in the tensile strength due to maximum load resistance property of E-glass fiber and low moisture absorbent property of sisal fiber. It also noted that tensile strength of composite increases along the direction of fiber.

Flexural Strength

The flexural test is also performed on three different combinations of sisal and epoxy, E-glass fiber and epoxy, sisal E-glass fiber and epoxy. And the results are obtained in following table.

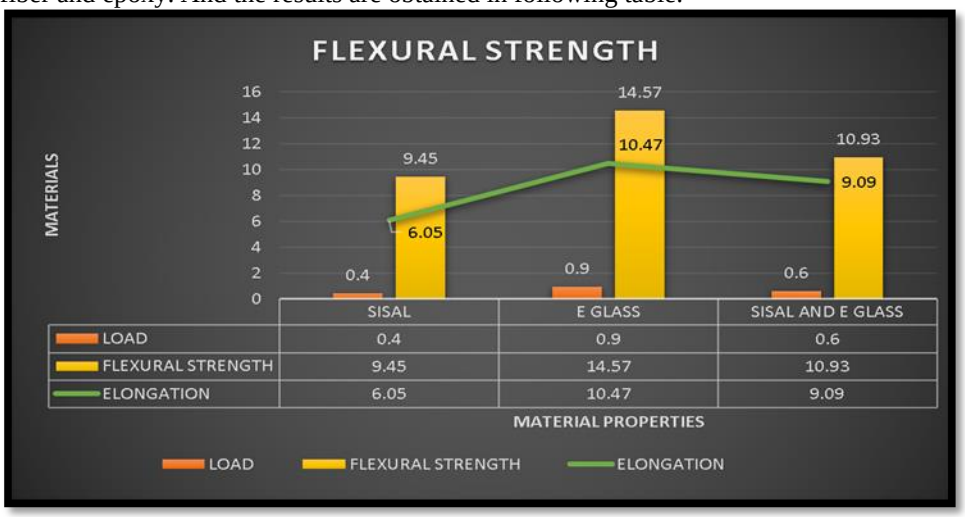

FIGURE 3. Flexural strength of the fabricated specimens

The flexural test is carried out by three-point bending equipment, with different material combinations. From results it is seen that sisal with epoxy produces less flexural strength. The performance of E-glass fibre is better the sisal fibre. The sisal glass fibre reinforced hybrid composite shows good increment in flexural strength due to longitudinal orientation of fibres. It is observed that as fibre content increases the strength also increases.

CONCLUSION

From the above experimental work, the hybrid composites are fabricated by hand layup technique. The specimens are tested and by results and analysis the conclusions are drawn.

1. The fiber orientation, fiber content and internal adhesive forces effects the mechanical properties of composite materials.
2. According to the study the composites orientation in longitudinal direction of fiber material increases the tensile and flexural strength.
3. It is seen that sisal fiber alone can't produce required result due to less cohesive forces between fiber and matrix. The reinforced glass fiber with sisal results in good mechanical property.
4. As the fiber and matrix content increases the internal adhesive forces increases which results in enhancement in properties.
5. The specimen fabricated using E-glass fibre shows excellent tensile and flexural properties, followed by the specimen fabricated using sisal-Eglass.

Although the Natural fiber reinforced hybrid composites are applicable in many engineering and industrial application, because of its superior properties like specific strength, low weight, good mechanical properties, ecofriendly nature and low cost. Hence the natural fibers with glass reinforced composites shows an improved result and incorporates to positivity effect in material science.

REFERENCES

1. A. May-Pat, A. Valadez-González and P.J. Herrera-Franco, "Effect of fiber surface treatments on the essential work of fracture of HDPE-continuous henequen fiber-reinforced composites", *Polymer Testing*, 32 (6) (2013), pp. 1114–1122.
2. Nikbakt S, Kamarian S and Shakeri M. "A review on optimization of composite structures" Part I: *Laminated composites. Compos Struct* 2018; 195: 158–185.
3. M. J. John and R. D. Anandjiwala. "Recent developments in chemical modification and characterization of natural fibre-reinforced composites". *Polymer composites*, 2008, Volume 29 (2): page number (187–207)
4. Govind Pathak, Om Prakash Dubey and Prafful Kumar Manoharan, "Mechanical properties of sisal/glass fiber einforced hybrid composites ", 2018 , pp.(70 – 76)
5. S. N. Monteiro, L. A. H. Terrones and J. R. M. D'Almeida. "Mechanical performance of coir fibre/polyester composites". *Polymer Testing*, 2008, Volume 27 (5): page number (591–595).
6. T. M. Gowda, A. C. B. Naidu and R. Chhaya. "Some Mechanical Properties of Untreated Jute Fabric-Reinforced Polyester Composites". Composites Part A: *Applied Science and Manufacturing*, 1999, Volume 30 (3): page number (227–284).
7. Ashish kumrea, R S Ranab and Rajesh Purohitc "A Review on mechanical property of sisal glass fiber reinforced polymer composites Proceedings 4 (2017) 3466–3476.
8. N Madhavi, K Sreelakshmi and M. Satyanarayana Gupta, "Evaluation of Ply Orientation on Failure of Composites", *International Journal of Civil Engineering & Technology* (IJCIET), Vol:8, Issue No:5, page No:409 - 417, ISSN No:0976 - 6316, May-2017.
9. John K and Naidu SV. "Effect of fiber content and fibertreatment on flexural properties of sisal fiber/glass fiber hybrid composites". J Reinf Plast Compos 2004; 23: 1601–1605.
10. N. Prabhu Kishore, "Performance Comparison of GFRP Composite I Section With An Aluminium I section", *International Journal of Civil Engineering and Technology*, 8 (4) (2017) ,pp. 278–286..
11. Kar KK. "Composite materials: Processing, applications, characterizations". 1st ed. Springer, 2017, p. 498.
12. Muhammed Anaz Khan, A. Vivek Anand, Lokasani Bhanuprakash, A. Ravindra and V. Hariprasad, "Mechanical Properties of E-Glass Fiber- Basalt Fiber Reinforced Polymer Matrix Composite", *International Journal of Recent Technology and Engineering*, 9 (2) (2020), pp. 1019-1022.6477

13. L. Bhanuprakash, S. Parasuram and S. Varghese, "Experimental investigation on graphene oxides coated carbon fibre/epoxy hybrid composites: Mechanical and electrical properties", *Composites Science and Technology*, 179 (2019), pp. 134-144.
14. S.S. Mathapati, B. Suresh. "Experimental Investigation and Failure Analysis of Glass Fibre Reinforced Epoxy Composite", *International Journal of Science and Research (IJSR)*, Vol. 4, no. 12, 2015.
15. Johnson, A.; Sims, G.: "Mechanical properties and design of sandwich materials". Composites **17**(4), 321–328 (1986)

RESEARCH ARTICLE | MAY 22 2023

Mechanical testing of coconut sheath fibre reinforced polymer composite in effect to various treatments with alkaline solutions

G. Manikandan ✉; P. Senthil Kumar; N. Dhavaneeswaran; R. Vinothini; R. K. Yokesvaran; M. R. Harish Kumar; M. Srikanth

AIP Conference Proceedings 2492, 040068 (2023)
https://doi.org/10.1063/5.0113219

Mechanical Testing of Coconut Sheath Fibre Reinforced Polymer Composite in Effect to Various Treatments with Alkaline Solutions

G. Manikandan[1 a)], P. Senthil Kumar[1], N. Dhavaneeswaran[2], R. Vinothini[2], R.K. Yokesvaran[2], M.R. Harish Kumar[2], M. Srikanth[3]

[1] *Department of Automobile Engineering, Kongu EngineeringCollege, Perundurai, Tamil Nadu, India.*
[2] *Department of Automobile Engineering, Kongu Engineering College,Perundurai, Tamil Nadu, India.*
[3]*Department of Aeronautical Engineering, MLR Institute of Technology, Hyderabad, India*

[a)] Corresponding author: manikandan.auto@kongu.edu

Abstract. Regular fiber strengthened polymer composites have arisen as a potential ecofriendly and financially savvy option in contrast to engineered fiber fortified composites. Over the previous decade, huge uses of characteristic fiber composites are utilized in significant ventures, like the development, bundling and car enterprises have shown an extensive interest in the advancement of new regular fiber fortified composite materials. The accessibility of normal fiber and the simplicity of assembling have enticed to consider the attainability of their application as fortification. Thus, the work towards is to study the mechanical properties of fiber made from coconut sheath and it is tested for tensile, flexural, impact and compressive load behaviors for the application in automotive bumpers. The Fiber Reinforced Polymer (FRP) composite was manufactured by hand layup technique after the NaOH solution treatment of coconut tree sheath. The manufactured samples are finished and tested according to the ASTM standards. The results obtained are compared with conventional materials (thermoplastic olefins, polyesters and polyurethanes) and found be greater than these materials. Thus the usage of coconut sheath fiber reinforced epoxy composite in automotive parts will be ecofriendly to the environment.

INTRODUCTION

It is clearly found that the characteristics of composite material rely on the fiber content, loading and orientation of the fiber. Pure epoxy resin has moderate wear resistance and impact strength. Natural fibers are added with the epoxy resin considerably enhances the tensile, compressive, impact properties. Tensile, compressive, wear resistance and impact strength differ as fiber functions and fibertreatment. The reason for treating fibers with NaOH solution i.e., improves fiber bonding with epoxy matrix. The characteristics like impact and tensile strength of coconut sheath fibers in epoxy matrix is comparatively good than other natural fiber. Hence the reinforcement of coconut sheath fibers is used in our project to get improved mechanical properties of the material.

FIBRE DESCRIPTION

The coconut sheath fibers (figure 1) are available plenty from Tamil Nadu and Kerala. These fibers areextracted by either by hand picking or mechanical cutting. The filaments were cleaned with water in the wake of splashing for 30 minutes. The strands were additionally dried in regular daylight to eliminate dampness content and long uniform filaments were acquired. Table 1 shows the propertiesof coconut sheath fiber. Coconut sheath filaments are effectively realistic in fiber and texture structures with great warm and mechanical properties among various normal strands. The inherent properties of coconut sheath fiber like low thickness, low lengthening at break, high pliable modulus, its particular solidness and strength similar to glass fiber.

Advancements in Aeromechanical Materials for Manufacturing: ICAAMM-2021
AIP Conf. Proc. 2492, 040068-1–040068-8; https://doi.org/10.1063/5.0113219
Published by AIP Publishing. 978-0-7354-4438-6/$30.00

FIGURE 1. Coconut Tree, Coconut Sheath Fiber

TABLE 1. Properties of Coconut Sheath Fiber

Properties (physical & mechanical)	Coconut sheath(experimental data)
Wax content (%)	0.41
Cellulose content (%)	68.36
Lignin content (%)	20.63
Moisture content (%)	8.79
Ash content (%)	1.04
Maximum stress (MPa)	119.8 – 128.6
Young's modulus (GPa)	7 – 18
Elongation (%) at break	5.5 – 6.8

PREPARATION PROCESS

Preparation of fibers and matrix

The coconut sheath fibers are cut at 19 cm × 19 cm (l×b) and it is used as reinforcement. For each sample of composite 3 layers of coconut sheath is used as reinforcement. Totally 3 samples of composite are made. Out of those samples first one is dry sample which consists of only coconutsheath layers, the second sample is treated with 2% NaOH and the third sample is treated with 4% NaOH. The coconut sheath fibers are immersed in NaOH for 10 to 15 minutes and then taken. The coconut sheath fiber samples are shown in the figures below.

FIGURE 2. Raw Coconut Sheath

FIGURE 3. 2% NaOH Treated Sheath

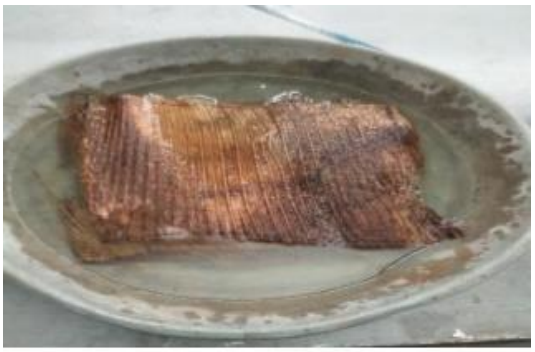

Figure 4. 4% NaOH Treated Sheath

Composite Preparation

In this, the composites are created by utilizing epoxy resin as a grid and coconut sheath fiber as a fortification material. Absolutely 3 examples were set up in various organizations to consider the mechanical properties of the coconut sheath fiber strengthened epoxy composites. The composite material was set up by customary hand lay-up method in mellow steel shape (75 mm × 75 mm × 10 mm) at room temperature. The form is extraordinarily intended to create 10 mm thickness plate. Here7 mm thickness composite example is readied. Epoxy resin LY 556 and hardener HY 951 wereutilized as the network materials. Figure 5 shows the resin and the hardener utilized. The pitch and hardener were blended and mixed precisely in a proportion of 10:1 by weight. The layup composite creation procedure is utilized and stacked layers one over the other is kept. Absolutely 3 layers of coconut sheath is kept and afterward, the resins were filled the shape and shut firmly. The materialwas permitted to fix in room temperature for around 10 to 12 hours. The test examples were set up according to ASTM guidelines. Figure 5. shows the example subsequent to cooling in the room temperature.

FIGURE 5. Composite Specimen

Preparation of Specimen According to Standards of ASTM

The examples are sliced to the accompanying measurements according to ASTM principles appearedin figure 6.

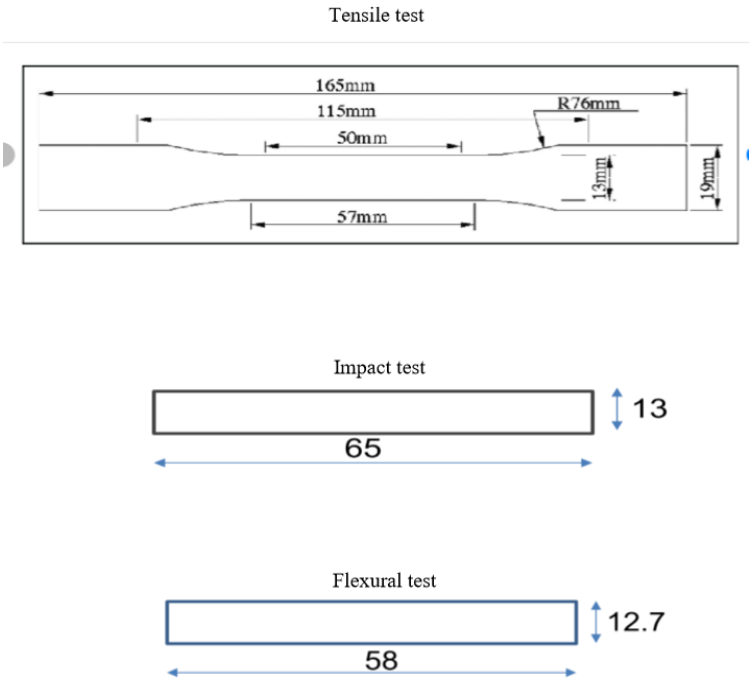

FIGURE 6. ASTM Standard Dimensions for Testing

SPECIFICATIONS OF SAMPLES

1.MATRIX	-	**Epoxy resin**
2.REINFORCEMENT	-	**Coconut sheath fiber**
3.VOLUME FRACTION	-	
Sample 1 - **Dry coconut sheath fiber**		
Sample 2 - **2% NaOH treated fiber**		
Sample 3 - **4% NaOH treated fiber**		
4.PATTERN TYPE	-	**Vertical orientation**
5.PROCESS METHOD	-	**Hand lay-up**

Figure 7. Specification of samples

TESTING

Impact Testing

An Izod impact testing was performed to research the effect strength of the overlays utilizing an effect analyzer as per ASTM D256 norms with an example size of 65×13×7 mm3. Six indistinguishable examples were analyzed under every classification, and the normal qualities were accounted for. The consumed energy during impact is the measure of energy needed to crack the example totally. The examples recorded in the creation table are exposed to Izod impact test according to ASTM D256 guidelines. The determinations of the machine utilized for impact testing is given in the table 2.

Table 2. Specification of Impact Testing Machine

System status	Digital
Span length of charpy vice	Adjustable from 40 mm to 100 mm
Impact speed	3.46 m/s
scales	2 J, 5 J, 10 J, 15 J, 25 J
Results expressed in terms	J/mm
Hammers	Two hammers for Izod test

The impact strength graphs for the samples are shown in the above figures. The average impact strength is obtained from those graphs and finally the impact strength for dry sample, 2% NaOH sample and 4% NaOH samples have been plotted in the figure 8.

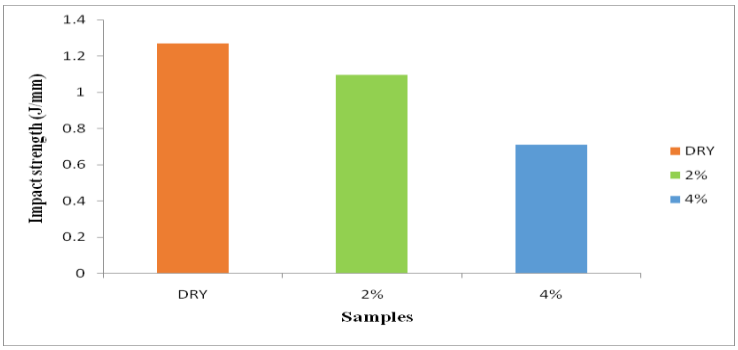

FIGURE 8. Impact Strength (J/Mm)

From the bar chart, it is inferred that 4% NaOH treated sample has very low impact strength when compared to remaining samples. The 2% NaOH treated sample and 4% NaOH treated sample exhibit 1.097 J/mm and 0.709 J/mm respectively. Pure dry coconut sheath fiber reinforced epoxy composite exhibited higher impact strength 1.269 J/mm. It was discovered that from the figure, there was abrupt drop in the effect strength because of expansion of NaOH in the composites. This shows that by expansion of NaOH, de-holding happens and the effect strength lessens. All the examples are contrasted and surmised and each other based on effect strength acquired. Accordingly, from the inference obviously the expansion of NaOH to the coconut sheath fiber strengthened epoxy composite diminishes the effect strength.

Tensile Testing

TABLE 3. Specification of Universal Testing Machine (Tensile)

Capacity	10 kN
Maximum cross head travel	1100 mm
Testing speed range	0.001 to 1000 mm/min
Maximum cross head speed	500 mm/min
Jog speed	0.001 to 1000 mm/min
Return speed	0.001 to 750 mm/min
Dimension (H × W × D)	1600 mm × 650mm × 450 mm

The tensile strength graphs for the samples are shown in the above figures. The tensile properties of composites for the most part rely upon the weaving idea of the texture, the layering design, the thickness, and the fiber/lattice grip. The average tensile strength is obtained from those graphs and finally the tensile strength for dry sample, 2% NaOH sample and 4% NaOH samples have been plotted in the figure 9.

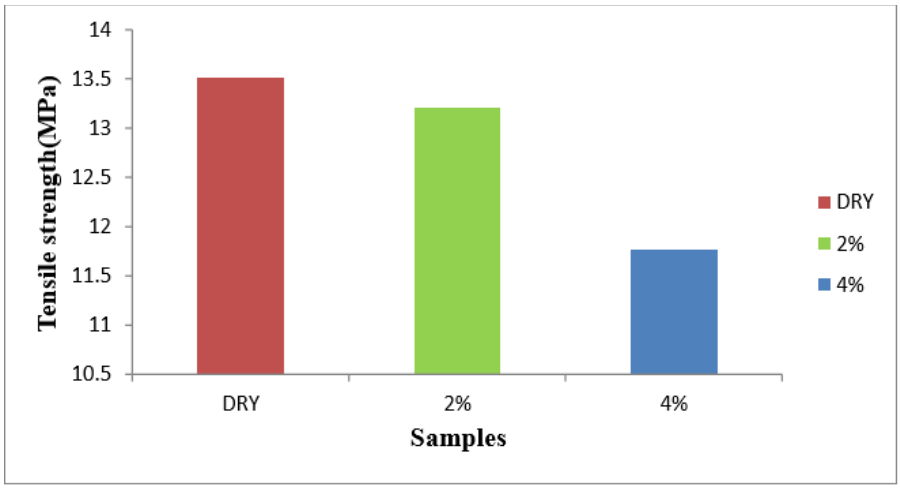

FIGURE 9. Tensile Strength (Mpa)

From the bar chart, it is inferred that 4% NaOH treated sample has very low tensile strength when compared to remaining samples. The 2% NaOH treated sample and 4% NaOH treated sample exhibit

13.21 MPa and 11.76 MPa respectively. Pure dry coconut sheath fiber reinforced epoxy composite exhibits higher tensile strength of about 13.51 MPa. It was discovered that from the figure, there was unexpected drop in the effect strength because of expansion of NaOH in the composites. This shows that by expansion of NaOH, bond property of fiber misfortunes and the elasticity diminishes. Accordingly, from the inference unmistakably the expansion of NaOH to the coconut sheath fiber strengthened epoxy composite diminishes the rigidity.

Flexural Test

Table 4. Specification of Universal Testing Machine (Flexural)

Capacity	10 kN
Maximum cross head travel	1100 mm
Testing speed range	0.001 to 1000 mm/min
Maximum cross head speed	500 mm/min
Jog speed	0.001 to 1000 mm/min
Return speed	0.001 to 750 mm/min
Dimension (H × W × D)	1600 mm × 650mm × 450 mm

The flexural strength graphs for the samples are shown in the above figures. The average flexural strength is obtained from those graphs and finally the flexural strength for dry sample, 2% NaOH sample and 4% NaOH samples have been plotted in the figure 10.

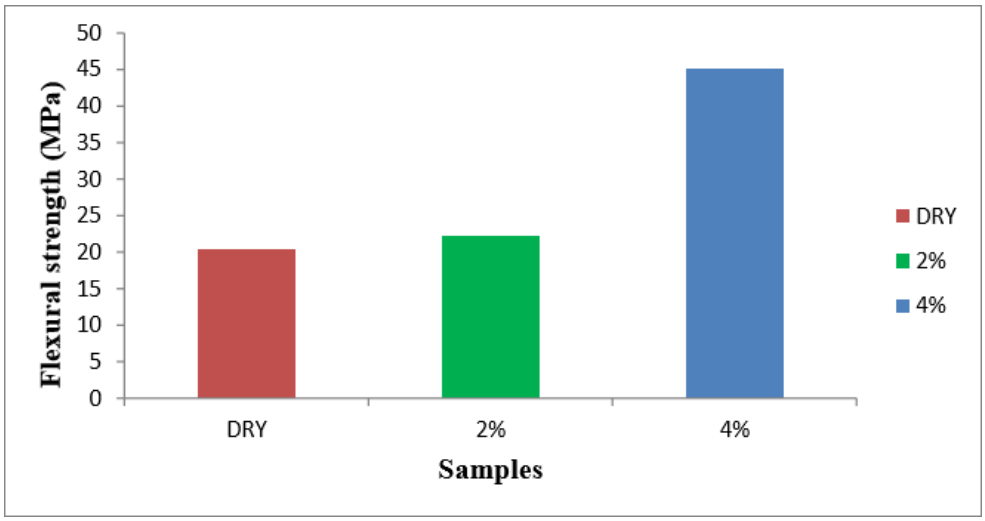

FIGURE 10. Flexural Strength (Mpa)

From the bar chart, it is inferred that 4% NaOH treated sample has very high flexural strength when compared to remaining samples. The 2% NaOH treated sample and dry sample exhibit 22.21 MPa and

20.35 MPa respectively. The 4% NaOH treated coconut sheath fiber reinforced epoxy composite exhibits higher flexural strength of about 45.07 MPa. Due to both tension and compression stresses acting on a bending specimen, it was found that both dry and 2% NaOH treated composite specimens were failed due to de-lamination. The flexural strength of composite plate specimen (4% NaOH) treated has better strength compare to other plates.

CONCLUSION

Fiber treatments were vital factor to fabricate common fiber composites since it can improve the flexural properties indeed by making great interfacial holding among strands and network. This implies that entomb surface assumes a predominant part in flexural and holding properties in a composite. The maximum value of impact strength is 1.269 J/mm which is identified in dry sample, the maximum value of tensile strength is 13.51 MPa which is exhibited in dry sample, the maximum value of flexural strength is 45.07 MPa which is exhibited in 4% NaOH treated sample. It is seen that the mechanical conduct of the composites for example, elasticity, and bowing strength of the composites are vitally biased by the treatment of NaOH to the fibers. The comparison with other material shows that coconut sheath fiber composites can be used as a replacement for automotive components.

REFERENCES

1. Naresinajan.M.P, Rajmohan.B, Devarajulu.S, “Effect of ingredients on mechanical and tribological characteristics of different Brake Liner Materials”. International Journal of Mechanical Engineering and Robotic research, IJMERR, ISSN 2278 – 0149.
2. Marimuthu.K.P, Kumar.S.M and Govindaraju, “Characterization of Mechanical Properties ofEpoxy Reinforced with Glass Fiber and Coconut Fiber”. Materials Today: Proceedings, Pg. (661-667)
3. Sinha.A.K, Narang.H.K and Bhattacharya.S, “Mechanical properties of natural fibre polymer composites”. Journal of Polymer Engineering, Pg. (879-895), 2017.
4. Zhezhen, Shicheng et al., “Jute fibers and powderized hazle nut shells as natural fibers innon-asbestos organic non-metallic friction composites”. Sciverse science direct – material and design, Pg. (847-853), 2013.
5. Albert.Y.M.L, Marc.A.M and Kenneth.S.V, “Mechanical properties and structure of Strombus gigas, Tridacna gigas, and Haliotis rufescens sea shells a comparative study”. Journal of Materials Science and Engineering, pg. (1380 – 1389), 2006.
6. C.W.Chin, B.F.Yousif et al., “Potential of kenaf fibers as reinforcement for tribological applications. Science direct – Wear, Pg. (1550-1557), 2009.

7. Siva Sravanan. S, V.K.Bupesh Raja et al., “Impact characterization of epoxy LY 556/ EGlassfiber Nano clay hybrid nano composite materials. Science direct, Procedia Engineering, Pg. (968-974), 2014.
8. Akhil. A.B et al., “Preparation and characterization of banana reinforced phenol formaldehyde composite”. Journal of Materials Science and Engineering, pg. 1380 – 1389, 2006.

RESEARCH ARTICLE | MAY 22 2023

Analysis of air flow distribution in raisin dryer

A. Saravanan; R. Naveen Kumar; K. Paramasivam; S. Kishore; A. Udaya Deepika

AIP Conference Proceedings 2492, 020074 (2023)
https://doi.org/10.1063/5.0114003

Analysis of Air Flow Distribution in Raisin Dryer

A Saravanan[1,a)], R NaveenKumar[1,b)] , K Paramasivam[1,c)] , S Kishore[1] and A Udaya Deepika[2]

[1] *Department of Mechanical Engineering, Kongu, Engineering College, Erode, India.*
[2]*Department of Aeronautical Engineering, MLR Institute of Technology, Hyderabad, India*

[a)] schatzsaravanan@gmail.com
[b)] nawinerd@gmail.com
[c)] param.mech@kongu.edu

Abstract. The aim of the project is to find the best and efficient arrangement for drying the grapes in short period of time, though there are many ways of drying the grape like from the traditional method this method provide good results and with some alterations in the setup the efficiency of the apparatus raise drastically as the temperature is increased highly with the help of the TEG chips.

Keywords-Grapedrying, TEGchips, Solarenergy, CFDanalysis.

INTRODUCTION

The usage of solar energy has been increased tremendously as it is a renewable energy. The rise of cost in fossil fuels and non-renewable energy sources made the renewable sources are in the emergence as the future energy source. Solar energy can be used directly and indirectly as energy or fuel for various processes. Here we use the both the ways as solar energy and solar heating for the purpose of drying. The first is the solar energy to run electric products like Thermo Electric Generator (TEG). The heat energy from the TEG chips is used to produce the necessary heat for the drying process and then heat is forced with the help of a blower in the form of air that is heated air. This setup is used for the purpose of drying raisins in short period of time. This setup is having good result but not that efficient so to improve the efficiency the setup is altered in different ways in the ANSYS CFD analysis to get the results so as to choose the best setup with higher usage and efficiency. The Analysis is done because doing all these in physical way will need lot of power and time so analysis will give near exact results so it will be easy to find the efficient method.

MATERIALS AND METHODS

Materials Used

The Materials used for the set up are Motor (775), GI Pipe, TEG Chip, Solar Panel, Aluminum foil, Battery, Fan, Metal Fame, Aluminum sheet.

Experimental Setup

The setup consists of a blower, container, heating element, aluminum foiling pipe. First the blower is connected to GI pipe having the heating element inside the pipe. The air from the blower carries the heat from the heating element

Advancements in Aeromechanical Materials for Manufacturing: ICAAMM-2021
AIP Conf. Proc. 2492, 020074-1–020074-5; https://doi.org/10.1063/5.0114003
Published by AIP Publishing. 978-0-7354-4438-6/$30.00

to the container. And the heating element and the blower speed are adjusted in order to maintain constant temperature. Aluminum foil is wrapped around the GI pipes inorder for more heating. With the help of the hot air the drying process is carried out. Solar power along with electric power is used for operating the setup. This setup is previously done practically and results are observed and found that the efficiency is very low so in order to get good results the following changes are carried out to get the best result.

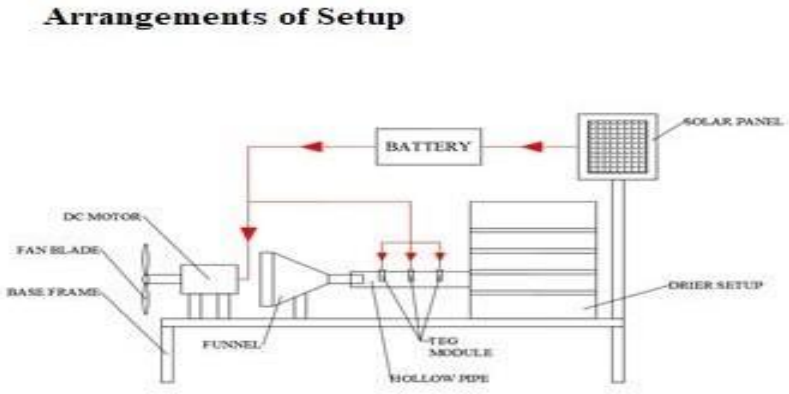

FIGURE1. The following are the arrangements done to the setup

Working Process

Initially this setup is placed in the region where the sun rays are high and also the materials which has to dried is loaded inside the container. The blower fan is turned on which absorbs atmospheric air to reach the system. The air from suction fan is allowed to pass through preheat chamber which consists of TEG module, this module also receives source from battery and thus liberates hot at one end and cold at another end due to Peltier effect. The atmospheric air crossing this module gets heated and this hot air is allowed to enter into the drier arrangement. This hot air when reaching the container again transfers the heat to the aluminum foil provided and this helps to maintain a hot temperature inside the chamber, which helps to remove the moisture content form the materials and thus the drying process takes place. This air is again excavated to the atmosphere through the provide exhaust holes. With the help of solar panel provided with our system the battery gets charged with the help of solar radiation and that stored energy is used to run the motor to blow air. This setup is made to dry about 3 to 5Kilograms of grapes in one run.

ANALYSIS

Objective

The setup runs very well upon practical testing but that is not as efficient as expected. The TEG Chips placed perpendicular to the flow of air will do the heating process but on the other side of TEG cold is produced, which in turn reduces the heat generated from the chip so that is not efficient. Also the flow of air is not uniform inside the chamber.

CFD Analysis

To overcome the above problems different setup are used and doing all them is physically not easy hence ANSYS software is used for simulation. First the setup is made as 3D model in solid works software and then the 3D model is imported to the ANSYS software. In the ANSYS software CFDANALYSIS is carried out for the various setup made. The CFD results are more near accuracy hence with that result we can easily find the most efficient setup.

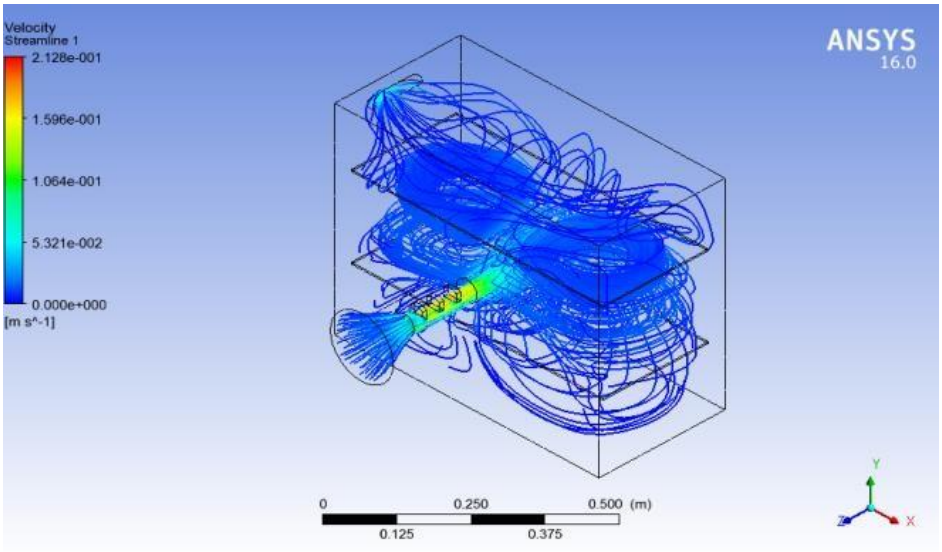

FIGURE2 . TEG placed perpendicular to the airflow

The Figure 2 consists of the setup with arrangement of TEG placed perpendicular to the air flow. It is the basic setup in which both the hot and cold sides are inside the pipe. This system is not that efficient as the cold produced inside may affect the heat generation inside.

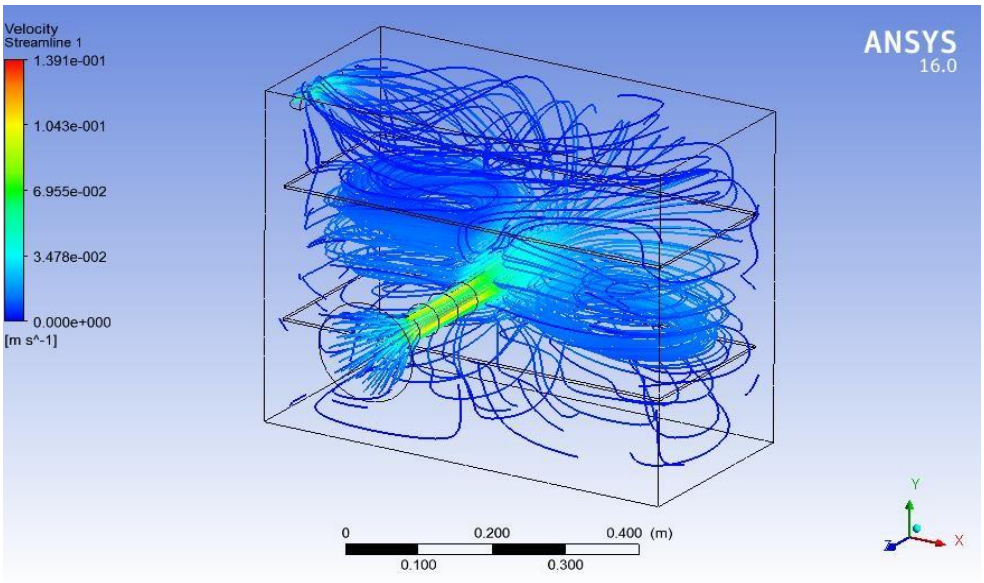

FIGURE3. TEG placed parallel to the air flow and the pipe is at the centre of the container

The figure 3 represents the setup with TEG placed parallel to the air flow and the pipe is at the centre of the container. Here the cold side is outside facing as the chip is mounted on the pipe itself, so only the heat will pass through and will have more heat inside.

Comparing these two the parallel arrangement have mare efficiency than the perpendicular placements in the upcoming setup the perpendicular setups are not taken only the parallel setup is used to have higher heat generation inside the container.

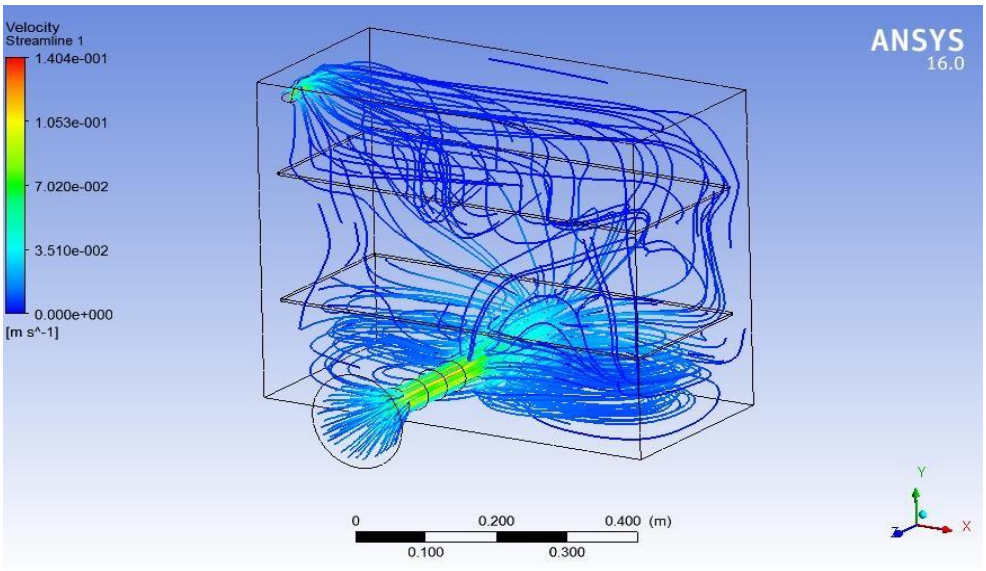

FIGURE 4. TEG parallel arrangement but the pipe is placed at the bottom portion of the container

Thefigure4 represents the TEG parallel arrangement but the pipe is placed at the bottom portion of the container in order to have good flow of air from bottom to top of the container. This setup gives better result than on the center portion.

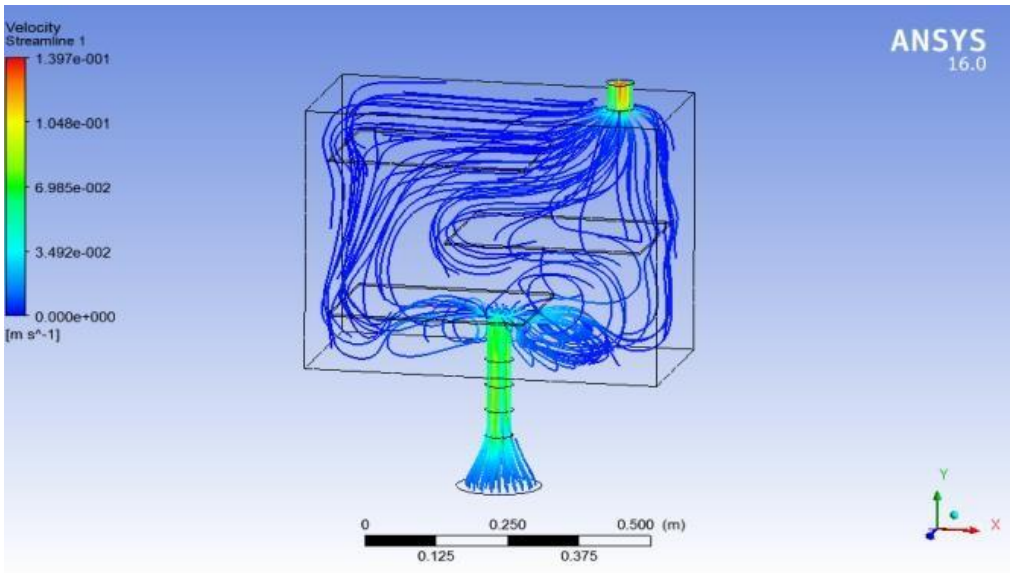

FIGURE 5. TEG parallel placement and the pipe at the bottom of the container and in addition to that the slits inside the container are arranged

The figure 5 represents the TEG parallel placement and the pipe at the bottom of the container and in addition to that the slits inside the container are arranged as shown in figure in order for good flow of air all around the container to have a even distribution of heat through the process.

With the result of these four setups, it is concluded that with constant velocity and pressure inversely proportional at constant the temperature is observed to be high at the setup with parallel placed TEG to the flow of air with pipe at the bottom of the container.

CONCLUSION

Thus, upon successful analysis, required results came with more efficiency and it will help the drying process more quickly as the tray arrangement in the setup will provide an even drying of the raisins and have a rich raisin. With this arrangement the drying will be quick and saves a lot of time than the traditional methods of drying which is the open and closed shade sun drying which will take week for the process to complete. This one uses the solar power effectively for the drying purposes. This setup may be used for large scale purpose also if the system is made at big scale with necessary amount to be dried.

REFERENCES

1. Adiletta G, Senadeera W, LiguoriL, Crescitelli A, AlbaneseD, RussoP. (2015).The influence of abrasive pretreatment on hot air drying of grape. Food and Nutrition Sciences, 6(3), 355–364.
2. Ayensu A., Dehydration of Food Crops Using Solar Dryer with Convective Heat Flow, 2000, Research of Department of Physics, University of Cape Coast, Ghana.
3. Boyer, R. Huff, Karleigh. Using Dehydration to Preserve Fruits, Vegetables, and Meats. Virginia Tech, Virginia state University, pp 348-597., April2008.
4. Gabas,A.L.;Menegalli,F.C.;Telis Romero, J.Effect of chemical pre treatment on the physical properties of dehydrated grapes. DryingTechnology1999, 17(6), 1215–1226.
5. Garg & Prakash, H. P. Garg, “Solar energy: fundamentals and applications”, Tata McGraw-Hill Education, 2000.
6. Hosseinpour,S.; Rafiee,S.; Mohtasebi,S.S. Application of image processing to analyze shrinkage and shape changes of shrimp batch during drying. DryingTechnology2011,
7. 29(12), 1416–1438.
8. Jairaj KS, Singh SP, Srikant K. (2009). A review of solar dryers developed for grape drying. Solar Energy, 83(9), 1698–1712.
9. OlaleyeD.O., The Design and Construction of a Solar Incubator, 2008, Project Report, submitted to Department of Mechanical Engineering, University of Agriculture, Abeokuta
10. Olayinka ADUNOLA, Design and construction of a Domestic Passive Solar Food Dryer, 2014, department of mechanical, Nigeria
11. Ong K.S, Results of investigation into forced convection and natural solar heater and dryers. Reg J Energy Heat and MassTransfer, 1982, 4 (1), pp. 29-45.
12. Patel, A; Shah, S.A; Bhargav, Hitesh. Review on Solar Dryer for Grains, Vegetables and Fruits. Birla Vishvakarma Mahavidyalaya Engineering College. International Journal of Engineering Research &Technology (IJERT), Vol. 2Issue 1, January-2013
13. RaviHosamani, Dr.Satish.R. Desai “Solar Based Temperature Controlled Fruit Drying System”, International Journal of Research in Instrumentation Engineering (IJRAIE), Vol. 1, Issue.2, Sep. 2013.
14. Sharma K, A. Colangelo & G. Spagna, "Experimental Performance Of Indirect Type Solar Fruit and Vegetable Dryer", ENEA-C. R.E. Trisaia, Italy
15. Sharma VK, Sharma S, Ray RA, Garg HP. (1986). Design and performance studies of a solar dryer suitable for rural applications.EnergyConversionandManagement, 26(1), 111–119.
16. SukhatmeS.P, Solar-Energy-Principles of Thermal Collection and Storage, Tata McGraw Hill Publishing Company Limited, 1996.

RESEARCH ARTICLE | MAY 22 2023

Topology optimization of aluminium alloy wheels for SUV

B. A. Rithish; J. Logeshwaran; S. Sanjeev; R. Balamurugan ✉; P. Arunkumar; K. Arun Kumar

AIP Conference Proceedings 2492, 040073 (2023)
https://doi.org/10.1063/5.0113358

Topology Optimization of Aluminium Alloy Wheels for SUV

B A Rithish[1], J Logeshwaran[1], S Sanjeev [1], R Balamurugan[2, a)], P Arunkumar [2], K. Arun kumar[3]

[1]*Department of Automobile Engineering, Bannari Amman Institute of Technology, Erode, India - 638401.*
[2]*Department of Mechatronics Engineering, Sri Krishna College of Engineering and Technology, Coimbatore, India - 641008.*
[3]*Department of Aeronautical Engineering, MLR Institute of Technology, Hyderabad, India.*

[a)] Corresponding author: balamuruganrs@bitsathy.ac.in

Abstract. In this technological era, there is a new technology developing every day. The matter is that these new technologies will have intense domination in future or not. Here, Inthis paper, we performed Topology optimization of aluminium alloy wheels for sports utility vehicle (SUV). Wheels are one of the most crucial components, and they should be designed sothat their dimensions and shape should suitably accommodate the type of tyre required for the vehicle. Here, we designed an aluminium alloy wheel suitable for the disc wheel category. We utilized Solid Works 2020 to design our 3D wheel rim, As the time spent developing our wheel rim is reduced drastically, and the software is very user friendly. Later, this model is imported to Ansys workbench 16.0 for meshing. We performed the meshing process in our model to create a fine mesh of 5mm using the tetrahedron element. Later, this mesh model has importedto Altair inspire 2019.4 software for further analysis and optimization process as it can producenear to real design topology optimization and exact simulation results. Initially, Altair inspire 2019.4 is utilized to simulate the different working conditions like vertical forces exerted by the vehicle, pressure load applied on the tyres, and the wheel's rpm. The analysis process is carried out, and the results are acquired for further procedures. By utilizing the analysis results,Topology optimization is performed on the wheel rim for reducing weight by 30% and 40% respectively. The optimized designs are acquired and subjected to an analysis process to check whether the design can withstand original working conditions. Later the analysis results are obtained and compared for the best design structure, withstand the working conditions, less weight and uncompromised performance.

INTRODUCTION

Car wheels have developed throughout a very long time, from early talked designs of wood and steel, level steel circles to the stepped metal arrangements and current cast and fashioned aluminium alloys rims of the present-day vehicles. Generally, impressive designs show up after a while of involvement and comprehensive field testing. Lately, the methodology has been improved by an assortment of experimental and scientific methods for structural analysis and unwavering quality methods for managing the varieties natural in designing structure have been applied to the car wheel. Wheels are unmistakably well-being-related components, and subsequently, fatigue execution and the condition ofstress in the rim under different loading conditions are prime concerns. Further, wheels keep ongetting a lot of consideration as a feature of industry endeavours to decrease weight through material replacement and downsizing. Even though wheels are loaded in a mind-boggling way and are profoundly stressed during their moving obligation, lightweight is one of the prime necessities, henceforth cast and produced aluminium alloys are primary in the design[1].

Wheels have a crucial significance for the vehicle's safety, and uncommon care must guarantee their durability. The vehicle business's advancement has unequivocally affected the design, material determination, and manufacturing processes of the wheels. They are loaded in a complex way, and further improvement and effective wheel design will be conceivable just if their loading will be better perceived. To accomplish an ideal design of the wheel, two necessities are required: the exact information on the loading and the mechanical properties and

Advancements in Aeromechanical Materials for Manufacturing: ICAAMM-2021
AIP Conf. Proc. 2492, 040073-1–040073-13; https://doi.org/10.1063/5.0113358
Published by AIP Publishing. 978-0-7354-4438-6/$30.00

allowable stresses of the material, whichrely upon the vehicle qualities, administration conditions and manufacturing processes[2]. Today, most producers build up the wheel design dependent on the consequences of the standard powerful outspread fatigue test, the rim roll test, and the dynamic cornering fatigue test called the rotating bending test[3].

Another possibility is to use the finite element method to establish the stresses in the wheel rim and compare the different design solutions. However, the rim's real loading model cannot be accurate enough, which is why the results should be used with precaution. This method is beneficial for comparing different design solutions and selecting the rim that should be tested further.

Accordingly, it is defended to have a definite analysis utilizing a strategy like FE for the stresses created during utilized. It is proposed to break down the car rim utilizing the FE approach for shifted calculation parametric boundary for optimizing its weight. Weight optimization in the car industry is a functioning subject of study and now daily expanding lightweight commercial vehicles because of its efficiency and right choice.

FIGURE 1. methodology of the project

These days, every industry tries to produce the necessary components utilizing a minimal number of raw materials and maintaining the component's primary qualities flawless or surprisingly better. The ideal choice utilizes the Topology optimization process of reducing the given component understudy's raw material until the best design and shape is achieved. A genuine model is how to arrive at the most grounded conceivable design and still utilize a minimal measure of material[4].

Additive manufacturing permits the manufacturers to fabricate even the weirdest and most complex designs. Consequently, The recent advancements empower makers to utilize the most advanced types of programming software's to acquire the best designs without agonizing over the manufacturability prospects accessible to use in the wake of completing the design stage[5].

OBJECTIVE

The main objective of the project is to develop a fancy aluminium alloy wheel utilizing topology optimization process, where the wheel can withstand the actually working conditions of the road. The project begins with the study of existing Alloy wheel's design in the market that allows us to sketch an alloy wheel to start the reverse engineering technique and checking the ability of the basic model in With standing the normal working conditions. Later the basic model is subjected to optimize topologically for weight reduction. Then follows the redesigning of alloy wheel to the shape obtained by the topology optimization. Then applied the selected material to the wheel to get the best out of the optimized wheel. Ultimately, the topology optimized wheel is analysed and compared with the basic wheel for its stresses and deformations[6-9].

MATERIAL PREFERENCE

Even though we care more about the durability of the material we use, researchers have built up an extraordinary interest in lightweight materials, for example, Magnesium, Titanium….and so forth. Close by the durability, there should be gorgeous car rims since it is perhaps the most alluring assistants to care for car lovers worldwide.

Considering durability, lightweight, manufacturability and cost as a concern, we choose aluminium alloy as it is very much suiTABLE for rim manufacturing both in the traditional and additive manufacturing method.

Aluminium alloy 2024 is used in this application as it requires high strength to weight ratio and good fatigue resistance[10-12].

TABLE .1 Physical properties of aluminium alloy 2024

Physical Property	Density	Young's modulus	Poisson's ratio	Shear modulus	Tensile yield strength	Tensile ultimate strength
metric	2.78 g/cc	73.1 GPa	0.33	28 GPa	324 MPa	469 MPa

DETAILED DESIGN

Design is where the whole concept of an idea takes its shape before manufacturing, and here wedisplay the design parameter of our rim below. We have designed the rim using Solid works 2020.

FIGURE 2. Detailed design view of our project (All dimensions are in inches)

Loading and Constraints

Considering various real-time values and random data, we finalized these values to minimize thestatistical uncertainty, concerning the results to be accurate.

- The average weight of SUV - 1400 kgs
- Average passenger weight - 400 kgs
- Standard tire pressure of SUVs ranges from 32-36 Psi. Its assumed 34 psi as ideal pressure.
- The maximum speed capability of the tire - 100km/hr

With respect to the above inferences, we calculated the following values applicable to the alloy wheel.

Vertical load

- Gross vehicle weight - 1800kgs
- Vertical force applied on wheel (F_v) = 1800*0.25*9.8= 4414.5 N

Tire pressure

- Psi into M Pa
- Psi - pounds-force per square inches1 psi = 0.00689Mpa
- So 34 psi = **0.2344 M pa**

Rotational velocity

Km/hr = Wheel Diameter (cm) * RPM * 0.001885100/(40.64*0.001885) = **1300 RPM**

The above calculations states that the Total weight of the car is converted into vertical force of **4414.5 N**, which is applied on the wheel rotating at **1300 rpm** along with the pressure of **0.2344 M pa**.

FINITE ELEMENT ANALYSIS

FIGURE 3. Weight determination

The plain rim's estimated mass-produced using the above design with Aluminum alloy 2024 is **26.132 kg s**. Further, This design is subjected to the real working conditions and topology optimization process for reducing the weight without compromising its performance.

TABLE .2 Mass details of the basic rim

Material	**Aluminium alloy 2024**
Mass	26.132 kg s

MESHING

In the finite element method, the fascinating part is partitioned into sub domains called elements, and we inexact every element's capacity independently. The development of the subdivision into elements is named discretization. The arrangement of all elements speaking to a subdivision comprises the finite element mesh. We can set up an alternate discretization for the part on the off chance that we need to get improved exactness from a finite element analysis, utilizing a more modest element size, which expands an enormous number of finite elements in the

analysis. The process of re- discretizing utilizing more subtle elements is named mesh refinement. We can say that as we refine the mesh, the rough, finite element solution will be nearer to the correct answer[13].

Each finite element has a few focuses called nodes, and it is advantageous to build up the nodal estimations of the fieldwork as the steady boundaries of the rough solution.

TABLE .3: Mesh Details

Element	Mesh type	Mesh size	No of Nodes	No of Elements
Tetrahedron	Fine	5 mm	124235	68494

ANALYSIS RESULTS OF THE BASIC RIM

The analysis is carried out utilizing Altair Inspire 2019.4 on the above design to determine the wheel rim's structural durability with the normal working conditions applied on the rim.

When an external force is applied to a structure, the structure will generally go through some deformation. Because of the connection between the particles, the body contradicts deformation.

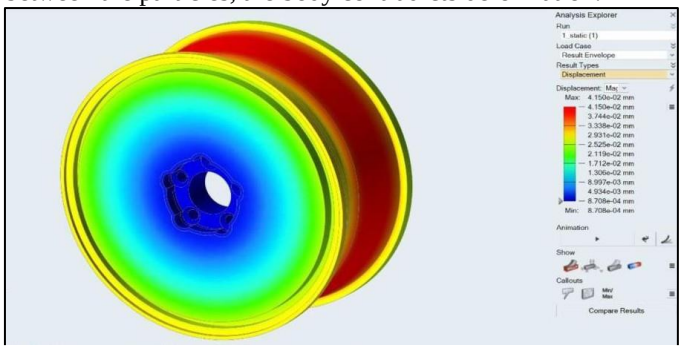

FIGURE 4: Total deformation of the basic rim

This obstruction by which material of the body opposes the deformation is known as the strength of the material. Inside a particular limit, the material's opposition corresponds to the deformation purchased out on the material by an external force. Likewise, inside the limit, the obstruction is

equivalent to the external force. In any case, past the elastic limit, the material's opposition is lower than the applied load. In such cases, the deformation proceeds until a failure happens.

TABLE .4 Total deformation of the basic rim

Input values			Output values	
Vertical load	**Pressure load**	**Rotational velocity**	**Max .Displacement**	**Min .Displacement**
4415 N	0.2344 M pa	1300 RPM	0.04150 mm	0.0008708 mm

Tension and Compression

When subjected to two equal and opposite pulls, the stress-induced in a body results in increasing the body's length is known as tensile stress or tension.

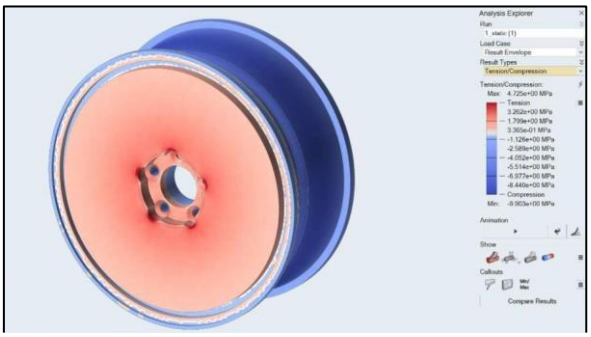

FIGURE 5: Tension and Compression of the basic rim

The stress-induced in a body, when subjected to two equal and opposite pushes results indecreasing the length of a body is known as compressive stress or Compression.

TABLE .5 Tension and Compression of the basic rim

Input values			Output values	
Vertical load	**Pressure load**	**Rotational velocity**	**Tension**	**Compression**
4415 N	0.2344 M pa	1300 RPM	4.725 M Pa	9.903 M Pa

Von-mess stress

Von Mess stress is a value used to determine if a given material will yield or fracture. It is mostly used for ductile materials, such as metals. The von Mess yield criterion states that if the von Mess stress of a material under load is equal or greater than the yield limit of the same material under simpletension, the material will yield.

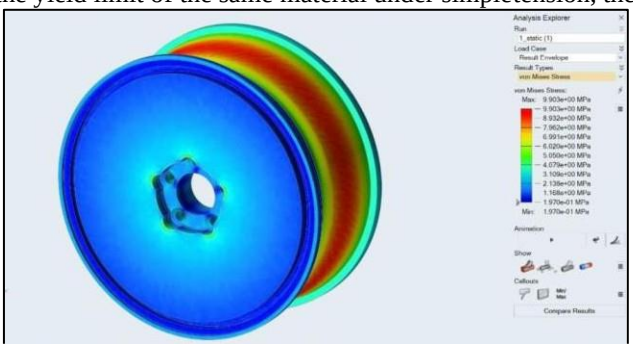

FIGURE 6. Von mess stress of basic rim

We can calculate a factor of safety as the maximum allowable stress ratio to the equivalent stress (Von-Mises) when using Yield Strength. It must be over 1 for the design to be accepTABLE. (Less than one means there is some permanent deformation.) When using Ultimate Strength, Maximum Principal stress is used to determine safety factor ratios.

Factor of safety = Tensile yield strength / Von-Mess Stress = 324 / 9.903 = **32.717**

TABLE .6 Von Mess Stress of the basic rim

Input values			Output values	
Vertical load	**Pressure load**	**Rotational velocity**	**Max .Stress**	**Min .Stress**
4415 N	0.2344 M pa	1300 RPM	9.903 M Pa	0.197 M Pa

Principal Strain

According to principal strain theory, the failure will occur in the material when the maximum principal Strain reaches the Strain due to yield stress in simple tension or when the minimum principal Strain reaches the Strain due to yield stress in simple Compression.

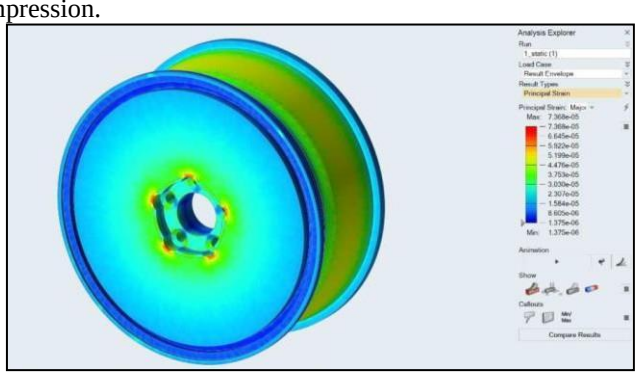

FIGURE 7. Principal Strain of basic rimYield stress is the maximum stress at the elastic limit.

TABLE .7 Principal Strain of basic rim

Input values			Output values	
Vertical load	**Pressure load**	**Rotational velocity**	**Max .Strain**	**Min .Strain**
4415 N	0.2344 M pa	1300 RPM	0.00007368	0.000001375

OPTIMIZATION RESULTS

The above design is subjected to Topology optimization by which the weight of the rim is reduced without compromising much on the performance aspect of the rim. Here the normal working conditions are applied on the rim to receive a perfect and fully optimized structure.

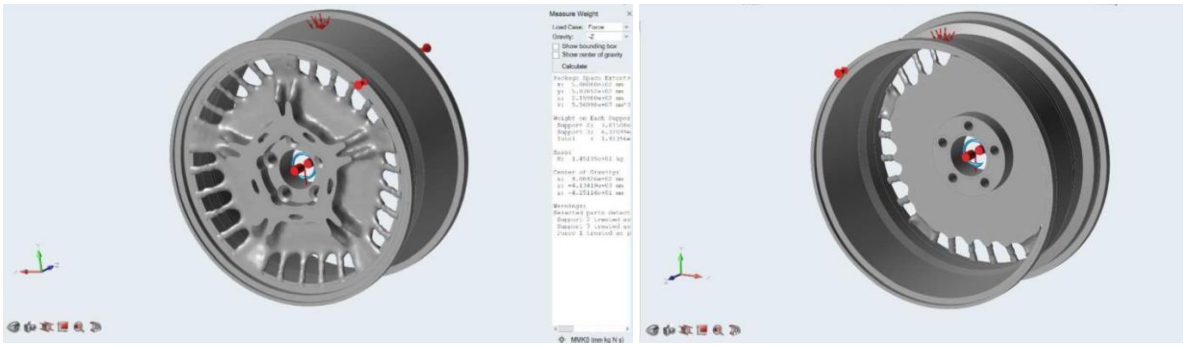

FIGURE 8. Front and Rear view of optimized design 1

The above design is topologically optimized for 30% weight reduction in optimization 1.

TABLE 8: Mass details of optimized design 1

Material	**Aluminium alloy 2024**
Mass	**14.513 kgs**

FIGURE 9. Front and Rear view of optimized design 2

The above design is topologically optimized for 40% weight reduction in optimization 2.

TABLE .9 Mass details of optimized design 2

Material	Aluminium alloy 2024
Mass	**13.371 kg s**

ANALYSIS RESULT OF OPTIMIZED DESIGN

The analysis is carried out utilizing Altair Inspire 2019.4 on the above Optimized design 1 to determine the wheel rim's structural durability with the normal working conditions applied on the rim.

TOTAL DEFORMATION

The loading constraints (i.e., Vertical loading, Tire pressure and Rotational velocity) are applied to theoptimized design 1 to obtain the deformation result.

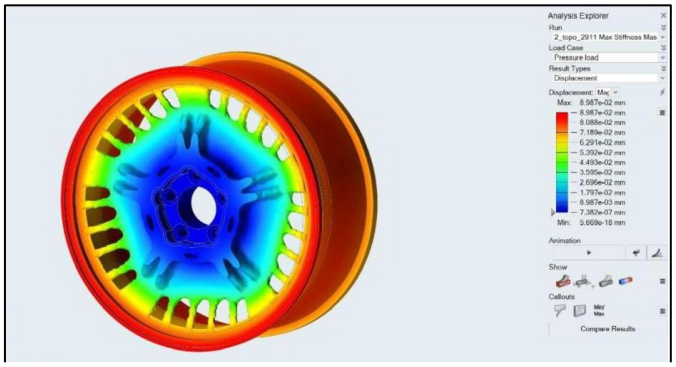

FIGURE 10: Total deformation of optimized design 1 The results are obtained from the above process and noted in the tabulation.

TABLE .10 Total deformation of optimized design 1

Input values			Output values	
Vertica lload	**Pressure load**	**Rotational velocity**	**Max .Displacement**	**Min. Displacement**
4415 N	0.2344 M pa	1300 RPM	0.08987 mm	5.669e-18 mm

TENSION AND COMPRESSION

The loading constraints (i.e., Vertical loading, Tire pressure and Rotational velocity) are applied to theoptimized design 1 to obtain the tension and compression results.

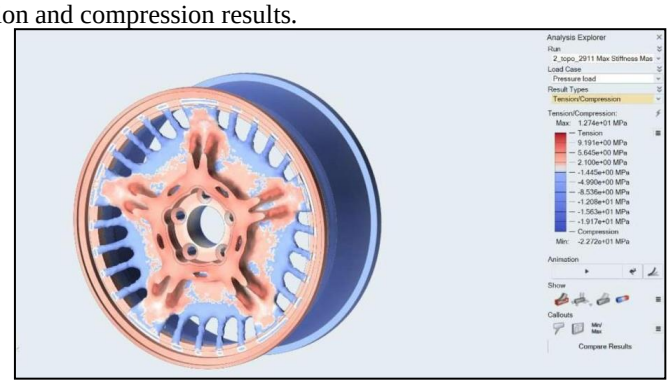

FIGURE 11. Tension and Compression of optimized design

The results are obtained from the above process and noted in the tabulation.

TABLE .11 Tension and Compression of optimized design 1

Input values			**Output values**	
Vertical load	**Pressure load**	**Rotational velocity**	**Tension**	**Compression**
4415 N	0.2344 M pa	1300 RPM	12.74 M Pa	22.72 M Pa

Von-mises stress

The loading constraints (i.e., Vertical loading, Tire pressure and Rotational velocity) are applied to theoptimized design 1 to obtain the von-mises stress result.

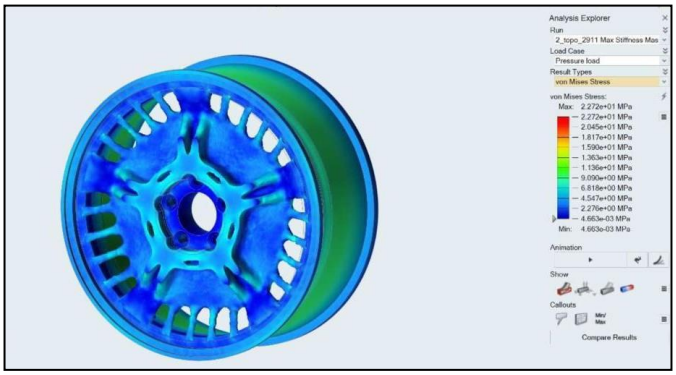

FIGURE 12. Von mises stress of optimized Design 1 The results are obtained from the above process and noted in the tabulation.

Factor of safety = Tensile yield strength / Von-Mises Stress = 324 / 22.72 = **14.260**

TABLE 12. Von mises stress of optimized Design

Input values			Output values	
Vertical load	Pressure load	Rotational velocity	Max.Stress	Min.Stress
4415 N	0.2344 Mpa	1300 RPM	22.72 MPa	4.663e-03 Mpa

Principal Strain

The loading constraints (i.e., Vertical loading, Tyre pressure and Rotational velocity) are applied to theoptimized design 1 to obtain the principal strain result.

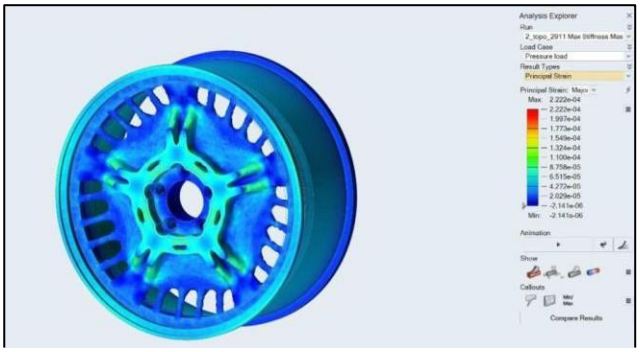

FIGURE 13. Principal Strain of optimized design 1

The results are obtained from the above process and noted in the tabulation

TABLE 13. Principal Strain of optimized design 1

Input values			Output values	
Vertical load	Pressure load	Rotational velocity	Max.Strain	Min.Strain
4415 N	0.2344 Mpa	1300 RPM	0.0002222	0.000002141

ANALYSIS RESULT OF OPTIMIZED DESIGN 2

The analysis is carried out utilizing Altair Inspire 2019.4 on the above Optimized design 2 to determine the wheel rim's structural durability with the normal working conditions applied on the rim.

Total deformation

The loading constraints (i.e., Vertical loading, Tire pressure and Rotational velocity) are applied to theoptimized design 2 to obtain the deformation result.

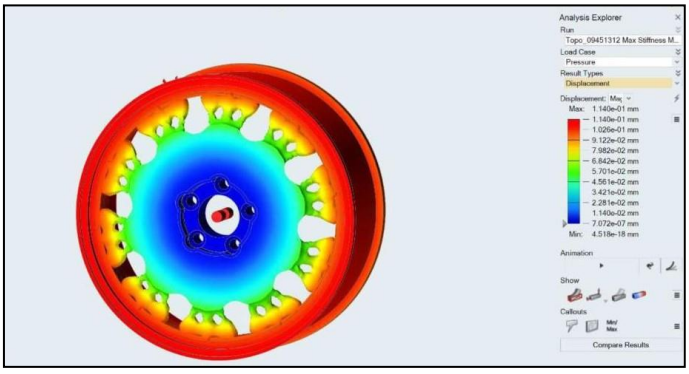

FIGURE 14. Total deformation of optimized design 2

The results are obtained from the above process and noted in the tabulation.

TABLE 14. Total deformation of optimized design 2

Input values			Output values	
Vertical load	**Pressure load**	**Rotational velocity**	**Max. Displacement**	**Min .Displacement**
4415 N	0.2344 M pa	1300 RPM	0.1140 mm	4.518e-18 mm

Tension and Compression

The loading constraints (i.e., Vertical loading, Tire pressure and Rotational velocity) are applied to theoptimized design 2 to obtain the tension and compression results.

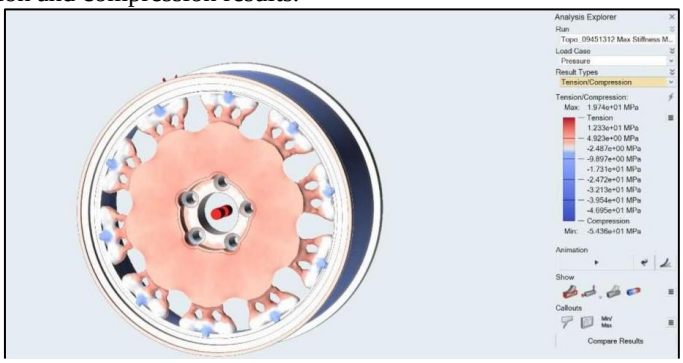

FIGURE 15. Tension and Compression of optimized design 2

The results are obtained from the above process and noted in the tabulation.

TABLE .15 Tension and Compression of optimized design 2

Input values			Output values	
Vertical load	**Pressure load**	**Rotational velocity**	**Tension**	**Compression**
4415 N	0.2344 M pa	1300 RPM	19.74 M Pa	54.36 M Pa

Von-mess stress

The loading constraints (i.e., Vertical loading, Tyre pressure and Rotational velocity) are applied to theoptimized design 2 to obtain the von-mises stress result.

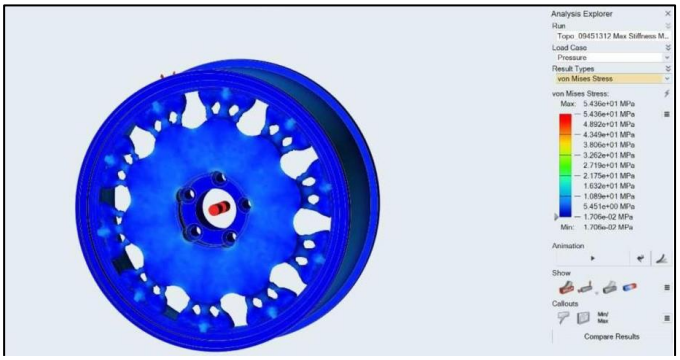

FIGURE 16. Von mess stress of optimized design 2

The results are obtained from the above process and noted in the tabulation.

Factor of safety = Tensile yield strength / Von-Mess Stress = 324 / 54.36 = **5.960**

TABLE .16 Von mess stress of optimized design 2

Input values			Output values	
Vertical load	**Pressure load**	**Rotational velocity**	**Max .Stress**	**Min. Stress**
4415 N	0.2344 Mpa	1300 RPM	54.36 M Pa	0.01706 MPa

Principal Strain

The loading constraints (i.e., Vertical loading, Tire pressure and Rotational velocity) are applied to theoptimized design 2 to obtain the principal strain result.

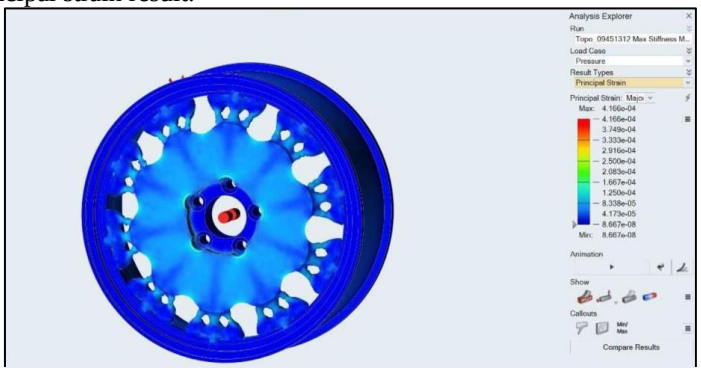

FIGURE 17. Principal Strain of optimized design 2

The results are obtained from the above process and noted in the tabulation.

TABLE .17 Principal Strain of optimized design 2

Input values			Output values	
Vertical load	**Pressure load**	**Rotational velocity**	**Max. Strain**	**Min. Strain**
4415 N	0.2344 M pa	1300 RPM	0.0004166	8.667e-08

CONCLUSION

From the above results, we can conclude the report by saying that:

- Compression force creates the maximum stress that is applied on the wheel rim in normal working conditions.
- According to Researchers, 1kg of un spring mass is equivalent to 10 - 15kg of the sprung mass, and 1kg decrease in mass on a car will raise mileage 5-8 meters on each litre fuel and so, the Optimized design 2 has the very low mass (i.e. 13.371 kg s) compared to the other two rims

- As far as performance is concerned, optimized design 1 is superior to optimized design 2 as optimized design 1 can withstand 14 times of normal working condition. Whereas optimized design 2 can only withstand six times of normal working condition, reducing the weight of 1.150kg s from optimized design 1.
- Further reduction of weight or topology optimization in optimized design 2 will result in fracture of the rim, As the structure can only withstand six times of normal working condition.

- Further weight reduction or topology optimization in optimized design 1 will result in a much more superior design with less reduction in the factor of safety, As the structure can withstand 14times of normal working condition.

SCOPE FOR FUTURE WORK

- Scope of work will focus on the material parametric analysis of the model as the accentuation of car businesses is on cost-saving by decreasing the weight of the model or utilizing the material with similar properties and less expense.
- Further work on various Rim thickness, extra force and rotational speed approval with practical information for the enhanced design will enhance this work.
- Another quickly developing field in the most recent decade is fast prototyping. Even though there are plentiful investigations in writing new calculations on the utilization of BESO, taking care of composite/practically reviewed materials, and considering backing and structure, meanwhile are the promising territories to examine.

REFERENCES

1. Meghashyam P,Girivardhan Naidu S and Sayed Baba N August 2013 IJAIEM *Design and analysis of wheel rim using CATIA & Ansys* **2(8)** pp 10-21
2. Prabha M V and Pendyala Veera Raju 2012 IJASET *Design and development of aluminium alloy wheels* **1(2)** pp 55-60
3. Siva Prasad, Krishnaiah T, Iliyas J Md and Jayapal Reddy M 2014International Journal of Innovative Science and Modern Engineering *A Review on Modeling and Analysis of Car Wheel Rim using CATIA & ANSYS* **2(6)** pp 05-11
4. PekguleryuzMO, Kainer K U and Kaya A A 2013 *Fundamentals of Magnesium AlloyMetallurgy* Oxford Woodhead Publishing p 151
5. Rashwan A 2019 IJEMS *Topologyoptimization and rim design* **4(4)** pp 93 – 100
6. Xiao D, Zhang H, Liu X, He T and Shan Y2014Journal of Mechanical Science and Technology
7. *Novel steel wheel design based on multi-objective topology optimization* **28(3)** pp 1007-1016
8. Jikai Liu, Andrew T Gaynor, Shikui Chen, Zhan Kang et al. 2018 Structural andmultidisciplinary optimization *Current and future trends in topology optimization for additive manufacturing* pp 10 – 40
9. Sabri M, Rezal M, Mu'az A, Shahril K and Ihsan JMarch 2015 International Journal of Engineering and Technology *Deformation Behaviour analysis of Car Wheel Rim under Different Loading Using Finite Element Method* **5(3)** pp 181-184
10. Sourav Das June 2014 International Journal of Scientific and Research Publications *Design and Weight Optimization of Aluminum Alloy Wheel* **4(6)** pp 4 -12
11. Sushant K Bawne October 2015International Journal of Engineering Research and Applications*Optimization of car rim* **5(10)** pp 01- 08
12. Ganesh S and DrPeriyasamy P 2014International Journal Of Engineering And Science *Design and Analysis of Spiral Wheel Rim for Four Wheeler* **3(4)** pp 29-37
13. Jaspreet singh and Siddhartha saha 2015 International Journal of Research in Engineering and Technology *Static analysis of alloy wheel using ansys15.0* **4(7)** pp 217-20

RESEARCH ARTICLE | MAY 22 2023

Fabrication and structural analysis of morphing wing of UAV

K. Veeranjaneyulu ✉; Sudhir Joshi; Vindhya Devalla; Kalavagunta Surya Kiran; Kushal

AIP Conference Proceedings 2492, 050044 (2023)
https://doi.org/10.1063/5.0113296

Fabrication and Structural Analysis of Morphing Wing of UAV

K Veeranjaneyulu[1, a)] , Sudhir Joshi[1, b)] ,Vindhya Devalla[2, c)], Kalavagunta Surya Kiran[3, d)] ,Kushal [1,e)]

[1]*Department of Aerospace Engineering, UPES, Dehradun, India*
[2]*Matdun Ltd, Hyderabad, India*
[3]*Department of Mechanical and Mechatronics Engineering, University of Waterloo, Ontario, Canada*

Corresponding author : [a)] veerak2k@mlrinstitutions.ac.in
[b)] sjoshi@ddn.upes.ac.in
[c)] vindsdevalla@yahoo.com
[d)]suryakk58k@gmail.com
[e)] kul.knight@outlook.com

Abstract. This paper explains the design, fabrication and structural analysis of spanwise morphing wing. The airfoil selected for the wing is Clark Y and the material used for the fabrication of the wing is balsa wood. The Clark Y airfoil is a thick one and the mechanism used to extend the wingspan is accommodated. The pressure loads are calculated when the airplane is flying at speed of 10m/s and 20m/s. The deformation of the structure due to the pressure loads are estimated. The stresses induced in the structure are analyzed with Ansys. The stresses are found to be high at the wing tips ,at the extension point and found to be within the acceptable levels.

Keywords: Morphing; Clark Y

INTRODUCTION

Morphing is also a technology that improves a vehicle's performance by changing certain characteristics to adapt the aircraft's configuration to the flight conditions and intended task[9]. Such wing concept has big potential to improvise the aircraft performance for multiple mission flight wings have been illustrated per their main components (structural, actuation, sensor, control, and skin systems). Morphing wing aircraft, compared to conventional rigid wing aircraft, are more capable in achieving optimum performance under different flight conditions[13]. Span-changing aircraft, in particular, have spurred attention owing to the benefits of achieving a suitable lift-to-drag ratio and specific fuel consumption, particularly for designs where the wing is the primary component[15].

Advancements in Aeromechanical Materials for Manufacturing: ICAAMM-2021
AIP Conf. Proc. 2492, 050044-1–050044-7; https://doi.org/10.1063/5.0113296
Published by AIP Publishing. 978-0-7354-4438-6/$30.00

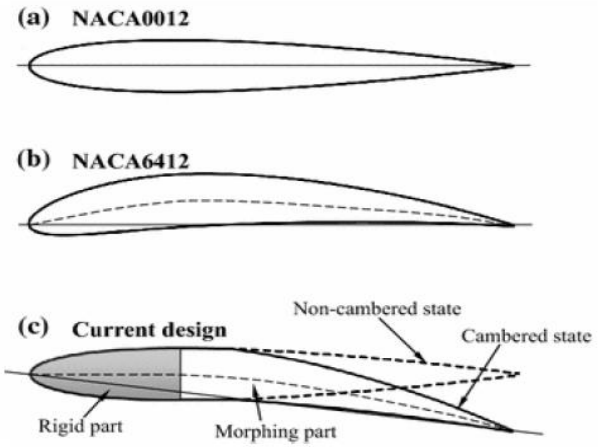

FIGURE 1. Airfoils for morphing

The simulation of bird flight is the main challenge of a morphing wing, and there are numerous stunning instances of adaptable structures in nature. Designers can build new structural systems that are entirely consistent with the rising Trigent airworthiness requirements by integrating more innovative technologies like reliable kinematic mechanisms, integrated servo-actuation, and smart materials systems.. The authors[14] report the characterization of an adaptable structure that resembles a wing trailing edge and is made up of a finger-like rib mechanism and a highly malleable skin with both soft and rigid portions.

Using shape **memory** alloy actuators, a robust fluid-structure interaction study of an adaptive airfoil was performed. An aero-structure interaction model is provided in this work for the fast modelling of morphing structures achieved with shape memory alloy (SMA) actuators[12]. The aerodynamic simulation method implements a potential flow method strongly coupled with an integral boundary layer method, which includes a transition prediction model and a simplified shear stress-transport equation for the turbulence closure in the context of a viscous-inviscid interaction approach[10]. The design, fabrication and structural analysis of spanwise morphing wing. The airfoil selected for the wing is Clark Y and the material used for the fabrication of the wing is high density balsa wood. The Clark Y airfoil is a thick one and the mechanism used to extend the wingspan can be accommodated. The pressure loads are calculated when the airplane is flying at speed of 10m/s and 20m/s. The deformation of the structure due to the pressure loads are estimated. The stresses induced in the structure are analyzed with Ansys. The stresses are found to be high at the wing tips ,at the extension point and found to be within the acceptable levels

WING DESIGN

The Airfoil selected for the model is taken for its Characteristics and the based on the requirements which include high thickness percentage which is required because of the mechanism. The airfoil selected for the wing is Clark Y airfoil.

The Specifications are:

- Max thickness 11.7% at 28% chord
- Max camber 3.4% at 42% chord
- At Reynolds's no = 200000
- Max Cl/Cd = 73.2 at Angle of attack = 4.75°

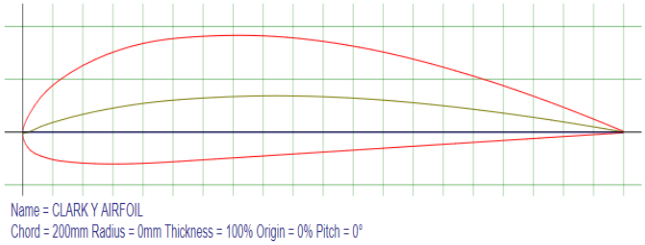

FIGURE 2. Airfoil

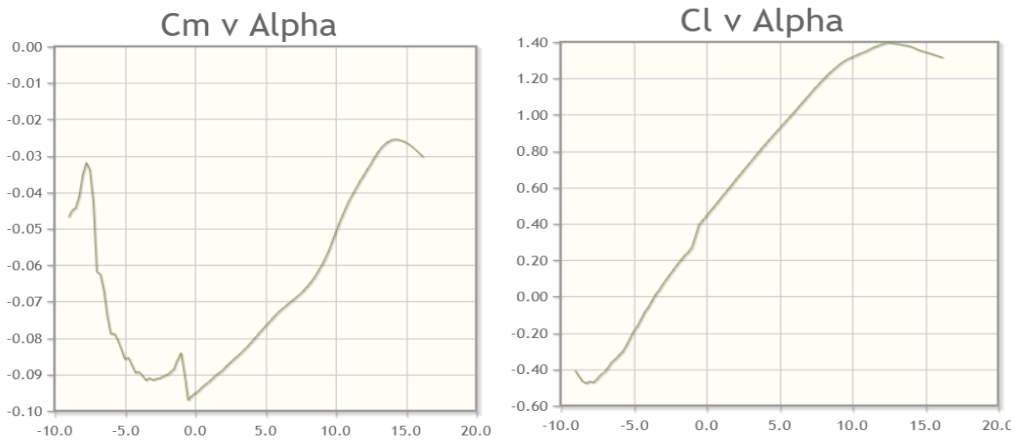

FIGURE 3. Graphs of Clark Y airfoil

FABRICATION

Bill of materials:

- Balsa wood sheet - 3mm * 1000mm * 95mm
- Balsa wood stiffeners - 6mm * 6mm
- Aluminium stiffener - 10mm diameter
- Servo Tower Pro - 45mm * 23mm * 50mm
- Transparent Film - 1000mm
- Mounting stand - 1 no
- Battery - 1500mAh
- Transmitter and receiver - 1 no

TABLE.1. Material properties:

Density	163 +- 10kg/m^3
Compressive Strengths	
low density	4.7Mpa
medium density	12.1Mpa
high density	19.5Mpa
Tensile strength	
low density	7.6Mpa
medium density	19.9Mpa
high density	32.2Mpa
Elastic modulus-Compression	460 +- 71Mpa
Elastic modulus-Tension	1280 +- 450Mpa

- Low Density = 75 kg/m³ (0.0027 lb/in³)
- Medium Density = 150 kg/m³ (0.0054 lb/in³)
- High Density = 225 kg/m³ (0.0081 lb/in³)

FIGURE 4.Wing ribs

ASSEMBLY

The assembly process was used to join the separate airfoil parts while including the leas screw mechanism. The motion was achieved by servo motors and those were powered by the batteries

FIGURE 5.Wing assembly

After the airfoil selection airfoil coordinates are taken and the material is cut into several airfoils and is arranged in series to form wing. Since the wing is tapered the chord value varies for every airfoil and the arrangement is done based on the chord value from root to tip of the wing. In the process of Assembly, as per selection of Airfoils material is cut,depending the number of airfoils required for the model. Then the series of airfoils are assembled to form a Wing and the airfoils cutting is taken to consideration because of the tapered wing type of the model. To strengthen the wing body stringers are used, they help the wing to bear more loads. During the process of assembly

measurement of the dimensions are calculated really specifically and electrical components are assembled with a great care

FIGURE 6. Wing spar assembly

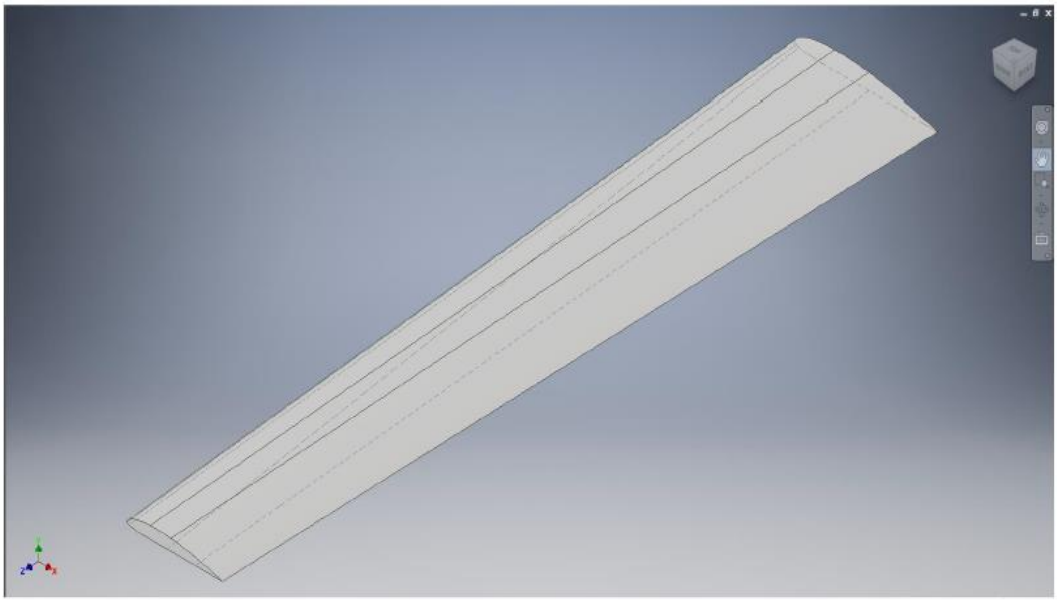

FIGURE 7. Morphed assembled wing

ANALYSIS

The flow all around the airfoil is investigated first. The term "airfoil" refers to a structure with curved surfaces that produces favourable lift and drag forces. When an airfoil structure is moved at a given speed through a fluid medium, it creates an aerodynamic force. The aerodynamic force is the force exerted on the airfoil structure by the fluid due to the relative velocity between the two surfaces. There are two explanations for this aerodynamic force. One is related to the fluid's pressure on the fluid's surface, and the other is due to the fluid's shear force on the body's surface owing to its viscosity. The pressure applied is perpendicular to the body's surface, whereas the shear force is parallel to the body's surface. When the pressure and shear forces are combined, the result is the aerodynamic force

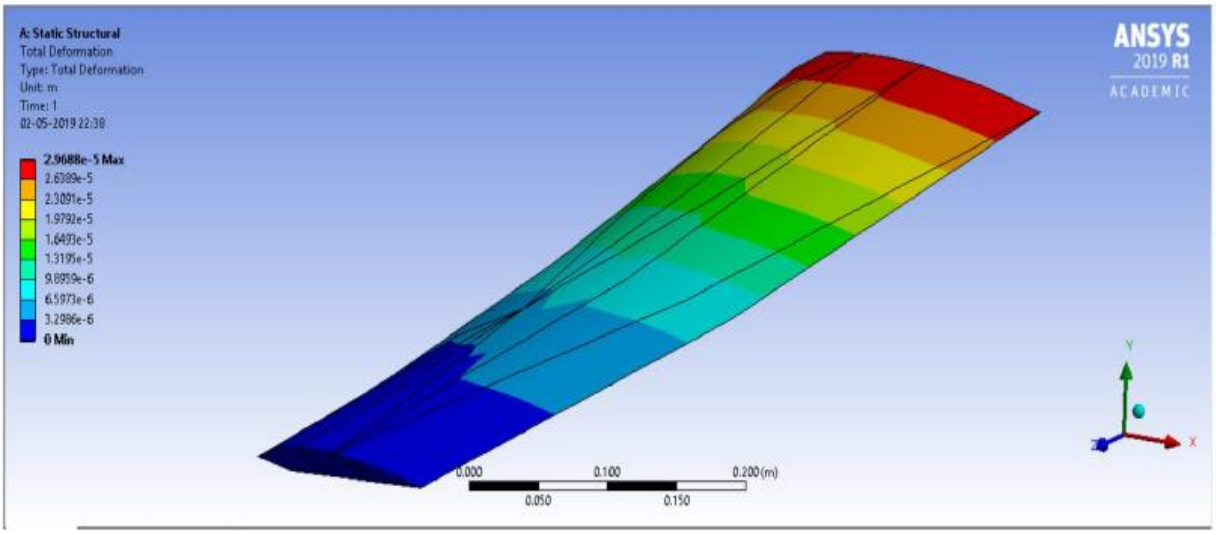

FIGURE 8. Deformation analysis on Tapered wing

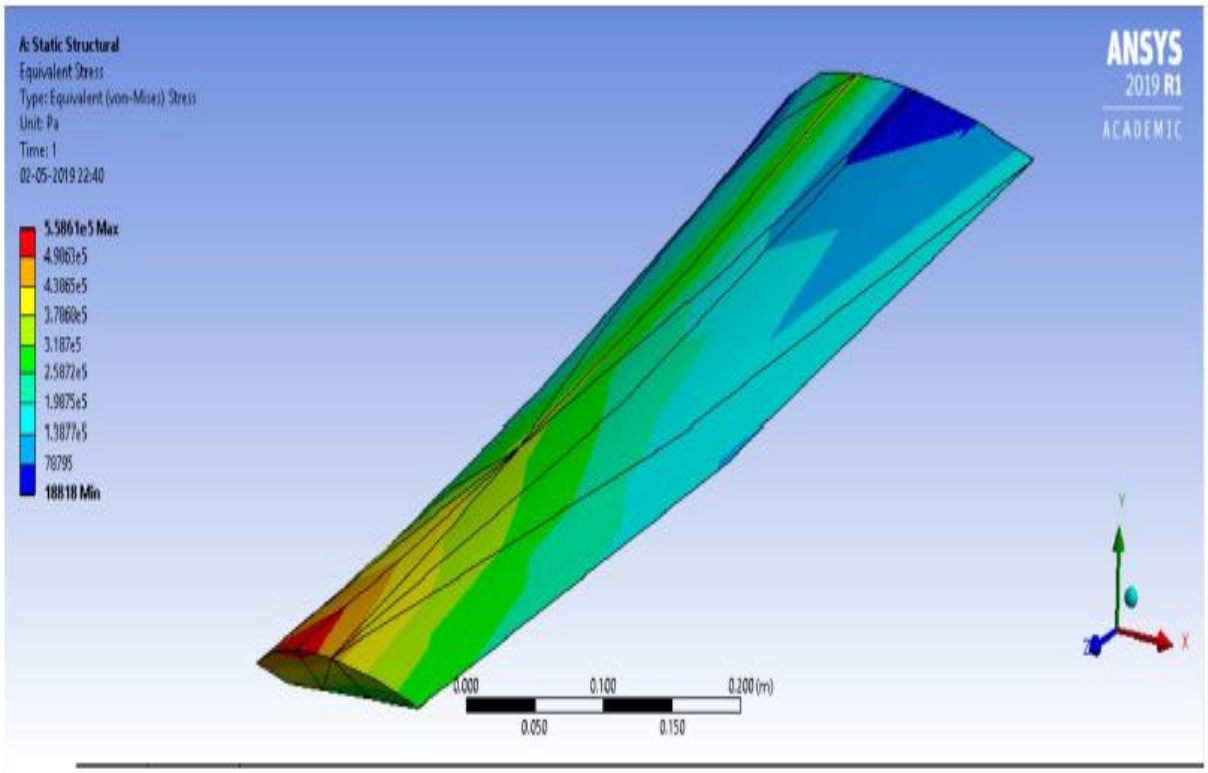

FIGURE 9. Stress analysis of morphed wing

CONCLUSIONS

The design, fabrication and stress analysis of spanwise morphing wing has been performed in this work. A Clark Y airfoil has been selected for the wing design. It imparts favorable L/D ratio at the given speed of flight. The analysis was carried out at low Reynolds number and at maximum cruise speed. The results shows that the maximum stress occurs at tip of the wing structure when the pressure load is applied on the surface of the wing. The deformation is high at the root of the wing and Stresses are also moderate at point of extension. All the stresses and deformations for the wing are with in the acceptable limits and the wing structure is safe to operate at all flight conditions.

REFERENCES

1. R. Mantena, P. (Dept. of Mechanical Engineering, The University of Mississippi); Mann, R.; Nori, and C. Low-velocity impact response and dynamic characteristics of glass-resin composites*; Journal of Reinforced Plastics and Composites*, 20, p 513-533, 2001.
2. ASTM D 3763, High Speed Puncture Properties of Plastics Using Load and Displacement Sensors, 1997.
3. W.R. Hoover, Effect of Test System Response Time on Instrumented Charpy Impact Data; Instrumented Impact Testing, ASTM STP 563, p203-214, 1974.
4. ASTM D 6110, Determining the Charpy Impact Resistance of Notched Specimens of Plastics; 2002.
5. D.F. Adams, L.A. Carlsson, R.B. Pipes, Experimental Characterization of Advanced Composite Materials, CRC Press, 3 rd ed. 2003.
6. Tomita, Yoshiyuki (Osaka Prefecture Univ); Tamaki, Toru; Morioka and Kojiro,Effect of fiber strength on notch bending fracture of unidirectional long carbon fiber-reinforced epoxy composites; Materials Characterization, 41, p 123-135, Oct, 1998.
7. C.B. Bucknall (Cranfield Inst of Technology), Relevance of impact testing in the materials science of polymers; Plastics, Rubber and Composites Processing and Applications, 17, p 141-145, 1992.
8. R.H. Toland, Impact Testing of Carbon-Epoxy Composite Materials; Instrumented Impact Testing, ASTM STP 563, p 133-145, 1974.
9. M. Nagai and H. Miyairi, The Study on Charpy impact testing method of CFRP; Advanced Composite Materials: The Official Journal of the Japan Society of Composite Materials, 3, p 177-190, 1994.
10. ASTM D 5628 Standard Test Method for Impact Resistance of Flat, Rigid Plastic Specimens by Means of a Falling Dart (Tup or Falling Mass), 1996.
11. S. Ujihashi, (Tokyo Inst of Technology); Intelligent method to determine the mechanical properties of composites under impact loading; Composite Structures, 23, p 149-163, 1993 Taylor, R.P.Fibre Composite Aircraft - Capability and Safety. Australia : Australian Transport Safety Bureau, 2008.
12. K Arunkumar, K Veeranjaneyulu, Om Prakash, Sreekanth Sura, M Srikanth," Mechanism and Performance Analysis of Morphing Wing", International Journal of Innovative Technology and Exploring Engineering (IJITEE) ISSN: 2278-3075, Volume-9 Issue-3, January 2020
13. Mr.Sreekanth sura, a.Sai kumar, Nirmith kumar mishra, Sohail raheman, "Design and fabrication of micro air vehicle (mav) with double-bubble fuselage" international journal of recent technology and engineering (ijrte) issn: 2277-3878, volume-8 issue-4, november 2019.
14. Ms.Narra Swetha and Sreekanth sura " Design and analysis of high speed helical gear with different helical angles" international journal of research, date: 10-10-2016, volume no:3.

RESEARCH ARTICLE | MAY 22 2023

Mounting plate design for section-IV of an aerospace vehicle under yawing mode

B. Manideep ✉; E. C. Prasad Nidumolu; B. Nagaraj Goud

AIP Conference Proceedings 2492, 040055 (2023)
https://doi.org/10.1063/5.0113329

Mounting Plate Design for Section-IV of an Aerospace Vehicle Under Yawing Mode

B Manideep[1, a)], E C Prasad Nidumolu[2, b)] and B Nagaraj Goud [1]

[1]*Department of Aeronautical Engineering, MLR Institute of technology, Hyderabad, India*
[2]*Department of Mechanical Engineering, MLR Institute of technology, Hyderabad, India*

[a)]Corresponding author: manideepbalusani.9@gmail.com
[b)]Prasadnidumolu555@gmail.com

Abstract. The structure of an aerospace vehicle is a group of several parts. Part IV is one of those sections, which covers electronic subsystems and avionics batteries. Includes a mounting plate interface that can accommodate a thermal battery for power train control and actuation systems. (No.3), 1, main electronic battery, secondary electronic battery pack, contractor box, monitoring circuit battery voltage (BVMC). The thermal battery and main electronic battery are attached to the clamp and holder plate, and the BVMC, secondary electronic battery and contractor box are attached with screws. Modeling was done in ProEngineer Wildfire 5.0 and analysis was done in ANSYS 12.0. The results were analyzed at various loads and, for theoretical calculations, the factor of safety of the mounting plate was within limits, so the overall design was considered reliable and safe.

Keywords— Battery, Analysis, Aerospace, Mounting Plate

INTRODUCTION

Aerospace Vehicle

In aerospace aircraft, the components must be mounted inside the airframe according to the configuration of the system and travel in a defined path with the help of guidance from control electronics must be installed to support all loads. Properties related to mass are important for the aircraft to follow the required path the main mass characteristics of a vehicle are body weight, COG, and MOI. A force exerted by Earth's gravity on the vehicle i.e. Weight. The vehicle's Mass (weight) is distributed efficiently, but knowing the lane distribution and vehicle stability is important. The main thing is to pay attention to the center of gravity and total weight[1-2].

Yaw Motion

During flight, the aircraft usually rotates around its CG. Since the axis of the coordinate system is perpendicular to one another, you must use the centroid to define the 3D coordinate system. The jaw axis is perpendicular to the horizontal and vertical axes. During the yaw movement, the car's nose moves from side to side. Moments can be observed in figure 1[3-4].

The deflection of the rudder of the aircraft allows you to create a yawning motion. The drawbar is articulated at the end of the vertical stabilizer. A slight change in the steering angle at the rudder end will change the lift produced by the longitudinal stabilizer. In the case of the longitudinal stabilizer and the rudder, the lateral force generated depends on the direction of the wing[5]. If the rudder leans towards left, the lateral force acts towards right side.

Advancements in Aeromechanical Materials for Manufacturing: ICAAMM-2021
AIP Conf. Proc. 2492, 040055-1–040055-8; https://doi.org/10.1063/5.0113329
Published by AIP Publishing. 978-0-7354-4438-6/$30.00

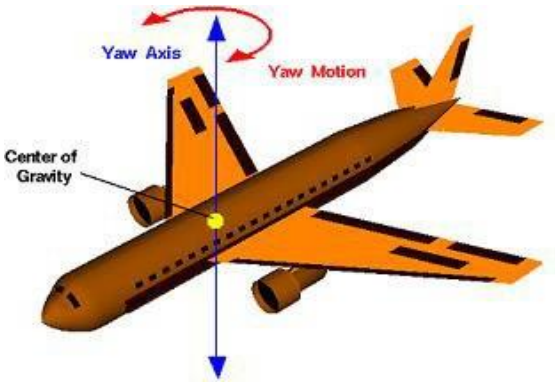

FIGURE 1 Flight Vehicle-Yaw Motion

MODELLING

Aerospace Machinery Part IV Subsystem for Order Fulfillment, Four brackets are used to assemble the section (cell) subsystem.

The Subsystems of mounting Plate are

- Control Actuation System's Thermal Batteries (3No's)
- Battery for Primary Avionics
- Circuit for Voltage Monitoring of BVMC-Battery
- Battery for Secondary Avionics
- Contactor Box.

The total mass of the assembly on the rack is approximately 17.7 kg and the total configuration is depicted as shown in Figure 2[5-8].

The weight of the auxiliary system is transmitted externally to the mounting plate as forces, moments. External load applied is 27.5 g in the vertical direction and 8 g in the horizontal direction, depending on the mass of the subsystem. The mounting plate is design is done and it is tested to check whether it can resist the acceleration loads.

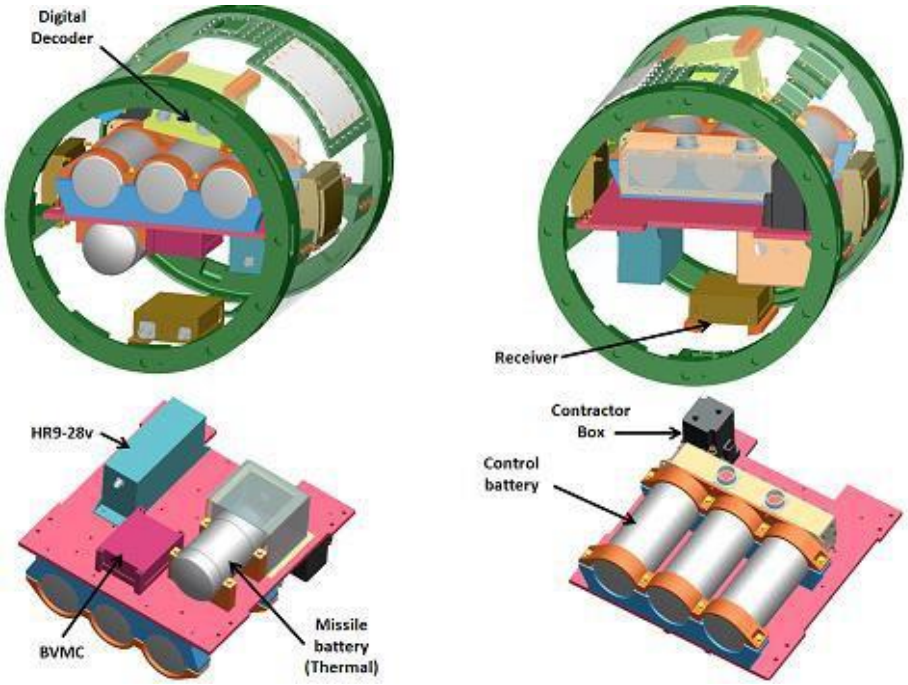

FIGURE 2.Section 4 airframe with packages mounted on plate

INDIVIDUAL PACKAGES DETAILS

Mounting Plate

Plate connected to a subsystem modeled in CAD Pro Engineer as showon in figure 3,

Plate is made up of Aluminium Alloy24345 (WP condition) material, its characteristics are as follows. Plate (IS:736): UTS:405 M Pa, PS:310 M Pa, %e:72

FIGIURE 3. Mounting plate

Control Battery (Thermal) along with Clamp, Brackets

Power for the control operating system is supplied by the control battery (thermostat). The size of the control spindle (thermostat) is Ø80 and 190 in length. The batteries are placed in series as shown in figure 4 with the lower bracket and secured with M5 screws (8 pcs) and upper clamps. Bakelite High Ram Grade F2IS: 2036 material is used for battery mounting and insulation

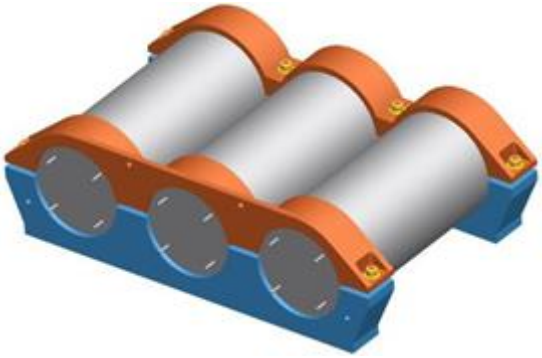

FIGURE 4 Control Battery with Clamps and Brackets

Avionics Battery (Thermal) mounted with Brackets and clamps

Use avionic (thermal) batteries to power the electronic assemblies installed in parts II to IV. The battery size is Ø80 and the length is 145. The battery is on the mounting bracket and is secured with an M5 8 screw and top clamp. Bakelite High Ram Grade F2IS: 2036 material is used for battery assembly and insulation, as shown in figure 5

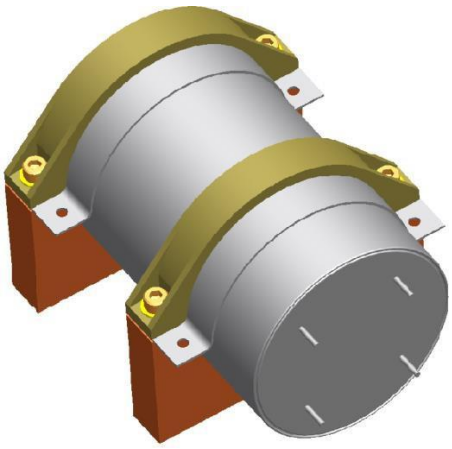

FIGURE 5. 3D Modeling of Avionics Battery Mounted on Clamps and Brackets

BVMC (Battery Voltage Monitoring Circuit) Package

The voltages of the different batteries installed in Part IV are monitored using the BVMC package which is shown in figure 6.For telemetry applications, the battery output voltage is monitored, converted to a digital format and then sent to the built-in computer.

FIGUIRE 6. Model of Battery Voltage Monitoring Circuit Package

HR-59VBattery

The HR59V battery is included to power autonomous aerospace destruction systems, AVDS and 1 Battery provides 5 amps at 9V for external AVDS is required.wchich is as shown infigure 7.

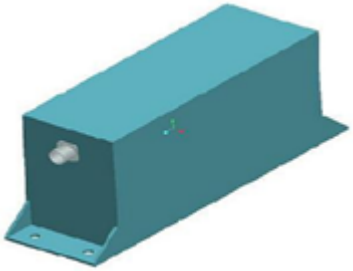

FIGURE:7 Model of HR5-9V

Contractor Box

Use the contractor's box to activate the control pin. Three control pins were connected in series. The battery packs a trigger voltage of 150V. The contractor's box shown in figure 8 receives a command to activate the transmit trigger voltage. These commands are obtained from the built-in calculator.

FIGURE 8. Model of Contractor Box

ANALYSIS

- In the inclined state, the plate experiences an external load and a moment due to the load caused by the packages attached to the plate. The analysis was carried out under inclined conditions [1-8]. The results are observed and tabulated.
- Mounting plates are imported into ANSYS software.
- eight node Shell element(Shell 281) is used to mesh the plate
- Uniform thickness of 8mm is provided.
- Lugs are modeled by a SOLID20, tetrahedral element (SOLID 187).
- The total number of items used in this assembly is 87471.
- No.of elements of plate are 4983.
- No.of elements of Lugs are 82488.

The node of the hole is at the pin level to connect to the stop cell at all degrees of freedom. The plate nodes and the interface holes of the heat sinks are interconnected with all degrees of freedom[9-12]

A Lateral Direction Loading (Yaw)

Each mounted package applies a direct load to each position on the plate, both left and right. Figure 9 shows the boundary conditions and forces acting on the plate. The stresses and flexures that occur on the plates and supports are shown in Figures 10 to 13.

Thermal battery weight (control) with bracket	=8.98Kg
Battery Force in 8g state	= 704.75N
The load onto the plate at each mounting hole	= 88.1 N
Thermal Battery (Avionics) weight with brackets =	2.26Kg
Battery Force in 8g state	= 177.4N
The load onto the plate at each mounting hole	= 44.4N
Battery (HR5-9v) Weight	= 1.95 Kg
Battery Force in 8g state	=150.7N
The load onto the plate at each mounting hole	= 150.7/4

Deflection &stress plot with plate and brackets

BVMC package Weight	= 0.7 Kg
Battery Force in 8g state	= 55 N
The load onto the plate at each mounting hole	= 13. N

Weight of Contact or package = 0.76Kg
Battery Force in 8g state = 59.6N
The load onto the plate at each mounting hole = 29.8 N

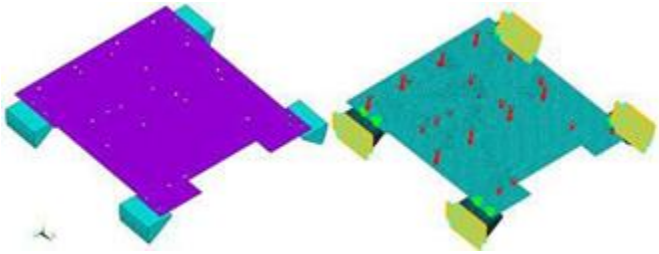

FIGURE 9. FE model and boundary condition plot

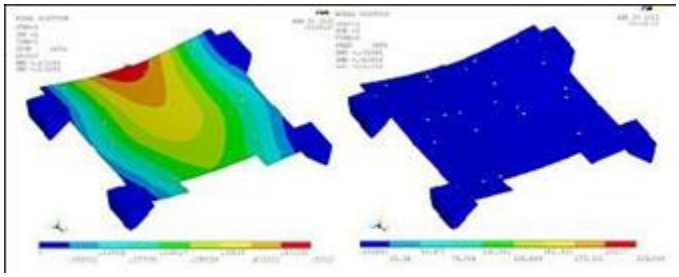

FIGURE 10. Deflection & stress plot with plate and brackets

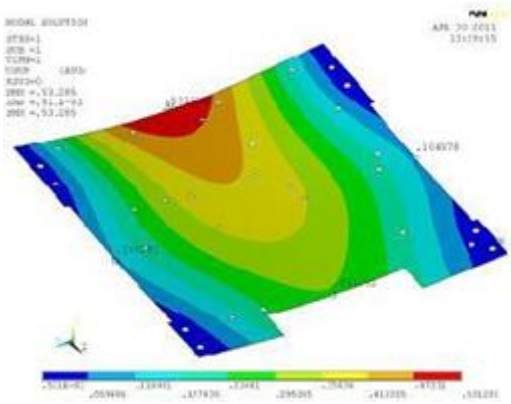

FIGURE 11..Deflection of plate under Yawing

From the Fig11, The max deflection got for Plate is 0.53mm.

RESULTS

The load on the plate is assumed as a rectangular plate having edges loaded in the center. [2], the load of all the packages including plate is 17 Kg. [3-4].

Plate b Length = 400 mm,
Plate a Width = 345mm,b/a = 1.2,
Plate Deflection $=\alpha(p\alpha^2/D)=3282051.3$
Where $\alpha=0.00647$, (based on b/a ratio)
P=Load on the plate= 1334.16 N
$D=Eh^2/\{12(1-\mu^2)\}$
=29.8N

Where E=0.7e5,
h=Thickness of the plate=8mm,
μ=0.3mm
By inducing the above results, Deflection of plate= 0.3 mm
The calculated deviation will be less than the result of FE. This is because the plate is firmly secured on all four sides. Calculations used for qualitative evaluation.

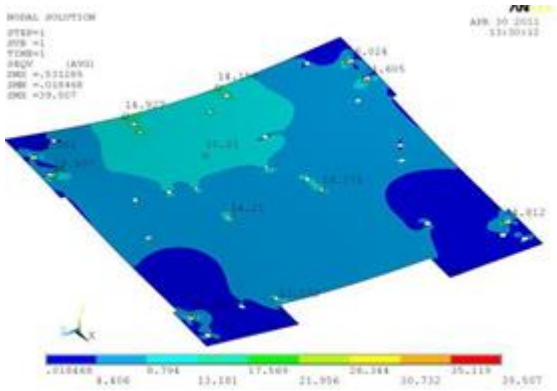

FIGURE 12. Induced Stresses in Plate Yawing

- The maximum deflection achieved with the mounting plate under elevation conditions is 0.055mm.
- The maximum stress obtained for the plate in yawing condition is 66 MPa, with an FOS equal to 4.7.shown in figure 12.

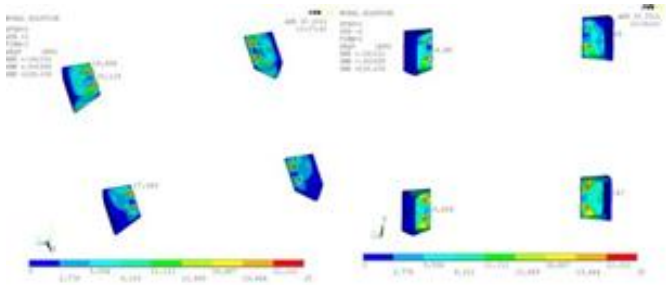

FIGURE13. Induced Stresses on Brackets under Yawing

From Figure 13, Maximum induced Stress for the Plate is =39.51MPa
FOS = 310 / 39.51 =8

CONCLUSION

In general the allowable safety factor for the structural design of aerospace aircraft is considered as 1.5. If the result of maximum deflection achieved with the mounting plate under elevation conditions is concidered, it is within limits, and the maximum stress obtained for the plate in yawing condition is acceptable as the FOS is greater than 1.5. Therefore, the mounting plate design is safe.

REFERENCES

1. *MIL-HDBK-5B, "Metallik Material and Elements for Aerospace Vehicle Structures", Department of Defence (DoD), Washington DC.*
2. "Theory of Plate & Shells-S, Timoshenko", Woinowsky-Krieger, Page No.206, and Table 37)
3. "Introduction to Finite Elements in Engineering Practice" *by "Tirupati R. Chandrapatta and Ashok D. Belugundu"*

4. M Ganesh, Nirmith Kumar Mishra, A. Sai Kumar, V. Vikas, K. Keerthi Krishna "Design and Analysis of UAV for High Payload" in *International Journal of Innovative Technology and Exploring Engineering* (IJITEE) Volume-9 Issue-2, December 2019
5. A. Sai Kumar, M Ganesh, Nirmith Kumar Mishra, Manish Choudhary, Yashwanth Rao Bandari "Design and Development of Man Portable Back Packable Multi-Purpose Drone" in *International Journal of Engineering and Advanced Technology* (IJEAT) Volume-9 Issue-2, December 2019
6. Dhanjal S., Arora R. "Stress analysis of a rectangular plate with circular hole using three dimensional finite element model". *International Journal of Engineering, Business and Enterprise Applications* (IJEBEA), Vol. 12, Issue 1, 2015, p. 77-80.
7. M. L. Pavan Kishore, A. Chandrashekha, M. Avinash and Raunak Das, "Stress analysis of rectangular and square plates with various cutouts",
8. Gunwant D., Singh J. P. "Stress and displacement analysis of a rectangular plate with a central elliptical hole". *International Journal of Engineering and Innovative Technology*, Vol. 3, Issue 3, 2013, p. 387-392.
9. . 'N.Madhavi, Muttangi Sushma, D.Mahesh Kumar, M Satyanarayana Gupta', 'Drones for Agricultural Land prediction', 'International Journal of Innovative Technology and Exploring Engineering (IJITEE)', ISSN: 2278–3075 (Online), Volume-9 Issue-2, December 2019, Page No. 5050-5053.
10. N.Madhavi, Vanaparti Ajay Kumar, Dr. M Satyanarayana Gupta" Design and Analysis of a Fuselage Using Helical Longerons", ijmetmr, ISSN No:2348-4845, Volume 3, sep,2016.
11. N Madhavi, Y.B.SudhirSastry, Pattabhi R.Budarapu," Buckling analysis of thin wall stiffened composite panels", Computational materials sciences, Volume 96, 459-471, Nov2015.

RESEARCH ARTICLE | MAY 22 2023

Modelling of battery thermal management system for improved battery efficiency

E. Prakash ✉; G. Rudissh Kanna; S. Kaarthi; B. Dharani Prasaad; D. Mahesh Kumar

AIP Conference Proceedings 2492, 050043 (2023)
https://doi.org/10.1063/5.0113915

Modelling Of Battery Thermal Management System for Improved Battery Efficiency

E Prakash[1, a)], G Rudissh Kanna[1, b)], S Kaarthi[1, c)], B Dharani Prasaad[1, d)] and D Mahesh Kumar[2]

[1]*Automobile Department, Bannari Amman Institute of Technology, Sathyamangalam, Tamil Nadu, India.*
[2]*Department of Aeronautical Engineering, MLR Institute of Technology, Hyderabad, India.*

[a)] Corresponding Author: prakashe@bitsathy.ac.in,
[b)]rudisshkanna.au17@bitsathy.ac.in,
[c)]kaarthi.au17@bitsathy.ac.in,
[d)]dharaniprasaad.au17@bitsathy.ac.in

Abstract. Electric vehicles (EV) are rapidly evolving and gaining popularity due to their zero-emission and high tank-to-wheels efficiency. However, some factors, particularly performance, cost, battery lifetime, and battery safety, are limiting the development of the electric vehicle. As a result, battery management is required to achieve maximum performance when operating in a variety of conditions. This project aims to study the different cooling systems adopted in the prevalent battery management system and to adopt a cooling system that gives maximum efficiency and to develop a battery management system in MATLAB/Simulink. Developing a battery management system involves selection of battery characteristics and develops equations for the different subsystems (pump, coolant, refrigeration system, radiator system and controller) and to identify the suitable international driving cycle. To evaluate the different subsystems and the relevant battery consumptions, to evaluate the heat flow rate across different systems, to plot the battery performance across different points of the driving cycle. According to the simulation results, BTMS is critical for controlling battery thermal behaviour. Combining the simulation model with battery thermal electric and CFD models could make future research more comprehensive and accurate.

INTRODUCTION

A vehicle that is propelled by at least one electric engine or footing engine is known as an electric vehicle (EV). An electric vehicle might be powered by off-vehicle sources via a gatherer framework, or it could be self-contained with a battery, solar panels, energy units, or an electric generator to convert fuel to electricity. Street and rail vehicles are examples of electric vehicles; however, they are far from the only ones. Electric vehicles include street and rail vehicles, surface and submerged watercraft, electric aeroplanes, and electric rockets.

The term "electric vehicle" (EV) refers to a vehicle that runs on electricity. Because of technological advancements, a greater emphasis on sustainable electricity, and the expected reduction of transportation's impact on environmental change and other natural challenges, EVs have seen a revival in the twenty-first century. Project Drawdown has named electric vehicles as one of the top 100 current solutions to climate change.

A half-electric vehicle (HEV) is a hybrid vehicle that combines an internal combustion engine (ICE) with an electric propulsion system (mixture vehicle drive train). It is proposed that the existence of an electric force train achieves either better efficiency or better execution than a conventional vehicle. There are various types of HEVs, and the capacity of each as an electric vehicle (EV) varies. The half-electric car is the most well-known type of HEV, but crossbreed electric vehicles (pickups and farm haulers), transporters, boats, and planes are also available. Regenerative brakes, which convert the vehicle's motor energy to electric energy, which is stored in a battery or super capacitor, are

Advancements in Aeromechanical Materials for Manufacturing: ICAAMM-2021
AIP Conf. Proc. 2492, 050043-1–050043-24; https://doi.org/10.1063/5.0113915
Published by AIP Publishing. 978-0-7354-4438-6/$30.00

used in current HEVs to improve productivity. Some HEVs use an internal ignition motor to run an electrical generator that either re-energizes the vehicle's batteries or controls the vehicle's electric drive engines directly. Many HEVs reduce inactive discharges by shutting down the motor out of gear and resuming it when necessary; this is known as a start-stop framework. In view of the fact that the crossover's fuel engine is typically more modest than that of a gas controlled vehicle, a half and half electric vehicle emits fewer tailpipe emissions than a similar estimated gas vehicle. If the motor isn't directly used to drive the vehicle, it is usually programmed to run at maximum efficiency, increasing efficiency even further.

EV Batteries

An electric-vehicle battery (EVB) is a battery that powers the electric motors in a battery electric vehicle (BEV) or hybrid electric vehicle (HEV). Lithium-ion rechargeable (secondary) batteries are the most common type. These batteries were designed to have a large ampere-hour (or kilowatt-hour) capacity. There are some types battery used in automobile:

- Starting, Lighting, and Ignition Batteries (SLI)
- Lithium ion battery
- Lead acid battery

Electric-vehicle batteries are deep-cycle batteries that give power for extended periods of time, as opposed to starting, lights, and ignition (SLI) batteries. The power-to-weight ratio, specific energy, and energy density of electric car batteries are all relatively high; smaller, lighter batteries are desirable since they reduce the vehicle's weight and so increase its performance. When compared to liquid fuels, most contemporary battery technologies have a substantially lower specific energy, which usually affects the cars' potential all-electric range.

Lithium ion Battery

An anode, a cathode, an electrolyte, and a separator make up a lithium-particle battery. The anode is the oxidised terminal that eliminates electrons to the outside circuit while releasing. The cathode, on the other hand, acts as an oxidising anode, receiving electrons from the outer circuit. The separator separates anodes from the electrolyte, which acts as a mechanism for transporting particles between terminals inside the cell. Furthermore, during the underlying charge, the strong electrolyte interface (SEI) is a delicate passivation layer that forms on the outside of the carbon anode. It lowers the current and slows down the response time. Furthermore, because a Li-particle battery is powered by a battery, its electrochemical responses are reversible. When lithium particles are released, they flow from the negative to the positive, and when they are charged, they move in the opposite direction. A lithium-particle battery's terminal is built of intercalated lithium compound rather than metallic lithium. The electrochemical responses of lithium cobalt in the positive and negative anodes are given blow:

The positive anode response is

$$\mathrm{Li}COO2 \Leftrightarrow Li1-xCOO2 + xLi+ + xe- \quad (1)$$

The negative electrode reaction:

$$\mathrm{x}Li+ + xe- + xC6 \Leftrightarrow xLiC6 \quad (2)$$

Other lithium batteries' electrochemical responses in the positive and negative cathodes are comparable.

There are numerous sorts of lithium-particle battery which are named by cathode oxides and every one has its own qualities as followings:

TABLE 1. Chemical composition and Description

Chemical name	Material	Short form	Description
Lithium cobalt oxide	$LiCoO_2$	Li-cobalt	High capacity; for cell phone laptop, camera
Lithium manganese oxide	$LiMn_2O_4$	Li-Manganese	Most safe; lower capacity than Li-cobalt but high specific power and long life. Power tools, e-bikes, EV, medical, hobbyist.
Lithium iron phosphate	$LiFePo_4$	Li-phosphate	
Lithium nickel manganese cobalt oxide	$LiNiMnCoO_2$	NMC	
Lithium nickel cobalt aluminum oxide	$LiNiCoAlO_2$	NCA	Gaining importance in electric power train and grid storage
Lithium titanate	$Li_4Ti_5O_{12}$	Li- titanate	

Thermal issues of Li-ion battery

Temperature and working voltage have an impact on the appearance of lithium-particle cells. When voltage and temperature are limited, lithium-ion cells function well. Something else will cause irreversible damage to the cells. The charging voltage exceeds the reasonable cell voltage in over-voltage situations, resulting in excessive current streams and messing up two at the same time.

Lithium-particles are saved faster than intercalation to the anode layers at high flows, and the Lithium particles are then stored as metallic Lithium on the anode's surface. This is referred to as lithium plating. It results in a decrease in free Lithium particles as well as an irreversible limit disaster. The two types of metal lithium plating are homogeneous and heterogeneous lithium plating; however the lithium plating is dendritic in nature. It may eventually result in a short between the anodes.

Under-voltage, like over-voltage, causes problems with the anode materials, resulting in their breakdown. For the anode, the copper current authority is short. It increases the battery's release rate and voltage, but the copper particles become metal copper, which is irreversible. Because of the possibility of a short between the anode and the cathode, the situation is hazardous. After a few of low-voltage cycles, the cobalt oxide or manganese oxide in the cathode will dissolve. Meanwhile, oxygen will be provided and the battery's power will be depleted. The battery's temperature should be meticulously monitored. Unreasonable warmth and an absence of warmth will both reason issues.

Temperature has a straight relationship with synthetic response rates. At the point when the working temperature is decreased, the response rate and current conveying limit are diminished during charging or releasing. As such, the battery's ability is decreased. Moreover, the more slow response rate makes it hard to embed lithium particles into intercalation spaces. Accordingly, force and lithium plating endure therefore.

The deficiency of limit High temperatures speeds up the response rate with higher force yield, yet they additionally increment heat dispersal and create much higher temperatures. The temperature will rise except if heat is disseminated quicker than it is produced, bringing about a warm out of control.

Warm rampant is made out of a few phases, every one of which causes irreversible cell harm. To start with, at around 800C, the SEI layer is broken up in electrolyte. Unnecessary current or a high surrounding temperature can cause essential overheating. After the SEI layer is separated, the electrolyte starts to respond with the anode. This is an exo-warm response, which raises the temperature. Second, the higher temperature makes natural solvents debase, bringing about the arrival of hydrocarbon gases. Regularly, this starts at around 1100 C. The gas has expanded the pressing factor inside the cells, and the temperature has transcended the flashpoint. Be that as it may, because of an absence of oxygen, the gas doesn't consume. To hold cells under legitimate pressing factor and stay away from a potential burst, a vent is needed to deliver the gas. At 1350 C, the separator melts and short-circuits structure between the anode and cathode. At long last, at 2000 C, the metal oxide cathode debases and delivers oxygen, permitting the electrolyte and hydrogen gas to consume.

Another issue with batteries is lopsided temperature dissemination. It is ordinarily brought about by high neighborhood temperatures, variable current in a cell, and the warm conductivity of the case, just as the arrangement of positive and adverse terminals, among different components. It causes neighborhood crumbling and surprisingly warm rampant, diminishing battery life.

Operating constraints

To keep away from warm issues and further develop execution, the battery temperature ought to be kept inside temperature limits. The temperature range impacts battery force and cycle life. Simultaneously, temperature circulation ought to be even to guarantee battery execution and life span. That is likewise why the battery warm administration framework is needed for the battery.

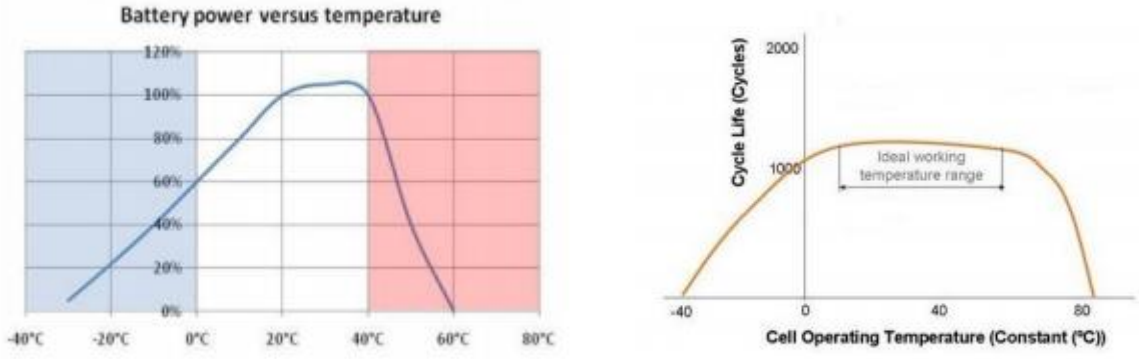

(a) (b)

FIGURE 1. (a)Battery power VS Temperature Graph, (b)Cell Life Cycle VS Battery Operating Temperature

Cycle life diminishes step by step beneath 10°C because of anode plating and quickly above 60°C because of cathode material breakdown (). To guarantee execution and cycle life, the temperature ought to be kept somewhere in the range of 20°C and 40°C. Besides, the temperature dispersion is held under 5K to guarantee the wellbeing and life span of the battery as shown in Fig 1.

BTMS and its types

For security, execution (both force and limit), and life expectancy reasons, the battery pack ought to be put away in a controlled climate where the temperature is controlled and there is no danger of warm rampant. As indicated by fundamental examination, the BTMS ought to be furnished with four fundamental capacities to guarantee the battery packs legitimate activity conditions:

Cooling

Battery cells produce power as well as warmth because of shortcoming. This warmth ought to be taken out from the battery pack when the battery temperature arrives at the ideal level, if conceivable. Therefore, BTMS requires a cooling capacity.

Heating

In chilly environments, the temperature of the battery pack is probably going to fall beneath the lower temperature limit. Accordingly, a warming capacity, like a PTC radiator, is needed to help the battery pack arrive at the legitimate temperature range in less time.

Insulating

The temperature contrast between within and outside of the battery pack is a lot more prominent in outrageous cold or blistering climate than in gentle climate. Subsequently, the battery temperature will fall (cold) or rise (hot) sooner outside of the appropriate temperature range. To keep away from this, great protection can moderate the fall or ascent of battery temperature, especially when the vehicle is left outside

Ventilation

To debilitate the unsafe gases inside the battery pack, ventilation is required. This capacity is joined with cooling and warming capacities in certain frameworks, for example, air frameworks.

Diverse warming and cooling innovations will be presented exhaustively in the accompanying areas, and their practicality and simplicity of ventilation will be assessed. Protection greaterly affects fixed conditions than driving conditions, so it won't be talked about further in this proposition.

Technologies in BTMS

Air cooling and heating

The warm medium in air frameworks is air. The admission air could be immediate from the environment or from the lodge, or it very well may be molded air from a climate control system's radiator or evaporator. The previous is known as an aloof air framework, while the last is known as a functioning air framework. Dynamic frameworks can give additional cooling or warming force. An inactive framework can give many watts of cooling or warming force, while a functioning framework is restricted to 1 kW. Since the air in the two cases is provided by a blower, they are additionally alluded to as constrained air frameworks. The chart underneath portrays a schematic depiction of frameworks as shown in Fig 2.

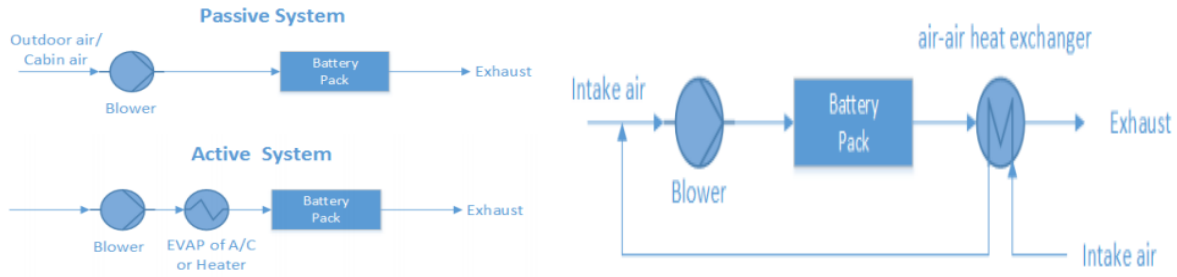

(a) (b)

FIGURE 2. (a) Passive and Active Cooling System Model, (b) Air Cooling System

It ought to be noticed that the air framework gives full warming, cooling, and ventilation capacities. There is no compelling reason to build a subsequent ventilator, however it ought to be noticed that the exhaust air can't be gotten back to the lodge. A warmth recuperation unit (air-air heat exchanger) is in some cases introduced after the battery pack to recuperate heat from the exhaust air. It can forestall the blending of exhaust and admission air while likewise giving extra reserve funds potential. The constrained air framework with heat recuperation is displayed in the graph underneath.

Liquid cooling and heating

Alongside from air, fluid is another warmth move liquid that can be utilized to move heat. There are two kinds of fluids utilized in warm administration frameworks. Mineral oil, for instance, is a dielectric fluid (direct-contact fluid) that can come into direct contact with the battery cells. The other kind is leading fluid (backhanded contact fluid), which can just connect with the battery cells, like a combination of ethylene glycol and water. Various formats are planned dependent on the various fluids. The standard design for direct-contact fluid is to lower modules in mineral

oil. A coat around the battery module, or discrete tubing around every cell, is a potential format for roundabout contact fluid, mounting the battery modules on a cooling/warming plate, or consolidating the battery module with cooling/warming blades and plates In this correlation, circuitous contact frameworks are favored on the grounds that they give better disengagement between the battery module and its environmental elements, bringing about better security execution.

Fluid frameworks can likewise be named aloof or dynamic dependent on the warmth sinks utilized for cooling. A radiator fills in as the warmth sink for cooling in an aloof fluid framework. This framework is unequipped for delivering heat. The methodical plan of a uninvolved fluid framework is portrayed in (). The siphon courses heat move liquid inside a shut framework. The flowing liquid assimilates heat from the battery pack and disperses it through a radiator. The cooling power is profoundly subject to the temperature distinction between the encompassing air and the battery. Fans behind the radiator can further develop cooling execution, yet on the off chance that the encompassing air temperature is higher than the battery temperature, or the thing that matters is too little, the aloof fluid framework becomes incapable.

The precise plan of a functioning fluid framework is portrayed in Fig 3. There are two circles in the framework. The upper circle is known as the essential circle, and the lower circle is known as the auxiliary circle. The essential circle is undifferentiated from the circle in a detached fluid framework, where the warmth move liquid is coursed by a siphon. The optional circle is a warming and cooling circle (A/C circle). Rather than being a radiator, the upper warmth exchanger fills in as an evaporator (EVAP) for cooling and interfaces the two circles. During warming, the 4 way valve is turned on, and the upper warmth exchanger capacities as a condenser (COND) and the lower heat exchanger capacities as an evaporator. The warming activity circle is additionally alluded to as a warmth siphon circle.

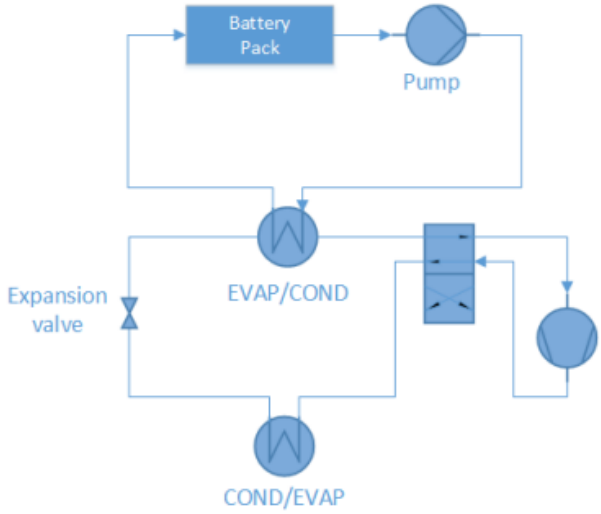

FIGURE 3. Liquid Cooling and Heating System

Direct refrigerant cooling and heating

An immediate refrigerant framework (DRS) is like a functioning fluid framework in that it has A/C circle, however DRS utilizes refrigerant straightforwardly as warmth move liquid coursing through the battery pack.() portrays the precise format in Fig 4.

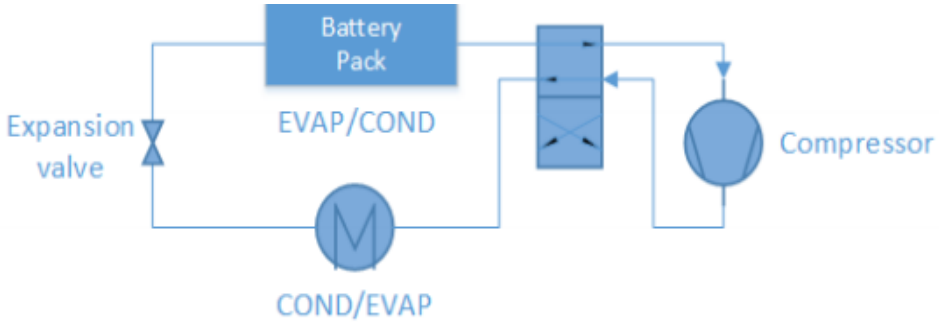

FIGURE 4. Direct Refrigerant Cooling and Heating System

PTC heater

PTC indoor regulators have a wide scope of self-warming applications because of their remarkable voltage current or current-time attributes. One of the applications is as a PTC radiator, which is an automatic warmer. The temperature of a PTC radiator can be kept consistent via naturally changing the obstruction of the PTC warmer, as displayed in Fig 5.

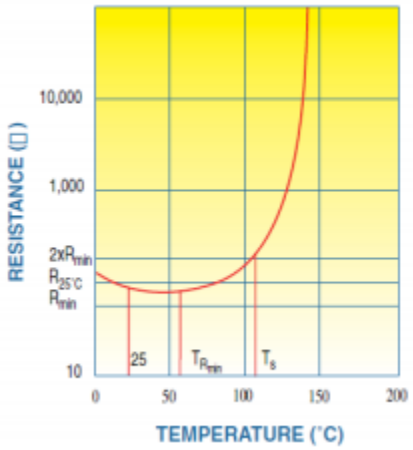

FIGURE 5. PTC Heater Characteristics

TOOL USED

Matlab/Simulink R2020 – Used to develop different mathematical model of subsystems in BTMS and to simulate the results

PROCEDURE

Theoretical Calculation

Heat Transfer Overall Heat Transfer Coefficient

The warmth move can as a rule be communicated utilizing the general warmth move co-productive by utilizing the condition underneath to gauge the proficiency of the warmth trade.

$$Q = UA\Delta Tm \quad (3)$$

Where,

q	Rate of warmth move (W)
U	Overall warmth move co-productive [(W/m2K)]
A	Heat move surface region (m2)
ΔT_m	Approximate mean temperature contrast (K)

The convective and conductive pieces of warmth move between the hot and cold liquids in the warmth exchanger are remembered for this condition. The radiation part and the warmth move between the warmth exchanger and the air are irrelevant.

The absolute warmth move coefficient for the un-finned, cylindrical warmth exchanger in Fig 6 can be communicated as Equation 2.4.

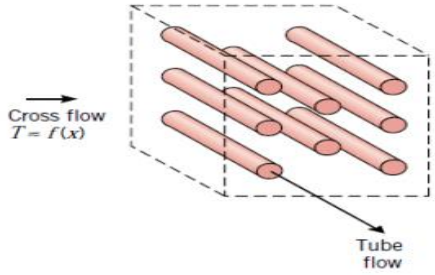

FIGURE 6. Un-finned, tubular cross flow heat exchanger

$$\frac{1}{UA} = \frac{1}{h_i A_i} + \frac{Rf''_i}{A_i} + Rw + \frac{Rf''_{,o}}{A_o} + \frac{1}{h_o A_o} \tag{4}$$

Where

UA	Product of U and A (W/K), A could either be A_o or A_i
h_o,h_i	Convective heat transfer co-efficient of outer and inner tube surface (W/m^2K)
A_o,A_i	Contact area of inner and outer tube surface (m^2)
Rf_i'',Rf_0''	Fouling factors (m^2K/W)
R_w	Conductive resistance (K/W)

For this situation, Rw represents the cylinder's conductive obstruction, which is determined utilizing the condition ln(Do/Di)/2πkL. Where Do is the cylinder's external breadth, Di is the cylinder's inward measurement, k is the cylinder's warm conductivity, and L is the cylinder's length. In the event that the convection of the external surface is especially solid, i.e., ho = ∞ and the fouling impact is unimportant, the terms $1/hoAo$, Rf_i''/A_i , Rf_o''/A_o in condition is irrelevant and the condition lessens.

$$\frac{1}{UA} = \frac{1}{h_i A_i} + \frac{\ln\left(\frac{D_o}{D_i}\right)}{2\pi kL} \tag{5}$$

If the calculation is based on the inner tube surface A = A_i and since $A_i = \pi LD_i$ the equation 3.3a is equivalent to

$$\frac{1}{U} = \frac{1}{h_i} + \frac{D_i \ln\left(\frac{D_o}{D_i}\right)}{2k} \tag{6}$$

Where ri and ro alludes to tube inward and external sweep. The condition 3.3c will be utilized to characterize the warmth move between battery cells and the warmth move liquid in the accompanying model unit "Battery Pack". One boundary, 'h' convective warmth move co-productive, is as yet unclear in Equations 3.3a to 3.3c. The accompanying conditions can be utilized to ascertain it:

$$N_{uD} = h_{fl} * \frac{D_h}{k_{fl}} \tag{7}$$

Where Dh is the water driven distance across, which is equivalent to Di on account of a filled roundabout cylinder, kfl is the warm conductivity of the liquid, and NuD is determined dependent on the different stream conditions (laminar or tempestuous). Since the worth of Re (Reynolds number) is < 2300, NuD is given by the accompanying condition

$$N_{uD} = 3.66 + \left[\left(\left(\left[\frac{0.668*\left(\frac{D}{L}\right)*R_e*P_r}{1} + (0.04)*\left(\left(\frac{D}{L}\right)*R_e*P_r\right)\right]\right)\right)^{0.67}\right] \tag{8}$$

In the equation 3.5 R_e is the Reynolds number which is determined by the following equation

$$R_e = \frac{\rho v D}{\mu} \tag{9}$$

The Prandtl number P_r, defined by the equation, interprets the ratio of momentum and thermal diffusivities

$$P_r = \frac{\mu C_p}{k} \tag{10}$$

Battery Unit

The areas of battery cells were believed to be homogeneous, and the interior warmth conductivity between cells moved toward vastness, permitting warmth to pass between cells quickly and guaranteeing that all focuses on the battery cells were at a similar temperature, alluded to as battery temperature Tba. The accompanying condition communicates the distinction in battery temperature over the long run:

$$\frac{dT_{ba}}{dt} = \frac{\left(Q_{gen} - Q_{dis}\right)}{\left(m_{ba} C_{p,ba}\right)} \tag{11}$$

Qgen and Qdis states the pace of warmth age and warmth scattering, individually. The previous is arranged utilizing the product inside signal generator or a warmth age rate profile from the driving cycle FTP - 75. This warmth is given by the electro-warm impacts of the battery. The last was controlled by the battery unit's sub-framework, which is communicated in Equation 3.8. The warmth disseminated during the warm cycle is addressed by this warmth (s). At the point when the warm cycle is cooling, the worth is positive. At the point when the warm cycle is warming, the worth is negative. Battery mass and explicit warmth limit are addressed by mba and Cp,ba individually.

$$Q_{dis} = UA(\overline{Tfl} - T_{ba} \tag{12}$$

To pass warmth to and from the battery, three discrete copper tubes are joined near the battery cells in the battery pack. As expressed in Section 3.1.1, the general warmth move coefficient U will be resolved. The contact region, which is the finished internal space of the three cylinders, is signified by the letter A. The assessed mean temperature distinction is addressed by ¯Tfl - Tba. ¯Tfl is the normal temperature of the liquid delta and outlet.

Air Conditioner (Active Cooling)

The fluid temperature differential is expressed as the following equation as heat transfer fluid flows through an air conditioner:

$$\frac{dT_o}{dt} = \left[\left(mdot_{fl} * C_p * \left(T_i - T_0 \right) \right) - \frac{Q_{Ac}}{\left(m_{fl,Ac} C_{p,fl} \right)} \right] \tag{13}$$

Since the climate control system extricates heat from the liquid, q in Equation (3.9) is consistently negative. Here q is swapped by QAc which represents cooling load and is consistently certain. The accompanying condition can be utilized to quantify Qac

$$Q_{Ac} = P_{el,Ac} * COP \tag{14}$$

Pel,Ac is the electrical energy devoured by the Air conditioner and COP is co-proficient of execution which is reliant upon working state of the Air Conditioner.

Radiator (Passive Cooling)

The fluid temperature difference in the radiator, like the air conditioner, can be expressed as:

$$mC_p * \frac{dT_{out}}{dt} = mdotC_p \left(T_{in} - T_{out} \right) + Q \tag{15}$$

Where Q is the warmer's warmth, Tin, Tout is the coolant in and out temperature, ṁ is the coolant mass stream rate, and m is the coolant mass in tubes.

$$P = P_{\max} = \text{constant} \tag{16}$$

Pump

The pump's electrical energy consumption is calculated as follows:

$$P = \frac{\gamma H mdot}{\eta} \tag{17}$$

The specific gravity γ is calculated by multiplying the coolant density by gravity and is expressed as: \

$$\gamma = \rho g \tag{18}$$

Where ṁ is mass flow rate, η is the efficiency of the pump, H is the total head and is related to the mass flow rate ṁ, refer Fig 7.

$$H = f\left(mdot \right) \tag{19}$$

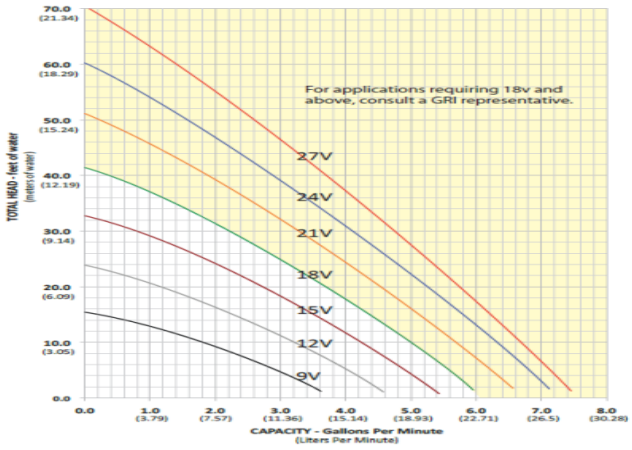

FIGURE 7. The relationship between flow rate and total head.

The performance of the water pump is shown in Figure 3.2, and the performance of other viscous coolants is determined using the correction.

$$mdot_{cl} = C_p mdot_w \tag{20}$$

$$H_{Cl} = C_h H_w \tag{21}$$

$$\eta_{cl} = C_\eta \eta_w \tag{22}$$

The force adjustment factor, head rectification factor, and productivity remedy factor are totally addressed by Cp, Ch, and Cη, individually. The amendment factors are picked as follows because of the coolant's low consistency and comparability to water:

$$C_p, C_h, C_\eta = 1 \tag{23}$$

Performance Parameters

The conditions for yield boundaries are momentarily displayed beneath. It includes the electrical energy utilization of every gadget, the battery's temperature, and the segment's functioning time.

The complete electrical energy utilization is determined as the measure of all electrical energy utilization. Every segment burns-through the accompanying measure of energy:

$$E_T = \sum E_{HT} + E_{BP} + E_{AC} \tag{24}$$

When the heater is turned on, the following equation is used to calculate the heater consumption:

$$E_{HT} = \int P_{Ptc} + P_{pump}\, dt \tag{25}$$

As the coolant passes through the bypass, the bypass consumption is determined by integrating pump power:

$$T_{b,\max} = \int P_{AC} + P_{pump}\, dt \tag{26}$$

The average temperature is calculated as:

$$T_{b,\max} = \max T_b(t) \tag{27}$$

The average temperature is calculated as:

$$T_{b,avec,c} = \overline{Tb(t1)} \tag{28}$$

The normal temperature of the battery Tb, avec, c is the normal battery temperature during detached and dynamic cooling. The accompanying condition portrays it: Tb, avec, c = ¯(Tb (t1)). There are additionally some different boundaries to assess the model's presentation. Tht,tbp,tpc, and tac are the working spans of warming, by-pass, latent cooling, and dynamic cooling, individually. T10 is the point at which the battery temperature transcends 10°C interestingly after the driving cycle starts in a virus state. tdes is characterized as when the battery temperature falls beneath the ideal temperature interestingly after the driving cycle starts in a hot state.

Modelling Of Battery Thermal Management System

A rationale model was created prior to beginning to foster a MATLAB/Simulink model to make a general rationale framework for the BTMS reenactment. It supported with the displaying steps that followed, yet in addition with likely alterations, expansions, and upgrades.

The logic modelling was primarily built in four steps:

Initial inputs and settings for thermal cycles

Actual boundaries, for example, warm limit and mass were determined as fixed boundaries beginning with the battery unit. With regards to the warm issues of the battery pack, there are two significant pieces of warmth move streams that impacted the battery temperature. The originally was the interior warmth age. This part was controlled by driving propensities, battery highlights, and other vehicle boundaries, for example, vehicle mass and streamlined execution. Since this postulation zeroed in on warm as opposed to electro-warm issues, the inside heat was produced by an outside electro-warm model. The other segment was outside heat scattering. This bit of the warmth came from the different warm cycles, which eliminated certain measures of warmth from the battery or, at times, carried warmth to the battery. The measure of warmth was dictated by both the warm cycle utilized and the encompassing warm conditions were considered. Thus, a few boundaries from the battery unit and testing conditions were gathered for estimation. Following this progression, the vital battery warm model was made.

Creating a control strategy

In most battery warm models, multiple warm cycles are planned. Some trademark boundaries, like battery temperature and encompassing temperature, were needed to figure out which cycle to run. An activity state was picked dependent on these boundaries. The state comparing to the dynamic warm cycle, just as some connected segments, like the siphon, would change their working state. At times, a sub-state inside the primary activity state might be acquainted with further develop activity highlights.

Simplifying and decoupling

Since some intricate estimation cases would bring about unlimited circles, a streamlined or inexact computation technique ought to be utilized to tackle the unlimited circles and accelerate the recreation. Decoupling was an elective arrangement in different cases. For instance, the actuated warm cycle devours power, bringing about expanded burden and, subsequently, expanded warmth. The coupling of the warm and electro-warm models would bring about startling programming issues. Accordingly, it was desirable over decouple these two models toward the beginning and interface them some other time when both were performing.

Data input and output

Not the entirety of the yield boundaries was important. Just boundaries addressing the model's yield were recorded. Some crude information was changed into execution boundaries to look at changed results utilizing a typical norm. A few figures were additionally plotted dependent on mathematical information for a superior visual agreement.

TABLE 2. Battery Specifications

Parameter	Value
Battery Capacity	29.5 kWh
Battery mass	270
Battery Specific Capacity	1000 J/kg.K
Vehicle mass	1700 kg

A few parameters were also changed to represent different scenarios.

Ambient temperature was the most important variable parameter

This temperature addressed the climate conditions in the space encompassing the driving vehicle. It was viewed as a chilly environment when the temperature went from - 20°C to 10°C. A gentle environment was characterized as temperatures going from 10°C to 20°C. It was viewed as a sweltering environment when the temperature went from 20°C to 40°C.

The initial temperature of the battery

It is generally accepted that the battery's underlying temperature is by and large equivalent to the encompassing temperature. Notwithstanding, when pre-molding is utilized, these two temperatures don't coordinate. At the point when a battery is pre-warmed in a cool environment, the underlying temperature of the battery is higher than the surrounding temperature. At the point when a battery is pre-cooled in a sweltering environment, its underlying temperature is lower than the encompassing temperature. Different degrees of pre-molding could be utilized.

Desired temperature

The ideal temperature is the temperature that the BTMS control unit focuses on, for example the producer's ideal working temperature point. The BTMS will utilize diverse warm cycles to attempt to keep the battery temperature as near the ideal temperature as could be expected. Temperature wanted is 25°C as a rule of this work, yet some unique cases with Temperature wanted = 20°C were additionally tried.

Testing driving cycle

This model zeros in additional on BTMS during driving. The driving cycle embraced for our task is the FTP – 75 driving cycle. This addresses the distinctive driving practices. The vehicle speed profile of the cycle is as displayed in the Fig 8. This driving cycle endures 1877 seconds for each single cycle. This cycle addresses a gentle driving conduct with greatest speed of 91.2 Kmph and a normal speed of 34.12 Kmph. For testing, the cycle was made to run multiple times as a testing condition input and the vehicle was driven after the speed profile until the accessible battery limit was depleted. This total cycle was named as the Testing Driving Cycle.

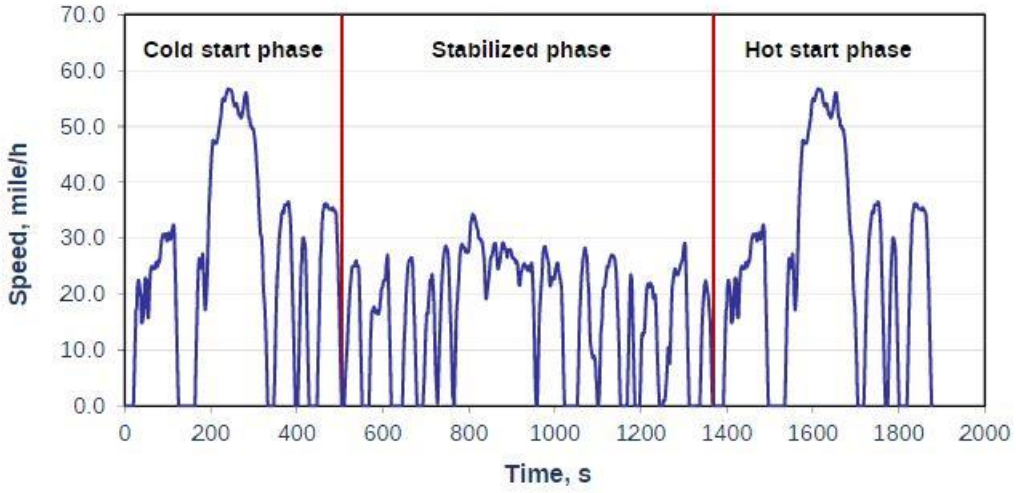

FIGURE 8. Speed Profile

Development of Combined Liquid System Model in Matlab

Following the four steps outlined at the start of the last chapter, a MATLAB/Simulink model was created.

A model design is displayed in the accompanying Fig 9. The temperature stream of warmth move liquid associates the principle parts in the fundamental format. The initial step was to stack testing information. The liquid was then warmed up, starting with the battery unit. Following that, the liquid courses through different parts, yet the control unit chooses just a single result. The siphon's stream rate was additionally administered by the control unit. At long last, the coolant was gotten back to the battery pack. This estimation technique was rehashed until the driving cycle was finished.

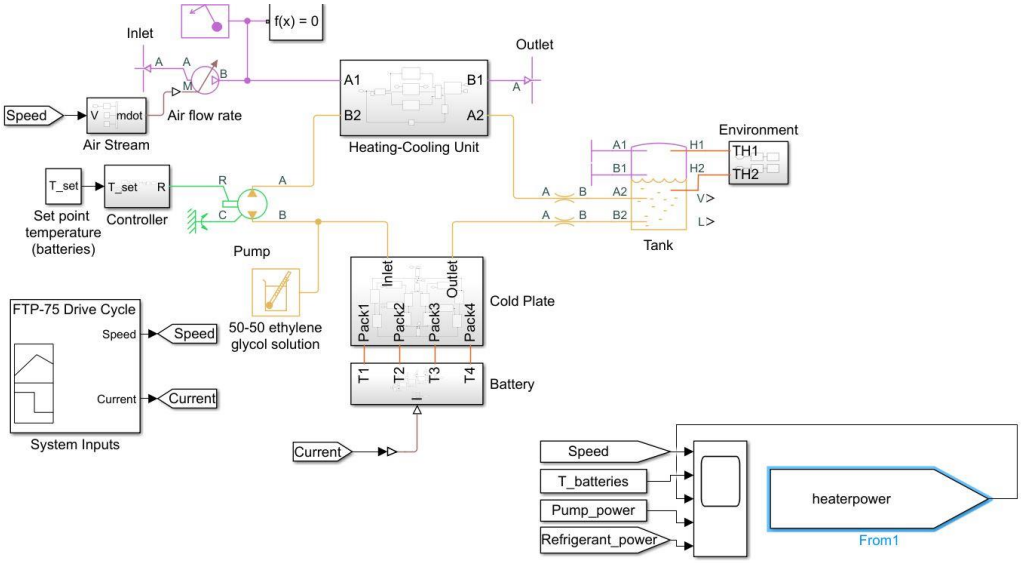

FIGURE 9. Battery Temperature management System (Combined Liquid System)

Driving Cycle

The driving cycle of FTP 75 was developed using the signal Builder block in Matlab as shown in Fig 10 which allows us to feed in the different values of Speed throughout the cycle and the relevant current depreciated.

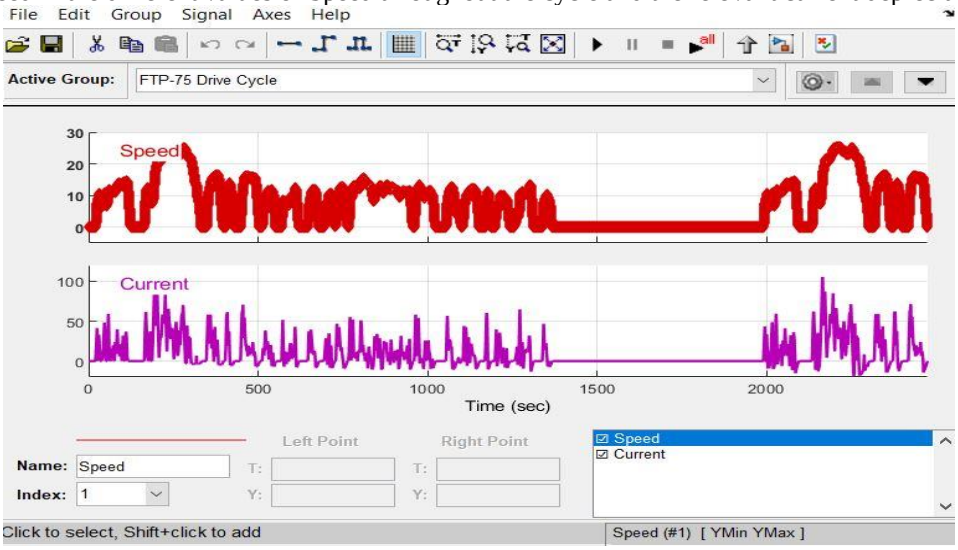

FIGURE 10. Speed Profile Signal in Signal Builder Block Matlab

Battery Unit

The battery unit is modelled as 4 battery packs connected in series consisting of 20 individual lithium cells as shown in Figure. The inputs from drive cycle are fed into the battery unit and the relevant heat flow is measured using heat flow sensor of simscape.

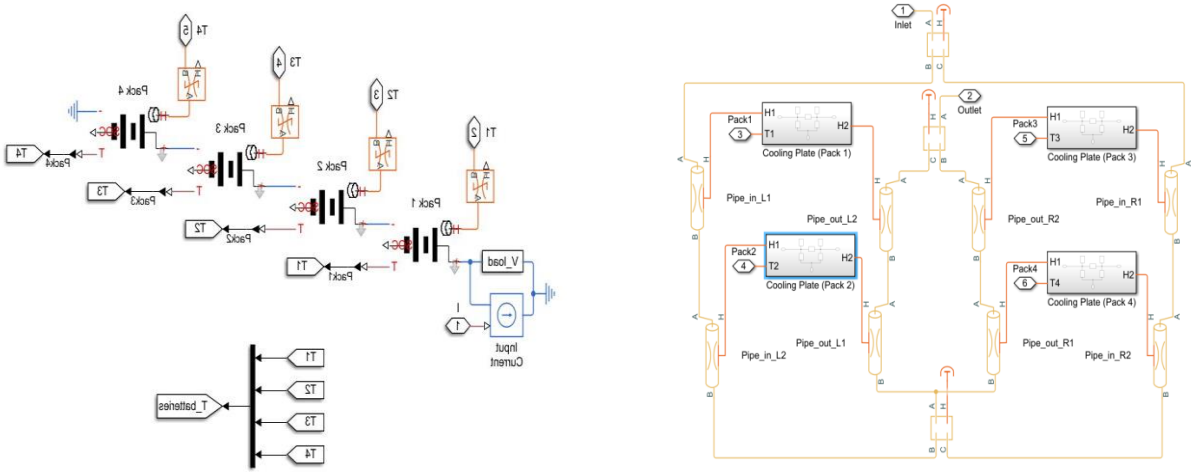

(a) (b)

FIGURE 11. (a) Battery Unit in Matlab, (b) 7 Cold Plate Cooling channels built into battery model

The coolant flowing through the battery is modelled in a separate subsystem known as the Cold plate where the heat flow battery measured is circulated to the incoming coolant as shown in the Fig 11.

Heating Cooling Unit

The heating cooling unit is the integral part of a Battery temperature Management System. Here in our Combined Liquid Cooling System that we adopted we have Radiator as a passive cooling system, PTC heater as a heating system and a refrigerant system as an active cooling system respectively with a controller and a 4 way valve to direct the coolant to the respective system with respect to the coolant temperature as shown in Fig 12.

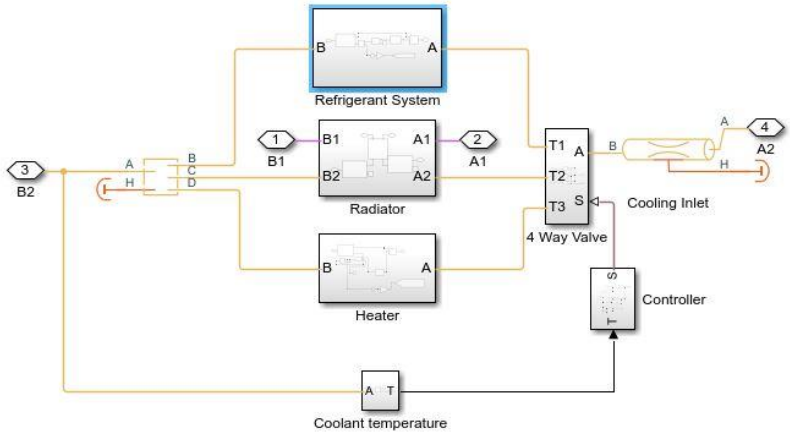

FIGURE 12. Heating Cooling Unit Overview

Radiator System (Passive Cooling)

The radiator system is developed as a passive cooling system so that it can be triggered during mild weather conditions where the temperature of the battery is between 25 to 30 deg Celsius. The flow rate of air for the radiator system is developed using another system which employs the speed of the vehicle to calculate the flow rate. The radiator system is modelled in Matlab as shown in the Fig 13 below.

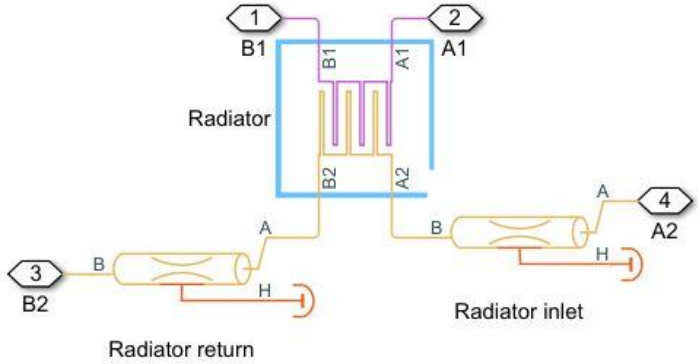

FIGURE 13. Radiator Model in Matlab

Refrigerator System (Active Cooling)

The refrigerated system is modelled in Matlab as shown in the Fig 14. The refrigerant system is employed for the hot weather conditions where the battery temperature rises above 30 deg Celsius. The refrigerant system is modelled considering the environmental conditions of above 30 deg Celsius. The refrigerant characteristics of the system used is the same as the popular refrigerant used in Air conditioner R 134 A.

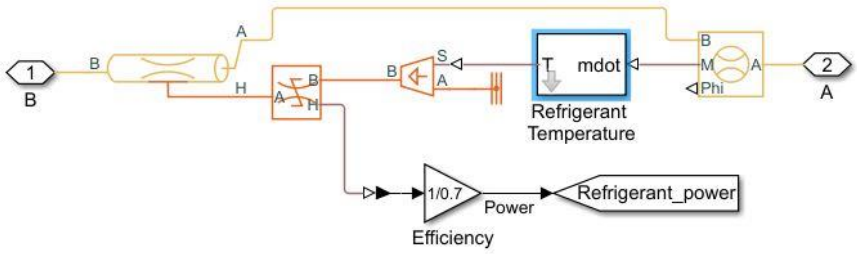

FIGURE 14. Refrigerant System Model in Matlab

Heater

The heating system is developed to operate in cold weather conditions where the environmental temperature is below 10 deg Celsius. We have developed a PTC heater kind of setup where the heater cut off is done automatically hence the heater system does not need any dedicated control system as shown in Fig 15.

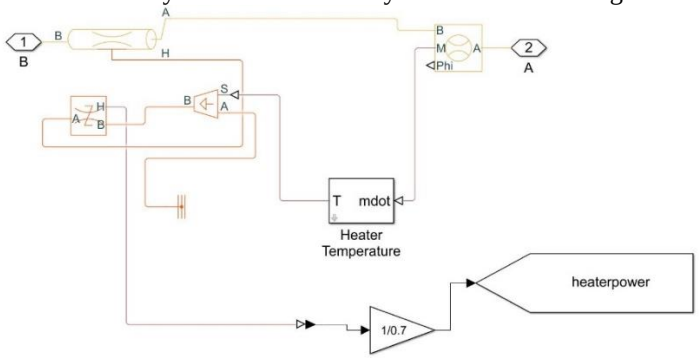

FIGURE 15. Heater System Model in Matlab

Control System

As a rule, a complex on-off control methodology is utilized as displayed in the Fig 16. Three on-off regulators with various exchanging temperatures make four expresses, every one of which compares to an activity mode. Regulator I is accountable for exchanging between States 1 (warming) and 2 (cooling) (Bypass). Regulator II is accountable for exchanging between States 2 and 3. (Aloof cooling). Regulator III is responsible for exchanging between States 3 and 4. (Dynamic cooling). The control System includes a PID regulator that is set at an ideal temperature scope of 20 to 22 deg Celsius.

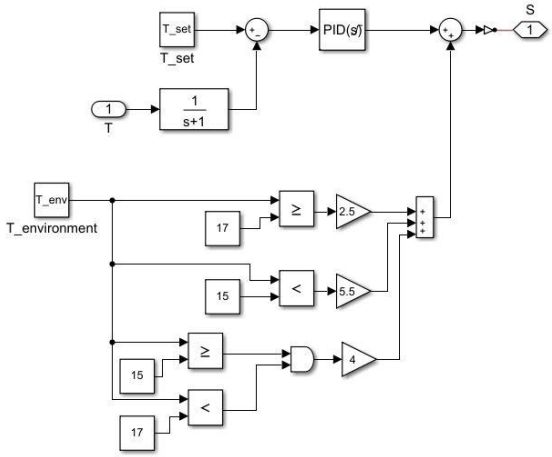

FIGURE 16. Control System of Heating Cooling Unit in Matlab

Ancillary Systems

Ambient Temperature

A separate Matlab system was setup to model the ambient characteristics which the heating and cooling unit has to monitor and also forms an integral part of the control strategy. The ambient system is setup using Simscape a subsidiary of the Simulink system as shown in the Fig 17.

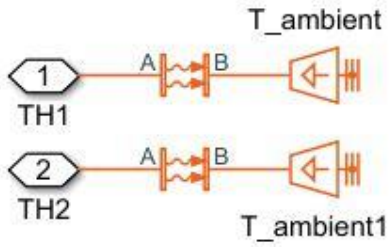

FIGURE 17. Ambient System Model in Matlab

Pump System

Pump system as shown in the Fig 18. Forms an integral part of the refrigerant system as it deploys the coolant into the refrigerant sysytem with respect to the required cooling rate. Hence developing the pump system with a proper control strategy is essential to minimize large cooling errors in the Matlab solution. This pump system was designed keeping in mind the required flow rate.

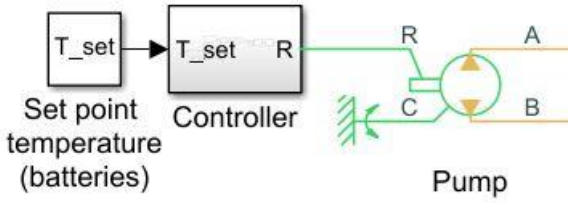

FIGURE 18. Pump System Model in Matlab

The controller becomes complex as we have to consider the temperature difference of the desired temperature and also the pump's rpm which acts as a relay to trigger the pump response which in turn pumps the coolant into the refrigerant system at a proper rate. This complex control system is as shown below in the Fig 19.

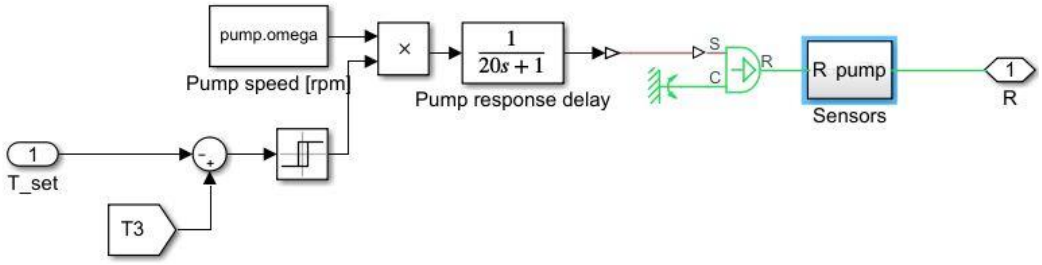

FIGURE 19. Pump Control System Model in Matlab

Airflow rate System

Similar to the role that the pump system plays in the refrigerant system. The airflow rate system forms an integral part of the radiator system. The radiator system as we know is a passive cooling system. Hence the airflow rate depends solely on the velocity at which the car travels and also the intrinsic properties of air. Thus setting up this system plays a pivotal role in the accuracy of the radiator system output. Here we have adopted a simple but effective strategy where we would feed in the speed data from the Test Driving Cycle into a flow rate calculator setup using the help of fundamental blocks in Simulink as shown in the Fig 20.

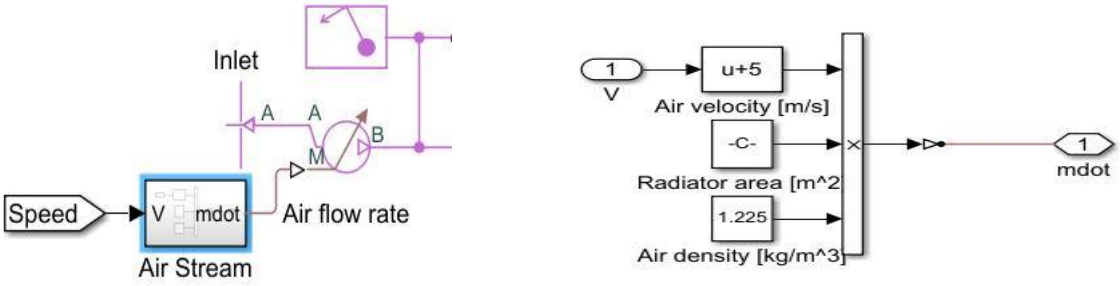

(a) (b)

FIGURE 20.(a) Air Flow Rate System Model in Matlab, (b) Air flow Rate Control System in Matlab

RESULTS AND DISCUSSION

With this we hereby conclude the different systems that have been developed in Matlab Simulink. This process of developing took a big chunk of our time as it involved multiple corrections of errors and studying the different Simulink and Simscape blocks and their functionalities.

In this Chapter we will be describing the various results obtained through simulating the Matlab/Simulink model of the Battery Thermal Management System. The results were taken under three different operating conditions (or) environmental conditions namely mild weather conditions, extremely hot and cold weather conditions. The General assertions made during the simulations are the battery temperature throughout the battery back remains even without any deviations and the battery is pre-conditioned that is the battery is pre-heated when operating under extreme cold conditions and pre-cooled when operating under extreme hot conditions. The former assertion was made to simplify and decouple the model and the latter is made to increase the battery performance of the designed Battery thermal model. The testing conditions for the different operating temperature are as follows

Hot Weather Condition

- The working ambient temperature is ranged between 38 – 45 deg Celsius
- The battery is pre-conditioned at 26 deg Celsius so that the energy savings is maximum

Cold Weather Condition

- The working ambient temperature is ranged between 0 – (-5) deg Celsius representing extreme cold conditions
- The battery is pre-conditioned at so that the energy consumed to heat the battery initially is reduced
- The pre-conditioning of the battery was found to increase the saving potential by almost 91% when pre heated

Mild Weather Condition

- The Mild Weather condition takes the ambient condition ranging from 20 – 28 deg Celsius
- The pre-conditioning is applied same as that of extremely hot and cold conditions but the energy spent to pre-condition is low

- The mild weather conditions favour the battery's performance and longevity. However, the designed Battery Thermal Management System achieves it in both the extreme cold and hot conditions as well.

Battery Performance

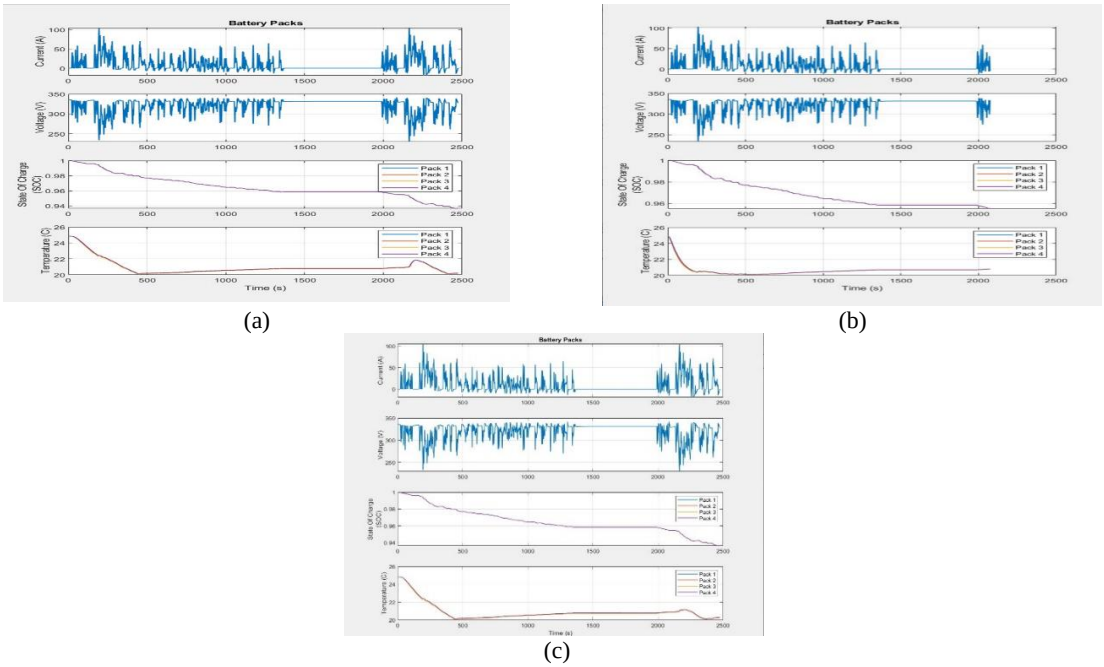

(a) (b)

(c)

FIGURE 21. (a) Battery Performance Hot Weather Condition, (b) Battery Performance Cold Weather Condition, (c) Battery Performance Mild Weather Condition

The above pictures show in Fig 21, the battery performance at hot, cold and mild weather conditions respectively. From the could understand that the battery performance remained fairly constant through different operating cycles which indicates that the designed Battery Thermal Management System has worked optimally in the different cycles. The temperature graph in cold condition falls rapidly from the pre-conditioned temperature similarly the temperature at hot condition falls gradually indicative of the prevalent ambient conditions which results in the sharp decrease of temperature during cold weather and gradual decrease during hot weather. The State of Charge remains fairly similar in different cycles.

Heat Flow

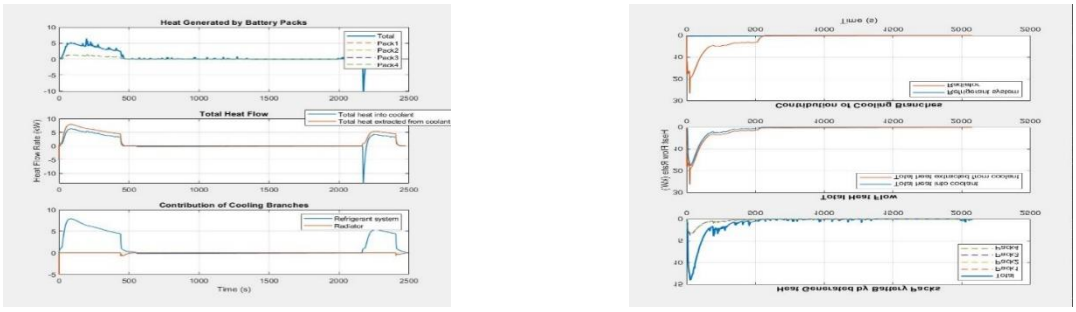

(a) (b)

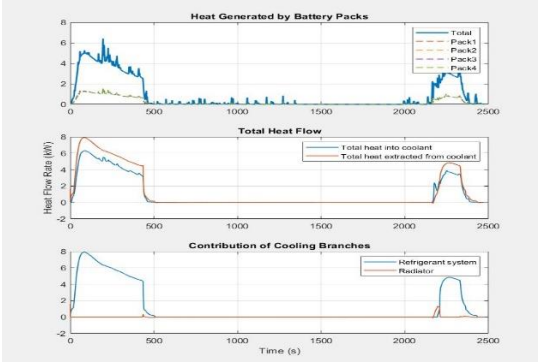

(c)

FIGURE 22.(a) Heat Flow through Battery pack and coolant Hot weather Condition, (b) Heat Flow through Battery Pack and coolant Cold Weather Condition, (c) Heat Flow through Battery Pack and Coolant Mild Weather Condition

The above pictures in Fig 22, represent the heat flow across the batteries, total heat flow into and extracted from the coolant and power contribution across the cooling branches for the hot, cold and mild weather conditions respectively. From these graphs we could see that the heat extracted from the coolant is always higher than that of the heat into coolant which is a positive sign that indicates that the radiator and refrigerant models are working in tandem with each other. We could also infer the heat generated by the batteries and also the contribution of the different cooling branches under different weather conditions. Under hot weather conditions we can observe that power contributed by the refrigerant is higher and under cold weather the radiator works more. The heat generated by the batteries is higher under cold weather conditions which is indicative of the heater working and pumping heat into the coolant to heat up the battery up to the desired operating temperature. Hence the heat flow graphs gives valuable insights to evaluate the BTMS.

Mechanical Power

The mechanical power used by the pump and the refrigerant system to pump the coolant and temperature extraction are studied in these results. The pump power is an essential parameter as it is solely responsible for the circulation of the coolant throughout the entire system. Hence it becomes imperative to study the pump and these results help us to do just that. As we could observe from the Fig 23 which represent the hot, cold and mild weather conditions respectively, the pump power is higher during the cold operating condition as the coolant has to be circulated to the heater at a higher rate compared to the hot and mild conditions. This gives a great outlook and reconfirmation that the heater system is working properly as designated.

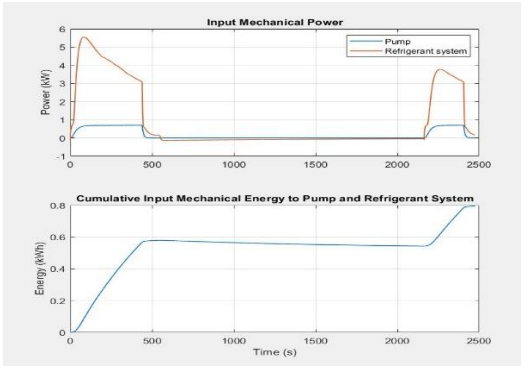

(a)

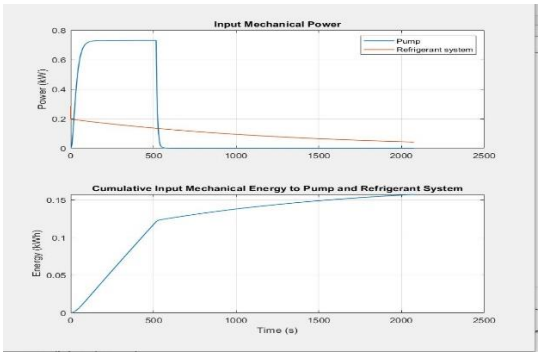

(b)

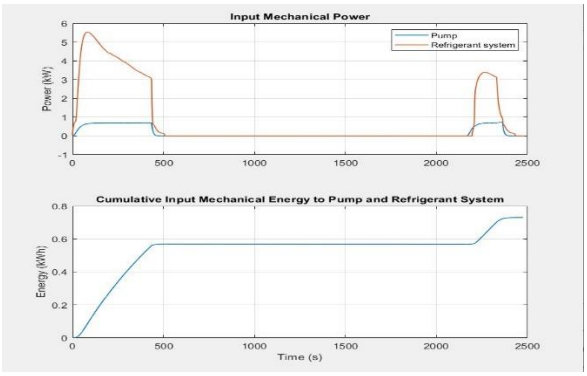

(c)

FIGURE 23. (a) Mechanical Power of Pump and Refrigerator System Hot Weather Condition, (b) Mechanical Power of Pump and Refrigerator System Cold Weather Condition, (c) Mechanical Power of Pump and Refrigerant System Mild Weather Condition

Power Consumption

Identifying the power consumed by the employed system remains our main objective to study the efficiency of the battery. Hence the below Fig 24 representing hot, cold and mild weather conditions with graphs that shows the speed map throughout the cycle, the operating temperature of the battery throughout the cycle, the heater , refrigerant and pump power respectively. These graphs gave us the right information to analyse the thermal efficiency of the designed BTMS. We could discern from the graph that the operating temperature operates predominantly in the desired temperature. And the power consumed correlates with the respective weather conditions which is indicative of the accuracy of the control system.

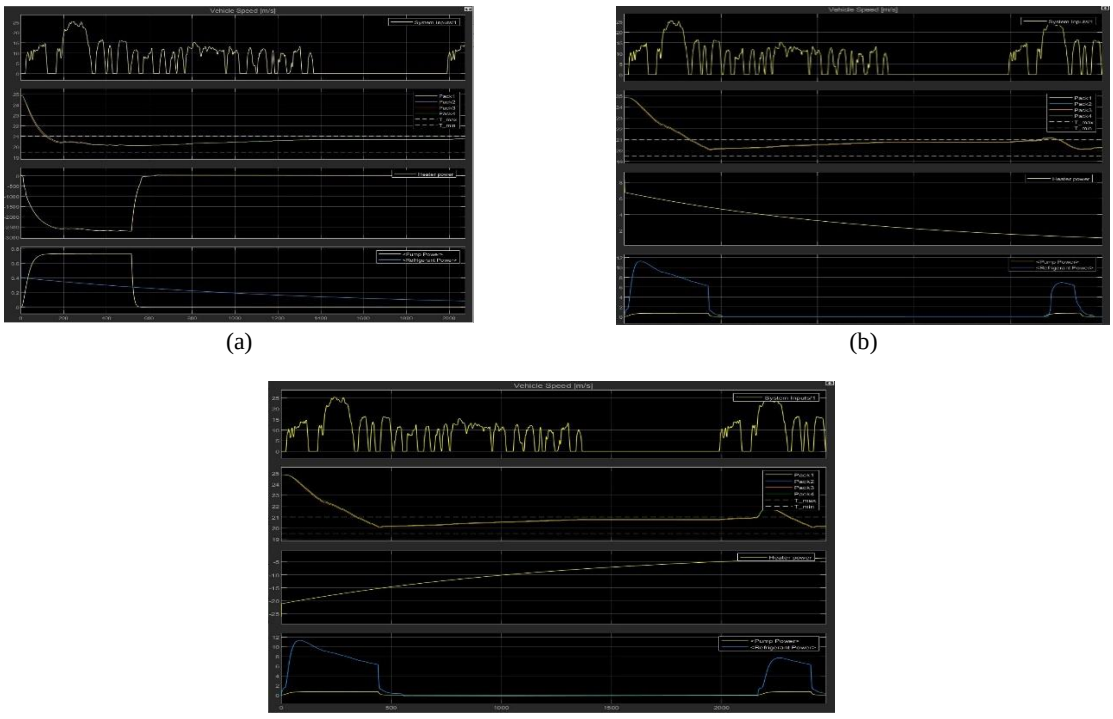

(a) (b)

(c)

FIGURE 24. (a) Power Consumption Cold Weather Condition, (b) Power Consumption Mild Weather Condition, (c) Power Consumption Hot Weather Condition

CONCLUSIONS

Under different climate, control, and driving conditions, mathematical outcomes with figures have been created. The anticipated electric energy utilization bodes well and had the right propensity. Besides, the displaying exhibited its flexibility to new frameworks with minor alterations.

The CLS model outcomes showed how driving conduct, battery introductory temperature, and encompassing temperature affected the BTMS and its related power utilization. As indicated by the discoveries, driving cycle changes significantly affected the BTMS highlight in blistering climate however not in chilly climate. The main variable for the BTMS was the surrounding temperature. The battery's underlying temperature, which addressed pre-molding treatment, essentially affected energy utilization, especially in outrageous blistering and chilly climate as displayed in the Fig 25.

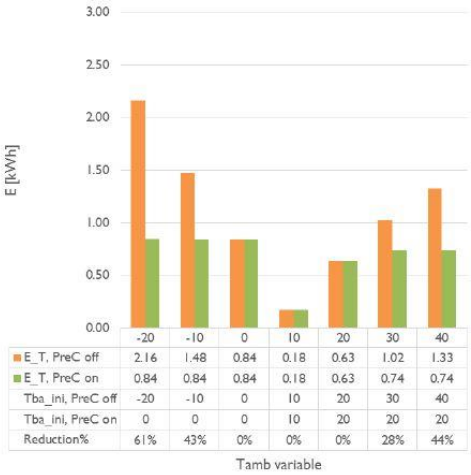

	-20	-10	0	10	20	30	40
E_T, PreC off	2.16	1.48	0.84	0.18	0.63	1.02	1.33
E_T, PreC on	0.84	0.84	0.84	0.18	0.63	0.74	0.74
Tba_ini, PreC off	-20	-10	0	10	20	30	40
Tba_ini, PreC on	0	0	0	10	20	20	20
Reduction%	61%	43%	0%	0%	0%	28%	44%

FIGURE 25. Difference of Power Consumption with and without Pre-Conditioning of the Battery

REFERENCES

1. Languang Lu et al., "A review on the key issues for lithium – ion battery management system in electric vehicles". *Journal of power sources*, Volume 226, 272-288 (2013)
2. Xuebing Han et al., "A review on the key issues of the lithium ion battery degradation among the whole life cycle". *Journal on eTransportation*, Volume 1, 100005. (2019)
3. Xuning Feng et al., "Mitigating Thermal Runaway of Lithium ion batteries". Joule, Volume 4, Issue 4, 743 – 770. (2020)
4. Huaqiang Liu et al., "Thermal issues about Li-ion batteries and recent progress in thermal management systems: A review". *Energy Conversion and Management*, Volume 150, 304-330 (2017)
5. Zhuqian Zhang and Ke Wei. "Experimental and numerical study of a passive thermal management system using flat heat pipes for lithium-ion batteries". *Applied Thermal Engineering*, Volume 166, 114660. (2020)
6. G.R.Molaeimanesh et al., "Experimental analysis of commercial Li-ion battery life span used in electric vehicle under extremely cold and hot thermal conditions". *Journal of Thermal Analysis and Calorimetry*, Volume 143, 3137-3146. (2020)
7. D. Thiruvonasundari and K. Deepa. "Electric Vehicle Battery Mdelling Methods Based on State of Charge – Review". *Journal of Green Engineering*, Volume 10, Issue 1. (2020)
8. Matthe R et al., "VOLTEC Battery Systems for Electric Vehicle with Extended Range". *SAE International Journal of Engines*". 4(1), pp.19441962. (2011)
9. Sabbah H et al., "Active (air-cooled) vs. passive (phase change material) thermal management of high power lithium-ion packs: Limitation of temperature rise and uniformity of temperature distribution". *Journal of Power Sources*, 182(2), pp. 630-638. (2008)
10. Tran T.H. et al., "Experimental investigation on the feasibility of heat pipe cooling for HEV/EV lithium –ion battery". *Applied Thermal Engineering*, 2(63), p.551-558. (2014)

11. Incropera F.P. “Fundamentals of Heat and Mass Transfer”. 6th edition Pesraran A.A. “Battery Thermal Management in EVs and HEVs: Issues and Solutions”. *Advanced Automotive Battery Conference*, p.10. (2001)
12. Battery University, 2014. *Battery University.* [Online]
Available at: http://batteryuniversity.com/learn/article/types_of_lithium_ion

RESEARCH ARTICLE | MAY 22 2023

Magnesium matrix reinforced with zirconium, garnet and graphite for improved mechanical properties

Muhammed Anaz Khan ✉; Lokasani Bhanuprakash; A. Vivek Anand

AIP Conference Proceedings 2492, 040077 (2023)
https://doi.org/10.1063/5.0116957

Magnesium Matrix Reinforced with Zirconium, Garnet and Graphite for improved Mechanical Properties

Muhammed Anaz Khan[1, a)], Lokasani Bhanuprakash[1, b)] and A Vivek Anand[2]

[1]*Department of Mechanical Engineering, MLR Institute of Technology, Hyderabad, Telangana, India-500043.*
[2]*Department of Aeronautical Engineering, MLR Institute of Technology, Hyderabad, Telangana, India-500043.*

[a)] Corresponding author: *muhammedanazkhan@mlrinstitutions.ac.in*,
[b)]*bhanuprakash_lokasani@mlrinstitutions.ac.in*

Abstract. Being the lightest metal constructional material, magnesium matrix composites are widely used in oceanic, structural, aerospace, and automobile applications for its lightweight, low density, better mechanical properties and resistance to corrosion. These composites incorporate attractive attributes of hard ceramics to the substrate material. In this study, magnesium based matrix is reinforced with Zirconium, Garnet and Graphite particulates. The reinforcement particles are blended with magnesium using stir casting process to ensure uniform particulate distribution across the matrix. The microstructure of the prepared composites was studied and hardness across the bulk is reported. It was observed that the bulk hardness increased with the garnet and graphite addition. Optimized parameters aid in uniform distribution of particulate reinforcement within the matrix pool. As-cast samples exhibited good bonding of reinforcement at the metal matrix-reinforcement interface. Agglomeration of garnet particle was observed to be minimal for 0.3 wt%, and increases with higher percentage. It is also observed that the porosity of the composites decreased with the increase in reinforcement weight percentage. The composite reinforced with 0.9 wt% of garnet and graphite exhibited and increased hardness of 70.2 HV0.1 compared to the 41 HV0.1 hardness exhibited by composite reinforced with 0.3 wt% of reinforcements. tensile properties.

INTRODUCTION

Magnesium and its alloys as scientific research material gained great attention in commercial application. Modern applications demand energy conservation and refined performance. Because of lower density, and higher specific strength compared with other structural metals, magnesium matrix alloys are considered for aerospace and automobile applications in order to minimize greenhouse emission and fuel consumption [1-3]. However, lower rate of wear, poor resistance to creep at higher temperatures, lower strength and modulus restricts the applications of these alloys for structural applications [4-5]. Reinforcing with industrial grade particle reinforcements impart better physical and mechanical properties. Such composites is being considered as a better alternative for Aluminium based metal matrix composites and possess several advantages such as high elastic modulus, strength, superior wear and creep resistances at elevated temperatures [6-7]. The properties of Mg MMCs can be tailored through judicious selection of reinforcement particles. The reinforcement is selected based on the working temperature and ambience. Some of the commonly used particle reinforcements are Aluminium Oxide (Al2O3), Titanium Carbide (TiC), and Silicon Carbide (SiC). It is reported that addition of carbides as reinforcement improves the yield strength, ultimate tensile strength, hardness, ductility and wear resistance of magnesium matrix alloys [8]. In the present work, Magnesium is reinforced with particulate Zirconium, Garnet and Graphite and its significance in improving the hardness of the composites is reported. In the area of the matrix, many metallic systems were considered as the matrix material including Al, Ag, Be, Co, Fe, Ti, Ni, and Mg. By far, aluminum matrix composites are considered to be the most considered for structural applications in aerospace and automobile applications. However, recent studies

Advancements in Aeromechanical Materials for Manufacturing: ICAAMM-2021
AIP Conf. Proc. 2492, 040077-1–040077-7; https://doi.org/10.1063/5.0116957
Published by AIP Publishing. 978-0-7354-4438-6/$30.00

claimed that magnesium could be considered to be a better alternative as matrix material as it offers lower density and better mechanical properties compared with Aluminum. Magnesium is lighter than structural materials such as aluminum, and steel [9]. Because of this, magnesium and its composites offer higher specific strength. The increase in demand for lightweight and high performance materials increases the need for magnesium matrix composites [10]. The magnesium matrix is reinforced with thermally stable reinforcements that make them suitable for high temperature applications [11]. For magnesium matrix composites, ceramic powders are considered to be the most widely used reinforcement. High-temperature stability and structural properties of ceramic materials make them favorable reinforcement candidates desirable for reinforcements. These properties include lower density and high levels of strength, thermal stability, hardness, and elastic modulus [12]. However, lower wettability, compatibility and reduced ductility are some of the problems associated with ceramic reinforcements to be used along with magnesium matrix. The most commonly used reinforcements are Titanium Carbide (TiC), Aluminium Oxide and, Silicon Carbide (SiC). K. B. Nie et al. [13] reported the microstructure and mechanical properties of SiC reinforced with magnesium matrix composites. Zhang Xiuqing et al. [14] reported the damping behaviour and mechanical properties of TiC particulates reinforced with magnesium matrix composites. It was observed that TiC as a reinforcement have a significant role on mechanical properties and damping capacity of the composites. Bhingole et al. [15] prepared and studied AZ91 alloy matrix composites reinforced with MgO and Al2O3 particles with. It was reported that formation of hard oxides improves the strain hardening exponent, hardness and ultimate strength of the composites.

EXPERIMENTAL

Powder Characterization

The Zirconium, Graphite and Garnet reinforcement particles having an average particle size of 30 microns were dispersed into the pure magnesium. The weight percentage of the particles was varied to understand the significance of elemental addition (Table 1). All castings were prepared using stir-casting furnace.

TABLE 1. Weight percentage of particle reinforcement

Sample Code	Zirconium weight %	Garnet weight %	Graphite weight %
MGG1	1	0.3	0.3
MGG2	1	0.3	0.6
MGG3	1	0.3	0.9
MGG4	1	0.6	0.3
MGG5	1	0.6	0.6
MGG6	1	0.6	0.9
MGG7	1	0.9	0.3
MGG8	1	0.9	0.6
MGG9	1	0.9	0.9

Microstructural and Mechanical Property Characterization

The microstructural specimens were polished using SiC papers of varying grit sizes followed by disc polishing using Al2O3 suspended distilled water. The disc polishing will provide mirror finish to the specimens' surface. The polished samples were etched using Keller solution to make microstructural features visible.

The Magnesium MMCs are reinforced with particles approximately 10-20 μm in diameter. The shape, size, and distribution of reinforced particles were observed using optical microscope (Olympus, BX41M). The hardness of the specimen is determined using a Brinell hardness tester and Vickers Hardness testing machine following the ASTM standard. The tensile properties were evaluated using UTM machine and the fractured surface was analyzed using SEM analysis[16].

RESULTS AND DISCUSSION

Microstructural Characterization

The Magnesium MMCs is reinforced with Zirconium, Graphite and Garnet particles having a particle size of approximately 10-20 μm in diameter. The microstructure exhibits the presence of reinforcement particles distributed across the magnesium matrix. Zirconium added is dissolved into the matrix during smelting of magnesium above 750 °C. The molten metal solidifies at a relatively high cooling rate and the dissolved Zr precipitates uniformly and is observed as α-Zr particles across the microstructure. Zirconium imparts grain-refining effect when it is added slightly above the solubility limit and subjected to a relatively lower cooling rate. Literatures reported that the zirconium acts an important grain refiner in magnesium used for commercial purpose [16]. However, addition of zirconium is limited by the cost-factor of the raw material and possible segregation at the bottom. This requires precise control over the process parameters to minimize the segregation of the zirconium.

Figure 1. (a-e) exhibits the microstructure of metal matrix composites fabricated through stir casting process. Distribution of particles is significant to impart superior structural properties to the fabricated composites. The lack of cracks attribute to the quality of castings. The volume fraction of the reinforcement is varied in different composition. It was observed that the microstructure of the composite consists of three phases: magnesium matrix, Graphite particles, and Garnet particles. It was observed that the Magnesium MMCs and the reinforcement particles are well bonded and few precipitates exist in the matrix or at the interface. The precipitate observed is formed from the elemental addition of Zirconium.

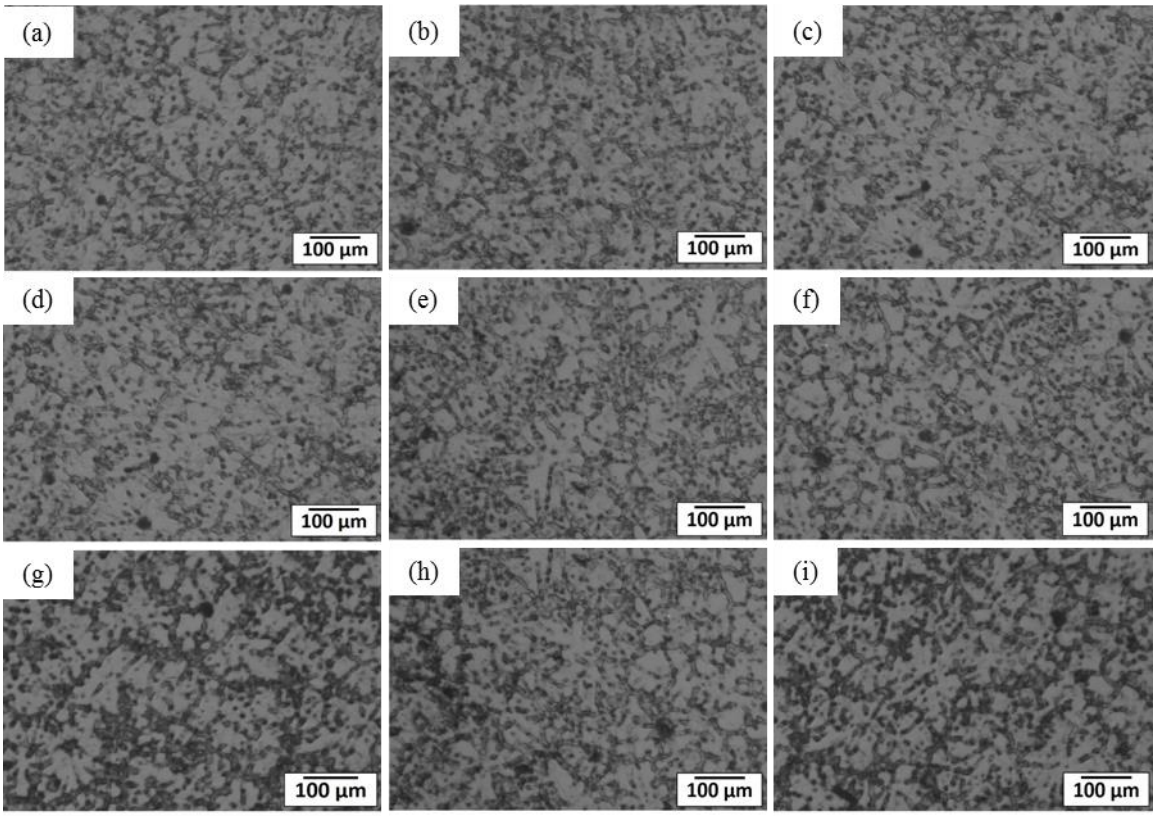

FIGURE 1. Optical Microscope images of Mg based metal matrix composites (a) MGG1, (b) MGG2, (c) MGG3, (d) MGG4, (e) MGG5, (f) MGG6, (g) MGG7, (h) MGG8 and (i) MGG9

From Figure 1. (a-c), it was observed that all castings exhibit good bonding along the Mg matrix-reinforcement interface. The stirring parameters were optimally adopted to minimize the agglomeration and segregation of the reinforcement particles.

The formation of bulk porosity across the cross-section of the fabricated composites is related to the wettability of the reinforcement. Inclusion of moisture along the periphery of the reinforcement particles entraps oxygen inside the molten metal matrix pool. This creates voids and acts as stress-nucleation sites. In order to remove the moisture, reinforcement particles were heated to a suitable temperature using a preheater. The dispersed graphite particles were observed to have a dendritic structure, and the density of these dendrites increased with graphite addition.

The variation in density of reinforcement was observed clearly with the increase in percentage of reinforcement. It was also observed that the porosity decreased with the higher percentage of reinforcement. The agglomeration of garnet particle was observed to be minimal for MGG1 where the percentage was limited to 0.3 wt%. However, agglomeration was observed for composites containing 0.6 and 0.9 wt% of graphite. This was attributed through higher binding force between the graphite particles. Optimized reinforcement percentage imparts improved bonding strength, which is attributed through matrix-reinforcement packing.

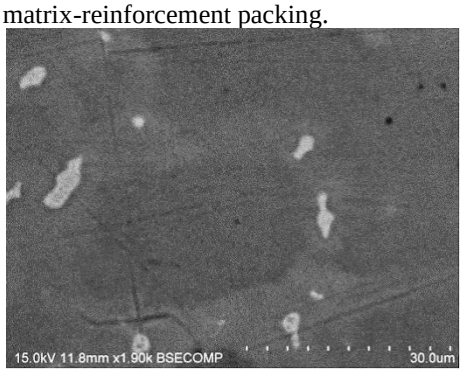

FIGURE 2. SEM image of as-cast MGG1 sample

Figure 2 shows the SEM image over the surface of as-cast MGG1. Peritectic reaction occurs between the zirconium and magnesium, and the zirconium reacts with matrix magnesium to form a solid solution enriched with zirconium. It is observed as the nuclei in the figure 2.

Hardness Characterization

Magnesium composites reinforced with 0.3 wt% of Garnet and Graphite exhibited a hardness of 37.32 BHN. The bulk hardness increased with weight percentage of reinforcement particulates. The Mg MMCs reinforced with 0.9 wt% of Garnet and Graphite exhibited a Brinell hardness of 78.14 BHN. Hardness at five different locations was measured and reported the average value. Much variation in hardness was not observed within the composites because of uniform particulate distribution. Higher weight percentage of reinforcement increases the micro-hardness value of the composites. The composite reinforced with 0.9 wt% of garnet and graphite exhibited a Vickers hardness of 70.2 HV0.1 compared to the 41 HV0.1 hardness exhibited by composite reinforced with 0.3 wt% of reinforcements. Higher volume fraction of refined dendritic structure attributed to higher micro-hardness. The Brinell and Vickers' hardness values obtained for all the fabricated composites are provided in Figure 3. (a) and (b).

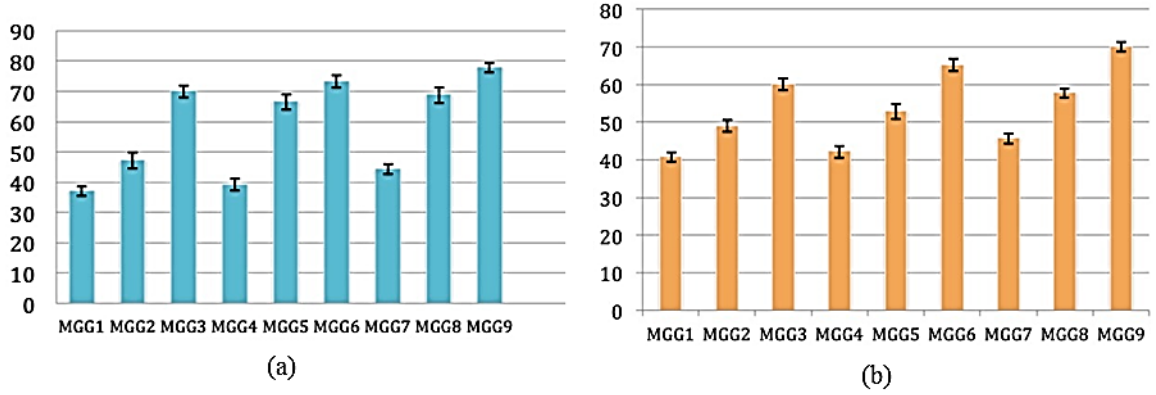

FIGURE 3. Hardness measurements for Mg MMCs (a) Brinell hardness and (b) Vickers' hardness

Tensile Property and Fractography

The tensile property of the fabricated composites was evaluated in accordance with ASTM standards. It was observed that the tensile properties increased up to 0.6 wt% of particulate addition and the property declined with further addition. Micro-fracture mechanism varies with varying volume fraction of reinforcement particles. The fractography of the fractured composites are given in Figure 4. The tested surfaces exhibit undulations and these were more for composites having higher weight percentage of garnet particulates. Higher cohesive strength between matrix and reinforcement particulates attributed to the undulated surface after the tensile test. It was observed that the reinforcement particles remained intact across the fractured surfaces. This exhibits the quality of bond between matrix and reinforcement particles. Existence of voids across the fractured surfaces exhibited the uniform distribution of reinforcement across the cross-section of the fabricated composites. Fractured surfaces were close examined and it was revealed that the tested samples followed a brittle mode of failure attributed through low fracture strain. SEM images given in Figure 5. (a-e) revealed the existence of submicron-sized voids. Fracture and/or loss of cohesion of graphite particles imparted the dimple structure over the fractured area. The micro voids present across the matrix-reinforcement interface acts as crack-nucleation sites during the tensile loading process. During progressive loading, these cracks propagate across the grain boundaries. The micro mechanism of the fracture varied with the reinforcement volume fraction.

Fractured surface of composites containing higher percentage of Garnet exhibited the presence of undulations. Higher cohesive force between the reinforcement and matrix material attributed to the formation of undulations and also imparted higher tensile strength to the fabricated composites. Surface cracks were observed across the fractured surfaces (Figure 5.(c)). The percentage of these cracks reduced with increase in the weight percentage of reinforcements. Higher percentage of graphite inhibited the propagation of cracks propagated across the soft matrix material.

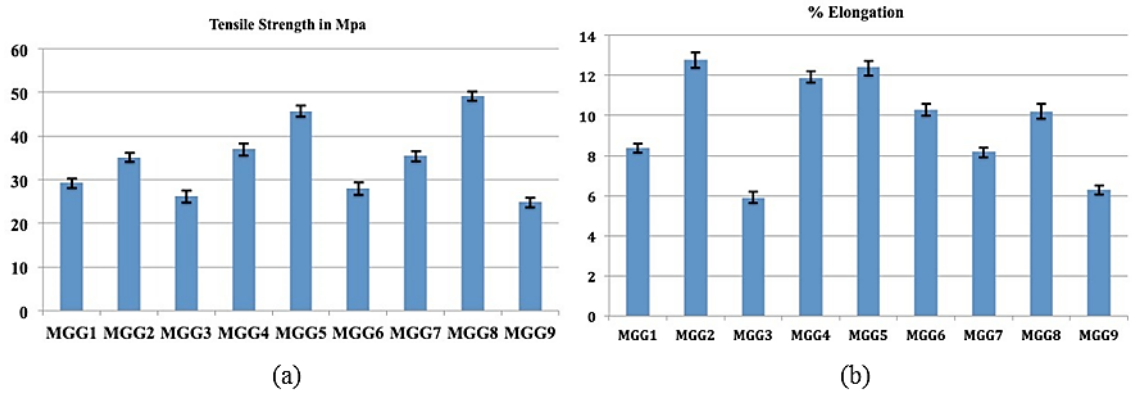

FIGURE 4. Tensile strength (a) and % Elongation values (b) of Mg based metal matrix composites

The importance of uniformly distributed reinforced materials can be observed from the microstructure of the fractured surfaces performed over the hybrid composites. All composite specimens exhibited brittle fracture. It was observed that the higher volume fraction of hardened reinforcement particles imparts higher degree of brittleness into the softer ductile-matrix material. The reinforcement particles void the crack nucleation. The size of the reinforcement particles and their distribution inside the matrix material significantly control the brittleness of the prepared composites.

Micro-voids where present over the fractographs of the composites containing 0.3 wt % of garnet particles, whereas, composite containing more than 0.6 wt% garnet were characterized by comparatively larger voids. Higher weight percentage of reinforcement result in the formation of clusters. However, the composites reinforced with higher weight percentage of reinforcement were observed to contain very less clusters. It was also observed that the dendrites were packed closely and were having lower primary arm spacing. This resulted in the formation of large size voids across the fractured surfaces of the composites containing larger weight percentage of reinforcement.

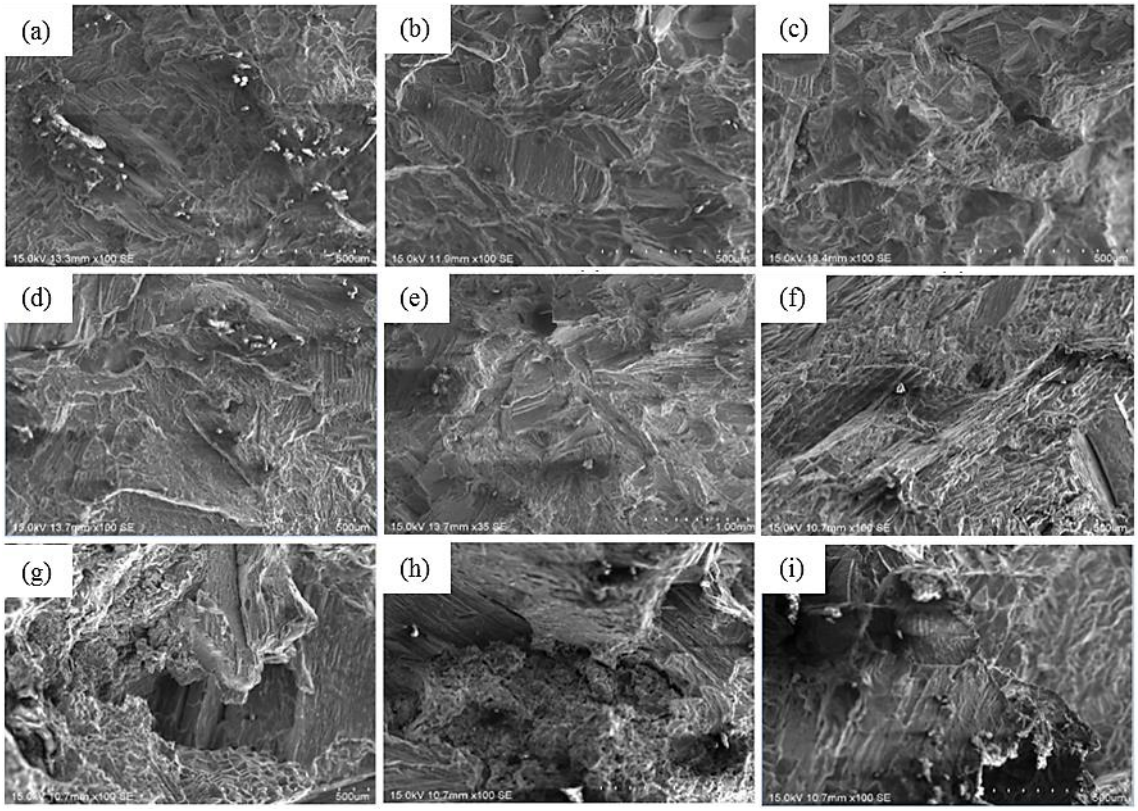

FIGURE 5. Fractographs of Mg based metal matrix composites (a) MGG1, (b) MGG2, (c) MGG3, (d) MGG4, (e) MGG5, (f) MGG6, (g) MGG7, (h) MGG8 and (i) MGG9

CONCLUSIONS

- Selection of optimal casting parameters resulted in the uniform distribution of reinforcement particles which in turn improved the bonding at the matrix-reinforcement interface.
- The dissolved Zirconium precipitated across the Mg and it was observed as α-Zr island-like structure in the SEM image.
- When the graphite percentage was limited to 0.3 wt%, minimal or no agglomeration was observed in the MGG1 sample, but, as the concentration of graphite was increased up to 0.6 and 0.9 wt%, agglomeration was clearly evident.
- The composite reinforced with 0.9 wt% of garnet and graphite exhibited the highest hardness of 70.2 $HV_{0.1}$ compared to the 41 $HV_{0.1}$ hardness exhibited by composite reinforced with 0.3 wt% of fillers.
- It was observed that the tensile properties increased with increase in particulate addition up to 0.6 wt%, beyond which the property declined with further addition.
- The tested surfaces exhibited undulations and they were more for the composites having higher weight percentage of garnet particulates.
- Higher cohesive force between the reinforcement and matrix material attributed to the formation of undulations has imparted higher tensile strength to the fabricated composites.
- The percentage of the cracks reduced with increase in the weight percentage of reinforcements. Higher percentage of graphite inhibited the propagation of cracks across the soft matrix material.

REFERENCES

1. 1. H.Z. Ye and X.Y. Liu, J. Mater. Sci. **39**, 6153–6171 (2004).

2. Z. Yang, J. P. Lib, J. X. Zhang, G. W. Lorimer and J. Robson, Acta Metall. Sin. (Engl. Lett.) **21**, 313–328 (2008).
3. D. J. Lloyd, Int. Mater. Rev. **39**, 1–23 (1994).
4. M. K. Habibi, S. P. Joshi and M. Gupta, Acta Mater. **58**, 6104-6114 (2010).
5. S. Wakeel, V. Manakari, G. Parande, M.S. Kujur and M. Gupta, Mater. Today: Proc. **5**, 28203-28210 (2018).
6. M. Shanthi, M. Gupta, A. E. W. Jarfors and M. J. Tan, Mater. Sci. Eng., A **528**, 6045-6050 (2011).
7. M. E. Alam, S. Han, Q. B. Nguyen, A. M. S. Hamouda and M. Gupta, J. Alloys Compd. **509**, 8522-8529 (2011).
8. S. Shang, K. Deng, K. Nie, J. Li, S. Zhou, F. Xu and J. Fan, Mater. Sci. Eng., A **610**, 243-249 (2014).
9. K. B. Nie, X. J. Wang, K. Wu, X. S. Hu, M. Y. Zheng and L. Xu, Mater. Sci. Eng., A **528**, 8709-8714 (2011).
10. S. F. Hassan and M. Gupta, Mater. Sci. Eng., A **392**, 163-171 (2005).
11. K. K. Deng, K. Wu, X. J. Wang, Y. W. Wu, X. S. Hu, M. Y. Zheng, W. M. Gan and H. G. Brokmeier, Mater. Sci. Eng., A **527** 1630-1635 (2010).
12. S. S. Zhou, K. K. Deng, J. C. Li, S. J. Shang, W. Liang and J. F. Fan, Mater. Des. **63**, 672-677 (2014).
13. K. K. Deng, K. Wu, Y. W. Wu, K. B. Nie and M. Y. Zheng, J. Alloys Compd. **504**, 542-547 (2010).
14. Zhang Xiuqing, Wang Haowei, Liao Lihua, Teng Xinying and Ma Naiheng, Mater. Lett. **59**, 2105-2109 (2005).
15. Sachin Vijay Muley, Satya Prakash Singh, Piyush Sinha, P. P. Bhingole and G. P. Chaudhari, Mater. Des. **53**, 475-481 (2014).
16. Yunting Guo, Guangyu Li, Yingchao Xu, Zezhou Xu, Mingqi Gang, Guixun Sun, Zhihui Zhang, Xiaohong Yang, Zhenglei Yu, Jianshe Lian and Luquan Ren, J. Mech. Behav. Biomed. Mater. **123**, 104759 (2021).

RESEARCH ARTICLE | MAY 22 2023

Evaluation of geometrical nonlinear behaviour of FRP composite plate using finite element method

Moyya Sundeep ✉; Jyothula Sunil Kumar; A. Udaya Deepika; Ravindra Ambatipud

AIP Conference Proceedings 2492, 040046 (2023)
https://doi.org/10.1063/5.0114419

Evaluation of Geometrical Nonlinear Behaviour of FRP Composite Plate using Finite Element Method

Moyya Sundeep[1, a)], Jyothula Sunil Kumar[1,b)], A. Udaya Deepika[2], Ravindra Ambatipud[1]

[1]*Department of Mechanical Engineering, MLR Institute of Technology, Hyderabad, Telangana, India-500043.*
[2]*Department of Aeronautical Engineering, MLR Institute of Technology, Hyderabad, Telangana, India-500043.*

[a)] Corresponding Author: moyya.sundeep@gmail.com
[b)] jyothula92@gmail.com

Abstract. In this paper prediction of nonlinear behavior of a square plate made of composite material under uniform transverse pressure using 3-D finite element analysis is analyzed. Transverse deflection, principal stresses and shear stresses are evaluated for different values of load and by varying the number of layers. The effect of loading and stresses in both the analyses for all the values of composite laminated plate with different stacking sequence are determined. In this the effect of layer thickness for different layup responses of laminate under the clamped boundary conditions is also studied. Using analysis software ANSYS linear static and geometric nonlinear static analysis is to be carried out.

INTRODUCTION

The requirements of the great ascent building and airplane business prompted the turn of events and use of composite materials. Advances in the assembling interaction and innovation of overlaid composites have changed the utilization of the composites from optional underlying segments to the essential ones. For all intents and purposes, covered composites are ordinarily utilized as a piece of building like sandwich punitive, aeronautical and aviation businesses as the principal part of the design as opposed to aluminium or other metallic materials. Low weight, high strength and more noteworthy unbending nature were of principal interest. An assortment of primary components like chambers, shafts, plates and shells could be utilized for the investigation of overlaid composites. The covered plate's high solidity-to-weight ratio, combined with the adaptability of the overlay plot selection, which can be custom-made to coordinate with the plan requirement, makes it an appealing primary segment for some businesses. Plates can be quite thick depending on their application. To utilize the covered composite plates effectively, it is important to foster proper investigation hypotheses to anticipate precisely their primary and dynamical conduct. The expanded use of composite materials in a few designing applications has prompted escalated research exercises in direct and non-straight, static and dynamic investigation of covered composite plates. Most of the examinations on overlaid plates use either the traditional overlay hypothesis (CLT), or the principal request shear misshaping hypothesis (FSDT). FRP composites are not the same as customary constructional materials like steel or aluminium. FRP composites are orthotropic, whereas steel or aluminium are isotropic. FRP composite properties are directional, implying that the best mechanical properties are in the heading of fibre arrangement. Sheik et al. [1] fostered a high accuracy shear deformable component for the examination of covered composite plates of various shapes. M. Ganapathi, B.P. Patel [2] utilized a C0 eight-nodded plate component created dependent on a precise higher-request hypothesis. The nonlinear elements examination of thick composite and sandwich plates are researched. The definition depends on a hypothesis that records the reasonable variety of in-plane and cross over relocations through the thickness. It additionally incorporates the inactivity terms relating to the higher-request terms engaged with the removal capacities. The plates were displayed using ANSYS 12.0, and the results were compared to the Limited Component Technique code. The base diversion was found at a point of 15 degrees for braced plate, and in the event of an essentially upheld plate the base avoidance was found at point 45 degrees. It is likewise seen that the diversion for clipped limit condition is not exactly just upheld limit condition for both isotropic and orthotropic plates. In isotropic plates, the avoidance of clipped plate is about half of essentially upheld. Furthermore, the diversion for clipped orthotropic plates is around (25 to 30) % of just upheld. Liércio André Isoldi [5] considered the mathematically nonlinear static and dynamic conduct of overlay composite

Advancements in Aeromechanical Materials for Manufacturing: ICAAMM-2021
AIP Conf. Proc. 2492, 040046-1–040046-6; https://doi.org/10.1063/5.0114419
Published by AIP Publishing. 978-0-7354-4438-6/$30.00

shells are investigated utilizing the Limited Component Strategy (FEM). Three-sided components with three hubs and six levels of opportunity for each hub (three relocation and three turn parts) are utilized. For static examination, the nonlinear balance conditions are settled utilizing the Summed-up Uprooting Control Technique (GDCM) while the unique arrangement is performed utilizing the traditional new imprint Strategy with a Refreshed Lagrangian Detailing (ULF). The arrangement of conditions is settled utilizing the Inclination Form Technique (GCM) and in nonlinear cases with limited revolutions and removals, an iterative gradual plan is utilized. Namik Kemal oztorun [6] approved limited component plan for the static and dynamic examination of direct versatile space structures made out of plate and bar type individuals is introduced in this investigation. As a rule, limited components can be utilized proficiently for the investigation of straight versatile constructions with shear dividers worked by utilization of passage structures. S.Oller, X. Martinez, F. Rrastellini [7] utilized computational system to introduce displaying of non-straight mechanical conduct of composite constructions made of FRP (Fiber-built up polymers) overlays. Sathya moorthy [8] has introduced a thorough investigation of the enormous sufficiency vibration of plates.

In the current paper, the mathematical nonlinear impacts of a square plate are assessed utilizing ANSYS programming. The portrayal of the issue, the subtleties of limited component demonstrating, material properties stacking and limit conditions are clarified in the accompanying segments.

PROBLEM MODELLING

Geometry

"A square plate of dimensions' length L=100, breath B=100, thickness H=10 units considered for the present analysis. The thickness H varies according to the no. of layers, and the transverse pressure 100Mpa is applied in five steps".

Finite Element Modelling

"The finite element mesh is generated using SOLID191 is a layered version of the 20-node structural solid designed to model layered thick shells or solids. The element is defined by 20 nodes having three degrees of freedom per node: translations in the nodal x, y, and z directions. SOLID191 has stress stiffening capabilities".

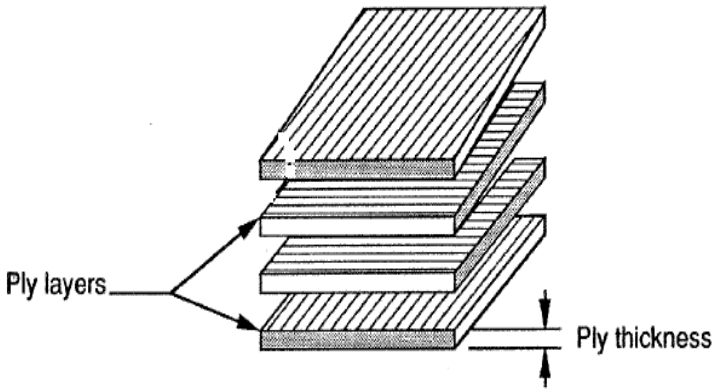

FIGURE 1. Boundary Conditions and Loading

"The clamped boundary conditions are applied along the square plate edges of FE model. A transvers pressure of 100MPa is applied on the top surface of the square plate. The analysis is performed by applying the total load in 5 equal number of steps".

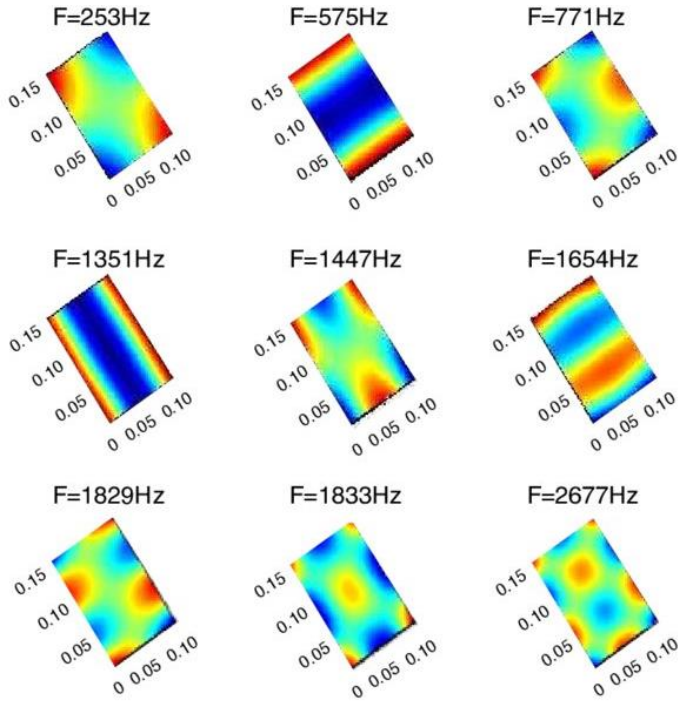

FIGURE 2. Material Properties

The following material properties are considered for the present analysis.

- Young'smodulus,-E1=175GPa, E2=E3=7GPa.
- Poisson's Ratio, ν12= ν13=0.27, ν23= 0.01.
- Rigidity-Modulus-G12=G13=3.5Gpa, G23=1.4Gpa.

RESULTS AND DISCUSSION

"Variety of the transvers avoidance estimated at the focal point of the plate (w) with various stacking succession of [0/ - 15/15/0] s, [0/ - 45/45/0] s and cross utilize of [0/90/90/0] s ('s' methods sign of evenness of number of layers in the composite construction). From the Figure.3, it very well may be seen that the variety of focus redirection (w) for both the straight and nonlinear examination are showing clear deviation regarding the distinctive stacking succession".

"It is seen that for point utilize of [0/ - 15/15/0] s, both the examination i.e direct and nonlinear reaction gives greatest deviation in uprooting of the composite design. The diversions are most extreme in the straight investigation contrasted with the nonlinear examination. A similar sort of investigation is performed for cross employ covered plate (0/90/90/0). The level of variety in removal between the point utilize [0/ - 15/15/0] s and the cross ply [0/90/90/0] limit of 8.47%. No progressions in the uprooting of the plate is seen at [0/15/15/0] and [0/45/45/0] utilize direction. Variety of stresses regarding applied burden ventures for point utilize's [0/15/15/0], [0/45/45/0] cross employ [0/90/90/0] are introduced in Figs. 6 to 8. It is seen that for point handle's [0/ - 15/15/0] s, and [0/ - 45/45/0] s, cross ply [0/90/90/0] pressure acquired from the nonlinear examination is lower than that of direct reaction. The most extreme reaction of stress (σx) is noticed for the fiber game plan of [0/ - 15/15/0], trailed by, [0/ - 45/45/0] and [0/90/90/0] lay-up. No particular deviation is acquired in nonlinear reaction for all considered utilize directions. An alternate conduct is seen in pressure in y heading for example (σy). [Fig.4] The most extreme pressure greatness is noticed for the lay-up of cross employ [0/90/90/0]. The conduct of composite plate showed comparative reaction for all viewed as lay-up as far as (σy). The variety of ordinary pressure (σz) appeared in Fig. 6. σz is acquired pinnacle reaction for cross handle cover. So for uniform calculation and uniform stacking and limit conditions same material composite plate reaction is diverse with various lay-up. Likewise, the variety of shear pressure as for employ direction and the variety of shearing stresses as for load steps is introduced in Figs.6-9. The reaction of τxy is same as that of σx. The shear pressure τyz is displaying same reaction for all lay ups. In any case, clear deviation among direct and nonlinear examination is noticed. The reaction of τxz is same as that of σz."

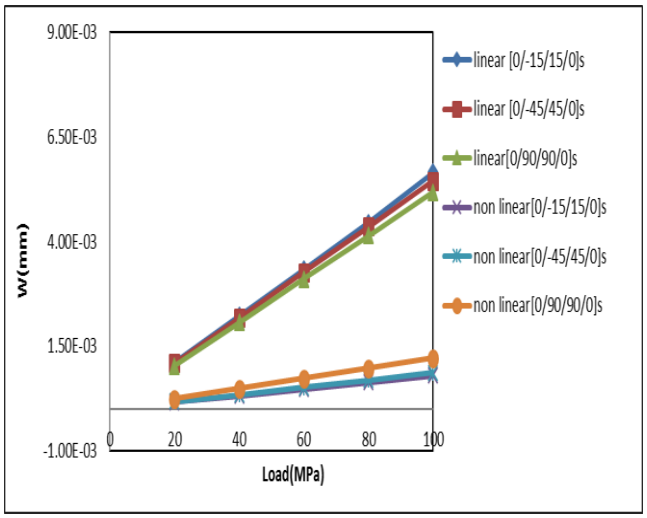

FIGURE 3. variation of 'w' with respect to load steps for fiber angles.

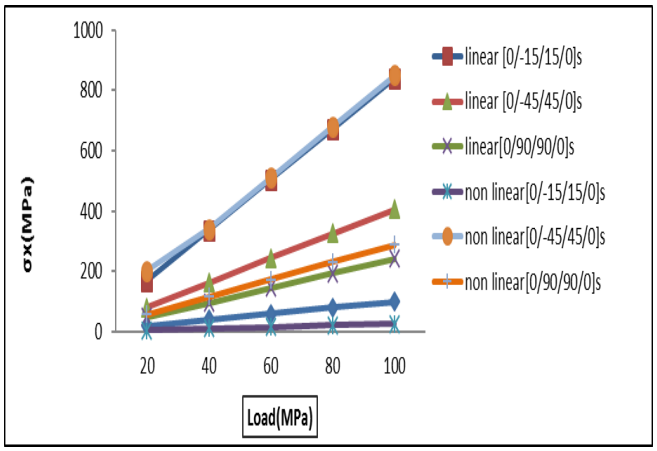

FIGURE 4. Variation of 'σ_x' with respect to load steps for fiber angles

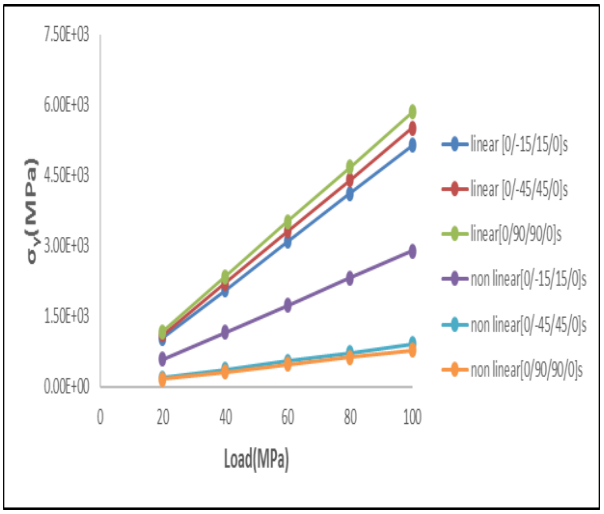

FIGURE 5. variation of 'σ_y' with respect to load steps for fiber angles.

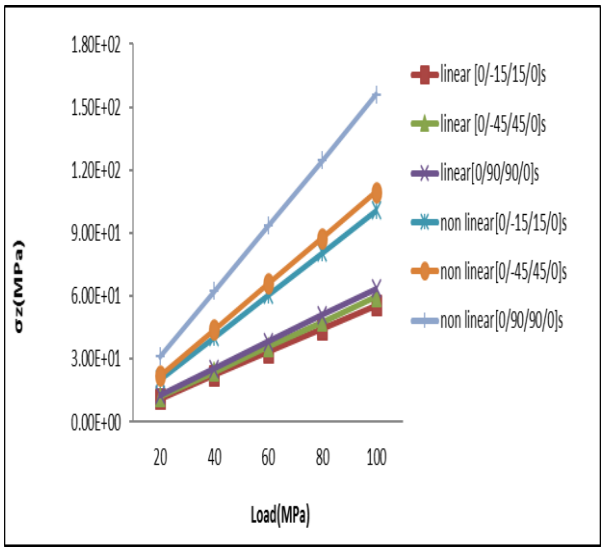

FIGURE 6. variation of 'σ_z' with respect to load steps for fiber angles.

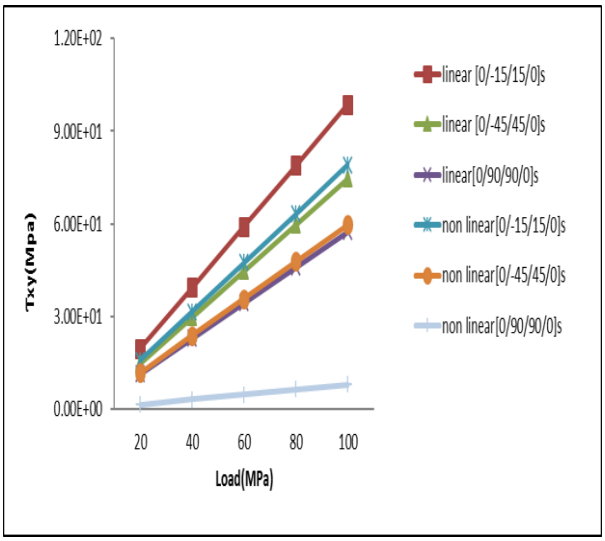

FIGURE 7. variation of 'τ_{xy}' with respect to load steps for fiber angles.

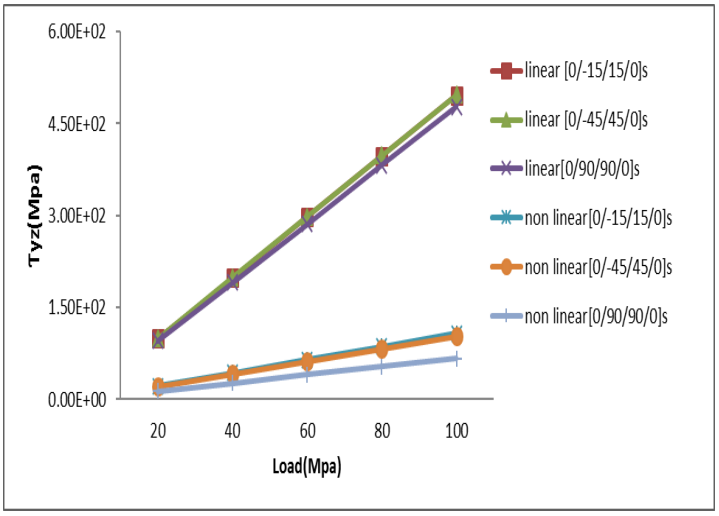

FIGURE 8. variation of 'τ_{yz}' with respect to load steps for fiber angles.

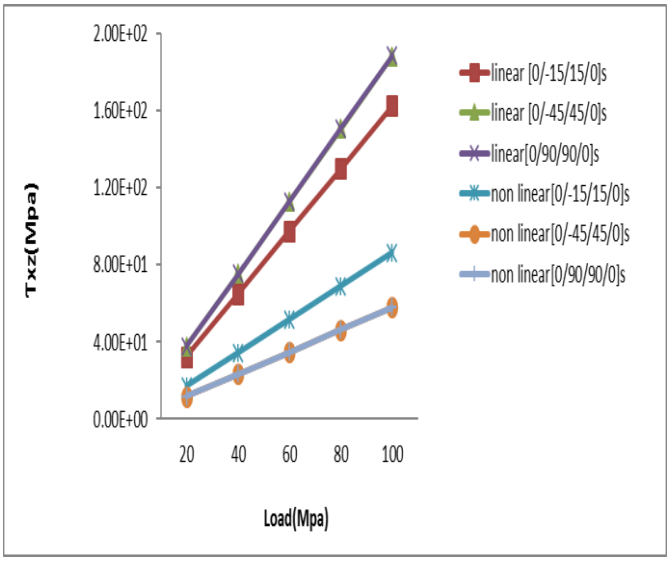

FIGURE 9. variation of 'τ_{xz}' with respect to load steps for fiber angles.

CONCLUSIONS

Significance of mathematical nonlinear investigation of a point utilize and cross handle FRP square plate exposed to uniform cross over pressure stacking has been examined in this paper. The plate is utilized examined utilizing direct and mathematical nonlinear investigation choices accessible in limited component programming ANSYS. Structure the current examination it is tracked down that the nonlinear investigation is must for the considered plate for all fiber directions considered for the examination.

REFERENCES

1. H Sheikh, S. Haldar and D. Sengupta, (2002). Composite Structures 55 pp.329–336.
2. M. Ganapathi, B.P. Patel*, D.P. Makhecha (2002). www.elsevier Composites, Part B 35 (2004) 345–355.
3. C.Sasi Rekha1,P.RaviKumar,K.VenkataRao (2013), IOSR Journal of Mechanical and Civil Engineering, Volume 9, Issue 6 (Nov. - Dec. 2013), e-ISSN: 2278-1684,p-ISSN: 2320-334X
4. Junaid Kameran Ahmed, V.C. Agarwal, P.Pal, Vikas Srivastav, (2013). International Journal of Innovative Technology and Exploring Engineering, Volume-3, Issue-6, (November 2013), (IJITEE) ISSN: 2278-3075.
5. Isoldi, Liércio André, Armando Miguel Awruch, Paulo Roberto de F. Teixeira, and Inácio B. Morsch. *Journal of the Brazilian Society of Mechanical Sciences and Engineering* 30, no. 1 (2008): 84-93.
6. Namik Kemal oztorun, Elsevier Science publishers volume 42, Issue 12 (August 2006),pages:1031-1052, year of publication :2006,ISSN:0168-874X.
7. S.Oller, X. Martinez, F. Rrastellini, journal of advanced composite Material Simulation Ciencia e-techno –logia dos materials, vol.20, 2008
8. ANSYS Reference Manuals.2007.
9. chandraputla T. and Belgundu.A.2002, "Theory of plates and shells", Mc Graw Hill, London.
10. Mahesh Kumar, T., Ravi Kumar, P., Anitha, D., Praveen, B., International Journal of Mechanical and Production Engineering, 10.24247/ijmperdapr20186.
11. Lokesh, S., Vivek, G.S., Praveen, L., International Journal of Mechanical and Production Engineering Research and Development. 10.24247/ijmperdoct20177.
12. Lokesh, S., Lakshmi Tulasi, C.H., Monica, T., Pranavi, U., International Journal of Mechanical Engineering and Technology.

RESEARCH ARTICLE | MAY 22 2023

Mechanical properties of sugarcane fibre and coconut fibre

N. Madhavi ✉; M. Harika; Sri Katyayani; Ch. Deepthi Sree; Sudhir Kumar Yadav

AIP Conference Proceedings 2492, 040010 (2023)
https://doi.org/10.1063/5.0116525

Mechanical Properties of Sugarcane Fibre and Coconut Fibre

N. Madhavi[1,a)], M Harika [1,b)], Sri Katyayani[1,c)], Ch Deepthi Sree [1,d)], Sudhir Kumar Yadav[1,e)]

[1]*Department of Aeronautical Engineering, MLR Institute of Technology, Hyderabad, India.*

[a)] Corresponding Author: madhunagireddy@mlrinstitutions.ac.in
[b)]harikamyneni15@gmail.com
[c)] katyayanisattiraju@gmail.com
[d)] sweetdeepthi7@gmail.com
[e)] sudhiryadava8@gmail.com

Abstract. The blend of two or more materials together is known as composite material. This paper presents the mechanical properties of sugarcane fibre and coconut fibre laminates, prepared using compression moulding. The main aim is to determine the properties of fibres such as tensile strength, impact resistance and flexural bending (3-point bend) properties. The usage of composite materials has seen a significant boost in the past decade in industries including aerospace, aeronautical, automobile, electronics and many more. The outcome of this work was obtained using Universal Testing Machine (UTM) and Pendulum Impact Tester (Charpy Test).

Keywords: Composite materials, Sugarcane and Coconut, Flexural bending, Compression Moulding.

INTRODUCTION

The first known usage of composite material dates back to 3400 B.C in Egypt in which the Egyptians used wood strips were glued together to form a plywood. While the first significant usage of composites in commercial aircrafts was in 1983 by Airbus in A300 and A310 fleets. Composite materials have shown significantly more strength per unit weight than compared to metals. Composites are 70% lighter than steel. Corrosion resistance in these composite materials is higher than steel, composites tends to show non-conductive nature and are considered as super insulators. Tensile strength is defined as the maximum load that a material can support without fracture when being stretched divided by the original cross-sectional area of the material. Impact strength is defined as the amount of energy that a material can withstand when the load is suddenly applied to it. Flexural bending is constant bending moment acts along the entire length of the beam.

Composites

Composites are materials that are made up of two or more components that are chemically different at the macroscopic scale, have distinct interfaces, and have properties that cannot be achieved by any of the components, individual activities. Polymer based composites were introduced during 1960's to overcome the mechanical issues faced by composite materials. Starting now and into the foreseeable future, composite materials have become fundamental planning materials and are arranged and created for various applications including auto sections, flight parts. The advancement in composite use moreover worked out as expected because of extended care concerning thing execution and extended challenge in the overall market for lightweight segments. Among all materials, composite materials replace commonly used steel and aluminium, generally with better performance. Replacing steel pieces with composite chips saves up to 60-80% of the weight of cross section, by exchanging aluminium parts 20% of the weight can be reduced.

Advancements in Aeromechanical Materials for Manufacturing: ICAAMM-2021
AIP Conf. Proc. 2492, 040010-1–040010-9; https://doi.org/10.1063/5.0116525
Published by AIP Publishing. 978-0-7354-4438-6/$30.00

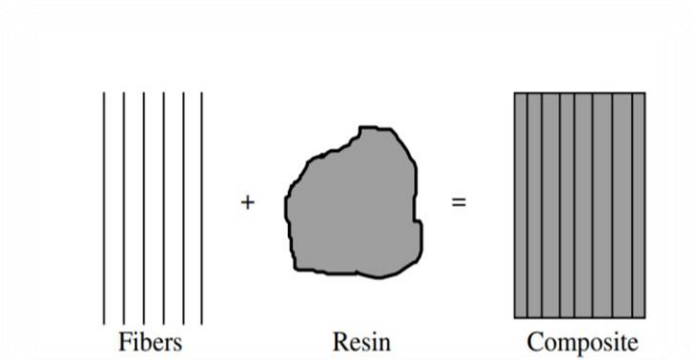

FIGURE 1. Composite composition

Types of Composites

Composite materials can be categorized according based on the matrix type, reinforcement type, length of fibre, number of layers, alignment of the fibre. Basically there are two types of composites. They are:

- Matrix based composite.
- Reinforcement based composite.

Below is the classification of the composites based on matrix type and reinforcement type.

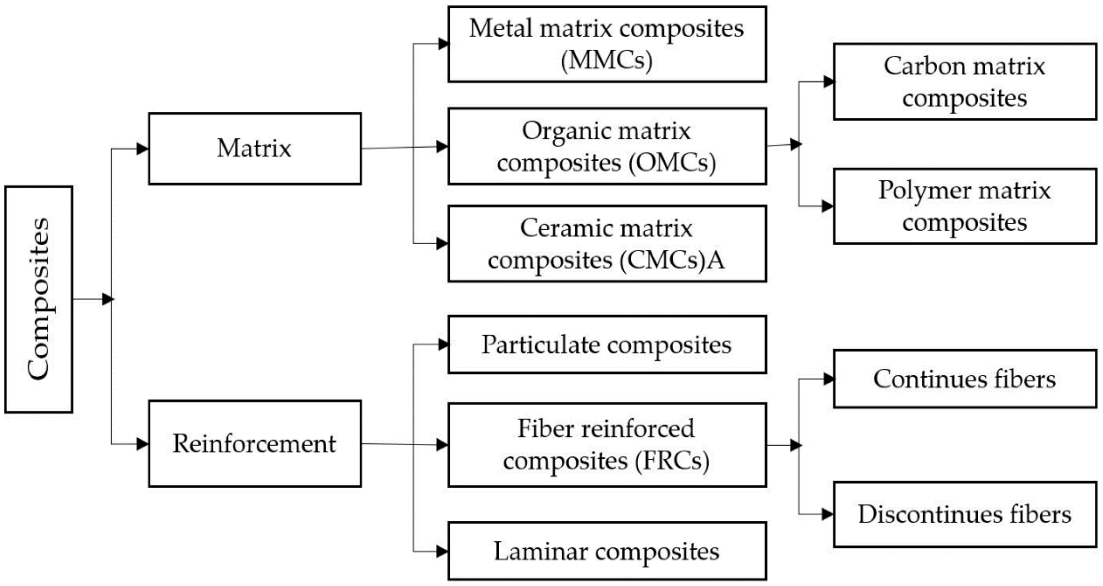

FIGURE 2. Classification of composites

Natural fibres:

Natural fibres are supported natural resources and are obtained directly from the animals, plants and minerals. These are usually short fibres and are called "staple fibres", except silk whose filaments are up to at least one kilometre long. Natural fibres are further classified into plant fibres, animal fibres.

Plant fibres are fibres which may be obtained from seeds, leaves, fruits, stalks and bast. Few samples of such fibres are banana, pineapple, coconut (coir), wheat, bamboo, straw, jute, hemp, vine, etc.Animal fibres are mostly obtained from animal hair and silk hair. These comprises of proteins such as collagen, keratin and fibroin, e.g.: silk, wool, alpaca, etc. Fibres or wool taken from animals such as sheep wool, goat hair, alpaca hair, horse hair comes under animal hair. Natural fibres used in composite materials such as in synthetic or glass fibre called as bio composites.

COMPRESSION MOULDING

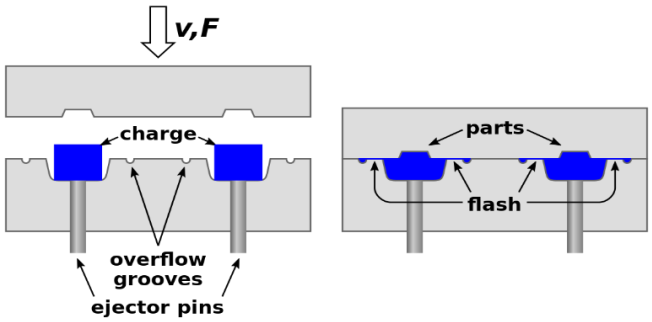

FIGURE 3. Compression Moulding

FIGURE 4. Sugarcane and Coconut Laminates – Compression Moulding

Compression moulding is generally used for high strength fibre reinforcements. This moulding uses a high volume and high pressure to force the material into the mould so that the material is in contact with all the areas of the mould. Heat and pressure are maintained till the material has cured and this process is known as 'Vulcanization'. Fibres can be in the form of woven, chopped strands, mats or knitted.

TESTING EQUIPMENT

Universal Testing Machine – UTM

Universal testing machines (UTMs), also called universal testers, perform tests used to measure the compressive, tensile and flexural strength of materials. These tests can include, standard tensile test and compressive tests, seal strength tests, bond strength tests, bend tests, puncture tests, and spring tests. The tests are done particular material type is specified by the ASTM International standards agency.

FIGURE 5: UTM

Pendulum Tester

A test specimen having a V-shaped notch is placed on the holder in such position that the notch is in the centre of the holder, and the specimen is struck at the back of the notched section with the weighted hammer. The Charpy impact value (kJ/m2) is calculated by dividing the fracture energy to the cross-section area of the specimen.

FIGURE 6. Pendulum Tester

TESTING

Tensile Strength:

The tensile strength of the fibre was determined using universal testing machine – UTM according to ASTM standards.

Length of the specimens, l = 250mm

Width of the specimens, w = 25mm

Thickness of the specimens, t = 3.1mm

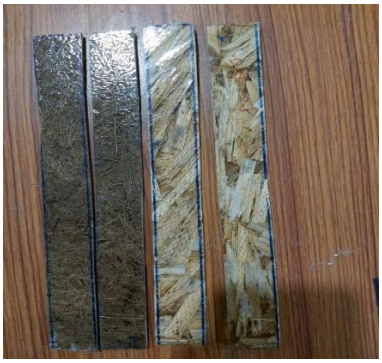

FIGURE 7. Sample specimen

(a)Sugarcane

(b)Coconut

FIGURE 8. Specimens after testing

Flexural Strength – 3 Point Bending:

The flexural strength of the fibre was determined using universal testing machine – UTM according to ASTM standards.

Length of the specimens, l = 115mm
Span length of specimens, ls = 99.2mm
Width of the specimens, w = 13mm
Thickness of the specimens, t = 3.1mm

FIGURE 9. Test specimen

(a)Sugarcane (b)Coconut

FIGURE 10. During Testing

Impact Strength Testing:

The impact strength of the fibre was determined using pendulum testing machine according to ASTM standards.

Length of the specimens, l = 60mm
Notch length of the specimens, ln = 2mm
Width of the sugarcane, w = 12mm
Width of the coconut, w = 13mm
Thickness of the specimens, t = 3.5mm

TABLE 1. Loads for different materials

Sl. No	Material	Length (mm)	Width (mm)	Load (kj)	Impact strength (j/m^2)
1	Sugarcane	60	12	4	95.23
2	Sugarcane	60	12	4	95.23
3	Coconut	60	13	8	175.82
4	Coconut	60	13	8	175.82

FIGURE 11. Test Specimen

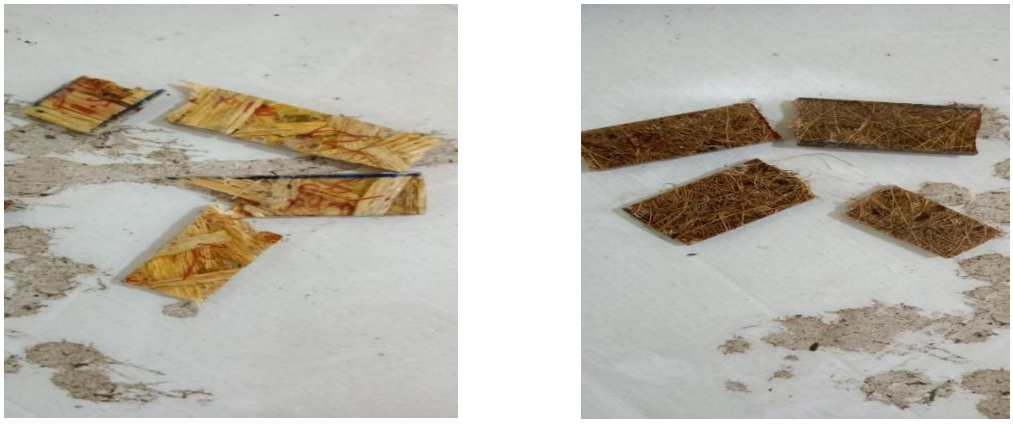

(a) Sugarcane (b) Coconut

FIGURE 12. After Testing

RESULT

Tensile

Sugarcane

The tensile strength of the fibre was determined using universal testing machine – UTM and deformation with respective the load applied is shown in the graphs.

From the below graphs we can observe that the first sample of sugarcane could withstand maximum force of 642.500N while undergoing the displacement of 4.330mm and the displacement at the maximum value of force was noted to be 3.620mm before failure. Second sample could withstand a maximum force of 434.500N while undergoing the displacement of 2.810mm and the displacement at the maximum value of force was noted to be 2.410mm before failure.

The average maximum force the material could withstand was 538.5N while undergoing the displacement of 3.57mm and the displacement at the maximum value of force was 3.015mm.

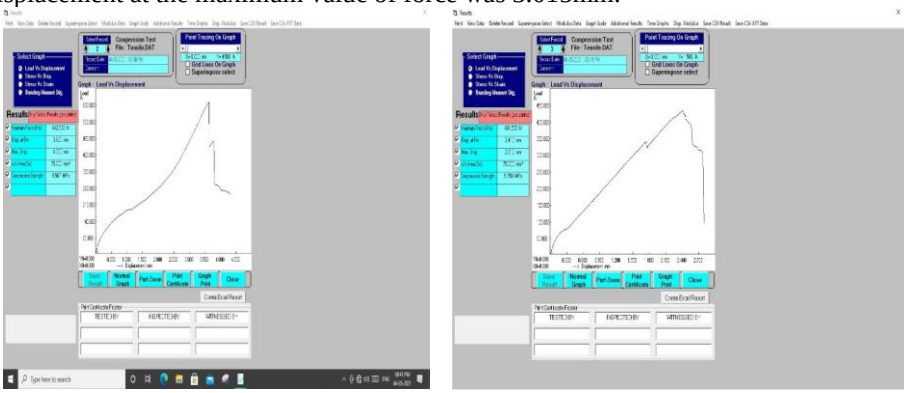

(a) Sugarcane (b) Coconut

FIGURE 13. Tensile Strength – Sugarcane

Coconut:

The tensile strength of the fibre was determined using universal testing machine – UTM and deformation with respective the load applied is shown in the graphs.

From the below graphs we can observe that the first sample of coconut could withstand maximum force of 1069.000N while undergoing the displacement of 3.260mm and the displacement at the maximum value of force was noted to be 3.230mm before failure. Second sample could withstand a maximum force of 1327.000N while undergoing the displacement of 3.430mm and the displacement at the maximum value of force was noted to be 3.420mm before failure.

The average maximum force the material could withstand was 1198.000N while undergoing the displacement of 3.345mm and the displacement at the maximum value of force was 3.325mm.

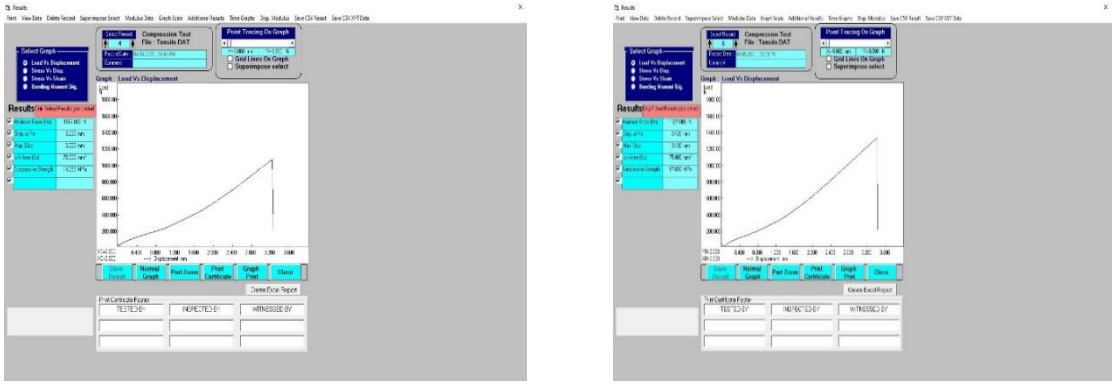

(a) Sugarcane (b) Coconut

FIGURE 14. Tensile Strength – Coconut

Flexural Strength – 3 Point Bend

Sugarcane

The flexural strength of the fibre was determined using universal testing machine – UTM and deformation with respective the load applied is shown in the graphs.

From the below graphs we can observe that the first sample of sugarcane could withstand maximum force of 8.000N while undergoing the displacement of 9.870mm and the displacement at the maximum value of force was noted to be 6.650mm before failure. Second sample could withstand a maximum force of 15.500N while undergoing the displacement of 9.480mm and the displacement at the maximum value of force was noted to be 7.230mm before failure. Third sample could withstand a maximum force of 11.500N while undergoing the displacement of 9.160mm and the displacement at the maximum value of force was noted to be 6.710mm before failure.

The average maximum force the material could withstand was 11.666N while undergoing the displacement of 9.573mm and the displacement at the maximum value of force was 6.863mm.

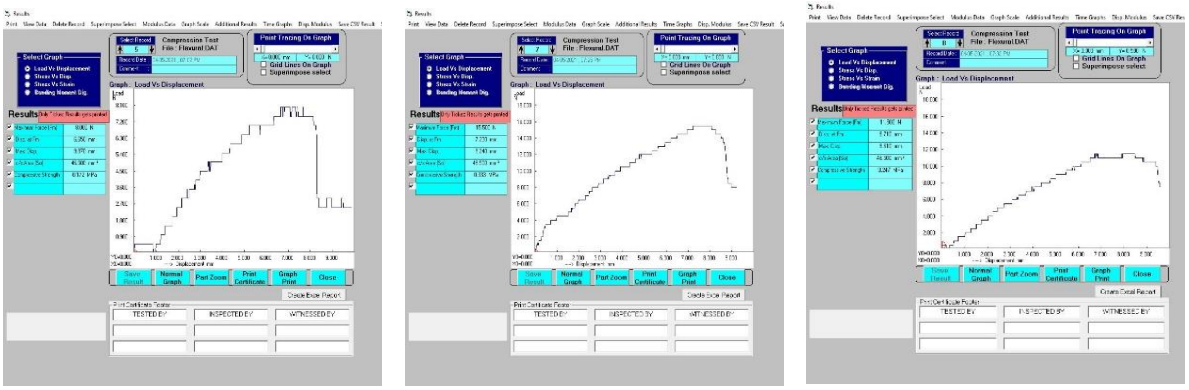

(a)Sample 1 (b) Sample 2 (c) Sample 3

FIGURE 15. Flexural Strength – Sugarcane

Coconut:

The flexural strength of the fibre was determined using universal testing machine – UTM and deformation with respective the load applied is shown in the graphs.

From the below graphs we can observe that the first sample of coconut could withstand maximum force of 44.500N while undergoing the displacement of 14.350mm and the displacement at the maximum value of force was noted to be 11.840mm before failure. Second sample could withstand a maximum force of 32.500N while undergoing the displacement of 12.270mm and the displacement at the maximum value of force was noted to be 11.210mm before failure. Third sample could withstand a maximum force of 38.500N while undergoing the displacement of 16.150mm and the displacement at the maximum value of force was noted to be 10.730mm before failure.

The average maximum force the material could withstand was 38.500N while undergoing the displacement of 14.256mm and the displacement at the maximum value of force was 11.260mm.

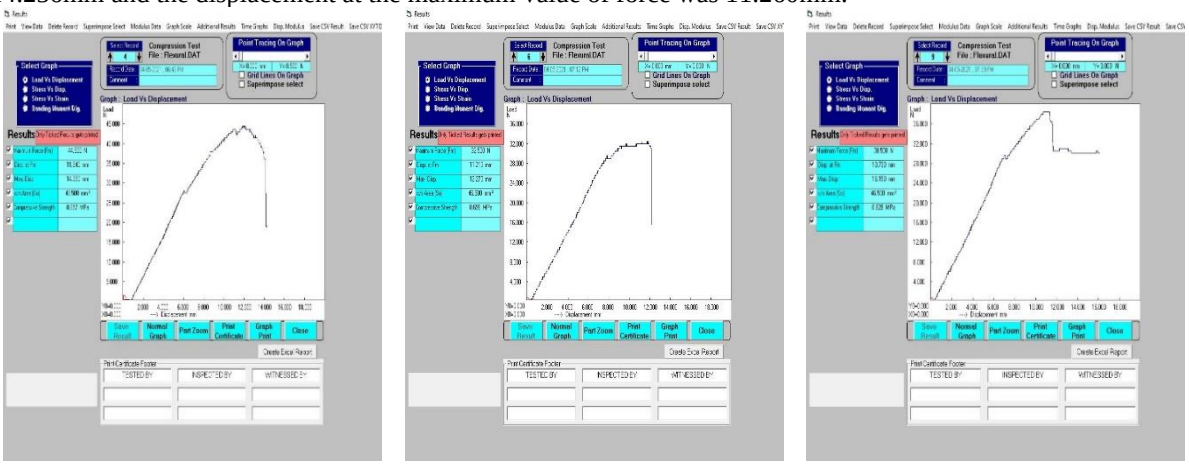

(a)Sample 1 (b) Sample 2 (c) Sample 3

FIGURE 16. Flexural Strength – Coconut

Impact Strength

Sugarcane:

The impact strength of the fibre was determined using pendulum testing machine according to ASTM standards.

The length of the sugarcane composite is 60mm and the vertical distance from the notch is 12mm and the notch width is 2mm. The load was observed to be 4J for both samples. The impact strength of the both samples was found out to be 95.23KJ/m^2.

Coconut:

The impact strength of the fibre was determined using pendulum testing machine according to ASTM standards.

The length of the coconut composite is 60mm and the vertical distance from the notch is 13mm and the notch width is 2mm. The load was observed to be 8J for both samples. The impact strength of the both samples was found out to be 175.82KJ/m^2.

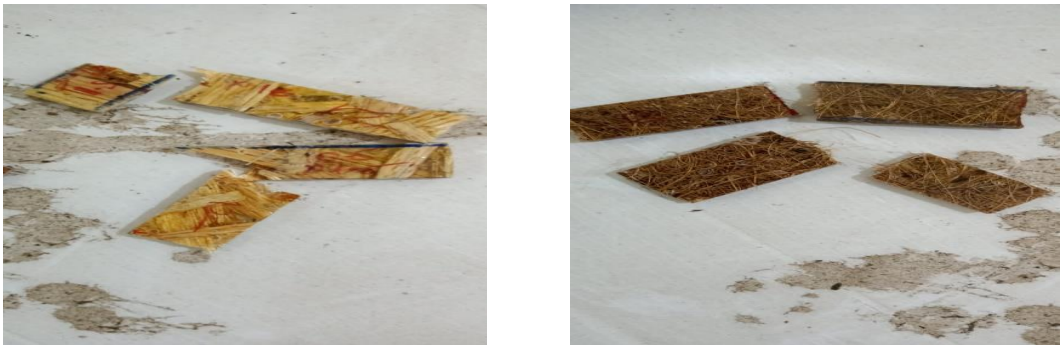

(a) Sugarcane (b) Coconut

FIGURE 17. After Testing

CONCLUSION

After studying the graphs of the both the laminates for tensile and flexural strength along with the impact strength values of the materials is was concluded that the coconut coir showed significantly higher values of strength when compared to sugarcane in the aspects of tension, bending and sudden loads.

The maximum tensile load coconut could withstand was 1198.000N while value of sugarcane was 538.5N.

The displacement for coconut was noted to be 14.256mm which is more than the sugarcane that is 9.573mm.

The impact strength for coconut was found out to be 175.82KJ/m^2 and the sugarcane's strength is 95.23KJ/m^2.

REFERENCE

1. N Madhavi, B Niharika M Satyanarayana Gupta Evaluation of ply orientation on failure of Kevlar Epoxy149 IJCIET, ISSN Print: 0976-6308 and ISSN Online: 0976-6316,Volume 8, May2017.
2. Madhavi, K Sreelakshmi and M. Satyanarayana Gupta, Evaluation of Ply Orientation on Failure of Composites, IJCIET, ISSN Print: 0976-6308 and ISSN Online: 0976-6316, Volume 8, May2017.
3. K. Sreelakshmi, N Madhavi, M Satyanarayana Gupta, Analysis of Interlaminar Stresses in a Composite Material with A Circular Hole by Using Finite Element Method, IJCIET, ISSN Print: 0976-6308 and ISSN Online: 0976-6316, Volume 8, May2017.
4. K Veeranjaneyulu, M S N Gupta, Dhana jayan and Vamsi V, 2017. Damage analysis of low speed impact on composite materials. International Journal of Civil Engineering & Technology (IJCIET) - Scopus Indexed.Volume:8,Issue:5,Pages:717-727
5. Mr. Veeranjaneyulu Professor Manohar Satti, Design and Analysis of Missiles Page 1570-1577 Volume No,3 Issue No.10 & ISSN: 2348-4845 IJMETMR Oct 2016
6. B. Nagaraj Goud, K. Shiva Shankar, B. Manideep, K. Veeranjaneyulu "Experimental Test on Glare Composite of an Aircraft Structure under Tensile Strength Failure", International Journal of Engineering and Advanced Technology (IJEAT) ISSN: 2249 – 8958, Volume-9 Issue-2, December, 2019.
7. B. Nagaraj Goud, K. Shiva Shankar, B. Manideep, K. Veeranjaneyulu "Experimental Test on Glare Composite of an Aircraft Structure under Tensile Strength Failure", International Journal of Engineering and Advanced Technology (IJEAT) ISSN: 2249 – 8958, Volume-9 Issue-2, December, 2019.
8. P. Anudeep , Babitha Kodavanla, P.Srinivas Rao and Madhavi Nagireddy,Experimental analysis on treated and untreated Grass/Carbon Hybrid Composite Structures, International Journal of Applied Engineering Research and Development (IJAERD), Vol. 8, Issue 1 Jun 2018, pp. 1-6 (ISSN (P): 2250-1584; ISSN (E): 2278-9383), Scopus Indexed).
9. A Vivek Anand, V Hariprasad, S Jayalakshmi, R Arvind Singh, V R Ravivarma and S Gollakota, 2018, "The Sisal/Coir/Glass fiber-based hybrid composite laminate structure", International Journal of Mechanical and Production Engineering Research and Development, Vol. 8, No. 7, pp. 1039-1046
10. Vivek Anand A, Gollakota S, Hariprasad V, Shunmugavelu N, Ahifkhan & Arumugam V, "Wettability Study on Microgroove Patterned Hierarchical SS304 Stainless Steel Surfaces", International Conference on Materials, Manufacturing and Machining (ICMMM - 2019), 8 & 9 March 2019, BIT Sathy, India.
11. Vivek Anand A, Gollakota S, Hariprasad V, Shunmugavelu N, Ahifkhan & Arumugam V, "Role of Micropatterns on Wettability and Corrosion Characteristics of SS304 Steel Surfaces", International Conference on Materials, Manufacturing and Machining (ICMMM - 2019), 8 & 9 March 2019, BIT Sathy, India.
12. Mohanty, A.K. Misra, M. Drzal, "L.T. Surface modifications of natural fibers and performance of the resulting biocomposites",: An overview. Compos. Interfaces 2001, 8, pp. 313–343.
13. Agarval, B. Broutman, L.J. Chandrashekha, K. 2006. "Analysis and performance of fiber composites". John Wiley & Sons, Inc., New Jersey.
14. Girisha, C. Sanjeevamurthy, Gunti Ranga Srinivas, 2012. "Sisal/Coconut Coir Natural Fibers–Epoxy Composites: Water Absorption and Mechanical Properties". International Journal of Engineering and Innovative Technology. Volume 2, Issue 3.
15. Van Voorn, B. Smit, H.H.G. Sniike, R.J. De Klerke, B. 2001. "Natural fiber reinforced sheet molding compound". Composite: Part A, 32, pp. 1271-1279.
16. Peças, P. Carvalho, H. Salman, H. Leite, M. Natural Fibre Composites and Their Applications: A Review. J. Compos. Sci. 2018, 2, 66.

RESEARCH ARTICLE | MAY 22 2023

Modeling and static structural analysis on stiffened panel for an aircraft structure

B. Nagaraj Goud ✉; Sreekanth Sura; Swetha Bala M. N. V. S.; B. Manideep

AIP Conference Proceedings 2492, 040007 (2023)
https://doi.org/10.1063/5.0113300

Modeling and Static Structural Analysis on Stiffened Panel for an Aircraft Structure

B. Nagaraj Goud [1, a)], Sreekanth Sura[1, b)], Swetha Bala MNVS[1, c)], B. Manideep [1, d)]

[1]*Department of Aeronautical Engineering, MLR Institute of Technology, Hyderabad, India.*

[a)] Corresponding Author*: nagaraj2107@gmail.com*
[b)] *sreekanthsuramlrit@gmail.com*
[c)] *swethabalamlr@gmail.com*
[d)]*manideepbalusani.9@gmail.com*

Abstract. The paper is focused on the modeling and analysis of an aircraft stiffener by using ANSYS. The stiffener of an aircraft is mainly used to support the structure of the aircraft. It is normally made using a metal of aluminum, steel and titanium. In this regard, the stiffener is made with aluminum alloy and is compared with steel material. and performed static structural analysis and analyzed material performance. To improve the structural stability of a stiffened panels are to be determined on account of their weight saving. When these stiffeners were permitted to buckle at ≤ to the design yield load. The response of stresses and deformation of the Stiffened Panel are addressed and the response of the structure. When the design is efficient, the constraint can be adjusted to allow local buckling at the design limit load, as long while the structure doesn't really fail at even a load lesser than the design maximum applied load. Improved structural integrity by supported by hat section arrangements to the stiffened panel. Therefore, the simulation analysis results for the stiffener supported by the hat section members were presented.

Key words: Aircraft, Stiffener, Design load, Static Analysis, ANSYS

INTRODUCTION

Stiffeners are secondary plates or sections that are attached to flanges or beam webs to strengthen the members against out-of-plane deformations[1]. Stiffeners will be installed on nearly all key bridge beams. Most, however, will have transverse web stiffeners connected to the web, so instead of vertical stiffeners. Longitudinal web stiffeners are often used in deep beams. Flange stiffeners are typically utilized on long length box girder bridges; however, they are infrequent elsewhere[2]. Weaving process through its thickness of the dry graphite-epoxy composite material can significantly decrease the effort required for panel fabrication and assembly. The pre-stacked skin portions, ribs, stringers, intercostals, and spar caps are stitched together across the thickness of the skin. Stitching provides a way to decrease damage progress caused by low-speed or discontinuous source impact, and mechanical fasteners are almost removed entirely. Conventional composite materials have used no-damage-growth technique and are tailored to withstand design limit loads in discrete-source-damaged components without damage dispersion[3]. As the structures that are partially noticeable after an impact can support the design of maximum load without damage occurs. The assembly constraint requires that allows the less strain than would be required in an original construction, resulting in a heavier structure and the composite material of stiffening panels are becoming more attractive in the aerospace applications[4].

The different types of stiffeners are used to stiffen the composite plate. These are divided into two categories: open form as well as closed form or box type. The open form is torsionally less, whereas the closed or box type is torsionally tough. Unless this design restriction could be altered to allow local buckling at design limit load, as far as

Advancements in Aeromechanical Materials for Manufacturing: ICAAMM-2021
AIP Conf. Proc. 2492, 040007-1–040007-6; https://doi.org/10.1063/5.0113300
Published by AIP Publishing. 978-0-7354-4438-6/$30.00

the component doesn't really fracture at such a load is below design maximum load, lighter, greater weight- and cost-efficient constructions can be produced[5]. The structural panels can be built in such a way that they are considered to handle loads far greater than that of the buckling loading and remain unchanged. The main aim of this research study about to see how considerable weight may be saved by allowing strengthened panels to buckle at loads lower than their bearing capacity as far as the panel doesn't quite fail. When the damage begins and growth on a local level, as well as nonlinear behaviour of post-buckling, If the structure fails due to the load is considered to be the ultimate load, it should be evaluated[6]. The method used in this study was to evaluate the behaviour of single-stiffener materials both analytically and experimentally then predict structural stability improvements for multi-type stiffened panels using analytical methods[7]. Stiffeners are divided into two categories. They are stiffeners that run the length of the web and are aligned in the span direction and other one is transverse stiffeners are placed perpendicular to the span direction of the beam as shown in figure.1

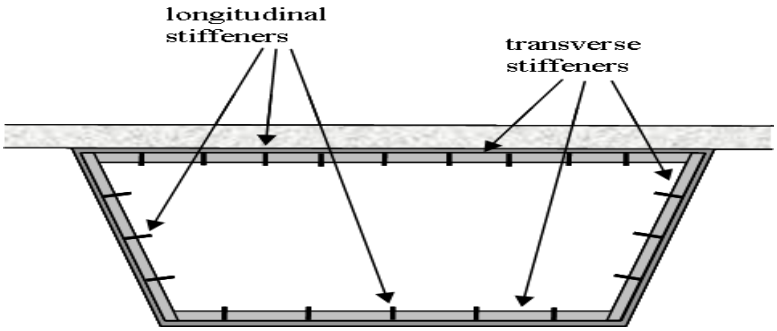

FIGURE.1 stiffener

Stiffeners have been utilized in the past in a number of ways, but the simple flat stiffener is virtually usually employed in the latest designs. The Stiffeners could be applied to one edge of the plate (single sided) or both edges of the plate (double sided) [8]. Joint stiffeners are commonly double-sided, while middle web shear walls are usually single. Stiffeners could be doubled, tripled, quadrupled, or even multi-legged. For the purpose of coupling torsional stiffening in between beams in a practical way, intermediate stiffeners on major beam webs are frequently required. If this is the case, the stiffener positions will be determined by the bracing locations[9]. However, for beams that do not requires including such transverse girders in the ladder deck bridge or if the design bracing is employed, intermediate stiffeners could be required. beam as shown in figure.2

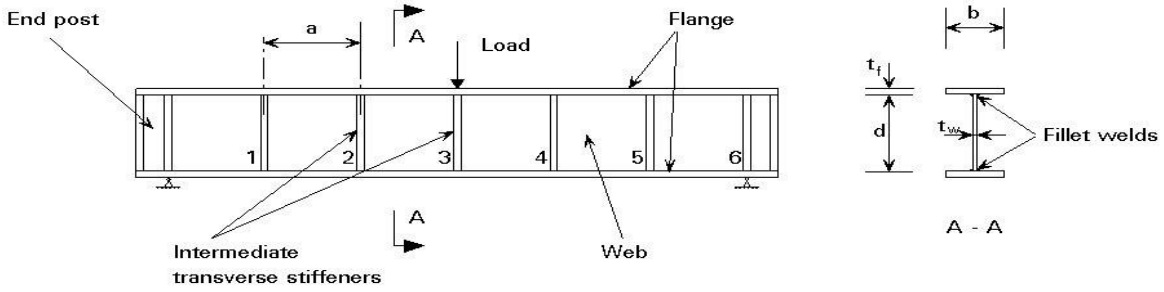

FIGURE.2 Intermediate transverse web stiffeners

In 1940, Massonnet presented a research study of the elastic stability of simply supported rectangular plates subjected to pure bending and strengthened with a 1/4 longitudinal stiffener. These studies concentrated primarily on the theory of optimal stiffener rigidity[10]. Later, Kromm and Chawla refined the minimum strength requirements for panel stiffeners by examining a longitudinal stiffened panel during pure bending[11]. Milosavljevic has developed a comprehensive study on treatment of the elastic stabilisation of a simply supported rectangular panel was subjected to an axial stress, shear stress and combined bending that strengthened to two transverse stiffeners and one longitudinal stiffener. The key was found by applying a series technique to the plate's differential equation. the stiffeners in the transverse direction at the 1/3 wide locations, the special situations of pure bending and bending

with shear were solved after a year. According to Dubas ideal portion of the stiffener in longitudinal direction which act a simply supported panel exposed to the pure bending is at 1/5, The American and British Specifications have since accepted this position.

DESIGN AND MATERIAL PROPERTIES

The design work in this research focuses on building and expanding the possibilities of those computational tools using the proposed methodology to improve modelling, design and development, thus the stiffened panel is designed entirely or in its discrete required components as shown in figure.3

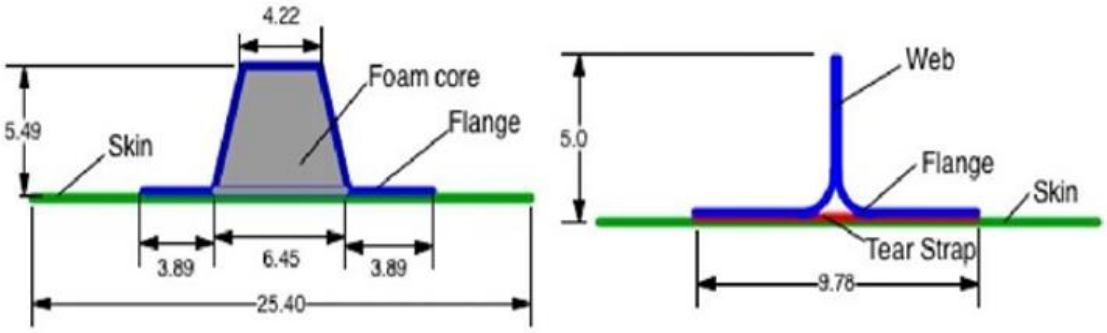

FIGURE.3 Hat and blade frame stiffener

The hat section stiffener design using CATIA and It includes a step-by-step simulation that demonstrates the main component with dimensions and their characteristics as shown a wireframe in figure.4 and the design part workbench in figure.5

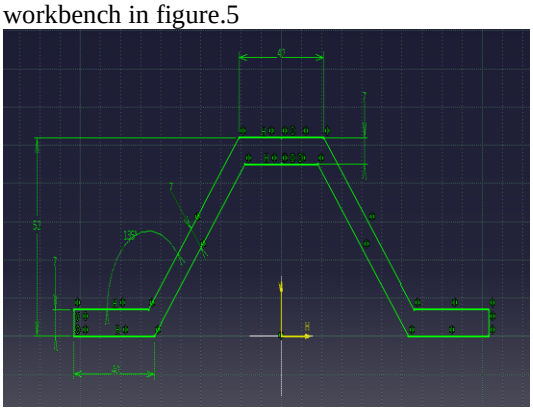

FIGURE.4 Geometry of the Hat section stiffener

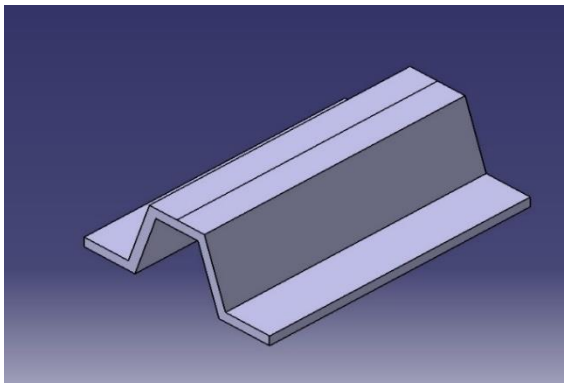

FIGURE. 5 Model of Single Hat section stiffener

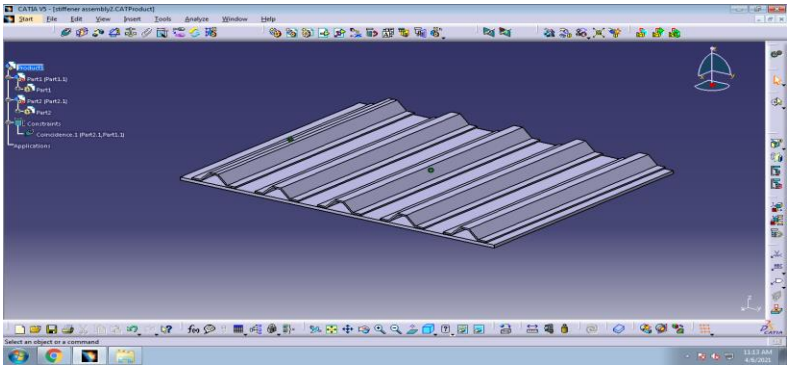

FIGURE.6 Model of Hat section stiffener

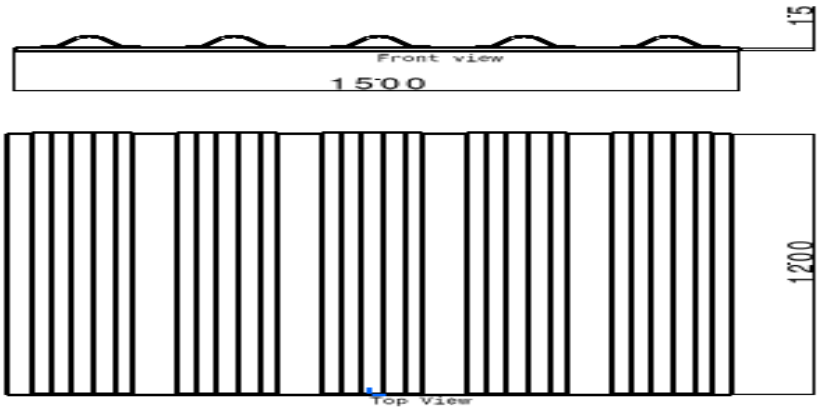

FIGURE.7 Front view and Top View of the Hat section stiffener

TABLE1. Shows the Material properties

Material	Poisson's Ratio	Modulus of Elasticity (GPa)	Density (kg/m^3)
Structural Steel	0.27	200	7850
Aluminium Alloy	0.33	70	2770

RESULTS AND DISSCUSSIONS

Based on selected materials and designs, the finite element analysis package ANSYS workbench was imported from CATIA and as per the required dimensions. Meshing, boundary conditions were applied, the rectangular panel was fixed at both ends and uniformly distributed pressure was applied, and static structural simulation analysis was performed for both aluminum alloy and steel materials.

For the given set of loading condition, the Maximum Deformation value was observed 40.092mm on the Aluminum stiffened panel and the minimum value was observed 4.45mm and von Mises stress, the Maximum value was observed 337.91Mpa and minimum value was observed 1.596Mpa as shown in figure.8 and 9.

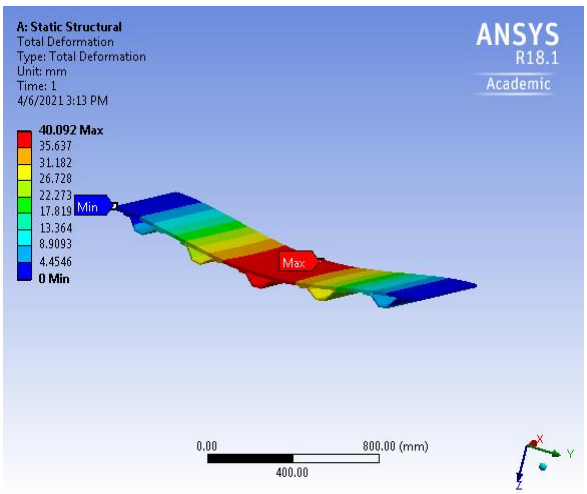

FIGURE.8 Maximum Deformation of an Aluminum Alloy Material

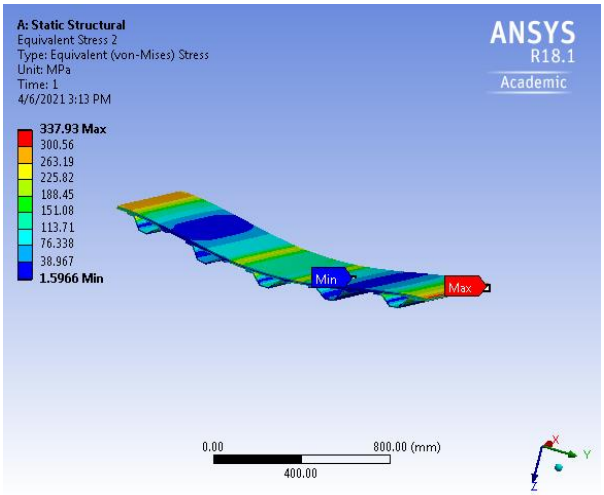

FIGURE.9 Von Mises stress of an Aluminum Alloy Material

Similarity on steel material, the given set of loading condition, the Maximum Deformation value was observed 14.68mm on the Steel stiffened panel and the minimum value was observed 1.6mm and von Mises stress, the Maximum value was observed 375.9Mpa and minimum value was observed 1.43Mpa as shown in figure.10 and 11.

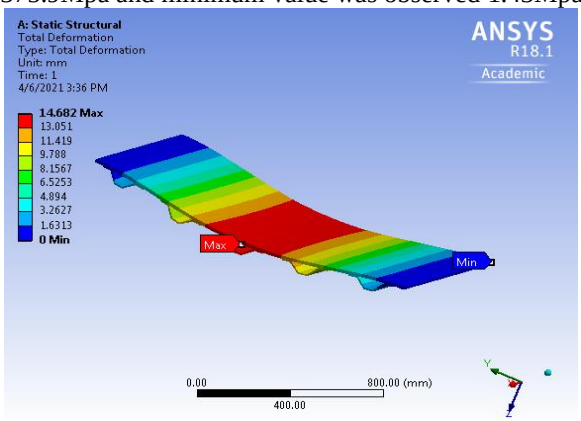

FIGURE.10 Maximum Deformation of the Steel Material

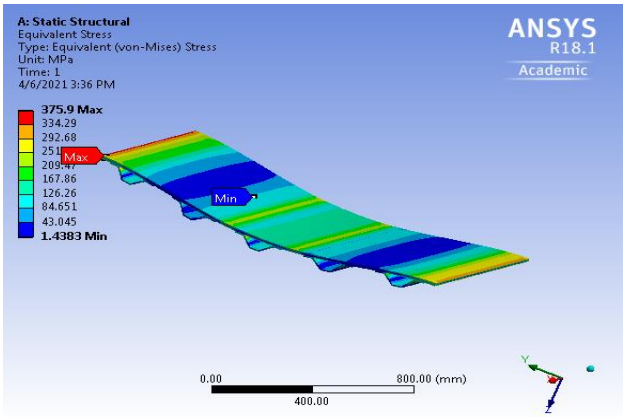

FIGURE.11 Von Mises stress of the Steel Material

The results of the static analysis presented in the form of total deformation and Von mises stresses under the pressure of 1atm was applied on the fixed rectangular plate carrying uniformly distributed load calculated by ANSYS.

TABLE 2. Shows the Stresses and Deformation Results

Materials	Pressure (MPa)	Von Misses Stresses (Mpa)	Displacement (mm)
Aluminium Alloy (AA6082)	0.101	337.93	40.09
Steel Alloy (Ferrium m54)	0.101	375.90	14.68

CONCLUSION

Aluminum is the primary material used in the manufacturing of aircraft in this article. However, larger aircraft manufacturers such as Boeing and Airbus have started to use carbon fiber in their planes. The FEA of the structural analysis for a fixed rectangular plate with uniformly distributed pressure load applied for both steel and aluminum material was performed in this work, and the following conclusions were reached. The total deformation and stress analysis results for a fixed stiffened panel are compared for two material qualities by ANSYS. By static analysis, von mises stress values are lower in aluminum than in steel stiffened panels, and overall deformation results are lower in aluminum than in steel stiffened panels.

REFERENCES

1. Uday Deepika A, Veeranjaneyulu K. Buckling analysis of stiffened panel for aircraft fuselage. *Int J Mech Prod Eng Res Dev*. 2018;8(1):1299-1308. doi:10.24247/ijmperdfeb2018150
2. Uday N, Goud R, Sawale A, Rakham B. Buckling Load Predictions of Panel and Shell using Vibration Correlation Technique. *Int J Eng Adv Technol*. 2019;9(2):1842-1845. doi:10.35940/ijeat.b2679.129219
3. Kumar DM, Madhavi N, Sushma M. Thin walled C-Sectional Beam under Axial Load. *Int J Innov Technol Explor Eng*. 2020;9(3):498-499. doi:10.35940/ijitee.c8512.019320
4. Ko WL, Jackson RH. Shear Buckling Analysis of a Hat-Stiffened Panel. *Nasa Tm-4644*. 1994;(November 1994).
5. A A V. Parametric study of castellated beam with varying depth of web opening. *Int J Sci Res Publ*. 2012;2(8):2250-3153. www.ijsrp.org
6. Kumar. Static and Dynamic Analysis of Aircraft Stiffened Panel. 3(2):134-139.
7. Kothapalli AKR, Mohanty A, Adika SRK. Finite Element Modeling And Analysis Of Fuselage Stiffened Panel Subjected To Cabin Pressurization. *ResearchgateNet*. 2012;(January):678-681. http://www.researchgate.net/publication/246546122_Finite_Element_Modeling_And_Analysis_Of_Fuselage_Stiffened_Panel_Subjected_To_Cabin_Pressurization/file/e0b4951d9b5233ed5e.pdf
8. Li X, Jia D, Meng C. Buckling analysis of airframe jointed panel under combined loading. *Int J Appl Mech Eng*. 2018;23(4):1035-1042. doi:10.2478/ijame-2018-0060
9. Anupriya B, Jagadeesan K. Shear strength of castellated beam with and without stiffeners using FEA (ANSYS 14). *Int J Eng Technol*. 2014;6(4):1970-1981.
10. Massonnet, C. (1940). "La Stabilite' De L`Ame Des Poutres Munies De Raidisseurs Horizontaux Et Sollicitees Par Flexion Pure (The Web stability of Longitudinally Stiffened Plate Girders Subjected to Pure Bending)."
11. Kromm, A. (1944). "Zur Frage der Mindeststeifigkeiten Von Plattenaussteifungen (On the Problem of Optimum Rigidity of Stiffened Plates)." Stahlbau, 17, p. 81.

RESEARCH ARTICLE | MAY 22 2023

Experimental investigation on surface characteristics of copper by roller burnishing process

Jyothula Sunil Kumar ✉; Arutla Udaya Deepika; Gummadi Ananda Rao; Moyya Sundeep; Jagadevapuram Laxmi Prasad; Gottipati Venkata Rambabu

AIP Conference Proceedings 2492, 040048 (2023)
https://doi.org/10.1063/5.0114438

Experimental Investigation on Surface Characteristics of Copper by Roller Burnishing Process

Jyothula Sunil Kumar[1,a)], Arutla Udaya deepika[1,b)], Gummadi Ananda Rao[1,c)], Moyya Sundeep[1,d)], Jagadevapuram Laxmi Prasad[1,e)] and Gottipati Venkata Rambabu[1,f)]

[1]*Department of Mechanical Engineering, MLR Institute of Technology, Hyderabad, India*

[a)] Corresponding author: jyothula92@gmail.com
[b)] udeepika.aero4825@mlrinstitutions.ac.in
[c)] gummadi68@gmail.com
[d)] moyya.sundeep@gmail.com
[e)] laxmiprasad.j@gmail.com
[f)] gvrambabu@mlrinstitutions.ac.in

Abstract. Surface finish will enhance the life of a product and it ensures durability and reliability. Roller burnishing process is a chip less machining process to finish the surface smoothly. It employs a rolling tool which rolls on the surface with high pressure to achieve the plastic deformation. In this process material will be displaced as a cold flow from peak to valley. It improves the surface texture like a mirror finish and produced hardness and toughness. In this paper an experimental study is presented which is carried out by doing burnishing process with hardened roller on a copper sheet. This surface hardness and surface structure was examined by varying burnishing parameters. A micro structure is then depicted for the burnished work piece.

INTRODUCTION

Surface texture of a machined part is very important in industries particularly in automotive and aircraft structures. A good surface finish will increase the life the product of a rubbing or sliding members. It also gives good appearance and smooth functioning of the parts. It's influences will be on fatigue, corrosion, and it also ensures the reliability and durability of the product. In early days with conventional machining process it is difficult to achieve required surface finish. Now-a-day we are using the modern technology to use computerized machines and precious measuring instruments to improve the surface quality.

Surface finish can be achieved by grinding, lapping, toning and also by removing the material in the form of minute chips (small amount of wastage of material). Other alternating process of finishing product is roller burnishing process. It is the cold working process that can be done on the ductile materials. In the burnishing process hardened rollers are used that are rolled with the high pressure on the surface that exceeds yield point of the work piece material resulting with a plastic deformation. These surface irregularities of peak and valleys are described as high and spacing. As the burnishing roller roll on the surface it displaces the material from the peaks to the valleys like cold flow. As a result, the surface which is grinded will have mirror like finish and it also has an excellent resistance against wear, corrosion and fatigue. The roller burnishing parameters like pressure, number of rollers and speed may be vary depending up on the material properties like ductility elasticity surface roughness.

Advancements in Aeromechanical Materials for Manufacturing: ICAAMM-2021
AIP Conf. Proc. 2492, 040048-1–040048-8; https://doi.org/10.1063/5.0114438
Published by AIP Publishing. 978-0-7354-4438-6/$30.00

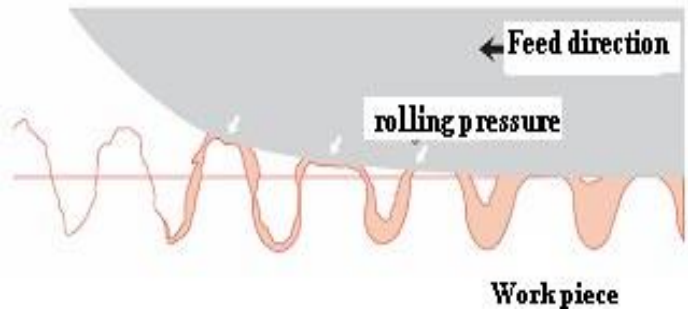

FIGURE 1. Burnishing operation principle

Many researches describe the burnishing process such for material and treatment of parameters and their studied on the shape of the rollers that are designed for milling. Thamizhmanii and B. Saparudin (2007), the surface of the material smoothened out and will become hardened to undergo with plastic deformation process but the residuals stresses will left with the associated cold work [1]. F. J. Shiou and C. Hsu (2008) Strain hardening occurred due to high pressure plastic deformation causes the growth in hardness [2]. U. Pettersson and S. Jacobson (2003). IN surface finishing process the quality depends on parameters like speed, feed, and numbers of passes [3]. M. H. Axir and A. A. Ibrahim (2005) Characteristics in surface rolling burnishing depends on number of passes [4]. M. H. El-Axir (2000) and the restore of one pass roller burnishing will be having ellipticity due to strain hardness [5]. H. J. Shiou and C. H. Chen (2003) studied the distribution of stress on the internal surface. If the force of the burnishing exceeds then it leads to discontinuities on the surface [6]. Y. K. Chou (2003) studied the speed and feed which is accompanied with the roughness of the surface finish [7]. Al-Qawabeha et al [2009] studied the influence of the rollers burnishing force that improve the hardness [8]. Nemat, M., Lyons,A.C.,(2001) the increase of number of passes that leads to depth of penetration and due to that surface hardness will be increased [9]. Gardin, Cet al (2007) This process is to lower or even to avoid the crack initiation and propagation which became one of the advantages to this process [10]. Loh N et al (1993) suggested that wear resistance can be achieved by the roller burnishing process [11]. In the below table1 various manufacturing methods with their achievability of surface finish are mentioned.

TABLE 1. Comparison of surface roughness with manufacturing process

Sl.No	ManufacturingProcess	Surface Roughness (Microns)
1	Turning	0.43 –26.0
2	Drilling	1.60- 21.0
3	Grinding	0.6-5.0
4	Broaching	0.4– 3.4
5	Burnishing	0.35- 0.8
6	Honing	0.25- 0.4
7	SuperFinishing	0.016–0.32
8	Lapping	0.012–0.16

EXPERIMENTALSET-UP

The following apparatus are required to conduct the experiment

1) Lathe machine
2) Dial gauge
3) Burnishing Tool (Roller)
4) Burnishing tool post assembly
5) Work pieces
6) Coolants.
7) Surface finish measuring instrument (Handy surf)
8) Micro Hardness testing instrument (Vickers Hardness).

Burnishing tool

High carbon chromium steel having 60 HRC hardness burnishing rollers are used for the material listed in the Table 2

TABLE 2. Materials used for the HRC hardness burnishing rollers

Element	C	Cr	Mn	Si	P	S
% of material used	1.10	1.60	0.50	0.35	0.025	0.025

A solid cylinder is chosen for the HCHCR material. This material is high carbon and high chromium alloy of steel, which has good hardness and is used for operations including burnishing.
The dimensions of the job are Ø30×10 mm thick.

Performed operations such as turning and a chamfering on lathe machine and made a job of dimensions 0.5×45° mm on both the sides of the job [12].

Performed operations turning and chamfering internally with the dimensions Ø21×10 mm and 0.5×45° mm on both the ends of the surface [13]. After this process is done the tool is heat treated and it's hardness reaches up to54HRC.

FIGURE 2. Burnishing Tool

Work piece

The work piece is used in the present study is used in the solid shafts. Burnishing operation is carried out on Copper material. The properties of this material are given in below table.

TABLE 3. Material properties of copper material

S.No	Material	Length	Diameter
1	Copper	60mm	29mm
Material	Young's modulus (GPa)	Poison's ratio	Density Kg/m3
copper	110–128 GPA	0.357	8950

EXPERIMENTALWORK

Operation of burnishing under different conditions:

1) Speed
2) Load
3) Passes

These operations are carried out under different conditions to obtain the readings for burnishing tool operations

- After fixing the tool post to lathe, then lathe is set in to a configuration of different feeds, speeds and loads required.
- The work piece is fixed on lathe machine and turning operation is performed to get desired diameter of raw material.
- After the turning operation is completed, the specimen is marked at a length of 25mm equally and using the lathe, slots are made at equal distance as marked on the work piece to test each specimen individually under different parameters.
- The work piece is held in between the chuck of the lathe and its tailstock center.
- Gears of the lathe are adjusted using the gearbox engage levers, for the required RPM of the spindle.
- There are eight variable speeds on the lathe machine which can be varied by using the gear engagelever which in turn is divided into two gearshafts which consists of four individual speeds respectively.
- After engaging the speed lever, feed is given to the carriage by using feed lever at certain speed, which is given by the engagement of lead screw to the carriage.
- This experiment is carried out for different values of speed, feed and number of passes and the hardness & surface roughness values are calibrated.

- The burnishing tool post if fitted on the lathe and the roller is made in contact with the work piece.
- The tool is given certain pressurized load by moving the tool post towards the work piece and the amount of load is calculated accordingly by the displacement of the dial indicator pointer.
- This load gives the work piece a stress which is generally termed as the contact stress and as the lathe spindle is turned on the centrifugal force acting tangentially on the roller component will make the roller to rotate on its own.
- This gives the surface a cold working process and the surface finish gets improved and also the hardness gets improved.

RESULTS AND DISCUSSIONS

Condition 1: Speed 62 rpm constant

As the load increases, the surface hardness increases.
As the load increases, the surface roughness decreases.

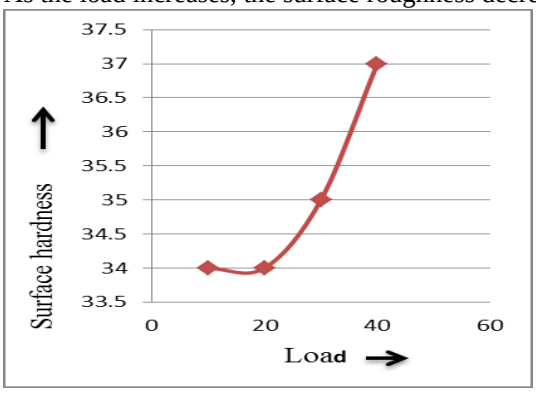

FIGURE 3. Load vs Surface hardness (Speed=62rpm)

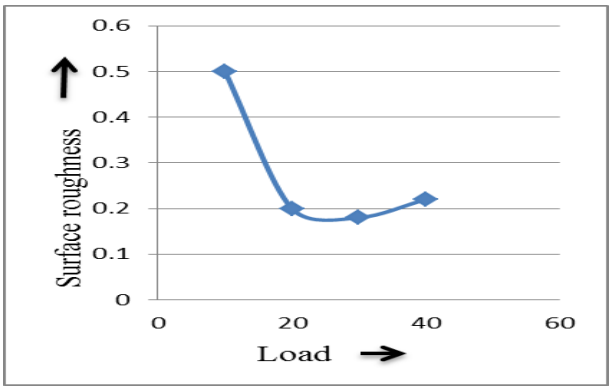

FIGURE 4. Load vs Surface roughness (Speed=62rpm)

Condition 2: Speed192 rpm constant.

As the load increases, the surface hardness decreases.
As the load increases, the surface Roughness Increase.

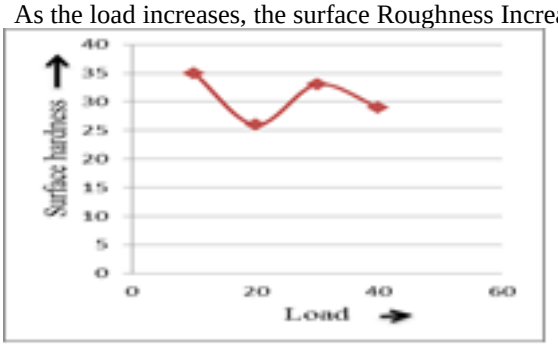

FIGURE 5. Load vs Surface hardness (Speed=192rpm)

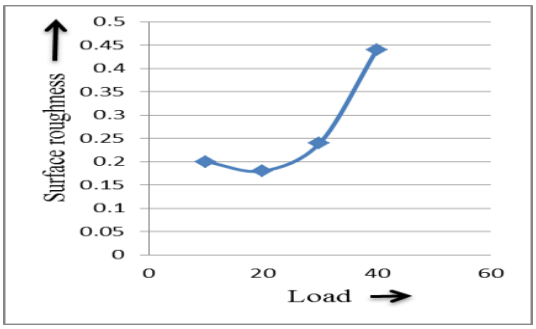

FIGURE 6. Load vs Surface Roughness (Speed=192rpm)

Condition 3: Speed 399rpm constant.

As the load increases, the surface hardness decreases and increases.
As the load increases, the surface roughness increases and decrease.

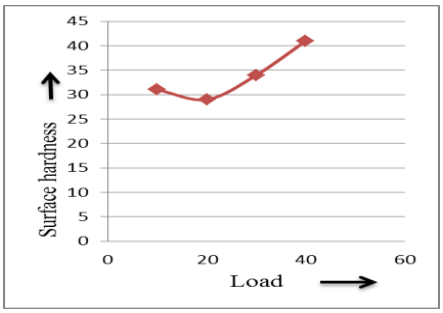

FIGURE 7. Load vs Surface Hardness (Speed=399rpm)

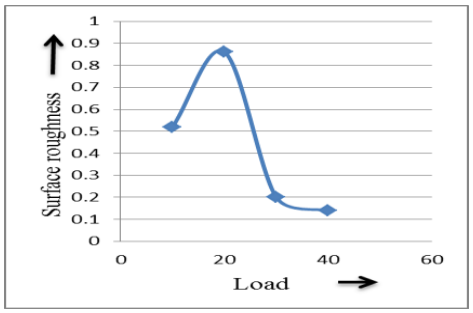

FIGURE 8. Load vs Surface Roughness (Speed=399rpm)

Condition 1: Pass1 constant

Taking load, a slow, medium and high with respect to the speed.
As the load increases, the surface hardness decreases.

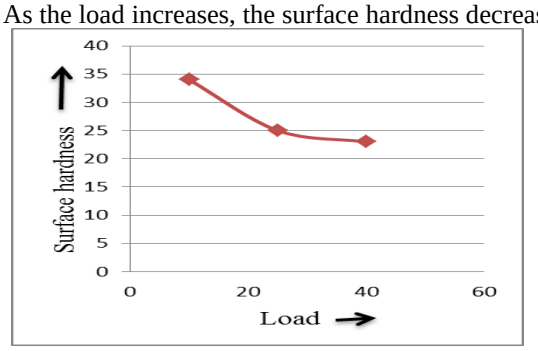

FIGURE 9 Load vs Surface hardness (Pass=1)

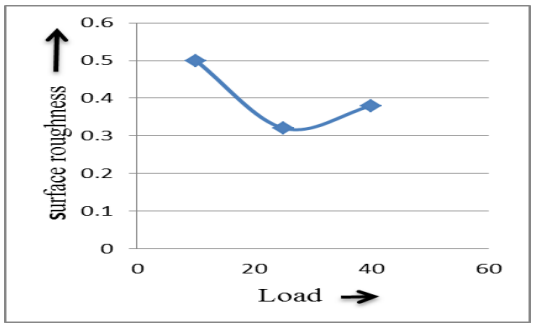

FIGURE 10 Load vs Surface roughness (Pass=1)

Condition 2: Pass 2 constant

As the load increases, the surface roughness decreases and increases.
Taking load in different conditions such as slow, medium and high with respect to the speed

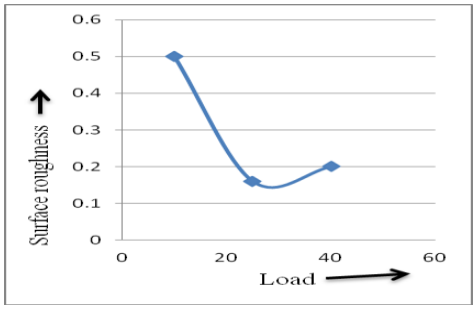

FIGURE 11. Load vs Surface roughness (Pass=2)

Condition 3: Pass 2 constant

As the load increases, the surface hardness decreases
As the load increases, the surface roughness increases.

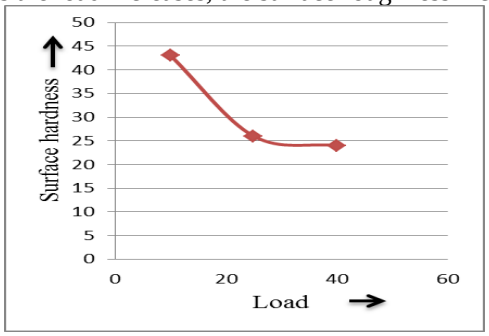

FIGURE 12. Load vs Surface Hardness (Pass=3)

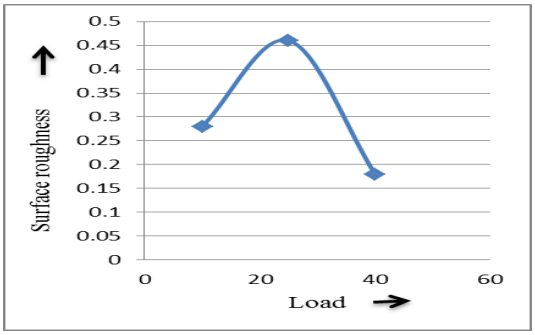

FIGURE 13. Load vs Surface Roughness (Pass=3)

Condition 4: Pass 4 constant

Taking load a slow, medium and high with respect to the speed,
As the load increases, the surface hardness decreases and increase
As the load increases, the surface roughness increases and decrease.

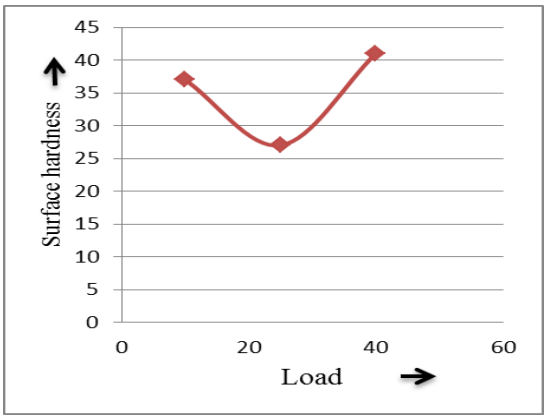

FIGURE 14. Load vs Surface Hardness (Pass=4)

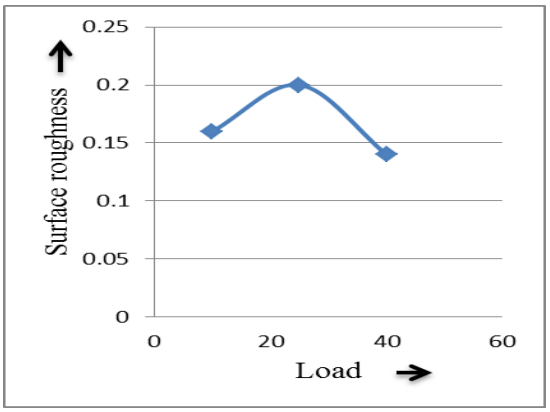

FIGURE 15. Load vs Surface Roughness (Pass=4)

Condition 5: Pass 5 constant

Taking load a slow, medium and high with respect to the speed. Load vs Surface Hardness (Pass=4). As the load increases, the surface hardness decreases and increase. Load vs Surface Roughness (Pass=4). As the load increases, the surface roughness increase and decrease [14].

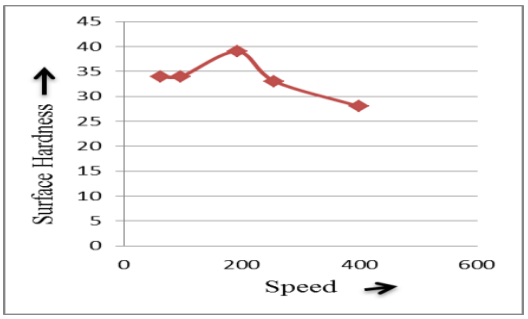

FIGURE 16. Load vs Surface Hardness (Pass=5)

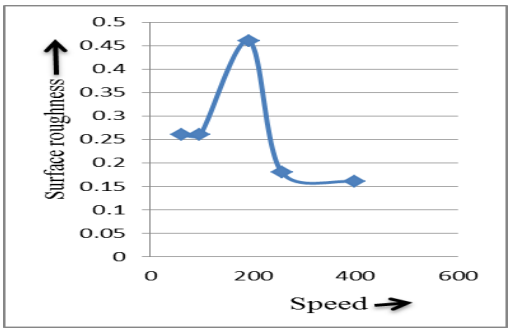

FIGURE 17. Load vs Surface Roughness (Pass=5)

As the load increases, the Surface hardness decreases. As the load increases, the Surface roughness increase and decrease.

Condition1: Load 10kg constant.

Speed vs surface roughness (Load=10kg)
Speed vs surface hardness (Load=10kg)

As the speed increases, the surface hardness Increase and decrease. As the speed increases, the surface roughness increases and decrease.

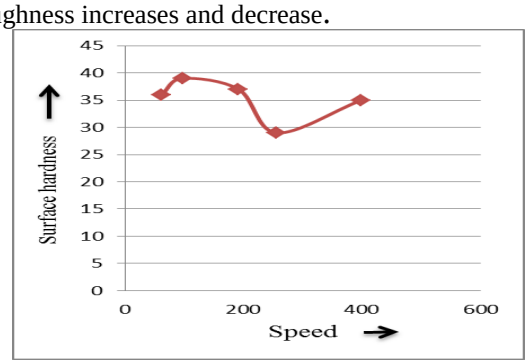

FIGURE 18. Speed vs surface hardness (Load= 25kg)

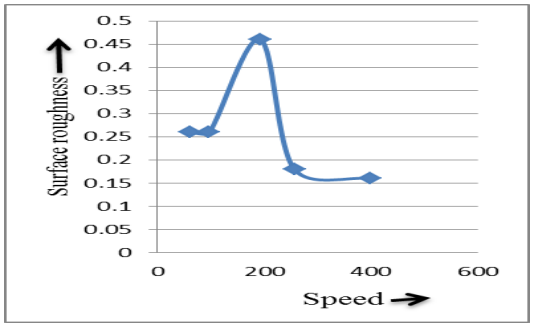

FIGURE 19. Speed vs surface roughness (Load=25kg)

Condition 2: Load 25kg constant as the speed increases, the surface hardness increases and decrease. As the speed increases, the surface roughness increase and decreases.

Condition 3: Load 40kg constant.

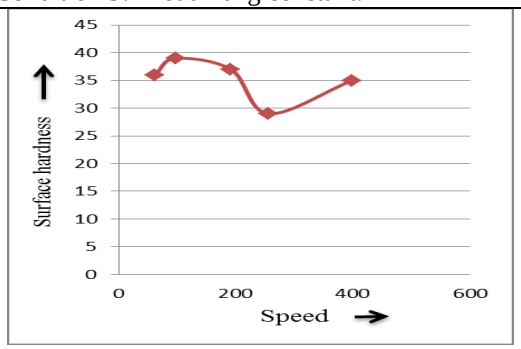

FIGURE 20 Speed vs surface hardness (Load= 40kg)

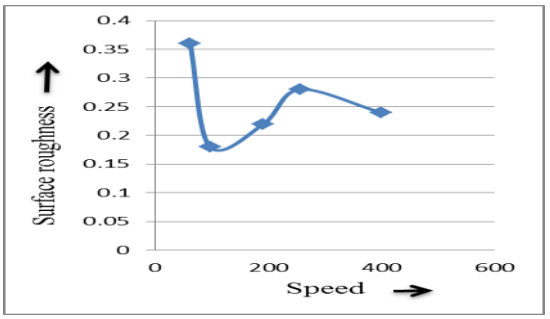

FIGURE 21 Speed vs surface roughness (Load= 40kg)

As the speed increases, the surface hardness Increase and decrease. As the speed increases, the surface roughness decrease and increase.

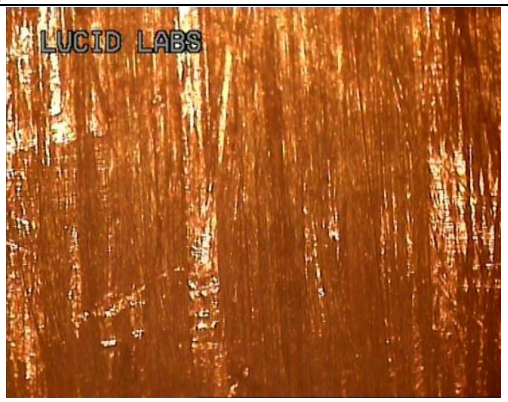

(a). Surface Hardness- 20 HRB Surface Roughness–0.12µm Magnification–50x

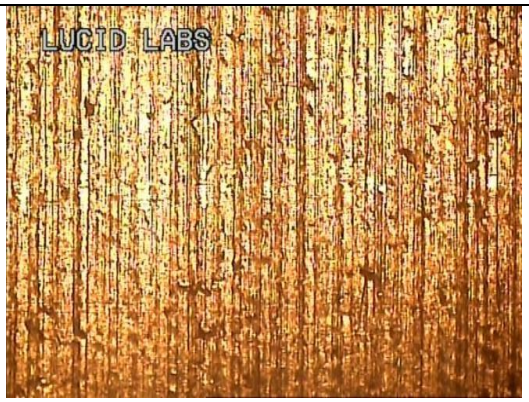

(b). Surface Hardness–43HRB Surface Roughness- 1.34µm Magnification–50x

FIGURE 22. Microstructure of copper before and after burnishing

CONCLUSION

Roller burnishing process was done on the copper work piece it was observed that improvement in the surface finishing increases the hardness. Work piece under different parameters such as surface roughness 0.16 µm, speed 399 rpm, force 25 Kg and Passes 5 results are mentioned in this paper. Surface hardness is 97 HRB and Speed 399 rpm, Force 40 Kgs and Passes 4 surface hardness is 43 HRB for copper. Investigation yields that Surface Hardness and surface roughness depends on force, passes and speed. The results shows that there is an improvement in surface roughness and increase in surface hardness are achieved by application of roller burnishing for copper work piece. Optimal values for surface roughness are: 0.16 µm and speed 399 rpm, force 25 Kg and passes5. Optimal values for surface hardness are: 43 HRB speed 399 rpm, force 40 Kg and passes4. Investigation yields that surface hardness and surface roughnesses depends on force, passes and speed for copper.

REFERENCES

1. S. Thamizhmanii and B. Saparudin, *J. Achiev. Mater. Manuf. Eng.*, **22**, 95 – 98 (2007).
2. F. J. Shiou and C. Hsu, *J.Mater. Proc. Technol.*, **205**, 249 – 258 (2008).
3. U. Pettersson and S. Jacobson, *Tribol. Int.*, **36**, 57 – 64 (2003).
4. M. H. Axir and A. A. Ibrahim, *J. Mater. Proc. Technol*, **167**, 47 – 53 (2005).
5. M. H. El-Axir, *Int. J.Machine Tools Manuf.*, **40**, 1603 – 1617 (2000).
6. H. J. Shiou and C. H. Chen, *Int. J.Adv. Manuf. Technol*., **3**, 177 – 185 (2003).
7. Y. K. Chou, *Wear*, **225**, 1388 – 1394 (2003).
8. Al-Qawabeha, U., Al-Rawajfeh, A.E., Al-Shamaileh, E., *Anti-Corrosion Methods and Materials*, **56**, 261 – 265 (2009)
9. Nemat, M., Lyons, A.C., *International Journal of Advanced Manufacturing Technology*, **16**, 469-473 (2001)

10. Gardin, C., Courtin, S., Bertheau, D., Bézine, G., Ben Hadj Hamouda, H., *Fatigue & Fracture of Engineering Materials & Structures*, **30**, 342 – 350 (2007)
11. Loh, N. H., Tam, S. C. and Miyazawa, S., *International Journal of Machine Tools Manufacturing*, **33**, 841-852 (1993)
12. Subramanyam, B., Vineeta, T.V., Garre, P, *IOP Conf. Ser.: Mater. Sci. Eng*., **455**, 1-11 (2018)
13. Prashanth Reddy M., Labesh Kumar C, *International Journal of Mechanical Engineering and Technology*, **8**, 502-509 (2017)
14. Snigdha M., Satya Sandeep C, *International Journal of Mechanical Engineering and Technology*, **8**, 1034-1051 (2017)

RESEARCH ARTICLE | MAY 22 2023

Design and fabrication of automatic sterilization system for industrial tools

J. Indira Priyadharshini ✉; P. Kapil; G. R. Manoj Eswar; M. S. Kailash; V. Kesava Viknesh; N. Madhavi

AIP Conference Proceedings 2492, 050022 (2023)
https://doi.org/10.1063/5.0113887

Design and Fabrication of Automatic Sterilization System for Industrial Tools

J Indira priyadharshini[1,a)], P Kapil[1], G R Manoj Eswar[1], M S Kailash[1], V Kesava Viknesh[1] ,N. Madhavi[2]

[1]*Department of Mechatronics Engineering, Sri Krishna College of Engineering and Technology, India*
[2]*Department of Aeronautical Engineering, MLR Institute of Technology, Hyderabad, India*

[a)] Corresponding author: indirapriyadharshinij@skcet.ac.in

Abstract. Covid19, which took place in 2020, had a profound impact on the entire human race. Because of its rapid and widespread spread, it is necessary to wear face masks and gloves to avoid touching anything with contact. Masks can shield humans, but industrial tools are not so well protected. They have a higher ability to spread disease, such asCovid19.As a result, hand-held industrial instruments must be sanitized. This complex problem is thus solved by using a smart electronic device controlled by a PIC controller. To solve this problem, a method of sterilization using ultraviolet-C lights is proposed and developed.The proposed device employs a pair of UV-C tubes to ensure a successful outcome.

INTRODUCTION

Covid 19 has altered people's perceptions of the world. People sanitize their hands, but they forget to sanitize their possessions most of the time in a world where deadly illness spreads through the air and through contact. By touching an infected person's object, you have a greater chance of spreading deadly disease. The tools in the industries are one of the most commonly used items. They have a higher risk of spreading diseases like covid19.As a result, hand-held tools used in industries must be sanitized.

This work prevents germs from spreading from one person to another. Sterilization on a regular basis would aid in the promotion of hygiene in the workplace.

STERILIZATION SYSTEM METHODOLOGY

The Automatic Sterilization for Machine Tools follows the mechatronics device methodology intending to provide automation. Automation, in general, is concerned with their modal of manual labor by the use of automated processing of mechanical job control mechanisms.

It is made up of three major components:

1. Input unit
2. Processing unit
3. Output unit

InputUnit: The input unit of the Automatic Sterilization for Machine Tools consists of the components needed to obtain input from the company's Machine tools.

Processing unit: The processing units made up of the components needed to ensure signal reception. On insertion of a PIC controller card into the Automatic Sterilization for Machine Tools, it also signalstheoutputdevicetodeliverthecompletedSterilizedproductofthemachinetools.

Output unit: The output unit is made up of the components required to produce the sterilized product of machine tools manufactured in the industry. It is regulated by the processing unit's instructions.

Advancements in Aeromechanical Materials for Manufacturing: ICAAMM-2021
AIP Conf. Proc. 2492, 050022-1–050022-6; https://doi.org/10.1063/5.0113887
Published by AIP Publishing. 978-0-7354-4438-6/$30.00

Electronic system

The PIC microcontroller with integrated chips is used in the electronic portion of the system to perform the system's processing. The entire processing is done on the microcontroller, which is programmed with the ―MP LAB IDE v8.92‖ software. The microcontroller was in charge of every component of the entire device. This involves the IR Sensor sensing the input machine components, the electrical motor running the conveyor belt, and the Ultra-violet Type C[UVC]portion being processed.

Mechanical system

The operating mechanism is representative of the mechanical part of the device. The frame, spur gear, bearing, shaft, and other mechanical components are among the mechanical components. This involves the power transmission from themotortothedeliveryoftheAutomaticSterilizationforMachineTools' sterilized goods. Mechanical practice also involves the construction of the machine's foundation and overall structure. The steel casing is fabricated using the welding and riveting processes, as required.

Electrical system

The motors and power supply unit are part of the electrical system in the Automatic Sterilization for Machine Tools. The input power supply must be stepped down to provide the necessary voltage of 12 volts to the microcontroller device. The electrical motor's power supply must also be considered. The type of electrical motor needed to deliver packaged goods from the machine must be selected.

COMPONENTS USED

Dc motor

An electric motor's operation is made possible through the principles of electromagnetism. When a conductor is exposed to a magnetic field, its current will be equal to the force it gets from the field. The opposite polarities will then attract each other

Spur Gear

The most basic sort of gear is spur gears, commonly known as straight-cut gears. They're made out of a cylinder or disc with teeth that protrude radially. The teeth are generally formed involute but also cycloid to maintain a constant drive ratio, even though they are not straight-sided. A straight edge runs perpendicular to the rotational axis on each tooth. Only when these gears are installed on parallel shafts do they mesh effectively. The tooth loads do not cause axial thrust. Spur gears perform well at moderate speeds, but at higher speeds, they can be noisy.

Bearing

A ball bearing is a rolling-element bearing that has two bearing races positioned on a flat surface. These races are designed to reduce rotational friction and support radial and axial stresses.

Conveyor belt

A plastic belt conveyor is a piece of industrial equipment used to transfer items or materials. The gadget works by putting products on a plastic belt that subsequently runs down a slotted track, making goods movement easier. This belt will rotate around the track, forming a continuous circle. Plastic belt conveyors with interlocking plastic components allow for bending, making the track more flexible and able to go in varied directions as needed.

PIC controller

The PIC16877FA is a 64-bit, CMOS FLASH-based microcontroller that is easy to program. It features a built-in 40-pin package and is compatible with the latest generation of PIC microcontrollers.

Relay

An electrical switching mechanism called a solid-state relay (SSR) turns on or off when an external voltage (AC or DC) is applied to its control terminals. It accomplishes the same task as an electromechanical relay, but it lacks moving parts, allowing it to endure longer. A control signal triggers a sensor, a solid-state electronic switching system distributes power to the load circuits, and a coupling mechanism allows the control signal to trigger the switch without the use of mechanical elements. It's possible that the relay will be set up to switch AC or DC loads.

LCD display

Data is tracked on an LCD display screen. A liquid-crystal display (LCD) is an electronically modified flat-panel display or other optical device that controls light using liquid crystals and polarizers.

Because liquid crystals cannot emit light directly, color or monochrome images are usually created with the help of a backlight or reflector. LCDs can show pre-programmed text, numerals, and seven-segment displays, as well as random or fixed pictures with limited information content that can be displayed or obscured (as in a general-purpose computer display) (as in a digital clock). They both use the same basic technique, with the exception that arbitrary images are created from scratch in one of them.

Sensor

A light-emitting diode (LED) and a receiver make up active infrared sensors. The infrared light from the LED bounces back and is detected by the receiver when an object comes close to the sensor. In obstacle detection systems, active infrared sensors are widely used as proximity sensors.

UVC Light

UVA, UVB, and UVC are the three kinds of UV radiation based on their wavelength. The more energetic and possibly hazardous the radiation is, the shorter the wavelength. On the other hand, shorter wavelength radiation has a harder time reaching human flesh. The sun's UVC rays are the most damaging, but they aren't strong enough to enter the atmosphere.

DESIGN CALCULATION

Belt Conveyor

Diameter of driving pulley(D)=30mmDiameterofroller(d)=30mm

For open drive,

$$L=2C+\pi/2(D+d)$$
$$=2(600)+\prod/2(30+30)$$
$$=1294.28mm$$
$$=1.28m$$

Length of belt=1.28m (1)

Resistance of belt on top

ω_0= cfl[(Gg + Gb) cos δ + Gro]±4 (Gg + Gb)c=Resistance factor=1.5,whereL=600mm

Gg=Weight of conveyor material/meter

=2.38/0.53

=4.49kgf/m. (2)

Gb=Weight of belt/meter

=0.3/1.29

=0.252kgf/m. (3)

δ=inclination of conveyor

ω_0=1.15*1*0.6[(4.49+0.23)cos0]

=3.25kgf. (4)

Resistance of belt on bottom

ω=0.Thereis no inclination

Total inclination=ω_0+ω

=3.25+0

ρ=3.25kgf. (5)

Tension in head drive (Tension in the belt)

T1=ρ[e^μd/ e^μd-1]

α= angle of wrap around pulleyα=180°

μ=coefficient of friction(0.3to0.8) (6)

T1=3.41[e^π*0.3/e^ π*0.3-1]

=3.41[e^0.942/e^ -0.037]

=3.41[2.565/0.944]

T1=9.26kgf (7)

T2=HGb=0T3=T2+ω_0

=0+0.016

=0.016kgf. (8)

T3=T4

=0.016kgf (9)

Total tension in the belt,T=T1+T2+T3+T4

=9.26+0+0.016+0.016

=9.292kgf. **(10)**

H.P of Drive

T=91.12N 1kgf=9.807N

= ρ*v/75

v=2m/s. **(11)**

H.R of Drive=3.25*2/75

=0.088kgfm/s

≈0.87Nm/s. **(12)**

Motor Selection

Power=Velocity*ForceForce=2kg=19.61N

Velocity=0.06m/s

=19.61*0.06

=1.1766Nm/s. **(13)**

Power= 1.1766 Watts.Torque=Force*Radius

= 19.61*0.021

=0.41181 Nm **(14)**

Speed

Power=Torque*(2πN)/60Power*60/Torque*2π=N

N= 1.1766*60/0.41181*2*3.14N=70.596/2.59

N=27.28rpm

N≈30rpm. **(15)**

Moment of Inertia(I)

Ixx=bh^3/12

=900*(75)^3

= 31.6*10^6. **(16)**

Iyy=hb^3/12

=75*(900)^3

=4556.25*10^6 **(17)**

Lowest value(I)=31.6*10^6mm^4

=31.6*10^9m^4 **(18)**

Bearing Calculation

Speed=60rpm

Lifetime=8000to14000hrs

C/P=3.36

Equivalent load,P=Fa+Fr

=23.8N **(19)**

C allowable= 190.64N

Basic Static Capacity,Cv=190kgf

Fa/Co=20/1900=0.0105. **(20)**

As,Fa/Co>e

Radial factor,x=0.56P=45.62N. **(21)**

C/P=3.36Ccal=3.36*45.62

=153.28 N. **(22)**

HARDWARE SETUP

Using the calculated data, the components are selected and assembled. On the frame,belt conveyor isattached.IR sensors is attached on the start and end of the frame. Beside the sensor, the motor is placed at one side of the frame.Battery is attached microcontroller and sensor to give power supply to work the system.

Once the power is generated, the IR sensor at the start point sense whether the object is detected or not,once detected the conveyor moves and the object enters the sterilization module and reaches the end of the conveyor. At the end, the IR sensor detects the object and the system will stop working.The typical setupofthe system was shown(fig. 2).

FIGURE.1. Typical setup of automated sterilization system

CONCLUSION

From the work, it was concluded that an automated sterilization system has the ability to deactivate the bacteria's and viruses in industrial tools. As we are using DC supply, this system is easy to use and portable. Its aim is to provide a product that is safe and eliminates the possibility of contamination. It Eliminates passive spreading of germs from one person to another. Routine sterilization can help in promoting hygiene in the industries. Hence, it is

recommended to use automated sterilization system in industries to kill the germs. The future work will be installed in industries and should be deactivate the bacteria's and viruses in real-time

REFERENCES

1. Tunggal, Tatiya Padang, et al. "Prototype of Hand Dryer with Ultraviolet Light Using ATMega8." *Journal of Robotics and Control (JRC)* 1.1 (2020): 7-10.
2. Ramos, Clysly Celine R., et al. "Use of ultraviolet-C in environmental sterilization in hospitals: A systematic review on efficacy and safety." *International Journal of Health Sciences* 14.6 (2020): 52.
3. Indrato, Tri Bowo, and Priyambada Cahya Nugraha. "AUTOMATIC HAND DRYER INCLUDING UV STERILLISATOR." *JURNAL TEKNOKES* 7.1 (2012).
4. Indirapriyadharshini, J., et al. "Design and fabrication of automated oil spraying machine for baking system." *Materials Today: Proceedings* (2021).
5. Jianping, Li. "Research on Sterilization of Recycled Urban Sewage for Landscape Water with Microwave/UV Method." *Environmental Science and Management* (2012): 10.
6. Upadhyay, Mr Piyushkumar V. "UV Light for Sterilization." (2015).
7. Hariono, B., et al. "Development of personal integrated sterilization machine for new normal phase preparation of the 2019-nCoV outbreak." *IOP Conference Series: Earth and Environmental Science*. Vol. 672. No. 1. IOP Publishing, 2021.
8. Saha, Puja, et al. "Photosweep: An Engineering Approach to Develop Cost Effective Sterilization System for Hospitals." *Advances in Decision Sciences, Image Processing, Security and Computer Vision*. Springer, Cham, 2020. 31-38.
9. Wigginton, Krista Rule, et al. "Virus inactivation mechanisms: impact of disinfectants on virus function and structural integrity." *Environmental science & technology* 46.21 (2012): 12069-12078.
10. Sharma, Aishwariya. "An ultraviolet-sterilization protocol for microtitre plates." *J Exp Microbiol Immunol* 16 (2012): 144-147.
11. Siva kumar, S. A., et al. "Electronic currency note sterilizer machine." *Materials Today: Proceedings* 37 (2021): 1442-1444.
12. Centers for Disease Control and Prevention. Update: influenza activity—United States, August30, 2009-January9, 2010.MMWRMorb MortalWklyRep 2010;59:38-43.
13. VelayatiAA, MasjediMR ,FarniaP, TabarsiP, GhanaviJ, ZiazarifiAH, etal. Emergence of newformsoftotallydrug-resistanttuberculosisbacilli:superextensivelydrug-resistant tuber culosisor totally drug-resistant strains in Iran.Chest2009;136:420-5.
14. Rastogi VK, Wallace, SmithLS. Disinfection of A cinetobacterbaumannii-contaminated surfaces relevant to medical treatment facilities with ultraviolet C light. Mil Med 2007;172:1166-9.
15. Hujer KM, Hujer AM, Hulten EA, BajaksouzianS, Adams JM, Donskey CJ, et al. Analysis of antibiotic resistance genes in multidrug-resistant Acine to bacter spisolates from military and civilian patients treated at the Walter Reed Army Medical Center. Antimicrob Agents Chemother2006;50:4114-23.
16. Loivukene K, Sepp E, Adamson V, Mitt P, Kallandi U, Otter K, et al. Prevalence and antibiotic susceptibility of Acine to bacter baumannii, Pseudomonas aeruginosa and Klebsiella pneumoniaein Estonian intensive care unit sincomparison with Europeandata.ScandJInfectDis2006;38:1001-8.
17. Guidancef or control of infection with carbapenem-resistantorcarbapenemase-producingnterobacteriaceaein acute care facilities, 2009.MorbMortalWklyRep 2009;58:256–260

RESEARCH ARTICLE | MAY 22 2023

Mounting plate design for section-IV of an aerospace vehicle under yawing mode

B. Manideep ✉; E. C. Prasad Nidumolu; B. Nagaraj Goud

AIP Conference Proceedings 2492, 040055 (2023)
https://doi.org/10.1063/5.0113329

Mounting Plate Design for Section-IV of an Aerospace Vehicle Under Yawing Mode

B Manideep[1, a)], E C Prasad Nidumolu[2, b)] and B Nagaraj Goud [1]

[1]*Department of Aeronautical Engineering, MLR Institute of technology, Hyderabad, India*
[2]*Department of Mechanical Engineering, MLR Institute of technology, Hyderabad, India*

[a)]Corresponding author: manideepbalusani.9@gmail.com
[b)]Prasadnidumolu555@gmail.com

Abstract. The structure of an aerospace vehicle is a group of several parts. Part IV is one of those sections, which covers electronic subsystems and avionics batteries. Includes a mounting plate interface that can accommodate a thermal battery for power train control and actuation systems. (No.3), 1, main electronic battery, secondary electronic battery pack, contractor box, monitoring circuit battery voltage (BVMC). The thermal battery and main electronic battery are attached to the clamp and holder plate, and the BVMC, secondary electronic battery and contractor box are attached with screws. Modeling was done in ProEngineer Wildfire 5.0 and analysis was done in ANSYS 12.0. The results were analyzed at various loads and, for theoretical calculations, the factor of safety of the mounting plate was within limits, so the overall design was considered reliable and safe.

Keywords— Battery, Analysis, Aerospace, Mounting Plate

INTRODUCTION

Aerospace Vehicle

In aerospace aircraft, the components must be mounted inside the airframe according to the configuration of the system and travel in a defined path with the help of guidance from control electronics must be installed to support all loads. Properties related to mass are important for the aircraft to follow the required path the main mass characteristics of a vehicle are body weight, COG, and MOI. A force exerted by Earth's gravity on the vehicle i.e. Weight. The vehicle's Mass (weight) is distributed efficiently, but knowing the lane distribution and vehicle stability is important. The main thing is to pay attention to the center of gravity and total weight[1-2].

Yaw Motion

During flight, the aircraft usually rotates around its CG. Since the axis of the coordinate system is perpendicular to one another, you must use the centroid to define the 3D coordinate system. The jaw axis is perpendicular to the horizontal and vertical axes. During the yaw movement, the car's nose moves from side to side. Moments can be observed in figure 1[3-4].

The deflection of the rudder of the aircraft allows you to create a yawning motion. The drawbar is articulated at the end of the vertical stabilizer. A slight change in the steering angle at the rudder end will change the lift produced by the longitudinal stabilizer. In the case of the longitudinal stabilizer and the rudder, the lateral force generated depends on the direction of the wing[5]. If the rudder leans towards left, the lateral force acts towards right side.

Advancements in Aeromechanical Materials for Manufacturing: ICAAMM-2021
AIP Conf. Proc. 2492, 040055-1–040055-8; https://doi.org/10.1063/5.0113329
Published by AIP Publishing. 978-0-7354-4438-6/$30.00

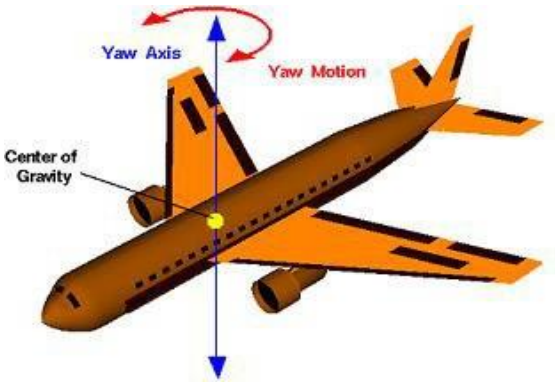

FIGURE 1 Flight Vehicle-Yaw Motion

MODELLING

Aerospace Machinery Part IV Subsystem for Order Fulfillment, Four brackets are used to assemble the section (cell) subsystem.

The Subsystems of mounting Plate are

- Control Actuation System's Thermal Batteries (3No's)
- Battery for Primary Avionics
- Circuit for Voltage Monitoring of BVMC-Battery
- Battery for Secondary Avionics
- Contactor Box.

The total mass of the assembly on the rack is approximately 17.7 kg and the total configuration is depicted as shown in Figure 2[5-8].

The weight of the auxiliary system is transmitted externally to the mounting plate as forces, moments. External load applied is 27.5 g in the vertical direction and 8 g in the horizontal direction, depending on the mass of the subsystem. The mounting plate is design is done and it is tested to check whether it can resist the acceleration loads.

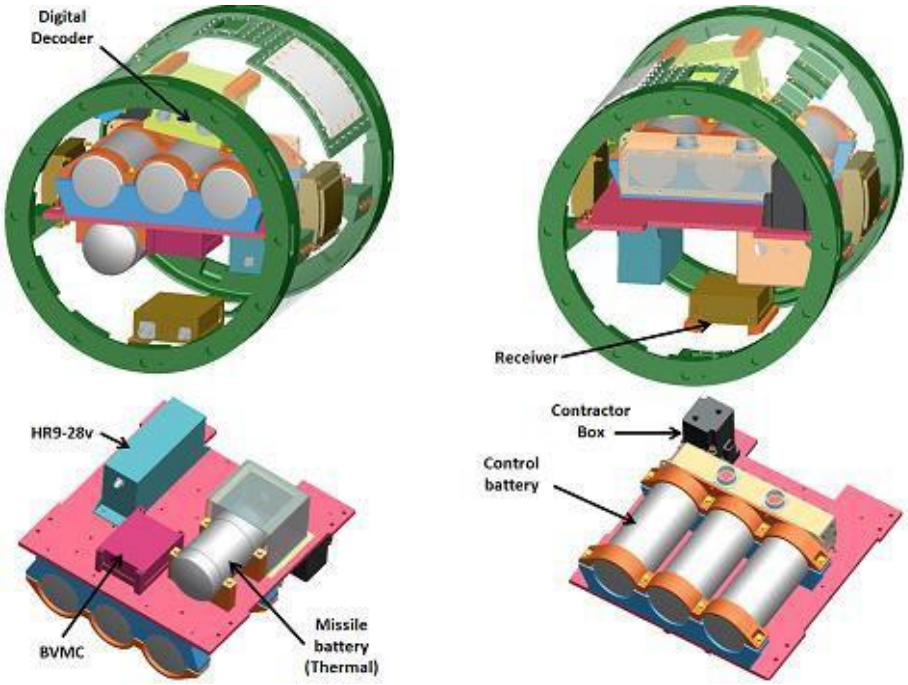

FIGURE 2.Section 4 airframe with packages mounted on plate

INDIVIDUAL PACKAGES DETAILS

Mounting Plate

Plate connected to a subsystem modeled in CAD Pro Engineer as showon in figure 3,

Plate is made up of Aluminium Alloy24345 (WP condition) material, its characteristics are as follows. Plate (IS:736): UTS:405 M Pa, PS:310 M Pa, %e:72

FIGIURE 3. Mounting plate

Control Battery (Thermal) along with Clamp, Brackets

Power for the control operating system is supplied by the control battery (thermostat). The size of the control spindle (thermostat) is Ø80 and 190 in length. The batteries are placed in series as shown in figure 4 with the lower bracket and secured with M5 screws (8 pcs) and upper clamps. Bakelite High Ram Grade F2IS: 2036 material is used for battery mounting and insulation

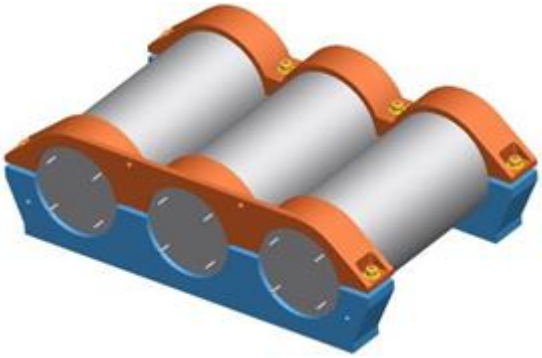

FIGURE 4 Control Battery with Clamps and Brackets

Avionics Battery (Thermal) mounted with Brackets and clamps

Use avionic (thermal) batteries to power the electronic assemblies installed in parts II to IV. The battery size is Ø80 and the length is 145. The battery is on the mounting bracket and is secured with an M5 8 screw and top clamp. Bakelite High Ram Grade F2IS: 2036 material is used for battery assembly and insulation, as shown in figure 5

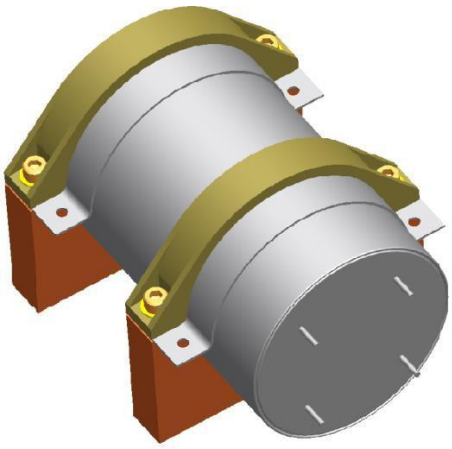

FIGURE 5. 3D Modeling of Avionics Battery Mounted on Clamps and Brackets

BVMC (Battery Voltage Monitoring Circuit) Package

The voltages of the different batteries installed in Part IV are monitored using the BVMC package which is shown in figure 6.For telemetry applications, the battery output voltage is monitored, converted to a digital format and then sent to the built-in computer.

FIGUIRE 6. Model of Battery Voltage Monitoring Circuit Package

HR-59VBattery

The HR59V battery is included to power autonomous aerospace destruction systems, AVDS and 1 Battery provides 5 amps at 9V for external AVDS is required.wchich is as shown infigure 7.

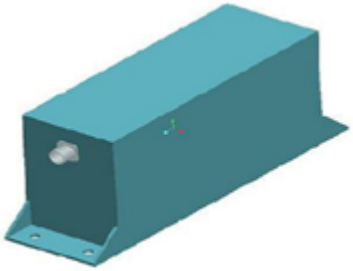

FIGURE:7 Model of HR5-9V

Contractor Box

Use the contractor's box to activate the control pin. Three control pins were connected in series. The battery packs a trigger voltage of 150V. The contractor's box shown in figure 8 receives a command to activate the transmit trigger voltage. These commands are obtained from the built-in calculator.

FIGURE 8. Model of Contractor Box

ANALYSIS

- In the inclined state, the plate experiences an external load and a moment due to the load caused by the packages attached to the plate. The analysis was carried out under inclined conditions [1-8]. The results are observed and tabulated.
- Mounting plates are imported into ANSYS software.
- eight node Shell element(Shell 281) is used to mesh the plate
- Uniform thickness of 8mm is provided.
- Lugs are modeled by a SOLID20, tetrahedral element (SOLID 187).
- The total number of items used in this assembly is 87471.
- No.of elements of plate are 4983.
- No.of elements of Lugs are 82488.

The node of the hole is at the pin level to connect to the stop cell at all degrees of freedom. The plate nodes and the interface holes of the heat sinks are interconnected with all degrees of freedom[9-12]

A Lateral Direction Loading (Yaw)

Each mounted package applies a direct load to each position on the plate, both left and right. Figure 9 shows the boundary conditions and forces acting on the plate. The stresses and flexures that occur on the plates and supports are shown in Figures 10 to 13.

Thermal battery weight (control) with bracket	=8.98Kg
Battery Force in 8g state	= 704.75N
The load onto the plate at each mounting hole	= 88.1 N
Thermal Battery (Avionics) weight with brackets =	2.26Kg
Battery Force in 8g state	= 177.4N
The load onto the plate at each mounting hole	= 44.4N
Battery (HR5-9v) Weight	= 1.95 Kg
Battery Force in 8g state	=150.7N
The load onto the plate at each mounting hole	= 150.7/4

Deflection &stress plot with plate and brackets

BVMC package Weight	= 0.7 Kg
Battery Force in 8g state	= 55 N
The load onto the plate at each mounting hole	= 13. N

Weight of Contact or package = 0.76Kg
Battery Force in 8g state = 59.6N
The load onto the plate at each mounting hole = 29.8 N

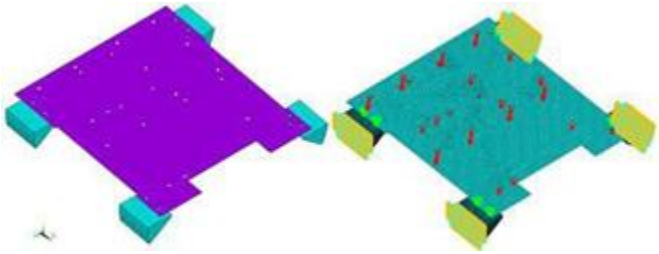

FIGURE 9. FE model and boundary condition plot

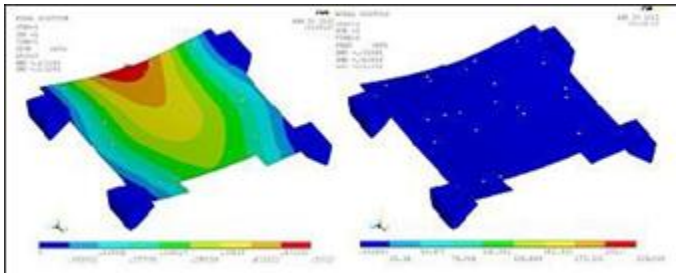

FIGURE 10. Deflection & stress plot with plate and brackets

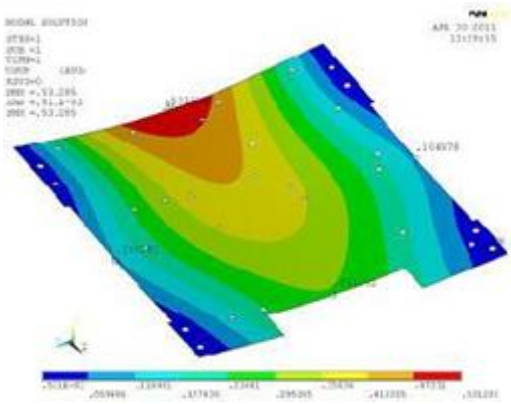

FIGURE 11..Deflection of plate under Yawing

From the Fig11, The max deflection got for Plate is 0.53mm.

RESULTS

The load on the plate is assumed as a rectangular plate having edges loaded in the center. [2], the load of all the packages including plate is 17 Kg. [3-4].

Plate b Length = 400 mm,
Plate a Width = 345mm,b/a = 1.2,
Plate Deflection $=\alpha(p\alpha^2/D)=3282051.3$
Where $\alpha=0.00647$, (based on b/a ratio)
P=Load on the plate= 1334.16 N
$D=Eh^2/\{12(1-\mu^2)\}$
=29.8N

Where E=0.7e5,
h=Thickness of the plate=8mm,
μ=0.3mm
By inducing the above results, Deflection of plate= 0.3 mm
The calculated deviation will be less than the result of FE. This is because the plate is firmly secured on all four sides. Calculations used for qualitative evaluation.

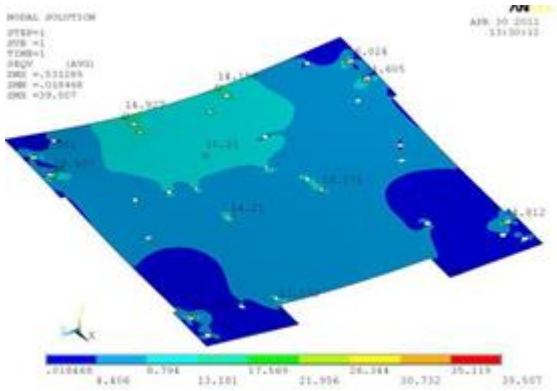

FIGURE 12. Induced Stresses in Plate Yawing

- The maximum deflection achieved with the mounting plate under elevation conditions is 0.055mm.
- The maximum stress obtained for the plate in yawing condition is 66 MPa, with an FOS equal to 4.7.shown in figure 12.

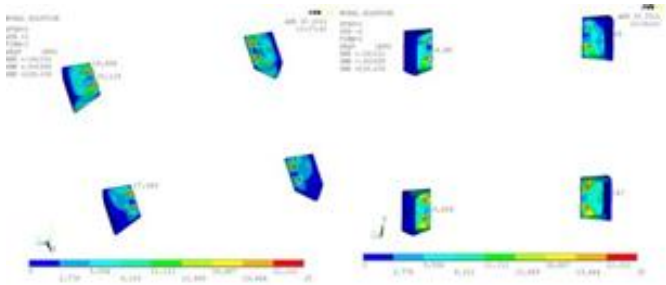

FIGURE13. Induced Stresses on Brackets under Yawing

From Figure 13, Maximum induced Stress for the Plate is =39.51MPa
FOS = 310 / 39.51 =8

CONCLUSION

In general the allowable safety factor for the structural design of aerospace aircraft is considered as 1.5. If the result of maximum deflection achieved with the mounting plate under elevation conditions is concidered, it is within limits, and the maximum stress obtained for the plate in yawing condition is acceptable as the FOS is greater than 1.5. Therefore, the mounting plate design is safe.

REFERENCES

1. *MIL-HDBK-5B, "Metallik Material and Elements for Aerospace Vehicle Structures", Department of Defence (DoD), Washington DC.*
2. "Theory of Plate & Shells-S, Timoshenko", Woinowsky-Krieger, Page No.206, and Table 37)
3. "Introduction to Finite Elements in Engineering Practice" *by "Tirupati R. Chandrapatta and Ashok D. Belugundu"*

4. M Ganesh, Nirmith Kumar Mishra, A. Sai Kumar, V. Vikas, K. Keerthi Krishna "Design and Analysis of UAV for High Payload" in *International Journal of Innovative Technology and Exploring Engineering* (IJITEE) Volume-9 Issue-2, December 2019
5. A. Sai Kumar, M Ganesh, Nirmith Kumar Mishra, Manish Choudhary, Yashwanth Rao Bandari "Design and Development of Man Portable Back Packable Multi-Purpose Drone" in *International Journal of Engineering and Advanced Technology* (IJEAT) Volume-9 Issue-2, December 2019
6. Dhanjal S., Arora R. "Stress analysis of a rectangular plate with circular hole using three dimensional finite element model". *International Journal of Engineering, Business and Enterprise Applications* (IJEBEA), Vol. 12, Issue 1, 2015, p. 77-80.
7. M. L. Pavan Kishore, A. Chandrashekha, M. Avinash and Raunak Das, "Stress analysis of rectangular and square plates with various cutouts",
8. Gunwant D., Singh J. P. "Stress and displacement analysis of a rectangular plate with a central elliptical hole". *International Journal of Engineering and Innovative Technology*, Vol. 3, Issue 3, 2013, p. 387-392.
9. . 'N.Madhavi, Muttangi Sushma, D.Mahesh Kumar, M Satyanarayana Gupta', 'Drones for Agricultural Land prediction', 'International Journal of Innovative Technology and Exploring Engineering (IJITEE)', ISSN: 2278–3075 (Online), Volume-9 Issue-2, December 2019, Page No. 5050-5053.
10. N.Madhavi, Vanaparti Ajay Kumar, Dr. M Satyanarayana Gupta" Design and Analysis of a Fuselage Using Helical Longerons", ijmetmr, ISSN No:2348-4845, Volume 3, sep,2016.
11. N Madhavi, Y.B.SudhirSastry, Pattabhi R.Budarapu," Buckling analysis of thin wall stiffened composite panels", Computational materials sciences, Volume 96, 459-471, Nov2015.

RESEARCH ARTICLE | MAY 22 2023

Design and fabrication of blended wing body UAV

A. Sai Kumar ✉; Nirmith Kumar Mishra; M. Ganesh; ... et. al

AIP Conference Proceedings 2492, 020070 (2023)
https://doi.org/10.1063/5.0113330

Design and Fabrication of Blended Wing Body UAV

A Sai Kumar[1, a], Nirmith Kumar Mishra[1, b], M. Ganesh[1, c], Swethabala MNVS[1, d]

[1]*Department of Aeronautical Engineering, MLR Institute of Technology, Hyderabad, India.*

[a)] Corresponding Author: ask.mraj@gmail.com
[b)]nirmithmishra@gmail.com
[c)]ganesh.manikonda@gmail.com
[d)]swethabalagnvs@gmail.com

Abstract: Unmanned Aerial Vehicles are the class of aircrafts that fly without on-board pilots. This is the most emerging technology advancement in the world. Blended wing bodies are the aircrafts in which the fuselage is integrated within the wings. However, a confluence of recognized needs and technological advancements over several years has brought about a marked change in perceived value of these blended wing bodies. The paper presents the conceptual design and analysis of blended wing UAV. The present work is a scale down approach to check the feasibility of these blended wing bodies as Transport and commercial aircrafts for the near future. The work aim is to develop a remote-controlled aircraft to take-off, maneuver, and land while carrying as much payload as possible. In this, the design of a blended wing aircraft is carried out based on the requirements using tradition approach. The design is then analyzed for aerodynamics and structural characteristics using ANSYS. A detail study was made and the selection materials to fabricate the aircraft are also suggested. A test aircraft was also fabricated

Keywords: Blended wing, Unmanned Aerial Vehicle, Design, Analysis, ANSYS 18, Material etc.

INTRODUCTION

The Blended wing Body (BWB) is basically a flying wing with a delta-shaped wing/fuselage in the center, large enough for a passenger cabin [1-4]. BWB is a hybrid of flying-wing aircraft and the conventional aircraft where the body is designed to have a shape of an airfoil and carefully streamlined with the wing to have a desired plan form [2-7]. The advantages of using a Blended wing are reduced wetted area and improved structural efficiency. The major problem with this configuration is pitch stability.

The objective of present work is to design and fabrication of a Blended Wing Body aircraft which can carry maximum payload with highest payload fraction. The design shall be an initial approach to develop a commercial Blended wing aircraft in future. Hence, to replicate the passengers, 5 footballs are considered as payload. Along with these footballs a payload which is the cargo that has to be carried by the aircraft is also considered. The aircraft must fly with full control for the specified range with endurance. The detailed requirements are given in further sections.

DESIGN OPTIONS AND INITIAL SKETCH

Since design also an artistic work, a number of configurations are studied to overcome the stability issue. Two of the design alternatives were considered initially first one was use of tail booms shown in Figure.1(a) and second one was to use canard surfaces which contribute to additional lift as shown in Figure 1(b). For both configurations, it was assumed to have a pusher type propulsive system.

Advancements in Aeromechanical Materials for Manufacturing: ICAAMM-2021
AIP Conf. Proc. 2492, 020070-1–020070-11; https://doi.org/10.1063/5.0113330
Published by AIP Publishing. 978-0-7354-4438-6/$30.00

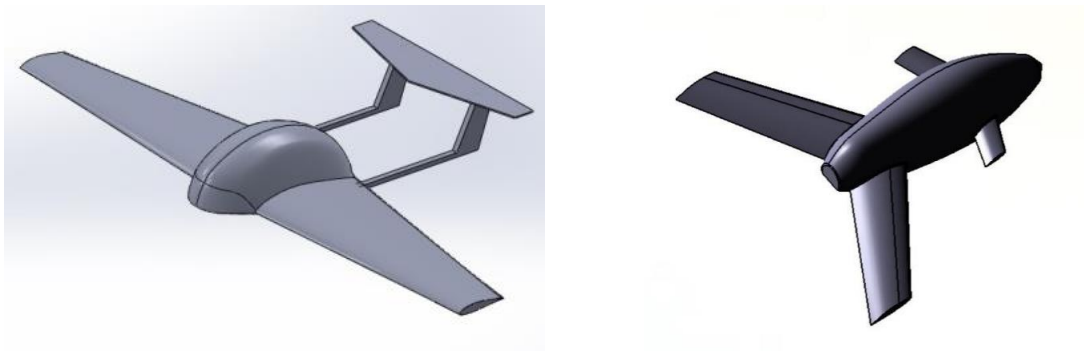

(a) Tail Boom Configuration (b) Canard configuration

FIGURE 1: Initial configurations

After detail study of these two models, first model was considered as a better option over the second as the volume is high and the needed stability can be achieved easily when compared to canard

DESIGN PROCESS

A traditional design approach was followed to develop the aircraft. The design process is outlined in the flow chart shown in Figure. 2.

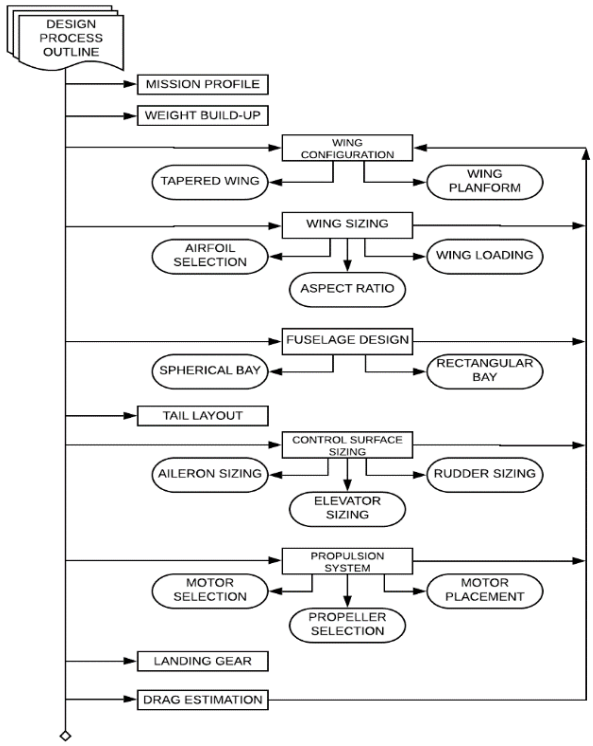

FIGURE 2. Design process

Weight Build-up

Weight estimation is the initial step to start the design of an aircraft as details the necessary lift that has to be generated by the aircraft. An approximate initial weight was calculated using statistical group weight. The components and their weight contribution are tabulated in Table 1.

TABLE 1. Weight build-up

S.NO	Component	Quantity	Weight (lb.)
1	Structure		12
2	Motor	1	2.5
3	Esc	1	0.5
4	Servos	4	2
5	Battery	1	3
6	Landing Gear	1	2
7	Propeller	1	1
8	Rectangular Payload	1	8
9	Circular Payload	4	4
	Total		**35**

The weight of the model including payload was approximated to an exact value of 35 lbs.

Wing Sizing

Airfoil Selection: The selection of the Airfoil for an aircraft's wings is a crucial to ensuring the aerodynamic performance of an aircraft [3]. Many parameters such as lift to drag ratio, take-off, landing performances depend on airfoil, after continuous research and analysis of airfoils E209 as selected and modified same airfoil for bulky middle portion of aircraft using spline tool (XFLR Software)[15-17]. As E209 couldn't meet all the design requirements, we have further optimized the airfoil for our requirements by inverse foil analysis in XFLR based on following parameters. The airfoil for the mid-section and wing are studied in XFLR and are plotted below in Figure 3.

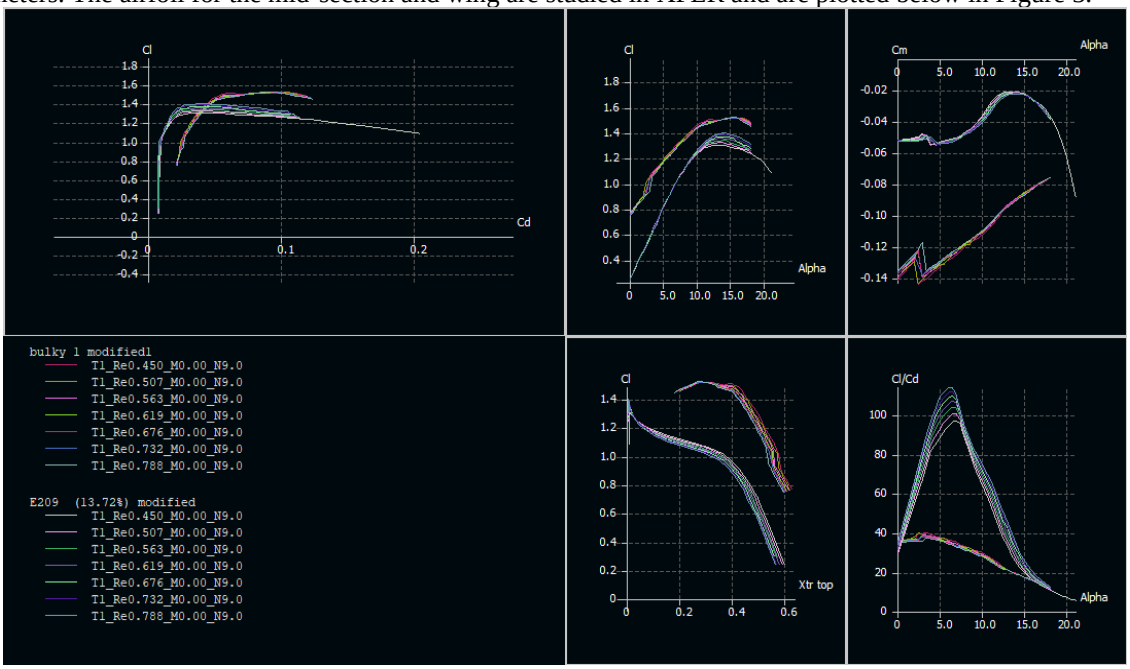

FIGURE 3. Modified E209 and Bulky Airfoil Characteristics

TABLE 2. Required parameters for wing and fuselage section

Location of Airfoil	L/D ratio	C_L	C_m	Thickness ratio (t/c)
Wing section	> 90	maximum	minimum	15%
Mid-section (Fuselage)	> 30	maximum	maximum	> 28%

Wing Loading: It is one of the critical parameters which decided the wing planform dimensions. It is the ratio of takeoff weight to that of area of the reference wing. It affects stall speed, rate of climb, takeoff and landing distances,

and turn performance. Larger wingspan has less wing loading, but leads to increase in drag and empty weight as penalty. Hence, an optimum value has to be predicted. The plot shown in F*igure 4* represents such iteration with velocity. As per wing loading of 1.46 lb/ft^2 is obtained which matched the historical data trend of RC a/c.

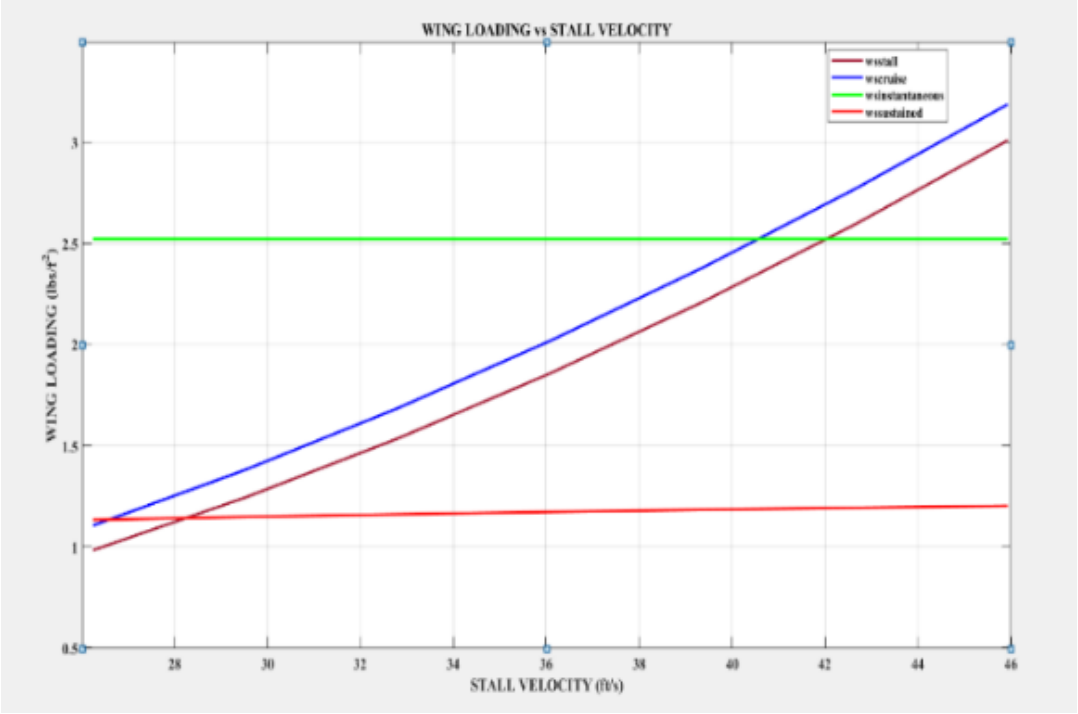

FIGURE 4. Wing Loading and Stall Velocity Graph

Empennage Configuration

H-type high boom tail is used for the empennage because it helps to escape the wake effects produced by bulky blended portion and provides more ground clearance at the empennage section during ground roll. Their sizing was iterated and calculated from the volume coefficients method and the thumbs rule[8-14].

Horizontal and Vertical Stabilizer: Horizontal stabilizer is a small horizontal tail or tail plane located at the rear of the aircraft. This stabilizer helps to counter the moment created by the wing to destabilize the plane and provides stability to the aircraft. Vertical stabilizer provides directional stability. It is mounted to the empennage (the rare fuselage) and helps to reduce aerodynamic side slip. Iterations are done for various percentages of wing areas to calculate tail size. The estimated horizontal stabilizer is 22% of wing area and that of vertical stabilizer is 36% of horizontal stabilizer. The detail tail dimensions are given in Table 3.

TABLE 3. Horizontal & Vertical Tail Specifications

Stabilizer	Span (ft.)	Root Chord (ft.)	Tip Chord (ft.)	Area (ft2)	Sweep Angle	Taper Ratio	Aspect Ratio
Horizontal	3.7204	1.6669	0.7933	4.6177	24.519°	0.48	3
Vertical	0.9842	1.1902	0.7309	1.6623	25.016°	0.61	1.8

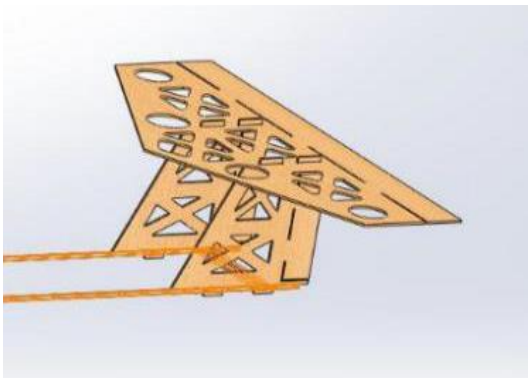

FIGURE 5. Empennage Construction

Winglets

Winglets are the devices used to restrict the flow from high pressure region to low pressure region. Winglets reduce the wingtip vortices. End Flat Plates are used as winglets for our design, which helps to achieve high L/D ratio by reducing drag with a minimal weight addition[15].

Control Surface Sizing

For the required rolling moment, the aileron span is 50% of wing semi span on each side and its aileron chord is 25% of wing chord is estimated. For the elevator span 100% of horizontal stabilizer span, the elevator chord is estimated to be 25% of horizontal stabilizer. Similarly, the rudder span is 100% of vertical stabilizer span and rudder chord is 25% of vertical stabilizer. The complete dimensions of control surfaces are tabulated below in table 4.

TABLE 4. Control Surfaces Sizing

Control Surface	Chord(m)	Span(m)	Area(m^2)
Ailerons	0.1705	0.75	0.1278
Elevator	0.0945	1.13	0.1067
Rudder	0.0752	0.52	0.0387

Servo Sizing: The main objective of the servo sizing is to calculate the torque required to overcome moments generated by control aerodynamic loading. Inertia ratio is the ratio of the load's inertia divided by the motor. Servo drives can be controlled via several interfaces. Futaba S3003 is chosen for our a/c. The torque requirements are given below in table 5.

TABLE 5. Torque Required & Produced for The Control Surface Deflection.

Control Surface	Torque required for control surface deflection (lbs.-ft)	Torque produced by servo (lbs.-ft)
Aileron	0.01088	0.0275
Elevator	0.00908	0.0275
Rudder	0.00329	0.0275

Power Plant Matching

The minimum power required is the function of Drag. Power required is equal to drag times velocity.

$$P = V x D \quad (1)$$

Total Drag is sum of Induced drag and Skin friction drag. As thrust is directly proportional to drag, the minimum thrust required for the aircraft is taken from the drag forces that the aircraft produces. The variations of Thrust with speed are plotted in Figure 6.

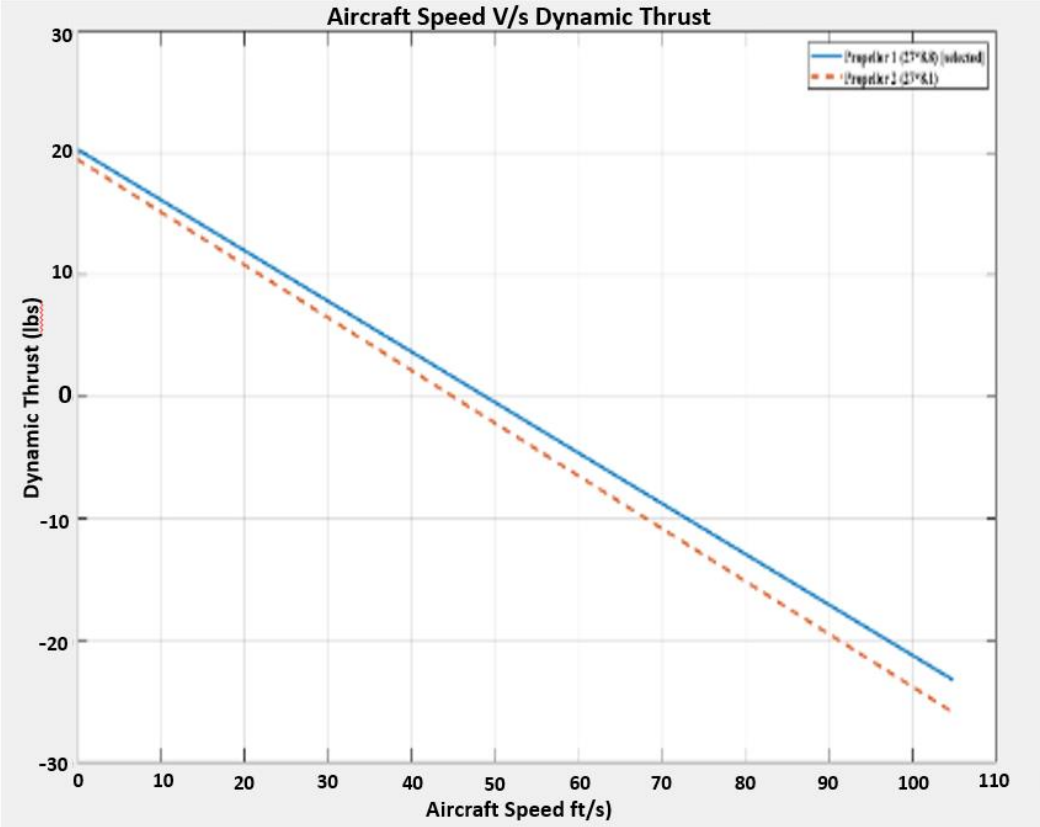

FIGURE 6. Dynamic Thrust Vs Aircraft Speed

Landing Gear

Tail dragger configuration is chosen for this design as it provides

- Greater propeller clearance.
- Takeoff distance is comparatively shorter

While landing the strut absorbs the impact load and acts as like shock absorbing pneumatic landing gear system. They are designed to with stand impact load of 70 lbs (FoS=2). Based on preliminary studies, the dimensions of Landing gear along with tyres are given in Figure 7.

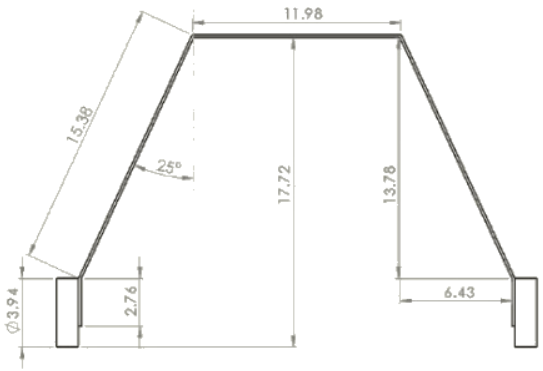

FIGURE 7. Landing Gear Design

Dimensional Drag Analysis

Drag is one of the most important parameters for an aircraft. It limits the forward movement of aircraft. It should be calculated to estimate the required thrust for our model. It is calculated as follows from the conventional drag formulae and tabulated in Table 6. The drag contributions are of wing and fuselage is plotted in Figure 8.

$$D = \frac{1}{2}\rho v^2 C_d S C_f \tag{2}$$

$$C_d = \left(C_{df} + \frac{C_l^2}{\pi * AR * e}\right)(1 + F) \tag{3}$$

Where,

$$F = 1 + 2\left(\frac{t}{c}\right) + 60\left(\frac{t}{c}\right)^4 \tag{4}$$

TABLE 6. Drag Calculation Table

Velocity (m/s)	Horizontal Tail (lb.)	Vertical Tail (lb.)	Wing (lb.)	Bulky Wing (lb.)	Landing Gear (lb.)	Induced Drag (lb.)	Total Drag (lb.)
8	0.0477	0.0366	0.2146	0.0833	0.0116	3.4585	4.8895
9	0.0589	0.0452	0.2653	0.1014	0.0142	4.4584	6.2265
10	0.0712	0.0545	0.3207	0.1227	0.0171	5.6948	7.8316
11	0.0845	0.0647	0.3809	0.1459	0.0202	7.1232	9.6599
12	0.0987	0.0756	0.4456	0.1708	0.0236	8.6217	11.588
13	0.1140	0.0872	0.5149	0.1975	0.0271	10.3675	13.7950
14	0.1303	0.0997	0.5887	0.2260	0.0309	12.0288	12.7571

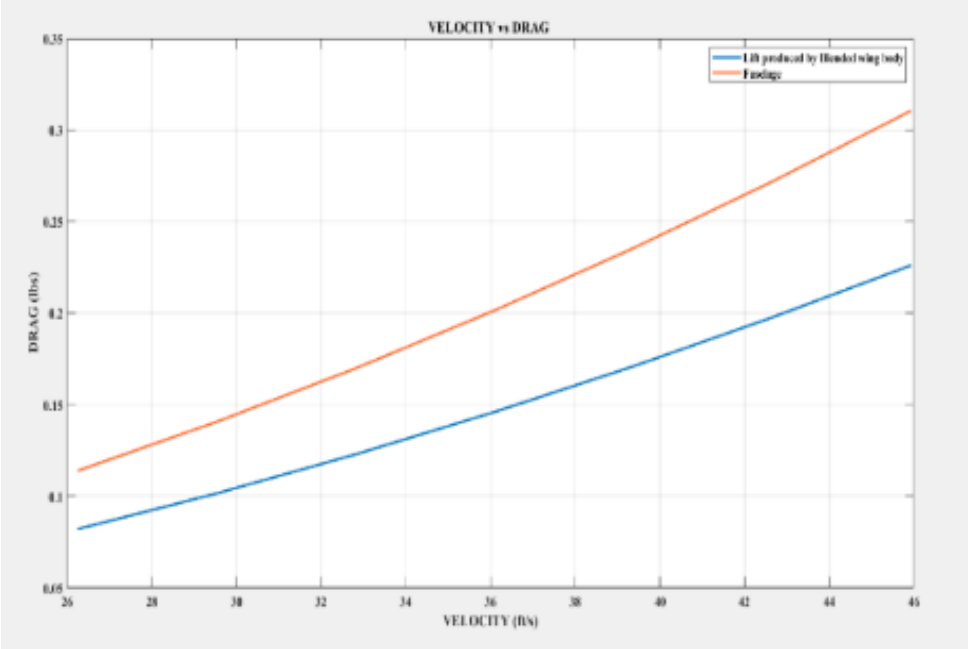

Figure 8. Comparative drag estimation between fuselage and blended wing section

PERFORMANCE AND STABILITY

Takeoff Performance

The calculated take-off velocity is 13m/s and the take-off ground distance calculated is 41.20ft. The co-efficient of ground friction is assumed 0.04. The value of Vstall is calculated as 10m/s. The calculations were performed with formulae displayed in equation 5 and 6.

$$T - \left[D + \mu_r(W - L)\right] = m\frac{dv}{dt} \tag{5}$$

$$S_{TO} = \frac{V_{TO}^2\left(\frac{W}{S}\right)}{2\left(T - \left[D + \mu_r(W - L)\right]_{av}\right)} \tag{6}$$

Landing Performance

The landing distance calculated is found to be 71.19ft. This is estimated from the formulae stated below. Approach velocity is considered 1.2Vstall as per FAR criterion i.e., 13m/s.

TABLE 7. Take-Off & Landing Performance

Characteristics	Results
V_{TO}	13 m/s
V_{TD}	11.5m/s
Friction co-efficient	0.04
Approach velocity	13 m/s
Take-off distance	41.20ft
Landing distance	71.19ft

ESTIMATION OF CENTRE OF GRAVITY

Centre of Gravity (C.G) of plane should be at the aircraft Aerodynamic Centre for longitudinal stability. The C.G of this aircraft is estimated as (20.708, 0, 2.125) with and without payload. Aerodynamic center of the wing is 20.708 inch from datum. C.G estimation is done using SOLID WORKS software with a static margin of 10% is assumed for a stable UAV.

TABLE 8. Estimation of Center of Gravity

Component	Weight (lbs.)	Position of C.G (in.)
Motor	0.992	(1.02,0,0)
Battery	1.984	(3.07,4.09,1.19)
Payload	10.36	(14.77,0,0.98)
Electronic Speed Controller (ESC)	0.44	(3.86,4.09,0.5)
Wing servos	0.528	(30.90, +31.49,1.96)
Horizontal Tail servo	0.264	(74.8,0,11.81)
Vertical Tail servos	0.528	(78.74, +5.9,1.96)
Landing gear servo	0.264	(70.86,0,3.93)

MODELING AND ANALYSIS

Modeling

The assembled design part is generated in SOLIDWORKS. The crucial role in the weight and strength of aircraft lies in fabrication. Balsa wood is used for the entire body structure of aircraft. To get the high stiffness and strength,

aluminum is used. Glue is used to join the wooden parts together. Covering film is used for covering the entire assembled skeletal framework and gives a proper finishing.

Main Assembly

At last, the aircraft members are completely mono coated with the covering film to attain a finest finishing, minimizing the surface drag. The final preparation is made to test the flight. Checks will be made on servos and their functioning while flight testing. Final touches will be conducted in order to ensure a successful and safe flight.

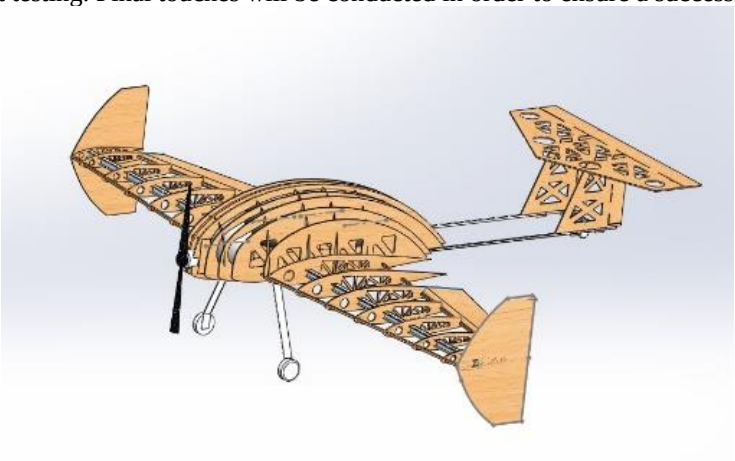

FIGURE 9. Final Assembly

Flow Analysis

The flow analysis was carried out on complete wing using CFD. Computational fluid dynamics is the branch of fluid dynamics that utilizations numerical strategies and calculations to examine the issues [3]. In the ANSYS workbench fluid flow, fluent analysis is selected, and the model is imported into the design modular geometry. A domain of 4m*4m*4m is enclosed around the body, with the help of Boolean operation we unite and subtract the individual parts and the enclosure around the structure. The computational analysis results which are obtained are validated with the manual calculation done with the standard formulas. The analysis proved the calculation worthiness and paved the way for location needed for aerodynamic design optimizations and structural reinforcements. The velocity contour is given in Figure 10.

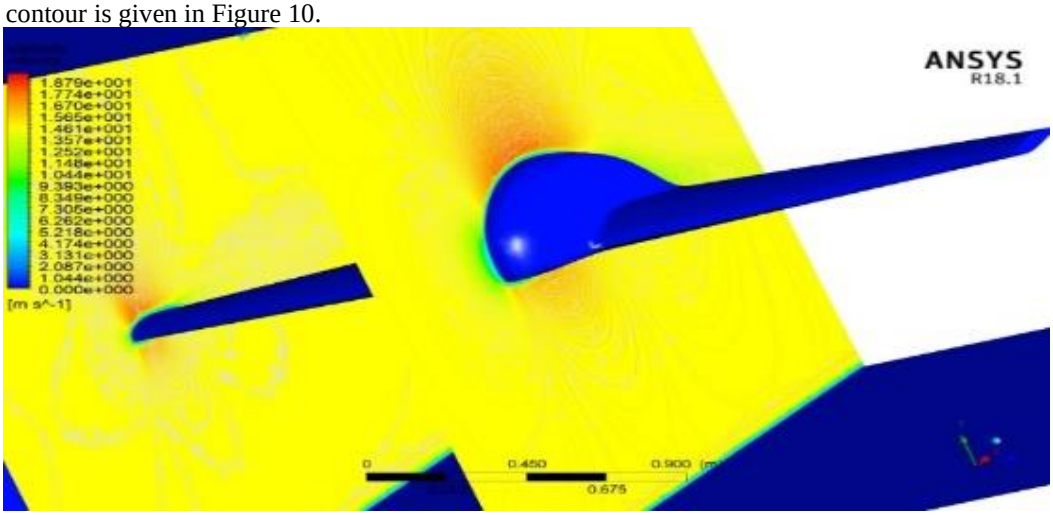

FIGURE 10: Velocity Magnitude Over aircraft

Structural Analysis

Structural analysis of wing and landing gear of aircraft are performed on ANSYS software it is used to analyze the structural integrity of components prior to the construction. Static loads tests were carried out on wings constructed with, spars and trussed structures landing gear. Materials selected are balsa wood, plywood, aluminum 2024 T3 (for spar) and aluminum 7075 T6 (for landing gear) used for construction and its material properties are mentioned as given in the table 10 illustrated below. Structural analysis with load of 60 lbs. is performed on the wing and load of 40 lbs. on landing gear. The results are illustrated below.

TABLE 9. Material Properties

Material	Young's modulus (N/m^2)	Mass density Kg/m^3	Shear modulus (N/m^2)	Poison's ratio
Balsa wood	3	160	0.3	0.38
Aluminum 2024 T3	72.4	2780	28	0.33
Aluminum 7075 T6	72	2810	26.9	0.33

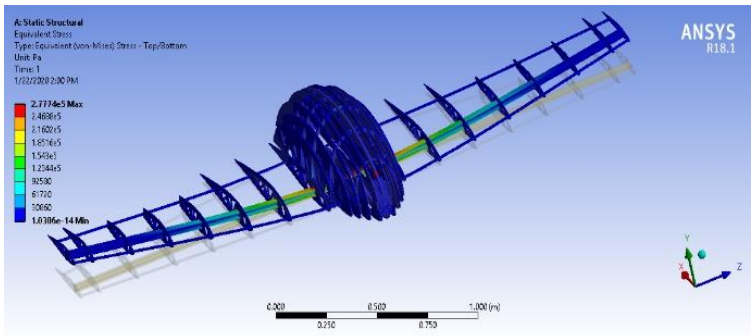

Figure 11. Stress Induced in the Wing Structure

The results for Wing and Landing gear were analyzed and it was observed that the deformation and stress experienced by the wing for the considered load are within the limit of material. The contour of Von Moises stress for wing and Landing gear are given in Figure 11 and Figure 12 respectively. The details are given in table 10.

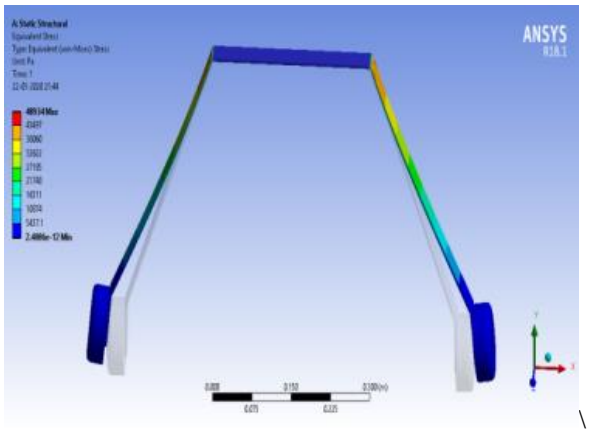

Figure 13. Stress Distribution on Landing Gear

TABLE 10. Structural analysis results

Parameter	Wing	Landing Gear
Von Moises Stress	2.77 e5 Pa	4 e5 Pa
Deformation	1 mm	0.24 mm

CONCLUSION

A blended wing aircraft was designed, fabricated by performing engineering analysis, and completed the construction of final design which meets all the design constrains. All the calculations were performed at mean sea level i.e., Standard atmospheric environments at lower altitude. A successful wide body UAV has been designed with maximum efficiency which can carry huge volumetric cargo. It could carry 5 soccer balls of 27-inch circumference. This lays the path for further research and enhancement of the UAV for commercial use.

Table 11. Conclusion

S. No	Parameter	Achieved
1	Dimension	118 In. Wingspan
2	Empty Weight	26.45lbs.
3	Take-Off Ground Roll	41.20 ft.
4	Landing Ground Roll	71.19ft.
5	Payload (Lbs.)	10.36 lbs.

REFERENCES

1. K. Simhachalam Naidu, G. Shruthi Keerthi, V.V.S. Nikhil Bharadwaj, "CFD Analysis of Blended Wing Body and B2 Wing", *International Journal of Engineering Sciences & Research Technology*,**5,** 2, (2016), pp. 492-513
2. K Shiva Shankar, B Nagaraj Goud, Sreekanth Sura, "An UAV with Twin Propellers Driven by Single Motor", *International Journal of Innovative Technology and Exploring Engineering*, **9**, 2, (2019), pp. 4109-4113
3. K Sreelakshmi and Kota KSR Jagadeeswar, "Aerodynamic analysis over Unmanned Aerial Vehicle (UAV) using CFD", *IOP Conference Series: Materials Science and Engineering*, **455**, (2018), pp. 1-10.
4. S. B. Tiwari, R. Suresh, C. K. Krishnadasan. "Design, Analysis and Qualification of Elevon for Reusable Launch Vehicle", *Journal of The Institution of Engineers (India)*: Series C, 2017.
5. Andy Lennon, "R/c Model Aircraft Design", Air age Media Inc. ISBN:0-911295
6. Daniel P.Raymer, "Aircraft Design: A Conceptual Approach", Fourth Edition, AIAA, 2006.
7. John D Anderson Jr, "Introduction to Flight", Fifth Edition, Tata Mc Graw Hill, 2007.
8. Pascual Marque's, "Fight Stability and Control of Tailless Lambda Unmanned Aircraft".
9. Prof. T.G. Talapurkara, Airplane Design, NPTEL Lectures
10. Zhou Jie Lyu's, "Aerodynamic Design Optimization Studies of a Blended-Wing-Body Aircraft".
11. Liebeck, R. H., "Design of Subsonic Airfoils for High Lift," Journal of Aircraft, **15**, (1978), pp. 549–561.
12. Liebeck, R. H., Page, M. A., Rawdon, B. K., Scott, P. W., and Wright,R. A., "Concepts for Advanced Subsonic Transports," NASA CR 4624, (1994).
13. Liebeck, R. H., Page, M. A., and Rawdon, B. K., "Blended-Wing-Body Subsonic Commercial Transport," AIAA Paper 98-0438, (1998).
14. ArunKumar K, Veeranjaneyule K, "Mechanism and Performance analysis of Morphing Wing", IJITEE,2019.
15. Mr. K Veeranjaneyulu "Design and Computational Analysis of Fixed Wing of Micro Aerial Vehicle", IJMETMR Volume 2 Issue 12.
16. Mr. K.Veeranjaneyulu, Karupalli, Anvesh, M Satyanarayana Gupta, "Aerodynamic Design of Wing for Supersonic Flight Vehicle" , ISSN: 2320-3706, Yuva Engineers Sept 2016.

RESEARCH ARTICLE | MAY 22 2023

"Numerical simulation of a blunt body to investigate drag characteristics with active and passive device"

Dharavath Easwer ✉; B. Manideep; A. Sai Kumar

AIP Conference Proceedings 2492, 020067 (2023)
https://doi.org/10.1063/5.0137243

"Numerical Simulation of a Blunt Body to Investigate Drag Characteristics with Active and Passive Device"

Dharavath Easwer[1, a)], B. Manideep [1, b)] and A Sai Kumar[1,c)]

[1]*Department of Aeronautical Engineering, MLR Institute of Technology, Hyderabad, Telangana, India.*

[a)] Corresponding Author: dharavtheaswer@gmail.com
[b)] manideepbalusuni.9@gmail.com
[c)]ask.mraj@gmail.com

ABSTRACT: Many researchers have been taken to examine novel designs for good and safe, dependable and inexpensive hyper-sonic personal flights by showing interest in space tourism and business transport systems. The hypersonic vehicle has always been significantly protected by aerodynamic heating and drag. Various techniques/methods for reducing aero heating and drag levels have been developed, with counter/lateral flowing and aerospikes/disks proving to be particularly effective and cost-effective. Many studies have concentrated on the flow of jets, and others have concentrated on the use of aerospikes to solve these challenges. However, few studies have focused on the combination of the two. As a result, in this study, a unique combination of flowing jet and aerospike is examined for reducing aero-heating and drag levels on the re-entry vehicle's blunt forebody. The investigation will be based on the numerical approach, the CFD solver fluent will be used for the investigation. Initially, a code verification will be performed, consequently followed by the numerical investigation of the blunt body with a combined (flow jet and spike) concept.

Keywords: the research is numerically based and the CFD solver is utilized fluently for the study. A code verification will initially be done, followed by a numerical examination of the body of the blunt body with a combined idea (flow jet and spike).

INTRODUCTION

A fluid-moving body has a drag force generally split in two parts: the friction drag and the pressure drag. It's because of the viscosity. Frictional drag (viscous drag) is the result of friction between the fluid and its surface. It creates border layers. Pressure drag (drag) is the eddying movement generated by the passage of the body in the fluid. This trajectory is linked to the creation of a wake, which is clearly visible behind a boat.

Many of the innovative and interesting vehicles planned for the twenty-first century will be dedicated to hypersonic flow. Hypersonic flights have been accomplished, both called and unidentified, although it is far from simple. Decades ago, the North American X-15 and other launch vehicles attained hypersonic speeds. Even with extensive flight testing and analysis, these vehicles require a great deal of careful engineering. A hypersonic flow over Mach 5 may be defined as a standard thumb rule. This number, however, is not in stone and relates solely to a specific max number of physical flow phenomena such as powerful impact waves, thin shock layers, entropy layers, viscous interactions, and high temperatures, heavy enthalpy flows. Viscous forces and high temperature gas dynamics are two significant phenomena that influence hypersonic flow characteristics. The viscous force that works on the test body can generate complicated border layers, typically leading to the transitional layer flow.

Laminar-turbulent transition is a cutting-edge research area. The analysis of viscous boundary layers is necessary in order to correctly capture heat transfer and skin friction values across the test body of a hypersonic vehicle in flight. Mach number, number of reynolds, assault angle, nose shape, and test body temperature all influence the laminar-

Advancements in Aeromechanical Materials for Manufacturing: ICAAMM-2021
AIP Conf. Proc. 2492, 020067-1–020067-9; https://doi.org/10.1063/5.0137243
Published by AIP Publishing. 978-0-7354-4438-6/$30.00

turbulent transition. It is extremely difficult to replicate the same transition point on the same shape at similar free-stream circumstances across numerous wind tunnels.

The high temperatures at the limiting layer and behind shock waves, on the other hand, stimulate fluid molecules at the microscopic level. These excited molecules can increase the vibration energy and dissociate and ionize if they are high enough. On the other hand, the high temperatures on the border layer and the fluid molecules are excited by shock waves at the microscopical level.

LITERATURE SURVEY

A space vehicle's trajectory might be non-lifting, lifting, terminal, or thrusting (jet-on). The base pressure and heat flux are important for the successful landing of a spacecraft and the efficient deployment of a parachute. Cassanto [4] determined the base pressure using a series of wind tunnel and free-flight experiments. Lamb et al. [5] investigated how wake flow characteristics, freestream conditions, and boundary layer edge features at the module's shoulder impact the base pressure on the reentry vehicle at high speed.

A supersonic research is carried out with computer fluid dynamics (CFD) and wind tunnel experiments done by SPR's INT-blunted cone flare. The experimental and computational simulations of the flow behind a truncated cylinder in a supersonic flow by Togiti et al [6] show a virtually constant base pressure coefficient. The Apollo AS-202 base flow analyses are provided by Wal pot et al. [7]. The arc shock wave comes in front of the blunt body surrounded by a sub-supersonic area.

Chester [8] investigated the wall pressure distribution, sonic line location, and shock stand-off distance on the spherical cap surface at extremely high speeds with an adiabatic index close to unity, which predicts a single point at 60° from the stagnation point. The analytical approach for high-speed flow over the blunt-body, on the other hand, is judged to be the most difficult and complex. The flow field above the reentry capsule is further complicated by the presence of a bevel at the shoulder and the shape of the reentry module's base shell.

High-speed aerodynamic simulations were conducted on the Commercial Experiment Transport (COMET) reentry capsule. The thin layer laminar Navier-Stokes equation must be solved. Yamamoto and Yoshioka [9] computed flow fields across the Orbital Reentry Experiments using the CFD method in conjunction with flight aerodynamic data (OREX).

The aerodynamic characterization of the CARINA reentry module in low supersonic Mach regimes was carried out using theoretical and experimental techniques [10]. Ross et al. [11] tested the orion crew module (OCM) in a wind tunnel to estimate aerodynamic forces. The team investigated a variety of wind tunnels in order to represent not only the aerodynamics but also the aero-acoustic environment that the Orion may experience during normal ascents and launch aborts.

Viviani et al. [1] undertake CFD assessments of space vehicles using H3NS and FLUENT programmes to study the flow field over different capsules.

Researchers have been researching hypersonic flow through cones for almost 60 years. Tables for symmetrical hypersonic flow have been created using several mathematical approximation models, such as Bartlett's [12]. Sapunkov [13] expanded on his research into hypersonic flow through yawed cones, providing solutions for the flow field between the shock and the cone surface. However, his method had surface singularities and was thus inapplicable near the cone surface. In recent decades, CFD has been widely used to analyse hypersonic flows over conical shapes and other space vehicles. LaBeau, Moss and Glass [14] investigated the Mach 10 flow in a low-density wind tunnel through a steep double cone using the direct simulation Monte Carlo (DSMC) method. In the solver, they identified A unique sensitivity to grid resolution. Gosse and Kimmel [15] ran Mach 8 simulations on an elliptic cone and discovered that CFD and experiment agreed quite well.

The primary goal of the Blunt vehicle's design is to function as a shield to protect the vehicle from extreme aerodynamic heating. The goal of the hypersonic Blunt vehicle is to reduce heat accumulated by the vehicle upon reentry into the atmosphere. As a result, a well-constructed Blunt vehicle may function as a protective cover for the produced heat while also reducing aerodynamic drag. Concerning the significance of wind tunnels in fluid propulsion research, von Neumann stated in 1946, "Indeed, to a large degree, experimentation in fluid dynamics is done under situations where the fundamental scientific principles do not appear to be uncertain, wherever the quantities to be determined are completely defined by existing equations

Wind tunnels, for example, are now employed as computer devices to integrate the PDE's of fluid dynamics." F.J. Schrijer, F. Scarano, and B.W. van Oudheusden [16] used the QIRT method on a Blunt Cone-Flare and experimented with boundary layer detachment and reattachment. Under Quantitative Infrared Thermography, transient heat transfer

data are distributed on a Blunted cone flare model for a relatively brief period of time in a hypersonic facility at Mach 9 mistreatment (QIRT). The surface temperature was measured using an infrared vision camera, and the temperature data was successfully correlated to the heat transfer coefficient using two separate reduction approaches.

THE METHODOLOGY

All fluid dynamics simulations will be carried out using ANSYS FLUENT. FLUENT uses a finite volume technique to solve the complete Navier-Stokes's equation, and its numerical methods are continually updated to employ the most recognized and newest algorithms discovered in the academic community. For simulation setup and simulation, ANSYS WORKBENCH 16.0 is utilized.

ANSYS DESIGNMODELER should be used to model the selected shape to recreate the hypersonic flux areas. The geometry is then meshed using the structural mesh tools included in the solver's meshing module. The grid is therefore crucial in the CFD-post.

For the desired flow field, FLUENT is utilized to solve. And the post-processing is confirmed for hypersonic flow and its CFD code's reliability and limits are investigated. This will be accomplished by choosing experimental test cases and reproducing them with the CFD solver.

These test cases will be carefully chosen to address the key flow phenomena seen in the hypersonic region. FLUENT's hypersonic viscous effects at the boundary layer will be confirmed. These findings will be contrasted with shock tunnel data.

FLUENT's CFD code may then be appropriately used as a design tool for the following study, which is the flow analysis of the Blunt vehicle using shock tunnel data, once the validation simulations are completed and its credibility and limits are established.

ANSYS CFD: The engineering technique to modelling systems, processes and equipment, including gas and liquid motion, heat- and mass-transfer, chemical reactions, and related physical phenomena, is computational fluid dynamics (CFD). It may be used for reducing the pressure drops, aerodynamic lift prediction, or dragging simulation, etc. Airflow determination in air conditioning rooms, adequate cooling, optimization of mixing rates etc.

When you successfully mix the more recognized brands for fluid simulation - ANSYS® FLUENT® and ANSYS® CFX® - you generate CFD needs at a time when the dependability, reliability, and performance of the goods are critical. ANSYS provides a comprehensive set of advanced CFD software tools, as well as unique modelling capabilities, to assist you in reducing total time. To solve the problem, ANSYS software is trusted by more product developers throughout the world for its fluid simulation platform's accuracy, dependability, and speed.

ANSYS is committed to providing highly accurate fluid dynamic technology for the creation of simulation-driven products. The ANSYS® Workbench TM platform is built on the ability to co-emulate, in addition to providing the most validated and widely used CFD solutions on the market. Users of ANSYS CFD solutions can combine them with our other industry-leading solver solutions for structural mechanics or electrical characteristics to create a model. This lowers engineering assumptions and makes their models more consumer-friendly.

CFD ANSYS solutions provide exceptional efficiency, allowing you to analyzed a large number of automated design variants without the need for complex programming. ANSYS provides integrated tools that not only assist you discover the most vulnerable parameters in your design, but also highlight which design parameters require the most stringent control. Including tools for integrated design (shape) and Six Sigma analysis. ANSYS Simulation Software helps you to design and deliver better products more rapidly for solid performance.

The governing equation of cfd

Continuity Equation:

- We use the physical principle is **"conservation of mass"** to derive the equation.
- The Physical principal is =

Net mass flow across the surface S from the control volume to Time rate of mass reduction within control

$$\frac{\partial}{\partial t}\iiint_{\mathscr{V}} \rho \, d\mathscr{V} + \iint_{S} \rho \mathbf{V} \cdot \mathbf{dS} = 0$$

The momentum equation:

the fundamental physical principal used is Newton's second law.
The X-Momentum of N-S equation:

$$\frac{\partial(\rho u)}{\partial t} + \nabla \cdot (\rho u \mathbf{V}) = -\frac{\partial p}{\partial x} + \frac{\partial \tau_{xx}}{\partial x} + \frac{\partial \tau_{yx}}{\partial y} + \frac{\partial \tau_{zx}}{\partial z} + \rho f_x$$

similarly, in Y and Z moments also follows.

The energy equation:

We use the physical principle here is **first law of thermodynamics Energy is conserved**. This law states that

The rate of energy change inside a fluid element. → The net flux into the fluid element is → The amount of work done on an element as a result of body and

The energy equation can be written as:

$$\rho \frac{D}{Dt}\left(e + \frac{V^2}{2}\right) = \rho \dot{q} + \frac{\partial}{\partial x}\left(k \frac{\partial T}{\partial x}\right) + \frac{\partial}{\partial y}\left(k \frac{\partial T}{\partial y}\right) + \frac{\partial}{\partial z}\left(k \frac{\partial T}{\partial z}\right)$$
$$- \frac{\partial(up)}{\partial x} - \frac{\partial(vp)}{\partial y} - \frac{\partial(wp)}{\partial z} + \frac{\partial(u\tau_{xx})}{\partial x} + \frac{\partial(u\tau_{yx})}{\partial y} + \frac{\partial(u\tau_{zx})}{\partial z} + \frac{\partial(v\tau_{xy})}{\partial x} + \frac{\partial(v\tau_{yy})}{\partial y}$$
$$+ \frac{\partial(v\tau_{zy})}{\partial z} + \frac{\partial(w\tau_{xz})}{\partial x} + \frac{\partial(w\tau_{yz})}{\partial y} + \frac{\partial(w\tau_{zz})}{\partial z} + \rho \mathbf{f} \cdot \mathbf{V}$$

STRUCTURE ANALYSIS AND MODELING OF ELEMENTS

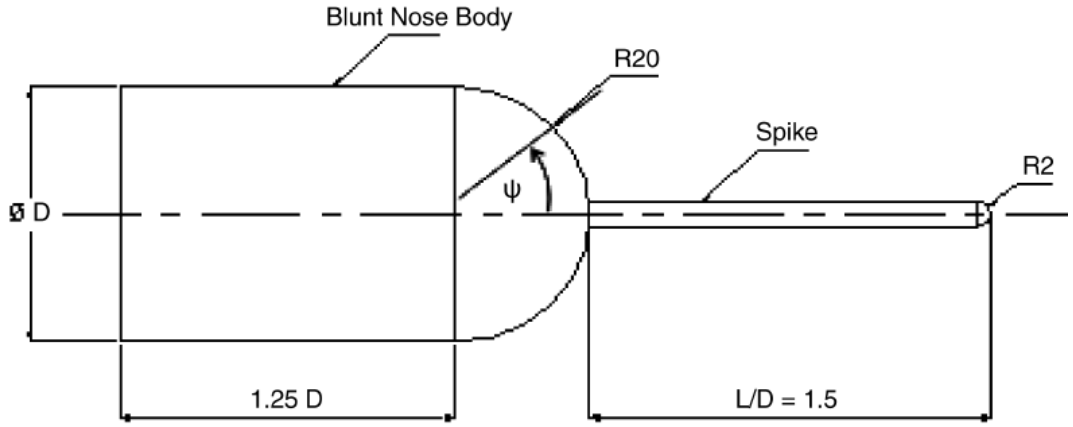

FIGURE 1. The 2-D geometry for a Blunt body.

The main screen of workbench has several modules; for this study, Fluent code is used. We chose and opened the fluent code. It consists of several phases, the first of which is to build a geometry. A 2-D axisymmetric geometry is constructed to decrease the computing cost of the study.

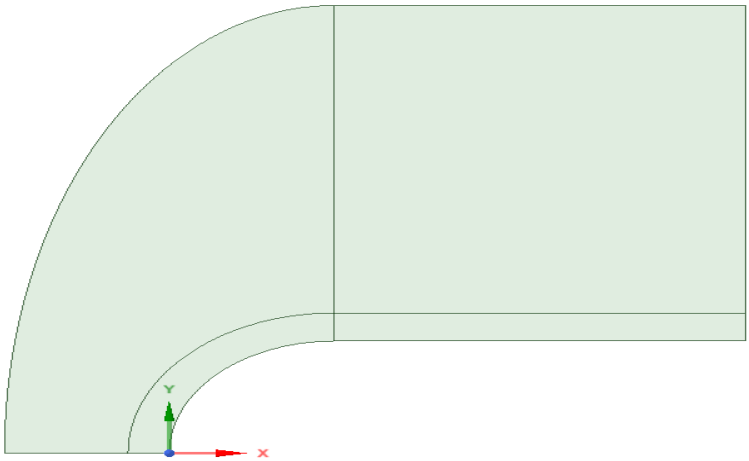

FIGURE 2: Creating of the geometry- non-Spike

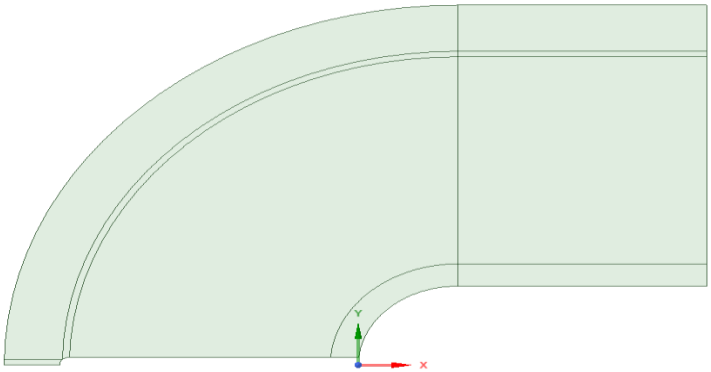

FIGURE 3: The geometry – spiked for the Blunt Body.

The Hypersonic Vehicle's measurements are in Millimetres. Various studies have investigated the axi-symmetric technique of analysis, and it has proved to be useful for analysis involving symmetric geometries. Various scholars investigate the axi-symmetric technique of analysis, and it has shown to be useful for analysis involving geometries with symmetry across the central axis. As a result, we must construct a side perspective of the vehicle.

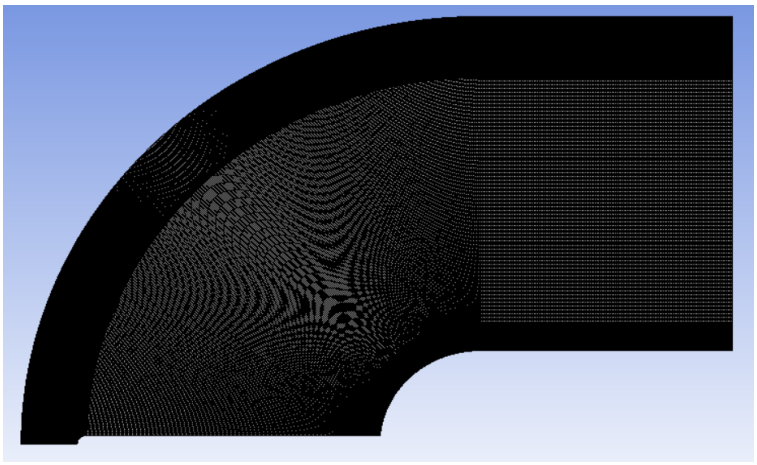

FIGURE 4. Domain

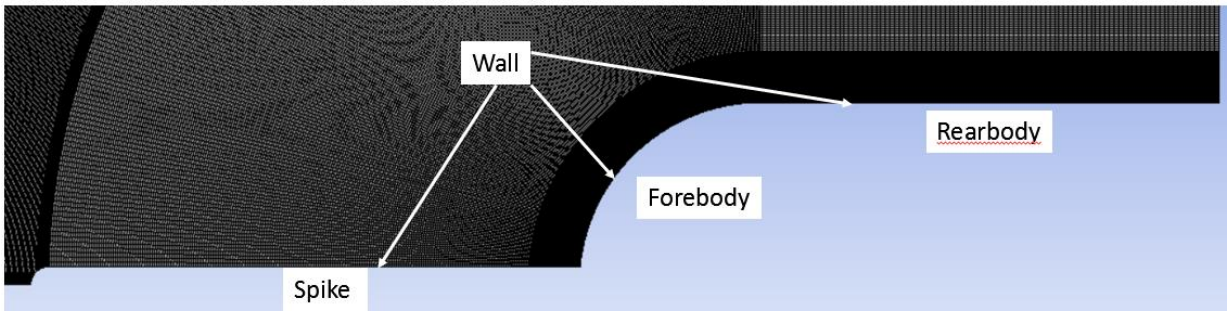

FIGURE 5. Meshed Blunt Body

RESULTS AND DISCUSSION

After completing the simulation process, different parameters are analysed to compare the hyper-sonic parameters of the vehicle, first of all, the plots are extracted with the body parts, for the variation in the static pressure over the fork and for the vehicle with and sans spike and temperature variation

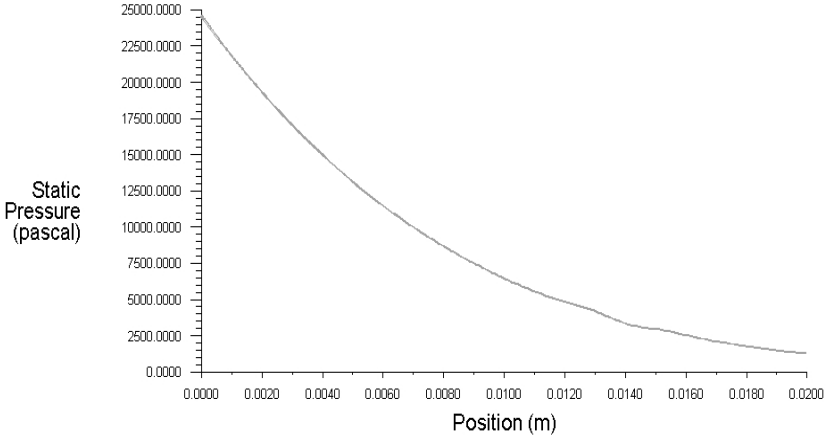

FIGURE 6: Static Pressure – Forebody – Non spike

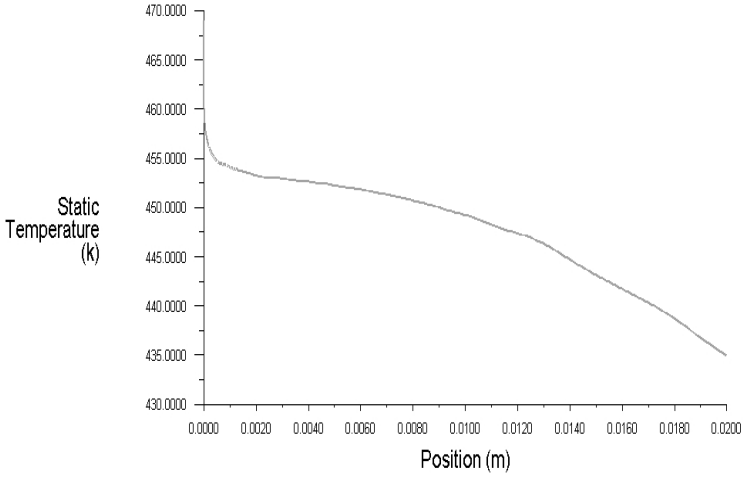

FIGURE 7: the static Temperature – Forebody – Non spike of the Blunt Body

TABLE 1. Data set

S.NO	Experimental [20]	Numerical (Present)	Blunt body with Flat Aerospike
Without spike	0.89	0.897	-
With spike	0.255	0.25	0.195

The flow configuration of the Mach Number for the specified model equipped with a combination of Counter Flowing Jet and the Aerodisk is represented in the figures above. The passage of high-pressure air from the aerodisk surface to upstream flow may be detected using stream traces. The counter, which flows throughout, changes the shear layer out of the aerodisk. The shear layer is pushing away from the aerodisk and the overall flow arrangement is changed. This increases the recirculation zone by the flow field (as seen in the above figure). This recirculation zone crosses an overall lowering of the drag coefficient and traverses a low velocity and pressure zone.

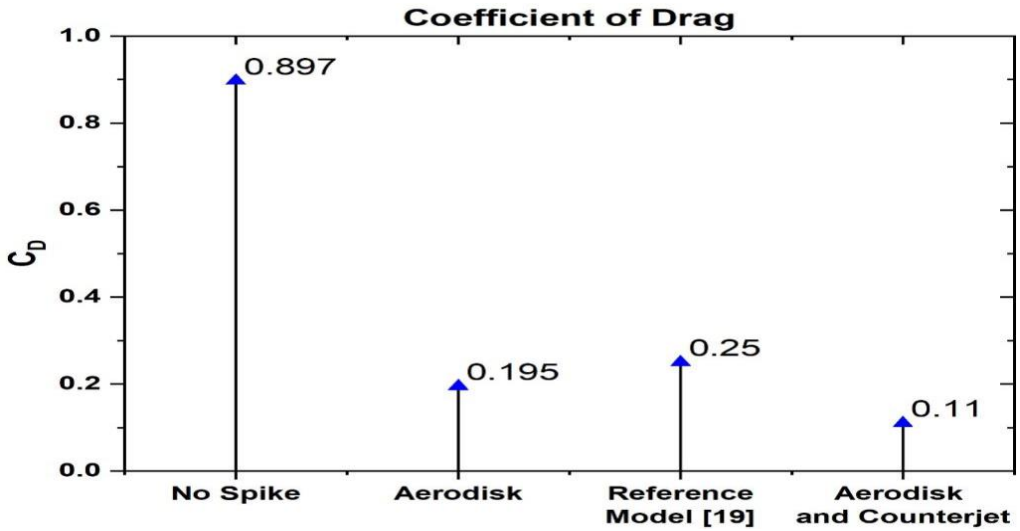

FIGURE 8: Coefficient of Drag of a Blunt Body for all the models investigated

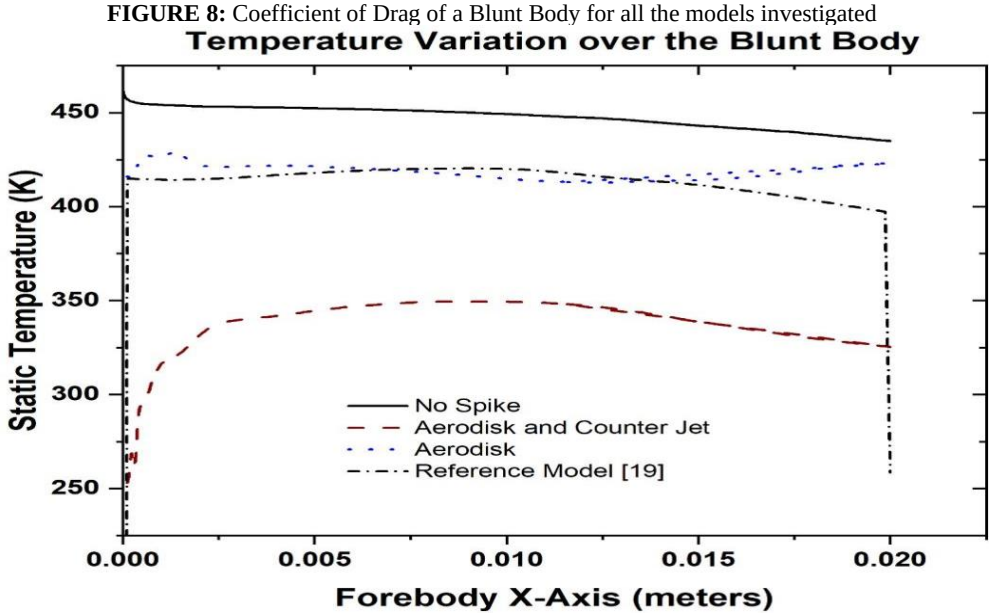

FIGURE 9: the Static Temperature variation over the Blunt Body

CONCLUSION

This experimental scenario is numerically done using commercial CFD software to test its strengths and.weakness when hypersonic flow is applied to a blunt body.

It has been revealed via research that the spike causes two significant changes in the flow field upstream of the forebody. To begin, it replaces the strong detached shock wave with a succession of smaller oblique shock waves. Second, it will act as a "flow separator," causing the boundary layer to separate from the surface and the creation of a shear layer. The latter extends downstream, reattaches to the body surface, and surrounds a zone of recirculation with low pressure and velocity values. Because this zone screens a major portion of the blunt forebody surface, surface pressure and temperature are significantly reduced. Only at the zone of shear layer reattachment on the blunt forebody are the local heating rate and surface temperature high. At the reattachment zone, a shock wave is also generated to move the flow beyond the shear layer parallel to the forebody surface. Just downstream of this reattachment shock, flow pressure reaches high local levels. Regardless, the overall consequence is a significant reduction in drag and aerodynamic heating.

Using all of the models evaluated in the study, the counterflowing jet in conjunction with the aero disk showed to be the most effective in lowering total forebody drag and surface temperature.

REFERENCES

1. A. Viviani and G. Pezzella, "Aerodynamic and Aerothermodynamic Analysis of Space Mission Vehicles". 2015.
2. J. D. Anderson, “Hypersonic and High Temperature Gas Dynamics.” McGraw-Hill Book Company.
3. C. J. Roy and F. G. Blottner, Review and assessment of turbulence models for hypersonic flows: 2D/Axisymmetric cases, vol. 12, no. January. 2006.
4. J. M. Cassanto, “A base pressure experiment for determining the atmospheric pressure profile of planets,” *J. Spacecr. Rockets, vol. 10, no. 4, pp. 253–261, 1973, doi: 10.2514/3.61875.*
5. J. P. Lamb and W. L. Oberkamp, “Review and development of base pressure and base heating correlations in supersonic flow,” *J. Spacecr. Rockets, vol. 32, no. 1, pp. 8–23, 1995, doi: 10.2514/3.26569.*
6. *S. J. Cameron Tropea, New Results in Numerical and Experimental Fluid. .*
7. L. Walpot, “Numerical Analysis of the ARD Capulse in S4 Wind Tunnel,” *4th Eur. Symp. Aerothermodyn. Sp. Appl., no. July, 2001.*
8. W. Chester, “Supersonic flow past a bluff body with a detached shock Part I Two-dimensional body,” *J. Fluid Mech., vol. 1, no. 4, pp. 353–365, 1956, doi: 10.1017/S0022112056000214.*
9. Y. Yamamoto and T. Ik, “CFD and FEM Coupling Analysis of OREX Aerothermodynamic Fligh Data,” *AIAA J., 1995.*
10. P. GASBARRI, M. A. SOLAZZO, and A. SANSONE, “Aerodynamic Characterization of the CARINA Re-Entry Module in the Low Supersonic Regimes,” *Aerothermodyn. Sp. Veh. Proc. 2nd Eur. Symp., vol. ESA SP-367, no. May, pp. 41–49, 1994.*
11. J. C. Ross and G. J. Brauckmann, “Aerodynamic and aeroacoustic wind tunnel testing of the orion spacecraft,” *29th AIAA Appl. Aerodyn. Conf. 2011, no. June, pp. 1–19, 2011, doi: 10.2514/6.2011-3160.*
12. B. R. S. Bartlett and B. R. S. Bartlett, “Tables of Supersonic Symmetrica ! Flow around Right Circular Cones , with and without the Addition of Heat at the Wave Tables of Supersonic Symmetrical Flow around Right Circular Cones , with and without the Addition of Heat at the Wave,” 1968.
13. I. G. Sapunkov, “Hypersonic flow past a circular cone at an angle of attack,” *J. Appl. Math. Mech., vol. 27, no. 5, pp. 1422–1436, 1963, doi: 10.1016/0021-8928(63)90081-9.*
14. J. N. Moss, “Hypersonic Shock Interactions About a 25°/65° Sharp Double Cone,” *vol. 425, pp. 425–432, 2003, doi: 10.1063/1.1581578.*
15. R. Gosse and R. Kimmel, “CFD study of three-dimensional hypersonic laminar boundary layer transition on a Mach 8 elliptic cone,” *39th AIAA Fluid Dyn. Conf., no. June, pp. 1–11, 2009, doi: 10.2514/6.2009-4053.*
16. F. F. J. Schrijer, F. Scarano, and B. W. van Oudheusden, “Experiments on hypersonic boundary layer separation and reattachment on a blunted cone-flare using quantitative infrared thermography,” 12th AIAA Int. Sp. Planes Hypersonic Syst. Technol., no. December, 2003, doi: 10.2514/6.2003-6967.
17. Y. Liu and Z. Jiang, “Concept of non-ablative thermal protection system for hypersonic vehicles,” *AIAA J., vol. 51, no. 3, pp. 584–590, 2013, doi: 10.2514/1.J051875.*

18. D. Dirkx and E. Mooij, “Optimization of entry-vehicle shapes during conceptual design,” Acta Astronaut., vol. 94, no. 1, pp. 198–214, 2014, doi: 10.1016/j.actaastro.2013.08.006.
19. J. Peter Reding “Effects of external burning on spike-induced separated flow,” J. Spacecr. Rockets, vol. 20, no. 5, pp. 452–453, 1983, doi: 10.2514/3.25628.
20. R. Kalimuthu, R. C. Mehta, and E. Rathakrishnan, “Experimental research on spiked body in hypersonic flow,” Aeronautical Journal, vol. 112, no. 1136, pp. 593–598, 2008, doi:10.1017/S0001924000002554.
21. R. Yadav, G. Velidi, and U. Guven, “Aerothermodynamics of generic re-entry vehicle with a series of aerospikes at nose,” Acta Astronaut., vol. 96, no. 1, pp. 1–10, 2014, doi: 10.1016/j.actaastro.2013.11.015.

RESEARCH ARTICLE | MAY 22 2023

Modelling and CFD analysis of supercritical airfoil with slotted flap at various flight segments

A. Sai Kumar ✉; M. Ganesh; Nirmith Kumar Mishra

AIP Conference Proceedings 2492, 020043 (2023)
https://doi.org/10.1063/5.0113316

Modelling and CFD Analysis of Supercritical Airfoil with Slotted Flap at Various Flight Segments

A Sai Kumar[1,a)], M Ganesh[1,b)] and Nirmith Kumar Mishra[1,c)]

[1]*Department of Aeronautical Engineering, MLR Institute of Technology, Hyderabad, India.*

[a)] Corresponding author: ask.mraj@gmail.com
[b)] ganesh.manikonda@gmail.com
[c)] nirmithmishra@gmail.com

Abstract. This paper presents the CFD analysis for a Supercritical Airfoil with a slotted flap. The analysis has been carried out for the Flight segments- Takeoff, Cruise & Landing. The elements were Modelled in CATIA V5 R20 and then analyzed in ANSYS fluent to obtain the lift and drag Coefficients, the results were then compared with a Cambered Airfoil of similar configuration analyzed separately. For the flight segments Takeoff & Landing, the airflow is considered to be subsonic and for the flight segment Cruise the airflow is considered as transonic as to study the Critical Mach Number and the behavior of transonic buffet around the airfoil. The contours for transonic regime were then compared with Cambered Airfoil to validate the efficiency of Supercritical Airfoil and to observe the location of Shock waves formed at Critical Mach Number for both Supercritical Airfoil and Cambered Airfoil configurations respectively.

Keywords: Supercritical Airfoil, NACA 0012, Critical Mach Number, Turbulent viscous Models, Mach Number.

INTRODUCTION

The concept of Supercritical Airfoils was introduced by Richard Whitcomb in order to avoid quarter chord formation of wave drag in Conventional Cambered airfoils. The rise in wave drag would allow formation of shock waves and instant reduction in overall lift produced by the wing. The issue with cambered airfoils is that they show poor Aerodynamic characteristics at transonic speeds due to the curved/ cambered upper surface which accelerates the air. This acceleration of air is best suitable for subsonic flows but not the transonic flow where the freestream Mach Number is accelerated on the upper surface which becomes equal to Speed of Sound or more forming Supersonic flow. When the flow becomes equal to speed of sound or more, the shock formation is inevitable [10-11]. To avoid such a behavior, the concept of airfoil with flat upper surface and cambered bottom surface with a large leading edge nose radius is more suitable, which is the concept behind the Supercritical Airfoils. In case of flap, Cambered Airfoils such NACA 2412 or 4412 cannot be taken into consideration because they produce positive pitching moment at zero angle of attack. Hence, Symmetric Airfoil is chosen for the flap to avoid such consequences. In this paper, a detailed study of analysis is performed on Supercritical Airfoil and Cambered Airfoil (for Comparison) with slotted flap. NACA 4415 is considered for Cambered Airfoil. Moving on, the results and contours of pressure and velocity were compared for both Supercritical and cambered Airfoil configuration.

Geometry and Aerodynamics

The considered airfoil is a Whitcomb Integral Supercritical Airfoil with a chord length of 950mm, and NACA 0012 considered as flap is 25% chord of Supercritical Airfoil. In the present study, for the analysis, gap of 5% chord of flap has been considered between the airfoil and flap. During takeoff, the overall camber of the airfoil becomes insufficient to generate lift for the given takeoff weight which is 80-100 tons for general single aisle aircrafts. Hence, flaps are used to increase the camber thereby producing enough lift to lift the aircraft at particular velocity and distance. The flaps do also increase the Critical Angle of attack and CLmax of the aircraft. At Takeoff the flaps are extended to 100 which increases the camber.

Advancements in Aeromechanical Materials for Manufacturing: ICAAMM-2021
AIP Conf. Proc. 2492, 020043-1–020043-10; https://doi.org/10.1063/5.0113316
Published by AIP Publishing. 978-0-7354-4438-6/$30.00

In the case of a slotted flap, the gap between airfoil and flap helps in reenergizing the boundary layer thereby avoiding Adverse pressure gradients. Speaking of Cruise segment, in this paper we will be discussing the transonic flow effect. The freestream Mach number which is subsonic accelerates upon reaching the upper surface of airfoil, local velocity becomes equal to speed of sound or more giving rise to wave drag. The freestream Mach number at which local wave drag forms on the airfoils upper surface is known as the Critical Mach number. Thus, a Supercritical Airfoil due to its flattened surface doesn't accelerate the flow until aft section where the surface begins to curve, here airflow accelerates allowing wave drag and shocks waves to form at this location. Due to this phenomenon, the Critical Mach number at which cambered airfoils show instant increase in drag; the Supercritical Airfoils can delay the location of wave drag which supports in giving higher drag divergence Mach number. Here, the Airfoil is deflected to 30 degrees whereas flap left undeflected. During landing since more drag is required, the flaps are deflected to higher angles up to 350 which helps in producing wake region around the top of flap, which helps in reducing overall lift at the wing. In this paper we shall be showing the pressure and velocity contours of these configurations and a comparison will be made with a Cambered Airfoil for validation.

Modelling of the Configuration

For the CFD analysis, the coordinates of the Whitcomb Integral Supercritical Airfoil for 1000m chord length have been taken from Airfoil tools. Similarly for the flap with 25% chord of Supercritical Airfoil, the coordinates for NACA 0012 were taken from Airfoil tools and were imported into CATIA V5 R20[7-10]. Once the coordinates are imported, the gap of 5% chord of the flap has been defined between the Airfoil and flap to provide a slotted flap configuration. The provided gap will help the bottom airflow to enter and energize the viscosity of boundary layer. This way the boundary layer will not separate and the flow will remain laminar and reverse pressure gradients can be avoided. The elements were extruded to 20mm, and using the Fill tool a domain is sketched around it for performing analysis later in fluent. The figures on the left show the modelled configuration for Takeoff, Cruise & Landing.

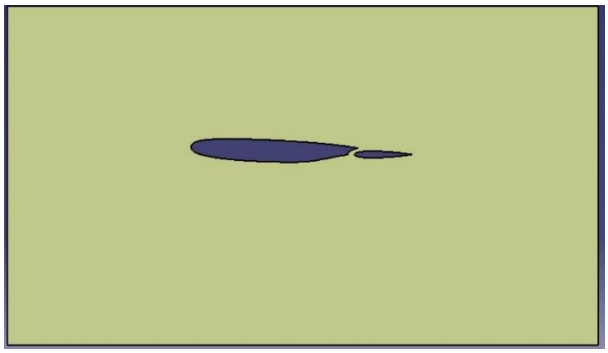

FIGURE 1. Supercritical airfoil with Flap

FIGURE 1 shows modelled configuration for takeoff. Here the flap has been deflected to 100 degrees, this way the camber increases and Cl value increases as well. This way Critical angle of attack increases and thereby increasing CLmax for the airfoil. Once modelled, the Takeoff configuration in converted to stp file and the geometry is imported to ANSYS fluent.

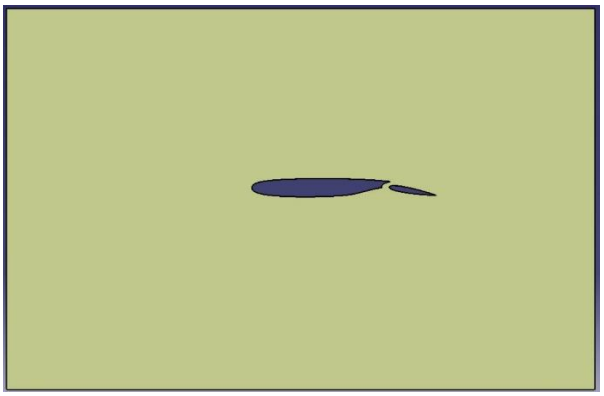

FIGURE 2. Supercritical airfoil with Low Flap deflection

FIGURE 2 is the modelled configuration for Cruise segment where the flap must be set to zero degrees. For our analysis, the element airfoil is set to 30 degrees for better aerodynamic efficiency and CFD analysis. After modelling, the configuration is converted to stp file and imported to ANSYS fluent.

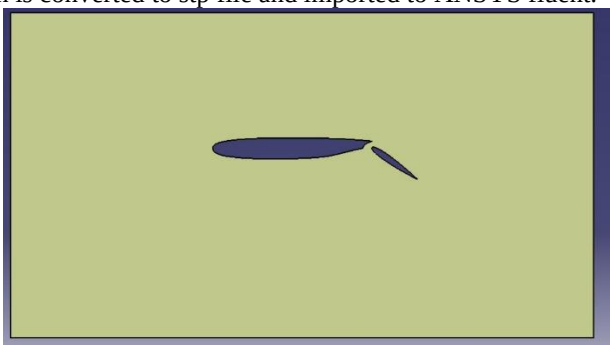

FIGURE 3. Supercritical airfoil with Flap high Flap deflection

Similarly, **Figure 3** represents the model of airfoil for Landing segment where the flap is deflected to 350 degrees to reduce the lift and increase the overall drag. This will separate flow from the upper surface of flap by making the airflow turbulent and wake region is formed which drops lift on upper surface of flap. Once modelled, similar to previous configurations this configuration is imported to ANSYS fluent for further calculations. In ANSYS fluent, the elements are meshed and after providing boundary conditions the calculation is initialized and results are computed respectively.

Mesh Generation

This section refers to meshing performed on configurations of Takeoff, Cruise & Landing. For the Takeoff Geometry, meshing has been performed separately for the domain and then using edge sizing the meshing values defined for airfoil are different from values specified for the domain[1]. The element size for the mesh for the domain is 0.008m and for the edge sizing the defined element size is 0.002m. This separate meshing allows the analysis for airfoil to be more accurate in terms of Lift and Drag Coefficients and to study the behavior of transonic flow at Cruise. All Triangles method is chosen for meshing the required geometry[3-5]. Meshing is an important step since a fine mesh can help in obtaining better flow characteristics upon Analysis.

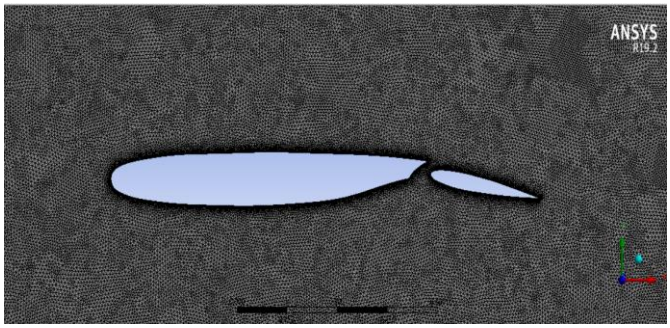

FIGURE 4. Mesh generated for takeoff with flap at 10^0

The Mesh nodes recorded for this geometry are 148910 whereas the Mesh elements are 295019 respectively. The average skewness obtained for Takeoff after Meshing is 5.4377e-002 and average orthogonal quality as 0.966. Similarly for Cruise the defined Mesh size is discrete from size defined for Takeoff and Landing. This is because the flow regime for Cruise is transonic and through a much finer mesh the flow properties can be analyzed very efficiently. Therefore, the defined Mesh size for the domain is 0.008m whereas for the airfoil, edge sizing is chosen and defined with element size as 0.0009m for better analysis results. For this geometry All Triangles method was chosen alone. The value of Mesh nodes for this geometry is 130517 and the value for number of elements is 256789 respectively.

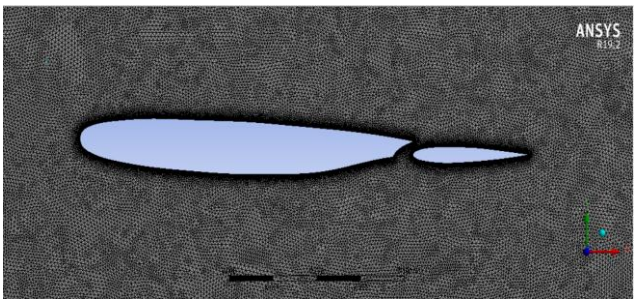

FIGURE 5. Mesh for Cruise with Airfoil at 3^0

Similarly for the Landing, the Meshing is performed using All Triangles method alone and the obtained showed better flow characteristics after Analysis. The Mesh size defined for the domain is 0.008m. the airfoil has been defined edge sizing with Mesh element size as 0.002m. For the Takeoff and Landing the Mesh sizes has been considered similar since a subsonic flow analyzed for both these segments with Mach Number below 0.3, making the airflow Incompressible. The generated Mesh shows 120034 nodes and 237392 elements respectively. For all these flight segments, the generated mesh was successful in performing analysis which yielded efficient flow characteristics and Aerodynamic Coefficients.

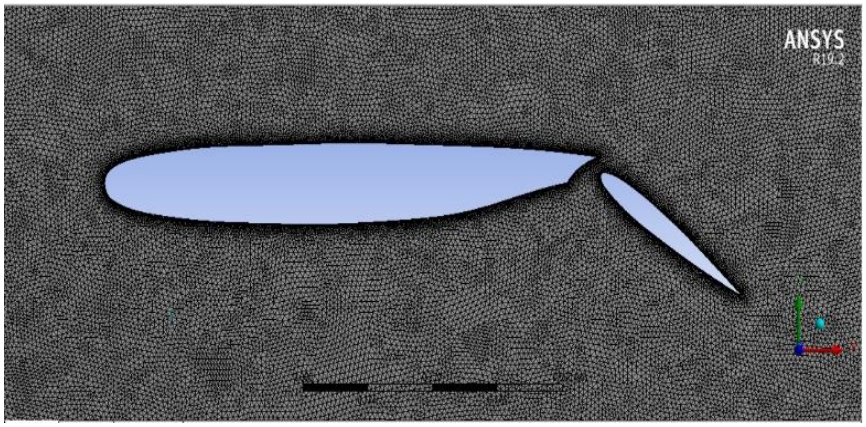

FIGURE 6. Mesh for Landing with flap at 35^0

RESULTS AND DISCUSSION

Once the configurations are meshed, the geometries are moved forward for analysis. In this section we'll be discussing the solver models used for analysis for all the flight segments discussed above. This paper presents a study on Aerodynamic Coefficients obtained for Supercritical Airfoil and Cambered Airfoil and compares the results for validation as well as to identify which Airfoil provides better efficiency at all flight segments. Also, all flight segments in this section are discretely presented.

At Take-off:

For this flight segment the freestream Mach Number defined is 0.23 and Reynolds Number $5*10^6$ million. During Takeoff, generally altitude is near to sea level which allows us to consider air as ideal gas since the flow is incompressible. Viscous Model used for this flight segment is Transition SST (4 eqn). The operating pressure considered is 101325 Pascals and viscosity as 1.7894e-05 kg/m-s & the operating Pressure as 300K. Once all these properties are updated into fluent, the calculations begin. Therefore, the solution **converges at 118 iterations** and yielded Lift and Drag Coefficients are **4.1802e-01 & 1.8907e-02**. The calculation has been performed for Cambered Airfoil as well simulating similar flow inputs and the Lift and Drag Coefficients yielded are **2.2522e-01 & 1.0309e-02** respectively. One can observe that Coefficient values for Supercritical Airfoil are more efficient in terms of lift than Cambered Airfoil. This is due to the geometry of Supercritical Airfoil which sustains high pressure values compared to Cambered Airfoil. The plotted graphs for Coefficients are shown below.

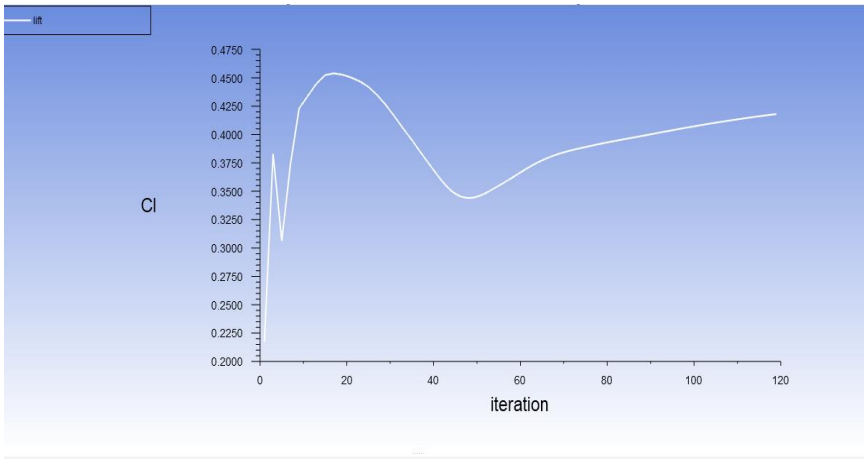

FIGURE 7. C_l during Takeoff

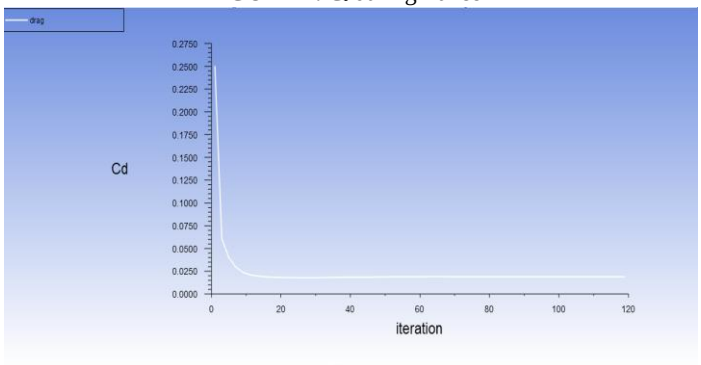

FIGURE 8. C_d for Takeoff

After obtaining the solution, the contours for Pressure and Velocity are obtained which are shown below. The pressure Contour shows the stagnation points for both Supercritical Airfoil and flap. Also, a sustained pressure force is seen on the upper surface. Whereas, the aft section of Supercritical Airfoil shows a varying pressure value due to the varying Camber. The Trailing edge has been collapsed for Supercritical Airfoil which provides a slot to allow the air moving at the bottom surface to enter the upper surface and disallow Adverse Pressure gradients caused due to less viscosity in the Boundary layer.

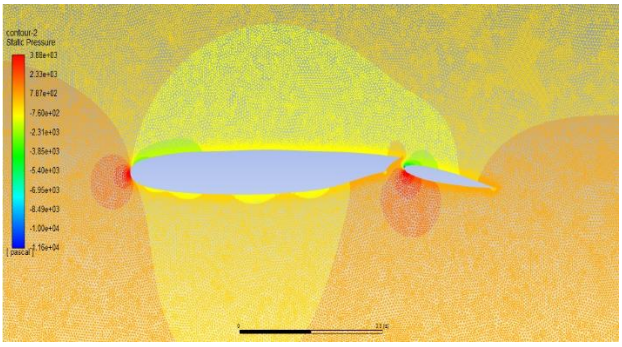

FIGURE 9. Pressure Contour for Take-off

Coming to Velocity Contour, the flow acceleration is seen only at the Leading edge until quarter chord and beyond that it remains constant and again starts varying at aft section near the trailing edge. The instant high velocity at the leading edge of flap is due to the deflection of flap which accelerated the velocity to reach trailing edge to meet the bottom surface air since the bottom surface will reach the trailing edge earlier than upper surface.

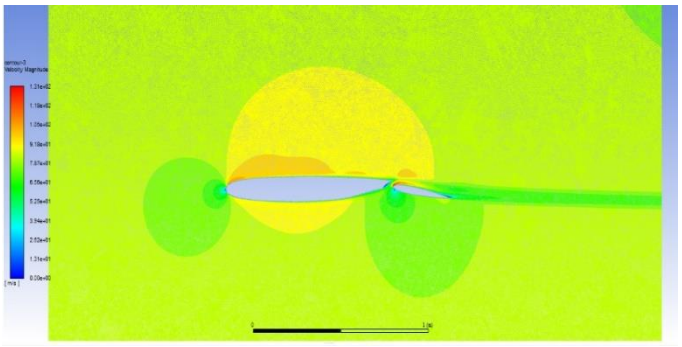

FIGURE 10. Velocity Contour for Take-off

This does contribute to overall lift on the wing. The constant velocity on upper surface is helpful at Critical Mach Number to delay the position of wave drag.

During Cruise

Cruise is the longest flight segment consuming at least 80% of the whole flight time. The Aircraft in this segment should fly sustaining all situations it may encounter without giving up. In this paper, we will consider the freestream Critical Mach Number as 0.85 as to evaluate the flow properties and to obtain changes in Lift and Drag Coefficients. The Reynolds Number is considered as $7*10^6$ million. Since Aircrafts Cruise at higher altitudes ranging between 35,000 feet & 40,000 feet, we have considered an average of 37,000 feet we obtain the flow properties as, operating Pressure as 20960 Pascals and viscosity as 4.213e-05 kg/m-s respectively. Also, the air is considered to be ideal gas since for our calculation the boundary conditions for inlet is specified as Pressure far-field. The viscous model chosen is k-omega (2 eqn) with SST production. k-omega viscous model is suitable for Transonic flow regimes since they yield efficient results. For this analysis the airfoil is set to 3^0 degrees and flap left undeflected. Once these properties are added, the solution is calculated. The **solution converges at 260 iterations** and yielded Lift and Drag Coefficients are **2.8185e-01 & 1.5322e-01** respectively. Analysis is performed on Cambered Airfoil as well where the Coefficients yielded are **8.6075e-02 & 7.8055e-02** respectively. One can observe that the lift value for Supercritical Airfoil if higher than Cambered Airfoil which makes Supercritical Airfoil more efficient at Critical Mach Number with delayed position of shock waves. The plots for lift and Drag Coefficients are shown below.

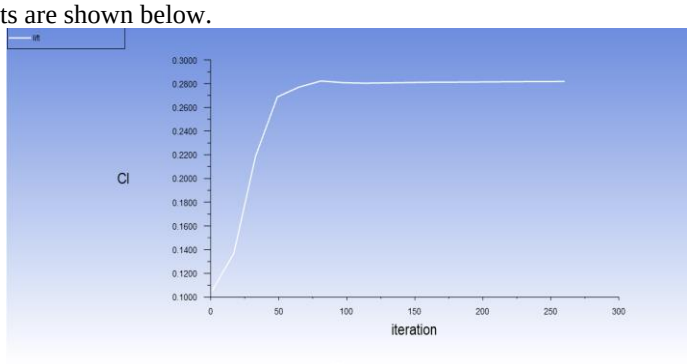

FIGURE 11. C_l for Cruise

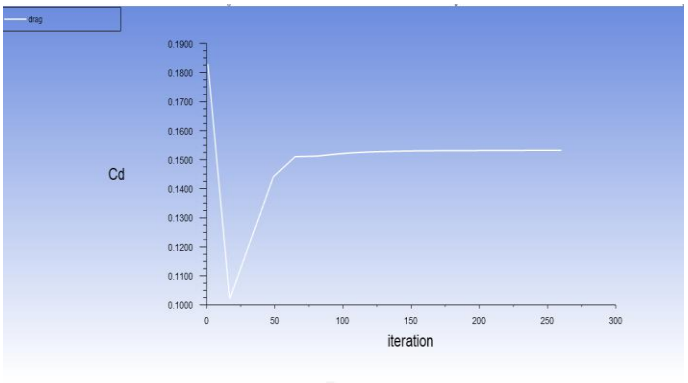

FIGURE 12. C_d for Cruise

The Contours for Pressure and Velocity are shown further for both Supercritical Airfoil and Cambered Airfoil respectively.

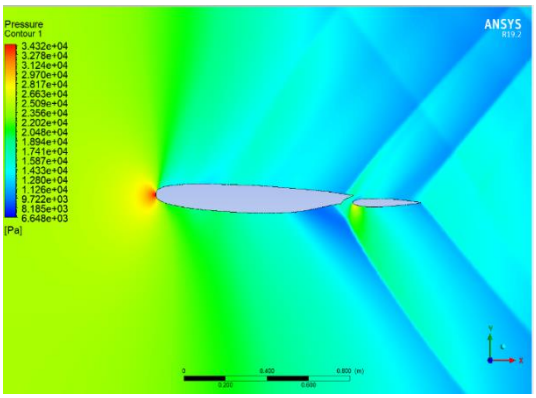

FIGURE 13. Pressure Contour for Supercritical Airfoil at Cruise

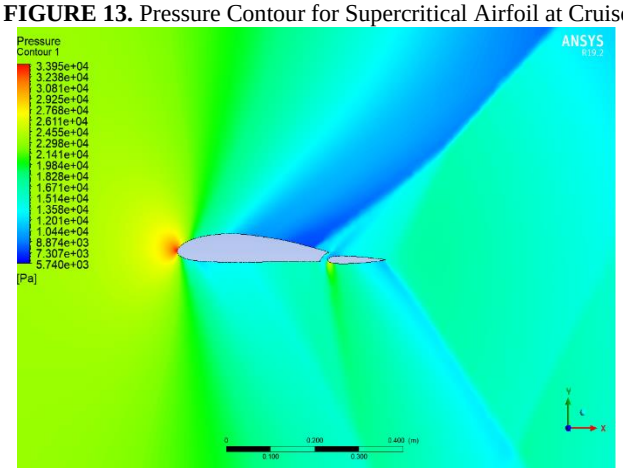

FIGURE 14. Pressure Contour for Cambered air foil at Cruise

The above two images define the shock formation at Critical Mach Number for both Supercritical Airfoil and Cambered Airfoil respectively. The images show the shock formation for Cambered Airfoil beginning from quarter chord which is not the case with Supercritical Airfoil. Thus, this is the cause for reduction of lift on cambered airfoil whereas in supercritical Airfoil the lift is sustained until the aft camber where the shocks begin to form. Similarly, we compare the velocity contours for both Supercritical Airfoil and Cambered Airfoil. We observe that flow on top accelerate from the quarter chord only, in Cambered Airfoil. But due to the flatness on the top and large leading edge nose radius of the Supercritical Airfoil, the local Mach number stays stable until it reaches the aft camber where it is further accelerated leading to increase in velocity. The gap provided helps in disallowing Adverse pressure gradients by keeping the Boundary layer reenergized and the shock waves though their formation doesn't affect the flow at quarter and mid chord of the airfoil. The velocity contours for both the Airfoils are shown below for the reference.

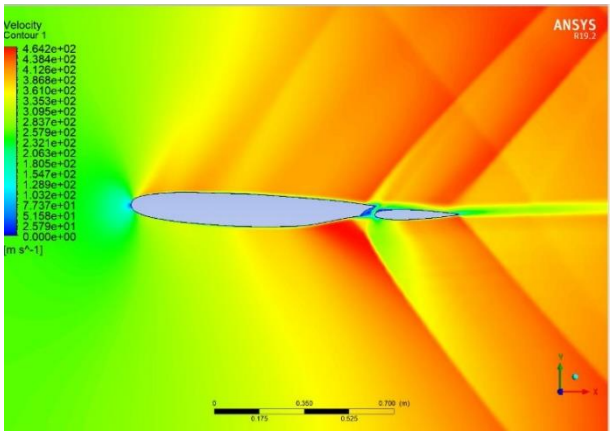

FIGURE 15. Velocity Contour for Supercritical Airfoil at Cruise

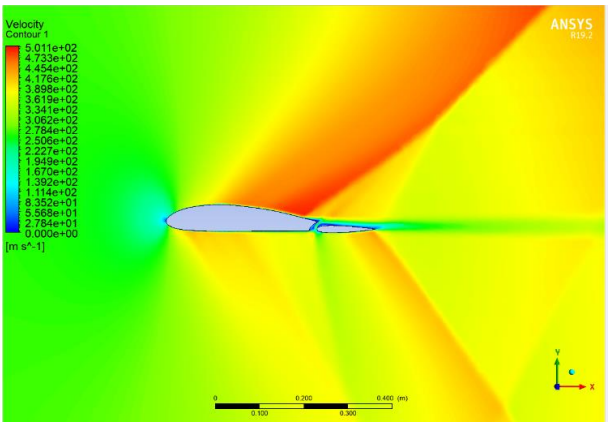

FIGURE 16. Velocity Contour for Cambered Airfoil at Cruise

For Landing

This being the final segment of the whole flight, the analysis has been performed at a specific flap deflection angle which is 35^0. During the landing the main criteria is to land without instant loss of lift irrespective of weather conditions, wind gusts etc. neither the pitching moment is to be compromised which plays an important role. The viscous model selected for this flow analysis is Spalart-Allmaras (1 eqn) with vorticity-based production. This option was chosen because vortices are inevitable during landing due to high downwash from wings and also due to induced drag. The fluid is considered as ideal gas with inlet velocity as 68.6 m/s or Mach 0.20. The operating pressure is 101325 Pascals with viscosity as 1.7894e-05 kg/m-s. The operating Reynolds number is similar to Takeoff, $5*10^6$ million. The solution is **converged at 227 iterations** with the Lift and Drag Coefficients obtained as **9.2160e-01 & 1.2863e-01** respectively. Whereas, the Coefficients for Cambered Airfoil are **4.8252e-01 & 5.5010e-02** respectively. On comparing both the values, we can observe that lift generated for Supercritical Airfoil is still higher than Cambered Airfoil as well as the Drag is high which is a requirement during the landing stage.

Below are the Coefficients of Lift and Drag plotted in terms of number of iterations:

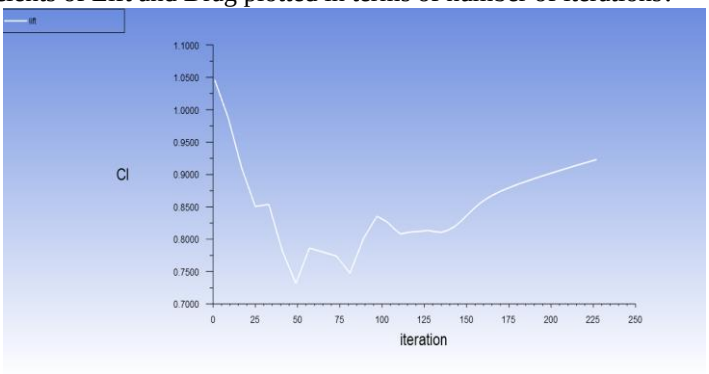

FIGURE 17. Cl for Landing

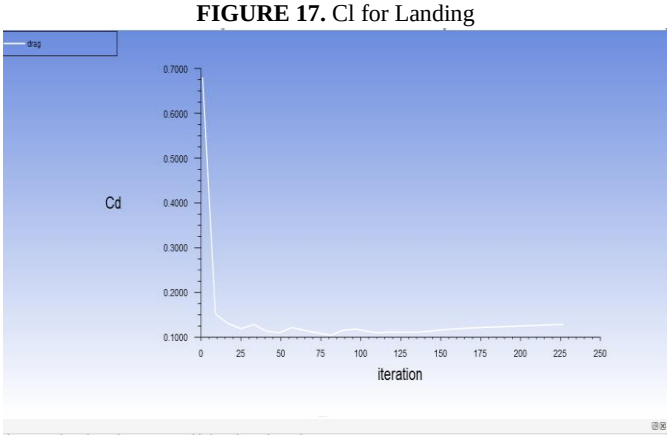

FIGURE 18. Cd for Landing

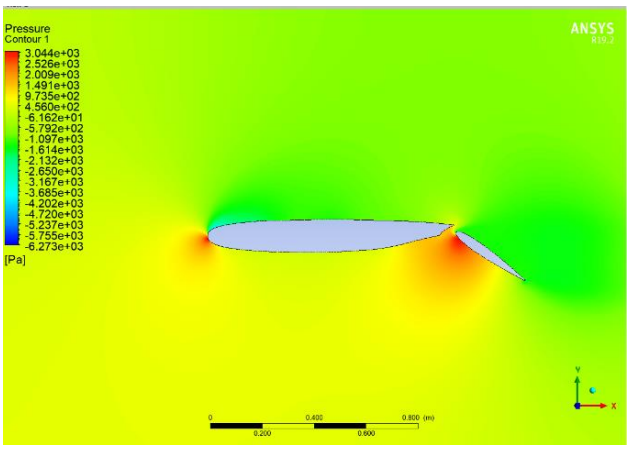

FIGURE 19. Pressure Contour for Landing

In the above image for pressure contour, we can observe that stagnation points occur at Leading edge of both Airfoil as well as flap. Also, the space between the Airfoil and flap is helping in creating drag due to collapsed trailing edge of Supercritical Airfoil and flap deflected too low that air flowing from bottom surface finds it difficult to escape hence increasing overall drag on the wing.

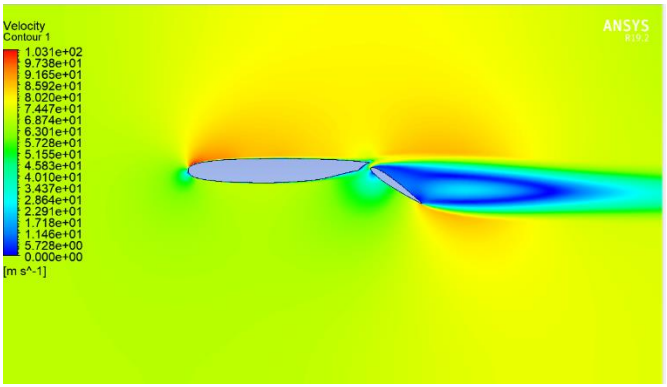

FIGURE 20. Velocity Contour for Landing

Coming to Velocity Contour, the upper surface is accelerated as generally it does only up to quarter chord. But at the flap wake region is seen on the top which is a result of high deflection of flap to 350. This results in flow separation thereby reducing the local lift. This is for a 2D case but when it comes to 3D wing, the induced drag due to winglets contribute higher amount of drag during landing giving rise to vortices.

Conclusion

TABLE 1. Comparison of Aerodynamics Characteristics

Flight Segment	Supercritical Air foil		Cambered Air foil	
	Cl	Cd	Cl	Cd
Take-off	4.1802e-01	1.8907e-02	2.2522e-01	1.0309e-02
Cruise	2.8185e-01	1.5322e-01	8.6075e-02	7.8055e-02
Landing	9.2160e-01	1.2863e-01	4.8252e-01	5.5010e-02

From the CFD analysis performed for the Configuration of Airfoil with slotted flap we obtain that,

- Supercritical Airfoil show better results when concerned to Lift and Drag. They also perform well during Cruise at transonic flow with ability of delaying shock waves until aft camber near the trailing edge. The Lift and Drag Coefficients obtained in all flight segments yield better results than Cambered Airfoil Configuration as discussed earlier.

- Whereas, Cambered Airfoil showed poor results compared to Supercritical Airfoil at all flight segments in terms of lift and drag. This study doesn't demotivate the application of Cambered airfoil rather, it provides a better option for operations through Supercritical Airfoils.
- This analysis is limited to steady state analysis and not Transient state analysis. Analysis has been performed for only one Mach Number for each flight segment.
- Other Cruise effects such as wind gusts, effect of severe weather conditions, icing effect during takeoff and Landing are not included in this study and to yield results for these, further study and analysis will be performed.

REFERENCES

1. João Alves de O. Neto, Carlos B. Júnior, "Aerodynamic study of high-lift device configurations for take-off and landing conditions- 25th INTERNATIONAL CONGRESS OF THE AERONAUTICAL SCIENCES
2. "An Experimental Study of Transonic Flow About a Supercritical Airfoil".
3. Shaowei Li, DanjieZhou, Yuanjing, Zhang, QiulinQu, "Aerodynamic investigation of RAE2822 airfoil in ground effect". *Procedia Engineering-Elsevier*, 2015.
4. "Numerical Simulation of Gurney Flap on RAE-2822 Supercritical Airfoil" *AIAA Publications*.
5. TongZhao,YufeiZhang, "Supercritical Wing Design Based on Airfoil Optimization and 2.75D Transformation". *Aerospace Science and Technology-Elsevier.2016*
6. https://ntrs.nasa.gov/search.jsp?R=19740058562-
7. "Optimization of Supercritical Airfoil Considering the Ice-Accretion Effects", *AIAA Publications*.
8. "Computation of shock buffet onset for a conventional and supercritical airfoil" AIAA Publication.
9. ArunKumar K, Veeranjaneyule K, "Mechanism and Performance analysis of Morphing Wing", IJITEE,2019.
10. Mr. K Veeranjaneyulu "Design and Computational Analysis of Fixed Wing of Micro Aerial Vehicle", IJMETMR Volume 2 Issue 12.
11. Mr. K.Veeranjaneyulu, Karupalli, Anvesh, M Satyanarayana Gupta, "Aerodynamic Design of Wing for Supersonic Flight Vehicle" , ISSN: 2320-3706, Yuva Engineers Sept 2016.